



BRNO UNIVERSITY OF TECHNOLOGY

VYSOKÉ UČENÍ TECHNICKÉ V BRNĚ

CENTRAL EUROPEAN INSTITUTE OF TECHNOLOGY BUT

STŘEDOEVROPSKÝ TECHNOLOGICKÝ INSTITUT VUT

**QUANTITATIVE 3D CHARACTERIZATION OF BIOLOGICAL
STRUCTURES BY X-RAY COMPUTED
MICROTOMOGRAPHY**

KVANTITATIVNÍ 3D CHARAKTERIZACE BIOLOGICKÝCH STRUKTUR POMOCÍ RENTGENOVÉ
POČÍTAČOVÉ MIKROTOMOGRAFIE

DOCTORAL THESIS

DIZERTAČNÍ PRÁCE

AUTHOR

AUTOR PRÁCE

Ing. Markéta Tesařová

SUPERVISOR

ŠKOLITEL

doc. Ing. Tomáš Zikmund, Ph.D.

BRNO 2022

Summary

Modern developmental biology uses a broad spectrum of methods for analysing structures of interest. Multi-disciplinary teams are currently pushing forward the understanding of biological questions using 3D approaches. However, one major challenge of 3D imaging techniques in biology is a lack of methodology for quantifying observed phenomena that are often the cause of developmental or genetic disorders. One of the methods whose application has been widely spread in recent years is X-ray computed microtomography (microCT). This technique provides isotropic resolution up to 1 μm and, when a sample is appropriately prepared, a wide variety of tissue differentiation. However, biological structures are usually diverse in size and shape, and every task requires a specific solution regarding data processing. This work addresses the implementation of microCT for imaging and mainly 3D characterization of biological structures *ex-vivo*. Particular emphasis is given to analysing soft tissues in mouse embryos' heads and imaging salamander species, focusing on their regeneration ability. This work describes the relevant information for microCT users dealing with biological samples; it includes the preparation of the sample for measurements, selecting suitable parameters for the experiment and mainly subsequent quantitative analysis of 3D datasets. The latest technological advancements in 3D imaging were studied and tested on concrete projects in the field of developmental biology, where 3D information from microCT played a key role.

Abstrakt

Moderní vývojová biologie využívá široké spektrum metod k analyzování studovaných struktur. Multioborové týmy v poslední době prosazují využívání 3D přístupu k porozumění biologickým procesům. Jedna z hlavních překážek při využívání 3D zobrazovacích technik v biologii je nedostatek metodologie pro kvantifikování pozorovaných jevů, které často bývají příčinou vývojových či genetických onemocnění. V posledních letech se v biologických výzkumech rozšířilo využití rentgenové počítačové mikrotomografie (mikroCT). Technika mikroCT dokáže poskytnout izotropní rozlišení až 1 μm a při správné přípravě vzorku širokou škálu tkáňové diference. Biologické struktury jsou však rozmanitých velikostí a tvarů a každá struktura vyžaduje specifický přístup v oblasti zpracování dat. Tato práce se zabývá využitím mikroCT pro zobrazování, ale především 3D charakterizaci biologických struktur *ex-vivo*. Zvláštní důraz je kladen na analýzu měkkých tkání v hlavách myších embryí a zobrazování různých druhů mloků se zaměřením na jejich regenerační schopnosti. Tato práce popisuje relevantní informace pro uživatele mikroCT zabývajících se biologickými projekty: To zahrnuje přípravu vzorku pro měření, výběr vhodných parametrů k samotnému měření, a především analýzu vzniklého 3D datasetu. Nejnovější technologické pokroky ve 3D zobrazování byly studovány a testovány na konkrétních projektech vývojové biologie, kde 3D informace získaná pomocí mikroCT hrála klíčovou roli.

Keywords

X-ray computed microtomography, microCT, CT, 3D imaging, biology, mouse embryos, salamanders

Klíčová slova

rentgenová počítačová mikrotomografie, mikroCT, CT, 3D zobrazování, biologie, myší embrya, mloci

TESAŘOVÁ, Markéta. *Quantitative 3D characterization of biological structures by X-ray computed microtomography*. Brno, 2022. Doctoral Thesis. Vysoké učení technické v Brně, Středoevropský technologický institut VUT, Central European Institute of Technology BUT. Supervisor Tomáš Zikmund.

I declare that I carried out this doctoral thesis *Quantitative 3D characterization of biological structures by X-ray computed microtomography* independently, and only with the cited sources, literature and other professional sources.

Ing. Markéta Tesařová

I would like to thank my supervisor, Associate Professor Tomáš Zikmund, not only for his comments during my dissertation work but also for his guidance in the laboratory since my bachelor's study. I would like to also thank the head of the research group Professor Jozef Kaiser for the opportunity and trust to participate in the research projects. Furthermore, my thanks belong to Doctor Lucia Mancini, who was my supervisor during my internship at Elettra synchrotron, and she was a motivator during the complex proteus research. Also, I would like to thank my colleagues working in the field of biology for coming up with new ideas. Namely, I would like to thank Professor Igor Adameyko and his entire research group, Doctor Markéta Kaucká, Professor Shahragim Tajbakhsh, Doctor Glenda Comai and Doctor Eglantine Heude. Special thanks belong to my family for their support throughout my studies. For the financial support, I acknowledge the Brno City Municipality as a Brno Ph.D. Talent Scholarship Holder and Martina Roeselova Memorial Fellowship. Part of this work was carried out with the support of the project CzechNanoLab Research Infrastructure supported by the Ministry of Education, Youth and Sports of the Czech Republic (LM2018110).

Na tomto místě bych ráda poděkovala svému školiteli docentu Tomáši Zikmundovi nejen za jeho komentáře během mé dizertační práce, ale i za jeho vedení v laboratoři už od bakalářského studia. Ráda bych poděkovala vedoucímu výzkumné skupiny Jozefu Kaiserovi za příležitost a důvěru zapojit se do vědeckých projektů. Mé díky patří doktorce Lucii Mancini, která byla mojí vedoucí během mé stáže na synchrotronu Elettra a byla velkou motivátorkou během komplexního výzkumu macarata jeskynního. Také bych chtěla poděkovat mým kolegům biologům za jejich stále nové nápady. Konkrétně děkuji profesoru Igoru Adameykovi a celé jeho výzkumné skupině, doktorce Markétě Kaucké, profesoru Shahragimu Tajbakhsh, doktorce Glendě Comai a doktorce Eglantine Heude. Zvláštní dík patří mé rodině za její podporu během mých studií. Za finanční podporu děkuji Magistrátu města Brna jako držitel stipendia Brno Ph.D. Talent a nadačnímu fondu Martiny Roeselové. Část této práce byla vypracována za podpory projektu CzechNanolab Research Infrastructure za podpory Ministerstva školství, mládeže a tělovýchovy České republiky (LM2018110).

Ing. Markéta Tesařová

Table of Contents

1	Literature review	2
1.1	X-ray Computed Tomography	2
1.1.1	History	2
1.1.2	Principle of measurement	3
1.1.3	X-ray sources	5
1.2	3D imaging in biology	7
1.2.1	Staining	7
1.2.2	Phase-contrast	9
1.2.3	Dual-energy CT	9
1.3	Data segmentation	10
2	Aims of Doctoral Thesis	12
2.1	MicroCT measurement and data segmentation of biological samples	12
2.2	Quantification of segmented 3D models	12
2.3	Implementation of the results to particular biological projects	12
3	Methods	13
3.1	Sample preparation	13
3.2	MicroCT	15
3.2.1	Laboratory measurements	15
3.2.2	Synchrotron measurements	16
3.3	Data analysis	16
4	Results	18
4.1	Regeneration of salamander limbs	18
4.2	3D-cell distribution in the regenerative muscle-skeletal system	21
4.2.1	Number and density of cells within the extracellular matrix	22
4.2.2	The polarity of the cells in 3D	25
4.2.3	Joint formation	27
4.3	Adaptation of <i>Proteus anguinus</i> to dark habitats	28
4.3.1	Frequency response analysis and future work	31
4.4	Vertebrate cartilage growth studied on mouse embryos	32
4.4.1	Wall thickness analysis	35
4.4.2	Shape comparison	35
4.4.3	Modelling of cell division based on microCT models	37
4.4.4	Re-use potential	37

4.5	Extraocular muscles development	38
4.5.1	Ventralization of the eyeball	39
5	Combination of microCT with other methods.....	43
5.1	Neck muscles and associated connective tissues.....	43
6	Conclusion	47
7	References.....	48
8	List of symbols and shortcuts	56
9	Author publications and other outputs.....	57
9.1	Publications	57
9.1.1	First-author	57
9.1.2	Co-author.....	57
9.1.3	Submitted publications.....	58
9.2	Products.....	59
9.3	Grants	59
9.4	Conferences.....	59

Introduction

3D imaging approaches based on CT have become increasingly accessible with technological advancements. The synergy of material and life sciences has impacted industrial and scientific research with new tools for investigation. Multi-disciplinary collectives composed of clinical doctors, biologists, engineers and imaging experts are pushing forward the use of 3D approaches to understanding biological questions. However, one major challenge of 3D techniques in biology is a lack of methodology for quantifying observed phenomena. Biological structures are usually diverse in size and shape, and every task requires a specific solution.

This dissertation work addresses the implementation of X-ray computed microtomography (microCT) for imaging and mainly 3D characterization of biological structures. Particular emphasis is given to challenges that arise with the measurement of biological samples that are not typical for material sciences. Furthermore, the work is written so that students and scientists who want to use microCT for biological projects could take this work as the manual for the complete procedure, starting with preparing samples and ending with the 3D analysis of measured data.

X-ray computed tomography (CT) is a 3D imaging method that can provide information about the internal structures non-destructively from the metres down to micrometres length scales. The first chapter starts with a literature review and introduces the microCT technique by explaining its principles and technological setup. This chapter also addresses the preparation of biological samples for microCT measurement. Data analysis and segmentation are also discussed.

The second chapter defines the dissertation work aims, and the third chapter describes the methodology used. It includes a complete pipeline starting with sample preparation, parameters of microCT measurement and data processing.

The main part of this thesis can be found in the fourth chapter. Each section is dedicated to one specific biological project. The motivation for using the microCT method is given and detailed procedure and analysis are explained. Sections refer to published manuscripts that originated from the presented work and can be found in the appendix of the thesis.

The fifth chapter then focuses on combining microCT with other imaging methods. It describes the motivation for why different techniques were needed, so it naturally defines the capability of microCT imaging. Specifically, it explains the combination of microCT with classical microscopy and histological staining on an example of muscle imaging and connective tissues.

The appendix of the thesis contains a list of author outputs – publications, products, conferences and grants associated with this dissertation work. First-author and co-author publications can be then found in the attachment.

1 Literature review

1.1 X-ray Computed Tomography

1.1.1 History

The development of X-ray computed tomography methods started at the end of the 19th century. Since then, this method has passed significant technological advancement, but it is still based on the same physical principle. This imaging method is connected with several Nobel prize winners, and the first to mention is Wilhelm Conrad Röntgen. He detected hitherto unknown rays on the evening of 8th November 1895. He found out that when running a high-voltage discharge tube enclosed in thick black cardboard, a paper plate covered on one side with barium platinocyanide would fluoresce, even when it was as far as two metres from the discharge tube. Röntgen concluded that the discharge must be emitting a new form of invisible radiation, and he named the radiation X-rays [1]. In 1901, he was awarded the first Nobel Prize in physics in recognition of the extraordinary services he had rendered by discovering the remarkable rays named after him [2].

From this Röntgen's discovery, X-rays found their application in diverse fields and disciplines throughout the 20th century. Another important name to mention in connection with the development of the X-ray computed tomography method is R. N. Bartholomew and R. M. Casagrande. In 1957, they used X-rays when they were discovering the density of the particles of the fluid layer inside steel piping. By taking X-ray projections from different angles, they were working the first tomographic data ever [3]. Despite this first industrial application, the first CT machines were used mainly for medical purposes thanks to Godfrey Hounsfield. He came up with an idea for viewing and examining organs from outside the body. However, Hounsfield was unaware that other scientists had already come up with this idea, but only in theory (Johann Radon and Allan Cormack). But they did not take this idea further in terms of creating an instrument that could carry this out. Also, when rumours of a cross-sectional X-ray imaging technique first emerged, research and development departments in the traditional X-ray companies were highly sceptical [4].

Hounsfield's first experimental system used gamma rays to scan bottles or perspex jars filled with water and pieces of metal and plastic. A lathe bed provided the means for moving and rotating the gamma-ray source, and sensitive detectors were placed on either side of the bottles or jars. This measurement took nine days, and such time wasn't convenient for measuring live patients. With an X-ray tube and a generator, time was reduced to nine hours. Other Hounsfield's experiments were done on bullock's and pig's brains, and he produced the first pictures in which white and grey matter could be clearly differentiated [5]. In 1979 Allan M. Cormack and Godfrey N. Hounsfield received the Nobel Prize for physiology and medicine "for the development of computer-assisted tomography" [6].

By 1980 the number of CT installations had expanded rapidly. Also, there was an urgent need to share the knowledge. As a result, teaching and training courses sprang up all over the World [4]. This method has been used for industrial and laboratory purposes to a more considerable extent since the 1990s [7]. The application of microCT has spread across science, metrology and manufacturing, engineering, biological or geological sciences [8]. Today, it is possible to perform X-ray imaging at the resolution of nanometres and to visualise complex 3D structures.

1.1.2 Principle of measurement

During CT measurement, a series of 2D X-ray projections are recorded from different sample angles. The taken projection is a result of the interaction of X-rays with a scanned sample. When an electromagnetic X-ray wave passes through an object, both the intensity and the phase change vary according to the refractive index, n

$$n = 1 - \delta + i\beta, \quad (1.1)$$

where the attenuation, i.e. absorption of the samples, is given by the imaginary part (β), and the phase shift is given by the real part (δ) [8].

The attenuation of radiation is then described by Beer-Lambert Law. For radiation with an intensity I_0 generated by the source, passing the distance x through the sample, the intensity at the detector I is described as

$$I = I_0 e^{-\mu x}, \quad (1.2)$$

where μ is the attenuation coefficient that is specific for every material. In non-homogenous material, attenuation coefficient μ is not constant, and it differs along the direction of propagation. The greyscale values on the detector pixels correspond to the absorption of the measured object. Specifically, a ratio of $\frac{I}{I_0}$ is recorded

$$\int \mu(x) dx = -\ln \frac{I}{I_0}. \quad (1.3)$$

When non-chromatic radiation passes through the sample, the intensity I of the radiation is a function of the energy (E). In other words, for a polychromatic beam with different energies, spectral intensity $j_0(E)$ must be considered

$$I = \int_E j_0(E) \exp\left(\int_x \mu(x, E) dx\right) dE. \quad (1.4)$$

One of the aims of the tomographic measurement is then to find function f that describes attenuation μ in the sample. This function can be derived by merging equations (1.3) and (1.4):

$$f = \int \mu(x) dx = -\ln \left(\frac{\int_E j_0(E) \exp\left(\int_x \mu(x, E) dx\right) dE}{I_0} \right). \quad (1.5)$$

A computed reconstruction algorithm is then used to create a stack of cross-sectional slices from these 2D projections (radiographs) of the object [8]. There are various approaches how to perform the tomographic reconstruction. One of the most widely-used algorithms is filtered back projection (FBP). Tomographic reconstruction with FBP can be described as computing a value of the integral in one point, and then the value is assigned to each point of the line (back projection). The methodological basis used for describing reconstruction is presented in detail in the work of Kak and Slaney [9] and Rosenfeld and Kak [10]. Another critical work written by Herman [11] describes reconstruction methods based on the algebraic reconstruction technique.

The resulted 3D data are made up of many cubic volume elements called voxels. The voxel resolution is then described as the cube edge length. Depending on the scanning conditions, spatial resolution is typically larger than the voxel resolution. Conventional (medical or heavy industrial) CT generally refers

to submillimetre resolutions or poorer (voxel sizes $\geq 100 \mu\text{m}$), microCT machines usually state micrometre resolutions (voxel sizes $\geq 0.1 \mu\text{m}$) and nanoCT goes down to voxel sizes about 10nm [8]. Voxel size is generally connected with the size of the scanned object; higher resolution usually means accepting a smaller object size. CT for laboratory purposes uses a similar principle as CT scanners used for medical diagnosis. The main difference is that the sample rotates between source and detector, and the X-ray source and detector stay still. The principle of laboratory CT machine is schematically shown in Fig. 1.1. The real experimental setup at the Laboratory of X-ray computed micro and nanotomography at Central European Institute of Technology (CEITEC) in Brno is shown in Fig. 1.2.

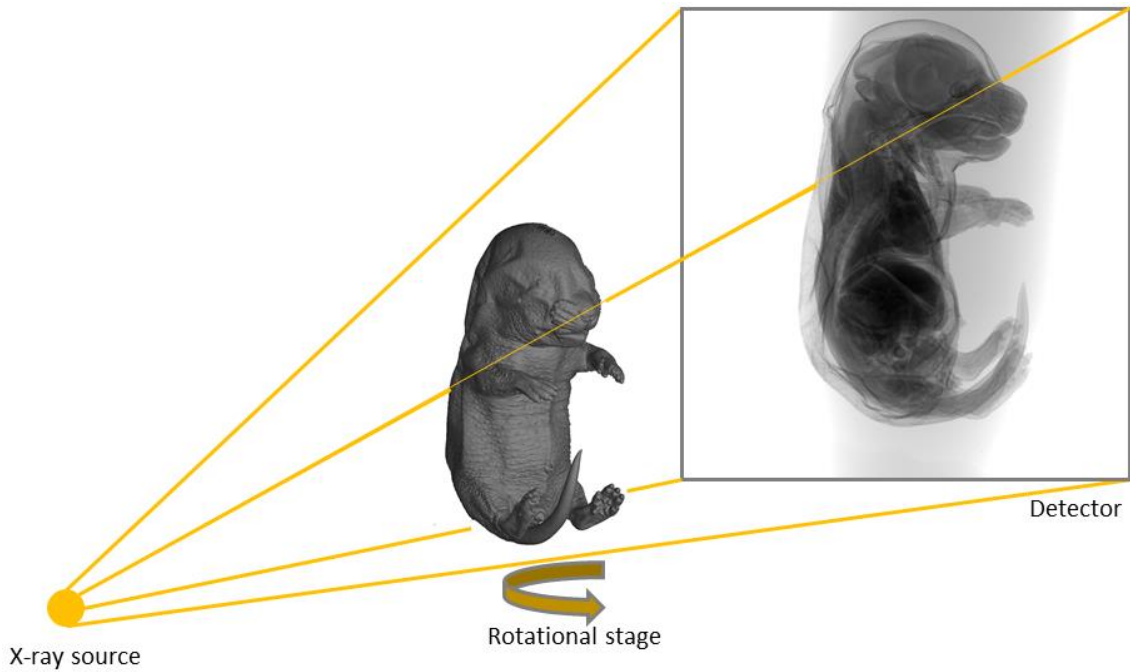


Figure 1.1: Principle of X-ray computed tomography scanning. A sample is placed on the rotation stage between the X-ray source and detector.

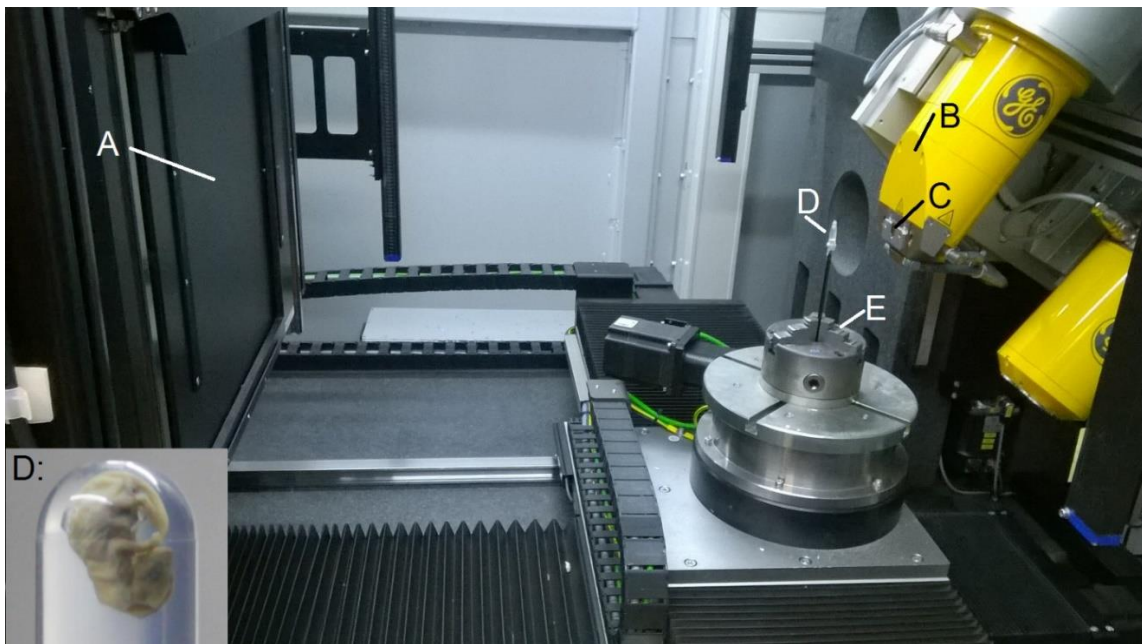


Figure 1.2: Experimental setup of microCT measurement inside in GE phoenix v|tome|x L 240 machine: A – detector; B – X-ray tube; C – filter; D – sample; E – rotational stage [11].

1.1.3 X-ray sources

The X-ray source is one of the essential components of a CT system as they supply the necessary X-ray photons to perform the scan. In most cases, the source is either an X-ray tube or a synchrotron storage ring. In both cases, X-rays are produced by the acceleration of electrons [8].

Although the size and appearance of the X-ray tube have changed significantly since its invention by Röntgen, the fundamental principle of X-ray generation has not changed, and X-ray tubes are (relatively) simple. The essential components of an X-ray tube are a cathode and an anode, both stored in a vacuum. The cathode supplies electrons, and the anode provides the target. When a target is bombarded with electrons, X-ray photons are produced. The intensity of the radiation produced is proportional to the atomic number of the target material and the number of electrons bombarding the target. The tube current controls this number. The energy of the generated X-ray photons depends on the electric potential difference between the cathode and the anode [12]. Both reflection and transmission targets exist; transmission targets are said to have a finer spot because they limit the mean free path of the incident electrons.

Commercially available machines are mostly cone-beam setups. They are straightforward in terms of imaging and utility. Their main advantage is that they are very flexible in terms of sample size and the resolution of reconstructed data. Magnification of the data is then given by the geometry of the experiment and by placing the sample at the proper distance between a sample and a detector, as schematically shown in Fig. 1.3. For the highest resolutions, the sample-source distance must be small (range of millimetres) [13]. Another approach is usually applied in nanoCT devices where the source-detector distance is fixed, and the sample is placed close to the detector. The beam is then considered semi-parallel because only a small part of the cone-beam is used. The detector consists of a scintillator, followed by an optical system providing magnification of the image. The small voxel size is achieved by small pixels of CCD or sCMOS detectors [14].

A more powerful source of X-ray is a synchrotron. Synchrotron research facilities can be dedicated to generating tuneable beams of electromagnetic radiation from the far-infrared to the hard X-ray regime with intensities of many orders of magnitude greater than those produced by laboratory-based sources [15]. Synchrotron consists of an evacuated storage ring in which high-energy electrons circulate at highly relativistic velocities and so-called beamlines tangential to the storage ring that utilise synchrotron light emitted by the electrons tangentially to their orbital path. The path of circulating electrons is bent and accelerated radially either by bending magnets or by insertion devices such as undulators or wigglers. Synchrotrons provide many orders of magnitude more flux than classic X-ray tubes. Also, they possess the ability of monochromatic beam that is selected and filtered from white beam X-ray spectrum. This improves sensitivity and can limit certain artefacts such as beam-hardening. Often the beam is spatially coherent, which is a critical condition for phase-contrast imaging. The X-ray beam reaching the specimen is typically highly parallel because the X-ray source is tens to hundreds of metres from the object [8].

Compared with the wide use of classic X-ray tubes, there are relatively few synchrotron facilities worldwide. Their beams differ in X-ray flux, source size and X-ray energy spectrum [15]. To experiment at a synchrotron facility, submitting an official application is usually required. An international panel then reviews the application. When the experimental proposal is approved, the applicants are given the required number of shifts for such measurement at the synchrotron facility.

One of the trends in X-ray imaging is the use of liquid metal jet X-ray sources. A solid metal anode is replaced by liquid metal here. This type can tolerate much higher electron-beam power because it is not focused only on one place, but the electrons hit the flowing jet of metal. The resulting X-ray beam has a very high flux and brightness while maintaining a small and stable focal spot. The classical power limit of an X-ray source, when the electron beam permanently damages the anode, may be disregarded. On the other hand, the operation of a metal jet X-ray source is significantly more expensive in comparison with classic X-ray tubes [14, 16].

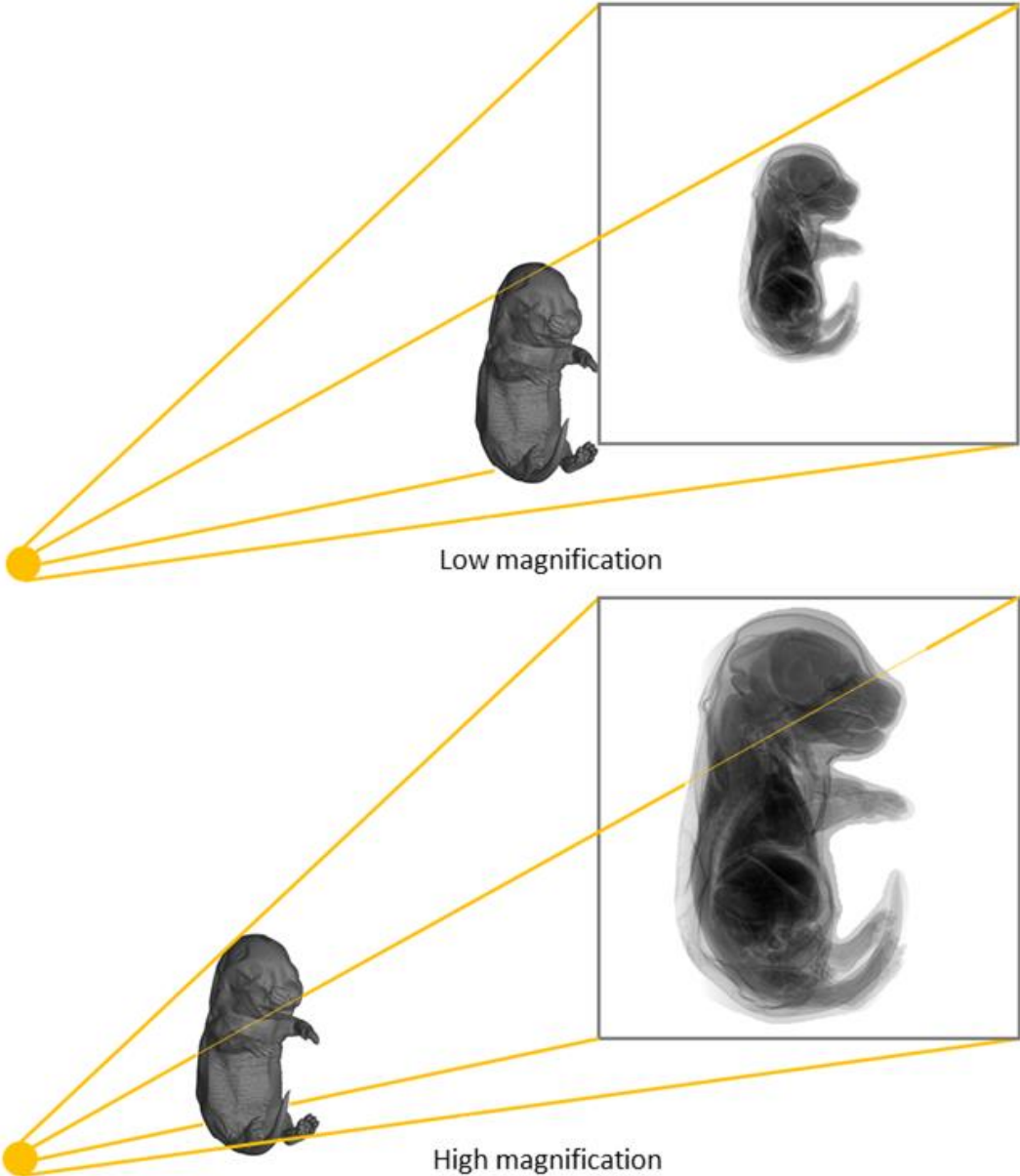


Figure 1.3: Magnification of imaging system determined by cone-beam geometry and position of the scanned sample. For the highest resolution, the sample-source distance must be small.

1.2 3D imaging in biology

Historically, pre-clinical and clinical studies usually rely on conventional imaging such as magnetic resonance imaging (MRI), positron emission tomography (PET), single-photon emission computed tomography (SPECT) and X-ray computed tomography (CT). Each of these methods has advantages and disadvantages; MRI provides high contrast of soft tissues, PET/SPECT delivers a high level of sensitivity, and CT provides high resolution of biological structures with high absorption. On the other side, MRI suffers from a long acquisition time for high-resolution images. PET/SPECT doesn't have a high spatial resolution, and CT is limited by patients' exposure to ionizing radiation [17].

In developmental biology, analysis of histological sections has remained a mainstay. However, it requires elaborate preparation and destruction of the specimen. Also, it can generate heterogeneous distortions [18]. The reconstruction of 3D volumes from 2D slices provides important information to analyse developing structures in a 3D context and understand the pathogenesis of various disorders [19-21]. The use of high resolution, 3D visualization has been receiving growing interest within life sciences, with non-invasive imaging tools becoming more readily accessible [22]. Such technologies capable of 3D imaging have become an important part of research works. They include confocal microscopy and light-sheet methods [23-25], optical projection tomography (OPT) [26-28] or microCT [29-32].

However, a considerable limitation of X-ray techniques, in general, is their low contrast for soft tissues. Indeed, these techniques are suitable for investigating high absorbing samples, such as bones and mineralized tissues. Still, it struggles with discriminating non-mineralized or soft biological tissues with similar or low X-ray absorbing properties [33]. Therefore, to increase the capability of microCT for low-absorbing tissues, contrast-enhancing techniques exist based on diverse principles, i.e. staining by chemical compounds, phase-contrast and dual CT.

1.2.1 Staining

Chemical compounds containing high atomic number elements that bind to soft tissues have been adopted as contrast/staining agents for X-ray Computed Tomography. There are contrast agents that can be applied *in-vivo* as well as *ex-vivo*. *In-vivo* contrast agents include iodine-based, lanthanide-based, and gold and other metallic nanoparticles [34]. Their detailed description can be found in the review by Lusic and Grinstaff [34], and they are not discussed further in this chapter, as the focus of this work is imaging of biological tissues *ex-vivo*. Particular emphasis is given to protocols suitable for the characterization of musculoskeletal tissues.

The goal of staining sample *ex-vivo* is to get a contrast agent uniformly to the whole sample or to stain the targeted tissue uniformly only. The example of an adequately stained mouse embryo is shown on X-ray projection in Fig. 1.4. In this Figure, there is also an X-ray projection of the sample that was only partially stained, i.e. the staining time was not sufficient, and some parts of the sample still miss the contrast agent. Also, it can happen that the contrast agent doesn't penetrate to the tissue at all, and the sample remains transparent to X-ray except for the mineralized parts. Therefore, when choosing a contrast agent, it is crucial to consider the tissue type and the size of the sample to be stained.

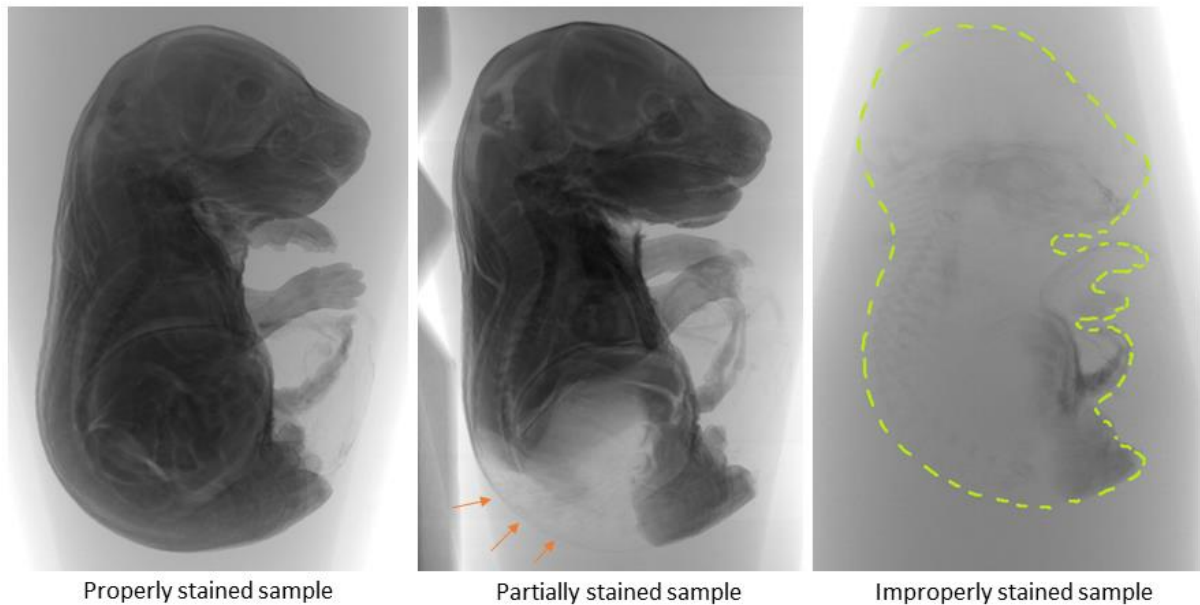


Figure 1.4: Staining of soft tissues on the X-ray projection of mouse embryo. The left image shows a properly stained sample. Orange arrows in the middle image show areas where staining wasn't efficient. The right image shows an improperly stained sample. Tissues that started ossification can be barely seen; the soft tissues are transparent for X-ray.

One of the first contrasting agents used for X-ray Computed Tomography was osmium tetroxide [35]. The use of this compound was logical as it is commonly used for soft tissues in electron microscopy. In 2009, Metscher [36, 37] came up with studies investigating the staining potential of several commercially available chemical compounds for different sample types. Also, Pauwels et al. [38] compared the contrasting enhancement of 28 other chemicals on samples larger than one cm^3 . These studies showed that the best contrasts are obtained by using solutions of osmium tetroxide, phosphomolybdic (PMA), phosphotungstic acid (PTA), or inorganic iodine. However, osmium tetroxide is a highly toxic stain, and its penetration is limited. On the other side, the main advantages of iodine and PMA/PTA staining are the simple sample preparation and their safer nature than osmium tetroxide. Nevertheless, also these stains have some limitations as the shrinking of stained samples.

After Metscher's publications in 2009, a number of studies dealing with staining protocols with a focus on specific tissues started to appear. MicroCT contrast agents with polyoxometalate structure [39] or hexabrix for cartilage imaging were introduced by the group of Kerckhofs [40, 41]. The complete review of studies dealing with contrasting agents from 2006 to 2019 can be found in the review of Bournonville [33].

An alternate approach to visualise bone and cartilage simultaneously was described by Gabner et al. in 2020 [42]. Their protocol is based on ethanolic fixation and staining with ruthenium red. Bone mineral stays preserved during staining; thus, the entire embryonic skeleton can be imaged with high contrast. Furthermore, differences in X-ray attenuation of ruthenium and calcium enable the spectral separation of cartilage matrix and bone by dual-energy CT. This protocol is promising for distinguishing bone and cartilage without advanced segmentation methods.

1.2.2 Phase-contrast

Although attenuation contrast suffices for visualizing objects containing very different materials, many specimens contain materials that attenuate similarly. Therefore, better contrast can be obtained by exploiting the materials' X-ray phase-contrast [8]. This technique also enables extending the capabilities of X-ray imaging to the details that don't possess enough absorption contrast to be visualised only by measuring the decrease in X-ray intensity. Hence, phase-contrast X-ray imaging is a promising technique for observing the structure inside biological soft tissues without staining and severe radiation exposure [43-45]. The captured X-ray projection image will always contain a mixture of contributions from both the absorption and the phase shifts in samples [46, 47].

X-ray phase-contrast imaging techniques are evolving fast, and different approaches exist, i.e. Zernike phase contrast, interferometry, grating-based or analyser-based methods. The most common X-ray computed tomography imaging approach is the free-space propagation technique (also called in-line phase-contrast imaging) [48]. Free-space propagation techniques require a simple set-up as introducing an appropriate propagation distance between the sample, and the image detector can be sufficient to make the phase effects detectable. The set-up is identical to a conventional CT except that the detector is far from sample [8]. Detectors cannot measure phase, but it is possible to decode the phase shifts from the recorded intensity patterns. The process that aims at making this type of imaging quantitative by calculating the phase and amplitude of the sample is called phase retrieval. An example of the phase-retrieval algorithms can be found in [49, 50].

Moreover, the X-ray beam needs to have spatial coherence and parallel geometry to observe phase change. These are typical characteristics of a synchrotron beam CT systems using synchrotron sources. They are capable of fine resolution because the synchrotron's electron beam can be used to generate high-brilliance X-ray beams that have narrow bandwidths. However, under certain conditions, the laboratory-based CT machines are also capable of phase-contrast imaging [8].

1.2.3 Dual-energy CT

Dual-energy CT (DECT) has recently demonstrated technological progress in clinical applications such as tumour visualization. It has the potential to improve soft-tissue contrast and reduce artefacts caused by beam hardening and metal [51]. DECT is generally used to distinguish two compounds with a similar attenuation but with a different K-edge. Two CT scans of the same subject are performed, each with different energy (i.e. accelerating voltage and current for X-ray tubes). As described in section 1.1.2, μ changes abruptly at the element-specific energies corresponding to these edges. This can enhance contrast in X-ray CT or identify the presence of different elements [8]. By scanning at two different energies (before and after the specific K-edge), contrast enhancement can be achieved [52].

Another possibility is a combination of DECT with contrasting agents. For example, the dual-energy technique combined with the dual contrast agent has been shown by Honkanen et al. [53] in the example of articular cartilage. However, the performance of conventional CT systems is usually limited by beam hardening and long acquisition times. Therefore, synchrotron microCT shows greater potential using a monochromatic X-ray beam and fast image acquisition for the dual contrast technique [54].

1.3 Data segmentation

The term segmentation of microCT data means dividing the 3D dataset into subgroups which helps in reducing the complexity of the dataset to make further processing or analysis simpler. In other words, segmentation means delineating anatomical structures or other regions of interest [55]. If the histogram of microCT data is bimodal or multimodal (has more peaks), the data segmentation can be done automatically. One of the most widely applied techniques for histogram segmentation is thresholding, which assumes that homogeneous objects in the image manifest themselves as clusters. The key to the histogram-based technique is selecting a set of thresholds that can discriminate objects and background pixels [56].

Biological data after staining often don't meet up criteria for histogram-based segmentation. Anatomical structures, i.e. clusters to be segmented, have similar greyscale values. For example, fig. 1.5 shows microCT data of the head of adult *Ambystoma Mexicanum*. Greyscale values are similar, and the histograms of anatomical structures (brain, cartilage, bone, eyes and muscles) overlap (Fig. 1.6). Therefore, it is challenging to segment data into classes using the conventional segmentation methods. Manual contouring is still the standard way to segment the structures, but it is time-consuming and user-biased [11, 57].

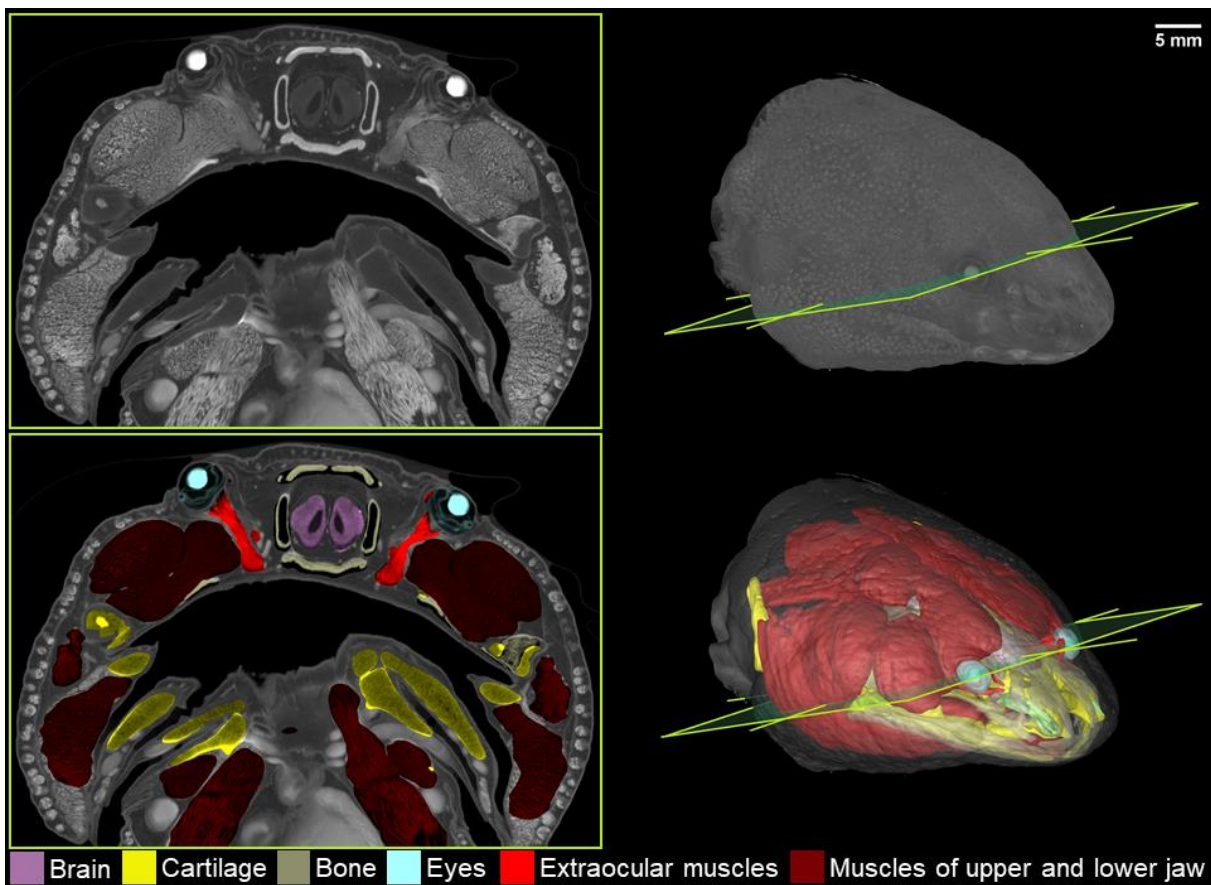


Figure 1.5: Segmentation of soft tissues in the head of adult *Ambystoma mexicanum*. The upper image shows the original CT slice in grayscale values. The lower image shows segmented structures. The green plane on the 3D model indicates the position of the 2D CT slice.

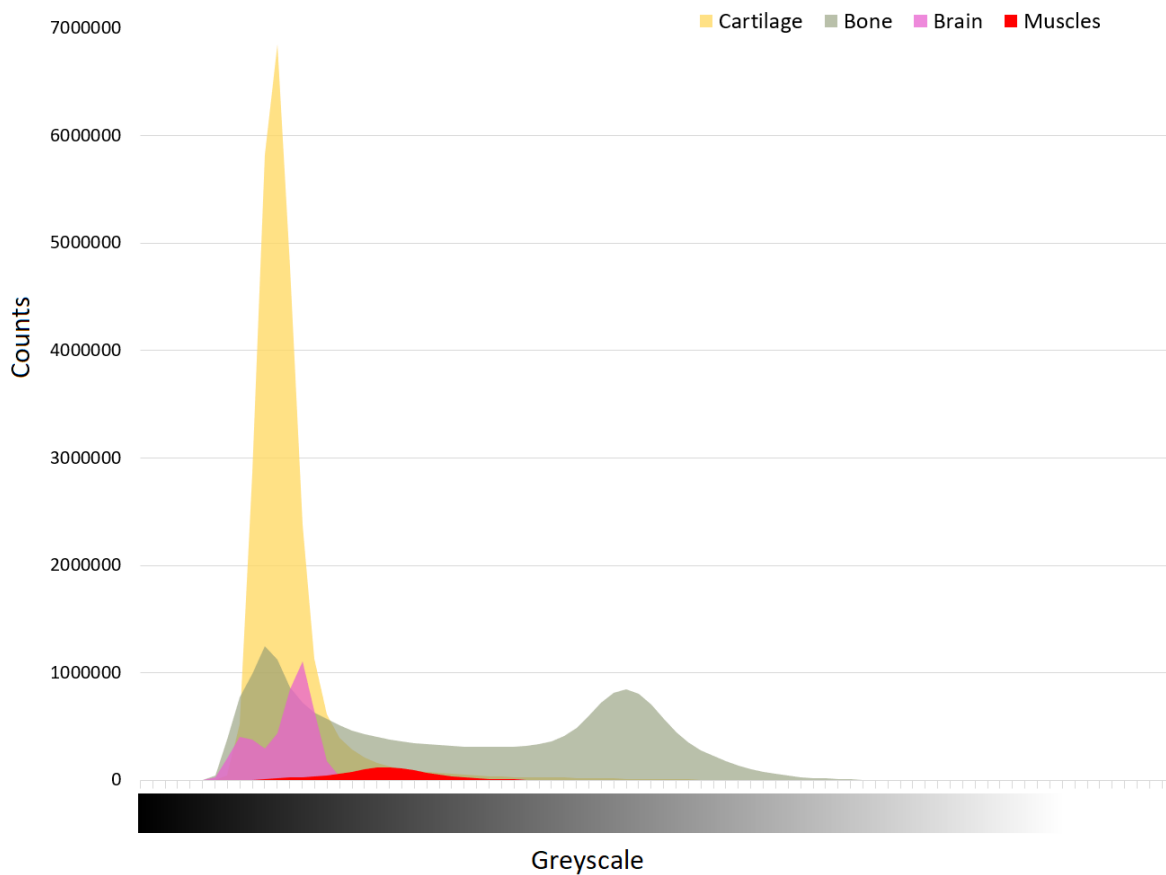


Figure 1.6: Schematic histogram of selected segmented structure from the head of adult *Ambystoma mexicanum* showed in Fig.1.5. Note the overlap of greyscale intervals.

One promising way seems to be a 3D fully convolutional neural network (CNN). For example, Léger et al. [57] utilized U-net to automatically segment mineralized cartilage from bone microCT images of the Achilles tendon-to-bone interface. Using the 3D U-net, they reached a high similarity of the samples an average Dice Similarity Coefficient that statistically describes the similarity of samples was 0.85 at the manual annotations for twelve 3D datasets.

Another recent successful example of using CNN was presented by Schultheiss et al. [58], who focused on CNN for lung nodule detection in the presence of foreign bodies. In their study, CNN was trained and evaluated. The presented CNN has the potential to help radiologists during a clinical routine. The CNN's decisions can be followed by inspection of individual lesion scores and box predictions, which is advantageous over other CNN architectures [58].

2 Aims of Doctoral Thesis

Even though microCT imaging has made significant progress in biological imaging in the last few years, many challenges still need to be addressed. The main aim of this dissertation is to bring new insight into microCT imaging and mainly subsequent 3D analysis of biological structures. As described below, the thesis aims can be divided into three parts: MicroCT measurement and data segmentation of biological samples, quantification of segmented 3D models and implementation of the results to particular biological projects.

2.1 MicroCT measurement and data segmentation of biological samples

There are three basic approaches for imaging biological samples by microCT: Staining, phase-contrast imaging, dual CT or a combination of these methods. Staining by chemical substances is often used because of the tissues' very similar attenuation coefficient. However, the staining has some limitations: generally, it is usually applied only on ex-vivo samples; shrinking tissue can appear with a longer staining time [59]; penetration of stains is limited etc. [36, 37]. In some cases, phase-contrast imaging is more convenient. The combination of staining and phase-contrast can give a good differential contrast and a higher resolution [46, 47, 60]. After getting the 3D dataset, data analysis and segmentation is another challenging task. Because of the complex structures of biological samples, it is hard to find a universal algorithm for the segmentation of biological data. Above that, the staining of soft tissues gives the same greyscale value to various tissue types. Thus, it is challenging to segment data into anatomical structures using conventional segmentation methods. On the other hand, due to the staining, a large variety of tissue can be observed by the human eye. Therefore, manual segmentation is taken as a golden standard [55]. However, this approach can be time-consuming and suffers from operator variability [11].

Therefore, this dissertation aims to set the appropriate strategy for microCT measurement of soft tissues, segment the structures and create a database of segmented data. Then, this database would serve as an input for machine learning algorithms, specifically convolutional neural networks (CNN).

2.2 Quantification of segmented 3D models

To answer the question of biological issues and to reveal and describe complex phenomena, visualization is usually not enough. Developmental studies in biology require the exact number of comparisons of groups with different ages, treatments, or mutations of the samples. Thus, this work should focus on finding ways to quantify differences among different developmental stages or how to compare wild types and mutants quantitatively.

2.3 Implementation of the results to particular biological projects

The main aim of this work is to implement obtained results in practical biological projects with an impact on the biological community. Particular attention should be given to soft tissues that have not been analysed by microCT before, like cartilaginous chondrocranium in mouse embryos, muscles with attachment points, tendons, and supportive tissues with a focus on their developmental programs. The dissertation work should also interactively reflect the needs of biologists for the segmentation and quantification of the studied structures.

3 Methods

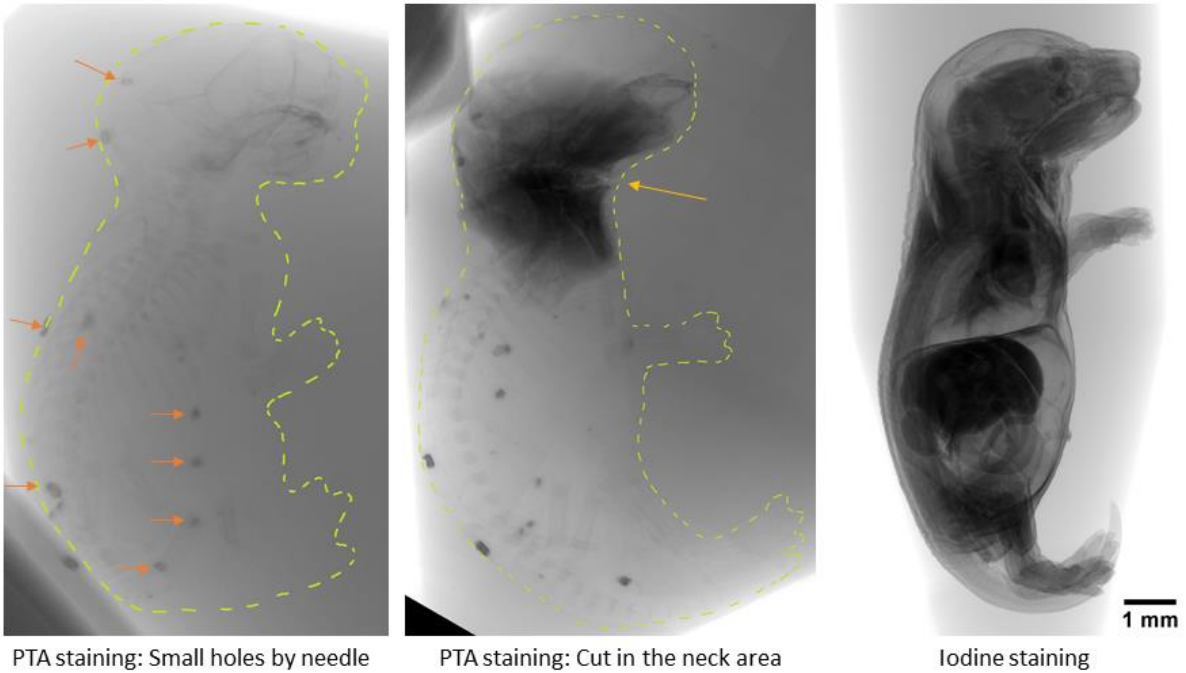
All animal work (mouse embryos and salamanders) was approved and permitted by the Ethical Committee on Animal Experiments (Norra Djurförsöksetiska Nämnd) and conducted according to the Swedish Animal Agency's Provisions, and Guidelines for Animal Experimentation and international guidelines and regulations were followed (Institutional Review Board/Institutional Animal Care and Use Committee). Mouse embryos for extraocular muscles project and investigation of neck muscles were handled as per European Community guidelines, and the ethics committee of the Institut Pasteur (CTEA) approved protocols (APAFIS#6354–20160809 I2028839).

3.1 Sample preparation

Staining with elements with higher atomic numbers turned out to increase the contrast of the soft tissues as the best option. Several staining protocols were tested to visualize mouse brain structures by microCT. Samples were stained in PTA, iodine or a combination of both solutions for various periods [59]. The staining protocols were modified by the work of Metscher [36; 37]. In summary, the staining in iodine exhibited more clear contours of fibres than in the case of PTA-stained samples. Fixation of samples in 4% PFA demonstrated higher contrast to tissues fixed in 10% PFA. Also, when iodine is compared to PTA, PTA appears as a larger molecule with much slower tissue penetration rates [36].

The staining time depends on the size of the sample. For samples larger than a few millimetres (i.e. mouse embryos 17.5 days post fertilisation and older), PTA penetration to the samples is limited. To improve the penetration of staining agents to the sample, we applied a few small holes by the needle to the skin of the sample (see Fig. 3.1). However, it turned out that they don't serve as the input for staining the whole sample. Another attempt was to cut to some parts to fasten the staining. The dissected area had faster perfusion of contrasting agents and decreased the staining time. However, the staining of PTA was still very slow and limited, and the sample did not stay intact. By applying iodine, it has turned out that staining time decreased significantly (from weeks with PTA to days with iodine, depending on the size of the sample). A comparison of iodine and PTA staining on the example of a mouse embryo is shown in Fig. 3.2. Both, the PTA and iodine stains were found to impart strong tissue contrast to soft tissues [36]. On the example of mouse embryo, soft tissues are stained almost equally, and they give similar input for segmentation, both manual and semi-automatic. A more detailed comparison of iodine and PTA staining with different concentrations and staining times can be found in the attached manuscript [59].

The next step after staining the sample is the sample's fixation for microCT measurement. Mechanical stability (both the CT machine and the specimen) is essential for high data quality. The motions must be smaller than the voxel size; otherwise, the reconstructed 3D volume will be blurred, as shown in Fig. 3.3. Biological samples were placed in polyimide/capton tubes filled with 1% agarose gel to ensure stability.



PTA staining: Small holes by needle

PTA staining: Cut in the neck area

Iodine staining

Figure 3.1: Problems of staining by PTA for samples larger than a few millimetres. The left image shows an improperly stained mouse embryo with holes by needle – only the areas of the needle marks (orange arrows absorbed some of the contrasting agents, but staining didn't penetrate to the sample). The middle image shows the cut in the neck area (yellow arrow). The right image shows staining by iodine instead of problematic PTA.

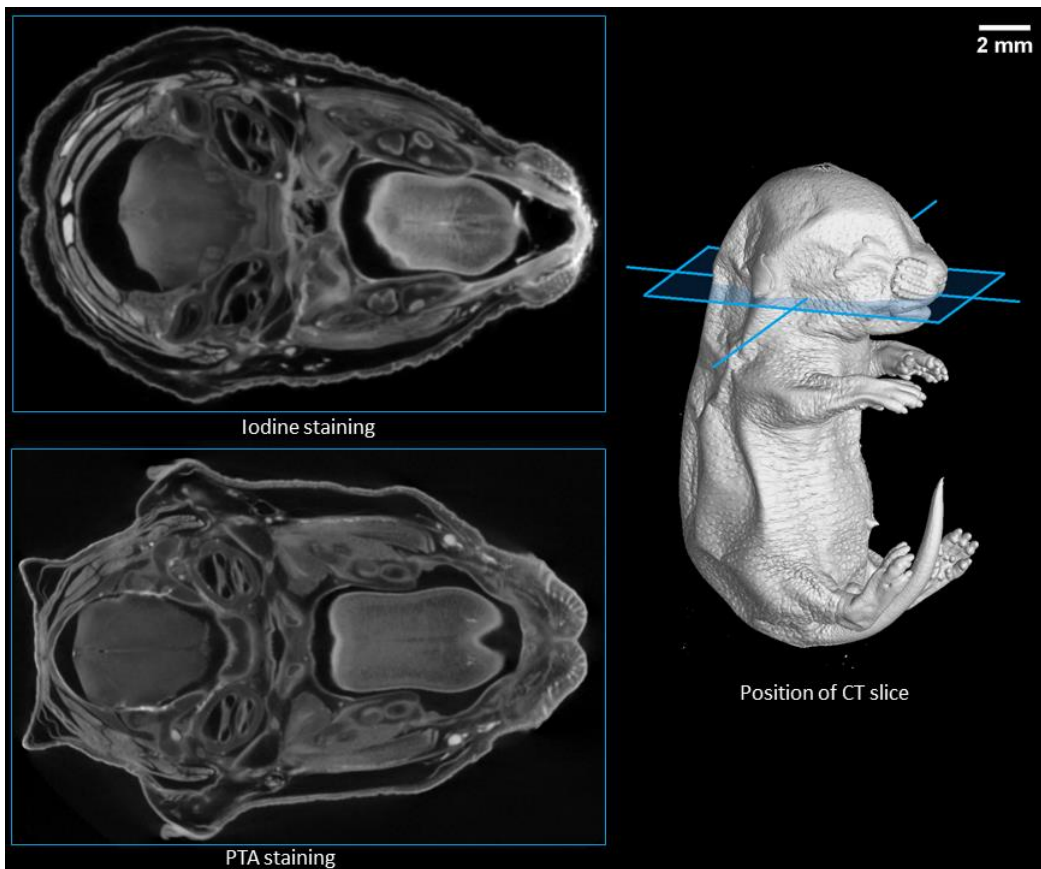


Figure 3.2: Comparison of iodine and PTA staining on mouse embryo 17.5 days post fertilisation. The blue plane on 3D models schematically indicates the position of the CT slice.

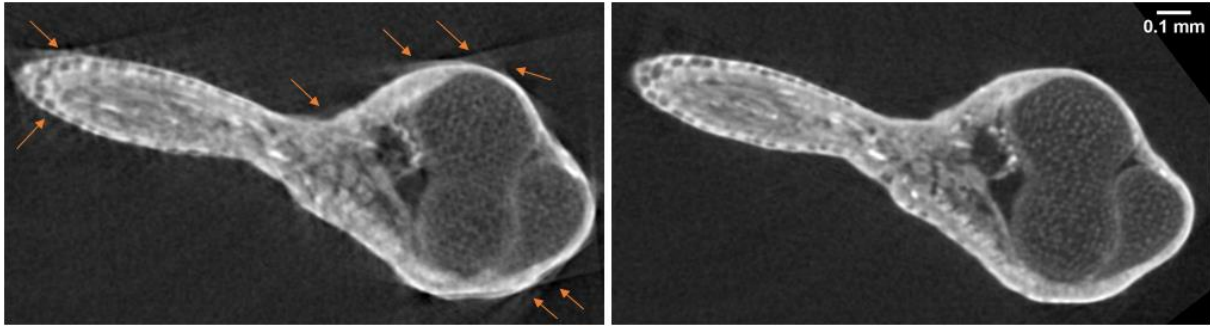


Figure 3.3: Artefacts caused by movement of the sample during microCT measurement in the reconstructed CT slices of a salamander limb. Orange arrows show blurred areas in the CT slice.

3.2 MicroCT

3.2.1 Laboratory measurements

CT measurements on laboratory equipment were realized in the laboratory of X-ray micro and nanocomputed tomography at CEITEC BUT in Brno. MicroCT machine GE phoenix v|tome|x L 240 is equipped with a 180 kV/15W maximum power nanofocus X-ray tube and high flat-panel dynamic 41|100 with 4000 × 4000 pixels and a pixel size of 100 × 100 μm.

The first step was to find suitable parameters for microCT measurement. It means to find proper sample-source and source-detector distance and find X-ray tube parameters for sufficient contrast. Because the illumination provided by X-ray sources is not uniform, and detectors show pixel to pixel variations in sensitivity, a projection must be acquired without the sample between source and detector. A bright, featureless image is captured to normalize the optical defects. The projection must be collected under the same conditions as the CT scan (i.e. same source-detector distance and parameters of the X-ray tube). This process compensates for these variations and is called a flat field correction [8].

As described in the previous section, mechanical stability is essential for microCT measurement. At the same time, the stability of the sample is ensured by putting the sample in agarose gel. Furthermore, the mechanical stability of the system is secured by granite slabs that dampen vibration that could affect the fluency of rotation of the sample during microCT scanning. Anyway, there is always some motion except the rotation of the sample during the scanning. To compensate for this motion, GE phoenix v|tome|x L 240 has a module that manages to compensate for a slight movement called scan|optimizer. The projections acquired at 0° and 360° should be identical. Scan|optimizer captures several X-ray images from different angles before the measurement. The module compares the images captured before and during the measurement at appropriate angles to ascertain whether there has been any movement during tomographic measurement. If there is a motion, the module can compensate for it during the reconstruction.

Information about applied acceleration voltage, current, exposure time, and the number of projections and filters for each sample are specified in publications (see section 9.1). The voxel size of obtained volumes was in the range of 1 μm for samples in the range of a few mm to 10-20 μm for samples in the range of a few cm.

3.2.2 Synchrotron measurements

Synchrotron experiments were conducted at Sincrotrone Elettra in Italy under the supervision of Dr. Lucia Mancini. Measurements were held at SYRMEP (Synchrotron Radiation for Medical Physics) beamline using the white beam radiation mode. The samples were fixed in 1% agarose gel in polyimide or plastic tubes. During the first measurements, some motion artefacts occurred. Tiny bubbles were found in agarose gel, probably created by overheating the samples. Also, a change in the colour to blue was observed. Thus, we optimized scanning parameters to reduce the scanning time. After optimization, we decreased from the original 40 minutes to 17 minutes per scan: Exposure time was 1.0 s per projection, with 1000 projections acquired over a total scan angle of 180°. The X-ray spectrum of the beam was filtered with 1.5 mm of silicon and 0.025 mm of molybdenum. The sample-detector distance was set at 100 mm. The first set of experiments was realized with a voxel resolution of 2.5 μm , and according to the size of the sample, it was tuned up to 1 μm . The tomographic slices were reconstructed using the SYRMEP Tomo Project (STP) software. The phase retrieval algorithm was implemented in STP software, which became crucial for visualising cells. Details of the synchrotron experiment realized on salamander limbs can be found in [60].

3.3 Data analysis

Tomographic data from GE phoenix v|tome|x L 240 were reconstructed with GE phoenix datos |x 2.0 3D computed tomography software (Waygate Technologies GmbH Germany). A scan optimiser module was applied during the reconstruction as described in the previous section regarding laboratory measurement to compensate for the small and smooth drift of the axis (samples and detector) and focus (X-ray tube) position. The output of the reconstructed CT slices was a 16-bit integer. For manual segmentation, 3D datasets were transformed to 8bit DICOM format to save processing time and reduce the size of the data to save space on the disk. Segmentation of structures was performed using software Avizo and VG Studio Max (Volume Graphics GmbH, Germany) as described in [11]. Firstly, the structures of interest were outlined in every 3rd to 5th slice manually or semi-automatically using watershed segmentation. Then, the mask was interpolated between slices. Segmentation along one direction caused disfluencies in the perpendicular direction.

For this reason, the segmented masks were transformed into STL model and smoothed in VG Studio MAX software. The smoothing was controlled to preserve the small details in the original data. The disfluencies after interpolation and the smoothed model are shown in Fig. 3.4. Quantitative analyses on the segmented structures were performed in VG Studio MAX software. Details of the analysis can be found in section 4 of this work.

Another challenge of microCT imaging is effectively and intuitively sharing complex datasets between scientists from different fields. Generally, 3D datasets need special software for visualisation or are reduced to 2D images in which important information might be lost. For this reason, we created a manual that describes individual steps for creating an interactive 3D PDF file allowing rotation, movement or magnification to provide an intuitive approach to analysing structures in a 3D context. This manual is widely applicable in biological research and can be used to analyse volumetric data from any research field relying on 3D rendering and CT-biomedical imaging [61].

This manual can be found in the attachments of this document and was published as supplementary material in my work about interactive and intuitive visualisation methods for 3D data [61]. It contains a detailed description of the pipeline to create a personalised interactive 3D PDF file. Our procedure

involves a combination of free (Meshlab, Blender) and commercial (Avizo, VG Studio, 3D PDF Maker) software. Alternatively, segmentation or remeshing of the model can be done with other appropriate software [61].

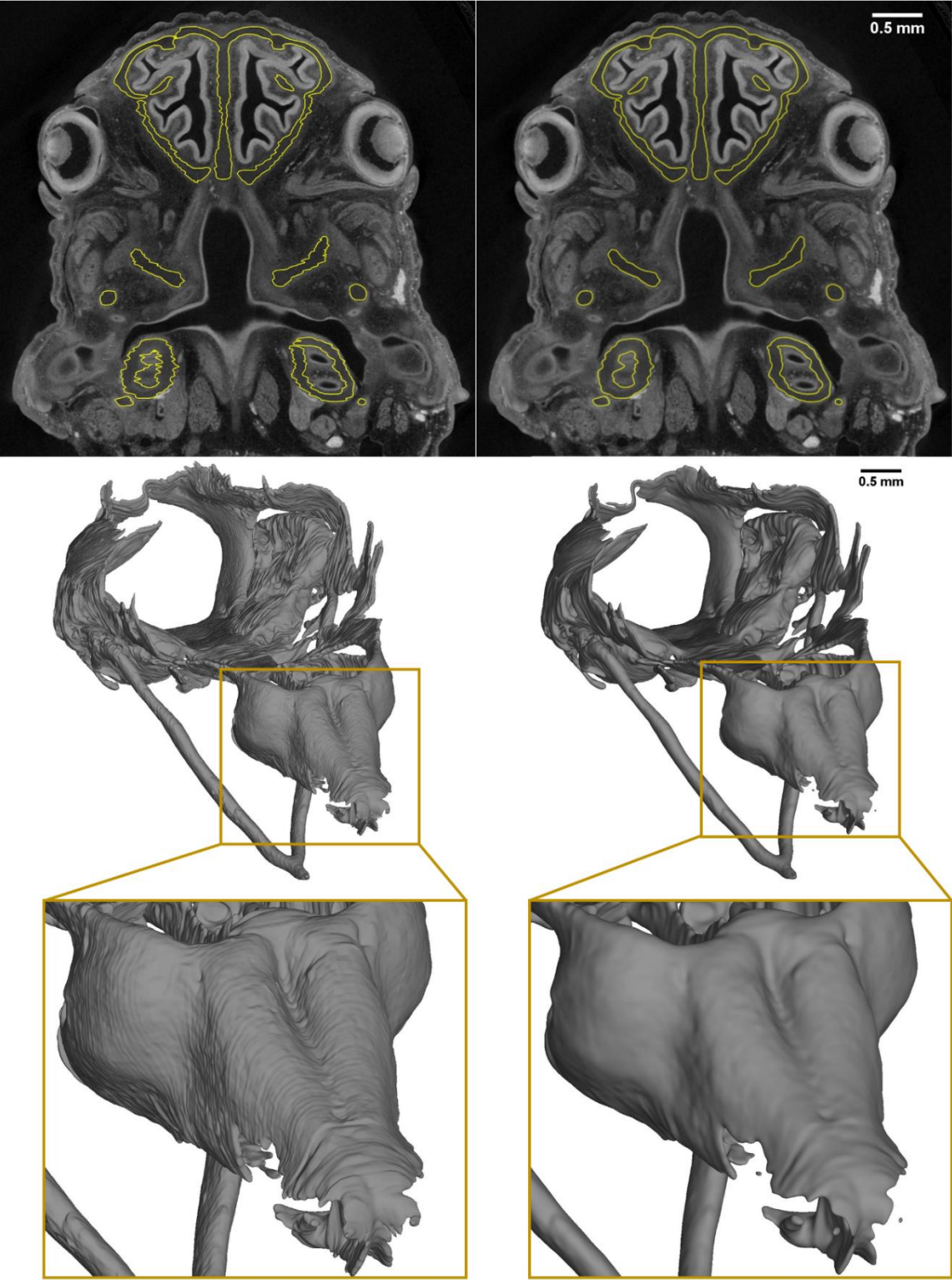


Figure 3.4.: A comparison of mouse chondrocranium directly after manual segmentation (left) with model after smoothing to get rid of artefacts caused by interpolation between manually segmented slices. The top images show CT slices with yellow contour outlining cartilaginous chondrocranium. The middle images show a completed 3D model, and the bottom images show a nasal capsule detail.

4 Results

4.1 Regeneration of salamander limbs

Regeneration of human tissue has been an interest of scientists for centuries and could be an essential element for the future of healthcare [62]. Knowing the principles and limitations of regeneration is necessary for controlling the opportunity to restore damaged tissues or organs. While humans show poor regenerative ability, other vertebrates can regenerate diverse body structures. Salamanders exhibit the most remarkable regenerative ability among amphibians. They can regrow ocular tissues, nervous system, whole body parts and organs such as the heart [62]. Such conservation of regenerative principles gives hope to applying the basic knowledge obtained in salamanders to human regeneration in the distant future. Limb regeneration in salamanders is a well-established model system [49-51]. The speed of salamander limb regeneration varies among species and developmental stages, and they can regenerate entire limbs in a range of days to weeks. [63].

In past years, experimental techniques, including lineage tracing, DNA transformation, and gene knockdown in regeneration model organisms, have shed new light on the regeneration process [62]. Regeneration is often interpreted as a repetition of embryonic development. It is believed that a regenerated limb is an entirely normal anatomical and functional limb. However, whether each regenerated limb is really an unequivocal copy has not been confirmed. Regeneration results in a limb of the same size; however, the regeneration process is not perfect, and the patterning defects and anomalies have been documented in regenerated limbs [64]. Certainly, developmental mechanisms play an essential role during regeneration. However, structures have much larger size and speed of growth together with environmental conditions in a regenerating limb are different. To question the exactness of the regenerative process, we focused on *Ambystoma mexicanum* (also known as axolotl) and *Pleurodeles waltl*. We used the microCT technique to trace the transformation of the blastema to the new limb by scanning the salamander limb in the different stages after amputations to compare developmental and regenerative formation mechanisms. The blastema is formed after injury of the limb and provides cell material for the limb morphogenesis [65]. The blastema itself originates from the complex mixture of cell types, including muscle, cartilage, dermis, and Schwann cells. Already three weeks after amputation, we observed cartilage in the regenerating limb. Every week, a limb was collected, and a 3D model was created. Thus, we were able to follow the regeneration process in time.

In fully regenerated limbs, we also looked at the process of ossification. It was challenging to find and segment ossified cartilage and newly formed bone in microCT data. Developing and regenerating limbs undergo different ossification types, as shown in Fig. 4.1. To segment cartilage, the semi-automatically method worked as cartilage is stained significantly weaker than surrounding tissue [11]. However, mineralized bone has higher X-ray attenuation and appears in lighter areas. Stained muscles also show higher attenuation with similar contrast to the bone. Above that, muscles touch the bone and thus, it is hard to find the border of the bone automatically. Therefore, special attention was given to these areas. The best method for segmentation turned out to semi-automatically segment the whole limb as described in section 3.3. In another step, bone and cartilage were separated based on their greyscale value (Fig. 4.2).

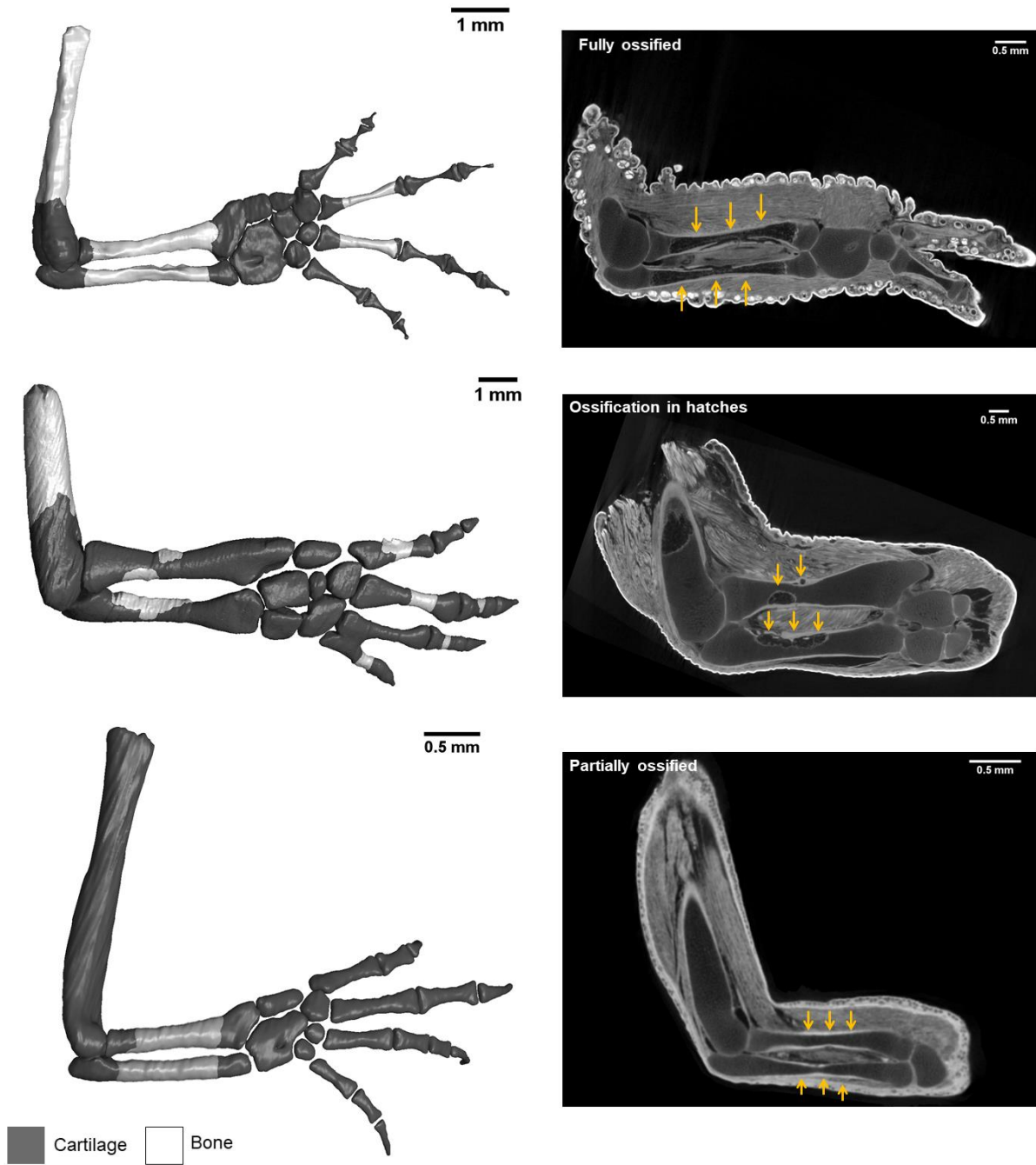


Figure 4.1: Different types of ossification in salamander limbs. The fully ossified ulna and radius in the top image; Ossification in patches in the middle image, and ossification in the border of the skeletal element in the bottom image. The left row shows segmented 3D models. The right row shows tomographic slices; yellow arrows show ossification in CT data.

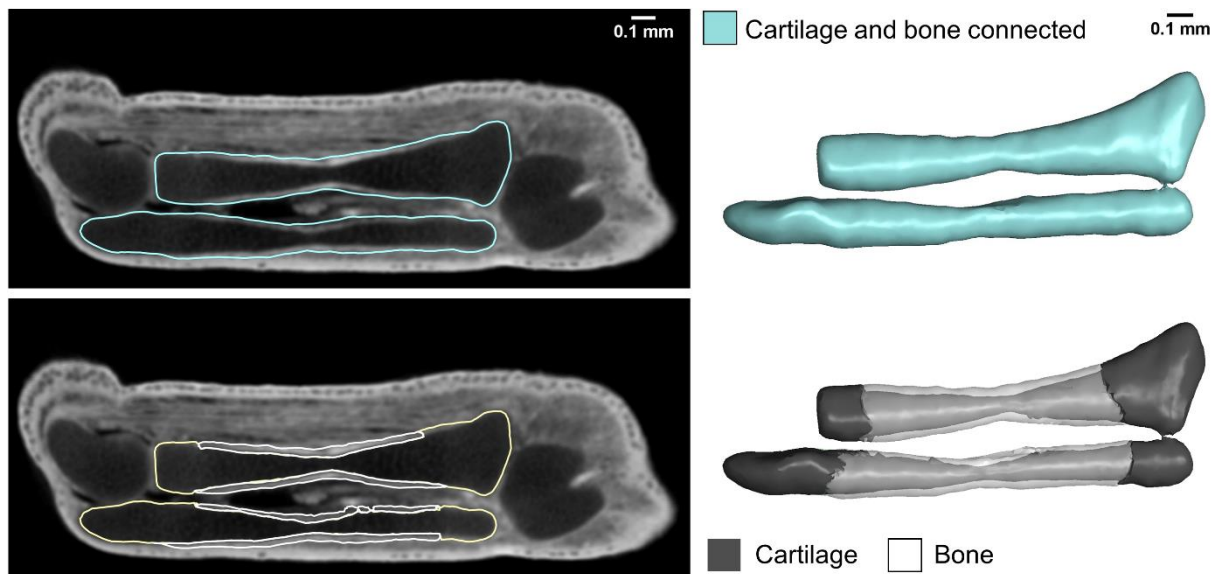


Figure 4.2: Semi-automatic segmentation of bone and cartilage in *ulna* and *radius* in salamander limb. The top image shows the segmentation of skeletal elements as one 3D model. The bottom image shows separated models for bone and cartilage based on their greyscale value.

When having a 3D model of cartilage and bone, we looked at the shape of segmented structures in more detail. When looking at the segmented models, it seemed that regenerated limbs have thicker cartilage and bone, respectively, compared to control limbs undergoing normal development. Firstly, to confirm this hypothesis, I divided the 3D model of all segmented elements into sub-models. The anatomically corresponding parts were taken into the same coordinate system in the second step. By changing the opacity of the registered models, it became clear that the length of the models is comparable.

On the other hand, the thickness of regenerated elements is thicker. To gain some quantitative numbers for confirmation of this observation, nominal/actual comparison analysis in VG studio software was performed. This type of analysis was developed to compare two mesh models. The parts of the models with the same position are shown in green colour. When a deviation occurs, the distance between the meshes is computed and then demonstrated by colour-coding on the model. The whole process of shape comparison is shown in Fig. 4.3.

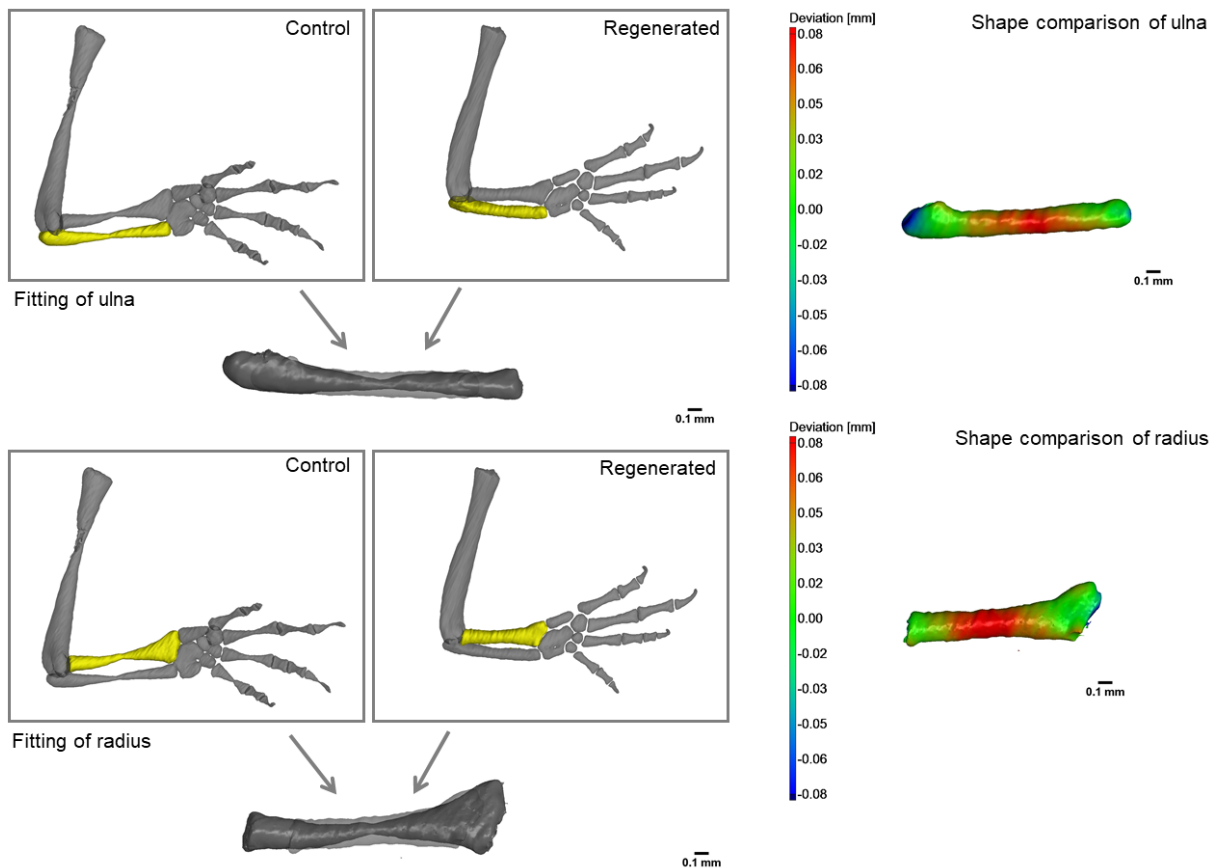


Figure 4.3: Shape comparison of ulna and radius of control and regenerated larval salamander limbs. There are no significant differences in the epiphysis. However, the diaphysis of control is narrowed compared to the regenerated limb.

4.2 3D-cell distribution in the regenerative muscle-skeletal system

During the measurements of salamander limbs with a conventional X-ray source at CEITEC BUT, we noticed very good contrast and resolution in tomographic data where the individual cells were detectable. However, automatic detection of the cells was not possible (Fig.4.4). As discussed in section 1.1.3, in synchrotron facilities, the small angular source size, the high intensity and the nearly-parallel geometry of the X-ray beam make it possible to obtain high spatial resolution. Furthermore, applying phase contrast could help the contrast of cells where only cell nuclei were stained. Thus, we applied for a synchrotron experiment at Elettra synchrotron (Trieste, Italy). Our goal was to perform tomographic measurements of salamander limbs to quantify cells inside cartilaginous elements of developing salamander (*Pleurodeles waltl*) limb [60]. Mapping the cells, their orientation and extracellular matrix distribution in 3D during salamander limb development could be taken as an input for computational modelling. This section describes individual steps to perform such quantitative analysis.

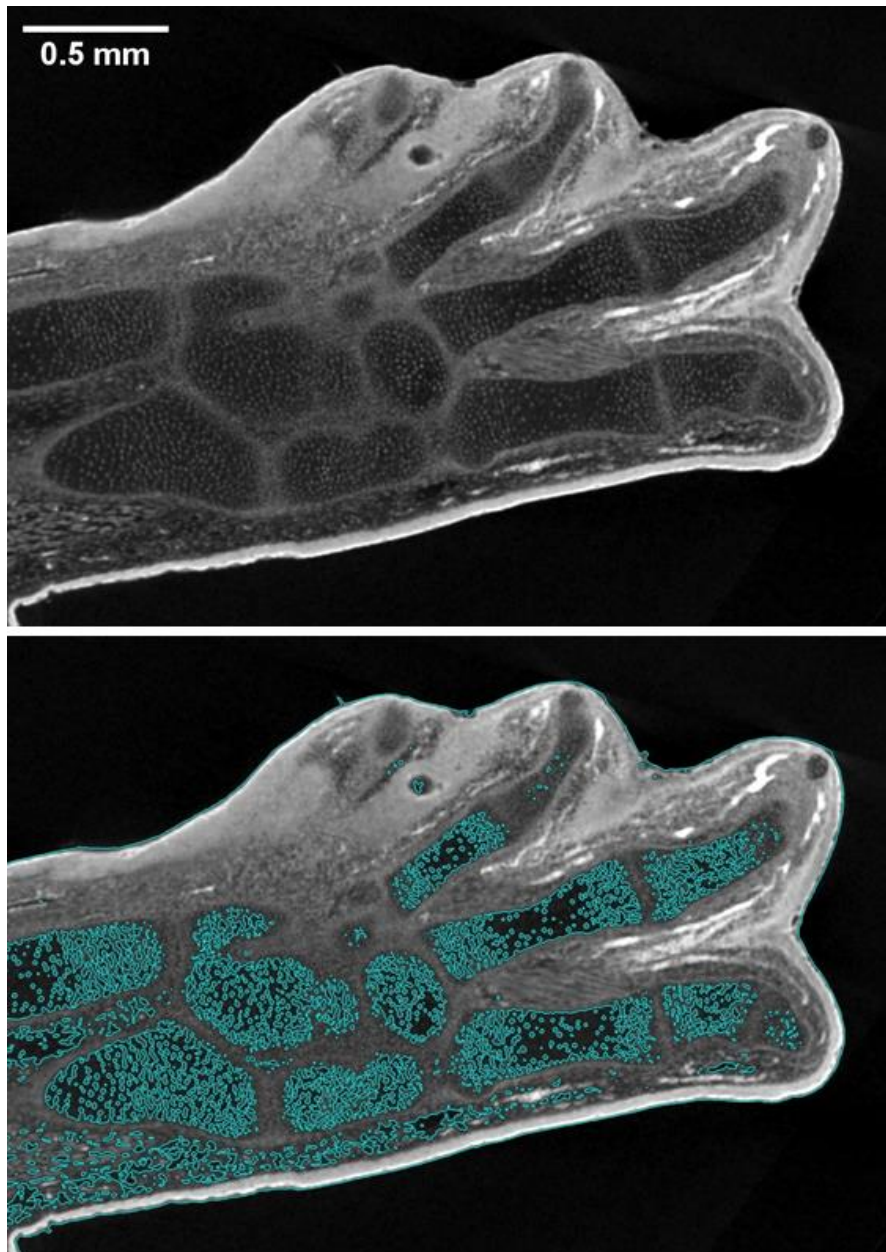


Figure 4.4: CT slice of salamander limb measured with conventional X-ray source. The upper image shows the original reconstructed data. White spots in cartilage represent cell nuclei. The blue line on the bottom image shows an attempt to segment the cells automatically. Errors are evident as connected regions of interest or missing some cells.

4.2.1 Number and density of cells within the extracellular matrix

The high spatial resolution (down to $1\ \mu\text{m}$) of synchrotron microCT at SYRMEP beamline at Elettra synchrotron achieved the cellular resolution needed for quantitative analysis of cell distribution. The details of the synchrotron measurement can be found in the methods section 3.2.2. Also, thanks to phase-contrast, the borders of cells in cartilaginous elements have been distinguished.

To perform a quantitative analysis of cells, several steps were required. The complete procedure is described in detail in the attached publication [60]: The first step was to segment individual cartilaginous elements (Fig. 4.5). However, the conventional segmentation algorithms failed on this task. Therefore, I used the freeware image analysis software ImageJ with its plug-in ABSnake. The

provided steps included the determination of the starting contour for segmentation (done manually by the user), the gradient threshold to be used in edge detection and the number of iterations of the segmentation cycles.

Nevertheless, by applying a contour on the non-filtered tomographic slices, the iteration process did not converge to the cartilage border (Fig. 4.6 a–c) because of the irregular boundary of the cartilage. To avoid this problem, the contour was applied to the median-filtered images. After filtering, the iteration procedure converged, and the resulted contour was the smooth cartilage border. The final line copied the perimeter of the cartilaginous elements (Fig. 4.6 d–f). Then, the segmented data could be taken as input for further steps in quantitative analysis [60].

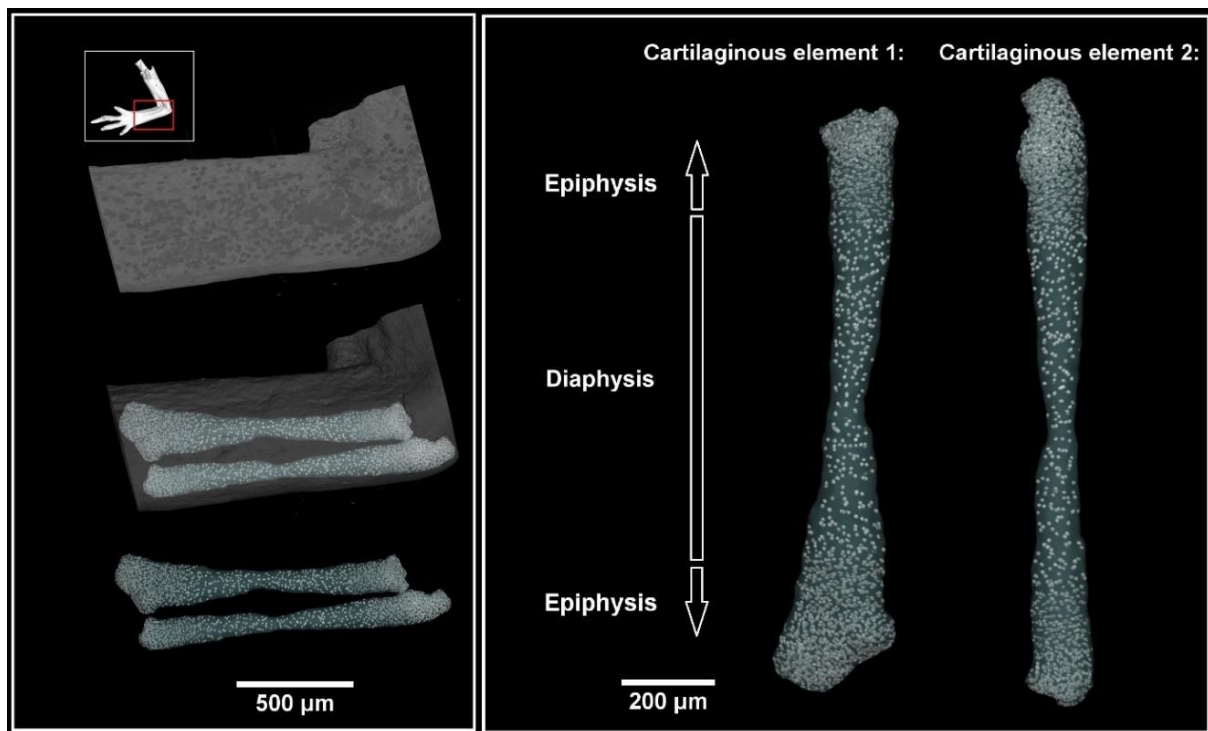


Figure 4.5: 3D visualisation of *ulna* and *radius* from an embryonic salamander limb (55A). White spots represent cell nuclei. Note difference density for epiphysis (high concentration of cells) and diaphysis (low concentration of cells). Modified from [60].

Another step was to count the cells, i.e. cell nuclei, inside segmented cartilaginous elements. The Pore3D software library [66] was used for this step. The 3D K-means clustering algorithm sorted data into three classes: the nuclei of cells, the extracellular matrix and the background. By evaluation of binarized data (comparison of Fig. 4.6 g and h), it is evident that some nuclei are connected into one blob (binary large object – blob). The red arrows show the example of connected blobs in Fig. 4.6.

Moreover, some border segments of the cartilage are miss-detected as cell nuclei (yellow arrows in Fig. 4.6). The erosion of the 3D data was the next step to getting rid of the miss-detected blobs. After the erosion, the data was well suited to determine the number of cells. Blob analysis [67] was performed to obtain the number of cells.

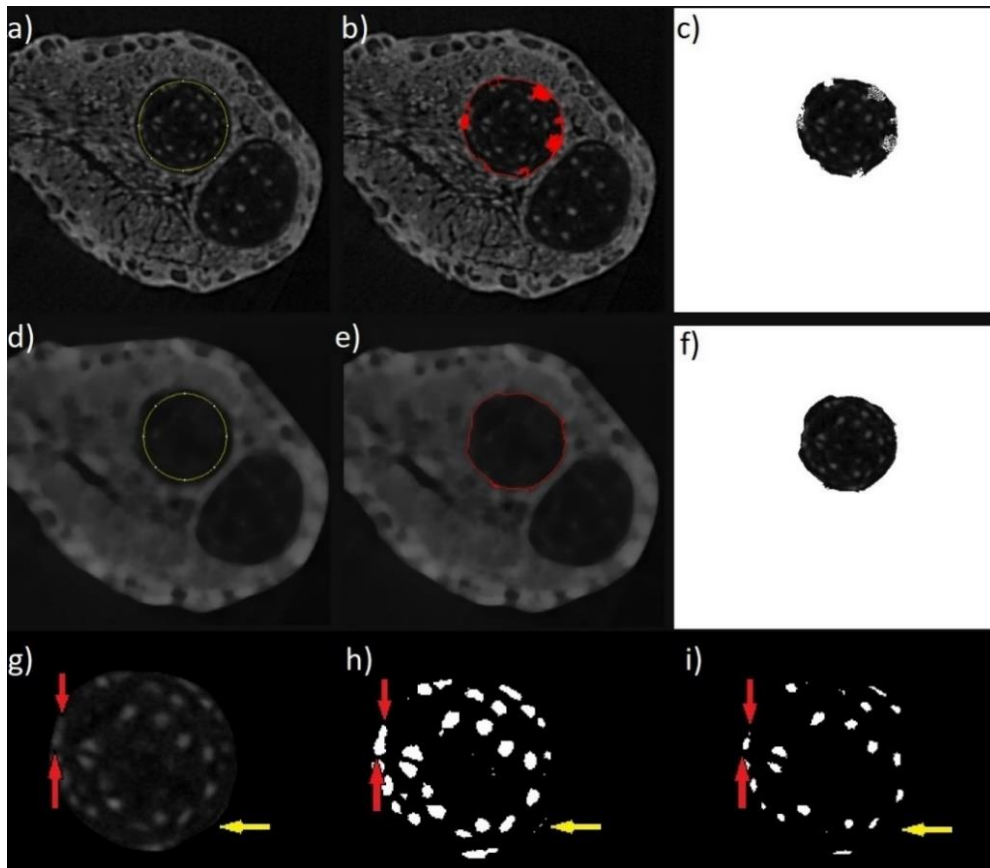


Figure 4.6: Individual steps of segmentation. (a–c) Shows the contour applied to non-filtered tomographic slices. (d–f) Shows the outline applied to filtered data. (g–i) Blob analysis in the Pore3D software. (g) Application of the 3D K-means clustering algorithm, (h) the results of the blob analysis, and (i) the eroded segmented image. Red arrows show two nuclei of the cells connected within the blob analysis. Yellow arrows indicate the light border of the cartilage [60].

The described procedure allowed us to determine the total number of cells, the volume of the cartilaginous elements, average size (given by the ratio of the volume of the whole element and number of cells) and density [60]. The difference between diaphysis and epiphysis is evident: the density of cells in the diaphysis is half compared to the density in the epiphysis (Table 4.1 and 4.2).

Table 4.1: Quantified criteria in the *radius*.

	Epiphysis	Diaphysis	Epiphysis
Number of cells	888	429	595
Volume of the whole element [mm ³]	0.0052	0.0071	0.0027
Average size of one cell [mm ³]	5.81×10^{-6}	1.65×10^{-5}	4.47×10^{-6}
Density of cells [mm ⁻³]	171,926	60,791	233,684

Table 4.2: Quantified criteria in the *ulna*.

	Epiphysis	Diaphysis	Epiphysis
Number of cells	441	333	1040
Volume of the whole element [mm ³]	0.0023	0.0058	0.0050
Average size of one cell [mm ³]	5.28×10^{-6}	1.74×10^{-5}	4.85×10^{-6}
Density of cells [mm ⁻³]	189,309	57,401	206,360

Another way to describe the density of cells inside cartilaginous elements is to calculate the distance between cell nuclei. To perform this, the binarized dataset was taken as an input. To determine this parameter, the circumscribed spheres were created for each binary object, i.e. cell nucleus. Then, the distance between these spheres was described as the *gap* parameter in VG Studio software. By this definition, some values can be negative (overlap of the spheres). This type of analysis gives a similar result to Tables 4.1 and 4.2 and is shown by colour-coding in Fig. 4.7.

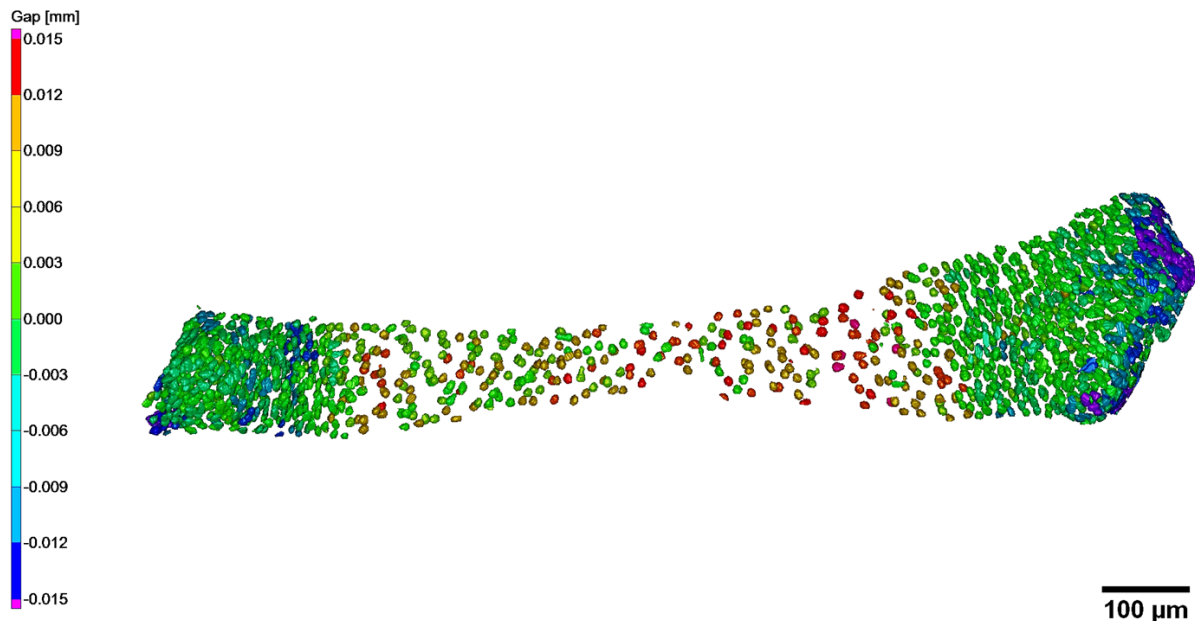


Figure 4.7: Calculating the distance between cell nuclei. The parameter *gap* indicates the minimum distance between the surfaces of the circumscribed spheres of two objects (i.e. cell nuclei).

4.2.2 The polarity of the cells in 3D

During analysing and segmenting cartilaginous elements, another interesting phenomenon was observed: When looking at the cells in the extracellular matrix, it seems that they are oriented, i.e. polarized, in specific directions. Moreover, the direction of polarization is different in different places in the cartilage. The tomographic slices with areas of polarized cells are shown in Fig. 4.8. To describe this phenomenon in detail and quantitatively, the 3D approach is needed again.

For this type of analysis, segmented binarized data were used. I used software VG Studio Max, with its module “Fiber orientation analysis”. Thus, every cell was considered the “fibre”, which means the direction of the axis of the element could be determined. Segmented data was registered in the coordinate system. The deviation angle of 0° corresponded to *yz* direction and blue colour. On the contrary, the deviation angle of 90° corresponded to *xy* direction and red colour. The result of the analysis is shown in Fig. 4.9.

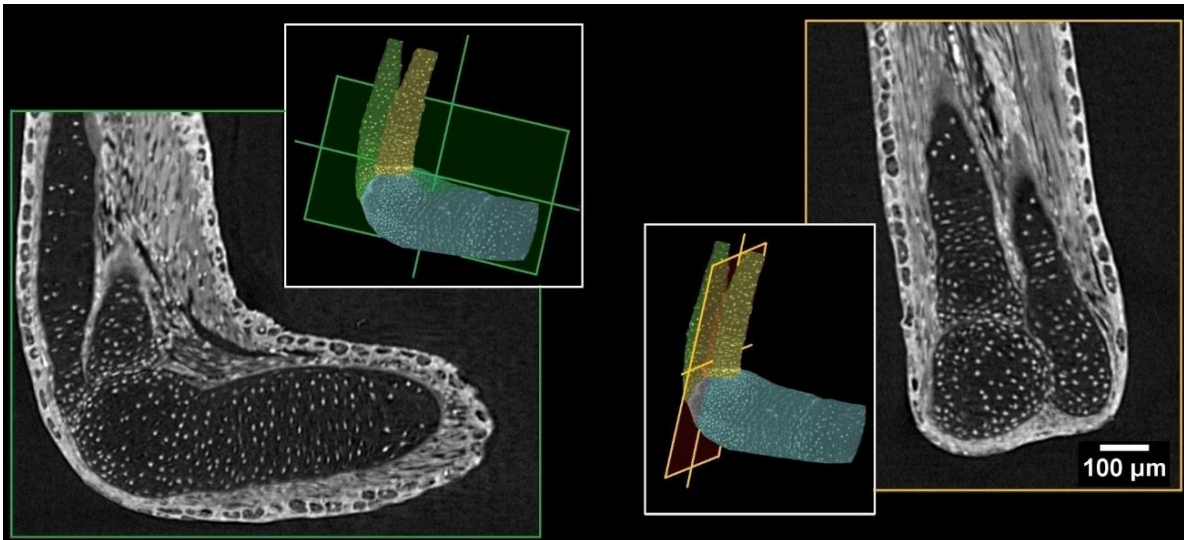


Figure 4.8: Tomographic slices in two orthogonal directions showing cellular resolution in tomographic slices [60].

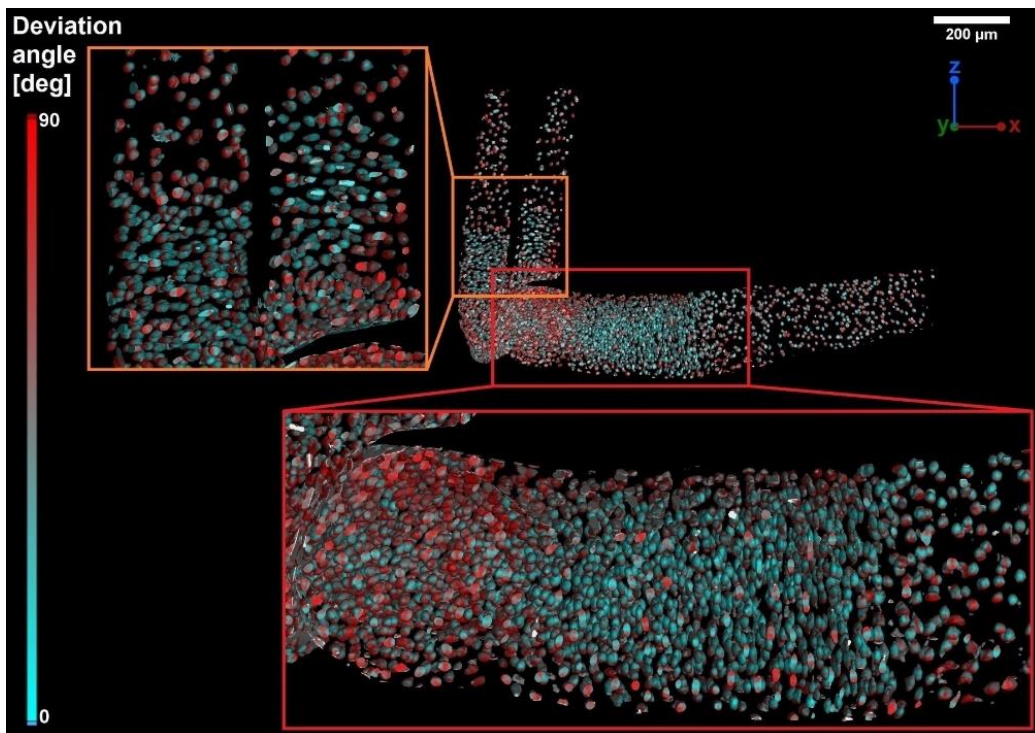


Figure 4.9: Polarization of the cells inside cartilage. There are polarized zones between the diaphysis and the epiphysis for all cartilaginous elements: *ulna*, *radius* and *humerus* [60].

“Fiber orientation analysis” provided detailed information about developing joint surfaces in the salamander limb. The impact of this observation is again described in the attached publication [60]: Orientation of chondrocytes in the developing joint correlated with the changing curvatures of joint surfaces. Also, the resolution and differential contrast was sufficient to map all chondrocytes' orientation inside the cartilage, which provided an essential foundation for future interpretation of the oriented cell behaviour during cartilage shaping. The results demonstrated that the predominant direction of chondrocytes in epiphyseal regions was different from rather central regions of the cartilage, where the cell density appeared low. In addition to this, superficial chondrocytes in epiphyseal regions were aligned with the developing surface of the cartilage (Fig. 4.10).

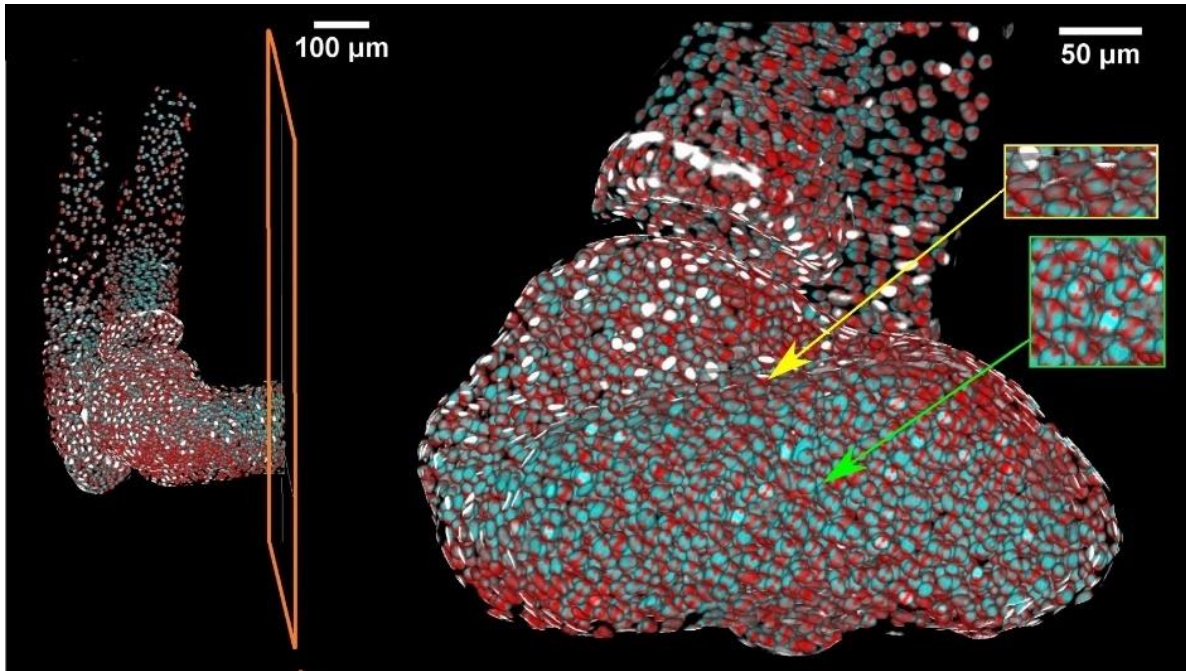


Figure 4.10: Detail of polarization of the cells on the salamander forelimb: Chondrocytes near-surface (yellow arrow) are aligned with the developing surface of the cartilage on the contrary with chondrocytes in the middle of the cartilage (green arrow). The orange plane on the 3D model indicates the position of the right image. Modified from [60].

4.2.3 Joint formation

Another area of interest was a joint formation within different stages of development. Here, we took advantage of the staining of the samples by PTA. In other words, we needed to be able to observe muscles and cartilage simultaneously. The development of muscles might guide cartilage and joint formation [68]. The visualization of these tissues in one 3D model showed some unexpected observations [60]: Three developmental stages were observed from a muscle-skeletal point of view. At the earliest analysed stage (41–42), only one small group of muscle around the elbow joint was found. However, different muscle groups (*biceps brachii*, *triceps brachii*, *brachioradialis* and *flexor carpi radialis*) were recognized in the following two stages.

Meanwhile, the elbow joint angle was decreased with the development of muscle. To calculate the elbow joint angle, the cylinders were fitted into humerus and radius and then, the angle between the cylinders' axes was measured. Interestingly, the decreasing elbow joint angle was observed with increasing developmental stages. The result of the analysis is shown in Fig. 4.11.

When looking at the visualisation of muscles in context with analysis of polarization of cells, there is a correlation between the cartilaginous cell polarity and attachment of the muscles. The chondrocytes next to the muscles' attachment points have a higher cell polarity. It means a correlation between the cell polarity inside cartilage and muscle attachment points. It is natural to speculate the mechanical force from muscle stretch may be delivered to attach point and then influence local chondrocytes' polarity. Hitherto unknown mechanisms can control chondrocytes' location and density together with cell polarity and muscle attachment points [60].

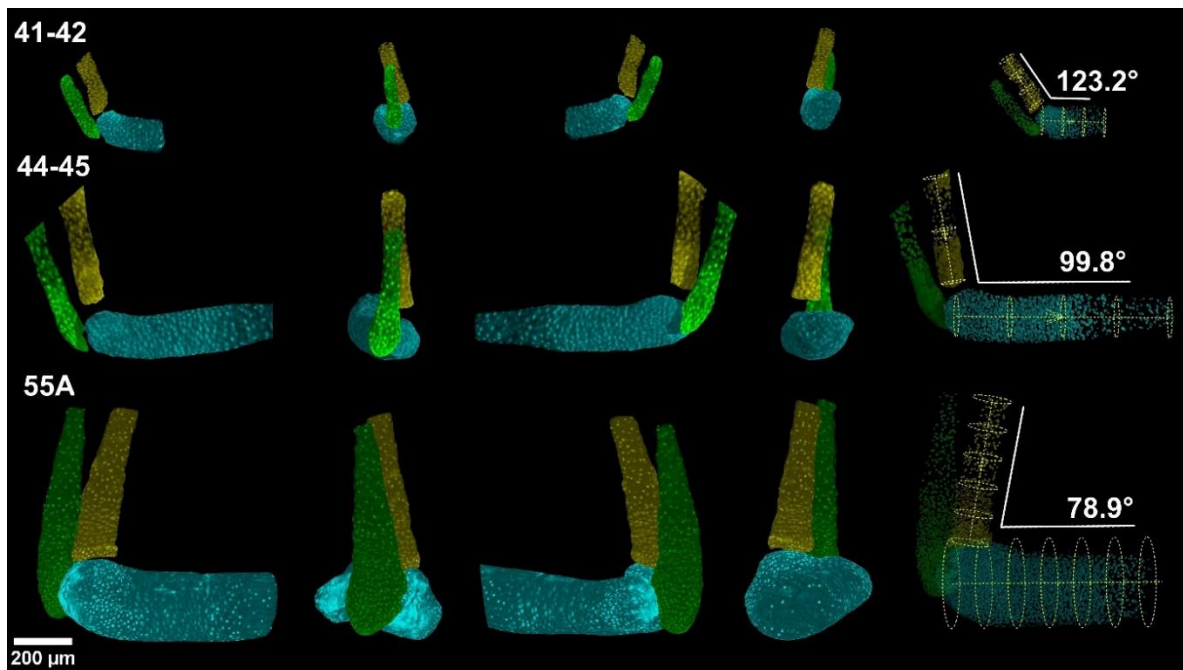


Figure 4.11: Development of the joint for three different developmental stages (41-42, 44-45 and 55A). The angle between *ulna* and *humerus* is decreasing with increasing developmental stage [60].

4.3 Adaptation of *Proteus anguinus* to dark habitats

The salamander species most often used in regeneration research are the *Ambystoma mexicanum* and three species of newts (*Notophthalmus viridescens*, *Cynops pyrrhogaster*, and *Pleurodeles waltl*) [63]. When exploring regeneration salamander species, we mainly worked on typical modern organisms *Pleurodeles waltl* and *Ambystoma mexicanum*. However, looking to the other, not so common species could give a new insight into the regeneration capabilities of amphibians. Thanks to the strategic partnership with synchrotron Elettra and its location in Dinaric karst, we got an opportunity to meet another salamander species – *Proteus Anguinus*, also known as olm or simply proteus. Proteus is the largest cave tetrapod and the only European amphibian living exclusively in subterranean environments. Its geographic distribution is limited to the Dinaric Karst; it ranges from the Gulf of Trieste in Italy through the southern half of Slovenia, the coastal mainland of Croatia and parts of Bosnia and Hercegovina, as far as adjacent parts of Montenegro [69, 70]. Proteus had a historical role during the formation of modern science from the 17th to 19th century, but also has the potential to answer the questions of today and future science (e.g., regeneration, cave-related adaptations, enormous genome, and conservation of subterranean biodiversity) [71]. However, specimens of proteus are rare and protected as proteus is currently classified as vulnerable [72].

For this reason, we accessed existing collections to avoid collecting them from nature. These animals died of natural causes, and their bodies were preserved (stored in 75% ethanol). We accessed the collection in Speleovivarium Trieste, Tular Cave Institute and the University of Ljubljana. We applied non-destructive staining and non-destructive imaging and then returned the specimens to the collection. The image of proteus captured in Tular Cave Institute is shown in Fig. 4.12.



Figure 4.12: Live image of *Proteus anguinus*. The image was taken by Gregor Aljančič at Tular Cave Institute.

For this study, we wanted to cover more developmental stages of proteus, and thus we accessed different collections to visualise larval and adult stages. Specifically: larva, 3 weeks old, captive breeding originating from the Postojna-Planina Cave System, from the collection of the Tular Cave Laboratory (Slovenia); juvenile, deceased at the collection site in a spring near Metković (Croatia), from the collection of the Department of Biology, Biotechnical Faculty, University of Ljubljana (Slovenia); adult, collected in Postojna-Planina Cave System (Slovenia, 1989), died in captivity of the Speleovivarium in 1999, from the collection of the Speleovivarium Erwin Pichl (Italy) [73].

Figure 4.13 shows 3D reconstructions of soft tissues in the head of proteus for three developmental stages. We focused on cartilaginous chondrocranium, brain and sensory organs, as olfactory epithelium and the presence of eyes. I was able to find eyes at larval and juvenile proteus, but no remnant of eyes was found in the adult. However, the absence of remnant eyes in microCT data can be caused by the low grayscale value contrast of the eye compared to other structures as the segmentation was done manually [73].

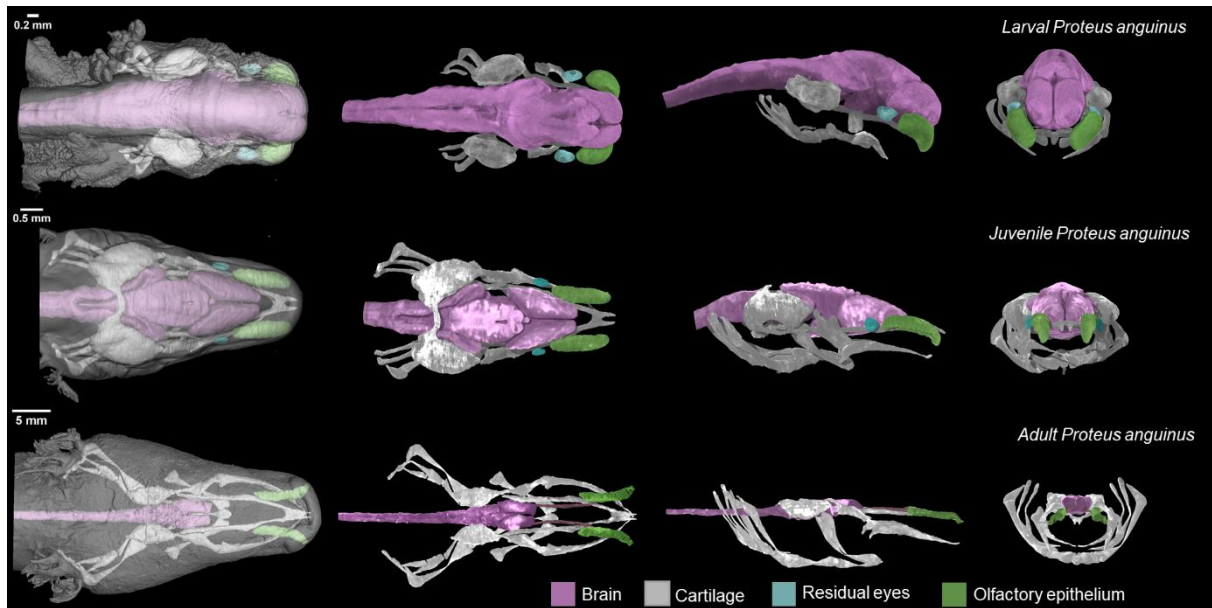


Figure 4.13: 3D reconstructions of proteus head. Larva (top), juvenile (middle) and adult (bottom). Images in the first column show semi-transparent 3D renderings of the head with skin in dorsal view. Dorsal, lateral and frontal views of the segmented internal soft structures are shown in the second to the fourth column [73].

Also, we compared proteus with *Ambystoma mexicanum*, also known as the axolotl, to make a model comparison between cave- and surface-dwelling paedomorphic salamanders. The visualisations and detailed commentary can be found in the attached manuscript [73]. By microCT scanning with a conventional source, we got excellent data quality, and single cells could be identified in cartilaginous elements. However, even though cells can be seen by the human eye, their automatic segmentation and quantification can be further challenging. The potential of X-ray microCT imaging with synchrotron imaging on salamander limbs has been discussed in chapter 4.2. Based on our partnership with Synchrotron Elettra and as this project was created in close cooperation with this institution, we decided to go also for synchrotron experiments. A comparison of the conventional and synchrotron X-ray microCT is reported in Fig. 4.14. Here, I show the potential of synchrotron imaging on larvae of *Ambystoma mexicanum* in the head structures (brain and eye). Such data can be used for mathematical modelling regarding joint shaping [74] or more general regenerative dynamics in various skeletal and non-skeletal tissues.

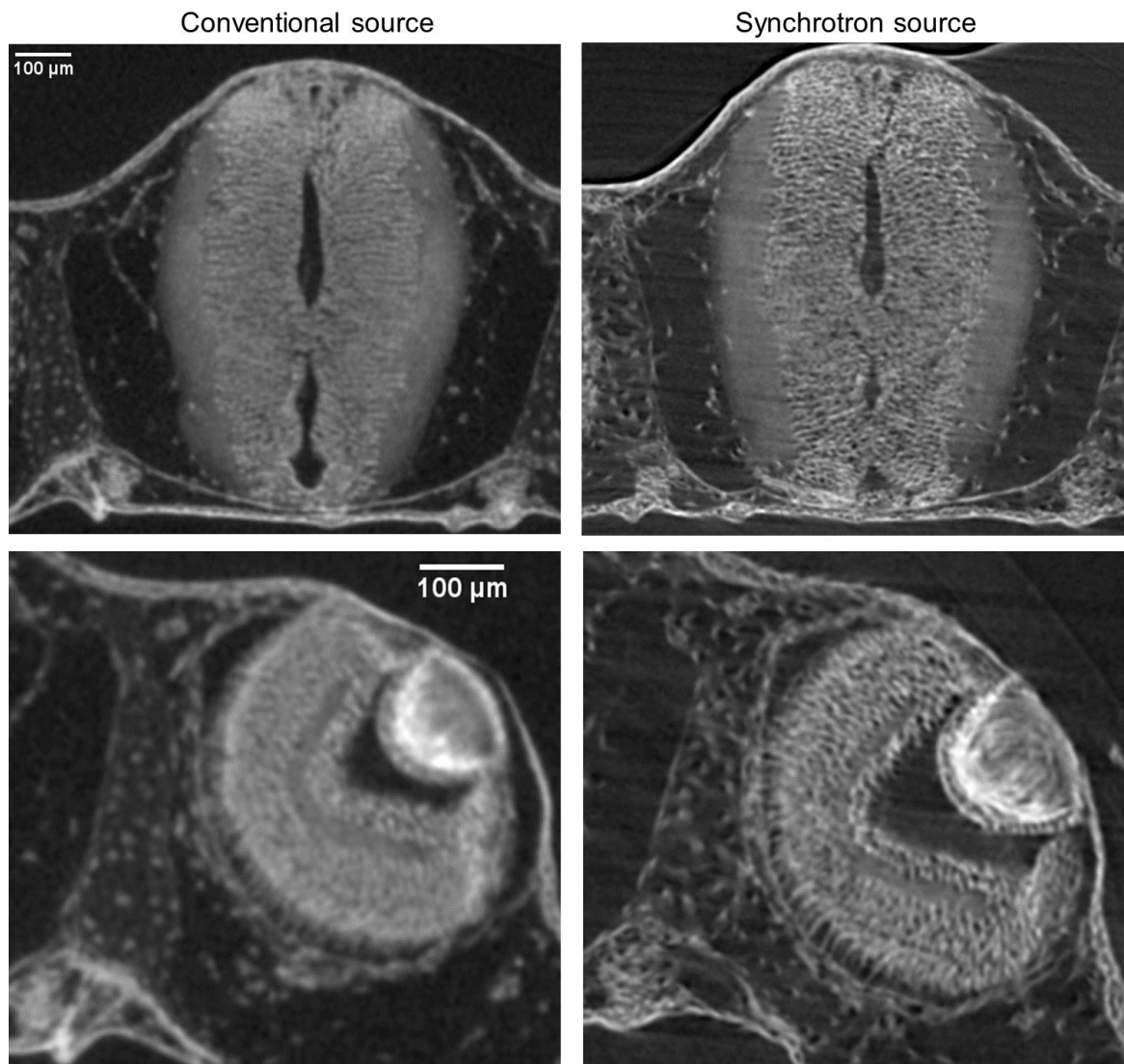


Figure 4.14: Comparison of conventional and synchrotron sources. The top images show the brain of *Ambystoma mexicanum* larvae, and the bottom images show its eye.

4.3.1 Frequency response analysis and future work

Based on microCT 3D reconstructions, we tried to understand how proteus adapts to living in the dark habitat. We hypothesized that proteus could rely on sound and vibrations transmitted by the elongated jaw bones. To prove that, we wanted to look at the resonating frequencies for such hypothetical sound transmission compared to the axolotl, another salamander living in the open air. We were able to reconstruct ear labyrinths for proteus and axolotl species, create STL models, and look at some simulations of resonating frequencies. Fig. 4.15 shows frequency response analysis for a frequency of 160 kHz. Frequency response analysis measures the ear labyrinth's response to an acoustic stimulus with an increasing frequency and a constant amplitude. We looked at the acoustic modes of the ear labyrinths and determined the resonating frequencies for the system. This simulation was done by Anass Bouchnita (University of Texas, USA). In our future work, we would like to look in more detail at all reconstructed ear labyrinths and try to understand the physics of sound transmission. Another interesting area for future work is understanding the predatory behaviour of proteus, and we would like to do biting analyses based on the 3D model of jaws and facial muscles. This type of analysis may shed light on the predatory abilities of proteus.

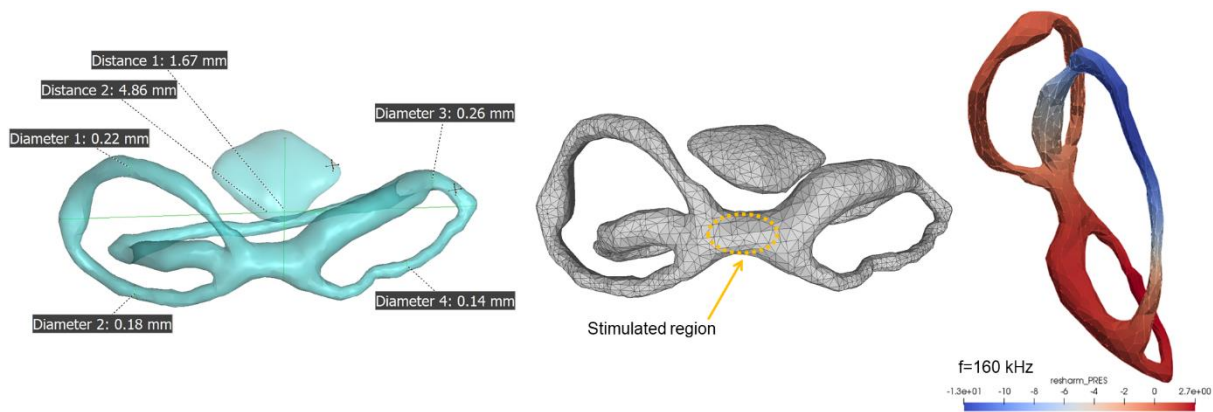


Figure 4.15: Detail analysis of ear labyrinth of adult proteus. The left image shows 3D reconstruction based on microCT data with dimensions measurements. The middle image shows the STL object with mesh and schematically shown area of stimulation for frequency response analysis ($f=160$ kHz).

Simulation done by Anass Bouchnita (University of Texas, USA).

4.4 Vertebrate cartilage growth studied on mouse embryos

Cartilage is the core of embryo growth and shaping before the bone forms. It is an essential skeletal and supportive tissue in our body. The shape and size of each cartilage element result from complex developmental processes. Cartilage elements vary widely in shape: they may be simple shapes like rods or bars (Meckel, cartilage templates of the future long bones and ribs) or sheet-like structures (in the head) but can be highly complicated with many irregular shapes [31, 32].

The craniofacial region consists of diverse embryonic cell types, including skeletal, muscular and nervous components [75]. The final shape of the face strongly depends on the geometry of the skeletal elements and their interaction with adjacent soft tissues such as muscles and the nervous system [31, 32]. In the human embryo, defects in cellular processes can affect the developmental program leading to congenital disabilities [31, 32, 76]. Numerous congenital craniofacial abnormalities affect the face's form and function, and explanations of these malformations still await the understanding [77]. According to the World Health Organization, genetic disorders have an incidence of 3 % in the human population [78], and they are causal for up to one-quarter of all reported neonatal deaths [79]. Thus, contextual visualisation of embryonic development is critical to clarify the origins of malformations [61].

The mouse model is a compelling experimental model: it is a mammalian system with similar embryology, anatomy and physiology to humans; genes, proteins and regulatory programs are largely conserved between humans and mice [80]. The developing cartilaginous skull, the chondrocranium, displays a complex geometry of mostly sheet-like cartilages resulting from coordinated anisotropic growth in all dimensions. To understand the changes in dimensions of chondrocranium growth at major developmental stages, we created 3D reconstructions of cartilaginous chondrocranium (Fig. 4.16). Based on 3D microCT reconstructions of mouse chondrocranium, we were able to report a novel principle of vertebrate cartilage growth based on introducing transversally-oriented clones into pre-existing cartilage [31]. The microCT analysis, followed by 3D quantification, has enabled the understanding of complex morphological aspects of face development [31, 32, 76], which is further described in this chapter.

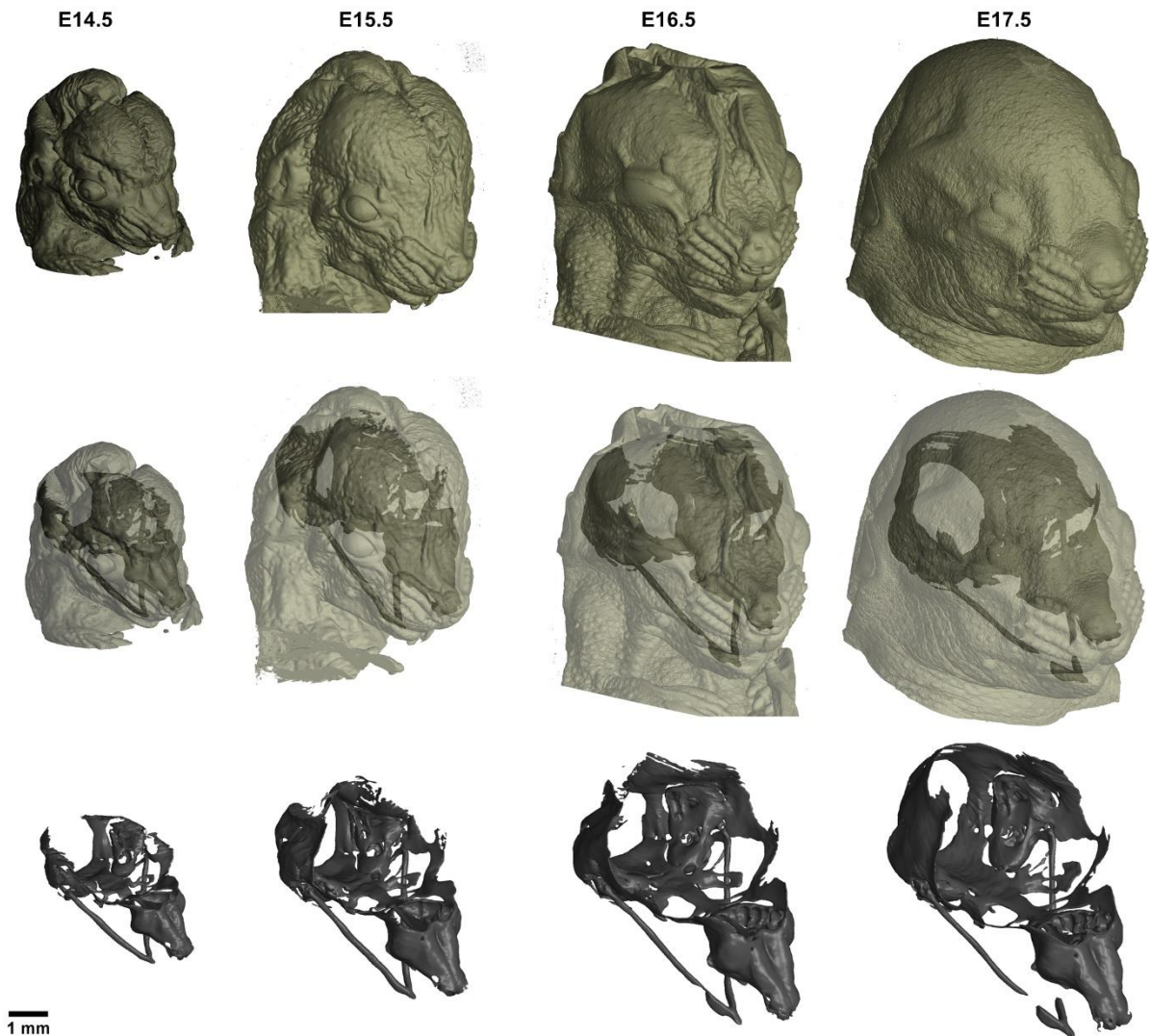


Figure 4.16: 3D reconstructions and segmentations of cartilaginous chondrocranium in mouse embryos, developmental stage E14.5-E17.5 The top row shows the 3D rendering of skin. The middle row shows semi-transparent heads with segmented chondrocranium. The bottom image shows only cartilaginous chondrocranium.

Also, in this project, it was crucial to distinguish mesenchymal condensations, cartilage and bone. Mesenchymal condensations are the stage before early cartilages start to form, and thus, the segmentation in microCT data was challenging. On the opposite, the transition of cartilage to bone was clearly recorded in the data as synchondroses are involved in this transformation. Synchondroses have a lower density than cartilage and newly formed bone, and thus, they can be detected as darker areas with lower attenuation (Fig. 4.17). Since growth plates or synchondroses are oriented towards a specific direction, expanding cartilage in other dimensions was unclear and required further investigation [31].

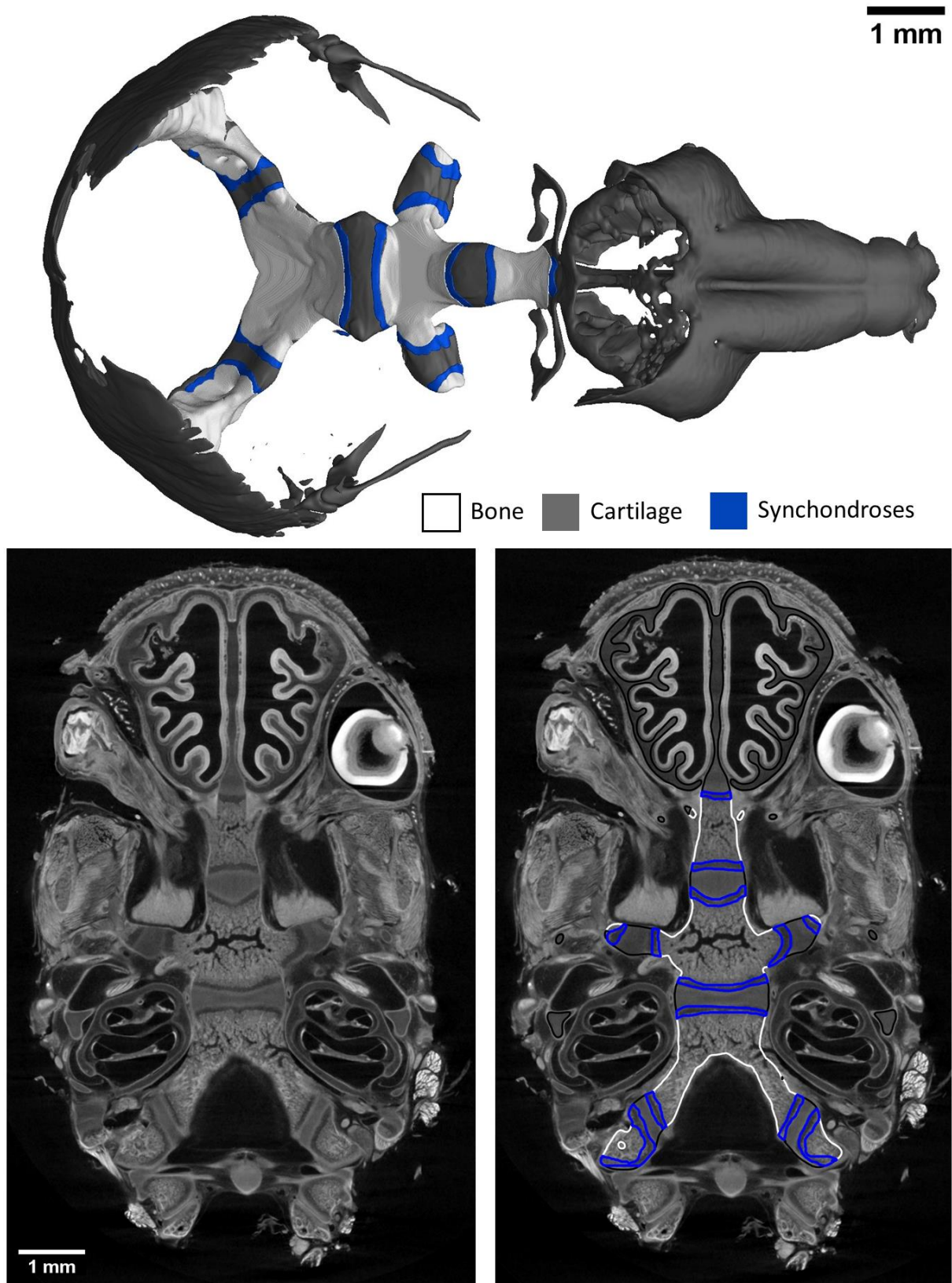


Figure 4.17: 3D reconstructions of cartilage, bone and synchondroses in mouse 2 days after born (P2). A corresponding CT slice with segmented structures is shown in the bottom part. Modified from [31].

4.4.1 Wall thickness analysis

By observing the results of cartilaginous nasal capsules from different developmental stages, E14.5 generally establishes the shape of the structure. Nevertheless, from E14.5 until E17.5 the cartilaginous nasal capsule is accurately scaled up with significant geometrical tuning. Therefore, we wanted to understand the mechanism of scaling and whether cartilage thickens or narrows during development. We applied wall thickness analysis in software VG Studio MAX to study this process. The analysis inscribes the sphere to the STL model, and the diameter of the inscribed sphere is taken as the “wall thickness”. Surprisingly, the thickness of the cartilaginous sheets did not change as much as the other dimensions during nasal capsule growth. Thus, the sheet-shaped cartilage expands mainly laterally (within the plane) during directional growth (Fig. 4.18) [31].

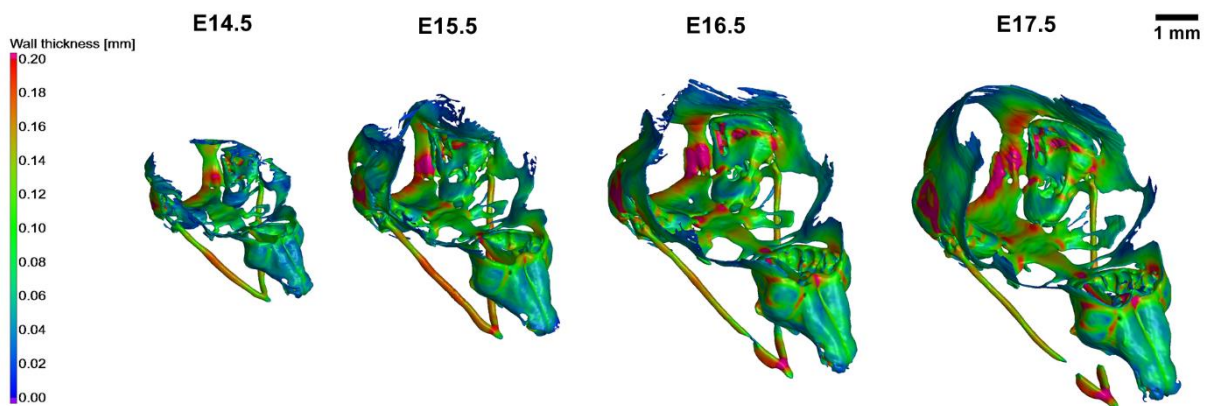


Figure 4.18: Wall thickness analysis of the cartilaginous chondrocranium of mouse embryos developmental stages E14.5-E17.5

4.4.2 Shape comparison

Also, we wanted to compare the shapes of the nasal capsules of major developmental stages and at five Wnt/PCP mutants ($Wnt5a^{-/-}$, $Vangl2^{-/-}$ and $Ror2^{-/-}$ together with $Vangl2^{+/-}Ror2^{+/-}$ heterozygous control). By simple look, the shape of the nasal capsules seemed very similar to one another for normally developing stages. However, we wanted some quantification to prove the exact shape of the segmented models. A typical way of comparison of 3D models is morphometric analysis. Traditional morphometrics relies on measurements such as linear distances, angles, weights or areas. However, most modern morphometric approaches are based on an analysis of landmarks. It means that set of landmarks is set on the 3D model. The assumption is that these landmarks are defined homologously across models. A particular landmark should unequivocally correspond to the same point across the stages etc. However, homology is a significant issue for morphometrics [81]. In our study, we defined the landmarks as shown in Fig. 4.19: Here, five representative distances were determined on the nasal capsule and these distances were measured for analysed developmental stages. Then, proportions were compared.

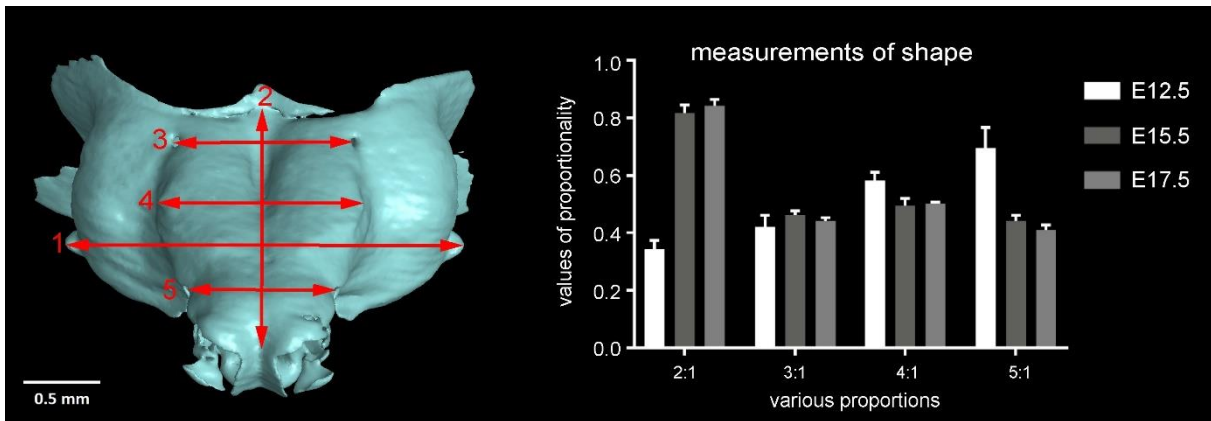


Figure 4.19: Morphometric analysis of E12.5, E15.5 and E17.5 stages. Red dimensions in the blue nasal capsule show the measurements used for morphometric analysis [31].

Even though morphometric analysis gave us logical and presumed data, we looked for further options on how to compare the shapes in a more intuitive demonstrative way that will not be dependent on the definition of landmarks. The best uniform option was given by the shape comparison analysis that is often used in the industrial sector for the comparison of two CAD/STL models. According to their septum, the nasal capsules were converted into STL files and registered in one coordinate system. Then, registered 3D models were compared (always the older one to the previous developmental stage) in a GOM Inspect Software by finding the closest distance between models with the searching angle of 30°. Finally, the same procedure compared E15.5 Wnt/PCP mutants to the same developmental stage of a wild-type control embryo. The result of the analysis is shown in Fig. 4.20.

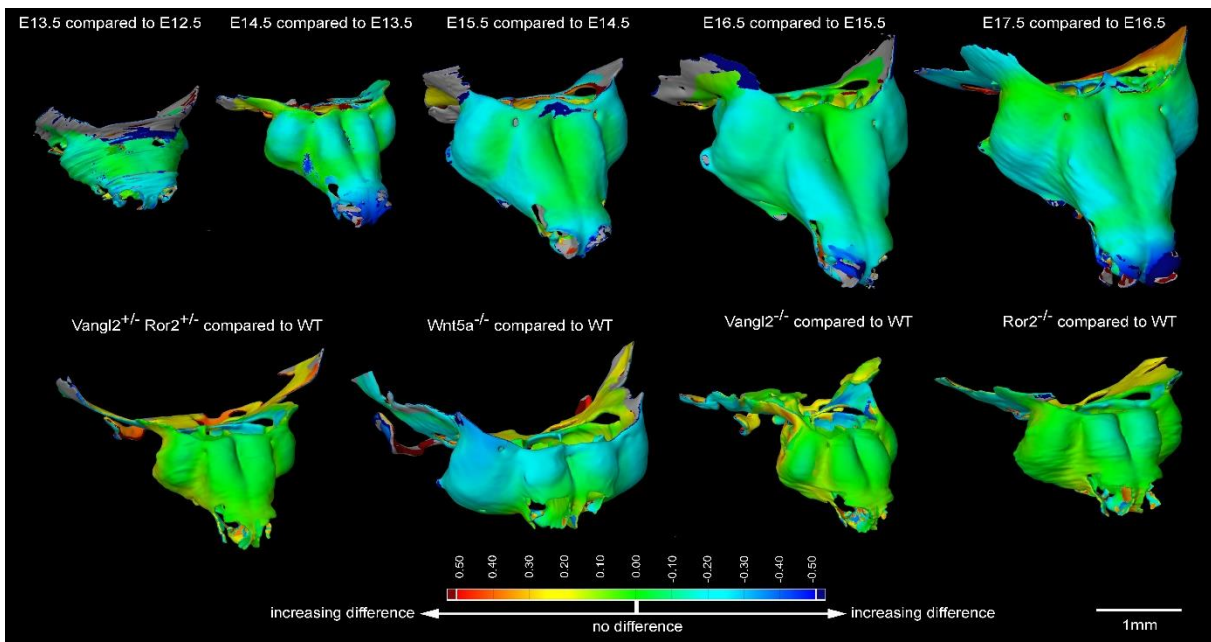


Figure 4.20: Shape comparison between control developmental stages and Wnt/PCP mutants. Colouration represents the incremental difference in the shape of the compared samples from green to red or blue colour [31].

4.4.3 Modelling of cell division based on microCT models

A significant advantage of segmented microCT 3D models is that they can be transformed into polygonal mesh suitable for other techniques such as 3D printing [11] or mathematical modelling. In this project, segmented cartilage was taken as an input to modelling uneven growth in shaping the nasal capsule. To exploit that, it was necessary to determine areas with different proliferation. To track and visualise the speed of proliferation, microCT data were combined with EdU labelling and fluorescence microscopy (Fig. 4.21). For each fluorescence image, a corresponding microCT slice was found and based on the number of tracked cells, sub-3D-models were created based on the original nasal capsule model. By tracking and matching the whole 3D microCT dataset with data from microCT, different proliferation was determined in 3D. More details on mathematical modelling can be found in the attached publication [31].

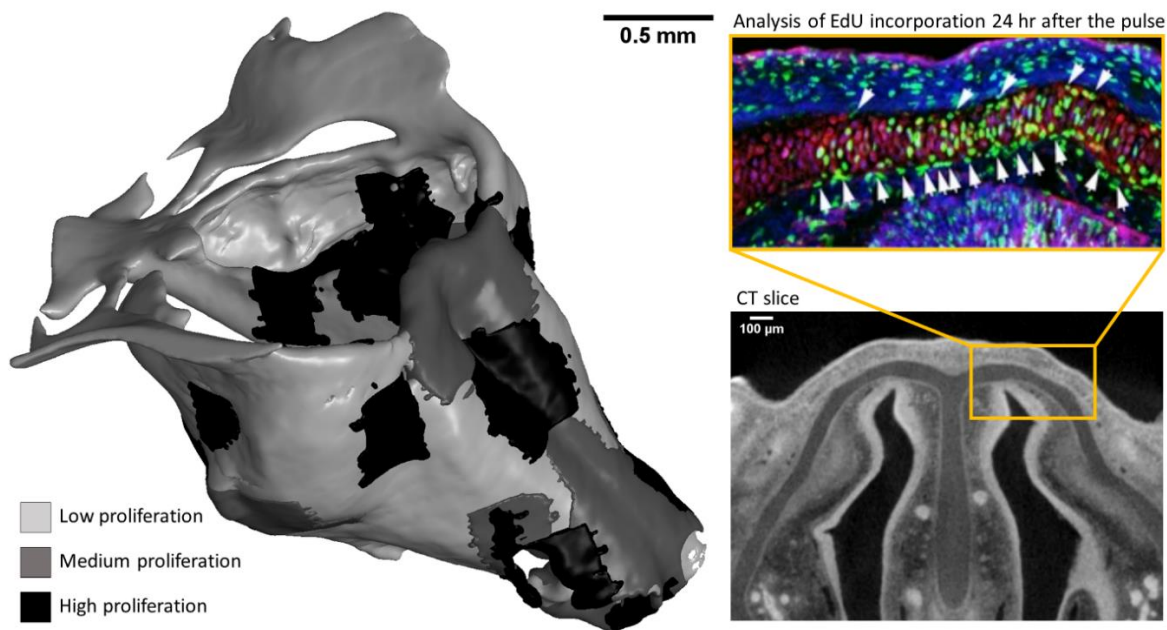


Figure 4.21: Input for modelling of uneven growth in a nasal capsule. The left image shows different cell proliferation in the 3D model. Right images show the creation of these growth zones based on matching EdU incorporation [31] with microCT slices.

4.4.4 Re-use potential

The presented 3D datasets with segmented craniofacial cartilage were published in Gigascience Database (GigaDB) [82]. In addition, reusable tomographic data from 7 full 3D scans of mouse embryo heads (E12.5-E18.5) were made publicly available. Such datasets published in public repositories such as GigaDB are linked and cited in the paper through a citable DOI (Digital Object Identifier), providing stability and, most importantly, additional discoverability and traceability [83]. This dataset can be taken as input in creating a robust method for segmentation cartilaginous structures from microCT data. Deep learning algorithms have lately dominated the field of image processing, and specifically, convolutional neural networks consistently achieve state-of-the-art results in fully automatic image segmentation tasks [84]. The dataset has been validated for deep learning algorithm 83 and can be used by other researchers for automatic and neural network segmentation. Also, there is a potential for biological re-use as mouse embryos are typical model organisms in developmental biology [80].

4.5 Extraocular muscles development

Among the craniofacial muscles, the morphology of the extraocular muscles (EOMs) has been a longstanding challenge in comparative anatomy and evolutionary biology. It had been unknown how the individual muscle masses emerge from the individual muscle anlagen and how the development of their tendons and attachment points is coordinated. These muscles do not have bone-to-bone attachments and constitute an evolutionary conserved cranial muscle unit. They are responsible for the coordinated movement of the eyeballs and vision. The basic EOM pattern is shared among all vertebrate classes. They include four recti muscles and two oblique muscles for eyeball movement [85-87]. Fig. 4.22 shows the anatomy of EOMs, and their responsible movements are described in Table 4.3.

This project investigated the morphogenesis of extraocular muscles (EOMs). The process of muscle patterning is essential for the acquisition of muscle shape and impacts the function of the adult muscles. While significant knowledge of the mechanisms of differentiation and patterning within individual tissues has been attained, much less about the patterning of different adjacent tissues [88, 89]. The study of muscles is usually done by confocal microscopy or optical projection tomography. However, these methods can visualize specific tissues such as muscles, but they do not give information about other anatomical structures such as eyeballs, cartilage, tendons etc. So knowing the position of the eyeball, lens and EOMs in the context of the whole head gives essential information about the developing structures. This project aimed to build a precise spatiotemporal map of EOMs and quantify changes between developmental stages and genetically modified mice or after inhibitor treatments. By creating microCT 3D reconstructions, we identified a time window in which individual EOMs emerge from a unique muscle anlage and establish insertions in the sclera [90]. Also, connective tissue, tendons, and attachment points were visualized to determine whether they are derived from neural crest lineage.

The detail of this project can be found in the attached publication [90]. This chapter then describes microCT analysis and quantitative measurements as ventralization of the eyeball or distance of *superior rectus* muscle from the eyeball.

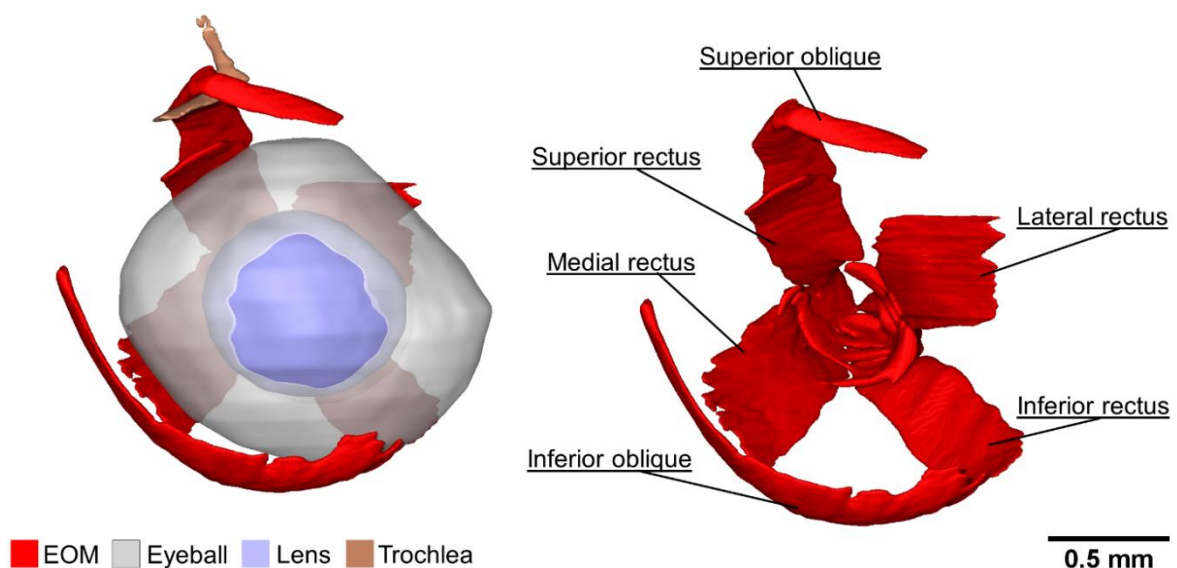


Figure 4.22: 3D reconstruction of extraocular muscles (EOM), eyeball, lens and trochlea in mouse embryo head 17.5 days post-fertilisation.

Table 4.3: Extraocular muscles and their responsible movement of the eye [91].

Name of the muscle	Responsible movement
<i>Superior oblique</i>	Downward and outward
<i>Superior rectus</i>	Upward
<i>Lateral rectus</i>	Outward
<i>Medial rectus</i>	Inward
<i>Inferior rectus</i>	Downward
<i>Inferior oblique</i>	Upward and outward

4.5.1 Ventralization of the eyeball

By PTA contrasting and subsequent segmentation of microCT data, we got a precise spatiotemporal atlas of the development of EOMs, eyeball, lens and optic nerve. We got information on these structures in one 3D dataset. Besides that, we observed these structures in the context of developing cartilage and the skin of the mouse embryos. To have the context of the developing structures was crucial when comparing normal development with genetically modified embryos. For BMS493-treated embryos, we noticed that eye of the mutant “looks down” compared to the control one. In other words, there is a ventralization of the eyeball. The ventralization for mouse embryos 13.5 days post fertilisation is shown in Fig. 4.23. We wanted to have a specific number representing the changes between the mutant and the control to describe this phenomenon. Therefore, we decided to measure the angle of inclination.

In geometry, the angle can be defined as the figure formed by two rays meeting at a common endpoint. For our purpose, we needed the definition of these two rays that will fit the geometry of the developing eye. Firstly, we fitted geometrical objects to selected biological structures: Two spheres were fitted to the eyeball and lens, and one cylinder was fitted into the eye nerve. Secondly, the first ray was defined as the axe of the cylinder and the second ray was defined as the vector for the nearest distance between eyeball and lens. Finally, the angle of inclination was den calculated as the angle of these two rays. The individual steps of this analysis and the computation result are shown in Fig. 4.24. In this way, the actual number was determined that describes the observed fact that mutant looks down in comparison with control.



Figure 4.23: Comparison of control and genetically modified (BMS493-treated) mouse embryos 13.5 days post-fertilisation. The top images show the 3D rendering of the skin of the whole head. The middle images show semi-transparent skin with the segmented eyeball, lens, optic nerve and EOMs. The bottom images show only segmented structures. The perspective of the eyeball in the whole head shows ventralization in the mutant.

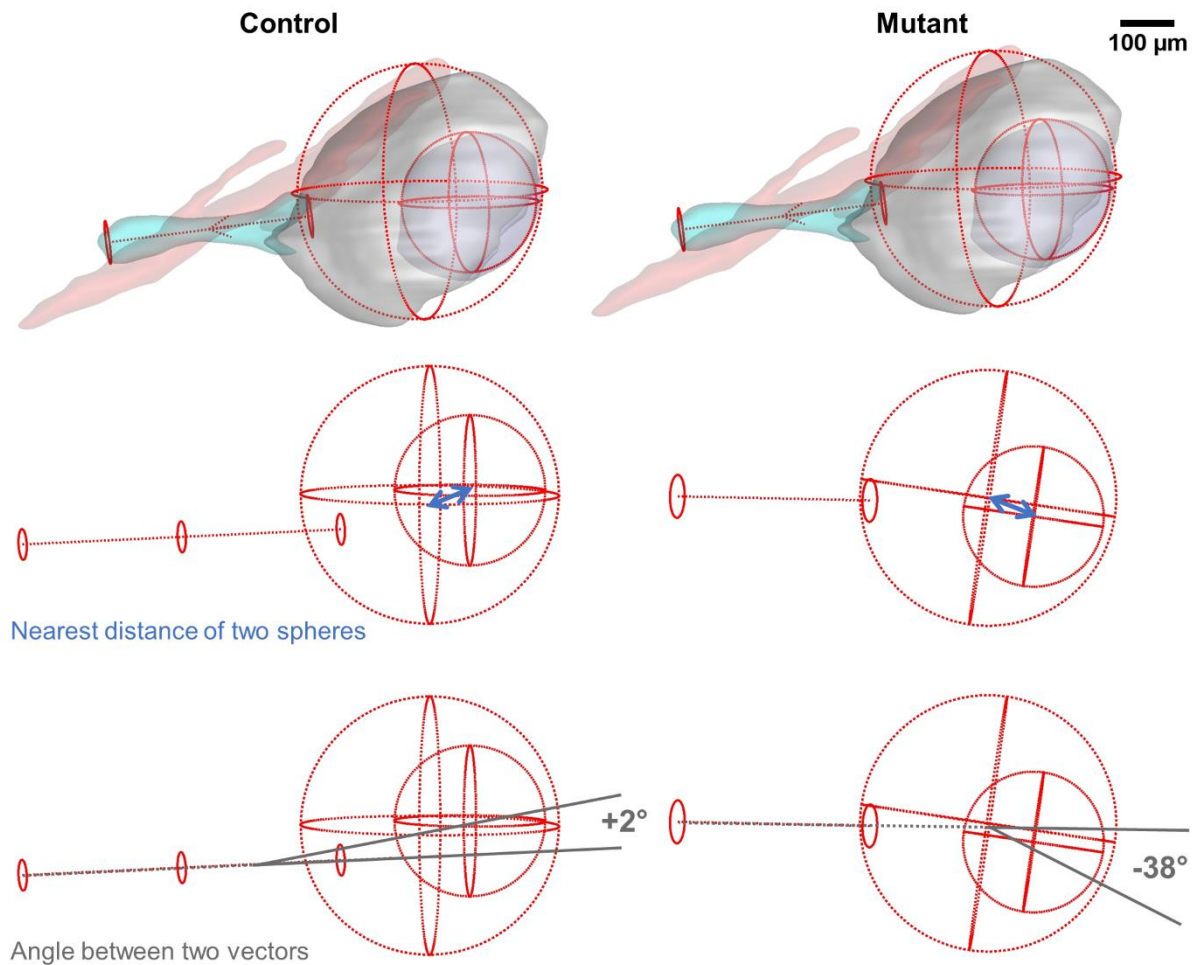


Figure 4.24: Fitting geometrical objects to biological structures. A cylinder is fitted to the optic nerve, and spheres are fitted to the eyeball and lens. The difference between a control and a mutant (BMS493-treated) is 40° .

Another interesting phenomenon observed in 3D models was the distance of the *superior rectus* muscle from the eyeball. It seemed that this muscle was going very near to the eyeball in the control embryo. However, at the mutant, the distance seemed farther. Firstly, we looked at tomographic slices of the reconstructed volume. As there is a ventralization of the mutant eyeball, it is very challenging to find corresponding orientation for two volumes of two different samples. Based on this fact, I fitted one point to the muscle and one point to the eyeball, but also this procedure is dependent on the operator, so I further looked for other options on how to determine this distance. The best option seemed to fit additional volume between the muscle and the eyeball. In the second step, I subtract the segmented structures from the volume. In the third step, I looked at the “thickness” of the gap between the structures. The result of this analysis is shown in Fig. 4.25. By calculating the thickness of this gap, the procedure becomes fully automatic and is not dependent on the operator. The manually measured distances can serve as the control for the automatic wall thickness analysis.

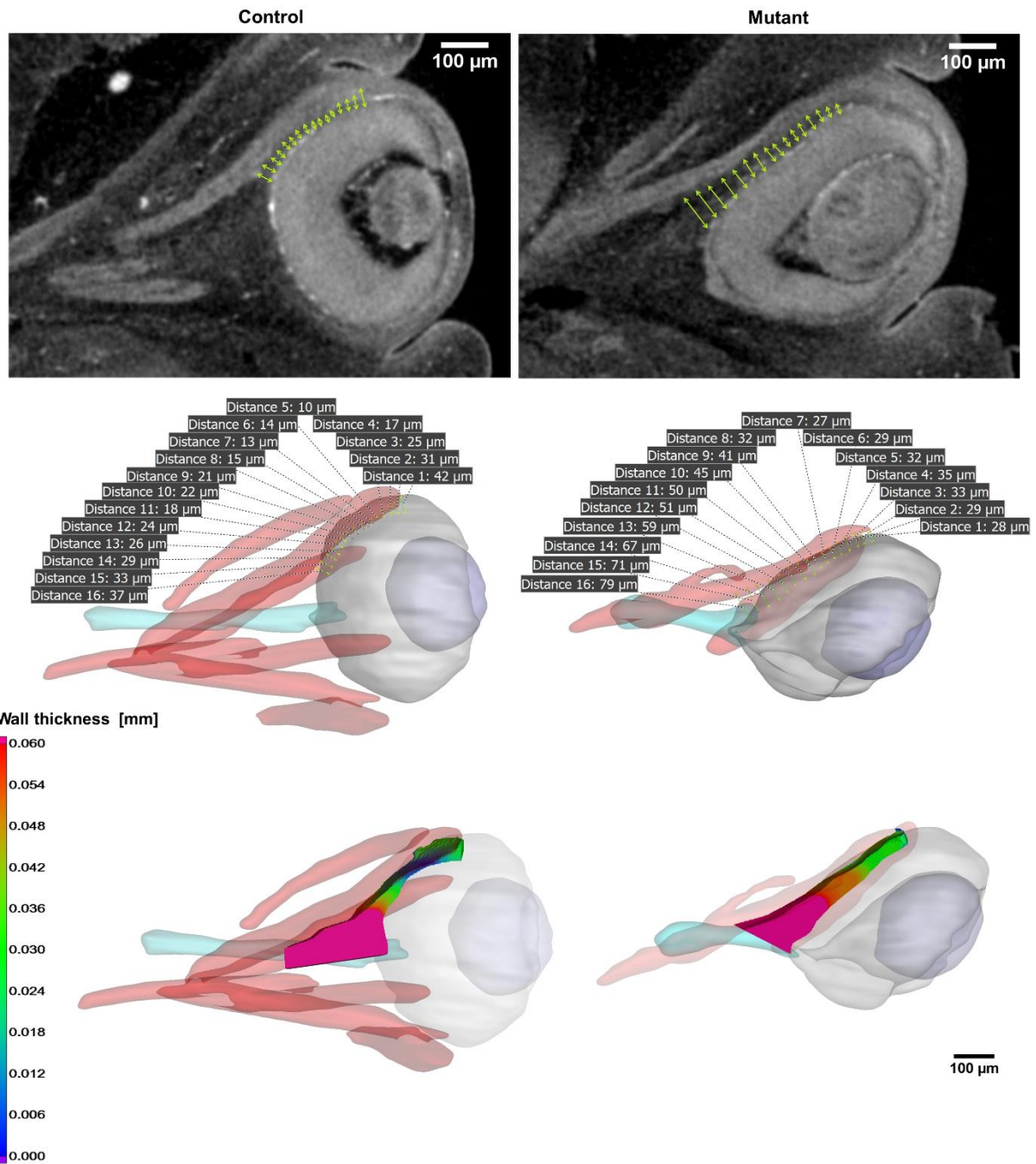


Figure 4.25: Measurement of distance between *superior rectus* muscle and eyeball for control and mutant embryo (BMS493-treated) 13.5 days post-fertilisation. The top images show CT slices, and green arrows indicate the distance to be measured between the muscle and eyeball. Middle images show manually measured distance. The bottom images show distance measured in 3D by determining wall thickness on volume inserted between the muscle and the eyeball.

5 Combination of microCT with other methods

5.1 Neck muscles and associated connective tissues

The neck is composed of approximately 80 skeletal muscles that allow head mobility, respiration, swallowing, and vocalization processes in humans. A robust network of muscles ensures these processes at the head-trunk interface, a transition zone subjected to a spectrum of human muscle diseases [92-94]. Neck muscles have remained poorly defined due to their complex morphogenesis and dual mesodermal origins [95]. Describing the embryology of these distinct muscle groups is crucial to understanding the mechanisms underlying specific muscles' susceptibility to muscular dystrophies. While myogenesis at the cranial and trunk levels has been studied extensively, the developmental mechanisms at the basis of neck muscle formation are poorly documented and often debated [96].

To describe the origins of different muscle groups, we combined immunostaining on sections and 3D microCT reconstructions of the neck and pectoral girdle of control and two genetically-modified embryos (Tbx1^{-/-} and Pax3^{-/-}) [95]. All samples were 18.5 days post-fertilisation. Because of the larger size of this developmental stage and possible limited staining penetration, we decided to cut off the area of interest for scanning. The cutting helped penetration a contrasting agent (PTA) into the sample. In other words, there was a dissection of the cervical region (including the mandible and scapular components). Thus, the staining time was reduced to 10 days. Another step for creating a 3D map of a neck region was to define the muscles of interest for 3D segmentation. When applying the staining procedure to soft tissues, segmentation is based on grayscale value and anatomical shape. However, using these criteria on muscles is quite challenging as they are hard to distinguish. To validate the neck muscles, we combined microCT data with immunostaining. Immunostaining clearly showed the individual muscles, but only on eight sections (Fig. 5.1) in the sample. In opposite, the resolution of microCT scanning was 5.7 μm for all samples but with lower differential contrast. The data showing both immunostaining and CT slices are shown in Fig. 5.2. When we combined information from both techniques by tracking marked muscles from immunostaining throughout microCT volume, we were able to get high-resolution reconstructions for muscles and skeletal elements in the context of the whole mouse embryo (Fig. 5.3).

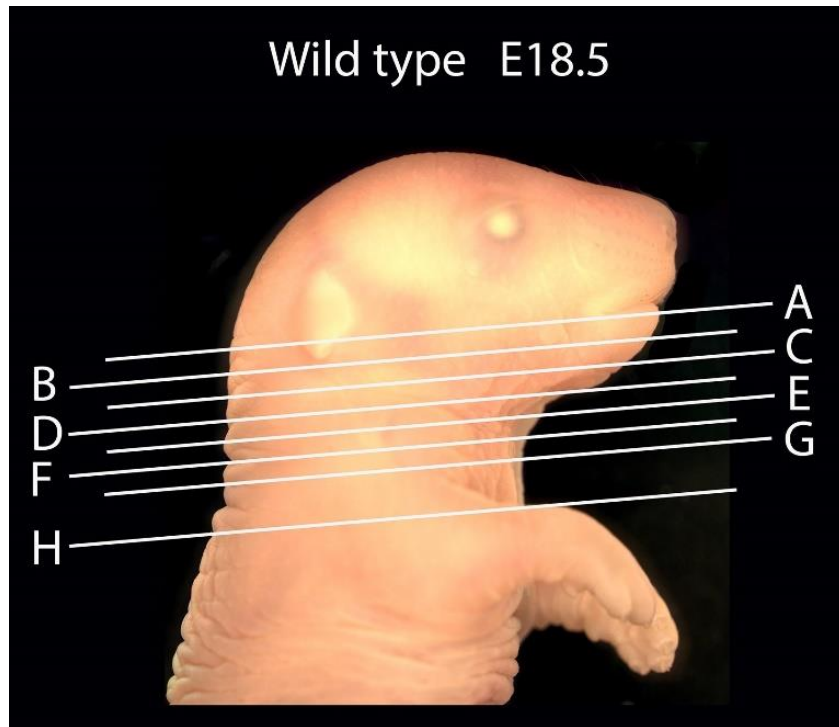


Figure 5.1. Mouse embryo 18.5 days post-fertilisation. Eight sections (A-H) indicate the planes of immunostaining that were subsequently matched with microCT data [97].

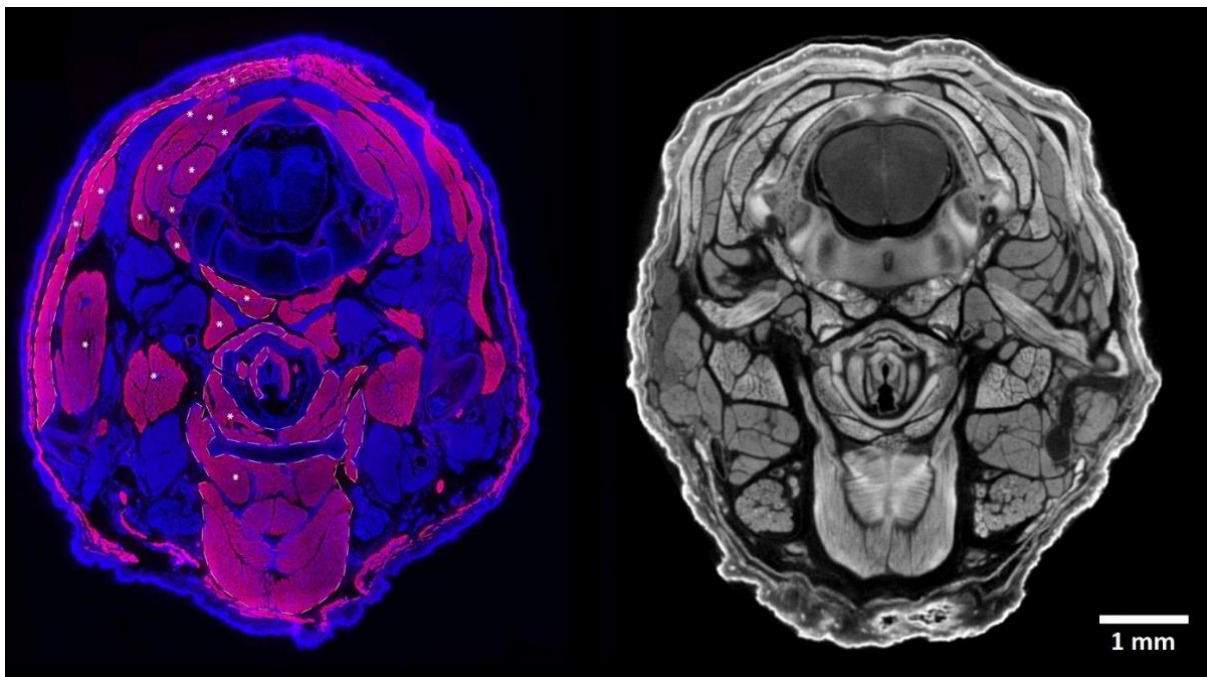


Figure 5.2. The immunostaining section (left) and corresponding CT slice of a mouse embryo (18.5 days post-fertilisation). The pink colour shows the muscles, and white asterisks mark the muscles that need to be visualized in 3D. Note similar contrast for muscles and other tissues at microCT slice [97].

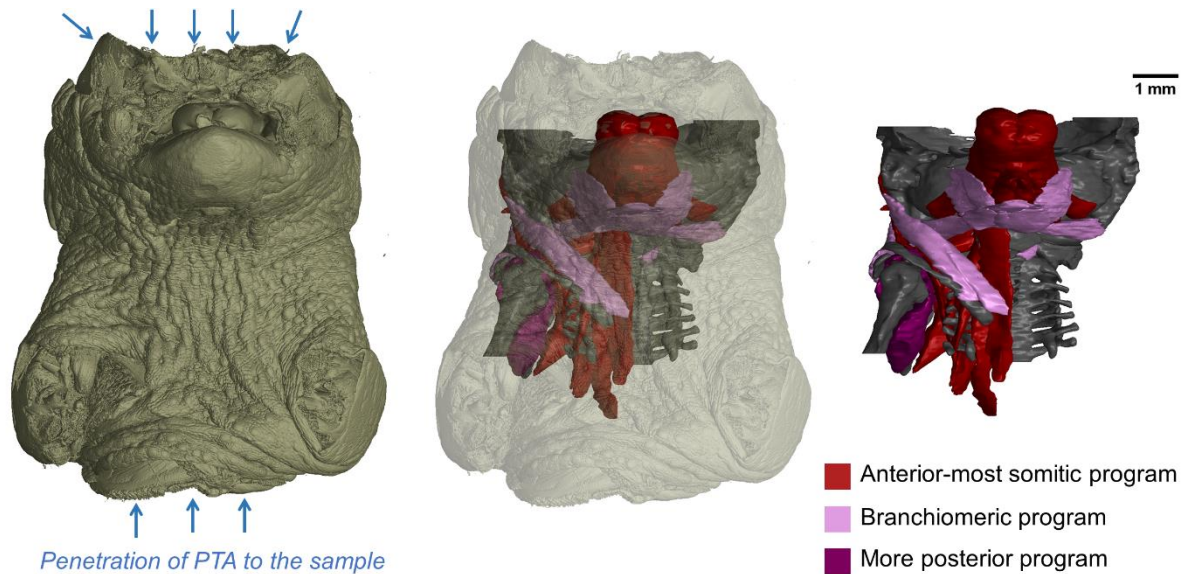


Figure 5.3: 3D reconstruction of the neck area of mouse embryo (18.5 days post-fertilisation). 3D rendering of skin (left), semi-transparent skin (middle) and segmented structures (right). Note cut in the area of head and abdomen. Blue arrows then indicate penetration of contrasting agent (PTA) to the sample in these areas.

Together with a 3D atlas of a control embryo, 18.5 days post-fertilisation, we analysed the effect of inactivation of *Tbx1* and *Pax3* genes on neck muscle formation, compared to the muscle phenotypes observed at cranial and trunk levels. Fig. 5.4 shows the reconstruction of the muscles and different colour-coding for anterior-most somatic, branchiomeric and more posterior programs. Fig. 5.5 shows then only cartilaginous reconstructions for better clarity. Note the malformation of trapezius muscle affected in *Pax3*^{Cre/Cre} and missing entirely in *Tbx1*^{-/-}. On the contrary, scapular muscles of the more posterior program are not significantly affected in *Tbx1*^{-/-} but missing in *Pax3*^{Cre/Cre}. Also, intrinsic laryngeal muscles were affected together with skeletal elements of the larynx. More details of biological observations can be found in the attached publications [95].

When comparing differences between genetically modified samples and developmental programs, we generated many 2D images with different transparency from the 3D models, different zooming etc. As a result, it became hard to get oriented in a generated data. For this reason, we began to look for the other way to put the 3D models into the publication so that anyone can access them without the need for specialised software. The best suitable option turned out to convert 3D models into interactive 3D PDF format. In this way, microCT data can be interpreted in small file format, readable on all operating systems using the widely used Portable Document Format (PDF). To convert the biological models into this type of document, I faced some challenges such as the size of the data, the colouring of the models with the conservation of sub-models hierarchy etc. First, I wrote down all the challenges that I faced during the creation of the model. Then, I formed a manual describing individual steps, starting with segmentation of the data and surface extraction to embedding models into interactive 3D PDF files. This manual was also published with an example of craniofacial structures, so anyone working with a 3D imaging technique can use our user-friendly protocol [61]. We believe that intuitive and interactive 3D PDF files have a great potential for data sharing, communication, and publications.

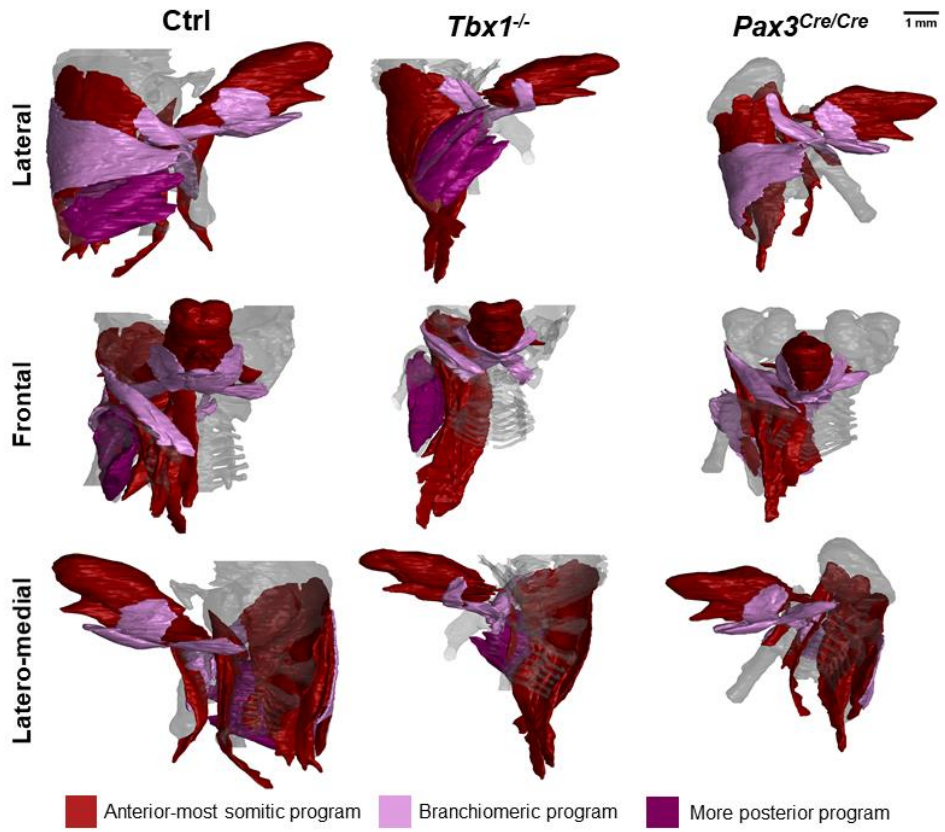


Fig. 5.4: 3D reconstructions of neck muscles in three mouse embryos: Ctrl (control) and two mutants (*Tbx1*^{-/-} and *Pax3*^{Cre/Cre}). Different colours correspond to different developmental programs.

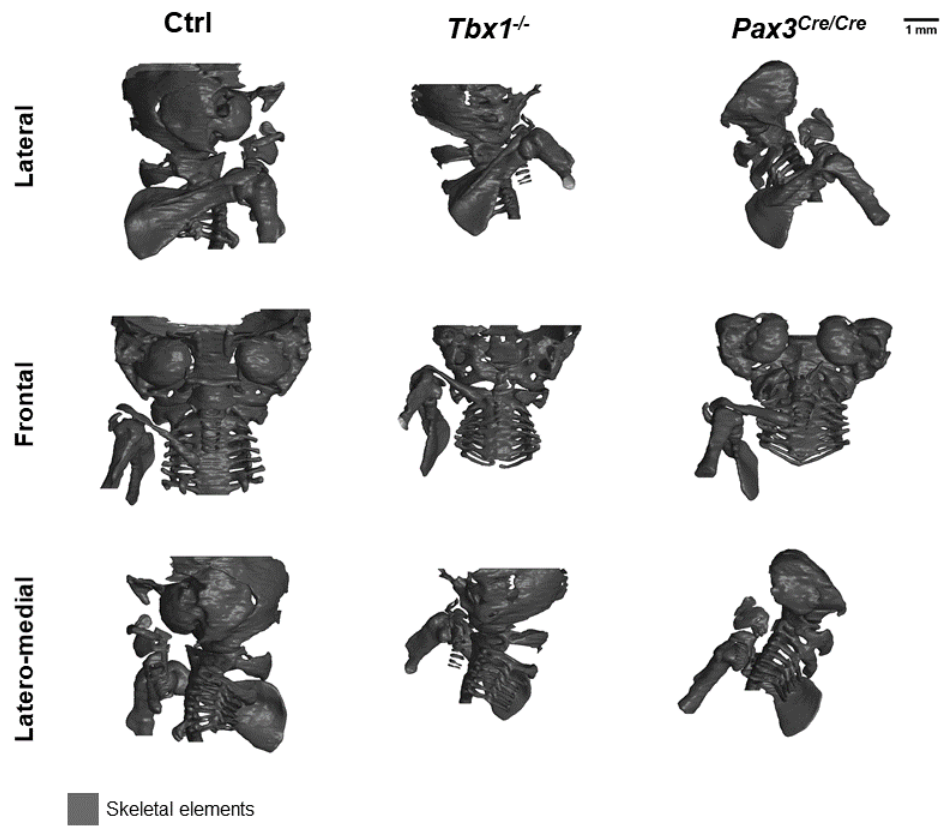


Fig. 5.5: 3D reconstructions of associated skeletal elements to which muscles attach.

6 Conclusion

This dissertation reflects the current need for the biological community for precise 3D characterisation of studied structures. The microCT technique has shown great potential in developmental biology in recent years. However, there has been a lack of methodology for the quantitative characterization of 3D structures.

The particular applicability of this work is demonstrated in the research projects that have been published in impact factor journals. Specifically, my dissertation focused on studying salamander limbs' regeneration down to cellular level in different salamander species: *Pleurodeles waltli*, *Ambystoma mexicanum* and rare cave amphibian *Proteus anguinus*. Above that, a digital atlas of proteus was created involving different developmental stages and comparison with surface-dwelling axolotl. Since these 3D models are published online, scientists worldwide can access and use these models in their research, which is particularly valuable given the proteus is an endangered and protected animal.

Another animal in which structures were thoroughly analysed was mouse and mouse embryos, respectively. Also here, we accessed a diverse range of developmental stages together with genetically-modified animals. Particular attention was given to soft tissues in the head that have not been analysed by microCT before. We focused on cartilaginous chondrocranium and quantitative comparison of thickness and shapes. Similarly, muscles with attachment points, tendons, and supportive tissues were visualised and analysed, focusing on their different developmental programs. Many samples were scanned and segmented, so also here, we created a digital atlas containing microCT data of major developmental stages and relevant segmentations. This mouse embryo atlas was again published online so that anyone can access this valuable data. The segmented cartilage was then used as an input for deep learning-based automatic segmentation. Thus, the effort and resources given to the 3D reconstructions can serve as the initial input for other scientific projects.

During the creation of 3D models and analysis, I faced many challenges: I fought with the contrast of soft tissues and staining protocols, unsolicited motion during microCT measurement and challenging data segmentation and 3D characterisation. In this work, I tried to address all topics relevant to microCT characterisation of biological structures in 3D, so any student or scientist dealing with a similar topic can take this document as a user-friendly recipe for their experiment.

7 References

- [1] J. Maddox, *The sensational discovery of X-rays*, *Nature* **vol. 375**, (1995).
- [2] *The Nobel Prize in Physics 1901 [online]*. Available from: https://www.nobelprize.org/nobel_prizes/physics/laureates/1901/ Visited on [2022-06-05].
- [3] J. Baruchel, *X-Ray Tomography in Material Science*, Hermes Science, Paris, ISBN 978-2-7462-0115-6 (2000).
- [4] J. Husband and G. Dombrowe, *X-ray computed tomography – a truly remarkable medical development*, *British Journal of Radiology* **vol. 78**, (2005).
- [5] V. Petrik, V. Apok, J. Britton, B. Bell and M. Papadopoulos, *Godfrey Hounsfield and the Dawn of Computed Tomography*, *Neurosurgery* **vol. 58**, (2006).
- [6] *The Nobel Prize in Physiology or Medicine 1979 [online]*. Available from: http://www.nobelprize.org/nobel_prizes/medicine/laureates/1979/ Visited on [2022-06-05].
- [7] W. Kalender, *Computed Tomography, Fundamentals, System Technology, Image Quality, Application*, 3rd, Publicis Publishing, Erlangen, ISBN 978-3-89578-317-3 (2011).
- [8] P. Withers, C. Bouman, S. Carmignato, V. Cnudde, D. Grimaldi, C. Hagen, E. Maire, M. Manley, A. Du Plessis and S. Stock, *X-ray computed tomography*, *Nat Rev Methods Primers* **vol. 1**, (2021).
- [9] A. Kak and M. Slaney, *Principles of Computerized Tomographic Imaging*, IEEE Press, New York, ISBN 0-87942-198-3 (1999).
- [10] A. Rosenfeld and A. Kak, *Digital Picture Processing, Computer Science and Applied Mathematics*, Academic Press Inc., ISBN 978-0-323-13991-5 (1982).
- [11] M. Tesařová, T. Zikmund, M. Kaucká, I. Adameyko, J. Jaroš, D. Paloušek, D. Škaroupka and J. Kaiser, *Use of micro computed-tomography and 3D printing for reverse engineering of mouse embryo nasal capsule*, *Journal of Instrumentation* **vol. 11**, (2016).
- [12] J. Hsieh, *Computed Tomography: Principles, Design, Artifacts, and Recent Advances*, 3rd, SPIE, Bellingham, Washington, USA, ISBN 978-1-62841-825-5 (2015).
- [13] P. Withers, *X-ray nanotomography*, *Materials Today* **vol. 10**, (2007).
- [14] D. Kalasová, *X-ray nano computed tomography of structured polymeric biomaterials*, Dissertation thesis. Brno University of Technology, Central European Institute of Technology (2019).
- [15] P. Willmott, *An Introduction to Synchrotron Radiation*, John Wiley & Sons, Ltd, Chichester, UK, ISBN 978-1-119-97095-8 (2011).

- [16] *The metal jet technology* [online. Available from: <https://www.excillum.com/our-products/metaljet/> Visited on [2022-04-02].
- [17] A. Astolfo, F. Arfelli, E. Schültke, S. James, L. Mancini and R. Menk, *A detailed study of gold-nanoparticle loaded cells using X-ray based techniques for cell-tracking applications with single-cell sensitivity*, *Nanoscale* **vol. 5**, (2013).
- [18] A. Carden, R. Rajachar, M. Morris and D. Kohn, *Ultrastructural Changes Accompanying the Mechanical Deformation of Bone Tissue: A Raman Imaging Study*, *Calcified Tissue International* **vol. 72**, (2003).
- [19] B. de Bakker, K. de Jong, J. Hagoort, R. Oostra and A. Moorman, *Towards a 3-dimensional atlas of the developing human embryo: The Amsterdam experience*, *Reproductive Toxicology* **vol. 34**, (2012).
- [20] B. de Bakker, K. de Jong, J. Hagoort, K. de Bree, C. Besselink, F. de Kanter, T. Veldhuis, B. Bais, R. Schildmeijer, J. Ruijter, R. Oostra, V. Christoffels and A. Moorman, *An interactive three-dimensional digital atlas and quantitative database of human development*, *Science* **vol. 354**, (2016).
- [21] B. de Boer, G. van den Berg, P. de Boer, A. Moorman and J. Ruijter, *Growth of the developing mouse heart: An interactive qualitative and quantitative 3D atlas*, *Developmental Biology* **vol. 368**, (2012).
- [22] E. Descamps, A. Sochacka, B. De Kegel, D. Van Loo, L. Van Hoorebeke and D. Adriaens, *Soft tissue discrimination with contrast agents using micro-CT scanning*, *Belgian Journal of Zoology* **vol. 144**, (2014).
- [23] M. Belle, D. Godefroy, G. Couly, S. Malone, F. Collier, P. Giacobini and A. Chédotal, *Tridimensional Visualization and Analysis of Early Human Development*, *Cell* **vol. 169**, (2017).
- [24] N. Renier, Z. Wu, D. Simon, J. Yang, P. Ariel and M. Tessier-Lavigne, *iDISCO: A Simple, Rapid Method to Immunolabel Large Tissue Samples for Volume Imaging*, *Cell* **vol. 159**, (2014).
- [25] M. Ragazzi, S. Piana, C. Longo, F. Castagnetti, M. Foroni, G. Ferrari, G. Gardini and G. Pellacani, *Fluorescence confocal microscopy for pathologists*, *Modern Pathology* **vol. 27**, (2014).
- [26] M. Dickinson, A. Flenniken, X. Ji, L. Teboul, M. Wong *et al.*, *High-throughput discovery of novel developmental phenotypes*, *Nature* **vol. 537**, (2016).
- [27] J. Sharpe, *Optical Projection Tomography as a Tool for 3D Microscopy and Gene Expression Studies*, *Science* **vol. 296**, (2002).
- [28] J. Sharpe, *Optical projection tomography as a new tool for studying embryo anatomy*, *Journal of Anatomy* **vol. 202**, (2003).

- [29] M. Wong, A. Dorr, J. Walls, J. Lerch and R. Henkelman, *A novel 3D mouse embryo atlas based on micro-CT*, *Development* **vol. 139**, (2012).
- [30] C. Hsu, L. Wong, T. Rasmussen, S. Kalaga, M. McElwee, L. Keith, R. Bohat, J. Seavitt, A. Beaudet and M. Dickinson, *Three-dimensional microCT imaging of mouse development from early post-implantation to early postnatal stages*, *Developmental Biology* **vol. 419**, (2016).
- [31] M. Kaucka, T. Zikmund, M. Tesarova, D. Gyllborg, A. Hellander, J. Jaros, J. Kaiser, J. Petersen, B. Szarowska, P. Newton, V. Dyachuk, L. Li, H. Qian, A. Johansson, Y. Mishina, J. Currie, E. Tanaka, A. Erickson, A. Dudley, H. Brismar, P. Southam, E. Coen, M. Chen, L. Weinstein, A. Hampl, E. Arenas, A. Chagin, K. Fried and I. Adameyko, *Oriented clonal cell dynamics enables accurate growth and shaping of vertebrate cartilage*, *eLife* **vol. 6**, (2017).
- [32] M. Kaucka, J. Petersen, M. Tesarova, B. Szarowska, M. Kastriti, M. Xie, A. Kicheva, K. Annusver, M. Kasper, O. Symmons, L. Pan, F. Spitz, J. Kaiser, M. Hovorakova, T. Zikmund, K. Sunadome, M. Matisse, H. Wang, U. Marklund, H. Abdo, P. Ernfors, P. Maire, M. Wurmser, A. Chagin, K. Fried and I. Adameyko, *Signals from the brain and olfactory epithelium control shaping of the mammalian nasal capsule cartilage*, *eLife* **vol. 7**, (2018).
- [33] S. de Bournonville, S. Vangrunderbeeck and G. Kerckhofs, *Contrast-Enhanced MicroCT for Virtual 3D Anatomical Pathology of Biological Tissues: A Literature Review*, *Contrast Media & Molecular Imaging* **vol. 2019**, (2019).
- [34] H. Lusic and M. Grinstaff, *X-ray-Computed Tomography Contrast Agents*, *Chemical Reviews* **vol. 113**, (2013).
- [35] J. Johnson, M. Hansen, I. Wu, L. Healy, C. Johnson, G. Jones, M. Capecchi, C. Keller and W. Frankel, *Virtual Histology of Transgenic Mouse Embryos for High-Throughput Phenotyping*, *PLoS Genetics* **vol. 2**, (2006).
- [36] B. Metscher, *MicroCT for comparative morphology: simple staining methods allow high-contrast 3D imaging of diverse non-mineralized animal tissues*, *BMC Physiology* **vol. 9**, (2009).
- [37] B. Metscher, *MicroCT for developmental biology: A versatile tool for high-contrast 3D imaging at histological resolutions*, *Developmental Dynamics* **vol. 238**, (2009).
- [38] E. Pauwels, D. Van Loo, P. Cornillie, L. Brabant and L. Van Hoorebeke, *An exploratory study of contrast agents for soft tissue visualization by means of high resolution X-ray computed tomography imaging*, *Journal of Microscopy* **vol. 250**, (2013).
- [39] G. Kerckhofs, S. Stegen, N. van Gastel, A. Sap, G. Falgayrac, G. Penel, M. Durand, F. Luyten, L. Geris, K. Vandamme, T. Parac-Vogt and G. Carmeliet, *Simultaneous three-dimensional visualization of mineralized and soft skeletal tissues by a novel microCT contrast agent with polyoxometalate structure*, *Biomaterials* **vol. 159**, (2018).

- [40] G. Kerckhofs, J. Sainz, M. Maréchal, M. Wevers, T. Van de Putte, L. Geris and J. Schrooten, *Contrast-Enhanced Nanofocus X-Ray Computed Tomography Allows Virtual Three-Dimensional Histopathology and Morphometric Analysis of Osteoarthritis in Small Animal Models*, *CARTILAGE* **vol. 5**, (2013).
- [41] G. Kerckhofs, J. Sainz, M. Wevers, T. Van de Putte and J. Schrooten, *Contrast-enhanced nanofocus computed tomography images the cartilage subtissue architecture in three dimensions*, *European Cells and Materials* **vol. 25**, (2013).
- [42] S. Gabner, P. Böck, D. Fink, M. Glösmann and S. Handschuh, *The visible skeleton 2.0: phenotyping of cartilage and bone in fixed vertebrate embryos and fetuses based on X-ray microCT*, *Development* **vol. 147**, (2020).
- [43] A. Momose, T. Takeda, Y. Itai and K. Hirano, *Phase-contrast X-ray computed tomography for observing biological soft tissues*, *Nature Medicine* **vol. 2**, (1996).
- [44] G. Albertini, A. Giuliani, V. Komlev, F. Moroncini, A. Pugnali, G. Pennesi, M. Belicchi, C. Rubini, F. Rustichelli, R. Tasso and Y. Torrente, *Organization of Extracellular Matrix Fibers Within Polyglycolic Acid–Polylactic Acid Scaffolds Analyzed Using X-Ray Synchrotron-Radiation Phase-Contrast Micro Computed Tomography*, *Tissue Engineering Part C: Methods* **vol. 15**, (2009).
- [45] P. Verboven, G. Kerckhofs, H. Mebatsion, Q. Ho, K. Temst, M. Wevers, P. Cloetens and B. Nicolai, *Three-Dimensional Gas Exchange Pathways in Pome Fruit Characterized by Synchrotron X-Ray Computed Tomography*, *Plant Physiology* **vol. 147**, (2008).
- [46] C. Dullin, R. Ufartes, E. Larsson, S. Martin, M. Lazzarini, G. Tromba, J. Missbach-Guentner, D. Pinkert-Leetsch, D. Katschinski, F. Alves and R. Roeder, *μ CT of ex-vivo stained mouse hearts and embryos enables a precise match between 3D virtual histology, classical histology and immunochemistry*, *PLOS ONE* **vol. 12**, (2017).
- [47] M. Krenkel, A. Markus, M. Bartels, C. Dullin, F. Alves and T. Salditt, *Phase-contrast zoom tomography reveals precise locations of macrophages in mouse lungs*, *Scientific Reports* **vol. 5**, (2015).
- [48] P. Cloetens, W. Ludwig, J. Baruchel, D. Van Dyck, J. Van Landuyt, J. Guigay and M. Schlenker, *Holotomography: Quantitative phase tomography with micrometer resolution using hard synchrotron radiation x rays*, *Applied Physics Letters* **vol. 75**, (1999).
- [49] T. Weitkamp, D. Haas, D. Wegrzynek and A. Rack, *ANKAphase: software for single-distance phase retrieval from inline X-ray phase-contrast radiographs*, *Journal of Synchrotron Radiation* **vol. 18**, (2011).
- [50] M. Endrizzi, *X-ray phase-contrast imaging*, *Nuclear Instruments and Methods in Physics Research Section A: Accelerators, Spectrometers, Detectors and Associated Equipment* **vol. 878**, (2018).

- [51] S. Sajja, Y. Lee, M. Eriksson, H. Nordström, A. Sahgal, M. Hashemi, J. Mainprize and M. Ruschin, *Technical Principles of Dual-Energy Cone Beam Computed Tomography and Clinical Applications for Radiation Therapy, Advances in Radiation Oncology* **vol. 5**, (2020).
- [52] J. Martins de Souza e Silva, J. Utsch, M. Kimm, S. Allner, M. Epple, K. Achterhold and F. Pfeiffer, *Dual-energy micro-CT for quantifying the time-course and staining characteristics of ex-vivo animal organs treated with iodine- and gadolinium-based contrast agents, Scientific Reports* **vol. 7**, (2017).
- [53] M. Honkanen, A. Saukko, M. Turunen, R. Shaikh, M. Prakash, G. Lovric, A. Joukainen, H. Kröger, M. Grinstaff and J. Töyräs, *Synchrotron MicroCT Reveals the Potential of the Dual Contrast Technique for Quantitative Assessment of Human Articular Cartilage Composition, Journal of Orthopaedic Research* **vol. 38**, (2020).
- [54] C. Dullin, F. di Lillo, A. Svetlove, J. Albers, W. Wagner, A. Markus, N. Sodini, D. Dreossi, F. Alves and G. Tromba, *Multiscale biomedical imaging at the SYRMEP beamline of Elettra - Closing the gap between preclinical research and patient applications, Physics Open* **vol. 6**, (2021).
- [55] D. Pham, C. Xu and J. Prince, *Current Methods in Medical Image Segmentation, Annual Review of Biomedical Engineering* **vol. 2**, (2000).
- [56] M. Li, L. Wang, S. Deng, C. Zhou and Y. Wang, *Color image segmentation using adaptive hierarchical-histogram thresholding, PLOS ONE* **vol. 15**, (2020).
- [57] J. Léger, L. Leysens, C. De Vleeschouwer and G. Kerckhofs, *Deep Learning-Based Segmentation of Mineralized Cartilage and Bone in High-Resolution Micro-CT Images*, in *Computer Methods, Imaging and Visualization in Biomechanics and Biomedical Engineering*, G. Ateshian, K. Myers and J. Tavares, eds., Springer International Publishing, Cham, (2020).
- [58] M. Schultheiss, S. Schober, M. Lodde, J. Bodden, J. Aichele, C. Müller-Leisse, B. Renger, F. Pfeiffer and D. Pfeiffer, *A robust convolutional neural network for lung nodule detection in the presence of foreign bodies, Scientific Reports* **vol. 10**, (2020).
- [59] T. Zikmund, M. Novotná, M. Kavková, M. Tesařová, M. Kaucká, B. Szarowská, I. Adameyko, E. Hrubá, M. Buchtová, E. Dražanová, Z. Starčuk and J. Kaiser, *High-contrast differentiation resolution 3D imaging of rodent brain by X-ray computed microtomography, Journal of Instrumentation* **vol. 13**, (2018).
- [60] M. Tesařová, L. Mancini, A. Simon, I. Adameyko, M. Kaucká, A. Elewa, G. Lanzafame, Y. Zhang, D. Kalasová, B. Szarowská, T. Zikmund, M. Novotná and J. Kaiser, *A quantitative analysis of 3D-cell distribution in regenerating muscle-skeletal system with synchrotron X-ray computed microtomography, Scientific Reports* **vol. 8**, (2018).
- [61] M. Tesařová, E. Heude, G. Comai, T. Zikmund, M. Kaucká, I. Adameyko, S. Tajbakhsh and J. Kaiser, *An interactive and intuitive visualisation method for X-ray computed tomography data of biological samples in 3D Portable Document Format, Scientific Reports* **vol. 9**, (2019).

- [62] E. Tanaka, *Regeneration, Cell* **vol. 113**, (2003).
- [63] A. Joven, A. Elewa and A. Simon, *Model systems for regeneration: salamanders, Development* **vol. 146**, (2019).
- [64] R. Diogo, E. Nacu and E. Tanaka, *Is Salamander Limb Regeneration Really Perfect? Anatomical and Morphogenetic Analysis of Forelimb Muscle Regeneration in GFP-Transgenic Axolotls as a Basis for Regenerative, Developmental, and Evolutionary Studies, The Anatomical Record* **vol. 297**, (2014).
- [65] T. Gerber, P. Murawala, D. Knapp, W. Masselink, M. Schuez, S. Hermann, M. Gac-Santel, S. Nowoshilow, J. Kageyama, S. Khattak, J. Currie, J. Camp, E. Tanaka and B. Treutlein, *Single-cell analysis uncovers convergence of cell identities during axolotl limb regeneration, Science* **vol. 362**, (2018).
- [66] F. Brun, L. Mancini, P. Kasae, S. Favretto, D. Dreossi and G. Tromba, *Pore3D: A software library for quantitative analysis of porous media, Nuclear Instruments and Methods in Physics Research Section A: Accelerators, Spectrometers, Detectors and Associated Equipment* **vol. 615**, (2010).
- [67] D. Zandomenighi, M. Voltolini, L. Mancini, F. Brun, D. Dreossi and M. Polacci, *Quantitative analysis of X-ray microtomography images of geomaterials: Application to volcanic rocks, Geosphere* **vol. 6**, (2010).
- [68] L. Brunt, J. Norton, J. Bright, E. Rayfield and C. Hammond, *Finite element modelling predicts changes in joint shape and cell behaviour due to loss of muscle strain in jaw development, Journal of Biomechanics* **vol. 48**, (2015).
- [69] B. Sket, *Distribution of Proteus (Amphibia: Urodela: Proteidae) and its possible explanation, Journal of Biogeography* **vol. 24**, (2003).
- [70] Š. Gorički, D. Stanković, A. Snoj, M. Kuntner, W. Jeffery, P. Trontelj, M. Pavičević, Z. Grizelj, M. Năpăruș-Aljančić and G. Aljančić, *Environmental DNA in subterranean biology: range extension and taxonomic implications for Proteus, Scientific Reports* **vol. 7**, (2017).
- [71] G. Aljančić, *History of research on Proteus anguinus Laurenti 1768 in Slovenia / Zgodovina raziskovanja človeške ribice (Proteus anguinus Laurenti 1768) v Sloveniji, Folia biologica et geologica* **vol. 60**, (2019).
- [72] S. Stuart, J. Chanson, N. Cox, B. Young, A. Rodrigues, D. Fischman and R. Waller, *Status and Trends of Amphibian Declines and Extinctions Worldwide, Science* **vol. 306**, (2004).
- [73] M. Tesařová, L. Mancini, E. Mauri, G. Aljančić, M. Năpăruș-Aljančić, R. Kostanjšek, L. Bizjak Mali, T. Zikmund, M. Kaucká, F. Papi, J. Goyens, A. Bouchnita, A. Hellander, I. Adameyko and J. Kaiser, *Living in darkness: Exploring adaptation of Proteus anguinus in 3 dimensions by X-ray imaging, GigaScience* **vol. 11**, (2022).

- [74] E. Comellas, T. Duerr, J. Farkas, J. Monaghan and S. Shefelbine, *Integrating macromolecular data in a tissue-level computational model of vertebrate joint morphogenesis*, 14th WCCM & ECCOMAS Congress (2020).
- [75] D. Noden and P. Trainor, *Relations and interactions between cranial mesoderm and neural crest populations*, *Journal of Anatomy* **vol. 207**, (2005).
- [76] M. Kaucka, E. Ivashkin, D. Gyllborg, T. Zikmund, M. Tesarova, J. Kaiser, M. Xie, J. Petersen, V. Pachnis, S. Nicolis, T. Yu, P. Sharpe, E. Arenas, H. Brismar, H. Blom, H. Clevers, U. Suter, A. Chagin, K. Fried, A. Hellander and I. Adameyko, *Analysis of neural crest-derived clones reveals novel aspects of facial development*, *Science Advances* **vol. 2**, (2016).
- [77] B. de Boer, A. Soufan, J. Hagoort, T. Mohun, M. van den Hoff, A. Hasman, F. Voorbraak, A. Moorman and J. Ruijter, *The interactive presentation of 3D information obtained from reconstructed datasets and 3D placement of single histological sections with the 3D portable document format*, *Development* **vol. 138**, (2010).
- [78] *Congenital anomalies, Fact sheet No. 370*, in *World Health Organization*, (2016).
- [79] *Birth defects: report by the Secretariat, Executive board 125th session EB125/7*, in *World Health Organization*, (2009).
- [80] A. Moon, *Mouse Models for Investigating the Developmental Basis of Human Birth Defects*, *Pediatric Research* **vol. 59**, (2006).
- [81] C. Klingenberg, *Novelty and “Homology-free” Morphometrics: What’s in a Name?*, *Evolutionary Biology* **vol. 35**, (2008).
- [82] J. Matula, M. Tesarova, T. Zikmund, M. Kaucka, I. Adameyko and J. Kaiser, *X-ray microtomography-based atlas of mouse cranial development*, *GigaScience* **vol. 10**, (2021).
- [83] T. Sneddon, P. Li and S. Edmunds, *GigaDB: announcing the GigaScience database*, *GigaScience* **vol. 1**, (2012).
- [84] O. Ronneberger, P. Fischer and T. Brox, *U-Net: Convolutional Networks for Biomedical Image Segmentation*, in *Medical Image Computing and Computer-Assisted Intervention – MICCAI 2015*, N. Navab, J. Hornegger, W. Wells and A. Frangi, eds., Springer International Publishing, Cham, (2015).
- [85] D. Noden and P. Francis-West, *The differentiation and morphogenesis of craniofacial muscles*, *Developmental Dynamics* **vol. 235**, (2006).
- [86] D. Suzuki, Y. Fukumoto, M. Yoshimura, Y. Yamazaki, J. Kosaka, S. Kuratani and H. Wada, *Comparative morphology and development of extra-ocular muscles in the lamprey and gnathostomes reveal the ancestral state and developmental patterns of the vertebrate head*, *Zoological Letters* **vol. 2**, (2016).

- [87] G. Young, *Number and arrangement of extraocular muscles in primitive gnathostomes: evidence from extinct placoderm fishes*, *Biology Letters* **vol. 4**, (2007).
- [88] P. Hasson, *“Soft” tissue patterning: Muscles and tendons of the limb take their form*, *Developmental Dynamics* **vol. 240**, (2011).
- [89] A. Huang, *Coordinated development of the limb musculoskeletal system: Tendon and muscle patterning and integration with the skeleton*, *Developmental Biology* **vol. 429**, (2017).
- [90] G. Comai, M. Tesařová, V. Dupé, M. Rhinn, P. Vallecillo-García, F. da Silva, B. Feret, K. Exelby, P. Dollé, L. Carlsson, B. Pryce, F. Spitz, S. Stricker, T. Zikmund, J. Kaiser, J. Briscoe, A. Schedl, N. Ghyselinck, R. Schweitzer, S. Tajbakhsh and S. Hughes, *Local retinoic acid signaling directs emergence of the extraocular muscle functional unit*, *PLOS Biology* **vol. 18**, (2020).
- [91] J. Porter, R. Baker, R. Ragusa and J. Brueckner, *Extraocular muscles: Basic and clinical aspects of structure and function*, *Survey of Ophthalmology* **vol. 39**, (1995).
- [92] A. Emery, *The muscular dystrophies*, Oxford University Press, New York, ISBN 9780199542161 (2001).
- [93] A. Martin, R. Reddy and M. Fehlings, *Dropped head syndrome: diagnosis and management*, *Evidence-Based Spine-Care Journal* **vol. 2**, (2011).
- [94] M. Randolph and G. Pavlath, *A muscle stem cell for every muscle: variability of satellite cell biology among different muscle groups*, *Frontiers in Aging Neuroscience* **vol. 7**, (2015).
- [95] E. Heude, M. Tesarova, E. Sefton, E. Jullian, N. Adachi, A. Grimaldi, T. Zikmund, J. Kaiser, G. Kardon, R. Kelly and S. Tajbakhsh, *Unique morphogenetic signatures define mammalian neck muscles and associated connective tissues*, *eLife* **vol. 7**, (2018).
- [96] R. Ericsson, R. Knight and Z. Johanson, *Evolution and development of the vertebrate neck*, *Journal of Anatomy* **vol. 222**, (2013).
- [97] M. Tesařová, *Quantitative 3D characterization of biological structures by X-ray computed microtomography*, Doctoral thesis topic. Brno University of Technology, Central European Institute of Technology (2020).

8 List of symbols and shortcuts

2D	two-dimensional
3D	three-dimensional
BUT	Brno University of Technology
Blob	Binary large object
CEITEC	Central European Institute of Technology
CNN	Convolutional Neural Network
CT	X-ray Computed Tomography
Ctrl	Control
DOI	Digital Object Identifier
E	Energy
EOM	Extraocular muscles
FBP	Filtered Back Projection
GigaDB	GigaScience Database
j_0	Spectral intensity
I	Intensity at the detector
I_0	Intensity generated by the source
microCT	X-ray Computed Microtomography
n	refractive index
PDF	Portable Document Format
PMA	Phosphomolybdic Acid
PTA	Phosphotungstic Acid
STP	SYRMEP Tomo Project
WT	Wild Type
β	Imaginary part of refractive index
δ	Real part of refractive index
μ	Attenuation coefficient

9 Author publications and other outputs

9.1 Publications

9.1.1 First-author

- **TESAŘOVÁ M.**; MANCINI L.; MAURI E.; ALJANČIČ G.; NAPARUS-ALJANČIČ M.; KOSTANJŠEK R.; MALI L.B.; ZIKMUND T.; KAUCKA M.; PAPI F.; GOYENS J.; BOUCHNITA A.; HELLANDER A.; ADAMEYKO I. and KAISER J. Living in darkness: Exploring adaptation of *Proteus anguinus* in 3D by X-ray imaging. *GigaScience*, 2022.
- **TESAŘOVÁ, M.**; HEUDE, E.; COMAI, G.; ZIKMUND, T.; KAUCKÁ, M.; ADAMEYKO, I.; TAJBAKSH, S. and KAISER, J. An interactive and intuitive visualisation method for X-ray computed tomography data of biological samples in 3D Portable Document Format, *Scientific Reports*, 2019.
- **TESAŘOVÁ, M.**, MANCINI, L., SIMON, A., ADAMEYKO, I., KAUCKÁ, M., ELEWA, A., LANZAFAME, G., ZHANG, Y., KALASOVÁ, D., SZAROWSKÁ, B., ZIKMUND, T., NOVOTNÁ, M. and KAISER, J. A quantitative analysis of 3D-cell distribution in regenerating muscle-skeletal system with synchrotron X-ray computed microtomography, *Scientific Reports*, 2018.
- **TESAŘOVÁ, M.**; ZIKMUND, T.; KAUCKÁ, M.; ADAMEYKO, I.; JAROŠ, J.; PALOUŠEK, D.; ŠKAROUPKA, D. and KAISER, J. Use of micro computed- tomography and 3D printing for reverse engineering of mouse embryo nasal capsule. *Journal of Instrumentation*, 2016.

9.1.2 Co-author

- KAMENEVA P.; MELNIKOVA V.; KASTRITI M.E.; KURTOVA A.; KRYUKOV E.; MURTAZINA A.; FAURE L.; POVERENNAYA I.; ARTEMOV A.; KALININA T.; KUDRYASHOV N.; BADER M.; SKODA J.; CHLAPEK P.; CURYLOVA L.; SOURADA L. NERADIL J.; **TESAŘOVÁ M.**; GASPAR P.; YAKUSHOV V.D.; SHEFTEL B.I.; ZIKMUND T.; KAISER J.; FRIED K. ALENINA N.; VORONEZSHKAYA E. and ADAMEYKO I. Serotonin limits generation of chromaffin cells during adrenal organ development. *Nature Communications*, 2022.
- MATULA J.; POLAKOVA V.; SALPLACHTA J.; **TESAŘOVÁ M.**; ZIKMUND T.; KAUCKÁ M.; ADAMEYKO I. and KAISER J. Resolving complex cartilage structures in developmental biology via deep learning-based automatic segmentation of X-ray computed microtomography images. *Scientific Reports*, 2022.
- BOUDERLIQUE T.; PETERSEN J.; FAURE L. ABED-NAVANDI D.; BOUCHNITA A.; MUELLER B.; NAZAROV M.; ENGLMAIER L.; **TESAŘOVÁ M.**; FRADE P.R.; ZIKMUND T.; KOEHNE T.; KAISER J. FRIED K.; WILD C.; PANTOS O.; HELLANDER A.; BYTHELL J. and ADAMEKO I. Surface flow for colonial integration in reef-building corals. *Current Biology*, 2022.
- MATULA, J.; **TESAŘOVÁ, M.**; ZIKMUND, T.; KAUCKÁ, M.; ADAMEYKO, I. and KAISER, J. X-ray microtomography-based atlas of mouse cranial development. *GigaScience*, 2021.
- COMAI, G.; **TESAŘOVÁ, M.**; DUPÉ, V.; RHINN, M.; VALLECILLO-GARCÍA, P.; DA SILVA, F.; FERET, B.; EXELBY, K.; DOLLE, P.; CARLSSON, L.; PRYCE, B.; SPITZ, F.; STRICKER, S.; ZIKMUND, T.; KAISER, J.; BRISCOE, J.; SCHEDL, A.; GHYSELINCK, N.; SCHWEITZER, R. and TAJBAKSH, S. Local retinoic acid signaling directs emergence of the extraocular muscle functional unit. *PLOS Biology*, 2020.
- HEUDE, E.; **TESAŘOVÁ, M.**; SEFTON, E. M.; JULLIAN, E.; ADACHI, N.; GRIMALDI, A.; ZIKMUND, T.; KAISER, J.; KARDON, G.; KELLY, R. G. and TAJBAKSH, S. Unique morphogenetic signatures define mammalian neck muscles and associated connective tissues. *eLife*, 2018.

- KAUCKA, M.; PETERSEN, J.; **TESAŘOVÁ, M.**; SZAROWSKA, B.; KASTRITI, ME.; XIE, M.; KICHEVA, A.; ANNUSVER, K.; PAN, L.; SPITZ, F.; KAISER, J.; HOVORAKOVA, M.; ZIKMUND, T.; SUNADOME, K.; MATISE, MP.; WANG, H.; MARKLUND, U.; ABDO, H.; ERNFORS, P.; MAIRE, P.; WURMSER, M.; CHAGIN, AS.; FRIED, K. and ADAMEYKO, I. Signals from the brain and olfactory epithelium control shaping of the mammalian nasal capsule cartilage. *eLife*, 2018.
- ZIKMUND, T.; NOVOTNÁ, M.; KAVKOVÁ, M.; **TESAŘOVÁ, M.**; KAUCKÁ, M.; SZAROWSKÁ, B.; ADAMEYKO, I.; HRUBÁ, E.; BUCHTOVÁ, M.; DRAŽANOVÁ, E.; STARČUK, Z. and KAISER, J. et al. High-contrast differentiation resolution 3D imaging of rodent brain by X-ray computed microtomography. *Journal of Instrumentation*, 2018.
- KAUCKÁ, M.; ZIKMUND, T.; **TESAŘOVÁ, M.**; GYLLBORG, D.; HELLANDER, A.; JAROŠ, J.; KAISER, J.; PETERSEN, J.; SZAROWSKA, B.; NEWTON, P.T.; DYACHUK, V.; LI, L.; QIAN, H.; JOHANSSON, A-S.; MISHINA, Y.; CURRIE, J.; TANAKA, E.M.; ERICKSON, A.; DUDLEY, A.; BRISMAR, H.; SOUTHAM, P.; COEN, E.; CHEN, M.; WEINSTEIN, L.S.; HAMPL, A.; ARENAS, E.; CHAGIN, A.S.; FRIED, K. and ADAMEYKO, I. Oriented clonal cell dynamics enables accurate growth and shaping of vertebrate cartilage. *eLife*, 2017.
- JAROŠ, J.; PETROV, M.; **TESAŘOVÁ, M.** and HAMPL, A. Revealing 3D Ultrastructure and Morphology of Stem Cell Spheroids by Electron Microscopy. *Methods Molecular Biology*, 2017.
- KAUCKÁ, M.; IVASHKIN E.; GYLBORG, D.; ZIKMUND, T.; **TESAŘOVÁ, M.**; KAISER, J.; XIE, M.; PETERSEN, J.; PACHNIS, V.; NICLOIS, S.K.; YU, T.; SHARPE, P.; ARENAS, E.; BRISMAR, H.; BLOM, H.; CLEVERS, H.; SUTER, U.; CHAGIN, A.S.; FRIED, K.; HELLANDER, A. and ADAMEYKO, I. Analysis of neural crest- derived clones reveals novel aspects of facial development. *Science Advances*, 2016.

9.1.3 Submitted publications

- KAUCKA M.; JOVEN A.; **TESAŘOVÁ M.**; CURRIE J.; PETERSEN J.; YAO Z.; BOUCHNITA A.; HELLANDER A.; ZIKMUND T.; ELEWA A.; NEWTON P.; FEI J.F.; CHAGIN A.; FRIED K.; TANAKA E. KAISER J.; SIMON A. AND ADAMEYKO I. Limb regeneration in salamanders leads to bulky long bones through variations of developmental programs. *Nature Communications*, 2022 (awaiting resubmission).
- SUNADOME K.; ERICKSON A.; KAH D.; FABRY B.; ADORI C.; KAMENEVA P.; FAURE L.; KANATANI S.; KAUCKA M.; DEHNISCH I.; **TESAŘOVÁ M.**; ZIKMUND T.; KAISER J.; EDWARDS S.; MAKI K.; ADACHI T.; FRIED K. and ADAMEYKO I. Directionality of developing skeletal muscles is set by mechanical forces. *Nature Communications*, 2022 (under review).
- PETERSEN J.; ENGLMAIER L.; ARTEMOV A.; POVERENNAYA I.; BOUDERLIQUE T.; **TESAŘOVÁ M.**; DEVIATIIAROV R.; SZILVASY-SZABO A.; AKKURATOV E.; ZEBERG H.; KAUCKA M.; KASTRITI M.E.; KRIVANEK J.; RADASZKIEWICZ T.; GRABOWSKI A. ZIKMUND T.; KAVKOVÁ M.; AXELSON H.; LINDGREN D.; KRAMANN R.; KUPPE C.; ERDÉLYI F.; MÁTÉ Z.; SZABO G.; KOEHNE T.; BRYJA V.; HARKANY T.; FRIED K.; KAISER J.; CSABA F.; GUSEV O. and ADAMEYKO I. A previously uncharacterized Kidney-Associated Membrane Protein (KAMP) is associated with evolutionary adaptation, energy balance and kidney physiology. *Nature Communications*, 2022 (awaiting resubmission).

9.2 Products

- ŠALPLACHTA, J.; **TESAŘOVÁ, M.**; ZEMEK, M. and KAISER, J.: Sample holder with a reference area (functional sample). Output of TAČR ZÉTA TJ02000127

9.3 Grants

- Bridge fund 2021-2022: “3D characterization of lymphotic leukemia cells’ migration by X-ray computed microtomography” – Cooperation between CEITEC research groups Advanced Instrumentation and Methods for Materials Characterization (Tomáš Zikmund) and Microenvironment of Immune Cells (Marek Mráz).
- TAČR ZÉTA – “Differentiation of soft tissues by dual-target tomography” - TJ02000127 (5/2019-4/2021) – main applicant. Cooperation between Brno University of Technology and Rigaku Innovative Technologies Europe s.r.o
- Martina Roeselova memorial fellowship 2020.
- BUT Internal projects – main applicant
 - “Shaping of skeletal elements during regeneration of salamander limbs by X-ray computed microtomography” - CEITEC VUT-J-21-7145 (2021).
 - “Morphogenesis of the extraocular muscles in 3D by X-ray computed microtomography” – CEITEC VUT-J-20-6317 (2020).
 - “Application of industrial X-ray computed tomography for muscle-skeletal imaging at vertebrates” – CEITEC VUT-J-19-5764 (2019).
- Brno PhD Talent 2018.
- AFM Telethon 21853 – “Investigating heterogeneities and morphogenesis of cranial mesoderm derived skeletal muscles” (2017-2018).

9.4 Conferences

May 2022	4 th International meeting SOS Proteus: Conservation of Proteus and its habitat facing climate change challenge, Trieste, Italy <i>Oral presentation:</i> 3D exploring of <i>Proteus anguinus</i> by X-ray computed microtomography
October 2021	35 th Conference of Czech Herpetological Society, Prague, Czech Republic <i>Oral presentation:</i> Rentgenová počítačová mikrotomografie jako nástroj ke studiu (nejen) macaráta jeskynního (in Czech language)
September 2021	Conference of The Visegrád Group Society for Developmental Biology (V4SDB), Szeged, Hungary <i>Oral presentation:</i> Revealing secrets of <i>Proteus anguinus</i> by 3D X-ray imaging
June 2019	Joint Retreat, Kouty u Ledče nad Sázavou, Czech Republic <i>Oral presentation:</i> Application of industrial X-ray computed tomography for muscle-skeletal imaging at vertebrates
July 2018	International symposium on morphological sciences, Prague, Czech Republic <i>Oral presentation:</i> Implementation of industrial approach of X-ray computed microtomography in developmental biology.
June 2018	European Workshop on laser ablation, Pau France

Poster: Combination of Laser-Induced Breakdown Spectroscopy and Computed Tomography for 3D chemical imaging.

September 2017

International workshop on Imaging, Varenna, Italy

Poster: Quantitative 3D analysis at cellular resolution with X-ray computed microtomography.

April 2017

Bioimplantology, Brno, Czech Republic

Oral presentation: Application of X-ray Computed Tomography for 3D imaging with cellular resolution.

Living in darkness: Exploring adaptation of *Proteus anguinus* in 3 dimensions by X-ray imaging

Markéta Tesařová¹, Lucia Mancini², Edgardo Mauri³, Gregor Aljančič⁴, Magdalena Năpăruș-Aljančič^{4,5}, Rok Kostanjšek⁶, Lilijana Bizjak Mali⁶, Tomáš Zikmund¹, Markéta Kaucká⁷, Federica Papi³, Jana Goyens⁸, Anass Bouchnita^{9,10}, Andreas Hellander⁹, Igor Adameyko^{11,12} and Jozef Kaiser^{1,*}

¹Central European Institute of Technology, Brno University of Technology, Purkyňova 123, Brno, 61200, Czech Republic

²Elettra-Sincrotrone Trieste S.C.p.A., S.S. 14 - km 163,5 in Area Science Park, Basovizza, Trieste, 34149, Italy

³Speleovivarium Erwin Pichl, Adriatic Speleology Society, Via Guido Reni, 2/C, Trieste, 34123, Italy

⁴Institute Tular Cave Laboratory, Oldhamska 8a, Kranj, 4000, Slovenia

⁵Research Centre of the Slovenian Academy of Sciences and Arts: Karst Research Institute, Titov trg 2, Postojna, 6230, Slovenia

⁶University of Ljubljana, Biotechnical Faculty, Department of Biology, Večna pot 111, Ljubljana, 1000, Slovenia

⁷Max Planck Institute for Evolutionary Biology, August-Thienemann-Str. 2, Plön, 24306, Germany

⁸Laboratory of Functional Morphology, University of Antwerp, Universiteitsplein 1, Wilrijk, 2610, Belgium

⁹Department of Information Technology, Uppsala University, Box 337, Uppsala, 755 01, Sweden

¹⁰Department of Integrative Biology, University of Texas at Austin, Austin, 78712, Texas, USA

¹¹Medical University of Vienna, Center for Brain Research, Department of Neuroimmunology, Spitalgasse 4, 1090 Vienna, Austria

¹²Karolinska Institutet, Department of Physiology and Pharmacology, Solnavagen 9, 17165 Solna, Sweden

*Correspondence address: Jozef Kaiser, Central European Institute of Technology, Brno University of Technology, Central European Institute of Technology, Brno University of Technology, Purkyňova 123, Brno, 61200, Czech Republic. E-mail: jozef.kaiser@ceitec.vutbr.cz

Abstract

Background: Lightless caves can harbour a wide range of living organisms. Cave animals have evolved a set of morphological, physiological, and behavioural adaptations known as troglomorphisms, enabling their survival in the perpetual darkness, narrow temperature and humidity ranges, and nutrient scarcity of the subterranean environment. In this study, we focused on adaptations of skull shape and sensory systems in the blind cave salamander, *Proteus anguinus*, also known as olm or simply proteus—the largest cave tetrapod and the only European amphibian living exclusively in subterranean environments. This extraordinary amphibian compensates for the loss of sight by enhanced non-visual sensory systems including mechanoreceptors, electroreceptors, and chemoreceptors. We compared developmental stages of *P. anguinus* with *Ambystoma mexicanum*, also known as axolotl, to make an exemplary comparison between cave- and surface-dwelling paedomorphic salamanders.

Findings: We used contrast-enhanced X-ray computed microtomography for the 3D segmentation of the soft tissues in the head of *P. anguinus* and *A. mexicanum*. Sensory organs were visualized to elucidate how the animal is adapted to living in complete darkness. X-ray microCT datasets were provided along with 3D models for larval, juvenile, and adult specimens, showing the cartilage of the chondrocranium and the position, shape, and size of the brain, eyes, and olfactory epithelium.

Conclusions: *P. anguinus* still keeps some of its secrets. Our high-resolution X-ray microCT scans together with 3D models of the anatomical structures in the head may help to elucidate the nature and origin of the mechanisms behind its adaptations to the subterranean environment, which led to a series of troglomorphisms.

Keywords: *Proteus anguinus*, *Ambystoma mexicanum*, olm, axolotl, X-ray microCT, microtomography, salamander, cave animal, subterranean adaptations

Data Description

Context

Proteus anguinus, also known as the olm or simply proteus, has attracted the attention of scientists and animal traders for centuries. *P. anguinus* is an apex predator of the karst underground waters. Its presence indicates the stability of food chains in the subterranean ecosystem. Its geographic distribution is limited to the Dinaric Karst; it ranges from the Gulf of Trieste in Italy, through the southern half of Slovenia, coastal mainland of Croatia and parts of Bosnia and Hercegovina, as far as adjacent parts of Montenegro. With its extremely fragmented and limited habitat, *P. anguinus* is particularly vulnerable to pollution of groundwater. Some populations have been locally destroyed or endangered by

pollution or habitat destruction [1, 2]. *P. anguinus* is an important object of research from at least 2 perspectives. First, *P. anguinus* played a historical role during the formation of modern science from the 17th to 19th century, puzzling the minds of most prominent early naturalists, from Valvasor to Linnaeus, Scopoli, Cuvier, and Humboldt, and from Lamarck to Darwin and Goethe. Second, *P. anguinus* has potential to answer the questions of the science of today and the future (e.g., regeneration, cave-related adaptations, enormous genome, and conservation of subterranean biodiversity) [3].

P. anguinus was first mentioned by Janez Vajkard Valvasor in 1689. Its scientific name *Proteus anguinus* was given by Josephus Nicolaus Laurenti in 1768, and thus *P. anguinus* became the first

Received: August 27, 2021. Revised: January 6, 2022. Accepted: February 27, 2022

© The Author(s) 2022. Published by Oxford University Press GigaScience. This is an Open Access article distributed under the terms of the Creative Commons Attribution License (<https://creativecommons.org/licenses/by/4.0/>), which permits unrestricted reuse, distribution, and reproduction in any medium, provided the original work is properly cited.

taxonomically described cave animal in the world [4]. In the past 2 centuries, more detailed research has been performed on *P. anguinus*. Two of the central figures of the early *P. anguinus* research were Žiga Zois, a naturalist from Ljubljana, who first described its behaviour and conducted the earliest physiological and ecological observations. Then, Karl von Schreibers, a Viennese zoologist, was the first to explore the anatomy of *P. anguinus* [5]. This mysterious animal, which retains larval features at the adult stage, started to interest the scientific community in the early 19th century, with a focus on its secretive mode of reproduction. In 1859, *P. anguinus* served as an example of blind cave animals in the famous monograph *On the Origin of Species*, where Charles Darwin attributed the reduction of eyes wholly to their disuse in darkness [6]. *P. anguinus* also became a model species in classical studies of comparative anatomy of the late 19th century. In the 20th century, more systematic research was enabled by overcoming the inaccessibility of *P. anguinus*'s subterranean habitat in captivity of cave laboratories worldwide, including France, Slovenia, and Germany; the studies focused on cave-related physiology, ecology, behaviour, and molecular phylogeny [3]. Fortunately, the attention to *P. anguinus* and its habitat has gradually received an important cultural and conservation attitude (1951 protected species in Slovenia, 1971 Ramsar convention, 1979 Bern convention, and 1992 EU Habitat Directive). The year 2019 represented another milestone in the research of *P. anguinus*. The public presentation of the *P. anguinus* genome sequencing project [7] aimed to decipher the *P. anguinus* genetic information coded in its genome, which is ~15 times larger than the human genome.

Obligate cave-dwellers often result in a set of specific morphological, physiological, and behavioural traits (i.e., troglomorphy). Compared with their epigeal relatives, cave-dwelling animals may have phylogenetically retained older sensory properties, improved them, or acquired new ones, enabling their survival in dark habitats [8]. *P. anguinus* evolved a range of adaptations such as the loss of pigmentation, slow metabolism, and capability of surviving extreme starvation. Moreover, the loss of eyesight is compensated by other specialized senses that enable navigation in complete darkness. The mode of cave life and other biological peculiarities of *P. anguinus* and other troglomorphs evoke the potential role of underwater audio-, mechano-, electro-, and magnetoreception [9, 10].

Specimens of *P. anguinus* are valuable study material because they are protected and vulnerable. Our knowledge of *P. anguinus* larval and juvenile stages is still scarce. For these reasons, we aimed to use *P. anguinus* specimens from existing collections to avoid collecting them from nature. These animals died by natural causes and their bodies were preserved. We accessed the collection, applied non-destructive staining and a non-destructive imaging method (X-ray computed microtomography [microCT]), and then returned the specimens back to the collection. In this way, we obtained high-quality and high-resolution 3D data without needing to kill any animal.

X-ray microCT has become a powerful method in developmental biology for exploring morphological changes in 3 dimensions. Geometric morphometrics based on X-ray microCT has already been used previously for an exploratory analysis of the morphology of the cranial osteology in the white and black subspecies of *P. anguinus* [11, 12]. However, without contrast-enhanced techniques, less dense tissues such as sensory organs would be unrecognizable or inaccurately captured owing to insufficient contrast for detailed 3D analysis. In our study, we use staining of soft tissues by phosphotungstic acid (PTA) or iodine to visualize soft tissues in the head of *P. anguinus*. For the first time, we look at vol-

umetric internal structures by using a non-destructive imaging technique and we show the sensory organ with a high spatial and contrast resolution.

P. anguinus has been an important object of study in the history of international nature research, intriguing scientists. Thanks to studies in the past 300 years [5], the mysteries of this cave amphibian are slowly being unravelled. However, *P. anguinus* still leaves gaps in our knowledge about its ecology, evolution, and physiology. Our high-resolution microCT scans, together with 3D models of anatomical structures in the head, could help to elucidate the nature and origin of the mechanisms behind its adaptations to the subterranean lightless environment, which led to the acquisition of the troglomorphic features.

Methods

Sample preparation

Approval for the capture, handling, maintenance, and breeding in captivity of the animals used in the study was granted by the Ministry of the Environment and Spatial Planning of the Republic of Slovenia, Slovenian Agency for the Environment (Permits Nos. 35701-36/01, 35601-95/2009-4, and 35601-132/2014-4), by the Italian Republic, Friuli Venezia Giulia Region (Permit Nos. 4105/6MU4/95/04/12), and by the Italian Republic, Ministry of Ecological Transition (Permits Nos. 3006/015590-93, 39/04). No animals were killed for this study. Our experimental plan involved scanning *P. anguinus* and the axolotl *Ambystoma mexicanum* samples at different stages to study various parts of the skull and sensory organs.

All 5 *P. anguinus* specimens (NCBI:txid221568) were stored in 75% ethanol. Specimens of *A. mexicanum* (NCBI:txid8296) had been reared at the Speleovivarium Erwin Pichl (Italy) since 2004 and included a 5-year-old adult female (died in 2009) with a total length of 194 mm, and a larva of 6 days old (died in 2012) with a total length of 11 mm. Specimens of *P. anguinus* included 1 larva, 3 weeks old (died in 2007), length 23 mm, captive breeding originating from the Postojna-Planina Cave System, from the collection of the Tular Cave Laboratory (Slovenia); 1 juvenile, 35 mm long, deceased at the collection site in spring near Metković (Croatia), from the collection of the Department of Biology, Biotechnical Faculty, University of Ljubljana (Slovenia); 1 adult, sex unknown, length 276 mm, collected in Postojna-Planina Cave System (Slovenia, 1989), died in captivity of the Speleovivarium in 1999, from the collection of the Speleovivarium Erwin Pichl (Italy).

We modified a contrast-enhancing protocol initially developed by Brian Metscher [13] that has been successfully applied on salamander tissues before [14]. Larval samples of both *P. anguinus* and *A. mexicanum*, and juvenile *P. anguinus* were stained with 1% PTA in 90% methanol for 7 weeks. The solution was exchanged with a fresh one once a week. The adult *P. anguinus* and *A. mexicanum* specimens were stained with 2% iodine (instead of PTA) in 90% methanol for 6 weeks to ensure that the contrasting agent would penetrate the entire sample because iodine penetrates better than PTA. Subsequently, the samples were gradually rehydrated in ethanol series (90%, 80%, 70%, and 50%), 1 day for each concentration (i.e., 4 days of rehydration). The samples were then stabled in polyamide tubes filled with 1% low-melting agarose gel to prevent sample movement during CT scan.

Image acquisition

The head region of the samples was scanned by using a laboratory X-ray microCT system GE Phoenix v|tome|x L 240 (Waygate Technologies / Baker Hughes Digital Solutions GmbH, Wunstorf,

Germany). The system was equipped with a 180 kV/15 W maximum power nanofocus X-ray tube and a high-contrast flat-panel detector DXR250 with $2,048 \times 2,048$ pixels resolution and $(200 \times 200) \mu\text{m}^2$ pixel size. A total of 2,000 projections over a total scan angle of 360° were acquired with an exposure time of 900 ms per projection. Each projection was captured 3 times, and an average of the signal was used to improve the signal-to-noise ratio. The acceleration voltage of the X-ray tube was set to 60 kV and the tube current to 200 μA for larval and juvenile *P. anguinus*; 80 kV and 250 μA were used, respectively, for voltage and current for adult samples. The X-ray beams of lower energies were filtered with a 0.2-mm-thick aluminium plate for larval and with a 1-mm-thick aluminium plate for adult samples. The voxel sizes of the reconstructed data were as follows: 3.5 μm for juvenile *P. anguinus*, 5.8 μm for larval *P. anguinus*, 25 μm for adult *P. anguinus*, 2.8 μm for larval *A. mexicanum*, and 27.5 μm for adult *A. mexicanum*.

Tomographic data processing

The tomographic reconstruction was performed using GE phoenix datos|x 2.0 software (Waygate Technologies / Baker Hughes Digital Solutions GmbH, Wunstorf, Germany) (Phoenix Datos|x 2.0, RRID:SCR_017996). A segmentation procedure was then applied to reconstructed slices. The Avizo 7.1 (Thermo Fisher Scientific, Waltham, MA, USA) (Avizo 3D Software, RRID:SCR_014431) image processing software was used for semi-automatic segmentation [15–17] of structures in the head. To reduce the load of the 3D segmentation volume, every third slice was manually segmented, and the rest was calculated by linear interpolation between manually segmented slices [17]. We converted the semi-manually segmented models into polygonal meshes and imported this in VG Studio MAX 2.2 software (Volume Graphics GmbH, Heidelberg, Germany) (VG Studio MAX, RRID:SCR_017997) for 3D visualizations.

Data validation and quality control

By contrast-enhanced X-ray microCT scan, we were able to visualize the internal structures of the *P. anguinus* head. Figure 1 shows the manually segmented cartilaginous chondrocranium, as well as the position and the shape of the brain, the remnant eyes, and the olfactory epithelium. A considerable portion of the cranial skeleton in the adult *P. anguinus* specimen remains cartilaginous.

A validation of the semi-automatic segmentation procedure is presented in Fig. 2. The 3D models were created by an operator based on the grey-scale value contrast and the shape of the structures. The detailed procedure is described in the Methods section and followed our previous study [17].

In Fig. 3, we compare the microCT datasets and segmentations of the internal head structures of the larval and adult specimens of both *P. anguinus* and *A. mexicanum*. The head of the troglolithic *P. anguinus* is narrower and more elongated in comparison with the epigeal *A. mexicanum*, which lives in open surface bodies of water but not underwater caves. Our 3D segmentations show remnant eyes at larval and juvenile stage *P. anguinus*, but no remnant of eyes was noticed in the adult specimen. The progressive degeneration of the eye in the development of *P. anguinus* may lead to the apparent disappearance of the eye in the adult animal [18]. By contrast, 3D models of *A. mexicanum* clearly show the eyes, together with an optic nerve that leads to the brain, in both the larval and adult stages. However, the absence of remnant eyes and optic nerves in our data could be caused by low contrast of these structures in microCT data because the segmentation was done

manually by the operator and based on their grey-scale values and their shape.

Reuse potential

Museum-type documentation of rare and endangered species

The presented datasets give insight not only into the developmental biology of *P. anguinus*. Together with 3D datasets of *A. mexicanum*, they are important study materials for the conservation efforts to preserve these endangered amphibians. According to the global assessment of the International Union for Conservation of Nature (IUCN), 43% of amphibian species are in decline while 32% are threatened with extinction [19]; *P. anguinus* is currently classified as vulnerable. The X-ray microCT method enables anatomical studies without damaging the morphology of the specimens and is therefore exceptionally appropriate for studying endangered species with a limited amount of available specimens. Semi-automatically segmented images and the extracted 3D models could also be taken as an input into a machine learning algorithm. The field of image processing is becoming dominated by deep learning algorithms and convolutional neural networks [20]. Creating an online database could also be beneficial for student studies and distance learning. Especially, last year showed the importance of easy access to online study materials because of Covid-19 restrictions.

Perspectives: Cellular resolution

Using microCT scan with a conventional X-ray source, we obtained data of excellent quality that depict single cells in the cartilaginous elements (Fig. 4). Despite the fact that the cells can be visually detected, their automatic segmentation and quantification is challenging. The potential of X-ray microCT imaging with synchrotron sources for the study of 3D cell distribution was demonstrated in our previous study on salamander limbs [12], and the potential for biomedical applications was shown before [21, 22]. The data with cellular resolution can be used as the input for the study of polarization of cells in the extracellular matrix in salamander limbs or for mathematical modelling of joint formation [14].

Research outlook

The morphology of the cranium carries important information related to mechanics involved in feeding, as well as competitive, reproductive, and anti-predatory behaviour. Even small differences in cranial skeleton may have important biomechanical and ecological implications [23]. The most detailed descriptions of the *P. anguinus* skull are those of Dolivo-Dobrovolsky [24, 25], Ivanović et al. [11], Papi et al. [12], and Bizjak Mali and Sket [26]. MicroCT contrast-enhanced data included overall 3D information and a further segmentation. Working on the provided data can be taken as an input for various type of analyses (Fig. 5). The visualization of muscles of the upper and lower jaw could be used for biting analyses that may shed light on the predatory abilities of *P. anguinus*.

In general, our datasets will help to investigate how evolutionary changes in the shape of the head and its integrated musculoskeletal apparatus, nervous system, and sensory organs would help for troglomorphic adaptation. Because *P. anguinus* is a cave-dwelling animal, the craniofacial design underwent a number of cave-related evolutionary adaptations, acquiring protracted and longitudinally elongated skeletal elements, in comparison with the epigeal *A. mexicanum*, as revealed by comparative microCT

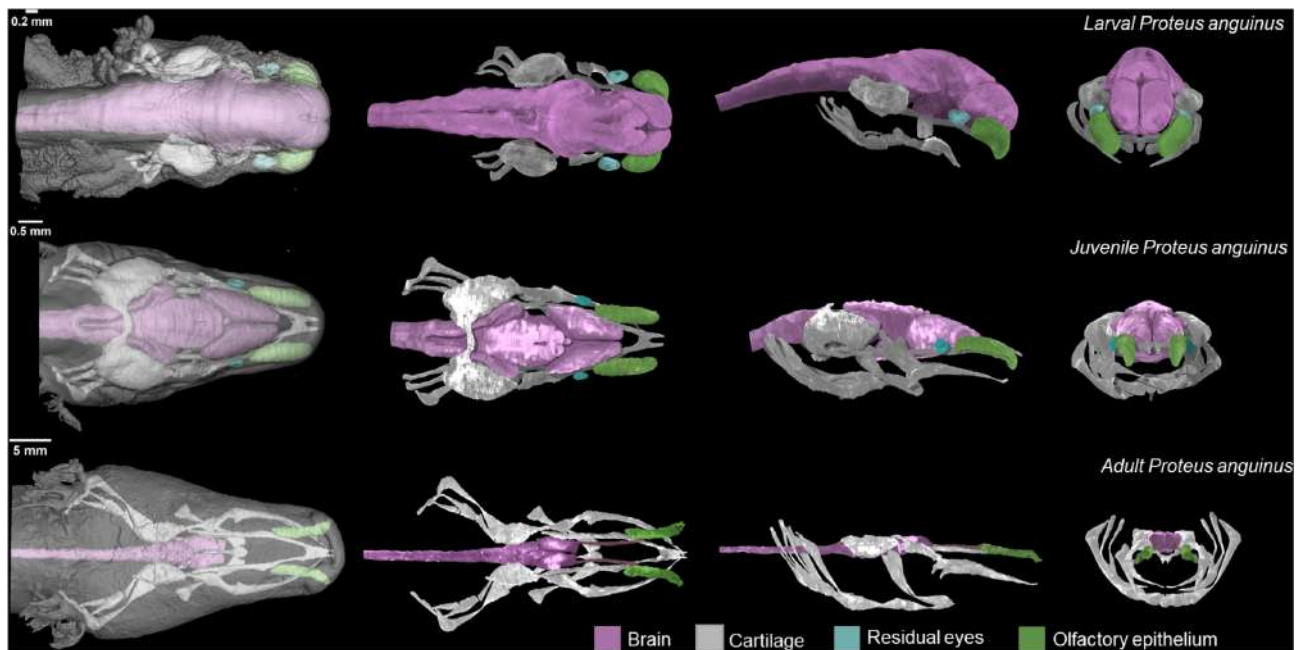


Figure 1: 3D reconstructions of *P. anguinus* head based on X-ray microCT data. Larva (top), juvenile (middle), and adult (bottom) *P. anguinus*. Images in the first column show semi-transparent 3D renderings of the head with skin in dorsal view. Dorsal, lateral, and frontal views of the segmented and color-coded internal soft structures are shown in the second to the fourth columns.

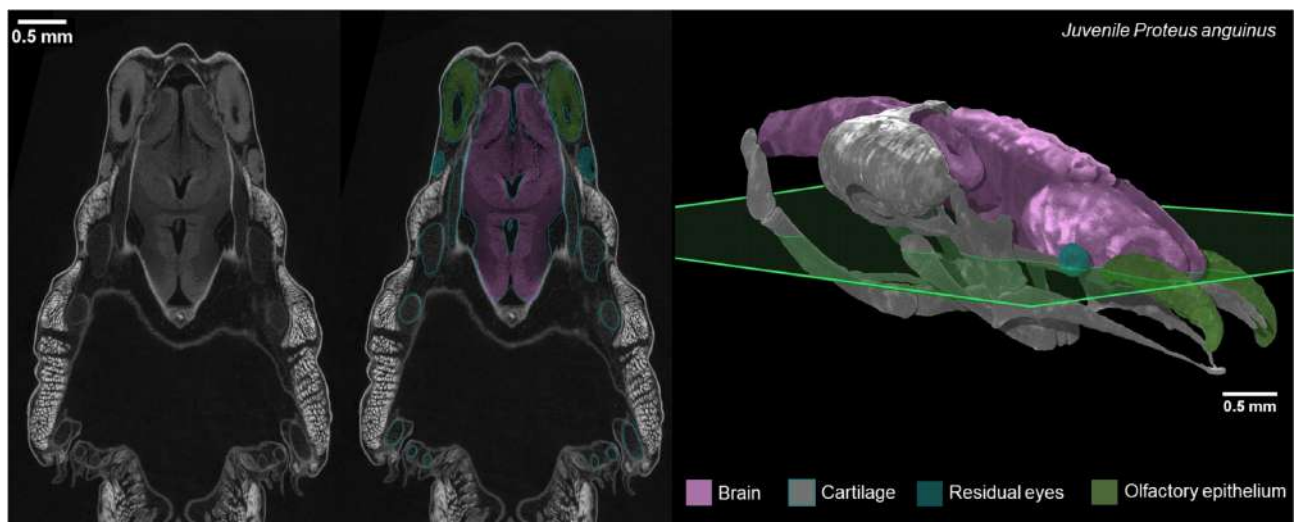


Figure 2: Accuracy validation of semi-automatic segmentations of X-ray microCT data in juvenile *P. anguinus*. Raw CT image (left) and the corresponding segmented image (middle) through the transverse plane (green) of the head of a juvenile *P. anguinus* (right).

scanning analysis and in-depth 3D analysis. Indeed, when compared to *P. anguinus*, *A. mexicanum* exhibits a wider skull with a massive jaw. Elongated skull, body, and limbs are common features of troglomorphy for organisms inhabiting subterranean habitats [27, 28]. Only 14 cave-obligate species are known (all plethodontid and proteid salamanders), but this number is likely to be an underestimate because of cryptic species [29]. In this regard, the results of our study provide insight into evolutionary trends in adaptive morphological traits as a result of convergent evolution across phyla. Even without evolutionary comparison across phyla, our results enable further studies on evolution of the skeletal parts in the adaptive landscapes individually for closely related species.

Not only evolutionary questions but also developmental patterns can be tackled with these data. For instance, to investigate whether the elongated skull shape develops evenly with the growth of the animal, we investigated the larval *P. anguinus*. The larva of *P. anguinus*, although small, revealed its miniaturized protracted chondrocrania with similar spatial proportions to the adult form. Thus, the elongated body and stretched cranium may indicate possible benefits at any phase of development. Such comparative developmental and growth-related studies open up new opportunities to look into the dynamics of skeletal shape development in relation to the specifics of the environment.

However, when it comes to the adaptations in sensory organs, the 3D analysis of the head revealed major differences in visual

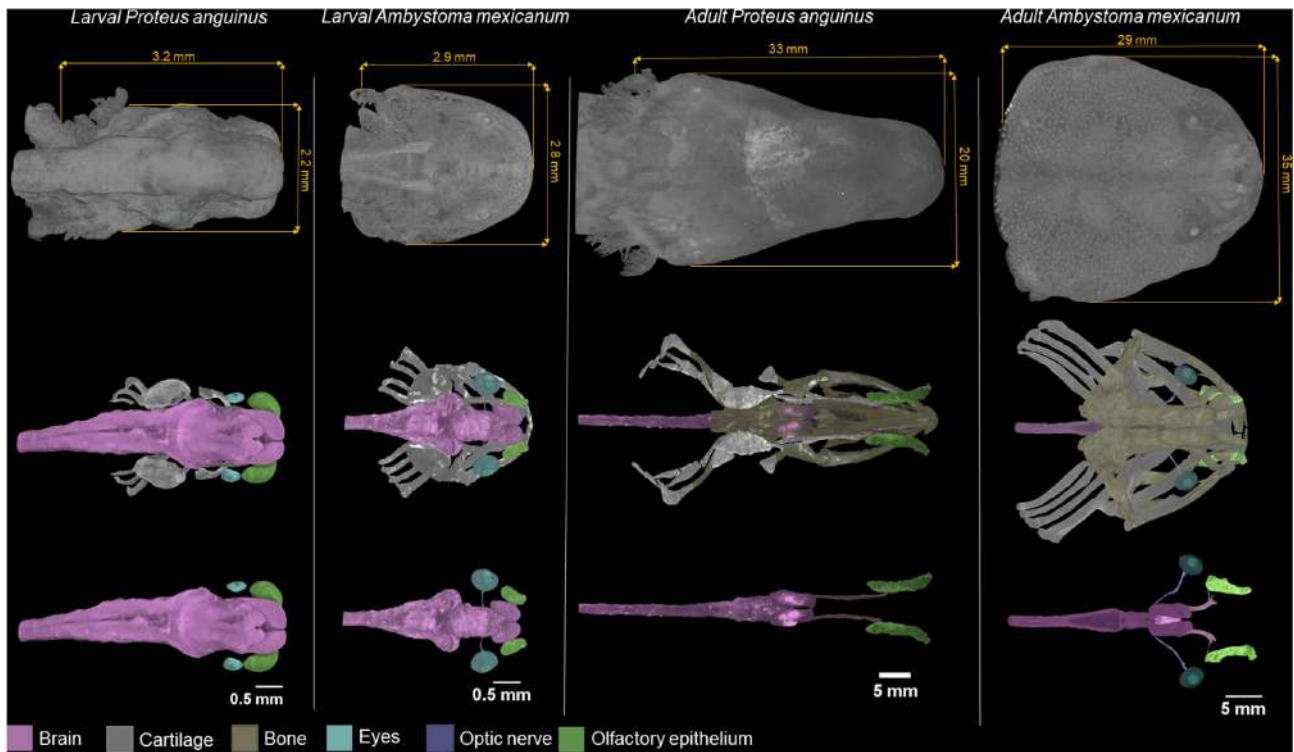


Figure 3: Comparison of the head and internal soft-tissue anatomy of the cave-dwelling *P. anguinus* with *A. mexicanum* in larval and adult specimens. Images in the first row show 3D renderings of the head with skin in dorsal view. The second row shows color-coded segmented brain, cartilage, bones, and eyes with optic nerve and olfactory epithelium. The third row shows these structures without bone and cartilage for better clarity.

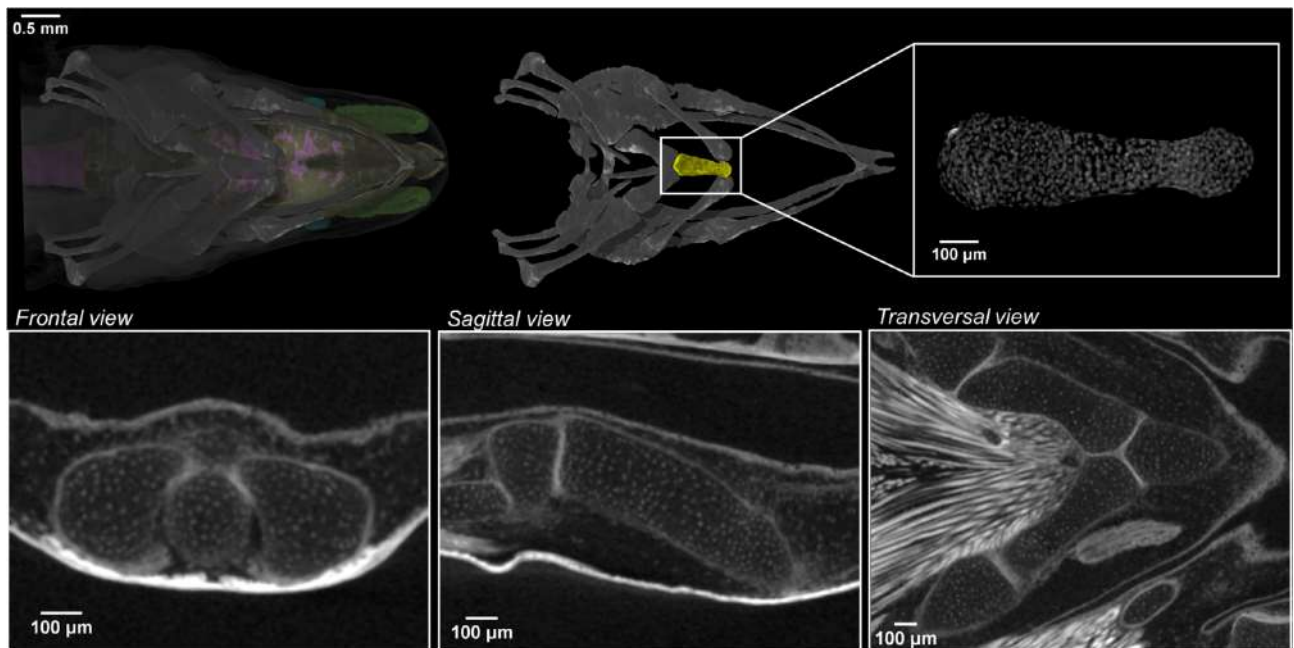


Figure 4: Images at near cellular-level resolution showing the cartilaginous elements in juvenile *P. anguinus* obtained by microCT. The white dots represent cell nuclei. 3D detail of the cartilaginous first basibranchial element of the hyobranchial apparatus in ventral view (yellow; top row) with 3 orthogonal CT slices along the frontal, sagittal, and transverse planes (second row).

and olfactory systems of *P. anguinus* and *A. mexicanum*. First, *P. anguinus* is blind, a typical troglomorphic trait that is explained by the troglomorphic way of life. The eye development in *P. anguinus* larva begins as in other amphibians. The regression of the almost normally formed eyes starts soon after hatching and gradually

leads to a considerable reduction of the eyes in adult *P. anguinus* [18], while surface-dwelling salamanders develop fully functional eyes. The morphological comparisons of the *P. anguinus* developmental stages with their gradual reduction of eyes may improve our knowledge on the mechanisms of eye degeneration in *P. angu-*

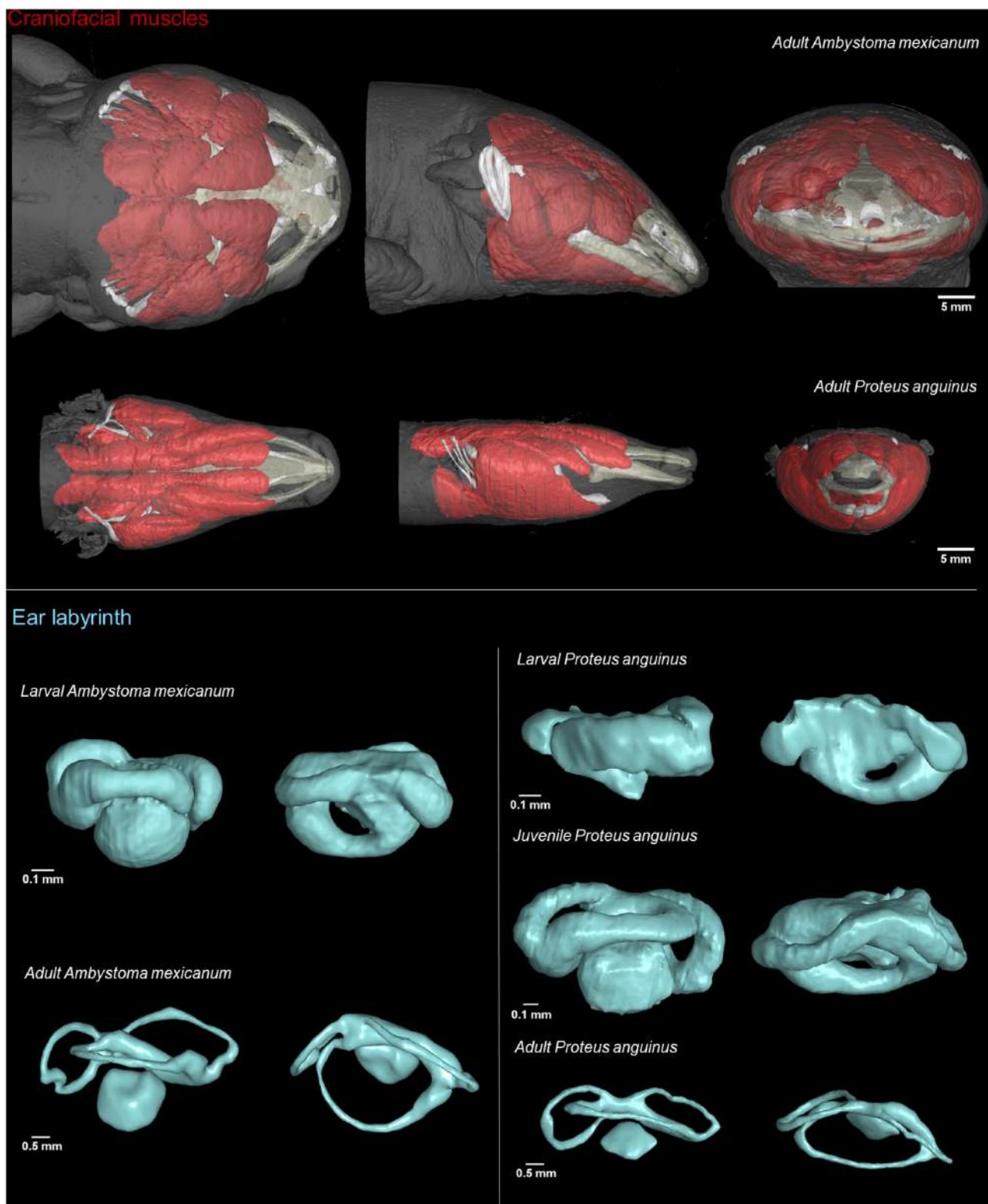


Figure 5: Potential use of contrast-enhanced X-ray microCT data. Segmentation of craniofacial muscles and ear labyrinth in *A. mexicanum* and *P. anguinus*.

nus and possibly other similar blind cave-dwellers. Moreover, the eyeballs develop in a complex conjunction with muscular apparatus [30] and optical nerve. Here, in *P. anguinus*, it is possible to question how the induction and degeneration of auxiliary tissues is achieved during the degradation of the pre-shaped eyeballs.

The animals with eye regression are generally known to inhabit caves; therefore vision is nearly useless to them. The blind Mexican cave fish (*Astyanax mexicanus*) is one of the popular model systems to study the loss of vision and developmental arrest of the visual system [31]. However, blind fish and other model or-

ganisms, including *P. anguinus*, still have a great potential for comparison with other eyeless vertebrates [32]. Therefore, our results and datasets may enable new insights into evolutionary trends in the eye development and degeneration strategies in cave-dwellers across vertebrate clades.

Olfaction plays an important role in the life of salamanders [8]. The analysis of 3D-rendered olfactory organs revealed striking differences between the surface-dwelling *A. mexicanum* and the cave-dwelling *P. anguinus*. Elongated and tube-shaped olfactory cavities in *P. anguinus* likely emerge as another adaptation to the cave environment, where enhanced olfaction capabilities pose an advantage in the absence of visual signals [33]. Comparing to *A. mexicanum*, the elongated olfactory cavities of *P. anguinus* might enable a higher dynamic range of sensitivity, owing to a more efficient longitudinal diffusion of signals upon entry via the nostrils. In line with this, the olfactory nerves of *P. anguinus* are also considerably elongated, which is explained by a rather long rostral part of the skull in *P. anguinus*. Therefore, studies of evolutionary divergence of the olfactory system and its sensitivity and general design could benefit from the deposited datasets.

Finally, salamanders represent a well-established model system for the research of regeneration, and the fundamental principles of multi-tissue regeneration have already been revealed [34]. Regeneration of *P. anguinus* has been described previously, yet the provided data offer an important insight into the evolutionary differences in regeneration among salamanders with fundamentally different lifestyles.

Data Availability

The datasets underlying this article are available in the GigaScience Database repository [35]. We provide reconstructed slices as DICOM image stacks and segmented structures in STL format for the head region of 3 specimens (1 larva, 1 juvenile, and 1 adult) of *P. anguinus* and 2 specimens (1 larva and 1 adult) of *A. mexicanum*. For segmented structures, we also provide segmented masks as DICOM image stacks—1 stack for each structure. The folders are structured so that each folder represents 1 sample containing a folder with DICOM stack, a folder with STL files, and a folder with segmented masks. The DICOM image stacks can be opened in any image viewer supporting this format; we recommend ImageJ for viewing the data [36]. To explore datasets in 3 dimensions, specialized free viewers are available—Drishti [37], DragonFly (Object Research Systems [ORS], Inc., Montreal, QC, Canada), or others. For analysis and further segmentation, we recommend the use of ITK-SNAP [38] or commercial software, e.g., Avizo or VG Studio MAX. A detailed description and a manual for segmentation of biological data can be found in our previous works [17, 39]. The STL files can be also explored in 3D mesh viewers: popular free open-source software, e.g., MeshLab [40] or Blender [41], as well as in the sketchfab repository [42].

Abbreviations

DICOM: Digital Imaging and Communications in Medicine; microCT: X-ray computed microtomography; PTA: phosphotungstic acid; STL: Standard Triangle Language.

Competing Interests

The authors declare that they have no competing interests.

Funding

We acknowledge CzechNanoLab Research Infrastructure supported by MEYS CR (LM2018110). M.T. acknowledges grant CEITEC VUT-J-21-7145, the Brno City Municipality as a Brno Ph.D. Talent Scholarship Holder and Martina Roeselova Memorial Fellowship. J.G. was funded the Fonds Wetenschappelijk Onderzoek-Vlaanderen by a postdoctoral fellowship (Grant No. 12R5118N).

Authors' Contributions

M.T.: Writing—original draft, Visualization; L.M.: Conceptualization, Methodology; E.M.: Investigation, Writing—original draft; G.A.: Investigation, Writing—original draft; M.N.A.: Investigation, Writing—original draft; R.K.: Validation, Writing—review & editing; L.B.-M.: Validation; T.Z.: Project administration; M.K.: Methodology; Writing—review & editing; F.P.: Methodology; J.G.: Data curation, Writing—review & editing; A.B.: Data curation; A.H.: Project administration; I.A.: Conceptualization, Project administration; J.K.: Funding acquisition, Supervision.

Acknowledgements

We thank Teo Deli c for collecting the juvenile *P. anguinus* specimens.








References

1. Sket, B. Distribution of *Proteus* (Amphibia: Urodela: Proteidae) and its possible explanation. *J Biogeogr* 1997;**24**(3):263–80.
2. Gori cki,  , Stankovi c, D, Snoj, A, et al. Environmental DNA in subterranean biology: range extension and taxonomic implications for *Proteus*. *Sci Rep* 2017;**7**(1):doi:10.1038/srep45054.
3. Aljan ci c, G. History of research on *Proteus anguinus* Laurenti 1768 in Slovenia. *Folia biol geol* 2019;**60**(1):39.
4. Laurenti, J. Synopsis reptilium. In: *Specimen Medicum, Exhibens Synopsin Reptilium Emendatam cum Experimentis Circa Venena et Antidota Reptilium Austriacorum*. Vienna: JT de Trattner; 1768:35–6.
5. von Schreibers, KA. Historical and anatomical description of a doubtful amphibious animal of Germany, called, by Laurenti, *Proteus anguinus*. *Philos Trans* 1801;**91**:241–64.
6. Charles, D. *On the Origin of Species*. John Murray; 1859.
7. Kostanjsek, R, Diderichsen, B, Recknagel, H, et al. Toward the massive genome of *Proteus anguinus*—illuminating longevity, regeneration, convergent evolution, and metabolic disorders. *Ann N Y Acad Sci* 2022;**1507**(1):5–11.
8. Schlegel, PA, Steinfartz, S, Bulog, B. Non-visual sensory physiology and magnetic orientation in the blind cave salamander, *Proteus anguinus* (and some other cave-dwelling urodele species). Review and new results on light-sensitivity and non-visual orientation in subterranean urodeles (Amphibia). *Anim Biol* 2009;**59**(3):351–384.
9. Bulog, B, Schlegel, P. Functional morphology of the inner ear and underwater audiograms of *Proteus anguinus* (Amphibia, Urodela). *Eur J Physiol* 2000;**439**(S1):r165–7.
10. Hervant, F, Mathieu, J, Durand, J. Behavioural, physiological and metabolic responses to long-term starvation and refeeding in a blind cave-dwelling (*Proteus anguinus*) and a surface-dwelling (*Euproctus asper*) salamander. *J Exp Biol* 2001;**204**(2):269–81.
11. Ivanovi c, A, Aljan ci c, G, Arntzen, JW, et al. Skull shape differentiation of black and white olms (*Proteus anguinus anguinus* and *Proteus a. parkelj*): an exploratory analysis with micro-CT scanning. *Contrib Zool* 2013;**82**(2):107–14.

12. Papi, F, Mauri, E, Pesaro, S, et al. Analysis of the skull of *Proteus anguinus* anguinus by high-resolution X-ray computed microtomography. *Nat Slov* 2018;**2**:43–5.
13. Metscher, B. MicroCT for comparative morphology: simple staining methods allow high-contrast 3D imaging of diverse non-mineralized animal tissues. *BMC Physiol* 2009;**9**(1):11.
14. Tesařová, M, Mancini, L, Simon, A, et al. A quantitative analysis of 3D-cell distribution in regenerating muscle-skeletal system with synchrotron X-ray computed microtomography. *Sci Rep* 2018;**8**(1): doi:10.1038/s41598-018-32459-2.
15. Bayle, P, Braga, J, Mazurier, A, et al. Dental developmental pattern of the Neanderthal child from Roc de Marsal: a high-resolution 3D analysis. *J Hum Evol* 2009;**56**(1):66–75.
16. Zanolli, C, Bondioli, L, Mancini, L, et al. Brief communication: Two human fossil deciduous molars from the Sangiran dome (Java, Indonesia). *Am J Phys Anthropol* 2012;**147**(3):472–81.
17. Tesařová, M, Zikmund, T, Kaucká, M, et al. Use of micro computed-tomography and 3D printing for reverse engineering of mouse embryo nasal capsule. *J Instrum* 2016;**11**(03):C03006.
18. Durand, J. Ocular development and involution in the European cave salamander, *Proteus anguinus* laurenti. *Biol Bull* 1976;**151**(3):450–66.
19. Stuart, SN, Chanson, JS, Cox, NA, et al. Status and trends of amphibian declines and extinctions worldwide. *Science* 2004;**306**(5702):1783–6.
20. Ronneberger, O, Fischer, P, Brox, T. U-Net: convolutional networks for biomedical image segmentation. In: N Navab, J Hornegger, W Wells, et al., eds. *Medical Image Computing and Computer-Assisted Intervention – MICCAI 2015*. Cham:Springer; 2015:doi:10.1007/978-3-319-24574-4_28.
21. Tromba, G, Longo, R, Abrami, A, et al. The SYRMEP Beamline of Elettra: clinical mammography and bio-medical applications. *AIP Conf. Proc* 2010;**1266**:18–23.
22. Du Plesis, A, Broeckhoven, C, Guelpa, A, et al. Laboratory x-ray micro-computed tomography: a user guideline for biological samples. *Gigascience* 2017;**6**(6):doi:10.1093/gigascience/gix027.
23. van der Meij, M, Bout, R. The relationship between shape of the skull and bite force in finches. *J Exp Biol* 2008;**211**(10): 1668–80.
24. Dolivo-Dobrovolsky, V. Das Kopfskelett des Grottenolmes (*Proteus anguinus* Laur.). *Zool Anz* 1923;**57**:281–4.
25. Dolivo-Dobrovolsky, V. Lobanja človeške ribice (*Proteus anguinus* Laurenti). *Rad Jugosl Akad Zna-nosti Umjetnost* 1926;**232**: 190–209.
26. Bizjak Mali, L, Sket, B. History and biology of the «black proteus» (*Proteus anguinus* parkelj Sket & Arntzen 1994; Amphibia: Proteidae). *Folia Biol Geol* 2019;**60**:5–37.
27. Culver, D, Pipan, T. *The Biology of Caves and Other Subterranean Habitats*. Oxford University Press; 2019:doi:10.1093/oso/9780198820765.001.0001.
28. Ribera, I, Cieslak, A, Faille, A, et al. Historical and ecological factors determining cave diversity: analysis and synthesis. In: O Moldovan, Ľ Kováč, S Halse, eds. *Cave Ecology*. Cham: Springer; 2018:doi:10.1007/978-3-319-98852-8_10.
29. Recknagel, H, Trontelj, P. From cave dragons to genomics: advancements in the study of subterranean tetrapods. *Bioscience* 2021;**72**(3):254–66.
30. Comai, G, Tesařová, M, Dupé, V, et al. Local retinoic acid signaling directs emergence of the extraocular muscle functional unit. *PLoS Biol* 2020;**18**(11):e3000902.
31. Jeffery, WR. Emerging model systems in evo-devo: cavefish and microevolution of development. *Evol Dev* 2008;**10**:265–72.
32. Tovar, R, Cantu, V, Fremaux, B, et al. Comparative development and ocular histology between epigeal and subterranean salamanders (Eurycea) from central Texas. *PeerJ* 2021;**9**:e11840.
33. Dumas, P, Chris, B. The olfaction in *Proteus anguinus*: a behavioural and cytological study. *Behav Processes* 1998;**43**(2):107–13.
34. Kumar, A, Godwin, J, Gates, P, et al. Molecular basis for the nerve dependence of limb regeneration in an adult vertebrate. *Science* 2007;**318**(5851):772–7.
35. Tesarova, M, Mancini, L, Mauri, E, et al. Supporting data for "Living in darkness: exploring adaptation of *Proteus anguinus* in 3 dimensions by X-ray imaging." *GigaScience Database*. 2022. <http://dx.doi.org/10.5524/102196>.
36. Schneider, C, Rasband, W, Eliceiri, K. NIH Image to ImageJ: 25 years of image analysis. *Nat Methods* 2012;**9**(7):671–5.
37. Limaye, A, Stock, S. Drishti: a volume exploration and presentation tool. *Developments in X-Ray Tomography* 2012;**8**: doi:10.1117/12.935640.
38. Yushkevich, PA, Gao, Y, Gerig, G. ITK-SNAP: an interactive tool for semi-automatic segmentation of multi-modality biomedical images. *Conf Proc IEEE Eng Med Biol Soc* 2016;**2016**:3342–5.
39. Tesařová, M, Heude, E, Comai, G, et al. An interactive and intuitive visualisation method for X-ray computed tomography data of biological samples in 3D Portable Document Format. *Sci Rep* 2019;**9**(1):doi:10.1038/s41598-019-51180-2.
40. Cignoni, P, Callieri, M, Corsini, M, et al. MeshLab: an Open-Source Mesh Processing Tool. *Computing* 2008;**1**:129–36, [10.2312/LocalChapterEvents/ItalChap/ItalianChapConf2008/129-136](https://doi.org/10.2312/LocalChapterEvents/ItalChap/ItalianChapConf2008/129-136).
41. Hess, R. *The Essential Blender: guide to 3D creation with the open source suite Blender*. No Starch Press; 2007.
42. *Salamander 3D Model Collection*. 2022. Sketchfab Repository. <https://sketchfab.com/GigaDB/collections/salamander>.

OPEN

An interactive and intuitive visualisation method for X-ray computed tomography data of biological samples in 3D Portable Document Format

Markéta Tesařová ¹, Eglantine Heude ^{2,3,4}, Glenda Comai ^{3,4}, Tomáš Zikmund ¹, Markéta Kaucká ^{5,6}, Igor Adameyko ^{5,6}, Shahragim Tajbakhsh ^{3,4} & Jozef Kaiser ^{1*}

3D imaging approaches based on X-ray microcomputed tomography (microCT) have become increasingly accessible with advancements in methods, instruments and expertise. The synergy of material and life sciences has impacted biomedical research by proposing new tools for investigation. However, data sharing remains challenging as microCT files are usually in the range of gigabytes and require specific and expensive software for rendering and interpretation. Here, we provide an advanced method for visualisation and interpretation of microCT data with small file formats, readable on all operating systems, using freely available Portable Document Format (PDF) software. Our method is based on the conversion of volumetric data into interactive 3D PDF, allowing rotation, movement, magnification and setting modifications of objects, thus providing an intuitive approach to analyse structures in a 3D context. We describe the complete pipeline from data acquisition, data processing and compression, to 3D PDF formatting on an example of craniofacial anatomical morphology in the mouse embryo. Our procedure is widely applicable in biological research and can be used as a framework to analyse volumetric data from any research field relying on 3D rendering and CT-biomedical imaging.

One of the formidable phenomena in developmental biology is how the shape diversity observed among living organisms is defined and controlled during development and growth. Embryonic patterning is a highly dynamic process implicating multiple molecular mechanisms and cell interactions at the basis of organ formation. In the human embryo, defects in such cellular processes can affect the developmental program leading to congenital disorders. Congenital defects have an incidence of 3% in the human population¹ and they are causal for up to one-quarter of all reported neonatal deaths². Thus, contextual visualisation of embryonic development is critical to elucidate the origins of malformations.

Multi-disciplinary collectives composed of clinical doctors, biologists, engineers and imaging experts are currently pushing forward the understanding of biological questions using three dimensional (3D) approaches. While the analysis of histological sections remains a mainstay in developmental biology, the reconstruction of 3D volumes from 2D slices has provided important information to understand morphogenesis in mouse and human embryos^{3–6}. Non-destructive technologies such as 3D imaging by confocal microscopy and light sheet methods^{7–9}, optical projection tomography (OPT)^{10–12} and micro-computed tomography (microCT)^{13–16} constitute emerging powerful methods to analyse the topography of developing structures in 3D context, to gain insight into the pathogenesis of congenital disorders. However, one major challenge of 3D approaches is sharing of complex datasets effectively and intuitively between colleagues from different fields for discussion, and ultimately

¹Central European Institute of Technology, Brno University of Technology, Brno, Czech Republic. ²Department Adaptation du Vivant, Museum national d'Histoire naturelle, CNRS UMR 7221, Paris, France. ³Department of Developmental and Stem Cell Biology, Stem Cells and Development Unit, Institut Pasteur, Paris, France. ⁴CNRS UMR, 3738, Paris, France. ⁵Department of Physiology and Pharmacology, Karolinska Institutet, Solna, Sweden. ⁶Department of Molecular Neurosciences, Medical University of Vienna, Vienna, Austria. *email: kaiser@fme.vutbr.cz

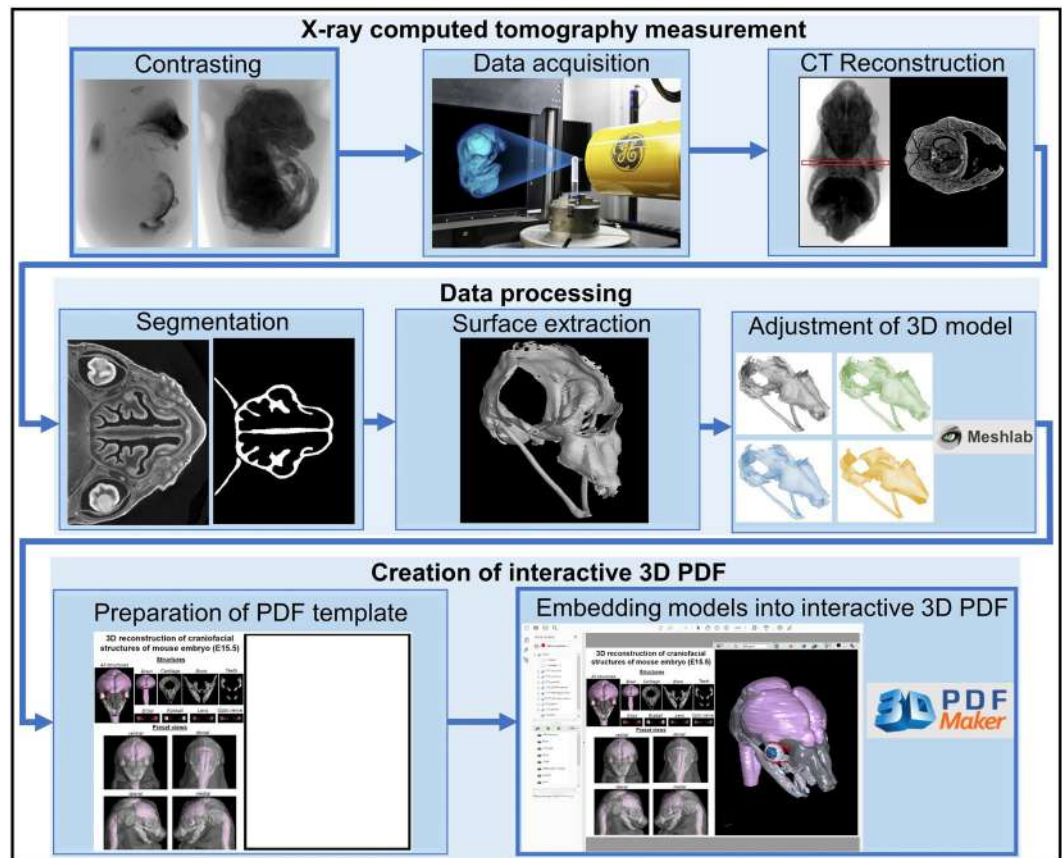


Figure 1. Overview of the method pipeline described in this study.

presenting them in a publication format. Generally, 3D datasets need special software for visualisation or are reduced to 2D pictures in which important information might be lost.

The study of the developing head constitutes a good example of the need for 3D approaches given its complex anatomy. The craniofacial region is built of diverse embryonic cell types giving rise to hard and soft tissues including skeletal, muscular and nervous components¹⁷. The final shape of the face strongly depends on the geometry of the skeletal elements and their interaction with adjacent soft tissues such as muscles and the nervous system^{15,16}. Numerous congenital craniofacial abnormalities affect the form and function of the face and explanations of these malformations still await the fundamental understanding of the underlying failure of morphogenesis¹⁸. The microCT approach followed by 3D reconstruction has enabled high-quality information of the complex morphological aspects of head and face development^{15,16}.

To facilitate assimilation and visualisation of microCT datasets, interactive 3D Portable Document Format (PDF) has been used in different field including in developmental biology^{6,19,20}, in human physiology and anatomy^{4,21–23}, in entomology²⁴ and marine biology^{25,26}. However, a major limitation of previously published methods is the requirement of advanced programming skills and/or installation of further prepaid software packages²¹. Most of these approaches depend on the use of Adobe Acrobat Pro Extended software^{4,6,19,23–28} or JavaScript programming language^{20,27}.

Here, we provide an alternative, user-friendly way to create interactive 3D PDF files from microCT datasets taking the complexity of mouse craniofacial anatomy as a model example. Our innovative and efficient pipeline comprises microCT data acquisition, segmentation and final establishment of a 3D PDF using a combination of free and pre-paid software. The resulting file can be viewed with standard PDF viewers and offers an interactive interface for microCT data sharing, analysis and presentation.

Pipeline for the Creation of Interactive 3D PDF

To create an interactive 3D PDF from microCT data, the critical steps are: (i) chemical contrasting of biological samples if soft tissues are to be visualized, (ii) data acquisition and (iii) CT virtual reconstruction (Fig. 1). This is followed by data processing, the most critical step consisting of segmentation, surface extraction, adjustment of segmented 3D models, and conversion into a final interactive PDF file. Here, we provide a detailed description of each step of the pipeline (see also Supplementary Material 1).

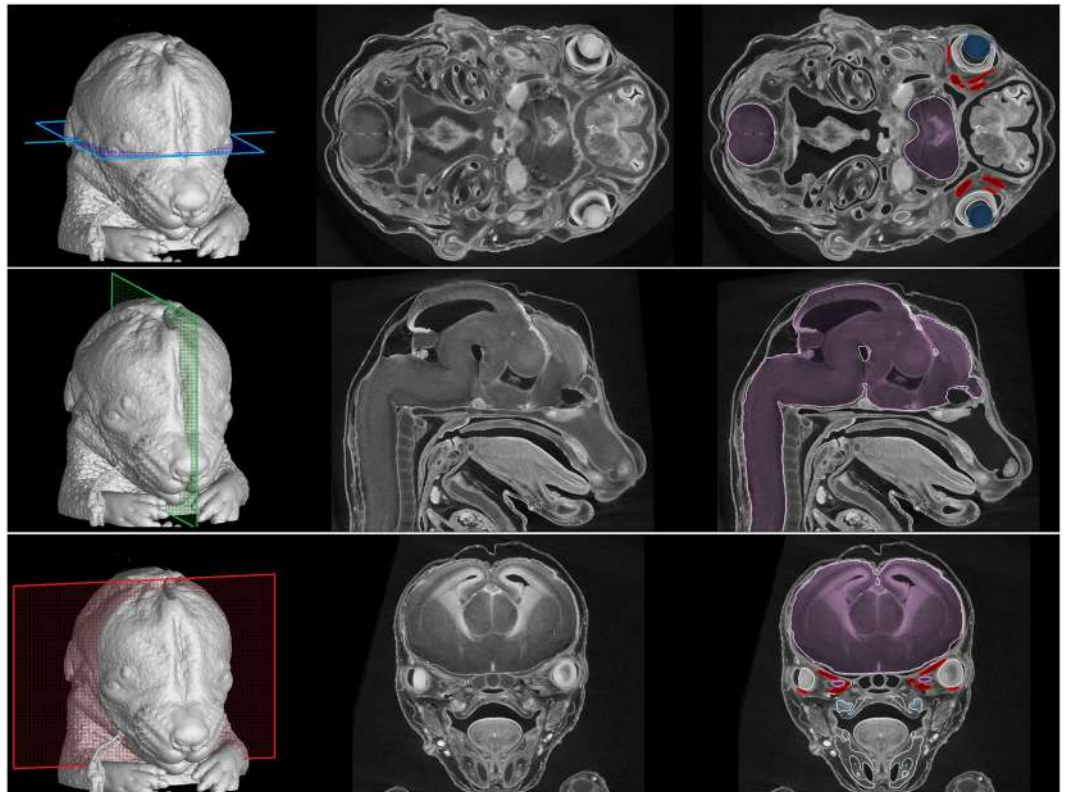


Figure 2. Tomographic measurements and segmentation of craniofacial structures in a mouse embryo 15 days post-fertilisation. Colour planes on 3D models (left panels) indicate the position of the raw tomographic slices (middle panels) and some segmented structures (right panels) including the central nervous system (purple), the lens (dark blue), the dental placodes (light blue) and extraocular muscles (red).

X-Ray Microtomography Measurement

MicroCT is an established technology for imaging mineralized tissues in animal specimens. However, its use in comparative morphology has been limited by the low intrinsic X-ray contrast of non-mineralised soft tissues. To overcome this problem, methods have been developed to increase tissue contrast, including chemical treatment with contrasting agents^{29,30}, phase-contrast imaging^{31–36} or dual-energy computed tomography (DECT)³⁷.

Chemical contrasting treatments have mostly been applied for the characterization of musculoskeletal tissues on small fixed samples. For *in vivo* CT imaging including clinical diagnoses, non-toxic iodine-based contrast agents (e.g. iohexol or hexabrix) are used for the analysis of the cardiovascular system and cavities, but not for direct analysis of muscle tissues^{38,39}. Clinical CT imaging of the musculoskeletal system is commonly performed without a contrasting agent, thereby limiting the analysis to discrete soft organs⁴⁰. Therefore, on small fixed samples, multiple contrasting protocols have been used, each with its own advantages and limitations^{41,42}. The stainings based on iodine, osmium or the toxic phosphotungstic acid (PTA) are the most commonly used^{29,30}. For the pipeline proposed here on the study of craniofacial mouse development, we propose the use of PTA contrasting treatment that permits high contrast imaging of a wide variety of soft and mineralised tissues composing the mouse head (Fig. 2). However, microCT data obtained with other contrasting agents or in their absence, such as clinical data or data from non-biological specimens, will be equally amenable for the subsequent steps of the 3D PDF pipeline.

Data Processing

Following the acquisition of high-contrast tomographic slices, the segmentation of complex craniofacial structures constitutes a major challenge. Fully-automatic approaches have been tried and were generally unsuccessful⁴³. Thus, the manual approach is usually the only method available to achieve precise and accurate segmentations⁴⁴. However, some semi-automatic methods such as local segmentation or interpolation between manually segmented slices can be used^{45,46}. For verification of the accuracy of manually segmented structures, Fig. 2 shows both original and segmented tomographic slices. This approach permitted the segmentation of soft tissues such as eyeballs, extraocular muscles and the central nervous system, as well as of hard tissues including the chondrocranium, bones and future teeth (dental placodes) (Fig. 3).

For 3D volume rendering, it is then more convenient to use 3D mesh formats rather than a stack of 2D images. 3D mesh formats represent a series of 2D polygons (typically triangles or quadrangles) linked together to recreate the surface of a 3D object²⁸. It encodes the 3D model's geometry, colours, textures, etc. For further work, the segmented masks need to be transferred to the meshes. Most software can transfer the mask into a wide range of

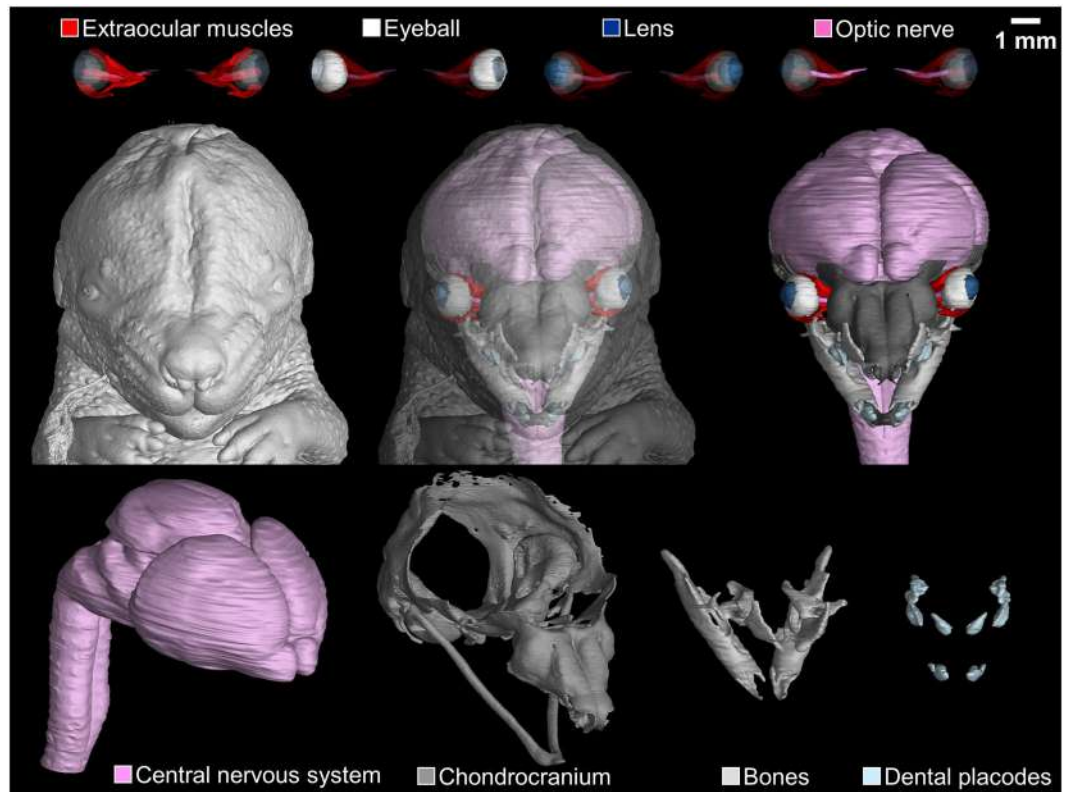


Figure 3. Surface rendering of segmented structures in a mouse embryo 15 days post-fertilisation. Structures of interest are colour-coded.

equivalent formats. However, only some of the formats contain information about the colour (e.g. OBJ, VRML and STEP) which is important for the visualisation of several structures in one model. Other formats represent only the mesh (e.g. STL and Matlab m-file).

Another problem to be solved is the size of the model (i.e. the number of faces in the mesh). When transferring the segmented mask into the mesh, an unnecessarily large number of faces can be created. Comparison of a different number of faces and corresponding size can be found in Fig. 4. Surprisingly, reducing by four times the number of faces does not significantly compromise details in the 3D models. Simple shapes such as the eyeball do not show notable errors besides the slight deformation of the sphere. However, further simplification of complex shapes, such as the chondrocranium and extraocular muscles (EOM), reduces the model quality and some details are lost (Fig. 4, red arrows). Thus, depending on the structures analysed and the resolution needed, different face reductions should be tested and validated before further analysis. Therefore, the compression of the data should be customised according to the complexity of the model and the resolution of tomographic slices.

Among the 3D printing software, some free software enable colour modifications or mesh simplification. Here, we made use of the Meshlab⁴⁷ and Blender⁴⁸ packages for this purpose. Notably, the latter allows unifying different sub-models into one mesh preserving the individuality of each object (see Supplementary Material 1 for more details).

Creation of an Interactive 3D PDF

Once the models are colour-labelled and simplified, they are then converted into an interactive file. We exploited 3D PDF Maker Standalone⁴⁹ taking advantage of the pre-prepared model that provides an interactive window in the PDF file by clicking on Add 3D button. Before embedding the model into an interactive file, the user can prepare an ordinary PDF file using standard software (e.g. Microsoft Office, Apache OpenOffice etc.). This file is used as a template showing, for example, individual structures or predefined views. These areas (i.e. images or signs) are taken into life in 3D PDF Maker by assigning whatever area in the page to specific view/structure (see for more details Supplementary Materials 1 and 2).

The model document presented here (Supplementary Material 3) consists of four predefined views (ventral, dorsal, lateral and medial) and a possibility of showing individual craniofacial structures (brain, cartilage, bone and teeth). It helps to manipulate the 3D model and can be set according to the areas/views of interest that are important to show. For example, for better visualisation, some structures can be set to the semi-transparent mode, or structures can be switched on/off individually in the model tree. The interactive 3D PDF also allows the user to rotate, turn and pan the model, change the pre-defined 3D-rendering, change the lights and background colour or add a virtual cross-section on the model.

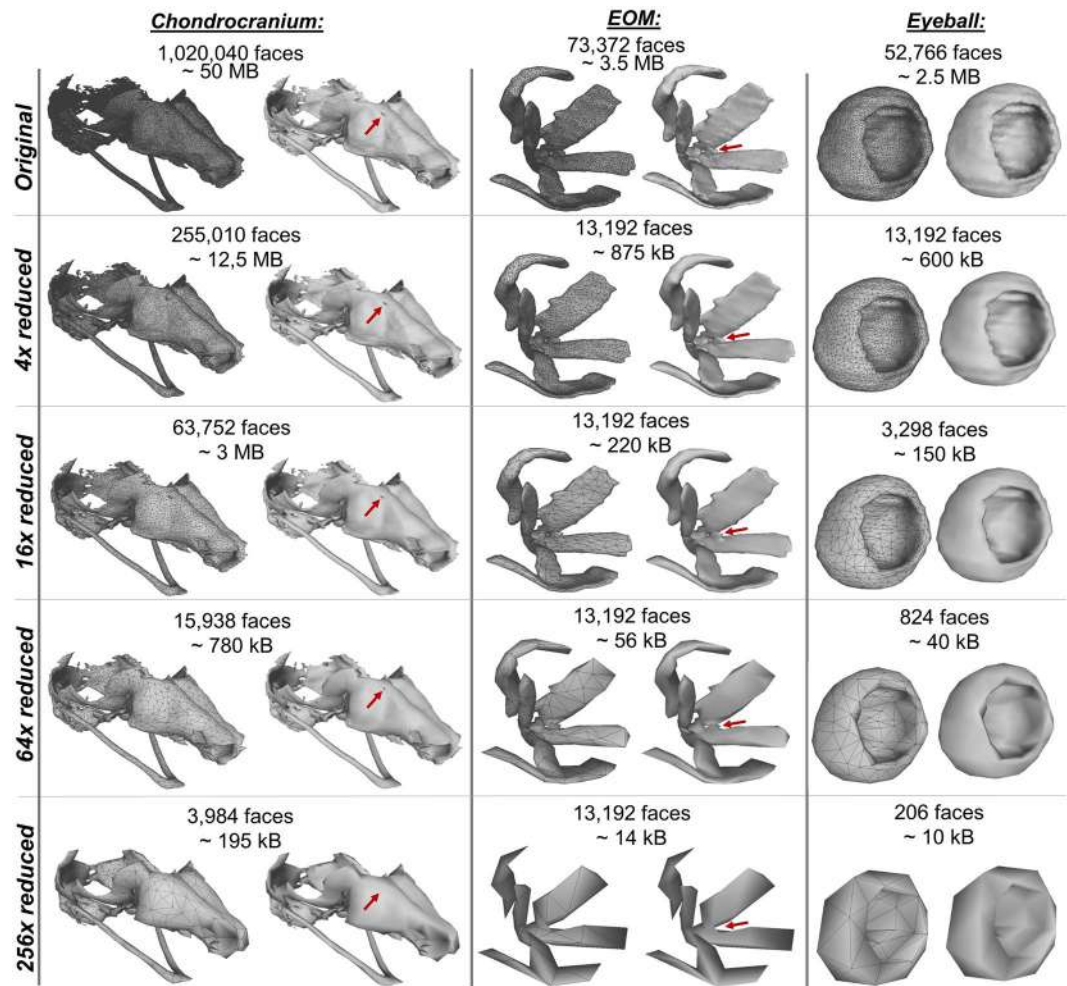


Figure 4. The number of faces affects the detection of details in chondrocranium, extraocular muscles (EOM) and eyeball models. Red arrows indicate details in the 3D model that disappear with model simplification.

Discussion and Conclusion

Comparative morphological studies in the field of developmental biology have been challenging, but contrast-enhanced X-ray computed tomography has brought new possibilities of high-resolution 3D visualisation^{15,16,50}. In this study, we present a detailed, user-friendly protocol for the surface rendering of craniofacial structures including soft tissues (muscles, eyeballs, central nervous system) as well as of hard tissues (cartilages, bones and teeth), with a step-by-step procedure from sample collection to the creation of an interactive 3D PDF. The final PDF is readable on all operating systems with the free standard AdobeReader®/AcrobatReaderDC (Adobe Inc., California USA).

Our 3D reconstruction methodology has already shown its utility and strength for visualisation and phenotypic analysis of complex structures such as the neck musculoskeletal system⁵⁰ and nasal capsules of control and mutant mouse embryos¹⁶. Therefore, a user-friendly method for creating such files will be of great utility for biologists. In addition, our procedure can be used as a framework to analyse volumetric data for any field of research that relies on 3D rendering, e.g. for visualisation of volumetric information of geological samples by laser-induced breakdown spectroscopy⁵¹.

The use of interactive 3D PDF files has a great potential for data sharing, communication and publications²¹, but is still sparsely used. We believe that our work will inspire researchers working with 3D imaging to present their data in such a user-friendly format.

Methods

Use of experimental animals. All animal work was approved and permitted by the Local Ethical Committee on Animal Experiments (North Stockholm Animal Ethics Committee) and conducted according to The Swedish Animal Agency's Provisions and Guidelines for Animal Experimentation recommendations. Mice were sacrificed with isoflurane (Baxter KDG9623) overdose or cervical dislocation, and embryos were collected into ice-cold PBS. Subsequently, tissue samples were fixed into freshly prepared 4% paraformaldehyde (PFA) in PBS solution for 24 hours at +4°C with slow rotation and washed in PBS.

Tissue contrasting. Staining protocol has been adapted and modified from the original protocol developed by Brian Metscher laboratory^{33,34}. After fixation, the samples were dehydrated in increasing concentration of ethanol series (30%, 50%, 70%, 90%), one day in each concentration to minimise the shrinkage of tissues. For tissue contrasting, samples were then transferred into 1% PTA (phosphotungstic acid) in 90% methanol for three weeks. The PTA-methanol solution was changed every two days. Subsequently, the samples were rehydrated by ethanol series (90%, 70%, 50% and 30%) and shipped to the CT-laboratory for scanning.

X-ray microCT measurements. After fixation and contrasting treatments, samples were fully rehydrated in distilled water, embedded in 1.0% agarose gel and placed in a polypropylene tube to avoid movement artefacts during tomography scanning. The polypropylene tube was fixed on a plastic rod by a silicone gun. The rod was put in the centre of the rotation stage axis. The microCT scanning was performed using the laboratory system GE Phoenix v|tome|x L 240 (GE Sensing & Inspection Technologies GmbH, Germany) with a 180 kV/15 W maximum power nanofocus X-ray tube and flat panel dynamic 41|100 with 4000 × 4000 px and a pixel size of 100 × 100 μm. The exposure time was 600 ms in each of the 2200 projections acquired over a total angle of 360°. Three projections were acquired and averaged in every position to reduce the noise in the tomographic data. Thus, the scanning time was 73 minutes. The acceleration voltage and current of the X-ray tube were 60 kV and 200 μA, respectively. The beam was filtered by a 0.2 mm-thick aluminium filter. The linear voxel resolution of the measurement was set to 4.2 μm in all dimensions. The tomographic reconstruction was conducted using the software GE phoenix datos|x 2.0 (GE Sensing & Inspection Technologies GmbH, Germany).

Data processing and analysis. Segmentation of craniofacial structures was performed semi-manually in Avizo (Thermo Fisher Scientific, USA). We used some automatic tools using a region growing method and thresholding on 2D slices. Segmentations were done on one of three to five slices, and the mask was interpolated. Subsequently, the segmented models were smoothed in VG Studio MAX 3.2 (Volume Graphics GmbH, Germany) according to⁴⁵. The segmented mask was then exported into a mesh (*.OBJ format) and was colour-labelled and adjusted in Meshlab⁴⁷ and Blender software⁴⁸. The colour-coded models were transferred into a pre-prepared PDF file in 3D PDF Maker Standalone⁴⁹. The detailed manual can be found in Supplementary Material 1. The use of the interactive 3D PDF is available in Supplementary Material 2.

Data availability

The datasets generated during and/or analysed during the current study are available from the corresponding author on reasonable request.

Received: 20 May 2019; Accepted: 25 September 2019;

Published online: 17 October 2019

References

- World Health Organization. Congenital anomalies, Fact sheet No. 370. <https://www.who.int/news-room/fact-sheets/detail/congenital-anomalies> (2016).
- World Health Organization. Birth defects: report by the Secretariat, Executive board 125th session EB125/7. <http://www.who.int/iris/handle/10665/2271> (2009).
- Weninger, W. *et al.* High-resolution episcopic microscopy: a rapid technique for high detailed 3D analysis of gene activity in the context of tissue architecture and morphology. *Anat Embryol* **211**, 213–221, <https://doi.org/10.1007/s00429-005-0073-x> (2006).
- De Bakker, B. *et al.* An interactive three-dimensional digital atlas and quantitative database of human development. *Science* **354**, 1019–1028, <https://doi.org/10.1126/science.aag0053> (2016).
- De Bakker, B., De Jong, K., Hagoort, J., Oostra, R. & Moorman, A. Towards a 3-dimensional atlas of the developing human embryo: The Amsterdam experience. *Reproductive Toxicol* **34**, 225–236, <https://doi.org/10.1016/j.reprotox.2012.05.087> (2012).
- De Boer, B., Van den Berg, G., De Boer, P., Moorman, A. & Ruijter, J. Growth of the developing mouse heart: An interactive qualitative and quantitative 3D atlas. *Dev Biol* **368**, 203–213, <https://doi.org/10.1016/j.ydbio.2012.05.001> (2012).
- Belle, M. *et al.* Tridimensional Visualization and Analysis of Early Human Development. *Cell* **169**, 161–173, <https://doi.org/10.1016/j.cell.2017.03.008> (2017).
- Renier, N. *et al.* iDISCO: A Simple, Rapid Method to Immunolabel Large Tissue Samples for Volume Imaging. *Cell* **159**, 896–910, <https://doi.org/10.1016/j.cell.2014.10.010> (2014).
- Ragazzi *et al.* G. Fluorescence confocal microscopy for pathologists. *Mod Pathol* **27**, 460–471, <https://doi.org/10.1038/modpathol.2013.158> (2014).
- Dickinson, M. *et al.* High-throughput discovery of novel developmental phenotypes. *Nature* **537**, 508–514, <https://doi.org/10.1038/nature19356> (2016).
- Sharpe, J. Optical Projection Tomography as a Tool for 3D Microscopy and Gene Expression Studies. *Science* **296**, 541–545, <https://doi.org/10.1126/science.1068206> (2002).
- Sharpe, J. Optical projection tomography as a new tool for studying embryo anatomy. *J Anat* **202**, 175–181, <https://doi.org/10.1046/j.1469-7580.2003.00155.x> (2003).
- Wong, M., Dorr, A., Walls, J., Lerch, J. & Henkelman, R. A novel 3D mouse embryo atlas based on micro-CT. *Dev* **139**, 3248–3256, <https://doi.org/10.1242/dev.082016> (2012).
- Hsu, C. *et al.* Three-dimensional microCT imaging of mouse development from early post-implantation to early postnatal stages. *Dev Biol* **419**, 229–236, <https://doi.org/10.1016/j.ydbio.2016.09.011> (2016).
- Kaucka, M. *et al.* Oriented clonal cell dynamics enables accurate growth and shaping of vertebrate cartilage. *elife* **6**, e25902, <https://doi.org/10.7554/eLife.25902> (2017).
- Kaucka, M. *et al.* Signals from the brain and olfactory epithelium control shaping of the mammalian nasal capsule cartilage. *eLife* **7**, e34465, <https://doi.org/10.7554/eLife.34465> (2018).
- Noden, D. & Trainor, P. Relations and interactions between cranial mesoderm and neural crest populations. *J Anat* **207**, 575–601, <https://doi.org/10.1111/j.1469-7580.2005.00473.x> (2005).
- Buchanan, E., Xue, A. & Hollier, L. Craniofacial Syndromes. *Plast Reconstr Surg* **134**, 128e–153e, <https://doi.org/10.1097/PRS.0000000000000308> (2014).

19. De Boer, B. *et al.* The interactive presentation of 3D information obtained from reconstructed datasets and 3D placement of single histological sections with the 3D portable document format. *Dev* **138**, 159–167, <https://doi.org/10.1242/dev.051086> (2010).
20. De Laurier, A. *et al.* The Mouse Limb Anatomy Atlas: An interactive 3D tool for studying embryonic limb patterning. *BMC Dev Biol* **8**, 1–7, <https://doi.org/10.1186/1471-213x-8-83> (2008).
21. Neue, A. & Becker, L. Three-Dimensional Portable Document Format (3D PDF) in Clinical Communication and Biomedical Sciences: Systematic Review of Applications, Tools, and Protocols. *JMIR Med Inform* **6**, e10295, <https://doi.org/10.2196/10295> (2018).
22. Danz, J. & Katsaros, C. Three-dimensional portable document format: A simple way to present 3-dimensional data in an electronic publication. *Am J Orthod Dentofac Orthop* **140**, 274–276, <https://doi.org/10.1016/j.ajodo.2011.04.010> (2011).
23. Valera-Melé, M. *et al.* A Novel and Freely Available Interactive 3d Model of the Internal Carotid Artery. *J Med Syst* **42**, 6, <https://doi.org/10.1007/s10916-018-0919-4> (2018).
24. Van de Kamp, T. *et al.* Three-Dimensional Reconstructions Come to Life – Interactive 3D PDF Animations in Functional Morphology. *PLoS ONE* **9**, e102355, <https://doi.org/10.1371/journal.pone.0102355> (2014).
25. Ruthensteiner, B. & Heß, M. Embedding 3D models of biological specimens in PDF publications. *Microsc Res Techn* **71**, 778–786, <https://doi.org/10.1002/jemt.20618> (2008).
26. Ruthensteiner, B., Baeumlner, N. & Barnes, D. Interactive 3D volume rendering in biomedical publications. *Micron* **41**, 886.e1–886.e17, <https://doi.org/10.1016/j.micron.2010.03.010> (2010).
27. Menn, J. & Seliger, G. Increasing Knowledge and Skills for Assembly Processes through Interactive 3D-PDFs. *Procedia CIRP* **48**, 454–459, <https://doi.org/10.1016/j.procir.2016.02.093> (2016).
28. Semple, T., Peakall, R. & Tatarinic, N. A comprehensive and user-friendly framework for 3D-data visualisation in invertebrates and other organisms. *J Morphol* **280**, 223–231, <https://doi.org/10.1002/jmor.20938> (2019).
29. Metscher, B. D. MicroCT for comparative morphology: simple staining methods allow high-contrast 3D imaging of diverse non-mineralized animal tissues. *BMC Physiol* **9**, 11, <https://doi.org/10.1186/1472-6793-9-11> (2009).
30. Metscher, B. D. MicroCT for developmental biology: A versatile tool for high-contrast 3D imaging at histological resolutions. *Dev Dyn* **238**, 632–640, <https://doi.org/10.1002/dvdy.21857> (2009).
31. Wilkins, S., Gureyev, T., Gao, D., Pogany, A. & Stevenson, A. Phase-contrast imaging using polychromatic hard X-rays. *Nature* **384**, 335–338, <https://doi.org/10.1038/384335a0> (1996).
32. Baran, P. *et al.* High-Resolution X-Ray Phase-Contrast 3-D Imaging of Breast Tissue Specimens as a Possible Adjunct to Histopathology. *IEEE Trans Med Imaging* **37**, 2642–2650, <https://doi.org/10.1109/TMI.2018.2845905> (2018).
33. Wagner, W. *et al.* Towards synchrotron phase-contrast lung imaging in patients – a proof-of-concept study on porcine lungs in a human-scale chest phantom. *J Synchrotron Rad* **25**, 1827–1832, <https://doi.org/10.1107/S1600577518013401> (2018).
34. Momose, A., Takeda, T., Itaj, Y. & Hirano, K. Phase-contrast X-ray computed tomography for observing biological soft tissues. *Nat. Med.* **2** (1996).
35. Saccomano, M. *et al.* Synchrotron inline phase contrast μ CT enables detailed virtual histology of embedded soft-tissue samples with and without staining. *J Synchrotron Radiat* **25**, <https://doi.org/10.1107/S1600577518005489> (2018).
36. Larsson, D. H., Vågberg, W., Yaroshenko, A., Yildirim, A. Ö. & Hertz, H. M. High-resolution short-exposure small-animal laboratory x-ray phase-contrast tomography. *Sci. Rep.* **6**, <https://doi.org/10.1038/srep39074> (2016).
37. Yang, M. *et al.* Theoretical variance analysis of single- and dual-energy computed tomography methods for calculating proton stopping power ratios of biological tissues. *Phys Med Biol* **55**, 1343–1362, <https://doi.org/10.1088/0031-9155/55/5/006> (2010).
38. Yan, D., Zhang, Z., Luo, Q., Yang, X. & Chen, C. A Novel Mouse Segmentation Method Based on Dynamic Contrast Enhanced Micro-CT Images. *PLoS ONE* **12**, <https://doi.org/10.1371/journal.pone.0169424> (2017).
39. Lusic, H. & Grinstaff, M. W. X-Ray Computed Tomography Contrast Agents. *Chem Rev* **3**, 113, <https://doi.org/10.1021/cr200358s> (2013).
40. Heude, E., Rivals, I., Couly, G. & Levi, G. Masticatory muscle defects in hemifacial microsomia: A new embryological concept. *Am J Med Genet Part A* **155**, 1991–1995, <https://doi.org/10.1002/ajmg.a.34095> (2011).
41. de Bournonville, S., Vangrunderbeeck, S. & Kerckhofs, G. Contrast-Enhanced MicroCT for Virtual 3D Anatomical Pathology of Biological Tissues: A Literature Review. *Contrast Media Mol. Imaging* **2019**, 1–9, <https://doi.org/10.1155/2019/8617406> (2019).
42. Zikmund, T. *et al.* High-contrast differentiation resolution 3D imaging of rodent brain by X-ray computed microtomography. *J Instrum* **13**, C02039–C02039, <https://doi.org/10.1088/1748-0221/13/02/C02039> (2018).
43. Weinhardt, V. *et al.* Quantitative morphometric analysis of adult teleost fish by X-ray computed tomography. *Sci Rep* **8**, 16531, <https://doi.org/10.1038/s41598-018-34848-z> (2018).
44. Boccardi, M. *et al.* Survey of Protocols for the Manual Segmentation of the Hippocampus: Preparatory Steps Towards a Joint EADC-ADNI Harmonized Protocol. *J Alzheimers Dis* **26**, 61–75, <https://doi.org/10.3233/JAD-2011-0004> (2011).
45. Tesařová, M. *et al.* Use of micro computed-tomography and 3D printing for reverse engineering of mouse embryo nasal capsule. *J Instrum* **11**, C03006–C03006, <https://doi.org/10.1088/1748-0221/11/03/C03006> (2016).
46. Tesařová, M. *et al.* A quantitative analysis of 3D-cell distribution in regenerating muscle-skeletal system with synchrotron X-ray computed microtomography. *Sci Rep* **8**, 14145, <https://doi.org/10.1038/s41598-018-32459-2> (2018).
47. Cignoni, P. *et al.* MeshLab: an Open-Source Mesh Processing Tool. <http://vcg.isti.cnr.it/Publications/2008/CCCDGR08/MeshLabEGIT.final.pdf> (2008).
48. Hess, R. *The essential Blender: guide to 3D creation with the open source suite Blender* (ed. Roosendaal, T.) (No Starch Press, 2007).
49. 3D PDF Maker [software] www.3dpdfmaker.com (2019).
50. Heude, E. *et al.* Unique morphogenetic signatures define mammalian neck muscles and associated connective tissues. *eLife* **7**, e40179, <https://doi.org/10.7554/eLife.40179> (2018).
51. Prochazka, D. *et al.* Joint utilization of double-pulse laser-induced breakdown spectroscopy and X-ray computed tomography for volumetric information of geological samples. *J Anal Atom Spectrom* **33**, 1993–1999, <https://doi.org/10.1039/c8ja00232k> (2018).

Acknowledgements

This research was carried out under the project CEITEC 2020 (LQ1601) with financial support from the Ministry of Education, Youth and Sports of the Czech Republic under the National Sustainability Programme II, CEITEC Nano Research Infrastructure (MEYS CR, 2016–2019) and) and Ceitec Nano+ project, CZ.02.01/0.0./0.0./16_013/0001728 under the program OP RDE. We acknowledge support by grant AFM Telethon 21853. J.K. and M.T. acknowledge the support of the Brno University of Technology through grant FSI-S-17-4506. M.T. was financially supported by grant CEITEC VUT-J-19-5764 and by the Brno City Municipality as a Brno Ph.D. Talent Scholarship Holder.

Author contributions

M.T., E.H. and G.C. worked on the data analysis and methodology. M.K. prepared the samples and stained them for CT measurement. M.T. and T.Z. performed CT measurements. I.A., S.T. and J.K. designed the experiments. M.T., T.Z. and J.K. wrote the manuscript. All authors reviewed the manuscript.

Competing interests

The authors declare no competing interests.

Additional information

Supplementary information is available for this paper at <https://doi.org/10.1038/s41598-019-51180-2>.

Correspondence and requests for materials should be addressed to J.K.

Reprints and permissions information is available at www.nature.com/reprints.

Publisher's note Springer Nature remains neutral with regard to jurisdictional claims in published maps and institutional affiliations.



Open Access This article is licensed under a Creative Commons Attribution 4.0 International License, which permits use, sharing, adaptation, distribution and reproduction in any medium or format, as long as you give appropriate credit to the original author(s) and the source, provide a link to the Creative Commons license, and indicate if changes were made. The images or other third party material in this article are included in the article's Creative Commons license, unless indicated otherwise in a credit line to the material. If material is not included in the article's Creative Commons license and your intended use is not permitted by statutory regulation or exceeds the permitted use, you will need to obtain permission directly from the copyright holder. To view a copy of this license, visit <http://creativecommons.org/licenses/by/4.0/>.

© The Author(s) 2019

An interactive and intuitive visualisation method for X-ray computed tomography data of biological samples in 3D Portable Document Format

Markéta Tesařová¹, Eglantine Heude^{2,3,4}, Glenda Comai^{3,4}, Tomáš Zikmund¹, Markéta Kaucká^{5,6}, Igor Adameyko^{5,6}, Shahragim Tajbakhsh^{3,4} and Jozef Kaiser^{1*}

¹Central European Institute of Technology, Brno University of Technology, Brno, Czech Republic

²Department Adaptation du Vivant, Museum national d'Histoire naturelle, Paris, France

³Department of Developmental and Stem Cell Biology, Stem Cells and Development Unit, Institut Pasteur, Paris, France

⁴CNRS UMR 3738, Paris, France

⁵Department of Physiology and Pharmacology, Karolinska Institutet, Solna, Sweden




⁶Department of Molecular Neurosciences, Medical University of Vienna, Vienna, Austria

*Corresponding author: kaiser@fme.vutbr.cz

Supplementary Material 1 Manual for creation of 3D PDF



The manual contains a detailed description of the pipeline for the creation of a personalised interactive 3D PDF file. Our procedure involves a combination of free (Meshlab, Blender) and commercial (Avizo, VG Studio, 3D PDF Maker) software. Alternatively, segmentation or remeshing of the model can be done with other appropriate software.

1a. Segmentation (Avizo)



- ✓ Import image stack into Avizo software (DICOM, tiff, raw etc.)
Click on: *Open data* - mark all images in the stack - option *Read complete volume into memory*.
- ✓ The loaded volume of data appears in a file format *samples_name.vol*.
Select this file for all processes with volumetric data.
- ✓ Open segmentation editor: Right click on file *samples_name.vol* - *Image segmentation* -option *Edit new label field*.
Each label field represents one object (anatomical structure) or a type of objects (e.g. dental placodes, muscles etc.)
- ✓ Adjust the contrast by changing the histogram in the right panel.
- ✓ The segmentation is performed using the following software tools:
 - 
 - Brush—manual drawing; Size of the brush can be changed according to the dimensions of the segmented object
 - 
 - 2D lasso—useful for filling borders of larger, in homogeneous areas.
 - 
 - Blow tool—uses region growing method for areas with distinct borders and homogenous filling inside. The segmented area spreads until it reaches a threshold represented by a grayscale value.
- ✓ Perform manual segmentation for approximately one from three to ten slices (depending on object heterogeneity).
Compute the slice gaps by interpolation (*ctrl + I*) and check the interpolated slices. This method can lead to incompleteness that should be corrected manually.
- ✓ After interpolation, click on *Add selected voxels*.
- ✓ To visualise the segmented area, move back to project scene tree and mark item *Labels – Display - Isosurface - Apply*.
- ✓ To export segmented mask into the mesh, mark selected item of labels - *Compute - Generate Surface – Apply*. The computed surface appears in the right panel as file *samples_name.surf*.

- ✓ Export the mesh by marking item file *samples_name.surf* - click on *Save Data As* - select any of formats (STL ascii, STL little endian etc.)

1b. Smoothing of the model (VG Studio) (Optional)

- ✓ Import image stack into the VG Studio software.
Click on: *File - Import – Image stack/Raw volume/DICOM image stack ...*
- ✓ Import mesh to VG studio software into raw data. Click on: *File - Import – Mesh.*
- ✓ Transfer mesh to the region of interest in the volumetric data — software function *ROI from the mesh* in the left panel:
 
- ✓ Use the function *Smoothing* (left panel) if distinct inaccuracies occurred during interpolation of manual segmentation:
 
- ✓ Right click on the smoothed region of interest – *Convert to mesh* – click on *Export – Convert.*

2. Remeshing and colour-labelling of the model (Meshlab)

- ✓ Import the meshes – take your mesh from the folder and drop it in the scene.
- ✓ Window with a sign *Unify duplicates* appears – click on *OK.*
- ✓ All meshes appear in the right panel. Change visibility by clicking on/off :
 
- ✓ When adjusting the model, select the appropriate mesh in the right panel.
- ✓ To visualise detailed structures (faces) of the mesh, click on *Wireframe* icon  in the top panel.
- ✓ To reduce the size of the model (i.e. the number of faces), in top panel click on: *Filters – Remeshing simplification and reconstruction – Simplification: quadric edge collapse* (or choose other appropriate options for model simplification).
In the new window, determine *Percentage reduction* (0.5 = reduction of 50%).
Repeat this step if needed. The simplified model can be observed in the window in real time.
The appropriate size of a final model is usually between 1-20 MB.
- ✓ Repeat these steps for all meshes.
- ✓ For complete colour-labelling of the model, colour-labelling of vertex and faces is required:
 - For vertex colour-labelling, click on: *Filters – colour creation and processing – perlin colour* (or choose other appropriate options).
 - For faces colour-labelling, click on: *Filters – colour creation and processing – transfer colour vertex to face – apply.*
- ✓ Once the models are remeshed and colour-labelled, export new meshes:
In the right panel, click on the mesh to be exported.
In the top panel, click on *Export mesh as* (choose the format that can contain information about the colour e.g. OBJ, VRML and STEP) – *OK.* Do not use diacritics or space in the model name.


3. Creation of mesh composed of sub-meshes (Blender)

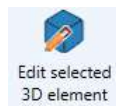
- ✓ Import mesh into Blender software, click on: *File – Import – OBJ* and select the mesh.
- ✓ Repeat this step for all meshes that will be merged into one 3D structure.
- ✓ Export final mesh, click on *Export as wavefront – OBJ.*
 - All meshes that have been imported individually will be exported altogether as one OBJ file, but keeping their individuality.

4. Pre-preparing of the PDF template (Powerpoint) (Optional)

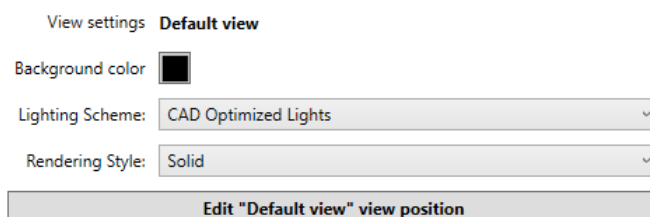
- ✓ Before creating an interactive file, you can prepare an ordinary PDF file from Powerpoint, which is used as a template for future 3D PDF. It can show e.g. signs, individual structures, predefined views, etc.

5. Creation of interactive 3D PDF (3D PDF Maker)

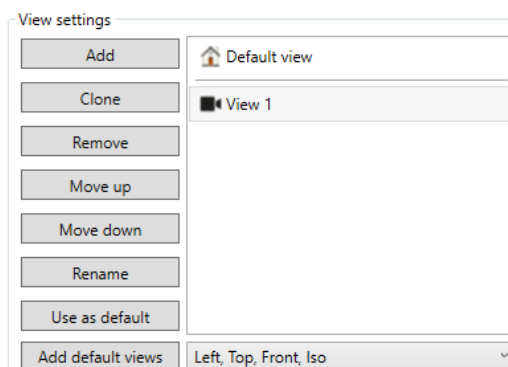
- ✓ Launch 3D PDF Maker Software. Then, you can choose between two options:
 - Open pre-prepared PDF template with static images.
 - Start with a new blank page.
- ✓ To add a 3D model into the page, click on *Add 3D* button  and select the mesh to be inserted.
- ✓ You can predefine the default view and background colour in this step (that can also be modified later). Then select an area for an interactive window by dragging the mouse.
- ✓ All options regarding the interactive window are set in the top panel by button *Edit selected 3D element*:



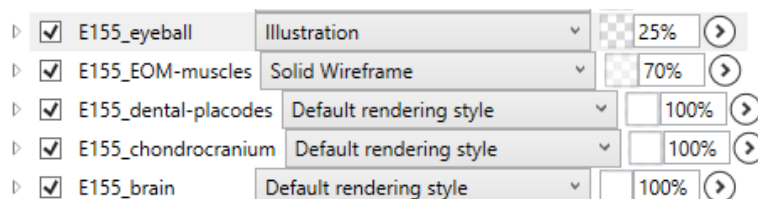
- ✓ By activating this button, you can:
 - Change default view, background colour, lighting scheme and rendering style:



- Add new views:



- Change transparency of objects:



- ✓ Linking pre-defined view with some image/sign can be done by clicking on *Add link to 3D view* button (this function allows the user to create interactive areas in the final PDF).

Drag the mouse in the area that you want to make interactive. The list with predefined views will appear, choose the view that you want to associate with this area.



- ✓ You can check the provisional form of the PDF by *Show preview with Adobe Reader* button:



- ✓ To save the final version, just click on the *Save icon*:



Note: A free 30-day trial to test the 3D PDF Maker software is available on www.3dpdfmaker.com.

SCIENTIFIC REPORTS

OPEN

A quantitative analysis of 3D-cell distribution in regenerating muscle-skeletal system with synchrotron X-ray computed microtomography

Markéta Tesařová¹, Lucia Mancini², Andras Simon³, Igor Adameyko^{4,5}, Markéta Kaucká^{4,5}, Ahmed Elewa³, Gabriele Lanzafame², Yi Zhang^{4,6}, Dominika Kalasová¹, Bára Szarowská⁴, Tomáš Zikmund¹, Marie Novotná¹ & Jozef Kaiser¹

One of the greatest enigmas of modern biology is how the geometry of muscular and skeletal structures are created and how their development is controlled during growth and regeneration. Scaling and shaping of vertebrate muscles and skeletal elements has always been enigmatic and required an advanced technical level in order to analyse the cell distribution in 3D. In this work, synchrotron X-ray computed microtomography (μ CT) and chemical contrasting has been exploited for a quantitative analysis of the 3D-cell distribution in tissues of a developing salamander (*Pleurodeles waltl*) limb – a key model organism for vertebrate regeneration studies. We mapped the limb muscles, their size and shape as well as the number and density of cells within the extracellular matrix of the developing cartilage. By using tomographic approach, we explored the polarity of the cells in 3D, in relation to the structure of developing joints. We found that the polarity of chondrocytes correlates with the planes in joint surfaces and also changes along the length of the cartilaginous elements. Our approach generates data for the precise computer simulations of muscle-skeletal regeneration using cell dynamics models, which is necessary for the understanding how anisotropic growth results in the precise shapes of skeletal structures.

Several experimental techniques have recently been used for the visualization of cells in three dimensions (3D). These techniques usually use electromagnetic radiation with wavelengths of visible light or X-rays (wavelength 10^{-6} – 10^{-10} m). Mainly due to the shape and composition of the investigated samples, all imaging methods have their own advantages and limitations. The 3D biological structures, in their natural shape, may be thick and highly scattering, preventing e.g. light from penetrating them without significant distortion. Advanced light microscopy techniques can image thicker biological specimens at a high spatial resolution such as confocal microscopy, multiphoton microscopy, and optical coherence tomography¹.

Confocal microscopy is considered to be one of the most convenient techniques for imaging cells in 3D. Moreover, this method has also been used specifically for the study of cell columns in the articular cartilage of rats². Also, an *in vivo* study of the collagen matrix was performed by high-resolution fluorescence confocal microscopy³. However, *in vivo*, fluorescence imaging or the immunostaining of labelled specific cells⁴ have high requirements for the sample preparation. Moreover, fluorescence-based techniques are used to visualize a fluorescent marker that was targeted to the structure of interest. The auto-fluorescent properties of the cells can provide sufficient contrast to allow for the identification of the desired structures¹. However, they cannot be used for all types of tissues, which can limit the utilization of this technique.

Additionally, imaging techniques based on the scattering of light are not suitable for imaging larger samples, e.g. the whole limbs of vertebrates. The penetration depth of confocal microscopy is limited to less than $100\ \mu\text{m}$ ^{5,6}.

¹Central European Institute of Technology, Brno University of Technology, Brno, Czech Republic. ²Elettra-Sincrotrone Trieste S.C.p.A., Basovizza, Trieste, Italy. ³Department of Cellular and Molecular Biology, Karolinska Institutet, Solna, 171777, Stockholm, Sweden. ⁴Department of Physiology and Pharmacology, Karolinska Institutet, Solna, 171777, Stockholm, Sweden. ⁵Department of Molecular Neurosciences, Medical University Vienna, Vienna, Austria. ⁶Department of Orthopaedics, Xiangya Hospital, Central South University, Changsha, Hunan Province, China. Correspondence and requests for materials should be addressed to J.K. (email: kaiser@fme.vutbr.cz)

Surface imaging microscopy has been compared to confocal microscopy imaging in order to visualize larger samples, such as whole embryos⁷. Despite the high spatial resolution for the whole body of an embryo, the method is destructive and highly demanding in terms of sample preparation.

A deeper sample penetration for 3D imaging can be achieved by multi-photon microscopy. This technique provides deep penetration mainly because of a scattered signal of photons which results from localized nonlinear signal generation. It can allow for optical sectioning in samples on a millimeter thickness scale, depending on the tissue type⁸. Such a thickness is comparable with the size of the skeletal elements of some embryonic vertebrates. However, this method cannot be applied to biological samples in general. The three-dimensional resolution of a two-photon excitation microscope is identical to that achieved in an ideal confocal microscope, i.e. hundreds of nanometers⁹.

Optical coherence tomography is a technique, which is capable of obtaining images from even thicker tissue samples¹⁰. On the other hand, the spatial resolution is lower (of the order of 5–10 μm)^{11,12}, which is not sufficient for a quantitative analysis of single cell distribution in vertebrates.

A number of improvements have developed in X-ray-based methods for cellular imaging. X-rays can penetrate cells and thick tissues (from millimeter- to centimeter-sized samples) without the need for sectioning the sample and it is possible to generate quantitative 3D data with spatial resolution of up to several dozen nanometers on the selected regions of interest^{13–15}. Soft X-ray microscopy or tomography and coherent diffractive imaging are techniques that examine even the subcellular structures. The soft X-ray microscopes usually use wavelengths in the so-called water window – the region of the spectrum between the K shell absorption edges of carbon and oxygen, which are the typical components for biological tissues. Carbon and nitrogen compounds absorb these X-rays more than water^{12,16}. However, visualizing an entire organ or a developing limb would generate an inhibitive amount of data. The feasible approach must allow for the 3D imaging of a large field of view (millimeter scale) with the eventual possibility of zooming into areas of interest¹⁷.

X-ray computed microtomography (μCT) is a non-destructive imaging method that provides high spatial resolution (from micron to sub-micron scale) of 3D data for samples with the size ranging from sub-millimeter to several millimeters. The result is a map of the X-ray attenuation coefficient within the sample volume and, if certain experimental conditions are fulfilled, then also phase changes can be detected^{18,19}. Recent developments of this method have significantly advanced biological imaging.

In synchrotron facilities, the small angular source size, the high intensity and the nearly-parallel geometry of the X-ray beam makes it possible to obtain not only a high spatial resolution on the macroscopic samples, but also to exploit the transverse coherence properties of the X-ray beam. This allows a very simple experimental approach to be used in the propagation-based phase-contrast imaging (PCI)^{20,21}. By using synchrotron radiation, μCT measurements of the different regions of the large-scale objects (centimeter range) can be imaged at high spatial resolution (on the micron scale)^{22–28}. Furthermore, the application of PCI techniques could allow different tissues with similar chemical compositions and radioscopic density, to be distinguished^{29,30}.

Staining with heavy elements such as iodine, tungsten or osmium-based compounds^{31,32} also enhances the contrast within the various types of tissues using advanced μCT instruments (either laboratory or synchrotron-based). A PCI of biological samples can be employed even for unstained samples^{33–35}. However, the combination of phase-contrast with the increasing X-ray absorption contrast by staining gives excellent image quality with better voxel resolution than absorption μCT setups^{25,26}.

The patterning of skeletal elements during limb development in salamanders differs from other tetrapods³⁶. Salamanders show an anterior or preaxial dominance in the order of formation and ossification of the zeugopodial and autopodial elements. Moreover, some proximal elements condense later than proximal ones³⁷, which is definitely isolated from the familiar order of proximal to distal limb development in other tetrapods. In contrast with mammals, salamanders have a remarkable ability to regenerate their extraordinary range of body structures such as limbs, tails, retina, and spinal cord, along with some sections of the heart and brain³⁸. Limb regeneration depends on the formation of a blastema, which is a pool of progenitor cells that arise after amputation. Blastema cells redifferentiate, proliferate and then restore the structured limbs³⁹. The basic anatomy of the salamander joints, with the apposed, articular surfaces between the adjacent long bones, encapsulated by the connective tissues, is very similar to mammals^{40–42}.

In many cases, the oriented cell dynamics and proliferation play an essential role in shaping and scaling, but the directional deposition of the matrix in the bone and cartilage is not very well understood. The majority of work so far has concentrated mainly on the analysis of the epithelial or migratory mesenchymal populations during limb or facial development, which has produced important knowledge on the asymmetric proliferation of mesenchyme and convergent extension processes in shape-making, in general^{43–45}. However, the sculpting of precise and highly complex cartilaginous structures has not been recently focused upon except for several published works^{46–50}. Despite attention to the cartilage shape, current works do not provide any comprehensive explanation for shape-making, but rather focuses on the importance of a multitude of factors for different aspects of cartilage and mesenchyme development with some general impact on shape.

Muscle is a tissue that lies immediately next to the developing cartilage tissue in the embryo and remains in close proximity to the cartilage template after birth^{51,52}. On the one hand, the mechanical forces, induced by muscle contraction, seem to directly influence the morphogenesis regulation. Animal models, where muscle contractions have been removed or altered, and mouse mutants, without forming skeletal muscles, have led to the underdeveloped and misshapen skeletal elements⁵³. Similar to humans, a short stature and scoliosis are common features in children with Duchenne Muscular Dystrophy⁵⁴. Moreover, the immobilized muscle can also lead to joint structures loosening, such as a cavity, articular surfaces and patella⁵³. On the other hand, muscle cells can release biochemical signals to regulate the cartilage gene expression indirectly⁵⁵. It is still unknown how the precise, three-dimensional shape of skeletal elements is established, scaled up and what is the interaction in muscle and cartilage development. Finding a way to visualize and analyse cell distribution in 3D would be a

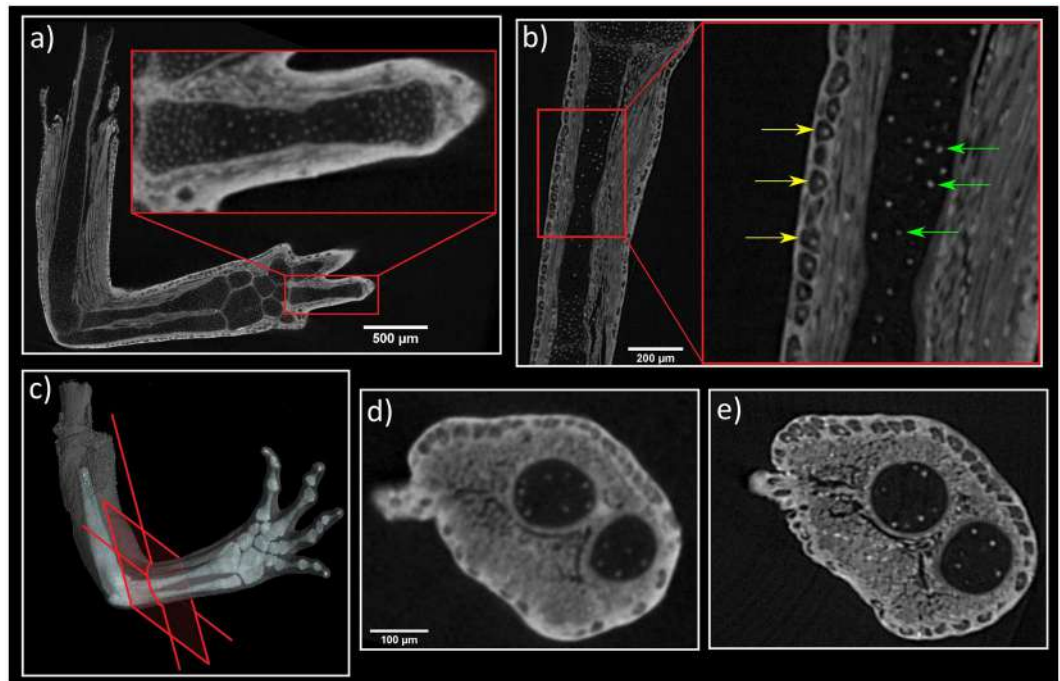


Figure 1. Comparison of the tomographic slices of a *P. waltl* forearm obtained by conventional and synchrotron μ CT. Despite near-cellular resolution, the employed conventional μ CT setup does not provide sufficient resolution for the automatic counting of cells with necessary accuracy. (a) Tomographic slice of the limb, the red area shows detail of one finger, (b) reconstructed slice obtained by phase-contrast μ CT at the SYRMEP beamline of the Elettra synchrotron facility, yellow arrows show cells of skin epithelium, green arrows show nuclei of cartilage, (c) 3D visualization of a limb with red plane representing the same plane of interest of tomographic slices: (d) Data obtained by conventional μ CT and (e) by synchrotron μ CT.

great step forward to answering these biological issues. 3D morphological characterization at cellular resolution using synchrotron-generated X-rays has already been successfully demonstrated. Furthermore, the spatial distribution of single cells inside the articular cartilage has been proven on stained⁵⁶ and unstained samples⁵⁷. Other tissues, such as Purkinje cells in the brain, were quantified using automated cell counting⁵⁸. However, previous approaches did not suffice in analysing cell polarization and the complex organization of multiple tissue types simultaneously with other 3D-analysis.

Here, we took advantage of the synchrotron-based X-ray μ CT technique in combination with chemical contrasting in mapping the actual cells, their orientation and extracellular matrix distribution in 3D, during salamander (*Pleurodeles waltl*) limb development in the simultaneous analysis of cartilage and muscles. We decided to use the larval limb of a Spanish ribbed newt because it is a promising emerging model of limb regeneration and development⁵⁹. The developing cartilages of *P. waltl* limbs are of the suitable size and are in the active growing and shaping phase. Our results demonstrated how the cell density and polarization within individual cartilaginous elements can be measured highlighting the localized accumulations of the extracellular matrix and changes in cell distribution and polarization during cartilage development. The method allowed for the mapping and 3D-reconstruction of several different tissue types at the same time, which is essential for understanding the development of a muscle-skeletal system. This study is a proof of the principle which shows the opportunity to use this type of analysis for exploring and modeling the development of skeletal structures with single-cell resolution.

Results

X-ray microtomography measurements. The conventional X-ray μ CT was exploited for overview experiments and the 3D visualization of developing *P. waltl* limbs stained with phosphotungstic acid (PTA). Here, we achieved an exceptional quality in chemical contrasting of the samples. However, the employed, conventional μ CT instruments, did not provide sufficient resolution for a quantitative analysis and counting every single cell. Nevertheless, the resolution delivered by conventional μ CT, gave basic information about qualitative cell distribution in the cartilage element (Fig. 1a,d). Though the information was only near-cellular, it was possible to detect some cell nuclei inside the limb.

The high photon flux, X-ray beam geometry and high spatial resolution (down to 1 μ m) of synchrotron μ CT achieved the cellular resolution for a quantitative analysis of cell distribution (see Fig. 1b,e). Moreover, the possibility to perform PCI experiments allowed the borders of cells in cartilaginous elements to be distinguished. A comparison of the same slice from conventional and synchrotron X-ray μ CT is reported in Fig. 1. A video of raw tomographic slices obtained by synchrotron μ CT measurement is in Supplementary Material 1.

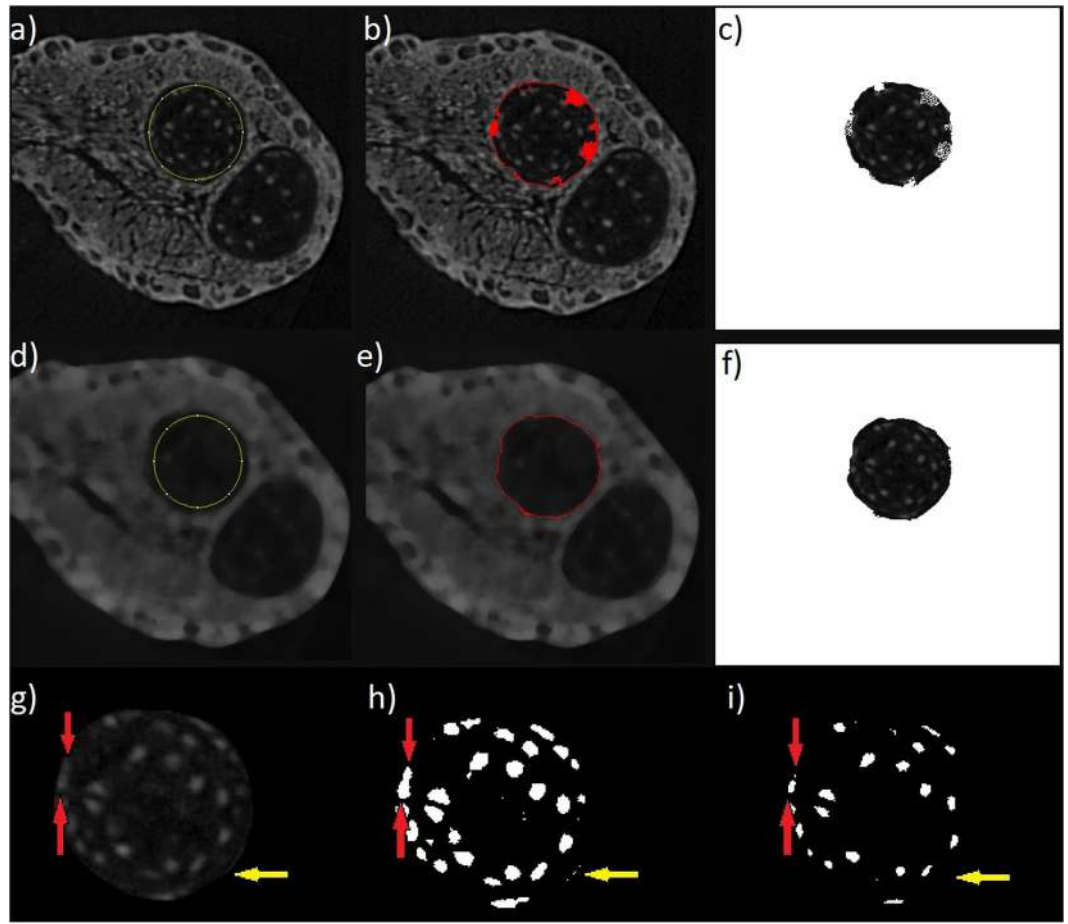


Figure 2. Automatic segmentation of skeletal elements performed by ABSnake^{65,66}. (a–c) Shows the contour applied to non-filtered tomographic slices; however, rough borders caused errors. (d–f) Shows the contour applied to a filtered image. The mask was obtained without any errors and the shape of the resulting data appears almost perfect. (g–i) *Blob analysis* in the *Pore3D* software⁶⁷. (g) One of the reconstructed slices used for the analysis, after the application of the 3D K-means clustering algorithm. (h) the results of the *blob analysis*, (i) the eroded segmented image. Red arrows indicate two nuclei of the cells that were connected within the *blob analysis*. The erosion of the binary image splits the blob into two parts. Yellow arrows show the light border of the cartilaginous element which should not be counted in the analysis. The erosion of the image also solved this problem.

Data processing and analysis. Obtaining high-contrast tomographic data is the first step in 3D analysis. By chemical contrasting, the cartilage is significantly less stained in comparison to the surrounding tissue, which leads to easier discrimination and outline of cartilage in μ CT data^{48–50,60}. The reason is that PTA provides a strong X-ray contrast as it is attached to proteins such as collagens and fibrils^{61,62}. Another important part is the data processing and analysis of the reconstructed tomographic volumes. Post-reconstruction data treatment requires segmentation of the investigated cartilage or bone elements by applying the appropriate algorithms for distinguishing every single cell in the desired area and then its quantitative analysis.

First, the detection and separation of a cartilaginous element is needed with segmentation. Conventional segmentation algorithms using the region growing method⁶³ are not suitable, due to the white spots inside the cartilage. These spots represent cell nuclei. Here, we applied the freeware image analysis software ImageJ⁶⁴ with its plug-in ABSnake^{65,66}. The next steps are to determine the starting contour for segmentation, the gradient threshold to be used in edge detection and the number of iterations of the segmentation cycles. Nevertheless, by applying a contour on the non-filtered tomographic slices, the iteration process does not converge to the border of the cartilage (Fig. 2a–c). This is due to the light spots (cell nuclei) in the cartilage body. Thus, the segmentation is not precise enough for the analysis. To avoid this problem, the contour is applied on the 3D median-filtered images. By filtering, the iteration procedure converges and the result of the process is the definition of the cartilage border. The final contour is smooth and perfectly copies the border of the cartilage body (Fig. 2d–f). The segmented data (cartilage element) can then be utilized for further analysis.

The next step for the quantification of cells was to count the cell nuclei represented by light spots in the image. For this purpose, the *Pore3D* software library⁶⁷ developed at Elettra, was employed. The 3D K-means clustering algorithm was used to sort data into three classes. The K-means algorithm converts an input image into vectors of

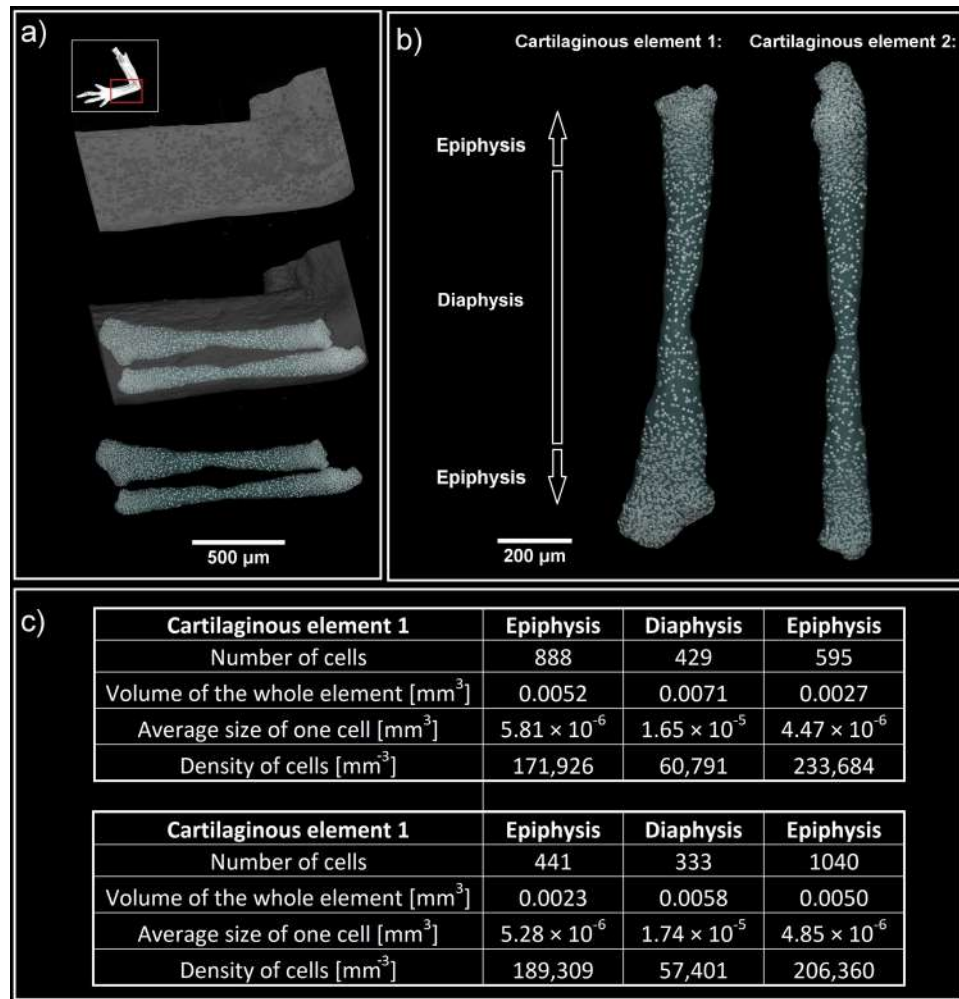


Figure 3. (a,b) 3D visualization of cartilaginous elements from a developing *P. waltl* limb forearm. White spots represent cell nuclei. c) Quantitative analysis allowed the determination of cell number, average size (given by ratio of volume of the whole element and number of cells), density and the volume of each cartilaginous element. The difference between diaphysis and epiphysis is evident: the density of cells in the diaphysis is half in comparison with the density in the epiphysis.

equal size and then by minimizing the sum of the squared distances from all points in a class to the class center⁶⁸. This way, the binary images were obtained for the nuclei of cells, extracellular matrix and the background. The binary image for the class, representing the cell nuclei (binary large object – blob) is shown in Fig. 2h.

By comparing Fig. 2g,h, it is evident that some nuclei are connected into one blob. This example is shown by the red arrows in Fig. 2. Moreover, some border segments of the cartilage are miss-detected as blobs (yellow arrows in Fig. 2). To correct these analytical issues, the erosion of the 3D data is the next step. After this step, the data is well suited to determine the number of cells (Fig. 2i). To obtain the final number of cells, the binary data of cell nuclei after erosion (Fig. 2i) was implemented for further blob analysis⁶⁹.

Basically, the limit of this type of analysis is determined by the resolution (spatial and contrast) of the system and by the size of the analysed structure. The spatial resolution of the detection system and the detectability of the given features of interest can be further influenced by working in phase-contrast mode⁷⁰. In our 3D image processing and analysis, the objects considered as cells and included in the computations, were those with size larger than 3 pixels = 27 voxels (=27 μm³ per blob). The video of segmented data is shown in Supplementary Material 2.

Biological results. Our analysis of developing ulna and radius cartilages from a *P. waltl* limb demonstrated zonation that included a wide central region inhabited by the chondrocytes submerged in much larger amounts of extracellular matrix as compared to developing epiphyseal regions defined based on the instant changes of a cell density on a histogram. The cell number of these sparse chondrocytes in the central regions of both the ulna and the radius appeared low, which could reflect the reduction of cell number by decreased proliferation and acquisition of a hypertrophic stage. According to a classical model, epiphyseal chondrocytes continue proliferation longer than chondrocytes in a central region of a cartilaginous element and, consequently, show much higher density according to our data (Fig. 3).

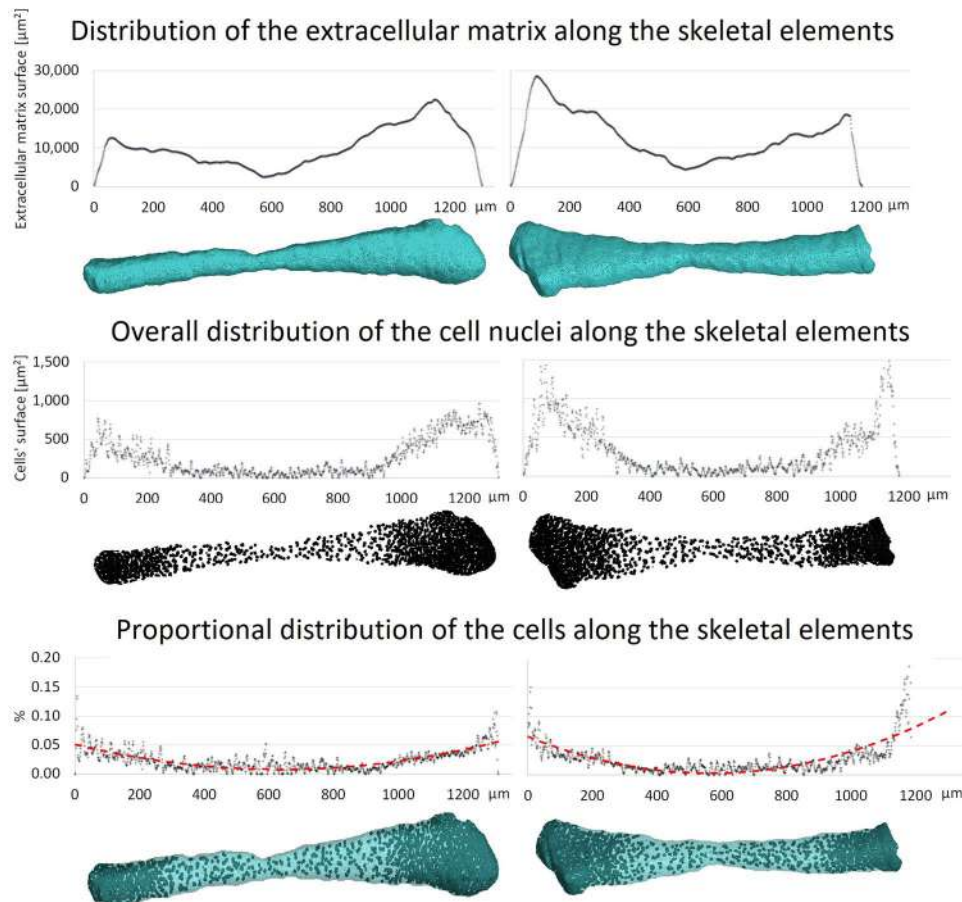


Figure 4. Distribution of extracellular matrix and cell nuclei along skeletal elements. Top: distribution of the area of extracellular matrix along the element. Middle: distribution of number of cells represented by the area of cell nuclei. Bottom: ratio between the area of cell nuclei and the area of extracellular matrix; the red-dotted line fits the data by a second order polynomial. The minimum of the parabola sits in the centre of the diaphyseal regions.

Further analysis showed more detailed distribution of cartilage along the growing skeletal element. For each slice, the area of the cell nuclei and area of the whole extracellular matrix were computed. Both structures showed uneven distribution in the distal direction. Interestingly, the ratio between cell nuclei and extracellular matrix areas changes (from approx. 0.1% to 0.01% - Fig. 4). The determined density of cells corresponds to the literature, which records estimated values for the cell density in cartilage between 30,000 and 110,000 cells mm^{-3} by confocal imaging⁷¹ or digital volumetric imaging by Jadin *et al.*⁷². However, the distribution in epiphyseal and diaphyseal regions has not been further discussed.

A key advantage of synchrotron X-ray μCT measurements enhanced by PTA staining is the large variety of tissues that can be detected simultaneously. Information from all structures in a sample is included in one dataset obtained by a single measurement, which determines the position of each structure within the sample (Fig. 5, Supplementary Material 3). Efficient analysis can be done for a wide spectrum of tissues. This allows to reveal connections between muscles and cartilage development simultaneously. The muscles showed incremental growth during the regeneration process in coordination with expanding cartilage and also appeared with their corresponding attachment points at different timing. The development of muscles then might guide cartilage and joint formation⁷³. Three developmental stages were observed in muscle-skeletal point of view. At the youngest analyzed stage (41–42), only one small group of muscle around the elbow joint was found. However, different muscle group (*biceps brachii*, *triceps brachii*, *brachioradialis* and *flexor carpi radialis*) were recognized in the next two stages (Fig. 6b). Meanwhile, the elbow joint angle was decreasing with the development of muscle. Interestingly, the decreasing angle between *ulna* and *humerus* was observed with increasing developmental stages (Fig. 6a). Beyond question, the development of *biceps brachii* and *brachioradialis* may contribute to the decreasing elbow joint directly (the physical function of *biceps brachii* and *brachioradialis* is to bend the elbow joint). Another important finding is shape and position of the developing muscles. Surprisingly, there is no muscle splitting at the youngest analysed stage (41–42). The muscle splitting occurs later together with shaping of the cartilaginous joint. Furthermore, there is a correlation between the cell polarity inside the cartilage and splitting of the muscles (Fig. 7). The chondrocytes next to the muscles attachment points have a higher cell polarity. In another word, there is a correlation between the cell polarity inside cartilage and muscle attachment point. It is natural to speculate the mechanical force from muscle stretch may be delivered to attach point and then influence

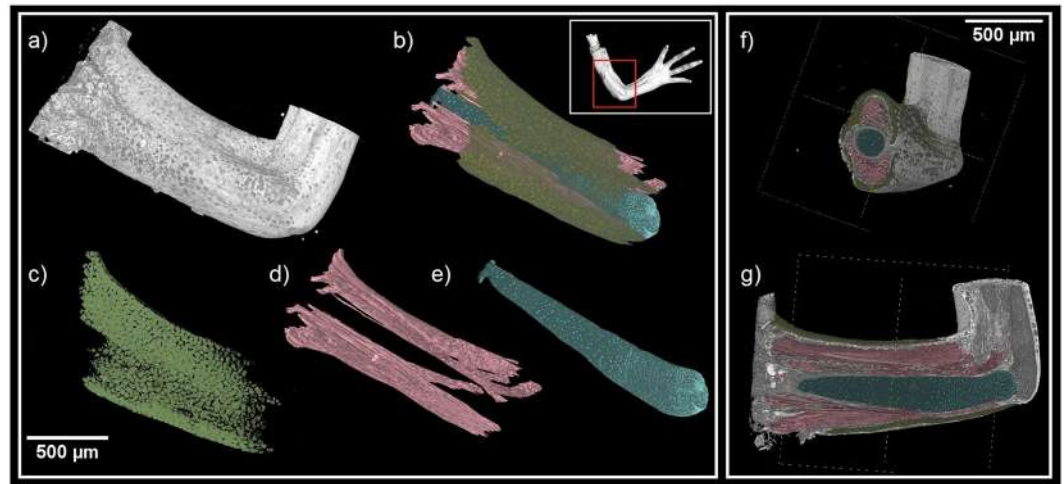


Figure 5. (a,b) 3D visualization of soft tissues showing other structures in the sample. (c–e) Sample segmentation showing cartilage (light blue), muscle fibers (red) and skin epithelium (yellow). (f–g) Clipping planes on the 3D model showing segmented structures inside the sample.

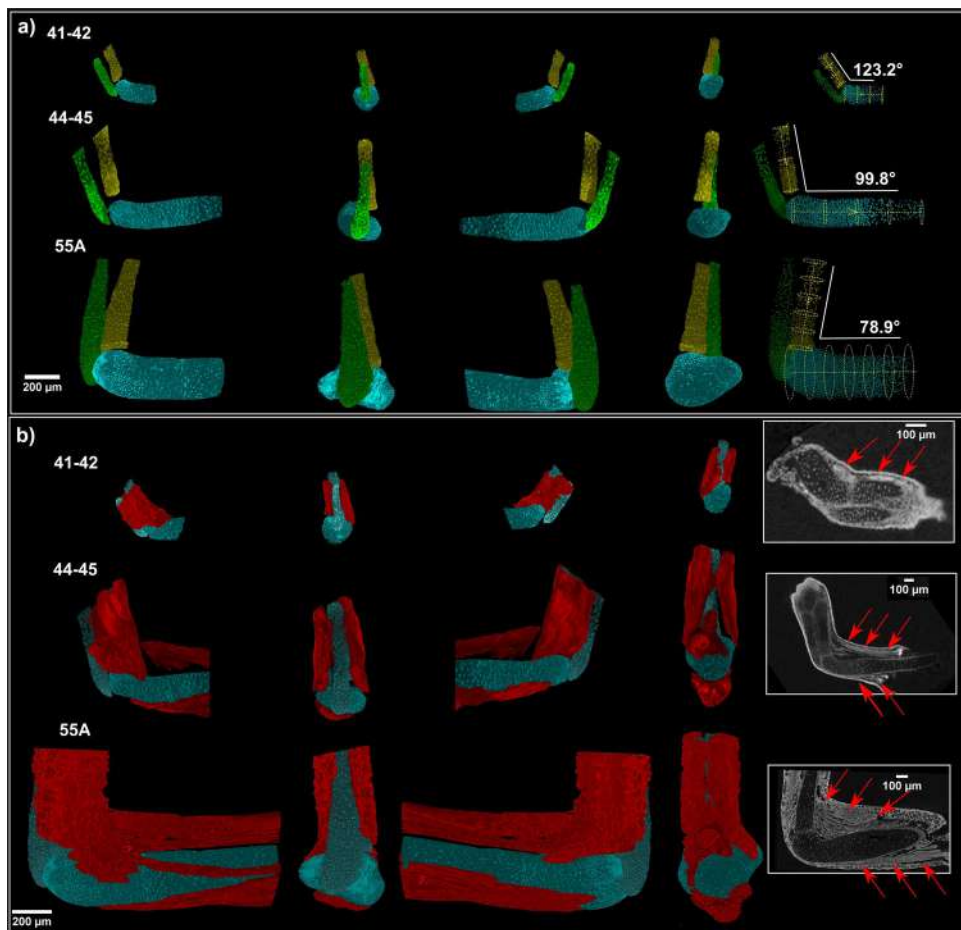


Figure 6. (a) Development of cartilage of the joint for three different developmental stages. The angle between *ulna* and *humerus* is decreasing with increasing developmental stage. (b) Visualization of joint simultaneously with developing muscles for three developmental stages. There is a correlation between decreasing angle and splitting of the muscles.

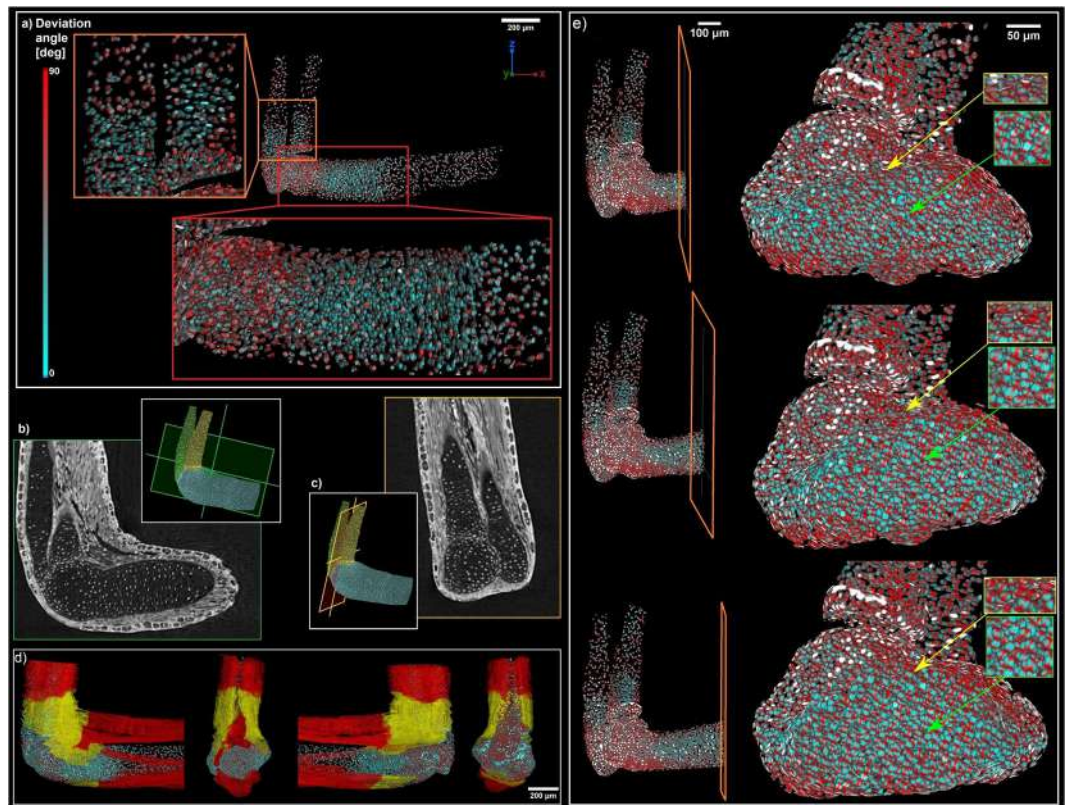


Figure 7. (a) Polarization of the cells inside cartilage. There are polarized zones between diaphysis and epiphysis for all cartilaginous elements: *ulna*, *radius* and *humerus*. Deviation angle 0° for *ulna* and *radius* was set to the plane x, y and for *humerus* was set to the plane y, z ; (b,c) Corresponding tomographic slices verifying the computation of polarization; (d) Muscle attachment points in correlation with cell polarization; (e) Detail of orientation of the cells: Superficial chondrocytes near surface (yellow arrow) are aligned with the developing surface of the cartilage in the contrary of chondrocytes in the middle of the cartilage (green arrow).

local chondrocytes polarity (Fig. 7d). It gives rise to a thought that a hitherto unknown mechanism controls the location and the density of chondrocytes together with cell polarity and muscle attachment points.

Our visualizations provided detailed information about developing joint surfaces at cellular resolution in 3D in the regenerating salamander limb. Development of surface geometry correlated in time with the formation of attached striated muscles. Orientation of chondrocytes in the developing joint, measured for the first time in the entire 3D volume by using X-ray computed tomography, correlated with the changing curvatures of joint surfaces. More generally, the resolution and differential contrast were sufficient to map the orientation of all chondrocytes within the cartilage, which provided important foundation for future inference of the oriented cell behaviour during cartilage shaping. Our results demonstrated that the predominant orientation of chondrocytes in epiphyseal regions was different from rather central regions of the cartilage, where the cell density appeared low. In addition to this, superficial chondrocytes in epiphyseal regions were aligned with the developing surface of the cartilage (Fig. 7e).

Taken together, our biological results show that development of cartilage geometry (including forming joints) correlates in time with developing skeletal muscles, which may influence the orientation of chondrocytes in epiphyseal regions, and through this, and in accordance with previously published data⁷³, regulate morphogenesis and fine shaping of specific regions in cartilage.

Discussion and Conclusion

In this study, we have demonstrated a novel, technical approach allowing for the quantitative analysis of polarization and 3D cell distribution inside the whole developing muscle-cartilaginous units from a regenerative animal model. This approach is based on the chemical contrasting of samples with PTA, followed by a high-resolution X-ray microtomography (μ CT) measurement and the subsequent 3D data-processing and analysis. The polarization of the cell is determined by analysing the shape of cells in the matrix or the shape of their nuclei within other soft tissues. The best results, suitable for the quantitative analysis, with a single cell resolution and qualified for the computer simulations, were achieved by the phase-contrast synchrotron X-ray μ CT analyses performed at the SYRMEP beamline of the Elettra facility. On the other hand, by using a conventional X-ray μ CT instrument, the resolution turned out to be near-cellular, whereas the quantitative analysis faced a number of additional problems.

Nevertheless, the data obtained by the conventional setup delivered important complementary information and allowed the visualization of many well-resolved internal structures.

Unexpectedly, our biological results show that the orientation of cells in the cartilage changes with cell density and position along the cartilaginous element and also in relation to the general position of the muscle attachment points and forming joint surfaces. The polarity of a cell may reflect so-called oriented cell behaviour, which might include oriented cell divisions, cell migration or other asymmetric processes important for shaping the structure⁷⁴. Geometrical signs of cell polarisation in the cartilage, obtained from tomographic data, suggest the potential role of mechanical forces in cartilage geometry formation via the control of the chondrocyte cell orientation within the extracellular matrix. The polarity of chondrocytes and perichondrial cells in the attachment point areas may result from tension in the developing muscles, which we mapped in terms of geometry and volume. Previous findings already established the role of the developing muscles in cartilage shaping⁷³. Brunt and co-authors⁷³ demonstrated that muscles are important for the morphogenesis of joints by using zebrafish as a model system together with computer simulations. The authors of the study concluded that the mechanical strain created by the muscles, influences cell orientation in the developing jaw joint of a fish⁷³, which goes along with our findings in the regenerative model system, where we provide 3D information of cell orientation suitable for further 3D-modeling efforts. On the other hand, according to our data, the muscles also expand in the direction following the attachment points that change their relative position in the growing cartilage with time.

In general, the obtained data, including the number of cells in 3D volume, their density, polarization, zonal distribution and the total volume of the skeletal elements, are important to understand growth, shaping, scaling and the regeneration of muscle and cartilaginous structures in the developing and regenerating vertebrates. Here, we have delivered proof of the principle study to show the possibility of visualizing and counting the individual chondrocytes in the cartilage of a vertebrate model system, suitable for both the developmental biology and the regenerative research. This approach can provide precise information about the incremental growth of a structure in terms of changes in cell polarity, cell numbers and simultaneously with the transforming shape. We envision that in the near future conventional laboratory μ CT setups will gain similar imaging capabilities to the synchrotron beamlines, opening new possibilities of studying biological structures in 3D with single-cell resolution. Hereby, the use of such conventional μ CT measurements in combination with open-source software for 3D image analysis, will enable new opportunities for the community of biologists and biomedical specialists, investigating the development and regeneration of skeletal and non-skeletal tissues.

Methods

Sample preparation. The *Pleurodeles waltl* (Spanish ribbed newt) colony was established from fertilized eggs produced in a laboratory colony located in Madrid, Spain. Animals originating from a wild population in the Doñana National Park (Spain) were obtained for research purposes by Agustin Gonzalez. The animals, used to prove the concept study were 4th/5th generation, developmental stage 41–42, 44–45 and 55 A (approximate length of the whole larva was 3.7 cm). Staging of the larva was performed according to Joven *et al.*⁷⁵. The frontal amputated limbs were briefly washed in PBS and fixed in freshly mixed 4% PFA for 12 hours at +4 degrees. A contrasting of the developing limbs was performed as follows: the samples were dehydrated in increasing ethanol grade (30%, 50%, 70%, 90%) at room temperature, 2 hours for each step, using a slow rotation of the samples. The samples were transferred into a solution of 0.7% PTA (phosphotungstic acid) in 90% methanol and incubated at +4 degrees for 5 days using slow rotation and the PTA-contrasting solution was changed after every 24 hours for a fresh one. The samples were washed with 90% methanol overnight at +4 degrees and then rehydrated in a decreasing ethanol grade (90%, 70%, 50%, 30%) at room temperature, 2 hours for each step and slow rotation.

Use of experimental animals. All procedures on newts were approved by local ethics committee (Stockholms Djurförsöksetiska Nämnd) and were performed in accordance with national regulations issued by the Swedish Board of Agriculture.

Conventional X-ray μ CT measurements. The contrast of the stained samples was checked by a conventional X-ray μ CT. Following that, the developing limbs were embedded in 1.0% of agarose gel and placed in polypropylene tubes to avoid movement artefacts during tomography scanning. A polypropylene tube was fixed on a plastic rod by a silicone gun. The rod, containing the sample, was put in the centre of the rotation stage axis. A μ CT scanning was performed using the laboratory system GE Phoenix v|tome|x L 240 (GE Sensing & Inspection Technologies GmbH, Germany) with a 180 kV/15 W maximum power nanofocus X-ray tube and a high contrast, flat panel detector DXR250 with 2048 × 2048 px² and a pixel size of 200 × 200 μ m². Exposure time was 900 ms in each of the 2200 projections acquired over a total angle of 360°. The utilized acceleration voltage and the current of the X-ray tube were 60 kV and 200 μ A, respectively. The beam was filtered by a 0.2 mm-thick aluminium filter to reduce beam-hardening artefacts. The tomographic reconstruction was done using the software GE phoenix datos|x 2.0 (GE Sensing & Inspection Technologies GmbH, Germany) with an isotropic voxel size of 2.5 μ m.

Synchrotron X-ray μ CT measurements. Phase-contrast synchrotron X-ray μ CT measurements were performed at the SYRMEP beamline of the Italian synchrotron radiation facility Elettra with the white beam mode. The X-ray spectrum of the beam was filtered with 1.5 mm of silicon and 0.025 mm of molybdenum. The sample-detector distance was set at 100 mm. The experiments were conducted with an isotropic voxel size of 1.05 μ m. The exposure time per projection was 1.0 s with 1000 projections acquired over a total scan angle of 180°. Thus, the total scanning time was about 17 minutes. The tomographic slices were reconstructed using the SYRMEP Tomo Project (STP) software developed at Elettra⁷⁶.

Data processing and analysis. Reconstructed slices were further analysed using the freeware ImageJ⁶² and the *Pore3D* software library^{65,67}. Firstly, the segmentation of cartilaginous elements was carried out using the

plugin ABSnake^{63,64} with a gradient threshold of 30 and a setting of 50 iterations. This plugin was applied to the dataset filtered by a Median 3D filter with a radius of 10 in all three dimensions. The final cartilaginous element (i.e. developing *P. waltl* forearm) was obtained in ImageJ by using the segmented slices as a transparent-zero mask on the original, non-filtered dataset. Further analyses were carried out by using *Pore3D*. To separate the background, the extracellular matrix and the bright cell nucleus, a 3D K-means clustering algorithm was applied to divide the data into three classes. The binary image of the class represented by the cell nuclei was consequently processed by the *erosion* and the *blob analysis* modules of *Pore3D*, which allowed for the determination of the number of *blobs*, i.e. the number of cells. Cell polarization was determined using the software, VGStudio Max 3.1, with its module *Fiber orientation analysis*. The different tissues such as the skin epithelium and muscles were segmented semi-automatically in combination with the software Avizo and VGStudio Max 2.2 according to Tesarova *et al.*⁶⁰.

Data Availability

The datasets generated and/or analysed during the current study are available in the Image Data Resource repository.

References

- Graf, B. W. & Boppart, S. A. Imaging and Analysis of Three-Dimensional Cell Culture Models. *Methods Mol Biol.* **591**, 211–227, https://doi.org/10.1007/978-1-60761-404-3_13 (2010).
- Hedlund, H., Brismar, H., Widholm, M. & Svensson, O. Studies of cell columns of articular cartilage using UV-Confocal scanning laser microscopy and 3D image processing. *J. Musculoskelet. Res.* **3**, 93–98 (1994).
- Artym, V. V. & Matsumoto, K. Imaging Cells in Three-Dimensional Collagen Matrix. in *Curr. Protoc Cell Biol.* Chapter 10: Unit10.18.1–20 <https://doi.org/10.1002/0471143030.cb1018s48> (2010).
- Morgan, F., Barbarese, E. & Carson, J. H. Visualizing cells in three dimensions using confocal microscopy, image reconstruction and isosurface rendering: application to glial cells in mouse central nervous system. *Scanning Microsc.* **6**, 345–56 (1992).
- Pawley, J. *Handbook of Biological Confocal Microscopy*. (Springer, 1995).
- Reihani, S. N. S. & Oddershede, L. B. Confocal microscopy of thick specimens. *J. Biomed. Opt.* **14**, 030513, <https://doi.org/10.1117/1.3156813> (2009).
- Ewald, A. J., McBride, H., Reddington, M., Fraser, S. E. & Kerschmann, R. Surface imaging microscopy, an automated method for visualizing whole embryo samples in three dimensions at high resolution. *Dev Dyn.* **225**, 369–375, <https://doi.org/10.1002/dvdy.10169> (2002).
- Helmchen, F. & Denk, W. Deep tissue two-photon microscopy. *Nat. Methods* **2**, 932–940, <https://doi.org/10.1038/nmeth818> (2005).
- Ustione, A. & Piston, D. W. A simple introduction to multiphoton microscopy: A simple introduction to multiphoton microscopy. *J. Microsc.* **243**, 221–226, <https://doi.org/10.1111/j.1365-2818.2011.03532.x> (2011).
- Schmitt, J. M. Optical coherence tomography (OCT): a review. *IEEE J. Quantum Electron.* **5**, 1205–1215, <https://doi.org/10.1109/2944.796348> (1999).
- Fercher, A. F., Drexler, W., Hitzinger, C. K. & Lasser, T. Optical coherence tomography—principles and applications. *Rep. Prog. Phys.* **66**, 239, <https://doi.org/10.1088/0034-4885/66/2/204> (2003).
- Campbell, J. P. *et al.* Detailed Vascular Anatomy of the Human Retina by Projection-Resolved Optical Coherence Tomography Angiography. *Sci. Rep.* **7**, 42201, <https://doi.org/10.1038/srep42201> (2017).
- Le Gros, M. A., McDermott, G. & Larabell, C. A. X-ray tomography of whole cells. *Curr Opin Struct Biol.* **15**, 593–600, <https://doi.org/10.1016/j.sbi.2005.08.008> (2005).
- Larabell, C. A. & Nugent, K. A. Imaging cellular architecture with X-rays. *Curr Opin Struct Biol.* **20**, 623–631, <https://doi.org/10.1016/j.sbi.2010.08.008> (2010).
- Langer, M. *et al.* Assessment of imaging quality in magnified phase CT of human bone tissue at the nanoscale. *Proc. SPIE.* 10391, <https://doi.org/10.1117/12.2272561> (SPIE, 2017).
- Attwood, D. T. *Soft X-rays and extreme ultraviolet radiation: Principles and application.* (Cambridge University press, 1999).
- Krenkel, M. *et al.* Phase-contrast zoom tomography reveals precise locations of macrophages in mouse lungs. *Sci. Rep.* **5**, 9973, <https://doi.org/10.1038/srep09973> (2015).
- Snigirev, A., Snigireva, I., Kohn, V., Kuznetsov, S. & Schelokov, I. On the possibilities of x-ray phase contrast microimaging by coherent high-energy synchrotron radiation. *Rev. Sci. Instrum.* **66**, 5486–5492, <https://doi.org/10.1063/1.1146073> (1995).
- Wilkins, S. W., Gureyev, T. E., Gao, D., Pogany, A. & Stevenson, A. W. Phase-contrast imaging using polychromatic hard X-rays. *Nature* **384**, 335, <https://doi.org/10.1038/384335a0> (1996).
- Baruchel, J., Buffière, J. Y., Maire, E., Merle, P. & Peix, G. X-ray tomography in material science, general principles. (Hermes Science Publications, 2000).
- Cloetens, P., Barrett, R., Baruchel, J., Guigay, J. P. & Schlenker, M. Phase objects in synchrotron radiation hard X-ray imaging. *J. PhysD Appl Phys* **29**, 133–146 (1996).
- Kaiser, J. *et al.* Investigation of the microstructure and mineralogical composition of urinary calculi fragments by synchrotron radiation X-ray microtomography: a feasibility study. *Urol Res.* **39**, 259–267, <https://doi.org/10.1007/s00240-010-0343-9> (2011).
- Astolfo, A. *et al.* In vivo visualization of gold-loaded cells in mice using x-ray computed tomography. *Nanomedicine* **9**, 284–292, <https://doi.org/10.1016/j.nano.2012.06.004> (2013).
- Larsson, D. H., Vågberg, W., Yaroshenko, A., Yildirim, A. Ö. & Hertz, H. M. High-resolution short-exposure small-animal laboratory x-ray phase-contrast tomography. *Sci. Rep.* **6**, <https://doi.org/10.1038/srep39074> (2016).
- Dullin, C. *et al.* μ CT of *ex-vivo* stained mouse hearts and embryos enables a precise match between 3D virtual histology, classical histology and immunochemistry. *PLoS one* **12**, e0170597, <https://doi.org/10.1371/journal.pone.2017> (2017).
- Saccomano M. *et al.* Synchrotron inline phase contrast μ CT enables detailed virtual histology of embedded soft-tissue samples with and without staining. *J. Synchrotron Radiat.* **25**, <https://doi.org/10.1107/S1600577518005489> (2018).
- Albers J. *et al.* X-ray-Based 3D Virtual Histology—Adding the Next Dimension to Histological Analysis. *Mol Imaging Biol.* <https://doi.org/10.1007/s11307-018-1246-3> (2018).
- Albers J. *et al.* X-ray based virtual histology allows guided sectioning of heavy ion stained murine lungs for histological analysis. *Sci. Rep.* **8**, <https://doi.org/10.1038/s41598-018-26086-0> (2018).
- Momose, A., Takeda, T., Itai, Y. & Hirano, K. Phase-contrast X-ray computed tomography for observing biological soft tissues. *Nat. Med.* **2** (1996).
- Beltran, M. A., Paganin, D. M., Uesugi, K. & Kitchen, M. J. 2D and 3D X-ray phase retrieval of multi-material objects using a single defocus distance. *Opt Express* **18**, 6423–36, <https://doi.org/10.1364/OE.18.006423> (2010).
- Metscher, B. D. MicroCT for comparative morphology: simple staining methods allow high-contrast 3D imaging of diverse non-mineralized animal tissues. *BMC Physiol* **9**, 11, <https://doi.org/10.1186/1472-6793-9-11> (2009).
- Metscher, B. D. MicroCT for developmental biology: A versatile tool for high-contrast 3D imaging at histological resolutions. *Dev Dyn.* **238**, 632–640. [10.1002/dvdy.21857](https://doi.org/10.1002/dvdy.21857) (2009).

33. Shinohara, M. *et al.* Atherosclerotic plaque imaging using phase-contrast X-ray computed tomography. *Am J Physiol Heart Circ Physiol* **294**, H1094–H1100 (2008).
34. Zanette, I. *et al.* Holotomography versus X-ray grating interferometry: A comparative study. *Applied Physics Letters* **103**, 244105 (2013).
35. Lang, S. *et al.* Experimental comparison of grating- and propagation-based hard X-ray phase tomography of soft tissue. *Journal of Applied Physics* **116**, 154903, <https://doi.org/10.1152/ajpheart.01149.2007> (2014).
36. Kumar A. *et al.* An orphan gene is necessary for preaxial digit formation during salamander limb development. *Nat Commun.* **6** <https://doi.org/10.1038/ncomms9684> (2015).
37. Frobisch, N. B. & Shubin, N. H. Salamander limb development: integrating genes, morphology, and fossils. *Dev. Dyn.* **240**, 1087–1099 (2011).
38. Godwin, J. W. *et al.* Macrophages are required for adult salamander limb regeneration. *Proc Natl Acad Sci USA* **23**, 9415–20, <https://doi.org/10.1073/pnas.1300290110> (2013).
39. Yun, M. H. *et al.* Regulation of p53 is critical for vertebrate limb regeneration. *Proc Natl Acad Sci USA* **43**, 17392–7 (2013).
40. Cosden, R. S. *et al.* Intrinsic repair of full-thickness articular cartilage defects in the axolotl salamander. *Osteoarthritis Cartilage* **19**, 200–205 (2011).
41. Khan, I. M. *et al.* The development of synovial joints. *Curr. Top. Dev. Biol.* **79**, 1–36 (2007).
42. Cosden-Decker, R. S. *et al.* Structural and functional analysis of intra-articular interzone tissue in axolotl salamanders. *Osteoarthritis Cartilage* **20**, 1347–1356, <https://doi.org/10.1016/j.joca.2012.07.002> (2012).
43. Adameyko, I. & Fried, K. The Nervous System Orchestrates and Integrates Craniofacial Development: A Review. *Front. Physiol.* **7**, 49, <https://doi.org/10.3389/fphys.2016.00049> (2016).
44. Davidson, L. A. Epithelial machines that shape the embryo. *Trends Cell Biol.* **22**, 82–87, <https://doi.org/10.1016/j.tcb.2011.10.005> (2012).
45. Boehm, B. *et al.* The Role of Spatially Controlled Cell Proliferation in Limb Bud Morphogenesis. *PLoS Biol.* **8**, e1000420, <https://doi.org/10.1371/journal.pbio.1000420> (2010).
46. Abzhanov, A. & Tabin, C. J. Shh and Fgf8 act synergistically to drive cartilage outgrowth during cranial development. *Dev Biol.* **273**, 134–148, <https://doi.org/10.1016/j.ydbio.2004.05.028> (2004).
47. Gros, J. & Tabin, C. J. Vertebrate Limb Bud Formation Is Initiated by Localized Epithelial-to-Mesenchymal Transition. *Science* **343**, 1253–1256, <https://doi.org/10.1126/science.1248228> (2014).
48. Kaucka, M. *et al.* Oriented clonal cell dynamics enables accurate growth and shaping of vertebrate cartilage. *Elife* **6**, e25902, <https://doi.org/10.7554/eLife.25902> (2017).
49. Li, L. *et al.* Superficial cells are self-renewing chondrocyte progenitors, which form the articular cartilage in juvenile mice. *FASEB J.* **31**, 1067–1084, <https://doi.org/10.1096/fj.201600918R> (2017).
50. Kaucka, M. *et al.* Signals from the brain and olfactory epithelium control shaping of the mammalian nasal capsule cartilage. *eLife* **7**, e34465, <https://doi.org/10.7554/eLife.34465> (2018).
51. Buckingham, M. *et al.* The formation of skeletal muscle: from somite to limb. *J Anat.* **202**, 59–68 (2003).
52. Stockdale, F. E. *et al.* Molecular and cellular biology of avian somite development. *Dev Dyn.* **219**, 304–21 (2000).
53. Roddy, K. A. *et al.* Mechanical Influences on Morphogenesis of the Knee Joint Revealed through Morphological, Molecular and Computational Analysis of Immobilised Embryos. *PLoS One* **6**, e17526, <https://doi.org/10.1371/journal.pone.0017526> (2011).
54. Rapaport, D. *et al.* Short stature in Duchenne muscular dystrophy. *Growth Regul.* **1**, 11–5 (1991).
55. Cairns, D. M. *et al.* The role of muscle cells in regulating cartilage matrix production. *J Orthop Res* **28**, 529–536 (2010).
56. Zehbe, R. *et al.* Characterization of oriented protein-ceramic and protein-polymer-composites for cartilage tissue engineering using synchrotron m-CT. *Int. J. Mater. Res.* **98**, 562–568, <https://doi.org/10.3139/146.101509> (2007).
57. Zehbe, R. *et al.* Going beyond histology. Synchrotron micro-computed tomography as a methodology for biological tissue characterization: from tissue morphology to individual cells. *J R Soc Interface* **7**, 49–59, <https://doi.org/10.1098/rsif.2008.0539> (2010).
58. Hieber, S. *et al.* Tomographic brain imaging with nucleolar detail and automatic cell counting. *Sci. Rep.* **6**, 32156, <https://doi.org/10.1038/srep32156> (2016).
59. Elewa, A. *et al.* Reading and editing the Pleurodeles waltl genome reveals novel features of tetrapod regeneration. *Nat. Commun.* **8**, 9, <https://doi.org/10.1038/s41467-017-01964-4> (2017).
60. Tesařová, M. *et al.* Use of micro computed-tomography and 3D printing for reverse engineering of mouse embryo nasal capsule. *JINST* **11**, C03006–C03006, <https://doi.org/10.1088/1748-0221/11/03/C03006> (2016).
61. Constantine, V. S. & Mowry, R. W. Selective staining of human dermal collagen. *J. Invest Dermatol.* **50**, 414–418 (1968).
62. Nemetschek, T., Riedl, H. & Jonak, R. Topochemistry of the binding of phosphotungstic acid to collagen. *J. Mol. Biol.* **133**, 67–83 (1979).
63. Adams, R. & Bischof, L. Seeded region growing. *IEEE Trans. Pattern Anal. Mach. Intell.* **16**, 641–647, <https://doi.org/10.1109/34.295913> (1994).
64. Schneider, C. A., Rasband, W. S. & Eliceiri, K. W. NIH Image to ImageJ: 25 years of image analysis. *Nat. methods* **9**, 671, <https://doi.org/10.1038/nmeth.2089> (2012).
65. Boudier, T. Elaboration d'un modèle de déformation pour la détection de contours aux formes complexes. *Innov. Techn. Biol. Med.* **18**, 1 (1997).
66. Andrey, P. & Boudier, T. Adaptive active contours (snakes) for the segmentation of complex structures in biological images. in *Centre de Recherche Public Henri Tudor Copyright Notice* 181 (2006).
67. Brun, F. *et al.* Pore3D: A software library for quantitative analysis of porous media. *Nucl. Instr. Meth. Phys. Res.* **615**, 326–332, <https://doi.org/10.1016/j.nima.2010.02.063> (2010).
68. Hartigan, J. A. & Wong, M. A. Algorithm AS 136: A K-Means Clustering Algorithm. *Applied Statistics* **28**, 100 (1979).
69. Zandomenighi, D. *et al.* Quantitative analysis of X-ray microtomography images of geomaterials: Application to volcanic rocks. *Geosphere* **6**, 793–804, <https://doi.org/10.1130/GES00561.1> (2010).
70. Viani, A. *et al.* Microstructural characterization of dental zinc phosphate cements using combined small angle neutron scattering and microfocus X-ray computed tomography. *Dent Mater* **4**, 402–417, <https://doi.org/10.1016/j.dental.2017.01.008> (2017).
71. Wong, M. *et al.* Zone-specific cell biosynthetic activity in mature bovine articular cartilage: a new method using confocal microscopic stereology and quantitative autoradiography. *J. Orthop. Res.* **14**, 424–432, <https://doi.org/10.1002/jor.1100140313> (1996).
72. Jadin, K. D. *et al.* Depth-varying density and organization of chondrocytes in immature and mature bovine articular cartilage assessed by 3D imaging and analysis. *J. Histochem. Cytochem.* **53**, 1109–1119, <https://doi.org/10.1369/jhc.4A6511.2005> (2005).
73. Brunt, L. H. *et al.* Finite element modelling predicts changes in joint shape and cell behaviour due to loss of muscle strain in jaw development. *J Biochem* **48**, 3112–22, <https://doi.org/10.1016/j.jbiomech.2015.07.017> (2015).
74. Kaucka, M. *et al.* Analysis of neural crest-derived clones reveals novel aspects of facial development. *Science Advances* **2**, e1600060, <https://doi.org/10.1126/sciadv.1600060> (2016).
75. Joven, A., Kirkham, M. & Simon, A. Husbandry of Spanish Ribbed Newts (*Pleurodeles waltl*). *Methods Mol Biol.* 47–70 https://doi.org/10.1007/978-1-4939-2495-0_4 (2015).
76. Brun, F. *et al.* Enhanced and Flexible Software Tools for X-ray Computed Tomography at the Italian Synchrotron Radiation Facility Elettra. *Fundamenta Informaticae* **141**, 233–243, <https://doi.org/10.3233/FI-2015-1273> (2015).

Acknowledgements

This research was carried out under the project CEITEC 2020 (LQ1601) with financial support from the Ministry of Education, Youth and Sports of the Czech Republic under the National Sustainability Programme II and CEITEC Nano Research Infrastructure (MEYS CR, 2016–2019). M.K. was funded by the SSMF fellowship. The authors acknowledge Elettra for access to synchrotron radiation computed microtomography facilities. J.K. and M.T. acknowledge the support of the Brno University of Technology with the grant FSI-S-17–4506. D.K. acknowledges the support of CEITEC Brno University of Technology with the grant FSI/STI-J-18–5337. We are grateful to the staff of SYRMEP for the experimental support during the experiments and to Adam Břínek who helped with the experiments at the synchrotron facility.

Author Contributions

A.S., I.A., and J.K. designed the experiments. M.K., A.E. and B.S. prepared the samples and stained them for μ CT measurement. Conventional μ CT experiments were performed by M.T., M.N. and D.K., synchrotron μ CT experiments were performed by M.T., L.M., D.K. and T.Z. Data analysis was done by M.T., L.M. and G.L. Biological part was discussed by I.A. and Y.Z. The manuscript was written by M.T., L.M., I.A. and J.K. All authors reviewed the manuscript.

Additional Information

Supplementary information accompanies this paper at <https://doi.org/10.1038/s41598-018-32459-2>.

Competing Interests: The authors declare no competing interests.

Publisher's note: Springer Nature remains neutral with regard to jurisdictional claims in published maps and institutional affiliations.



Open Access This article is licensed under a Creative Commons Attribution 4.0 International License, which permits use, sharing, adaptation, distribution and reproduction in any medium or format, as long as you give appropriate credit to the original author(s) and the source, provide a link to the Creative Commons license, and indicate if changes were made. The images or other third party material in this article are included in the article's Creative Commons license, unless indicated otherwise in a credit line to the material. If material is not included in the article's Creative Commons license and your intended use is not permitted by statutory regulation or exceeds the permitted use, you will need to obtain permission directly from the copyright holder. To view a copy of this license, visit <http://creativecommons.org/licenses/by/4.0/>.

© The Author(s) 2018

INTERNATIONAL WORKSHOP ON IMAGING
7–10 SEPTEMBER 2015
VARENNA, ITALY

Use of micro computed-tomography and 3D printing for reverse engineering of mouse embryo nasal capsule

M. Tesařová,^{a,b} T. Zikmund,^a M. Kaucká,^{c,d} I. Adameyko,^{c,d} J. Jaroš,^{e,f} D. Paloušek,^b
D. Škaroupka^b and J. Kaiser^{a,b,1}

^aCEITEC — BUT, Brno University of Technology,
Technická 3058/10, 616 00 Brno, Czech Republic

^bFaculty of Mechanical Engineering, Brno University of Technology,
Technická 2896/2, 616 69 Brno, Czech Republic

^cDepartment of Physiology and Pharmacology, Karolinska Institutet,
Nanna Svartz väg 2, Stockholm 17177, Sweden

^dDepartment of Molecular Neurosciences, Center for Brain Research, Medical University of Vienna,
Spitalgasse 4, Vienna 1090, Austria

^eDepartment of Histology and Embryology, Faculty of Medicine, Masaryk University,
Kamenice 3, 625 00 Brno, Czech Republic

^fInternational Clinical Research Center — Center of Biomolecular and Cellular Engineering,
St. Anne's University Hospital Brno, Pekařská 53, 656 91, Brno, Czech Republic

E-mail: jozef.kaiser@ceitec.vutbr.cz

ABSTRACT: Imaging of increasingly complex cartilage in vertebrate embryos is one of the key tasks of developmental biology. This is especially important to study shape-organizing processes during initial skeletal formation and growth. Advanced imaging techniques that are reflecting biological needs give a powerful impulse to push the boundaries of biological visualization. Recently, techniques for contrasting tissues and organs have improved considerably, extending traditional 2D imaging approaches to 3D. X-ray micro computed tomography (μ CT), which allows 3D imaging of biological objects including their internal structures with a resolution in the micrometer range, in combination with contrasting techniques seems to be the most suitable approach for non-destructive imaging of embryonic developing cartilage. Despite there are many software-based ways for visualization of 3D data sets, having a real solid model of the studied object might give novel opportunities to fully understand the shape-organizing processes in the developing body. In this feasibility study we demonstrated the full procedure of creating a real 3D object of mouse embryo nasal capsule, i.e. the staining, the μ CT scanning combined by the advanced data processing and the 3D printing.

KEYWORDS: Computerized Tomography (CT) and Computed Radiography (CR); Image reconstruction in medical imaging; Multi-modality systems

¹Corresponding author.



Contents

1	Introduction	1
2	Materials and methods	3
2.1	Preparation of samples for micro CT measurements, staining	3
2.2	CT measurement and gathering data for 3D printing	3
2.3	Additive manufacturing — 3D printing	4
3	Results	5
4	Discussions and ongoing work	6
5	Conclusions	9

1 Introduction

Despite the long-standing investigation of craniofacial development, this process is still not fully understood [1]. It is partially because of significant complexity of the structures in the head. These structures play an important role for vital functions through the whole life. The primary research of craniofacial development is often done on mouse embryos [2, 3]. Differences between the samples are usually investigated at craniofacial parts. Typical size of the mouse embryo nasal capsule at day 15 of embryonic development is in the range of few millimetres. There is a wide variety between different developmental stages or mutations that are manifested by small differences in the shape or thickness of the nasal capsule. In order to compare these fine details, high-resolution imaging techniques are needed.

For decades imaging has relied on optical and then also on electron microscopy of histological sections, which provides high resolution 2D data. Over time confocal microscopy enabled collection of optical sections through thicker samples [4]. Episcopic fluorescence image capturing is another technology for generating high-resolution 3D datasets. This method is based on capturing the autofluorescence of each of the histological slices. However, all above mentioned technologies are costly and time-consuming [5]. Optical projection tomography [6] is another approach for 3D imaging, but it is rather limited by sample size. The same accounts for light sheet microscopy (SPIM). Moreover, the sample preparation is rather complicated. Magnetic resonance imaging (MRI) currently represents an universal tool for different needs of soft tissue morphology [7]. This method uses magnetic field and radio waves in order to map various internal structures. MRI is suitable for imaging soft tissues such as internal organs, but it does not provide sufficient resolution for cartilage imaging [5].

One of the most convenient tools for imaging mouse embryonic samples from 12 to 17 days of embryonic development is X-ray computed tomography [3]. It is the oldest tomography imaging technique [8]. X-ray micro computed-tomography (μ CT), i.e. X-ray computed-tomography with high spatial-resolution down to $1\ \mu\text{m}$, has the same principle as CT machines used for medical scanning. The sample that is placed between the X-ray source and the detector is rotated by 360° around its axis perpendicular to the line connecting the source and the detector. In every rotation step a two dimensional projection is taken. The sequence of obtained projections is subsequently processed by tomographic reconstruction based on inverse Radon transform [8]. In this way different X-ray absorption at each sample point is visualized and the 3D volume map of object density is created. Due to the cone shape of the X-ray beam, geometric magnification can be used to reach high-resolution [8].

X-ray tomography imaging has been limited by low contrast of soft un-mineralized tissues. Phase contrast can be the solution for enhancement of image quality of the X-ray projections [9]. However, this method is not much convenient for industrial and laboratory μ CTs, where the image reconstruction rely predominantly on absorption contrast. Phase contrast is more applicable for monochromatic radiation used at synchrotrons [9, 10]. In the case of lab-based μ CT systems it is necessary to use contrasting agents for increasing X-ray absorption of soft tissues. There are various methods that are using contrasting agents for staining of biological samples [11]. Phosphotungstic acid (PTA) was utilized as standard histological technique for light and electron microscopy due to its capability to increase the contrast of soft versus mineralized tissues or different type of soft tissues [12–14]. PTA also confers strong X-ray contrast when attached to the collagens and fibrils [12, 13], and to various other proteins. It is considered to be suitable for visualizing soft connective tissue in general [15]. Here we found that cartilage is stained significantly weaker in comparison to surrounding tissue, therefore we took the advantage of that for discriminating and outlining cartilage in μ CT analysis.

Another step important for successful μ CT is the mounting of the biological sample. It is crucial to have the sample fixed appropriately during the μ CT scanning. Even a minuscule movement destroys the tomographic measurement and results in artefacts in the reconstructed tomographic cross-sections. It happens if samples are floating in aqueous or alcohol surrounding. Minimization of background can be reached by mounting the samples to hydrogels based on agarose, gelatine or alginate and by mechanical fixation of samples in standard laboratory equipment, like plastic tubes or polyimide tubes that are not very contrasting for X-rays.

If the contrast is sufficient, it is straightforward to visualize the 3D volume rendering of different features of the sample using proper tomographic software. The differentiation of these features is simply based on setting the appropriate gray values or gray value intervals in image histogram. However, it is difficult to set threshold for cartilage. As it was mentioned above, the cartilage is stained significantly weaker in comparison with surrounding tissue, so only its border is detectable (figure 1). In this case, data processing cannot be fully automated yet, but using suitable software tools enable relatively fast and precise manual segmentation of the craniofacial cartilage.

Here we present the whole process of reverse engineering of mouse embryo nasal capsule including staining and tomographic measurement combined with the advanced data processing for creating 3D model and its printing.

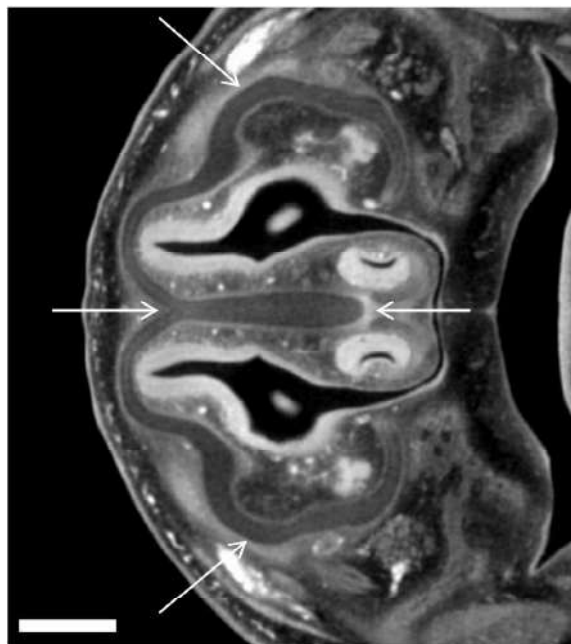


Figure 1. Reconstructed tomographic cross section of mouse embryo. Arrows show cartilage of nasal capsule. The length of the scale bar is 0.4 mm.

2 Materials and methods

2.1 Preparation of samples for micro CT measurements, staining

Our staining protocol has been modified from protocol developed by Brian Metscher [15]. After excision, the 15.5 days old C57BL strain mouse embryos were fixed with 4% formaldehyde in phosphate buffer saline (PBS) for 24 hours at +4°C. Samples were then washed with PBS and dehydrated by ethanol grade (30%, 50%, 70%), each concentration for 1 day.

We experimentally found out the best tissue contrast and penetration with PTA (10026-AP0, Lach-Ner, Czech Republic) dissolved in 90% methanol (21190-11000, Ing. Petr Švec-PENTA, Czech Republic). Therefore we transferred the samples from 70% ethanol (71250-11000, Ing. Petr Švec-PENTA, Czech Republic) to ethanol-methanol-water mixture (4:4:3) and then into 80% and 90% methanol, each bath for 1 hour. After that, 0.7% PTA-methanol solution was used to stain the samples for 6 days and exchanged every day with the fresh one.

The staining was followed by rehydration of the samples in methanol grade series (90%, 80%, 70%, 50% and 30%) to end up in sterile distilled water. After that, rehydrated embryos were embedded in 0.5% agarose gel (A5304, Sigma-Aldrich) and placed in 1.5 ml polypropylene tubes to avoid the movement artefacts during X-ray computer tomography scanning.

2.2 CT measurement and gathering data for 3D printing

The polypropylene tube was fixed on a plastic rod by a silicone gun. The rod was mounted in the chuck which provides the position of the sample in rotation axis (figure 2). The μ CT scanning was performed using laboratory system GE Phoenix v|tome|x L 240 (GE Sensing & Inspection

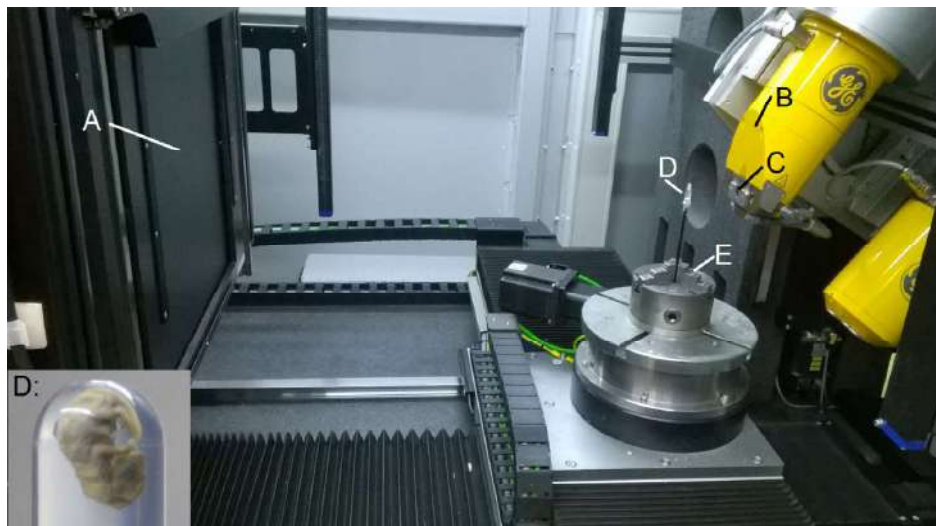


Figure 2. Fixing the sample for μ CT measurement. A — flat panel detector; B — X-ray tube; C — aluminium filter; D — embryo embedded in agarose gel in the tube; E — chuck.

Technologies GmbH, Germany), equipped with a 180 kV/15 W maximum power nanofocus X-ray tube and high contrast flat panel detector DXR250 with 2048×2048 pixel², $200 \times 200 \mu\text{m}^2$ pixel size. The exposure time was 900 ms in every of the 2200 positions. The utilized acceleration voltage and X-ray tube current were 60 kV and $200 \mu\text{A}$, respectively. The beam was filtered by the beryllium window of the X-ray housing and by 0.2 mm of aluminium filter. The voxel size of obtained volume was $5 \mu\text{m}$. The tomographic reconstruction was realized using 3D computed tomography software GE phoenix datos|x 2.0 (GE Sensing & Inspection Technologies GmbH, Germany). The data processing was realized in software VG Studio MAX 2.2 (Volume Graphics GmbH, Germany). Segmentation of nasal capsule was completed manually (approx. 8 hours of segmentation). The “smoothing” tool, with strength 20 was used to smooth the virtual 3D model in order to get rid of inaccuracies.

2.3 Additive manufacturing — 3D printing

The Parts have been manufactured by ZPrinter 650 (Peak Solutions, U.S.A.). Building volume is $254 \times 381 \times 203$ mm and layer thickness was established to 0.1016 mm. Color printing resolution in x and y directions is 600×540 dots per inch (DPI) and the minimum feature size is also 0.1016 mm. All data were adjusted in the 3D printing software ZPrint 7.15 (Peak Solutions, U.S.A.).

The STL data generated from μ CT measurements were scaled 50 times directly in the 3D printing software. Monochromatic green color, the same color that was used as a virtual color in VG studio MAX 2.2 software, was chosen. The printer spread 716 layers of plaster based powder, where each layer was bound by five Hewlett Packard print heads (CMYK binders + one Clear binder) with the resolution of 600×540 DPI. After 6 hours and 15 minutes the printing was finished and the printer dried up the part still surrounded by the powder in the building chamber. Dry part was carefully removed from the powder by vacuumer and brush and depowdered by compressed air in the post-processing unit. It was infiltrated by cyanoacrylate using drizzle method to give it additional strength, durability, and color vibrancy.

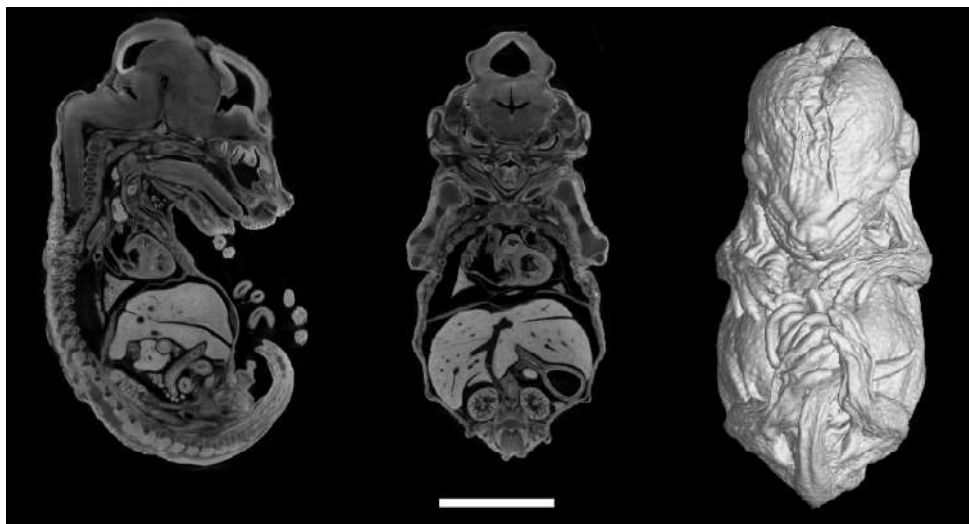


Figure 3. The obtained data from the μ CT measurement. The cross section in two perpendicular planes and the 3D render of the whole 15.5 days old embryo. The length of the scale bar is 3 mm.

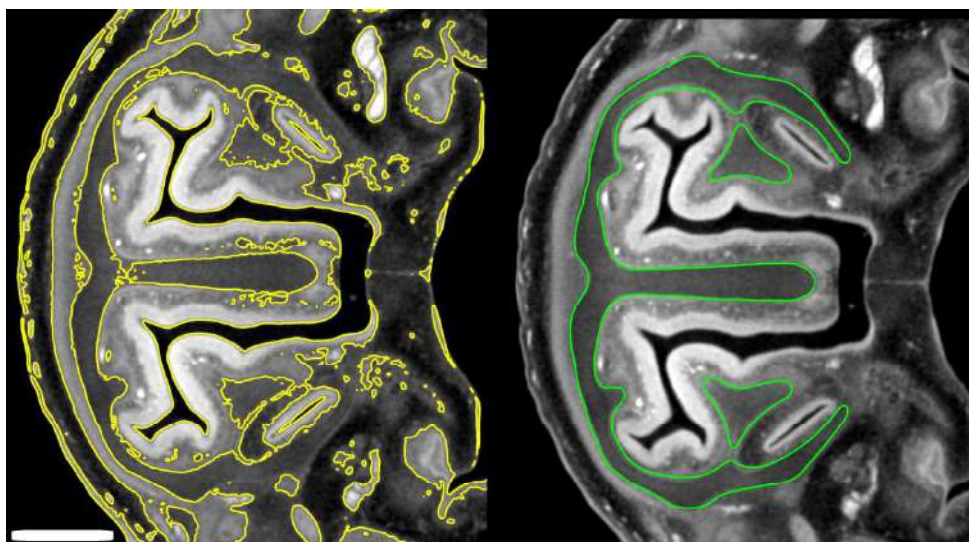


Figure 4. Comparison between automatic (yellow) and manual (green) segmentation. The length of the scale bar is 0.5 mm.

3 Results

The overall procedure is demonstrated on a representative 15.5 days old mouse embryo stained by PTA. The μ CT measurement had a satisfactory contrast for the overall 3D render of the mouse embryo (figure 3).

Gray value intervals for border of the cartilage was not sufficiently pronounced for automatic segmentation (figure 4). The manual segmentation was realized in one direction across the sample, along the cross section shown in figures 1 and 5, denoted x , y in figure 5. Using manual segmentation, a 3D model of a nasal capsule was created (figure 6).

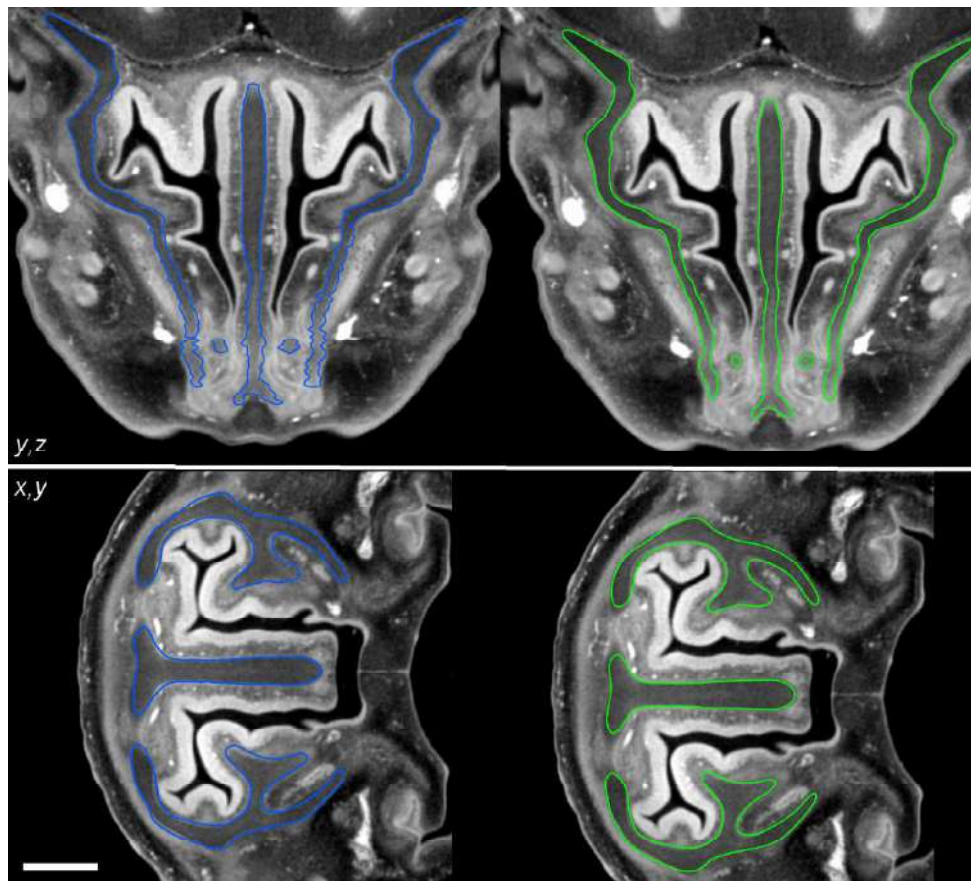


Figure 5. Using the “smoothing” tool. Blue line — before the application of the tool, green line — after the smoothing. The upper part shows the cross section y, z , perpendicular to the cross section x, y in which the segmentation was realized. The smoothing was controlled in the cross section x, y (bottom image) by comparing the segmented and smoothed data. The length of the scale bar is 0.35 mm.

Segmentation along one cross section caused disfluencies in the perpendicular cross section y, z (figure 5). After the segmentation these visible distinct inaccuracies were smoothed and fluent model was obtained. The smoothing parameter was optimized that way to preserve the small details. This was controlled by comparison with the original tomographic cross sections x, y (figure 5 and 6).

The finished virtual 3D model was exported to STL format for 3D printing. The printed 3D model is compared with the STL model in figure 7.

Figure 8 shows the comparison of the printed 3D model of an olfactory system with the human hand.

4 Discussions and ongoing work

Even if the proper combination of different techniques may represent a breakthrough with clinical significance, the use of advanced techniques in multi-disciplinary biological research is nowadays still a challenge [16]. Using μ CT, stereolithography computer-aided design (STL CAD) modeling and matrix-assisted laser desorption-ionisation — time of flight mass spectrometry (MALDI-TOF

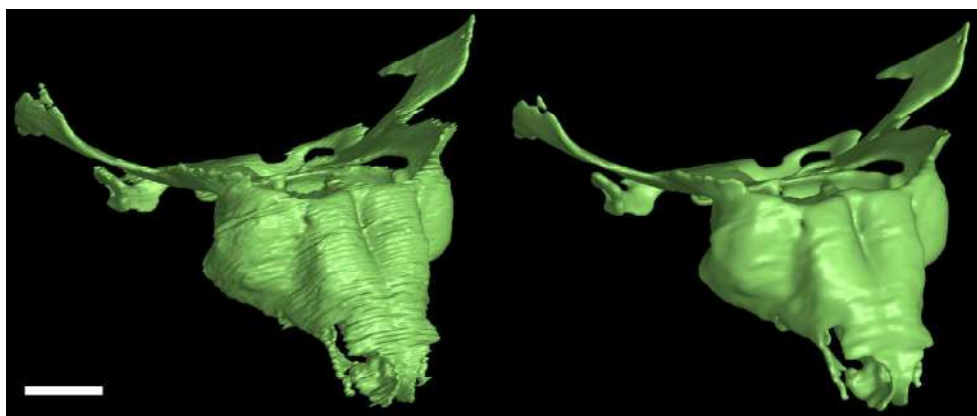


Figure 6. Segmented models without smoothing (left) and with smoothing (right). The length of the scale bar is 0.5 mm.

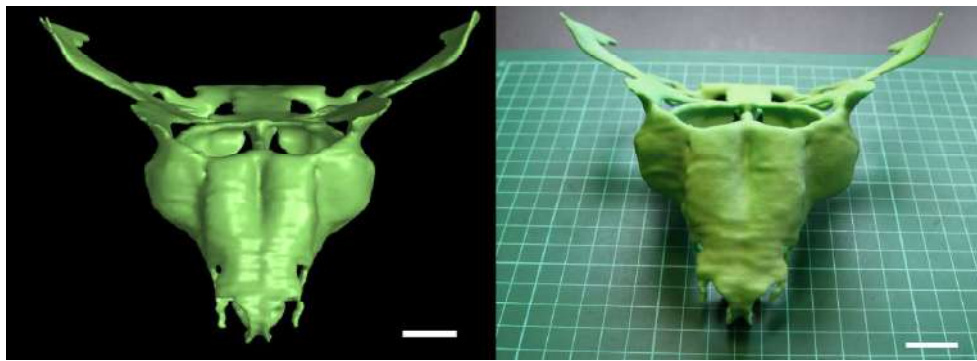


Figure 7. Comparison of the STL model (left) with the 50:1 upscaled model from 3D print (right). The scale bar is 0.4 mm (left) and 2 cm (right).



Figure 8. Comparison of the object from 3D print with human hand.

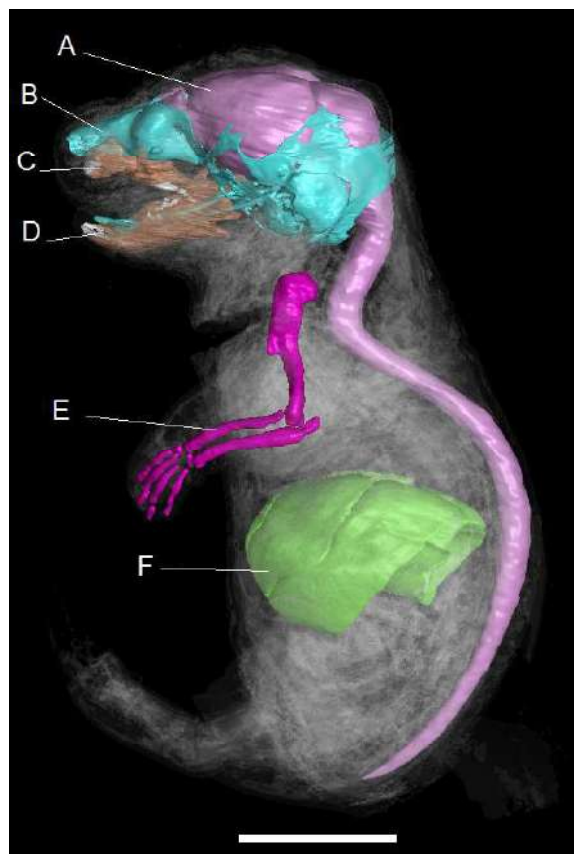


Figure 9. Segmented parts of 17.5 days old mouse embryo by using μ CT. A — brain with spinal cord; B — cranium; C — upper jaw; D — lower jaw; E — upper limb; F — liver. The length of the scale bar is 4 mm.

MS) we recently confirmed the causative role of absorbable suture material in the pathogenesis of hollow channel structures in some canine compound uroliths [17]. The straightforward combination of μ CT with 3D printing is however more common in medical practice [18–20]. In [18] the medical uses of 3D printing are reviewed, with the main emphasis on surgical training, special surgical planning and prosthetics applications. The overview of the main requirements for medical imaging affected needs of additive manufacturing (AM) formerly known as rapid prototyping is reviewed in [19]. It is shown that successful clinical cases of AM rely heavily in multi-disciplinary approach, i.e. on efficient collaboration between various disciplines, as operating surgeons, radiologists and engineers. The review also intends to narrow the potential communication gap between radiologists and engineers who work with projects involving AM by showcasing the overlap between the two disciplines. The possibilities to apply 3D printers in veterinary medicine are explored and illustrated in review [20]. It is stated that the increased use of this technology in human medicine together with the decreasing cost are making 3D printing more affordable also for veterinary use.

Combining the μ CT imaging, and 3D printing with tissue staining, the possibilities of reverse engineering are very broad. Here we created the real 3D cartilage model of the 15.5 days old mouse embryo to show that these techniques are suitable for demonstrating the complexity of biological structures (figure 9).

Using 3D printers, the physical exploration is extending observation of the samples by viewing from all sides, sensing surface roughness and wall thickness. Simple visualization of images on a computer does not allow all of these qualities for research, demonstrations and educational purposes.

Definitely, it is not easy to orient in such sophisticated geometry using only imagination even empowered by visualizing software. Researchers also may focus on developmental shape transformations of spine, limbs etc. The inner ear with its complex structure could be another part of the cartilaginous tissue suitable for such reverse engineering.

With sufficient resolution allowing the segmentation, one μ CT scan lasts about 2 hours. The relatively short scanning time gives an opportunity for creating entire real anatomical atlases or databases allowing researchers to browse in different structures, mutants etc. In addition, after one scan, objects can be printed in different scales or colors, which can also be used for educational purposes [18]. 3D print is a rapidly evolving technology and several methods exist like STL, digital light processing (DLP), laser sintering and laser melting, extrusion of thermoplastic material etc. Using this technology it is affordable to make such a collection.

μ CT also enables to display another soft tissues — liver, heart, gray matter i.e. brain and spinal cord (figure 7). μ CT so can complete other techniques that can image 3D structures (e.g. MRI, optical projection tomography [18] or high resolution episcopic microscopy). Using the specific advantages of each of these methods a complex and sophisticated 3D structure can be visualized and subsequently printed on 3D printers.

5 Conclusions

Here we have demonstrated the comprehensive process of the reverse engineering of mouse embryo nasal capsule. For this feasibility study a 15.5 days old mouse embryo was chosen as a representative sample that was contrasted by phosphotungstic acid. It was shown that the combination of micro computed-tomography with 3D printing brings new possibilities for exploring and understanding the processes in craniofacial development. Combination of these two methods can be also useful for various studies in developmental, comparative and quantitative biology.

Acknowledgments

This work is an output of cooperation between CEITEC — Central European Institute of Technology (CZ.1.05/1.1.00/02.0068) and NETME Centre, regional R&D centre built with the financial support from the Operational Programme Research and Development for Innovations within the project NETME Centre (New Technologies for Mechanical Engineering), Reg. No. CZ.1.05/2.1.00/01.0002 and, in the follow-up sustainability stage, supported through NETME CENTRE PLUS (LO1202) by financial means from the Ministry of Education, Youth and Sports under the National Sustainability Programme I. JJ acknowledge the support by FNUSA-ICRC Project (No. CZ.1.05/1.1.00/02.0123) from the European Regional Development Fund. JK acknowledge the support of Brno University of Technology on the frame of grant FSI-S-14-2494 (Application of Advanced Optical Methods). MK was supported by EMBO long-term fellowship.

















References

- [1] B. Hallgrímsson, D.E. Lieberman, W. Liu, A.F. Ford-Hutchinson and F.R. Jirik, *Epigenetic interactions and the structure of phenotypic variation in the cranium*, *Evol. Dev.* **9** (2007) 76.
- [2] T.E. Parsons et al., *Phenotypic variability and craniofacial dysmorphology: increased shape variance in a mouse model for cleft lip*, *J. Anat.* **212** (2008) 135.
- [3] K. Degenhardt, A.C. Wright, D. Horng, A. Padmanabhan and J.A. Epstein, *Rapid 3D phenotyping of cardiovascular development in mouse embryos by micro-CT with iodine staining*, *Circ. Cardiovasc. Imaging* **3** (2010) 314.
- [4] W.J. Weninger et al., *High-resolution episcopic microscopy: a rapid technic for high detailed 3D analysis of gene activity in the context of tissue architecture and morphology*, *Anat. Embryol.* **211** (2006) 213.
- [5] F.C. Norris et al., *A coming of age: advanced imaging technologies for characterising the developing mouse*, *Trends Genet.* **29** (2013) 700.
- [6] J. Kerwin et al., *3 dimensional modelling of early human brain development using optical projection tomography*, *BMC Neurosci.* **5** (2004) 27.
- [7] S.W. Ruffins et al., *Digital three-dimensional atlas of quail development using high-resolution MRI*, *Sci. W. J.* **7** (2007) 592.
- [8] W.A. Kalender, *Computed tomography: fundamentals, system technology, image, quality, applications*, 3rd edition, Wiley (2005).
- [9] J. Kaiser et al., *Investigation of the microstructure and mineralogical composition of urinary calculi fragments by synchrotron radiation X-ray microtomography: a feasibility study*, *Urol. Res.* **39** (2011) 259.
- [10] E. Ettl et al., *X-ray phase-contrast tomography with a compact laser-driven synchrotron source*, *Proc. Natl. Acad. Sci. USA* **112** (2015) 5567.
- [11] B.D. Metscher, *Micro-CT for comparative morphology: simple staining methods allow high contrast 3D imaging of diverse non-mineralized animal tissues*, *BMC Phys.* **9** (2009) 11.
- [12] V.S. Constantine and R.W. Mowry, *Selective staining of human dermal collagen*, *J. Inv. Derm.* **50** (1968) 419.
- [13] T. Nemetschek, H. Riedl and R. Jonak, *Topochemistry of the binding of phosphotungstic acid to collagen*, *J. Mol. Biol.* **133** (1979) 67.
- [14] R.N. Rao, P.M. Fallman, D. Greer Falls and S.N. Meloan, *A comparative study of PAS-phosphotungstic acid-Diamine Supra Blue FGL and immunological reactions for type I collagen*, *Histochemistry* **91** (1989) 283.
- [15] B.D. Metscher, *MicroCT for developmental biology: a versatile tool for high-contrast 3D imaging at histological resolutions*, *Dev. Dynam.* **238** (2009) 632.
- [16] H.G. Elmendorf and A.G. Rosenwald, *Biology of global health: preparing students for multi-disciplinary group work*, in *Proceedings of the 2014 ASCB/IFCB Meeting*, Philadelphia U.S.A., 6–10 Dec 2014.
- [17] J. Kaiser et al., *Determination of the cause of selected canine urolith formation by advanced analytical methods*, *J. Small Anim. Pract.* **53** (2012) 646.

- [18] F. Rengier et al., *3D printing based on imaging data: review of medical applications*, *Int. J. Comput. Assist. Radiol. Surg.* **5** (2010) 335.
- [19] E. Huotilainen et al., *Imaging requirements for medical applications of additive manufacturing*, *Acta Radiol.* **55** (2014) 78.
- [20] A.M. Hespel, R. Wilhite and J. Hudson, *Applications for 3D printers in veterinary medicine*, *Vet. Radiol. Ultrasoun.* **55** (2014) 347.

2016 JINST 11 C03006

Serotonin limits generation of chromaffin cells during adrenal organ development

Polina Kameneva^{1,2,19}, Victoria I. Melnikova ^{3,19}, Maria Eleni Kastriti ^{1,2}, Anastasia Kurtova ³, Emil Kryukov ^{1,2}, Aliia Murtazina², Louis Faure ¹, Irina Poverennaya¹, Artem V. Artemov^{1,4}, Tatiana S. Kalinina⁵, Nikita V. Kudryashov ^{5,6}, Michael Bader^{7,8,9,10}, Jan Skoda ^{11,12}, Petr Chlapek^{11,12}, Lucie Curylova ^{11,12}, Lukas Sourada ^{11,12}, Jakub Neradil ^{11,12}, Marketa Tesarova ¹³, Massimo Pasqualetti ^{14,15}, Patricia Gaspar ¹⁶, Vasily D. Yakushov¹⁷, Boris I. Sheftel¹⁷, Tomas Zikmund ¹³, Jozef Kaiser ¹³, Kaj Fried¹⁸, Natalia Alenina^{7,8}, Elena E. Voronezhskaya^{3✉} & Igor Adameyko ^{1,2✉}

Adrenal glands are the major organs releasing catecholamines and regulating our stress response. The mechanisms balancing generation of adrenergic chromaffin cells and protecting against neuroblastoma tumors are still enigmatic. Here we revealed that serotonin (5HT) controls the numbers of chromaffin cells by acting upon their immediate progenitor “bridge” cells via 5-hydroxytryptamine receptor 3A (HTR3A), and the aggressive HTR3A^{high} human neuroblastoma cell lines reduce proliferation in response to HTR3A-specific agonists. In embryos (in vivo), the physiological increase of 5HT caused a prolongation of the cell cycle in “bridge” progenitors leading to a smaller chromaffin population and changing the balance of hormones and behavioral patterns in adulthood. These behavioral effects and smaller adrenals were mirrored in the progeny of pregnant female mice subjected to experimental stress, suggesting a maternal-fetal link that controls developmental adaptations. Finally, these results corresponded to a size-distribution of adrenals found in wild rodents with different coping strategies.

¹ Department of Neuroimmunology, Center for Brain Research, Medical University Vienna, Vienna, Austria. ² Department of Physiology and Pharmacology, Karolinska Institute, Stockholm, Sweden. ³ Koltsov Institute of Developmental Biology, Russian Academy of Sciences, Moscow, Russia. ⁴ National Medical Research Center for Endocrinology, Moscow, Russia. ⁵ Federal state budgetary institution “Research Zakusov Institute of Pharmacology” (FSBI “Zakusov Institute of Pharmacology”), Russian Academy of Sciences, Moscow, Russia. ⁶ Sechenov First Moscow State Medical University (Sechenov University), Moscow, Russia. ⁷ Max-Delbrück Center for Molecular Medicine (MDC), 13125 Berlin-Buch, Germany. ⁸ German Center for Cardiovascular Research (DZHK), Partner Site Berlin, Germany. ⁹ Charité-Universitätsmedizin Berlin, 10117 Berlin, Germany. ¹⁰ Institute for Biology, University of Lübeck, 23562 Lübeck, Germany. ¹¹ Department of Experimental Biology, Faculty of Science, Masaryk University, Brno, Czech Republic. ¹² International Clinical Research Center, St. Anne’s University Hospital, Brno, Czech Republic. ¹³ Central European Institute of Technology, Brno University of Technology, Brno, Czech Republic. ¹⁴ Unit of Cell and Developmental Biology, Department of Biology, University of Pisa, Pisa, Italy. ¹⁵ Center for Neuroscience and Cognitive Systems @UniTn, Istituto Italiano di Tecnologia, Rovereto, Italy. ¹⁶ INSERM, Paris Brain Institute, Paris, France. ¹⁷ Severtsov Institute of Ecology and Evolution, Russian Academy of Sciences, Moscow, Russia. ¹⁸ Department of Neuroscience, Karolinska Institute, Stockholm, Sweden. ¹⁹ These authors contributed equally: Polina Kameneva, Victoria I. Melnikova. ✉email: elena.voronezhskaya@idbras.ru; igor.adameyko@ki.se

Adrenal glands are key hormonal regulators in our body, as they control major physiological processes of our daily life, and homeostasis cannot be maintained without their normal function. The structure of adrenal glands includes the cortical matter, consisting of cells that produce steroid hormones, and the centrally positioned medulla (adrenal medulla—AM), which orchestrates the response of our body to stress by releasing catecholamines (adrenaline and noradrenaline). Quite remarkably, there is another similar catecholamine-producing organ transiently present in our body, namely the Organ of Zuckerkandl (ZO)¹. The ZO eventually disappears during the first years of human life. Chromaffin cells represent the major catecholamine-producing cell type in the AM and in ZO (together called chromaffin organs).

Despite the importance for our physiology, the key details of adrenal gland development remain unclear. These details are important not only for the adrenal gland engineering attempts or for understanding associated congenital abnormalities, but also for coping with tumors arising from sympathoadrenal lineage, namely neuroblastoma, pheochromocytoma, and paraganglioma. According to a recent paradigm, tumor cells exploit and re-play developmental programs to elicit intra-tumoral plasticity and resist treatment². In addition, the good knowledge of developmental steps and molecular profiles assists better classification of tumors and helps to pinpoint the tumor-initiating cell types using transcriptional similarity of malignant cells to particular developmental cell states^{3–5}.

In line with this reasoning, recent studies showed that the initial stages of chromaffin cell development depend on the recruitment of local nerve-associated Schwann cell precursors (SCPs), which turn into a short-living transient population of “bridge” cells that rapidly transitions towards mature chromaffin cells in mouse and human embryos^{6–9}. This finding complicated the old picture of adrenal development (where migratory neural crest cells immediately generate chromaffin tissues), and raised a series of questions regarding the control of the number of chromaffin progenitors operating during the differentiation steps. These “bridge” cells are characterized by the expression of *Htr3a*^{6,8}—a gene encoding for a subunit of HTR3 receptor to serotonin (5-hydroxytryptamine, 5HT). Based on that, 5HT was recently hinted to be a part of the mechanism related to the development of adrenal medulla⁶.

More generally, 5HT is crucial for the embryonic development¹⁰ and for postnatal growth in the animal kingdom^{11–13}, including the formation of the nervous system^{14–16}. Moreover, 5HT is one of the main players shaping mood, fight-or-flight stress response, and aggressive behavior in mammals¹⁷. One of the key connection between embryonic development, chromaffin organs and 5HT comes from studies of animal domestication. Domesticated animals have higher levels of 5HT and less catecholamine-triggered aggressive behaviors¹⁸. Genetic differences between wild and tame animals of the same species include genes encoding for the enzymes of 5HT synthesis and degradation¹⁹. Moreover, the adrenal glands of domesticated animals are smaller than their wild relatives^{20,21}. Therefore, behavioral differences can be attributed to variations in 5HT and catecholamine systems and to the size of the respective endocrine organs, particularly the adrenal glands, which are shaped during embryonic development.

In this study, by analysing cellular composition and cell dynamics in the developing adrenal medulla and ZO, we show a 5HT-mediated regulatory negative feedback loop between chromaffin cells and their immediate precursor “bridge” cells. In line with this, we demonstrate that neuroblastoma cell lines with high expression of HTR3A are more tumorigenic and respond to HTR3A agonists with reduced proliferation rate. Finally, we

discover that high levels of mother-derived 5HT affect the development of embryonic adrenal medulla in a systemic way, being possibly involved in transmission of environmental signals and stress-related states from pregnant mother to her progeny. Indeed, we find that maternal mild stress induces smaller adrenal medullae in the progeny of stressed animals. Furthermore, the wild rodent population demonstrate a natural distribution of adrenal medulla sizes correlated with their preferred individual lifestyles. Taken together, these results support a major ecological and evolutionary role of the mechanisms controlling the development of adrenal glands and, in particular, chromaffin cells via a 5HT pathway.

Results

5HT-secreting and 5HT-sensitive cells in chromaffin organs.

To address the role of 5HT signaling in adrenal gland development, we re-analyzed the expression of related enzymes and receptors using previously published single-cell transcriptomics dataset of chromaffin and sympathetic development at E12.5 and E13.5 stages⁶ (Supplementary Fig. 1). As shown earlier by Furlan et al., chromaffin cells originate from SCPs and the differentiation progresses through the transitory “bridge” population. Thus “bridge” cells are immediate progenitors of chromaffin cells (Supplementary Fig. 1a). According to our analysis at E12.5, *Htr3a/3b* (encoding 5HT-receptor 3A/3B) are strongly expressed in the population of “bridge” cells and are only sporadically expressed in cells from other clusters. At E13.5, *Htr3a/3b* specifically marks the “bridge” cell population and also appears to be present in a minor portion of sympathoblasts (Supplementary Fig. 1b). To check if *HTR3A* is expressed in human adrenal medulla during development, we isolated adrenal glands at weeks 5-to-7 and subjected them to single-cell transcriptomics analysis with Chromium 10X approach. The results showed the sparse expression of *HTR3A* in “bridge” cells and rather consistent expression in sympathoblasts (Supplementary Fig. 2a, b). Although we detected only 6 *HTR3A*⁺ cells in a “bridge” population, the statistical test supports the significance of this find (Supplementary Fig. 2c). At the same time, this suggests low expression level of *HTR3A*, which we experimentally validated with RNAscope in situ hybridisation on slices of week 6 and week 8 human adrenal tissue (Supplementary Fig. 2d). Indeed, if the expression of *HTR3A* is truly present, it is weak and at the border of detection, which leaves the question about the role of *HTR3A* in human “bridge” cells open. Consistently, the data from other groups show almost absent expression of *HTR3A* from SCPs and “bridge” cells in developing human adrenal medulla despite its clear presence in sympathoblasts²². Again, a question of whether *HTR3A* is sufficiently present in “bridge” cells of human adrenal glands requires further investigation with more sensitive methods.

5HT, the ligand activating the ion channel receptor formed by HTR3A/3B proteins, can be supplied through the embryonic bloodstream, although it might be also produced locally by other cells of the developing adrenal medulla (AM). Thus, we explored different cell types in AM for the presence of enzymatic cascades necessary to produce local 5HT. It turned out that nearly all cells in AM express *Ddc* gene encoding the enzyme responsible for decarboxylating 5HTP (5-hydroxytryptophan) into 5HT, and *Maoa* gene encoding the enzyme responsible for monoamine degradation. At the same time, the synthesis of 5HT from tryptophan does not take place in AM cells, as most cells do not express the *Tph1* and *Tph2* genes at E12.5 and E13.5 (Supplementary Fig. 1c). Thus, the majority of immature and mature chromaffin cells, and a subset of SCPs and “bridge” cells are capable of producing 5HT from the chemical precursor

5HTP, but not from tryptophan. In addition to this, at E12.5, chromaffin cells are positive for *Slc29a4*, which encodes Plasma Membrane Monoamine Transporter (PMAT)—a non-selective transporter responsible for pumping 5HT inside the cells (Supplementary Fig. 1d). Therefore, embryonic chromaffin cells are capable of taking 5HT from the bloodstream, especially given that the adrenal glands are heavily vascularized. Moreover, chromaffin cells and sympathoblasts express *Slc18a1* and *Slc18a2*, which encode for VMAT1 and VMAT2, non-selective vesicular monoamine transporters responsible for the storage of monoamines in intracellular secretory vesicles. Therefore, chromaffin cells possess the necessary molecular machinery to uptake, synthesize, and secrete 5HT, and they originate from the 5HT-sensitive HTR3A⁺ “bridge” cells.

To characterize the local cell type composition and to assess the physical contacts between different cell types in AM and ZO, we took advantage of a standard combination of immunohistochemical markers (SOX10 for SCPs, tyrosine hydroxylase (TH) for chromaffin cells, and 5HT) together with genetically modified *Htr3a*^{EGFP} mice in order to visualize “bridge” cells and their newly-differentiated progeny²³. Because EGFP can be retained in cells up to 48 h after the cease of active expression²⁴, we additionally visualized “bridge” cells by *Htr3a* mRNA in situ hybridization, which revealed a proportion of *Htr3a*^{EGFP+} cells actively expressing *Htr3a* mRNA in developing AM at the time of the observations (Supplementary Fig. 3a). This result shows that *Htr3a*^{EGFP+} cells negative for *Htr3a* mRNA (post-bridge cells) rapidly differentiate into TH⁺ chromaffin cells. No chromaffin cells were found positive for *Htr3a* mRNA (Supplementary Fig. 3b). Therefore, the *Htr3a*^{EGFP} mouse strain can be used to trace the transition from the intermediate “bridge” cell population to the chromaffin cells by assessing the proportions of TH⁻/*Htr3a*^{EGFP+} “bridge” cells, TH⁺/*Htr3a*^{EGFP+} early chromaffin cells and TH⁺/*Htr3a*^{EGFP-} mature chromaffin cells.

AM and ZO are dynamically developing organs, and, therefore, the proportion of cells building AM and ZO changes between E12.5 and E14.5 towards more mature cell types (Fig. 1). Indeed, TH⁻/*Htr3a*^{EGFP+} “bridge” cells compose most of the AM and ZO at E12.5 (Fig. 1a–d, Supplementary Fig. 4a–d), and they rapidly differentiate into TH⁺/*Htr3a*^{EGFP+} early chromaffin cells and TH⁺/*Htr3a*^{EGFP-} mature chromaffin cells, composing most of the AM and ZO at E13.5 and E14.5 (Fig. 1f–o, Supplementary Fig. 4f–o). We validated the active transition from SCPs to “bridge” cells by visualizing the presence of SOX10⁺/*Htr3a*^{EGFP+} cells at E12.5 and E13.5 (Fig. 1b, g insets, Supplementary Fig. 4), as well as by assessing *Htr3a* mRNA expression at E13.5 (Supplementary Fig. 3a).

Next, our analysis revealed that already at E12.5, nearly 32% of early and mature chromaffin cells are 5HT⁺ in the AM (Fig. 1e). Soon after, around 58% and 77.8% of chromaffin cells became 5HT⁺ in the AM at E13.5 and E14.5 correspondingly (Fig. 1f–o). At the same time, SCPs did not show 5HT immunoreactivity (Supplementary Fig. 5a), and only 1.7–5.1% of all *Htr3a*^{EGFP+} cells were *Htr3a*^{EGFP+}/TH⁻/5HT⁺ (5HT-positive “bridge” cells) at E12.5–E14.5 (Fig. 1e, j, o). In ZO the proportion of 5HT⁺ cells among TH⁺ and *Htr3a*^{EGFP+} cells followed a similar pattern (Supplementary Fig. 4). Therefore, chromaffin cells contribute most of the local 5HT to the surrounding and neighboring cell types in the adrenal gland. In line with these observations, at E12.5–E13.5, *Htr3a*^{EGFP+}/TH⁻ “bridge” cells (sensitive to 5HT) are intermingled with chromaffin cells in the primordium of AM and ZO (Fig. 1a, e, Supplementary Fig. 4a–h), and are susceptible to 5HT generated by neighboring chromaffin cells. Based on this, we propose a mechanism of a paracrine control, where chromaffin cells release 5HT acting on neighboring “bridge” cells, with some contribution of the autocrine regulation, where

few 5HT⁺ “bridge” cells act on themselves and other HTR3A⁺ “bridge” cells in their vicinity. As the SCPs and few chromaffin cells express other receptors to 5HT, additional modes of local autocrine and paracrine control might be also present (Fig. 1p).

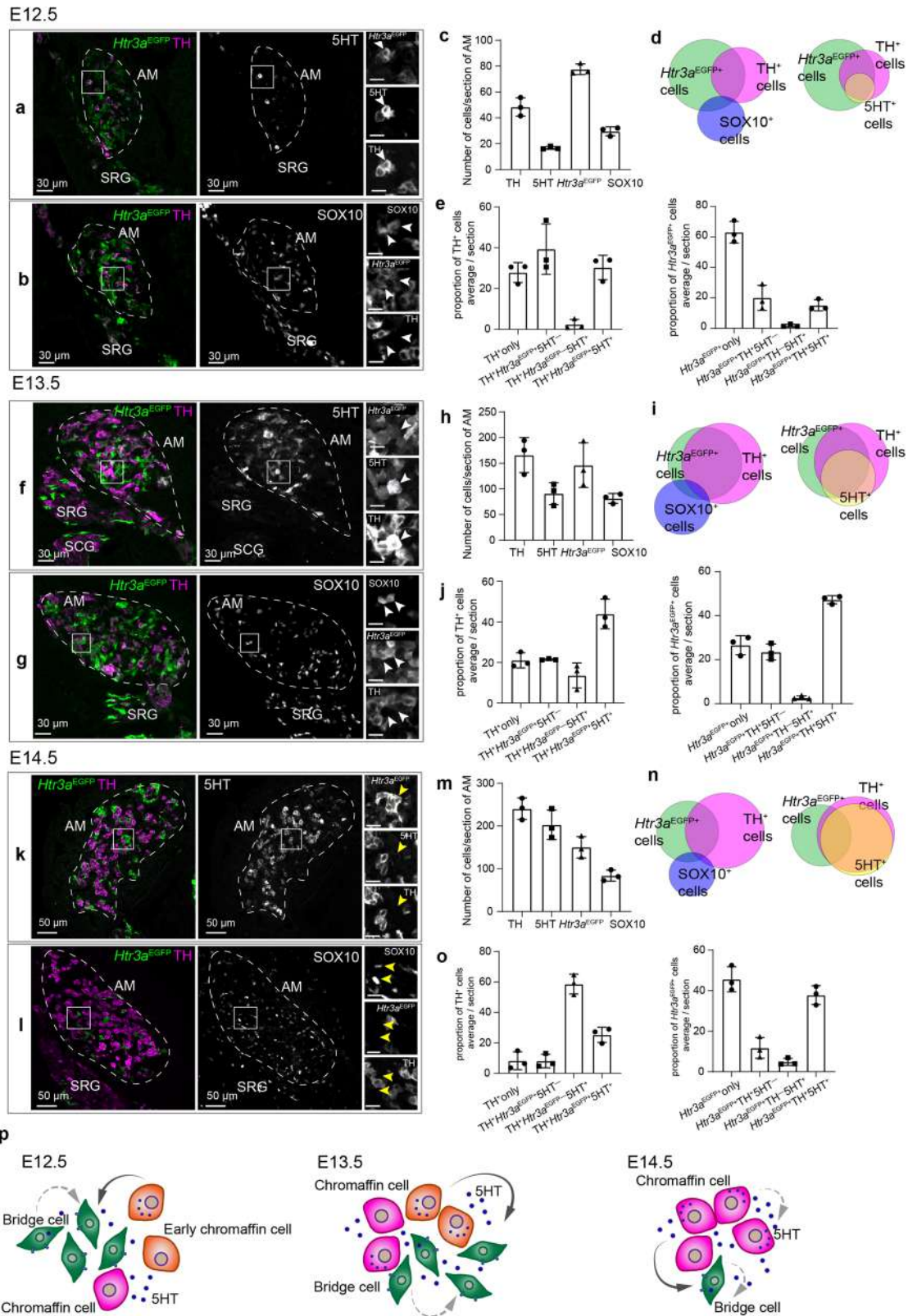
When the differentiation of chromaffin cells slows down around E14.5 (E13.5 in ZO)^{6,8}, the proportion of SOX10⁺/*Htr3a*^{EGFP+} cells decreases gradually (from 6.3% at E13.5 to 4.7% at E14.5), as the SOX10⁺ SCPs engage into the “bridge” fate at a decreasing rate (Fig. 1k–o, Supplementary Fig. 4f–o). Consistently, after E14.5, the majority of SOX10⁺ cells of AM and ZO are supporting glial cells and immature Schwann cells, as reported in the literature²⁵.

Thus, the observed transitions between SCPs, “bridge” and chromaffin cells suggest that the key 5HT-mediated regulatory phase occurs predominantly in a limited time window during chromaffin organ development (E11.5–E14.5). This is substantiated by the fact that *Htr3a*^{EGFP+}/TH⁺/5HT⁺ early chromaffin cells (reflecting the transition from *Htr3a*^{EGFP+} cells to chromaffin cells) are observed already at E12.5 within the AM (Fig. 1a, f insets), whereas at E14.5 the proportion of these cells drops two-fold in comparison with E13.5 (Fig. 1j, o). Moreover, at E14.5, a subset of TH⁺ chromaffin cells in AM undergoes further functional specialization as shown by the onset of expression of *Pnmt* gene encoding phenylethanolamine N-methyltransferase (PNMT) (Supplementary Fig. 5b), the enzyme responsible for converting noradrenaline to adrenaline. Even though the contribution of SCPs to “bridge” cells and their differentiation towards early chromaffin cells peaks at E13.5 and is reduced significantly after E15.5 in AM, in E14.5 ZO 90% of cells are represented by newly-generated *Htr3a*^{EGFP+}/TH⁺/5HT⁺ early chromaffin cells (Supplementary Fig. 4o). Importantly, during this time window and up to postnatal day 14 (P14) (the latest stage we checked), chromaffin cells in AM and ZO maintain 5HT-immunoreactivity (Supplementary Fig. 5c). Thus, chromaffin cells in mice are capable of releasing both 5HT and catecholamines during embryonic development and later during postnatal life^{26–30} being involved into a system of cell number control, which we specify below.

High 5HT causes developmental reduction of chromaffin organs.

To reveal the effects of 5HT on the developing AM, we performed a gain-of-function experiment by administering its biochemical precursor, 5HTP, to pregnant rats (Fig. 2a). The administration of 5HTP enables to increase the physiological concentrations of 5HT in embryos without disruption of pregnancy caused by direct 5HT administration³¹. Moreover, 5HTP is converted to 5HT by the placenta¹⁴. As expected, administration of 5HTP to pregnant females led to a significant increase of 5HT concentration in the placenta and trunks of E14.5 embryos (Fig. 2b), and enhanced the release of 5HT by the fetal adrenal glands (Fig. 2c), as measured by HPLC-ED. Thus, the administration of 5HTP to pregnant rodent females causes a stable and physiological increase of 5HT concentration in embryos, as previously shown for other tissues including the uterus^{32,33}.

Pregnant Wistar rats received 5HTP during E11.5–E15.5 stages, and the adrenal glands of E15.5 embryos were investigated in 3D by micro computerized tomography (microCT) (Fig. 2d). We observed a 37.2% reduction of the mean volume of adrenal glands in embryos upon 5HTP treatment (Fig. 2e, f). Immunohistochemical analysis of adrenal glands of littermates revealed a significant reduction of the AM, whereas the area of the adrenal cortex was similar in control and experimental offspring (Fig. 2g). The volume of kidneys in treated embryos did not change, confirming the lack of general developmental delay.



To make sure that the effect of 5HT on the AM size is consistent in a different rodent model, we analyzed the adrenal glands of mice and obtained consistent results (Fig. 2h). 5HTP treatment of pregnant rats and mice during the active differentiation of “bridge” cells into chromaffin cells resulted in a long-lasting reduction of AM size in embryonic and postnatal life in both species. Administration of 5HTP outside this critical

time window led to a less pronounced effect (Fig. 2h). Thus, we were able to influence the size of the adrenal glands in rodent offspring through the elevation of 5HT levels in pregnant animals during a limited developmental time window corresponding to the peak of chromaffin cell generation.

To pinpoint the specific medullary population affected by the increased levels of 5HT in developing AM and ZO, we repeated

Fig. 1 5HT-sensitive “bridge” cells and 5HT-producing chromaffin cells are present together in developing adrenal glands. **a, b** Transversal section of adrenal gland of *Htr3a*^{EGFP+/-} embryos immunostained for TH (marker chromaffin cells and sympathoblasts), EGFP (indicating expression of *Htr3a*), and 5HT (5-hydroxytryptamine, serotonin) (**a**), and for SOX10 (marker of SCPs) (**b**) at E12.5. White arrows point at TH⁺/*Htr3a*^{EGFP+}/5HT⁺ (**a**) and SOX10⁺/*Htr3a*^{EGFP+}/TH⁻ (**b**) cells, indicating formation of “bridge” cells and their differentiation into 5HT⁺ early chromaffin cells. **c** Cell numbers at E12.5. **d** Venn diagrams of *Htr3a*^{EGFP+}, TH⁺, SOX10⁺ (left), and 5HT⁺ (right) cells at E12.5. **e** Proportions of TH⁺ cells also positive for *Htr3a*^{EGFP} and 5HT (left), and proportions of *Htr3a*^{EGFP+} cells with TH and 5HT signal (right). **f, g** Immunohistochemistry on the transversal section of adrenal glands of *Htr3a*^{EGFP+/-} embryos stained for TH, EGFP, 5HT (**f**) and for SOX10 (**g**) at E13.5. White arrows point at TH⁺/*Htr3a*^{EGFP+}/5HT⁺ cells in (**f**) and SOX10⁺/*Htr3a*^{EGFP+}/TH⁻ cells in (**g**) at E13.5. **h** Cell numbers at E13.5. **i** Venn diagrams of *Htr3a*^{EGFP+}, TH⁺, SOX10⁺ (left), and 5HT⁺ (right) cells at E13.5. **j** Proportions of TH⁺ cells positive for *Htr3a*^{EGFP}, 5HT (left) and proportions of *Htr3a*^{EGFP+} cells positive for TH, 5HT (right). **k, l** Transversal sections of adrenal glands from *Htr3a*^{EGFP+/-} embryos stained for TH, EGFP, and 5HT in (**k**), and for SOX10 in (**l**) at E14.5. Yellow arrows point at TH⁻/*Htr3a*^{EGFP+}/5HT⁻ cells (**k**) and SOX10⁺/*Htr3a*^{EGFP-}/TH⁻ cells (**l**) indicating the end of “bridge” differentiation, SOX10⁺ represent supporting glial cells. **m** Cell numbers at E14.5. **n** Venn diagrams of *Htr3a*^{EGFP+}, TH⁺, SOX10⁺ (left), and 5HT⁺ cells (right) at E14.5. **o** Proportions of TH⁺ cells positive for *Htr3a*^{EGFP}, 5HT (left), and proportions of *Htr3a*^{EGFP+} cells positive for TH and 5HT (right). **p** Schematic representation of the proposed paracrine/autocrine regulation: chromaffin cells release 5HT activating HTR3A receptors on the surface of “bridge” cells (solid lines). Note that few “bridge” cells produce 5HT and can stimulate “bridge” population in an autocrine mode as well as some chromaffin cells can sense 5HT with other 5HT receptors (dashed lines). Scale bars for the insets are 10 μ m. Quantification is presented as mean \pm SD, biological *n* = 3. Adrenal medulla (AM) is outlined by the dashed line in all sections. SRG: suprarenal ganglion, SCG: sympathetic chain ganglion.

the 5HTP treatment in the transgenic *Htr3a*^{EGFP} mice. In order to target the same consistent stages across species, 5HTP was administered to pregnant mice at E11.5–E12.5, corresponding to E13.0–E15.0 in rats³⁴ (Fig. 3a). As a result, at E13.5, the numbers of early chromaffin cells (TH⁺/*Htr3a*^{EGFP+}) and mature chromaffin cells (TH⁺/*Htr3a*^{EGFP-}) were reduced by 39.1% and 38.8%, respectively (difference between mean values of control and 5HTP groups), in AM of the embryos from the treated mice (Fig. 3c). We did not detect a significant change in “bridge” cells number at E13.5. In the ZO, the number of “bridge” cells (*Htr3a*^{EGFP+}/TH⁻) was twice higher, and the number of mature chromaffin cells (TH⁺/*Htr3a*^{EGFP-}) was reduced (Fig. 3c). Schwann cell precursors (SOX10⁺) cell numbers were unaffected in both chromaffin organs (Fig. 3c).

To control for the systemic effect, we checked the cells in the sympathetic chain ganglia (SCG), which are directly derived from the migratory neural crest cells and do not transition through a “bridge” stage^{6,35}. Thus, SCG served as an internal control for the changes in size of chromaffin organs. 5HTP administration did not influence the size or cellular composition of SCG (Supplementary Fig. 6). Therefore, the reduction of chromaffin organs is specific and occurs at the expense of chromaffin cells.

To confirm that the observed phenotype emerged due to the activation of HTR3A, we used SR57227 hydrochloride, a potent and selective HTR3A agonist. Administration of SR57227 to pregnant mice at E11.5 and E12.5 caused a 30.6% reduction (difference between mean values of DMSO control and SR57227 groups) of early and mature TH⁺ chromaffin cells in AM at E13.5 (Fig. 3d). This is similar to the effect caused by 5HTP administration to pregnant mice during the same developmental time. To rescue the phenotype caused by the elevated 5HT level, we co-administered granisetron, a HTR3A antagonist, in combination with 5HTP. In this condition, the number of TH⁺ cells in AM turned out to be similar (Fig. 3d), whereas the administration of 5HTP alone caused a 34.5% reduction (difference between mean values of DMSO control and 5HTP groups) of the chromaffin cells in AM. The SCG (representing a control tissue with different genesis) showed the same numbers of TH⁺ sympathoblasts in all groups (Fig. 3d). Therefore, the HTR3A activation mediated 5HT-dependent signaling in the development of the chromaffin cell lineage and caused the decrease of chromaffin cells in AM and ZO upon 5HTP treatment.

To further investigate the reasons for the observed reduction in chromaffin cell numbers, we checked the dynamics of cell cycle in various populations of cells in the chromaffin lineage. For this purpose, we administered consecutively 5-ethynyl-2'-deoxyuridine (EdU) and 5-chloro-2'-deoxyuridine (CldU) thymidine

analogues at E12.5 with 4-h intervals to *Htr3a*^{EGFP} mice treated with 5HTP (Fig. 4a). At the time of CldU injection, EdU is not available for cells due to its rapid pharmacokinetics³⁶. This approach allowed calculating the proliferation rate as well as the proportion of Edu⁺Cldu⁻, Edu⁻Cldu⁺, and Edu⁺Cldu⁺ cells.

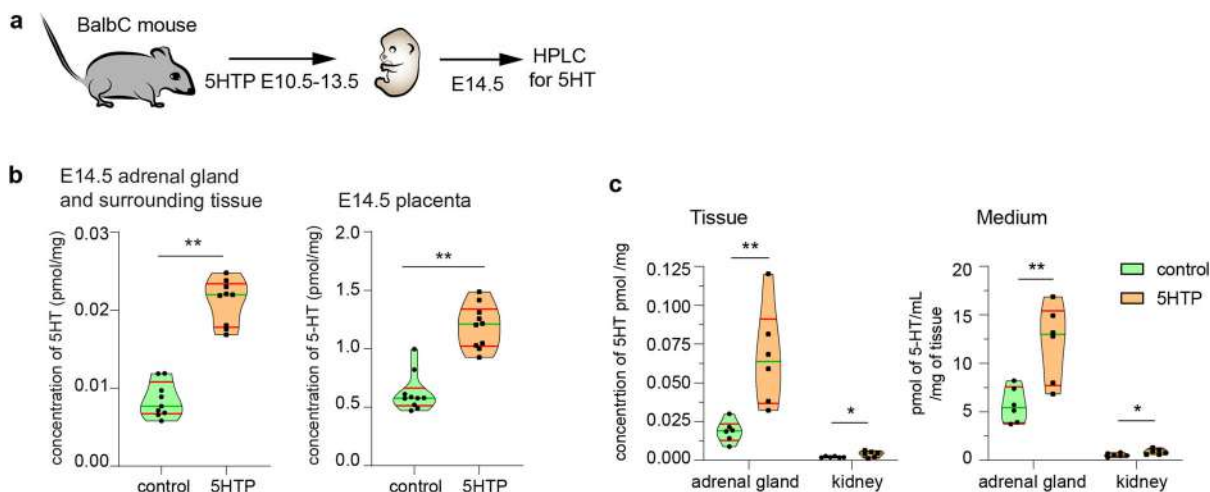
Despite the overall numbers of proliferating (incorporating one or both thymidine analogues) cells among SCPs, “bridge” cells, early chromaffin cells or mature chromaffin cells did not show a significant change in comparison with control (Fig. 4b), the length of a cell cycle in “bridge” cells appeared significantly increased in the 5HTP-treated group (Fig. 4c, d, Supplementary Fig. 7a). Delayed cell cycle progression resulted in the reduced number of “bridge” cells observed at this stage, soon after the injection (Fig. 4b). Such reduction of “bridge” cells was not observed at E13.5, due to a fast turnover of “bridge” cells and subsequent recruitment of new “bridge” cells from SCPs. Moreover, 5HTP and 5HT are rapidly depleted after the injection-dependent concentration peak due to pharmacokinetics. At the same time, the dynamics of cell cycle progression in SCPs and early chromaffin cells in AM did not change in control vs treatment group (Fig. 4c). The majority of mature chromaffin cells were negative for EdU or CldU, as they temporarily exit cell cycle in agreement with previous studies³⁷. Due to fast differentiation of chromaffin cells from progenitors in 14 h⁷, reduction of the progenitor pool has a major effect of chromaffin cell population. A majority of chromaffin cells do not proliferate at E12.5–E13.5 and are unable to compensate for the loss.

Contrary to the AM, in the E12.5 ZO, we observed a lower proportion and reduced absolute numbers of SOX10⁺ SCPs incorporating EdU only in the 5HTP-treated group (Supplementary Fig. 7), which suggests another mechanism of cell number control or delayed dynamics of 5HT's effects in the ZO.

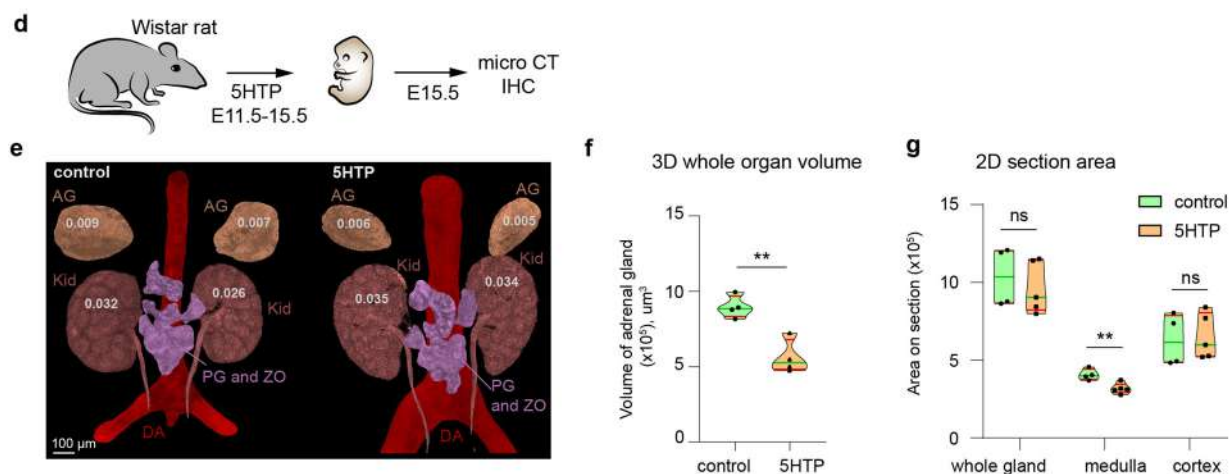
As we did not observe cleaved caspase-3 immunopositive (CASP3⁺) cells in any cell population in the AM and ZO (excluding exceptionally rare cases), the reduction of chromaffin cells in 5HTP-treated group cannot be mediated via increased apoptosis (Fig. 4e). Thus, the increase of 5HT causes a prolongation of the cell cycle of “bridge” progenitors leading to a decrease in their number, which results in a reduction of derived chromaffin cells (Fig. 4f).

Next, to dissect the potential changes of gene expression upon 5HTP administration, we performed single-cell RNA sequencing of the AM and ZO at E13.5 from 5HTP-treated and untreated embryos (Fig. 5a). We sequenced 1528 cells (both conditions combined) using Smart-seq2 technology, which allows an extraordinary deep sequencing of individual cells (7000/8000

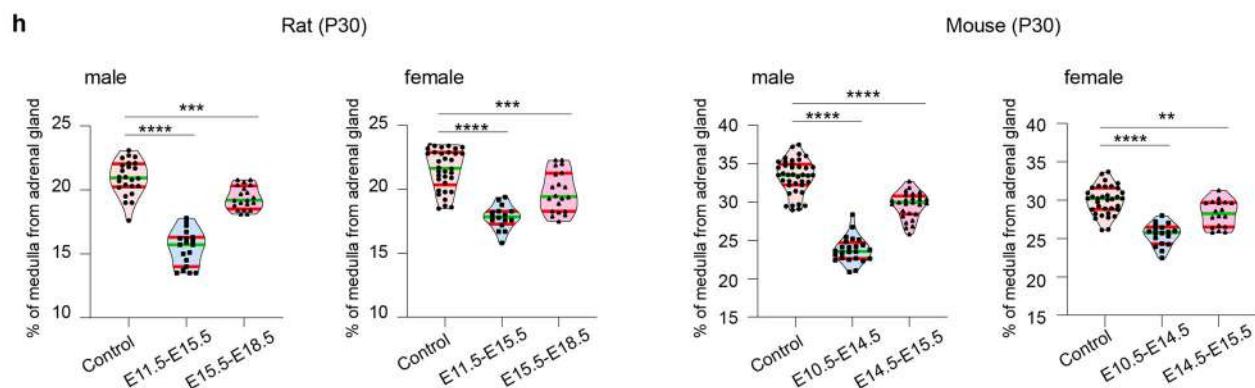
Serotonin is increased in adrenal glands after 5HTP treatment



Adrenal medullae are smaller in 5HTP-treated embryos



Reduction of adrenal medullae after 5HTP treatment



genes per cell on average). The general composition, cell type proportions, and the developmental sequence of cell types (SCPs, “bridge” cells, chromaffin cells, and sympathoblasts) (Fig. 5b, c) remained the same upon 5HTP treatment. At the same time, we detected a reliable change in expression of a gene responsible for

the regulation of splicing (*Cwc22*)^{38,39} (Fig. 5d, e). In line with this, we detected changes in differential splicing of several long non-coding RNAs (*Uph*, *Uph.AS2*, *Uph.AS3*, *Uph.AS4*) (Fig. 5e) controlling the expression of *Hand2*⁴⁰, a transcription factor essential for the transition to the catecholaminergic program in

Fig. 2 Administration of 5HTP, the immediate precursor of 5HT, to pregnant rodents reduces adrenal medulla in the progeny. **a** 5HTP was administered to pregnant BalbC mice at E10.5–E13.5. The embryos are collected at E14.5 for the HPLC-based analysis of 5HT. **b** Concentration of 5HT in the adrenal glands and surrounding tissues (left) and placentas (right) at E14.5 after 5HTP administration at E10.5–E13.5 stage. Unpaired double-sided *t*-test *p*-value $** < 0.001$, biological $n = 9$. **c** Adrenal glands from E14.5 embryos release 5HT into the surrounding medium measured by HPLC-ED. Note: kidneys, used as a control tissue, do not release 5HT. Unpaired double-sided *t*-test *p*-value $* < 0.05$, $** = 0.005$, biological $n = 6$. **d** 5HTP was administered to pregnant Wistar rats at E11.5–E15.5 followed by embryo collection at E15.5 and analysis by X-ray computed microtomography (microCT). **e** microCT X-ray reconstruction of adrenal glands and kidney volume from E15.5 rat embryos obtained from females in control and 5HTP-treated groups. Volumes of the organs in μm^3 ($\times 10^5$). **f** Adrenal gland volume normalized to the volume of adjacent kidneys. Biological $n = 4$. Unpaired double-sided *t*-test *p*-value $** < 0.005$. **g** Section areas of adrenal gland, adrenal medulla and adrenal cortex based on immunohistochemistry analysis with anti-TH immunostaining. Unpaired double-sided *t*-test *p*-value $\text{ns} > 0.05$, $* < 0.05$, biological $n = 4$ (control), 5 (5HTP). **h** Prenatal 5HTP exposure at the time of “bridge” cell differentiation (E11.5–E15.5 in rats and E10.5–E14.5 in mice) causes the decrease of postnatal adrenal medulla size in P30 animals, which was greater than decreased induced by 5HTP exposure after the time of “bridge” cell differentiation (E15.5–E18.5 in rats and E14.5–E15.5 in mice). Green line in all violin plots—the median, red lines—quartiles. One-way ANOVA test with Dunnett’s multiple comparison test $**p = 0.0017$, $***p = 0.0002$, $****p < 0.0001$, biological n (adrenal gland) = 24 (control male rat), 19 (E11.5–E15.5 male rat), 20 (E15.5–E18.5 male rat), 35 (control female mice), 16 (E11.5–E15.5 female rat), 20 (E15.5–E18.5 female rat), 40 (control male mice), 24 (E10.5–E14.5 male mice), 27 (E14.5–E15.5 male mice), 35 (control female mice), 18 (E10.5–E14.5 and E14.5–E15.5 female mice). For all experiments normality is checked with Shapiro–Wilk test. AG: adrenal gland, Kid: kidney, PG and ZO: paraganglia and organ of Zuckerkindl, DA: dorsal aorta.

chromaffin cells and sympathoblasts⁴¹. The other differentially spliced genes, *Apobec3* and long non-coding RNA *Cenpa.AS2*⁴², might be involved in the control of a cell cycle length in “bridge” cells, where they are enriched.

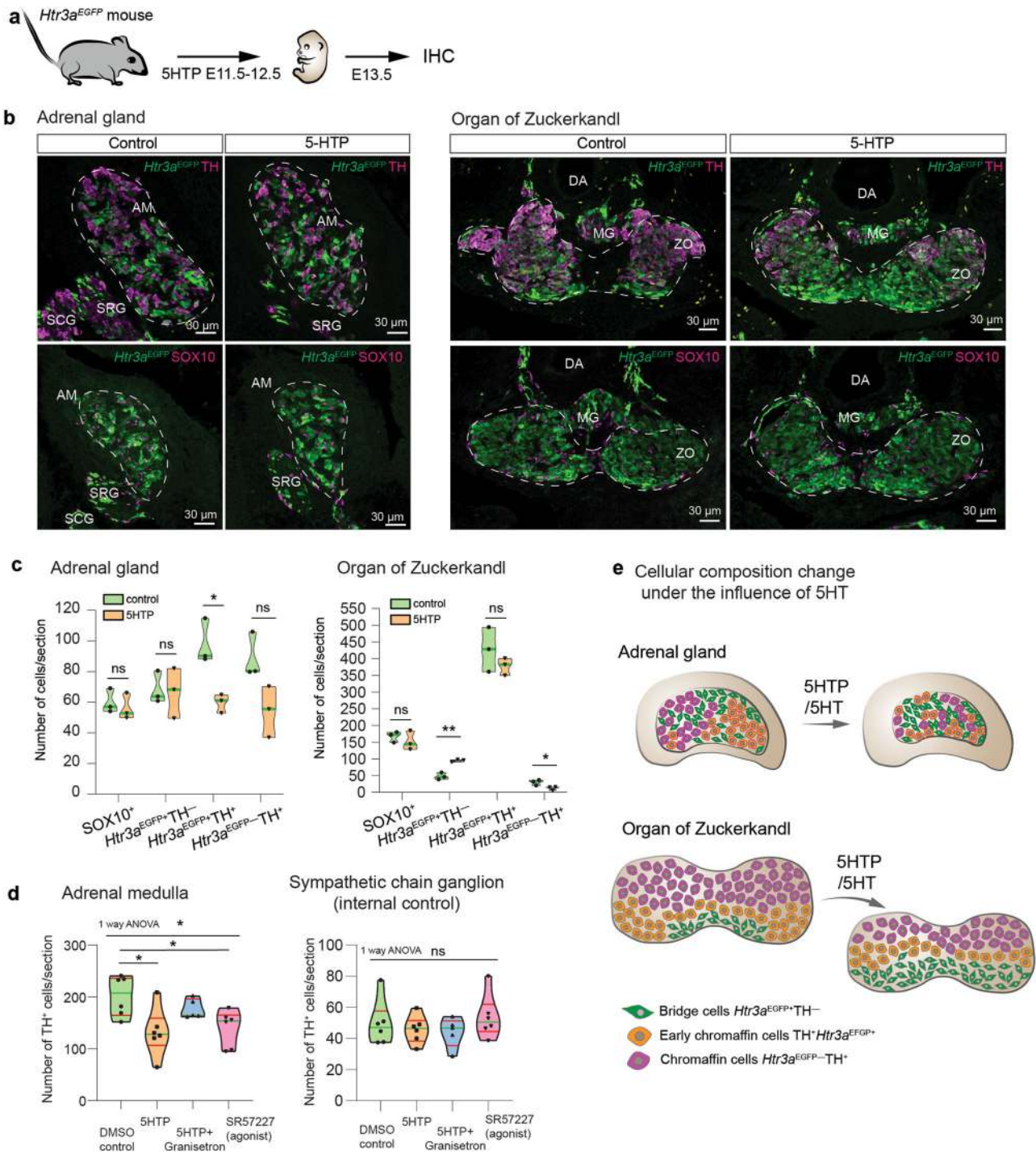
The deficit of 5HT has no effect on chromaffin cells. As the elevated levels of 5HT lead to a decreased chromaffin cell numbers in vivo by delaying the cell cycle of precursor “bridge” cells, we expected to see the opposite effect in the case of reduced levels of 5HT. However, the previously reported genetic loss-of-function of the HTR3A receptor failed to show any abnormal phenotype in adrenal glands⁴³. A potential explanation for these observations is that 5HT affects cell cycle progression in HTR3A⁺ “bridge” cells only when 5HT levels reach a certain threshold. Furthermore, HTR3A-dependent paracrine regulation may not be critical for the development of the adrenal gland, but is an important controller of excessive chromaffin tissue growth and pre-malignant states.

To explore how the deficit of 5HT affects chromaffin development, we analyzed several mouse models with a reduction of embryonic and maternal 5HT. *Pet1*^{-/-} embryos collected from *Pet1*^{+/-} females, as well as *Tph2*^{-/-} embryos collected from *Tph2*^{+/-} females, lack 5HT derived from the central nervous system of the mutant embryos, although maternal 5HT remains unchanged. The numbers of TH⁺ chromaffin cells did not differ in E15.5 *Pet1*^{-/-} and *Tph2*^{-/-} embryos in comparison with their *Pet1*^{+/-} and *Tph2*^{+/-} littermates serving as controls (Supplementary Fig. 8a, b). One of the major peripheral sources of 5HT in the embryo is represented by the enterochromaffin cells, which start to secrete 5HT at E15.5¹⁰ and therefore cannot contribute to the developing adrenal glands at E12.5–E13.5. Thus, the reduction of embryonic sources of 5HT is not critical for the development of chromaffin cells, while the extraembryonic 5HT might be important.

To address how a complete removal of 5HT from both maternal and embryonic sources affects the development of chromaffin cells in an embryo, we took advantage of the *Tph1*^{-/-}; *Tph2*^{-/-}, *Tph1*^{-/-}; *Scl6a4*^{-/-}, and *Tph1*^{-/-}; *Tph2*^{-/-}; *Scl6a4*^{-/-} mouse models, which lack the ability to produce central and peripheral 5HT and to selectively transport it into cells in both mothers and progeny. We analyzed E13.5 embryos from these mouse models for the number of chromaffin cells and 5HT⁺ cells in adrenal glands. At E13.5, the number of 5HT⁺ cells demonstrated 80% to 95% reduction in all knockout (KO) animals when compared with C57BL/6 controls (Supplementary Fig. 8c, d). The average number of TH⁺ chromaffin cells also appeared reduced in KOs (in *Tph1*^{-/-}; *Tph2*^{-/-} for 11.4%,

in *Tph1*^{-/-}; *Scl6a4*^{-/-} for 27.1%, in *Tph1*^{-/-}; *Tph2*^{-/-}; *Scl6a4*^{-/-} for 31.2%, based on the difference between mean values) (Supplementary Fig. 8d). To check whether the reduction of chromaffin cells was specific, we measured the number of cells in SCG. The number of TH⁺ sympathoblasts in SCG was significantly lower in KO embryos in comparison with wild type embryos (in *Tph1*^{-/-}; *Tph2*^{-/-} for 17.8%, in *Tph1*^{-/-}; *Scl6a4*^{-/-} for 30.2%, in *Tph1*^{-/-}; *Tph2*^{-/-}; *Scl6a4*^{-/-} for 48.6%, based on the difference between mean values) (Supplementary Fig. 8e), which indicated a general developmental delay and reduction of the embryonic growth, independently of cell origin and due to the lack of maternal 5HT. Therefore, the reduction of chromaffin cells in 5HT deficient models is not specific to the adrenal medulla. Of note, the numbers of SCPs, were not changed in AM and SCG in control and KO embryos (Supplementary Fig. 8f), because SCPs depend on the local innervation coming from elsewhere. The expression of *Htr3a* mRNA was evident in *Tph1*^{-/-}; *Tph2*^{-/-}; *Scl6a4*^{-/-} E13.5 adrenal glands, which indicated that “bridge” cells are still present in the KOs (Supplementary Fig. 8g). Overall, these experiments demonstrated that the reduction of maternal and embryonic 5HT has no specific effect on the number of chromaffin cells, contrary to the excess of 5HT during a critical developmental time window.

High expression of HTR3A in tumorigenic neuroblastoma cells. To investigate the possible action of 5HT on HTR3A in the progression of tumors originating from sympathoadrenal cells, we analyzed several clones of human-derived neuroblastoma for *HTR3A* expression and tumorigenicity using an immunodeficient mouse model. Based on mRNA (Fig. 6a) and protein expression levels (Fig. 6b, c), the examined neuroblastoma cell lines could be characterized as either *HTR3A*^{high} (SH-SY5Y, CHLA-15, and CHLA-20), expressing markedly high levels of *HTR3A*, or *HTR3A*^{low} (NBL-28, NBL-38, and NBL-40), with only weak *HTR3A* expression. While all cell lines were negative for *MYCN* amplification (two copies of gene in the genome), *HTR3A* protein expression was associated with expression of major drivers of aggressive neuroblastomas, N-MYC and c-MYC^{44,45}, or one of the core stemness factors SOX2 (Fig. 6b). Intriguingly, the same association was observed in NTERA-2 embryonal pluripotent carcinoma cells, which served as a positive control for *HTR3A* expression, and which are known to express high levels of N-MYC and share characteristics with early neural progenitors. To investigate the possible role of HTR3A receptor in regulation of proliferation in tumor cells, we treated the cells with the HTR3A agonists, N-methylquipazine dimaleate (NMQ) and SR57277, as well as antagonists, VUF10166 and granisetron HCl, in the



presence of 5HT. HTR3A agonists dramatically limited proliferation of HTR3A^{high} cell lines, whereas they did not affect HTR3A^{low} cell lines, or the effects were seen only at much higher doses (Fig. 6d, e). No cleaved caspase-3 was detected after the treatment with NMQ, indicating that such treatment does not induce apoptosis (Supplementary Fig. 9). In contrast, there was no significant effect of HTR3A antagonists on cell growth of both HTR3A^{high} SH-SY5Y and HTR3A^{low} NBL-28 cell lines (Fig. 6f, g).

We also tested the ability of cells to form spheres to check their stem cell-like properties (Fig. 6h). HTR3A^{high} cells formed spheres more frequently in comparison with HTR3A^{low} cell lines. Importantly, pre-treatment with 75 μM NMQ for 5 days did not reduce sphere-forming capacity of both HTR3A^{high} and HTR3A^{low}

cell lines. Therefore, the activation of HTR3A receptor does not compromise the stem-like state of neuroblastoma HTR3A^{high} cells, but only reduces their proliferation. When NMQ is removed the cells form spheres with the same or even increased efficiency (in case of NBL-38), as compared to vehicle-pretreated controls (Fig. 6i).

SH-SY5Y and CHLA-20 HTR3A^{high} cell lines formed large tumors in NOD/SCID gamma (NSG) mice, whereas HTR3A^{low} cells did not form xenograft tumors even in 4 months after injection (Fig. 6j, k). The tumor volume increase of the xenografts during the experiment (Fig. 6l) further demonstrated the association of HTR3A expression with the aggressive phenotype of neuroblastoma cells.

Fig. 3 Administration of 5HTP to pregnant females influences chromaffin and “bridge” cells in embryonic chromaffin organs. **a** 5HTP was administered to pregnant *Htr3a*^{EGFP+/-} females, which was followed by the analysis of embryonic adrenals at E13.5 by immunohistochemistry. **b** Transversal section through the adrenal glands (left) and Organ of Zuckerkandl (right) immunostained for TH, EGFP (indicating expression of *Htr3a*), and SOX10. The sections were obtained from E13.5 embryos collected from *Htr3a*^{EGFP+/-} females from control and 5HTP-treated groups. **c** Cell numbers in adrenal medulla (left) and Organ of Zuckerkandl (right) at E13.5 in control and treated groups. Note that early chromaffin cells (*HTR3A*^{EGFP+/TH+}) and mature chromaffin cells (*HTR3A*^{EGFP-/TH+}) decrease, whereas SCPs (*SOX10+*) and “bridge” cells (*HTR3A*^{EGFP+/TH-}) do not change in the treated group vs control in the adrenal medulla. At the same time, “bridge” cells (*HTR3A*^{EGFP+/TH-}) accumulate and mature chromaffin cells (*HTR3A*^{EGFP-/TH+}) decrease in the Organ of Zuckerkandl in the treated group. Cell number are presented as violin plots, where the green line indicates median, biological $n = 3$, Shapiro-Wilk test for normality and unpaired double-sided t -test p -value $ns > 0.05$, $* < 0.05$, $** < 0.002$. **d** Cell number in adrenal medulla and sympathetic chain ganglia across four groups of E13.5 embryos treated during E11.5–E12.5 with: DMSO (control), 5HTP, 5HTP and Granisetron (*HTR3A* antagonist), SR57227 (*HTR3A* agonist). Note that cell numbers change in the adrenal medulla, but not in the sympathetic chain ganglion. Biological $n = 6$ (DMSO, 5HTP, SR57227), 5 (5HTP + Granisetron), one-way ANOVA AM p -value $*0.0135$, followed by Tukey multiple comparison test DMSO vs 5HTP p -value $*0.0189$, DMSO vs SR57227 p -value $*0.0406$; ANOVA SCG p -value $ns 0.6265$. **e** Changes in size and cellular composition in E13.5 adrenal medulla and Organ of Zuckerkandl in mice under the influence of increased 5HT (E11.5–E12.5). Cell numbers are presented as violin plots, the green line—median and the red lines—quartiles. Adrenal medulla (AM) and Organ of Zuckerkandl (ZO) are outlined by the dashed line in sections. SRG: suprarenal ganglion, SCG: sympathetic chain ganglion, MG: mesenteric ganglion.

High 5HT alters catecholamine-mediated behavior in progeny.

To evaluate the long-term effect of elevated levels of 5HT during prenatal development in rodents, pregnant Wistar rats were administered 5HTP *per os* during E11.5–E15.5, a stage critical for the transition of “bridge” cells to chromaffin cells. The offspring of treated mothers was maintained until postnatal day 75 (P75), when the behavioral tests and measurements of respective catecholamine levels in blood and adrenal glands were performed (Fig. 7a).

The total body weight of P75 animals was similar in treated and control groups (Supplementary Fig. 10a, b), whereas the weight of adrenal glands was significantly reduced in males and females from the 5HTP-treated group (Fig. 7b). In embryonically-treated adult females, this reduction of adrenals correlated with significantly lower amounts of adrenaline, noradrenaline, and dopamine in the adrenal glands, and lower adrenaline in blood plasma (Fig. 7c). In males from the 5HTP-treated group, smaller adrenal glands contained respectively less adrenaline, but the levels of noradrenaline and dopamine did not show any significant difference (Fig. 7c). To ensure that the observed reduction of adrenaline in males and the reduction of adrenaline, noradrenaline, and dopamine in females were not associated with accelerated catabolism by catechol-O-methyltransferase in blood, we measured catecholamine metabolites: metanephrine and normetanephrine (Supplementary Fig. 10c). These measurements confirmed that the decrease in adrenaline supply from the adrenal glands in the 5HTP-treated group was not due to the acceleration of adrenaline catabolism (Supplementary Fig. 10c). On the other hand, the concentration of normetanephrine was significantly higher in 5HTP-treated males, suggesting an enhanced catabolism of noradrenaline that is typically observed in major pheochromocytoma subtypes in human^{46,47}. The elevation of normetanephrine is not observed in females. Of note, high metanephrine levels might not always reflect high catecholamine synthesis and following catabolism, as inhibition of monoamine oxidase may also lead to elevated levels of catecholamines/metanephrines, which we cannot rule out even though we consider this scenario unlikely based on the previous literature^{48–51}. The system of catecholamines and their metabolism is complex and stretches beyond the production of adrenaline and noradrenaline in chromaffin organs. Therefore, the observed differences in males and females, as well as the only partial correlations with behavioral data might be due to other systemic regulatory mechanisms, which are not covered by this study.

In the next line of behavioral experiments, we assessed how the prenatal exposure to enhanced 5HT during the critical time

window of chromaffin cell generation shaped the adaptive capacity of the offspring. According to the resident-intruder test and foot shock-induced aggression test, the males from 5HTP-treated mothers were less aggressive and did not defend their territory, compared with control males (Fig. 7d). Moreover, the experimental animals were more adaptive and flexible, demonstrating less anxiety and reduced stress-induced behavior (Supplementary Fig. 10d). These results are in line with *in vivo* measurements of catecholamines in adult mice revealing lower levels of adrenaline supplied by smaller adrenal glands (evident when measured as ng/organ, Fig. 7c) in animals prenatally exposed to elevated 5HT levels.

Stress affects fetal 5HT, medulla size, and progeny behavior.

The connection between embryonic 5HT levels and subsequent animal behavior allowed us to hypothesize a connection between the stress of a pregnant female, 5HT and the development of adrenals in progeny.

The following line of experiments based on the published method⁵² revealed that mild stress induced by 1-h-restrain of pregnant mice (E10.5–E14.5) significantly enhanced 5HT level in both placenta and fetuses (Fig. 7e, f), causing decreased medulla size in a progeny (Fig. 7e, f), similarly to 5HTP exposure (Fig. 2b, h). The resulting experimental progeny demonstrated less aggressive behavior according to the standard resident-intruder test: they showed cooperative behavior and reduced number of attacks on the intruder (Fig. 7f). Overall, the prenatally 5HTP-treated animals and the progenies from stress-induced mothers showed consistency in adrenal medulla reduction and behavioral changes. Although our data from mice and rats appear to be consistent, we do not claim that the effects of maternal stress on postnatal behavior are only rooted in decreased adrenals and embryonic influence from the mother. However, mild stress and 5HTP treatment during the same embryonic period result in similar behavioral outcomes in postnatal progeny, and are associated with a decreased AM size. Overall, the prenatal effects and postnatal effect are likely connected and correlate via the reduced number of chromaffin cells in adrenal glands.

The ratio of medulla to cortex changes in migrating voles.

As the experimentation on laboratory animals might not fully reflect the ecological and evolutionary situation, we committed to perform the analysis of adrenals in wild rodents with different well-documented intra-species modes of behavior. For this, we set out for an expedition to Yenisey Ecological Station “Mirnoe” (62.2 N; 89.0 W) in Siberia, to study the wild population of red-backed

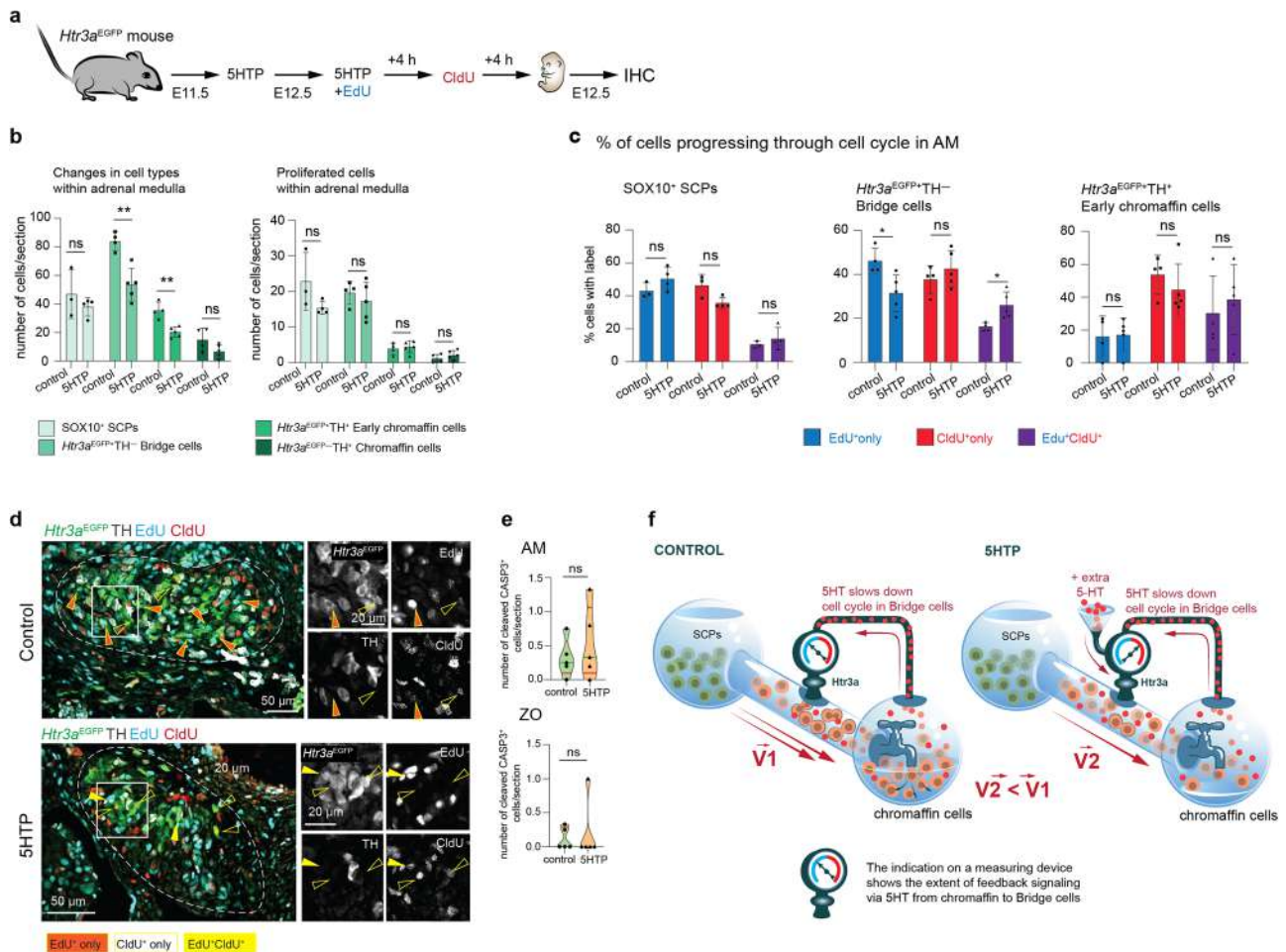


Fig. 4 Prenatal 5HT influences cell cycle length of the “bridge” progenitors in embryonic adrenal glands. **a** Pregnant *Htr3a^{EGFP/+}* females were administered 5HTP at E11.5; at E12.5, females received 5HTP together with 5-Ethynyl-2'-deoxyuridine (EdU); in 4 h females received 5-Chloro-2'-deoxyuridine (CldU); embryos were harvested in 4 h after CldU injection at E12.5. This allows identifying the proportions of cells, which incorporated EdU⁺ only, CldU⁺ only, or both thymidine analogues (EdU⁺CldU⁺). **b** Numbers of all cells (left) and numbers of proliferated cells (right) in populations of SCPs, “bridge” cells, early chromaffin cells, and mature chromaffin cells at E12.5 under the influence of 5HTP in adrenal medulla. Shapiro-Wilk test for normality and unpaired double-sided *t*-test *p*-value *ns* > 0.05, ** < 0.002, biological *n* = 3 (control SCPs), 4 (control other cell types), 4 (5HTP SCPs), 5 (5HTP other cell types). **c** Proportions of EdU⁺ only, CldU⁺ only, and EdU⁺CldU⁺ cells in populations of SCPs, “bridge” cells, and early chromaffin cells at E12.5 under the influence of 5HTP in adrenal medulla. Note that the cell cycle lengthened in “bridge” cells in the treated condition, as there are more EdU⁺CldU⁺ “bridge” cells. Shapiro-Wilk test for normality and unpaired double-sided *t*-test *p*-value *ns* > 0.05, * < 0.05, biological *n* = 3 (control SCPs), 4 (control other cell types), 4 (5HTP SCPs), 5 (5HTP other cell types). **d** Transversal sections of adrenal glands from *Htr3a^{EGFP/+}* embryos immunostained for TH, EGFP (indicating the expression of *Htr3a*), EdU, and CldU. Arrowheads point at EdU⁺ only, CldU⁺ only, and EdU⁺CldU⁺ cells. **e** Numbers of cleaved CASP3⁺ cells in adrenal medulla and Organ of Zuckerkandl. Note that the number of cleaved CASP3⁺ cells is exceptionally low. Cell numbers are presented in violin plots, the green line indicates median and the red lines are quartiles. Shapiro-Wilk test for normality and unpaired double-sided *t*-test (AM) and Mann-Whitney test (ZO), *p*-value *ns* > 0.05, biological *n* = 5. **f** Proposed mechanism of the paracrine/autocrine regulation of a cell cycle length in HTR3A⁺ “bridge” precursors by 5HT-releasing chromaffin cells in the developing adrenal medulla.

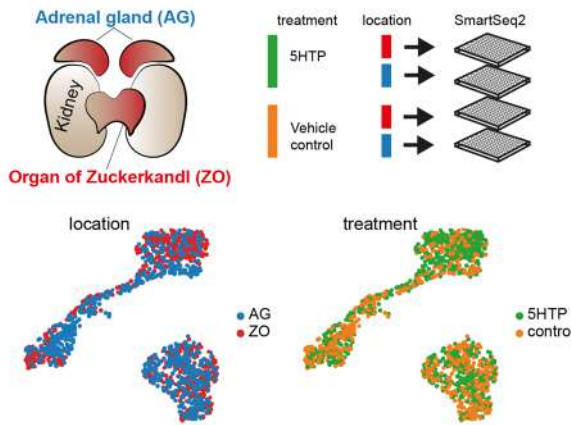
voles (*Clethrionomys rutilus*). *C. rutilus* represent a “cycling” population with periods of expansion and migration, with well-defined residents and migrants triggered by the spiking increase of density^{53–55}. To check if there is a correlation between the size of adrenal medulla and resident vs migrant profile in wild *C. rutilus*, we measured the medulla size in representatives of residents and migrants in the year of a peak population density accompanied by enhanced migration activity (2020). The results showed that the migrant animals of both sexes are characterized by reduced medulla size as compared to residents (Fig. 7g), which might be connected to the fact that the increase in population density is associated with increased chronic stress⁵⁶. According to our experiments with laboratory animals and previously published results⁵², increased level of stress in pregnant mothers elevates 5HT in the placenta and embryo. This, in turn, results in

reduced chromaffin organs in the offspring, altered hormonal profiles and more cooperative and flexible catecholamine-controlled behavior.

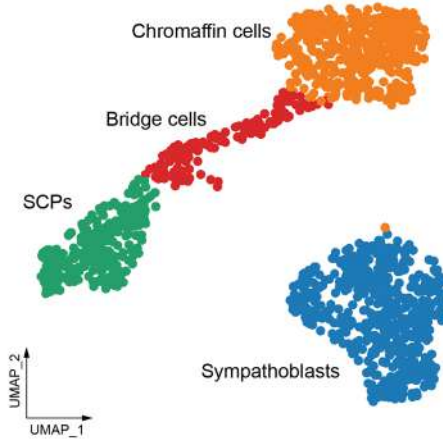
Discussion

Recent findings^{6,8} have challenged the older paradigm about the immediate origin of chromaffin cells from ventrally migrating neural crest cells⁵⁷, and raised questions about how the numbers of chromaffin cells are established and controlled during embryonic and postnatal life. These findings introduced intermediate cell states intercalating into the trajectory from the neural crest to chromaffin cells. One state is represented by nerve-associated Schwann cell precursors^{6,58} giving rise to “bridge” cells, which in turn transit into chromaffin cells⁶.

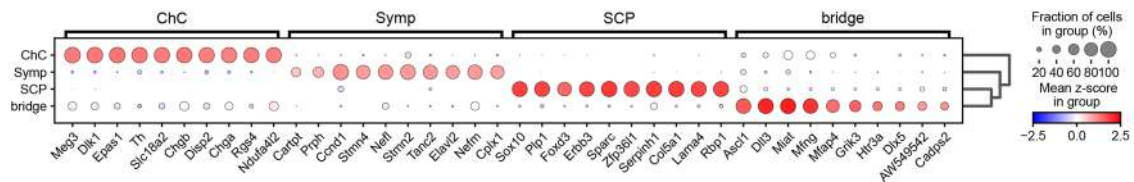
a Overview of the experimental design



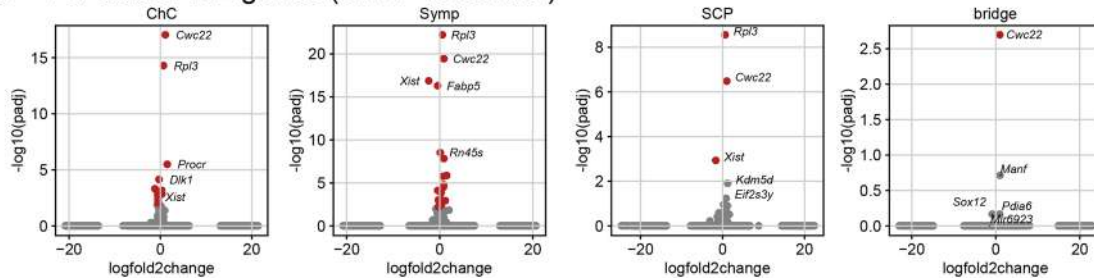
b Unbiased clustering and annotation



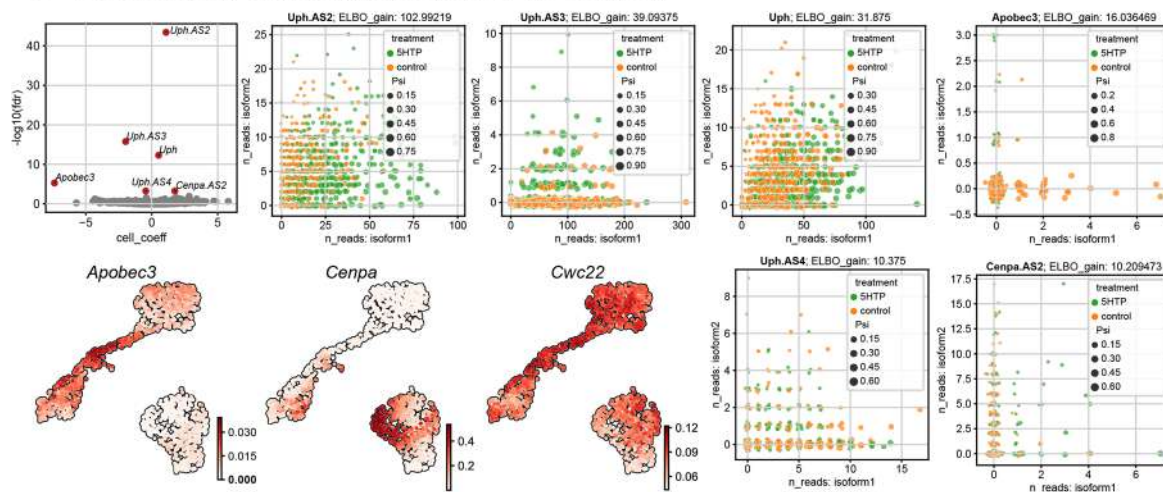
c Main markers for each clusters



d Per cluster DE genes (5HTP vs control)



e Differentially spliced genes (5HTP vs control)



Here we investigated how these intermediate cell types regulate their numbers and define the future size of the chromaffin population. We found that 32% of the chromaffin cells are 5HT positive as soon as they emerge at E12.5 in mouse and this number goes up to 77.8% at E14.5. The 5HT, which is derived from chromaffin cells and a small population of “bridge” cells, signals to neighboring HTR3A⁺ “bridge” cells, lengthening their

cell cycle. This causes a reduction of adrenal medulla because less “bridge” cells become available for differentiation into non-dividing chromaffin cells. Being 5HT-sensitive, “bridge” cells are a part of a negative feedback loop controlling the size of the 5HT-releasing chromaffin population. Similar modes of paracrine feedback loops were shown for retinoic acid signaling⁵⁹ or angiogenic growth factors⁶⁰ which are known to control

Fig. 5 Single-cell transcriptomics reveal differential changes in genes related to RNA splicing and cell cycle upon 5HTP treatment. **a** Adrenal glands (AG) and Organ of Zuckerkandl (ZO) were dissected from E13.5 *Wnt1-Cre^{+/−};R26R^{Tomato+/wt}* embryos; the tissue was dissociated, and *Wnt1^{Tomato+}* cells were sorted into 384-well plates for Smart-seq2 sequencing. Note the absence of statistically-tested compositional effects (see the “Methods” section) between 5HTP-treated and control conditions, shown as UMAPs (bottom panels). **b** Joint UMAP embedding of cells from AG and ZO from both treated and control groups. **c** Main marker genes defining each cluster. **d** Differential gene expression per cluster in 5HTP-treated vs control groups. **e** Statistically significant differentially spliced genes in 5HTP-treated vs control groups. Note that at least four long non-coding RNAs responsible for regulation of *Hand2* activity appeared differentially spliced (*Uph*, *Uph.AS2*, *Uph.AS3*, *Uph.AS4*) and well as *Cenpa*-related long non-coding RNA. The bottom: UMAP plots showing meaningful differentially spliced and differentially expressed genes.

organogenesis. Overall, the paracrine and autocrine role of 5HT in developing chromaffin organs results in two important aspects related to health and survival: protection from chromaffin tissue overgrowth or neoplasia, and prevention of excessive catecholamines and catecholamine-controlled behavior. In humans, the sparse expression of *HTR3A* appeared in “bridge” population at weeks 5-to-7 according to RNAseq and at weeks 6 and 8 according to experimental validations with RNAscope. Despite the expression was detected in principle, it appeared low and at the border of detection, leaving a question about the role of *HTR3A* in human “bridge” cells open. Contrary to this, the expression of *HTR3A* in sympathoblasts showed a strong and consistent pattern, also in agreement with other studies²². Therefore, the human-specific role of the described paracrine regulation via 5HT and chromaffin progenitor-specific *HTR3A* is probable, although it requires further experimentation to be validated. Of note, avian chromaffin cells²⁹ and the cells of the oxygen sensory organ (carotid body) are 5HT-positive as well⁶¹, and may employ the 5HT-dependent mechanism to control their numbers.

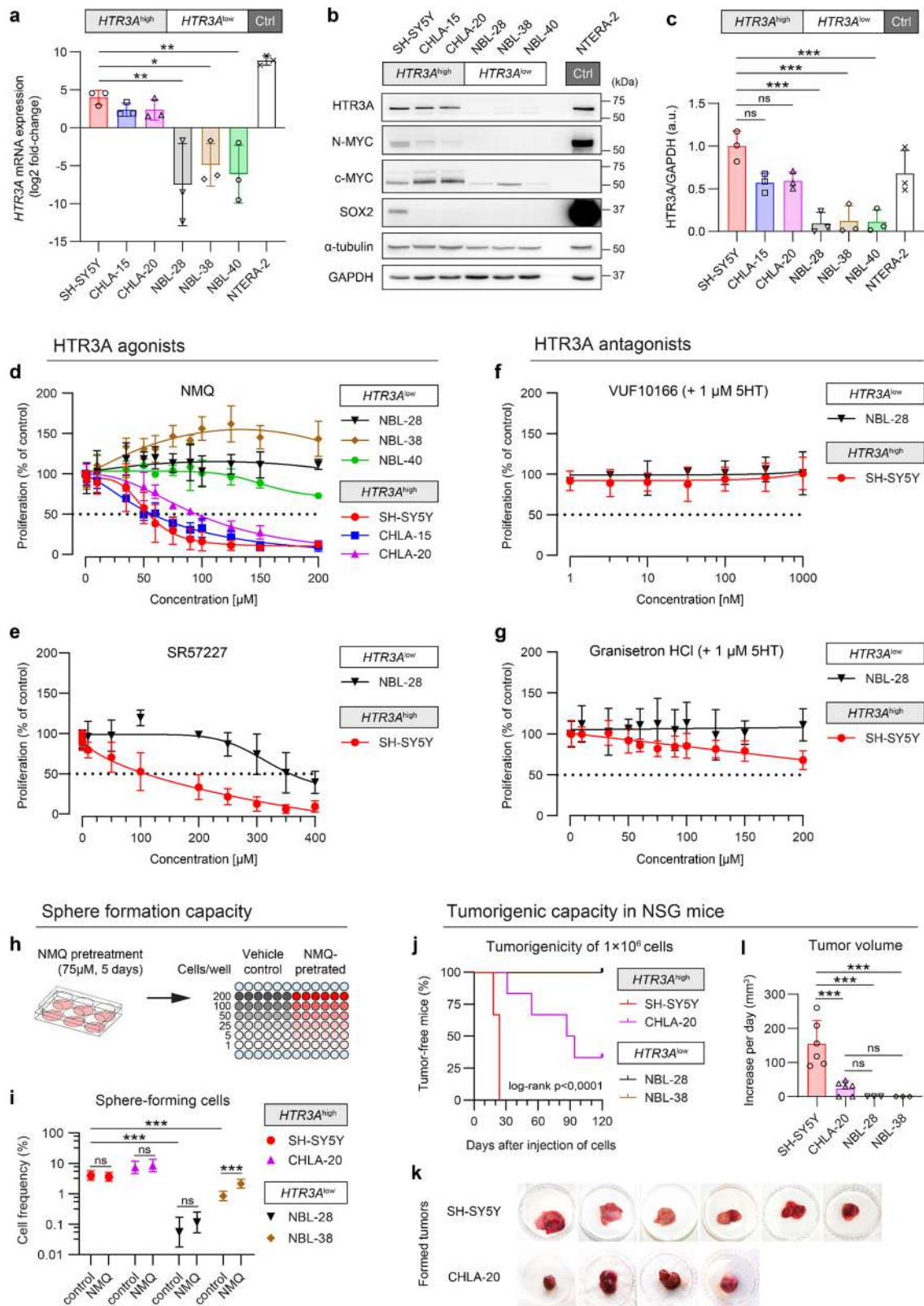
The single-cell transcriptomics analysis showed that elevated embryonic 5HT influences the expression of *Cwc22*—a key gene controlling splicing^{38,39}, and also changes the levels of differentially spliced proliferation—and differentiation-related genes expressed by a “bridge” population (*Apobec3*, long non-coding RNAs controlling *Hand2* and potentially *Cenpa*).

The proposed mechanism of chromaffin cell number control via 5HT-*HTR3A*-dependent paracrine regulation is unidirectional, as the complete elimination of 5HT and pharmacological blockage of *HTR3A* receptor do not result in overgrowth of chromaffin cell organs. This goes in line with previous reports showing that the excess of 5HT has stronger effects on brain development as compared to the lack of 5HT^{62,63}. For example, *Sert^{−/−}* mice demonstrate elevated levels of extracellular 5HT in the brain, which causes a number of structural abnormalities related to the role of 5HT during brain development together with depressive- and anxiety-like behavior⁶⁴, with no changes in adrenal gland morphology and catecholamine release⁶⁵. Conceptually similar results were obtained via inhibition of SERT with selective 5HT reuptake inhibitors at E8–E18 of mouse development^{62,66}. On the other hand, *Pet1* KO and *Tph2* KO mice lack 5HT, but have structurally normal brains (although *Pet1* KO mice lack serotonergic neurons) with altered anxiety-related behavior^{67,68}. These results are in line with our loss-of-function experiments, where the drastic decrease of embryonic and maternal 5HT did not yield any alteration of size of chromaffin organs, apart from the general reduction of an embryo size reported previously^{11,12}. Thus, the 5HT-dependent control of chromaffin cell numbers protects only against the excessive growth and, potentially, tumor-permissive situations.

Consistent with this reasoning, chromaffin organs within the sympathoadrenal complex represent the sites of childhood tumor neuroblastoma, as well as pheochromocytoma and paraganglioma. The comparison of human *HTR3A^{high}* and *HTR3A^{low}* neuroblastoma cell lines revealed that cell lines with *HTR3A^{high}*

expression level have higher tumor-initiating potential. Those cell lines had key characteristics of cancer stem cells and appeared tumorigenic in a mouse xenograft model system as well as formed significantly more spheres in vitro. In line with the in vivo cell cycle progression experiments, we managed to inhibit the proliferation rate of *HTR3A^{high}* neuroblastoma cells with a specific *HTR3A* agonist, which might be developed into a potential therapeutic strategy, especially in a combination with differentiation-inducing drugs^{69–71}. Still, it might be wise to keep in mind the potential difference between tumor and healthy *HTR3A⁺* cells, as the tumor cells might have additional, unpredictable effects following from *HTR3A* activation, and the relevance of 5HT paracrine regulation within tumors remains to be elucidated. Moreover, the origin of neuroblastoma is highly debatable^{9,22,72–75}, and our results regarding the feedback loop mechanism involving 5HT and *HTR3A* in “bridge” cells in vivo and in cancer cell lines should be interpreted with great care.

Hypothetically, beyond the anticancer-related roles, the 5HT-dependent chromaffin tissue control might have important behavioral, ecological and evolutionary dimensions. Indeed, in addition to local chromaffin cells synthesizing 5HT from 5HTP directly within chromaffin organs, the other major source of embryonic 5HT are represented by the maternal blood⁷⁶ and placenta^{14,77}. The biosynthetic enzymes TPH1 and DDC are produced in the syncytiotrophoblastic cell layer of the murine placenta, which is in line with previous observations of in vitro placental 5HT neo-synthesis at E10.5–E18.5 in mice. In line with this observation, human placental fetal villi demonstrated a similar biosynthetic capacity during early gestation⁷⁷. The combination of different 5HT sources and the switch from systemic (extraembryonic) to the local source of 5HT were previously noticed during embryonic brain development in mice¹⁴. Similar to brain development, the presence of extraembryonic-derived 5HT in the embryonic circulation adds another variable to the equation of chromaffin cell number control. In fact, not only local paracrine/autocrine regulation might take place in developing chromaffin organs, but also systemic extraembryonic 5HT might influence the future size of the adrenal medulla. In turn, the intensity of 5HT synthesis in placenta depends on the availability of mother-derived biochemical precursor 5HTP and tryptophan. This opens a potential for a non-genetic control of adrenergic organ development in a progeny of mothers capable of tuning the levels of tryptophan and 5HTP. This tuning might depend on stress factors or health conditions^{52,78,79}. Interestingly, chronic mild stress, excessive maternal inflammation, and hypoxia lead to the increased 5HT synthesis in the fetal placenta with increased output to the fetus, as was previously shown for rodents and humans⁸⁰. In our experiments, prenatal mild stress in pregnant females resulted in elevated levels of 5HT in progeny, which reduced adrenal medulla and changed the offspring behavior similarly to the experiment with chemically (5HTP)-treated mothers. In this “chemical” in vivo experiment, we mimicked the maternal-dependent elevation of 5HT by introducing higher levels of 5HTP into pregnant females. As a result, we detected a reduced number of chromaffin cells, smaller adrenal medulla and



decreased levels of catecholamines associated with changes in the behavior of the adult offspring.

One can admit that the molecular mechanisms controlling the size of chromaffin tissues are important for natural and artificial selection. Although we do not provide direct data supporting this idea, the low aggressiveness, changes in 5HT synthesis and degradation, and reduction of chromaffin organs were previously

reported as a part of the so-called “domestication syndrome”, observed in a number of domesticated species^{20,21}. In line with these domestication-associated behavioral patterns, our experimental rodents subjected to 5HT-driven reduction of adrenals showed less aggressive responses and altered levels of catecholamines. The individual levels of aggressive behavior are indeed related to how the animals react to a wide variety of

Fig. 6 HTR3A^{high} neuroblastoma cells are highly tumorigenic and reduce their proliferation under excessive HTR3A stimulation. **a** Gene expression analysis by qRT-PCR revealed marked differences in relative expression of *HTR3A* among individual human neuroblastoma cell lines. NTERA-2 pluripotent embryonal carcinoma cells served as a positive expression control (Ctrl). Data presented as mean \pm SD, biological $n = 3$, technical $n = 3$; $*p < 0.05$, $**p < 0.01$ using one-way ANOVA followed by Tukey's post hoc test. **b** Western blotting showed differences in HTR3A protein levels, which also corresponded to the differences in expression of N-MYC, c-MYC, and SOX2 proteins between HTR3A^{high} and HTR3A^{low} groups. Blots are representative of three experiments. **c** Densitometric quantitation of the HTR3A protein expression confirms the defined HTR3A^{high} and HTR3A^{low} groups. Data presented as mean \pm SD, biological $n = 3$; $**p < 0.01$ using one-way ANOVA followed by Tukey's post hoc test. **d–g** MTT assay on cells treated with agonists of HTR3A receptor (**d**, **e**) revealed significant dose-response decrease in proliferation of HTR3A^{high} neuroblastoma cells after 5 days of treatment with either N-methylquinazolinone dimaleate (NMQ, **d**) or SR57227 (**e**); treatments with HTR3A antagonists (**f**, **g**) did not exert a significant effect on cell proliferation. Data presented as mean \pm SD, biological $n = 3–5$, technical $n = 5$. **h** Schematic depiction of limiting dilution sphere formation assay: neuroblastoma cells were pretreated with 75 μ M NMQ or vehicle (DMSO) for 5 days and serially diluted in fresh serum-free media w/o the drugs at indicated numbers per well. **i** The frequencies of sphere-forming cells significantly differed between HTR3A^{high} and HTR3A^{low} cell lines, while NMQ pretreatment did not reduced sphere formation capacity of the tested cells. Data are shown as mean \pm 95% confidence interval, frequencies, and probability were computed using ELDA software⁷⁹. $**p < 0.01$, χ^2 pairwise test. **j–l** Only HTR3A^{high} neuroblastoma cell lines formed xenograft tumors in NOD/SCID gamma (NSG) mice (**k**). The higher levels of *HTR3A* expression in SH-SY5Y cells corresponded to the earlier onset of tumor formation (**j**) and increased tumor growth (**l**) when compared with CHLA-20 cells; $**p < 0.01$ using one-way ANOVA followed by Tukey's post hoc test.

environmental challenges including two major coping strategies—proactive and reactive⁸¹. Aggressive males typically express a more proactive type of behavioral response demonstrating rigid, cue-independent, and impulsive reactions and a tendency to defend their home territory. At the same time, non-aggressive reactive males are rather flexible, cautious, and open to the external cues, which can assist in variable or unpredictable environments, such as during migration^{81,82}. Our results demonstrated that prenatal exposure to enhanced 5HT during the critical time window (resulting from maternal mild stress or availability of 5HTP) leads to the birth of progeny with a preferentially reactive type of a coping strategy. This suggests a possible non-genetic information transmission from mother to progeny via the 5HT-dependent developmental control of chromaffin organ size. Conceptually, a similar 5HT-based mother-to-progeny information transmission was identified in invertebrates^{13,83,84} and, given our results, might be a more general strategy in nature⁸⁵.

Furthermore, the mechanism of 5HT-based mother-to-progeny information transmission might be more evident in a wild population under critical environmental stress. The oscillating population density in red-backed voles (*C. rutilus*) periodically reaches exceptional values and causes unprecedented social stress to individual animals⁵⁶. This, along with other factors, forces the voles to segregate into residents and migrants, shaping the population cycles⁸⁶. The difference between the animals forced to migrate and those who stay might involve a behavioral control of aggression, which is affected by the different size of chromaffin organs. We tested this hypothesis and found an association of the adrenal medulla size with the type of the coping strategy (resident—proactive and migrants—reactive) in wild rodents. This association supports the connection between stress in pregnant mothers, 5HT concentrations and the resulting size of chromaffin organs in progeny. Overall, the described mechanism of chromaffin cell number control via 5HT-sensitive precursor cells may provide a regulatory 5HT-mediated pathway of prenatal programming for long-lasting changes in progeny underlying the behavior of domesticated species as well as wild animals with active and reactive types of coping strategy. Future research should establish the role of genetic factors responsible for the variation of the chromaffin organs in wild animals as compared to the power of the 5HT-based mother-to-progeny information transfer mechanisms.

Methods

Animals and corresponding ethics. All experiments involving laboratory animals were done in accordance with European Convention on the Protection of

Vertebrate Animals Used for Experimental and Other Scientific Purposes (Strasbourg, 1986) and approved by the Ethics Committee for Animal Research of the Koltsov Institute of Developmental Biology (Russian Academy of Sciences, approval code: 22, approved on 15 March 2018) as well as in accordance with The Swedish Animal Agency's Provisions and Guidelines for Animal Experimentation recommendations and approved by Ethical Committee on Animal Experiments (Norra Djurförsöksetiska Nämnd, ethical permit N226/15).

Laboratory animals were kept in standardized conditions (24 °C, 12:12 h light–dark cycle, 40–60% humidity, food, and water ad libitum).

Htr3a^{EGFP} transgenic animals are Tg(Htr3a-EGFP)DH30Gsat/Mmnc) were received from MMRRRC and provided by the J. Hjerling-Lefler laboratory (Karolinska Institutet, Stockholm, Sweden) (https://www.mmrrc.org/catalog/sds.php?mmrrc_id=273). Animals were kept as heterozygotes for the EGFP transgene. *Wnt1-Cre* (The Jackson Laboratory, stock number 009107), full strain name B6.Cg-Tg(Wnt1-cre)11Rth Tg(Wnt1-GAL4)11Rth/J) and reporter mice line *R26R^{Tomato}* (The Jackson Laboratory stock number 007914) were used for the study. As wild type animals Wistar Rat, BalbC, and C57BL6 mice were used.

For all experiments, a single embryo was considered as a biological n , and the embryos from 1 to 2 litters were used in experiment to comply with the 3R policy about the usage of animals in research. Furthermore, the exact timing of the embryonic development varies depending on the time of conception and embryo implantation, which can be up to 12 h apart. The developmental difference within this time-window can affect the results and introduce the unwanted noise into the assessment of developing organs at E8–E14.5 stages. Based on our previous experience with such variation, pulling several litters into one comparison can result in much greater variability within the overall group, which can hide the true differences. Selecting and aligning the perfectly comparable litters requires the unnecessary sacrifice of higher numbers of without much of necessity. With this in mind, and with the goal to minimize the number of animals used, we focused on the analysis of adequate numbers of individual embryos (3–6) serving as biological replicates for our studies. For the majority of the experiments, we utilized 1–2 litters per experimental condition.

NOD/ShiLtSz-*scid*/Il2r γ ^{null} mice were used as a NSG model. All NSG mouse experiments were conducted in accordance with a study (21379/2011–30) approved by the Institutional Animal Care and Use Committee of Masaryk University and registered by the Ministry of Agriculture of the Czech Republic as required by national legislation.

E15.5 embryos (gender was not identified) from *Pet1^{-/-}* knockout mice were received from Patricia Gaspar (INSERM: Paris, France). E15.5 embryos (gender was not identified) from *Tph2* knockout mice were received from Massimo Pasqualetti (Dept of Biology, University of Pisa, Italy). E13.5 embryos (gender was not identified) from *Tph1*; *Tph2*, *Tph1*; *Sc16a4*, and *Tph1*; *Tph2*; *Sc16a4* knockout mice together with E13.5 embryos (gender was not identified) of C57BL/6 mice bred in the same facility were received from Natalia Alenina and Michael Bader (Max-Delbrück Center for Molecular Medicine (MDC), Berlin, Deutschland). Before shipment embryos were fixed in 4% paraformaldehyde in PBS (pH 7.4) at 4 °C 4–6 h depending on the embryonic stage. Samples were rinsed in PBS and placed in 30% sucrose in PBS for cryoprotection. Samples were sent in 30% sucrose in PBS solution incubated on ice and processed for immunohistochemical analysis after receipt.

All experiments involving wild animals red-backed voles *Clethrionomys rutilus* were approved by the Biomedical Ethics Commission of FSBI “Zakusov Institute of Pharmacology” (Russian Academy of Sciences, approval code: 01, dated 20 January 2017). Red-backed voles *C. rutilus* (Pallas, 1779) is not an endangered species. The wild representatives of red-backed voles *C. rutilus* were collected during August–September 2020 in the Yenisey ecological station “Mirnoe” (62.2 N; 89.0 W), Turukhansky region of Krasnoyarsk territory, within the Central Siberia Biosphere Reserve. The long-term population-ecological investigations demonstrated a 4-year

Long term effect of prenatal serotonin increase on behavior outputs

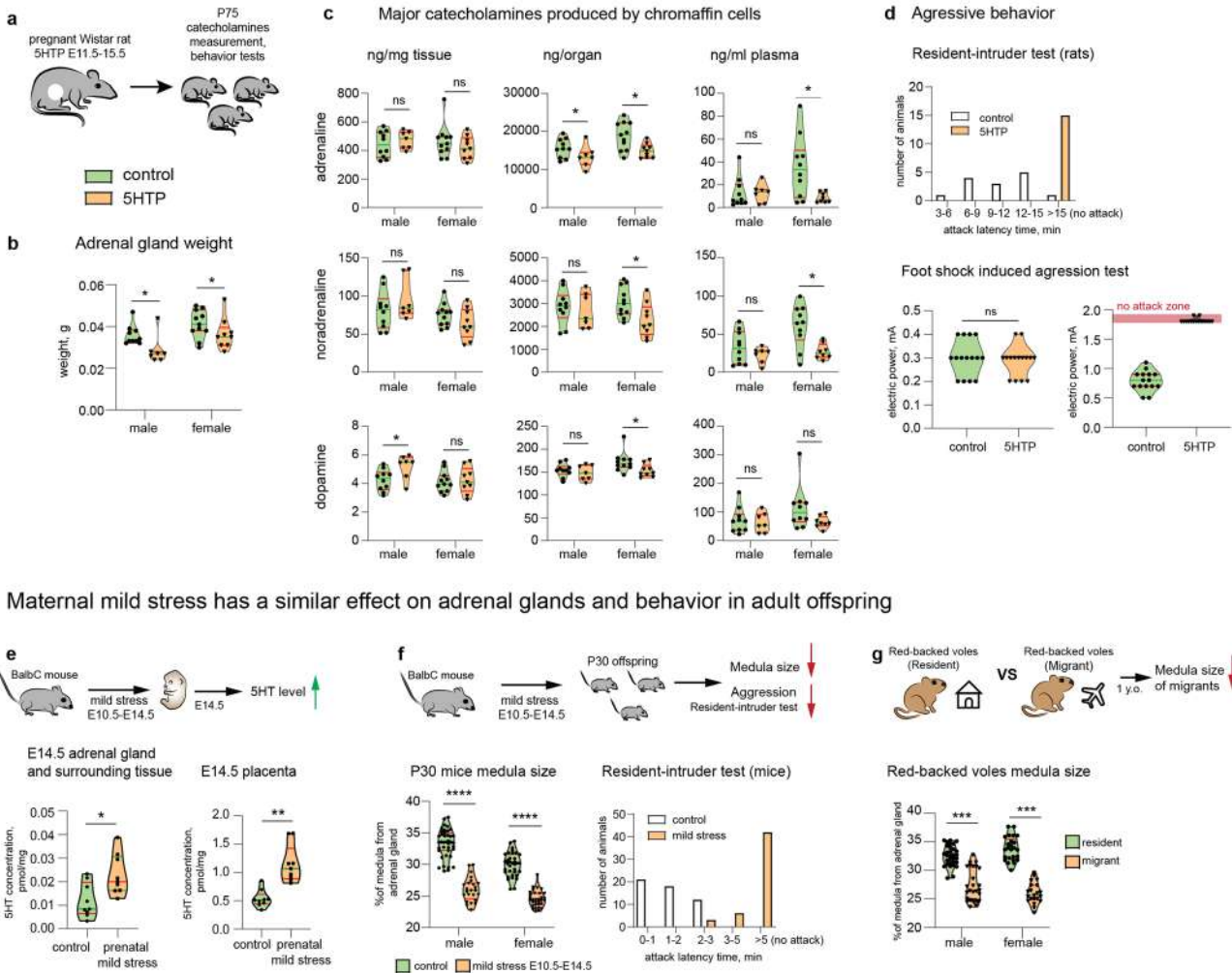


Fig. 7 Embryo-to-adult effects of prenatal 5HT on adult behavior and adrenals are similar to the effect of stress induced in pregnant mothers.

a Pregnant Wistar rats were administered 5HTP during E11.5–E15.5, and their offspring (P75) was analyzed with the behavioral tests and catecholamine measurements. **b** The size of adrenal glands in animals from the 5HTP-treated females was significantly smaller than from control group. Mann–Whitney test, p -value $* < 0.05$, biological $n =$ male: 11 (control), 8 (5HTP); female: 12 (control), 10 (5HTP). **c** Major catecholamines measured in ng/mg of tissue, ng/organ and ng/mL of plasma by HPLC–MS. Note: ng/mg of tissue reflects normal function of chromaffin cells, and does not change; ng/organ decreases in 5HTP-treated group. Mann–Whitney test, p -value $ns > 0.05$, $* < 0.05$, biological $n =$ male: 11 (control), 8 (5HTP); female 12 (control), 10 (5HTP), for plasma $n =$ male: 10 (control), 7 (5HTP); female 10 (female), 8 (female). **d** Aggression-assessing behavioral tests: “resident-intruder test” (top) and “foot shock-induced aggression test” (bottom) indicate the reduced aggression in the 5HTP-treated group. Mann–Whitney test, p -value $ns > 0.05$, biological $n = 14$ and 15 (control), 15 (5HTP group). **e** Pregnant BalbC mice were exposed to a mild stress (1 h restrain) at E10.5–E14.5, followed by 5HT measurements in the embryo trunks and placentas. Note: the 5HT levels were increased similarly to experiment with 5HTP-treatment (refer to Fig. 2a, b). Mann–Whitney test, p -value $* < 0.05$, $** < 0.002$, biological $n = 9$. **f** Pregnant BalbC mice were exposed to a mild stress (1 h restrain) at E10.5–E14.5, and their P30 offspring was tested for the size of adrenal medulla and aggression. Note: the proportion of adrenal medulla was significantly lower in the stress-induced group similarly to the 5HTP-treated group (refer to Fig. 2h). Shapiro–Wilk test for normality, unpaired double-sided t -test p -value, $**** < 0.0001$, n (adrenal gland) = 40 (control male), 24 (1 h restrain male), 35 (control female), 32 (1 h restrain female). **g** The ratio of adrenal medulla of the adrenal gland in *C. rutilus*. Mann–Whitney test, p -value $* < 0.05$, $*** < 0.001$, biological n (adrenal gland) = male: 31 (resident), 29 (migrant); female: 25 (resident), 21 (migrant). In all violon plots the green line—median, the red lines—quartiles.

cycle of population dynamics of Micromammalia which is stable in the conditions of Yenisey Central Siberia. *C.rutilus* population dynamic peak occurred in Central Siberia in 2020 (mean 29,1 animals per 100 traps per day in 2020, compared to mean 13,8 animals per 100 traps per day in 2018. Year monitoring of ecological station “Mirnoe”), and the collection period at the late summer/autumn considered the most relevant to estimate the wave dynamics in cycling population⁵⁵. Representatives of *C. rutilus* collected in Sherman traps (live traps) in taiga (dark coniferous forest consisting of Siberian cedar, fir, pine, and larch) were considered as settled individuals or residents. Representatives collected in pitfall traps in Yenisey River valley (meadows without tree communities) were considered as migrants. Trapped species were settled individually in plastic boxes for 2 h. The animals were weighed and adrenals were dissected under inhalant isoflurane anesthesia (SomnoSiute system, Kent Scientific, USA). The gender, pregnancy and

fertility status, approximate ages were determined visually after dissection. Altogether 24 females and 31 males of ~1 year old were used for the study.

5HTP administration to pregnant females and embryo collection. Three- to four-month-old females of Wistar rats, BalbC mice, and 2–4-month-old *Htr3a^{EGFP}* mice were placed in time-controlled mating and the day of plug was considered as embryonic day (E) 0.5 for mice, day of conception was considered as embryonic day (E) 0.5 for rats. 5-hydroxy-L-tryptophan (Sigma-Aldrich H9772) was dissolved in saline and fed (1 mg/kg BW, once a day) to pregnant rats through gavage or intraperitoneally injected (40 mg/kg BW, once a day) to pregnant mice females. At the stage of embryo harvest, the females were sacrificed by cervical dislocation after

anesthesia with 2–3% isoflurane, embryos were eviscerated and placed in ice-cold PBS. The gender of embryos was not identified.

HTR3A agonist and antagonist treatment. Three- to four-month-old pregnant BalbC females received intraperitoneal (i.p.) injections of the selective agonist of the HTR3A receptor, SR57227 hydrochloride (2 mg/kg BW, once a day) at E11.5 and E12.5 stages. Another group of animals was i.p. administered with the HTR3A antagonist, granisetron hydrochloride (2 mg/kg BW, once a day) in combination with 5HTP (40 mg/kg BW, once a day) at E11.5 and E12.5 stages. Drugs were purchased from Tocris (UK), dissolved in DMSO, and then diluted in sterile physiological saline. In the control group, mice received identical volumes of isotonic saline with DMSO (DMSO control). E13.5 embryos were fixed in 4% paraformaldehyde and processed for immunohistochemistry. The gender of embryos was not identified.

MicroCT tissue preparation and analysis. E15.5 rat embryos (gender was not identified) were fixed in 4% paraformaldehyde in PBS (pH 7.4) at 4 °C for 6 h. Samples were dehydrated by incubation in the ethanol gradient solutions in PBS (30%, 50%, 70%); incubation was done at 4 °C with agitation for 24 h in each concentration. For contrasting the samples were transferred to 1.0% PTA (Phosphotungstic acid, Sigma-Aldrich, P4006) in 90% methanol and incubated with rotation at 4 °C with agitation for 3 weeks; the PTA solution was changed weekly. After contrasting, the samples were rehydrated through a methanol gradient (90%, 75%, 50% and 30%). After that, rehydrated embryos were shipped on ice to Brno University of Technology, Czech Republic for microCT scanning.

Samples were placed in polypropylene tubes and embedded in 1% agarose gel to minimize movement during microCT measurement. MicroCT scanning was performed using system GE phoenix v|tome|x L 240, equipped with a 180 kV/15 W maximum power nanofocus X-ray tube and high flat panel dynamic 41|100 with 4000 × 4000 pixels and a pixel size of 100 × 100 μm. The exposure time was 900 ms in 2000 positions over 360°. The microCT scan was carried out at 60 kV acceleration voltage and with 200 μA X-ray tube current. The beam was filtered by a 0.2 mm-thick aluminum filter. The voxel size of obtained volumes was 2.2 μm for all samples. The tomographic reconstructions were performed using GE phoenix datos|x 2.0 3D computed tomography software. Segmentation of structures was performed manually by a combination of software Avizo (Thermo Fisher Scientific, USA) and VG Studio MAX 3.2 (Volume Graphics GmbH, Germany).

Thymidine analogues labeling during S-phase combined with 5HTP treatment. Double thymidine analogues labeling of cells in S-phase was based on the methods described previously⁸⁷. 5-ethynyl-2'-deoxyuridine (EdU, Life Technologies, E10415) and 5-Chloro-2'-deoxyuridine (CldU, Sigma-Aldrich, C6891) were dissolved in PBS at stock concentrations 5 mg/ml and 5.2 mg/mL and, respectively, intraperitoneally injected to 2–4-month-old *Htr3a*^{EGFP} mice pregnant females in equimolar concentrations to 50 mg/kg body weight of EdU with 4-h interval. Females also received 2 injections of 5HTP 40 mg/kg or vehicle control at E11.5 and at E12.5. To minimize the number of 5HTP injections, at E12.5 and the EdU dose were combined in one injection solution. Embryos were harvested 4 h after CldU injection E12.5, gender of the embryos cannot be identified.

Tissue preparation for immunohistochemistry. Whole embryos, dissected sympathoadrenal complexes were fixed in 4% paraformaldehyde in PBS at 4 °C with agitation for 2–6 h followed by rinse in PBS. After fixation samples were cryoprotected in 30% sucrose in PBS at +4 °C with agitation for 24 h. Samples were embedded in OCT and frozen at –20 °C. 14 μm serial sections were produced from each sample, collected on SuperFrost microscopy slides (Thermo Scientific) and kept at –20 °C before staining.

Immunohistochemistry. Cryosections were brought to room temperature and dried for at least 2 h before antigen retrieval. Antigen retrieval was done by submerging the slides in 1× Target Retrieval Solution (Dako, S1699) in water, bringing the solution to boiling and letting it cool down for 40–60 min. Sections were washed three times for 10 min in PBS containing 0.1% Tween-20 (PBST), encircled by Super PAP Pen (Invitrogen, 008899), and incubated at room temperature overnight with primary antibodies diluted in PBST in a humidified chamber. Then, sections were washed in PBST three times for 10 min and incubated with secondary antibodies and DAPI (5 μg/mL) diluted in PBST at RT for 90 min, washed again three times in PBST and mounted using Mowiol (Merck, 81381) mounting medium, prepared according to manufacturer's instructions.

Detection of thymidine analogues in combinations with IHC. Antigen retrieval was done by submerging the slides in 1× Target Retrieval Solution (Dako, S1699) in water, bringing the solution to boiling point, and cooling it down for 40–60 min. Sections were washed three times for 10 min in PBS. Sections were further permeabilized with 4% triton X-100 solution for 1 h followed by 3 washes 10 min in PBS.

EdU visualization was performed by click reactions. Sections were incubated in Click Buffer 1 (0.1 M Tris pH 7.5, 20 μL CuSO₄ 100 mM, 5 μM Alexa Fluor 647

azide (ThermoFisher, A10277) (stock 10 mM in DMSO), 100 mM ascorbic acid) for 15 min with gentle rocking. Washed three times for 5 min in PBS and incubated with Click Buffer 2 (20 μL CuSO₄ 100 mM, 40 mM ascorbic acid and 2 mM azidomethyl phenyl sulfide (Sigma-Aldrich) in PBS) for blocking of non-specific reactions of anti-BrdU (clone BU1/75) antibody with EdU⁶⁸. The sections were incubated for 15 min with gentle rocking followed by 3 washes for 5 min in PBS. For CldU visualization with antibodies, a DNA denaturing step by 2N Hydrochloric acid (incubation at 37 °C for 40 min) is critical to allow the antibody to bind to DNA. The sections were neutralized by washing in 0.1 M borate buffer (pH 8.0) two times for 10 min followed by three washes in PBS for 5 min. Then sections were blocked in 5% normal donkey serum (Sigma-Aldrich), 0.1% Triton X-100 in PBS for 1 h. Primary antibodies were dissolved in 5% normal donkey serum (Sigma-Aldrich), 0.1% Triton X-100 in PBS and incubated with sections overnight at RT with gentle rocking. A combination of anti-BrdU (recognizes CldU) antibody and cell type-specific antibodies was applied. Next day, the sections were washed in PBS three times for 5 min and incubated with the solution of secondary antibodies and DAPI in PBS for 90 min at RT. After incubation, the samples were washed in PBS three times for 10 min at room temperature and mounted using Mowiol mounting medium, prepared according to manufacturer's instructions.

Primary and secondary antibodies. The following primary antibodies were used: rabbit anti-TH (1:1000, Pel-Freez Biologicals, #P40101-150), sheep anti-TH (1:2000, Novus Biologicals, #NB300-110), rabbit anti-serotonin (1:2000, ImmunoStar, #20080), chicken anti-GFP (1:600, Aves Labs Inc., #GFP-1020), goat anti-human SOX10 (1:800, R&D Systems, #AF2864), rabbit anti-Ki67 (1:500, Thermo Scientific, #RM-9106), rabbit anti-Cleaved Caspase-3 (1:500, Cell signaling, Asp175), rat anti-BrdU (1:300, Abcam, BU1/75, also recognizes CldU).

For detection of the primary antibodies, secondary antibodies raised in donkey and conjugated with Alexa-405, -488, -555, and -647 fluorophores were used (1:1000, Molecular Probes, ThermoFisher Scientific). Goat anti-chicken conjugated to Alexa fluor-488 (1:600, Jackson ImmunoResearch, 703-545-155).

RNA scope® in situ hybridization. Fluorescent in situ hybridization manual assay against *Pnmt* (probe 426421-C3) and *Htr3a* (probe 411141-C3) was performed using the RNAscope Fluorescent® Multiplex Assay kit according to manufacturer's instructions (Advanced Cell Diagnostics). Immunostaining following the hybridization was performed as described above except for the antigen retrieval step.

Microscopy. Images were acquired using LSM700, LSM 710, and LSM 880 confocal microscopes (Carl Zeiss, Germany) equipped with ×10, ×20, and ×40 objectives. Images were acquired in the .ism format.

Cell counts and area measurements. Cell counts and area measurements were done manually using the Cell counter plugin and measurement functions of ImageJ (2.1.0/1.53c) software. The area of adrenal gland section was calculated by surrounding the area based on DAPI signal. The area of medulla was calculated based on TH⁺ signal within adrenal gland. The area of cortex was calculated by subtraction of adrenal medulla area from the area of the whole gland per individual section. Three section per gland and 2 glands per embryo were evaluated.

Venn diagrams were built with <https://www.meta-chart.com/venn#/your-charts> free on-line platform and redrawn in Adobe Illustrator 25.2.1. The percentage of Sox10⁺*Htr3a*^{EGFP+} cells was calculated as a fraction of Sox10⁺*Htr3a*^{EGFP+} cells from the sum of all Sox10⁺ and all *Htr3a*^{EGFP+} at E13.5 and E14.5 in adrenal medulla.

Measurements of relative medulla size in postnatal animals. The dissected adrenals of P30 BalbC mice and collected red-backed voles *Clethrionomys rutilus* were processed for whole-mount Benzyl alcohol/Benzyl benzoate tissue optical clearing method. The preparations were scanned using LSM 880 confocal microscope (Carl Zeiss, Germany) with a green channel determining the tissue autofluorescence. The optical section with maximal external volume was selected for relative medulla size analysis. The area of central medulla and the whole adrenal were measured using ImageJ software. Relative medulla size represented by the ratio: (medulla area/total area) × 100%.

Re-analysis of single-cell transcriptomic data published by Furlan et al., 2017. We re-analyzed single-cell RNA-seq data of mouse adrenal gland from Furlan et al.⁶. Gene counts were obtained from GEO database (GSE99933). Gene count matrix was analyzed with a standard Seurat (version 3.0.2) workflow⁸⁸. We used the original embeddings and clustering from ref. ⁶ (Figs. 5B and 5G). Downloaded from the published pagoda apps: http://pklab.med.harvard.edu/cgi-bin/R/rook/nc.SS2_16_249-2/pathcl.json and http://pklab.med.harvard.edu/cgi-bin/R/rook/nc.SS2_16_250-2/pathcl.json (json slots embedding/data for the embedding and col-clusters/data for the cluster labels).

Seurat function FeaturePlot and DotPlot were used to plot gene expression in individual cells on the embedding and average gene expression in the clusters as dot plots, respectively.

Single-cell RNA sequencing of mouse tissue by SmartSeq2. *Wnt1-Cre^{+/-}; R26R^{Tomato/+}* E13.5 embryos prenatally treated with 5HTP or vehicle for control at E11.5 and E12.5 were harvested in ice-cold PBS. Adrenal glands and Organ of Zuckerlandl were dissected under the stereoscope equipped with a fluorescent light source. Tissue was added to 500 μ L of 0.05% Trypsin/0.02% EDTA (Sigma, 59417-C) and incubated at 37 °C for 10 min. The tissue was triturated slowly with a P-200 pipette until complete dissociation. Trypsin was deactivated by adding 500 μ L of PBS containing 10% FBS. The cells were centrifuged at 500 \times g at 4 °C for 5 min. The cells were washed two times with PBS + 10% FBS followed by centrifugation. The non-single cell clusters of cells were removed by filtering through 40 μ m-pore size cell strainers. Fluorescent cells were sorted in single cells mode into 384-well plates pre-filled with lysis buffer according to a previously published protocol using a BD FACS Aria III Cell Sorter. One full 384-well plate was sorted and sequenced per organ and per treatment. Single-cell library preparation was done following Smartseq2 protocol⁸⁹.

Single-cell transcriptomics data analysis of SmartSeq2. First, generation of count matrices, QC and filtering was performed. The single-cell transcriptome data were generated at the Eukaryotic Single-cell Genomics facility at Science for Life Laboratory in Stockholm, Sweden. The samples were analyzed by first demultiplexing the .fastq files using deindexer (<https://github.com/ws6/deindexer>) using the NextEra index adapters and the 384-well plate layout. Individual .fastq files were then mapped to mm10_ERCC genome (https://www.ncbi.nlm.nih.gov/assembly/GCF_000001635.20/) using the STAR aligner version 2.7.5c using 2-pass alignment. Reads were filtered for only uniquely mapped and were saved in BAM file format; count matrices were subsequently produced. Estimated count matrices were gathered and converted to an anndata object. Cells with the following quantities were kept as high quality: having more than 10⁵ and less than 5 \times 10⁵ transcripts, containing more than 4000 and less than 8000 detected genes and or less than 15% of ERCC reads. Cells with low number of reads, potential doublets, cells with high fraction of ribosomal and mitochondrial genes were removed from the analysis. The resulting filtered count matrix contained 1361 high-quality cells (out of 1528 total cells sequenced).

The preprocessing and initial analysis of the count matrix was performed without any batch correction, using scanpy python package v1.7.2, scFates python package v0.2.4, and scvelo python package v0.2.3. Highly variable genes were detected using pagoda2 approach (scFates.pp.find_overdispersed, default parameters). Cell cycle genes were removed from the list of high variable genes to remove their effect. PCA was performed on the scaled count matrix using the high variable genes (scanpy.pp.pca, default parameters), kNN graph (scanpy.pp.neighbors, n_neighbors = 30, n_pcs = 30, metric = "cosine") was generated from PCA space, followed by UMAP embedding generation (scanpy.t.umap, default parameters) and leiden clustering (scanpy.t.leiden, Resolution = 0.3)⁹⁰. Differential gene expression analysis was performed per cluster between treated cells and control, using Wilcoxon rank-sum test.

To detect possible differentially spliced genes between the two conditions, BRIE2 algorithm was employed^{91,92}. Counting of the isoform-specific reads in each splicing event was performed for BAM files of the QC filtered cells, using filtered mouse annotation provided by the package maintainers. The annotation has the following characteristics: from GENCODE mouse vM17, exon skipping events located on autosome and chrX, not overlapped by any other AS-exon, surrounding introns are no shorter than a fixed length 100 bp. Length of alternative exon regions, between 50 and 450 bp. With a minimum distance, 500 bp, from TSS or TTS. Specific splice sites: surrounded by AG-GT, i.e., AG-AS.exon-GT. Splicing isoform proportion and variable splicing detection was performed in mode 3, by including a design matrix containing the both treatment and location as columns, location effect was removed as potential cofounder.

Ethical aspects of procedures involving human tissue. Human pre-natal tissue was obtained from clinical routine abortions with oral and written consent from the patient. Swedish Ethical Research Authority and the National Board of Health and Welfare has approved the acquisition of human pre-natal tissue for research purposes (ethical reference is 2018/769-31 with the addendum EPN2019-04595). The material was donated for a general research purpose especially with the focus on neuronal and nervous system-related cell types. Measurement of crown-rump-length (CRL) and anatomical landmarks were used to determine the post-conception age.

Human fetal cell isolation, storage in methanol, and rehydration. The tissue was received in ice-cold PBS and enzymatically digested to obtain the single-cell suspension. For this, tissue cut into smaller pieces was incubated with 500 μ L 0.05% Trypsin/0.02% EDTA (Sigma, 59417-C) for 15 min at 37 °C with gentle swirling every 5 min. Gentle pipetting up and down was used to mechanically dissociate bigger pieces if any. 500 μ L 10% FBS in PBS was added to cell suspension and the cells were pelleted at 500 \times g for 5 min at 4 °C. Cells were washed two times with 1000 μ L PBS, passed through the 35 μ m cell strainer (Falcon, 352235), pelleted at 500 \times g for 5 min at 4 °C and re-suspended in 100 μ L 0.04% BSA in PBS. Ice-cold methanol (400 μ L) was added for fixation of the cells and the cells were stored at -80 °C. For the preparation of the library the cells were brought to +4 °C and pelleted at 1000 \times g for 10 min at 4 °C. Cell pellet was re-suspended in 500 μ L of

rehydration buffer (1X DPBS (Gibco 14190144) containing 1.0% BSA (Sigma, B4287) and 0.5 U/ μ L RNase Out (ThermoFisher Scientific, 10777019) followed by two washes with 500 μ L of rehydration buffer. The rehydrated cell suspension was sorted to remove debris with BD FACS Aria Fusion instrument (BD Biosciences, San Jose, CA) equipped with 100 μ m nozzle. After FACS cells were pelleted to obtain concentrated cell suspension with 700–1200 cells/ μ L.

10x Genomics RNAseq library preparation and sequencing of human cells. 10x Genomics Chromium Single Cell 3' protocol for Reagent Kits v3 was used for library preparation aiming to recover 5000–8000 cells. Sequencing was done on Illumina NovaSeq 6000 Sequencing System (NovaSeq 6000 S1 Reagent Kit or NovaSeq 6000 S2 Reagent Kit were used) with the standard recommended read set up for 10X Genomics libraries: Read 1: 28 cycles (Cell barcode and UMI), i7 index: 8 cycles (Sample index), Read 2: 91 cycles. The 10X single-cell transcriptome data were generated at the Eukaryotic Single-cell Genomics facility at Science for Life Laboratory in Stockholm, Sweden.

Human single-cell transcriptomics data analysis with 10x Genomics. The count matrix for each sample was produced by Cell Ranger version 3.1.0 that processed, mapped, and counted raw sequencing data to the Cell Ranger GRCh38-3.0.0 genome and its corresponding annotation. Seurat package pipeline (v.4.0.2)⁹³ was used for the downstream analysis. Genes expressed in fewer than ten cells in each dataset were removed from further analysis. To keep only high-quality cells, the cells with less than 2000 or more than 25,000 transcripts and the cells with less than 1500 detected genes per cell were omitted. The cells with high mitochondrial content (more than 10%) were also excluded from the analysis. The putative doublets were predicted by Scrublet⁹⁴. The filtered datasets first were analyzed separately to extract the cells belonging to the neural crest-derived sympathoadrenal lineage and then integrated with Seurat function IntegrateData (2000 integration anchor features, 20 dims). The resulting integrated filtered dataset consisted of 3503 high-quality cells. The effects of cell cycle heterogeneity in gene expression were mitigated by regressing out the difference between G2M and S phase signatures by Seurat functions CellCycleScoring and ScaleData (vars.to.regress = "CC.Difference"). Then to perform a graph-based clustering and visualization by UMAP, the first 30 principal components and 30 nearest neighbors were used. Louvain clustering algorithm with resolution equal to 0.2 resulted into finding 13 clusters, two of them were removed due to containing the high doublet scores. The remaining clusters were re-analyzed using the same parameters except the resolution (30 PCs, 30 kNN, resolution = 0.1) and the resulting seven clusters were merged based on the expression of classical cell type-specific markers into four biologically meaningful clusters. To check whether the expression of *HTR3A* gene in the "bridge" cells is not noise-derived, the exact Fisher test was applied after removal of the sympathoblast clusters from the dataset.

Behavioral studies. The tests were performed on 21 male and 25 females P75 Wistar rats, weighing 180–200 g. Animals were acclimatized 15 min a day for 5 days before the tests⁹⁵.

Resident-intruder test was performed on rat and mice⁸¹. For the test on Wistar rats, each resident male was housed with the companion female in the resident cage (floor space of about half a square meter) for 1 week prior to testing. The companion females were sterilized 3 weeks before the test. The cages were not cleaned until the end of the experiment. Testing was performed once a day at 8:00 p.m. The companion female was removed from the cage and an unfamiliar male was introduced in the residential cage, followed by recording the behavior of the resident for 15 min. The time between the introductions of the intruder and the first clinch attack was considered as attack latency.

For the test on BalbC mice, male mice were singly housed for 1 week prior to testing. The cages were not cleaned until the end of the experiment. The male intruders were group-housed (five per cage) and matched with resident mice for approximate age and body weight. The unfamiliar male was introduced in the residential cage and behavior of resident mice was monitored during 5-min after exposure to male intruder. One trial per day was conducted at 8:00 p.m. The time between the introductions of the intruder and the first biting attack was considered as attack latency.

Foot-shock induced aggression test⁹⁶ was performed on rats. Two male rats were placed on the electrode floor of the test chamber for both, pain sensitivity and aggression, and then the current was gradually increased at a rate of 0.1 mA/s. The threshold of pain sensitivity was determined by the minimum current at which the animals made the first squealing. The minimum value of the current that causes the typical upright defensive postures (threat posture) in a rat was considered as the threshold of aggressiveness. The test was stopped at 1.8–1.9 mA/s.

Elevated Plus-maze (EPM) test was performed on rats. The apparatus for EPM test was constructed from 2 horizontal arms 50 cm long and 10 cm wide crossing each other in the middle at 90° angle. Two opposing parts of the maze have 40 cm high walls "closed arms". The maze was elevated 40 cm from the floor. The rat was placed in the middle of the apparatus facing one of the closed arms. The time the rat spent on the central part of the maze, in open and closed arms, and the number of entries to open and closed arms were recorded. The total time of one animal observation was 5 min⁹⁷.

Novelty-induced hypophagia test was performed on rats. The apparatus for Novelty-induced hypophagia test is a cylindrical platform 97 cm in diameter, with a 42 cm high wall made from white plastic. The floor of the platform has the marks of the central circle, 23 cm in diameter and the middle part, 18.5 cm wide, divided into 6 equal size sectors and the peripheral part 18.5 cm wide, divided into 12 equal size sectors. The source of light was 100 W lamp 1 m above the floor of the platform. In the center of the platform, the food was placed. During 10 min of the test the duration of food take latency was measured.

Extrapolation Escape Task was performed on rats. In this task animals need to find an escape solution from an acute stress situation. The apparatus consists of a basket with an internal cylinder 25 cm high and 10 cm in diameter. The basket is filled with 21–23 °C water up to 2 cm from the bottom of the internal cylinder. Rats were placed in the internal cylinder and their behavior was observed during 2 min. The dive latency and time to find the escape ladder was registered.

Catecholamine analysis. The catecholamine standards (norepinephrine (NE), epinephrine (E), and dopamine (DA)) and catecholamine metabolites (normetanephrine (NM), metanephrine (M)) were obtained from Sigma-Aldrich (USA). The catecholamine and catecholamine metabolites labeled internal standards (norepinephrine-d6, epinephrine-d3 and dopamine-d4, normetanephrine-d3, metanephrine-d3) were obtained from TRC (Canada). All reagents were of analytical grade. Methanol was obtained from Thermo Fisher Scientific (Fisher Scientific UK Ltd.). Ethyl ester was obtained from Panreac (Germany). 2-Aminoethyl diphenylborinate, Formic acid, Hydrochloric acid, Sodium hydroxide, Ammonium chloride were obtained from Sigma-Aldrich (USA). Water used in the entire analysis was prepared using Milli-Q water purification system from Millipore (UK).

A Shimadzu HPLC system (Japan) was used for chromatographic separation of analytes on an Eclipse XDB-C18 (150 mm, 4.6 mm, 5 mm) analytical column, maintained at 40 °C in a column oven. Gradient elution was used for the chromatographic separation of analytes. The mobile phase A: 0.1% formic acid in water, the mobile phase B: 0.1% formic acid in methanol.

A triple quadrupole mass spectrometer Shimadzu 8060 (Japan), equipped with electrospray ionization and operating in positive ionization mode was used for detection of analytes and ISs. For quantitation, multiple reaction monitoring (MRM) was used to monitor precursor-product ion transitions m/z 151.90 → 77.10 (norepinephrine), m/z 158.90 → 111.00 (norepinephrine-d6), m/z 183.90 → 107.00 (epinephrine), m/z 187.00 → 107.00 (epinephrine-d3), m/z 165.90 → 121.15 (normetanephrine), m/z 169.00 → 137.00 (normetanephrine-d3), m/z 153.90 → 91.10 (dopamine), m/z 157.00 → 94.00 (dopamine-d4), m/z 179.90 → 165.15 (metanephrine), m/z 183.00 → 168.00 (metanephrine-d3).

Calibration standards and quality control samples. Stock solutions of analytes (1 mg/mL) were prepared by dissolving accurately weighed reference standards in 0.1% HCl in water. Stock solutions of ISs (1 mg/mL) were prepared by dissolving accurately weighed reference standards in 0.1% formic acid in water. Calibration standards (CSs) and quality control (QC) samples were prepared by spiking blank sample (water) (10% of total volume of blank sample) with mixed stock solutions. CSs were made at concentration levels (Table 1).

QC samples were prepared at two concentration levels (Table 2).

All the solutions (standard stock, CSs and QC samples) were stored at –20 °C until use.

To extract catecholamines, adrenal glands were weighed, homogenized in 0.9% NaCl, and frozen in liquid nitrogen. Heparinized blood samples were collected from the heart and centrifuged. Samples were kept at –80 °C until the mass spectrometric analysis of catecholamines and their metabolites.

Prior to analysis, all frozen samples, CSs and QC samples were thawed in RT. To each glass tube (16 × 100 mm) 0.5 mL CSs, QC or sample; 20 µL of the internal standards mix and 0.8 mL of buffer containing a complexing agent (0.2% DPBA-ethanolamine ester and 5 g/L EDTA in 2 mol/L NH₄ Cl-NH₄ OH buffer, pH 8.5) was added. After mixing, the pH of the complexed sample preparation was checked with a pH probe or narrow range pH paper. If the pH was <7.5, it was adjusted with concentrated ammonia to be between 7.5 and 9.5. Ethyl Ester (1500 µL) was added to extract the analytes and vortex-mixed (10 min), and the sample was then centrifuged for 10 min at 3000 × g. The Ethyl Ester layer was removed (800 µL) and placed into a recovery vial (Waters Corp., Elstree, UK). The vial solution was then evaporated to dryness using a centrifugal vacuum evaporator (Eppendorf, USA).

Table 1 Composition of calibration standards.

Nº	Name	NM/D/E/M/NE concentration, ng/ml
1	Cal 1	1/50/5/1/5
2	Cal 2	10/100/25/10/25
3	Cal 3	50/250/50/50/50
4	Cal 4	100/500/100/100/100
5	Cal 5	500/750/250/500/250
6	Cal 6	1000/1000/500/1000/500

The samples were reconstituted in 200 µL (0.1% formic acid in water), and 2 µL was injected onto the column.

Quantification was performed using Shimadzu LabSolution software, version 5.3 (Japan) using the integration peak area ratio of analyte and labeled IS.

5HT measurement by high-performance liquid chromatography with electrochemical detection (HPLC-ED). 5HT concentration was determined after the following experiments: (1) Pregnant BalbC mice were subjected to mild stress based on a published method⁵² for 1 h daily from E10.5 to E13.5. 5HT was measured at E14.5 in placenta and fetal tissues; (2) Pregnant BalbC mice received 5HTP from E10.5 to E13.5. 5HT was measured at E14.5 in placenta and fetal tissues; (3) Pregnant BalbC mice received 5HTP from E10.5 to E13.5. At E 14.5 fetal adrenals and kidneys were dissected and incubated for 1 h in DMEM medium at 37 °C in a humidified 5% CO₂/95% air atmosphere. About 16–20 adrenals and 10–12 kidneys were pooled per sample. After the incubation 5HT was measured in culture medium and fetal tissues.

A Shimadzu HPLC-ED LC-20ADsp (Japan) was used for chromatographic separation of analytes on a reversed-phase ReproSil-Pur column, ODS-3, 4 × 100 mm with pore diameter of 3 µm (Dr. Majsch GMBH, Germany) at a temperature of 30 °C and a flow rate of 1.0 mL/min. The mobile phase consisted of 0.1 M citrate-phosphate buffer containing 0.3 mM sodium octanesulfonate, 0.1 mM EDTA and 7% acetonitrile (all reagents purchased from Sigma) (pH 2.56). Decade II electrochemical detector (Antec Leyden, Netherlands) was equipped with a glassy carbon working electrode (+0.85 V) and an Ag/AgCl reference electrode. Collected tissues were homogenized in 10 volumes of 0.1 N HClO₄ containing 3,4-dihydroxybenzylamine hydrobromide (internal standard, Sigma, St. Louis, USA) (25–250 pmol/mL) by an ultrasonic homogenizer (Sonopuls HD 2000.2, Bandelin, Berlin, Germany), centrifuged at 16,500 × g for 20 min, and 5HT in the supernatant were measured. Peaks corresponding to 5HT were identified according to elution time of the standard solution, and the contents of substances were estimated as a ratio of the peak area of the internal standard solution to that of the specimen using software LabSolutions (Shimadzu, Japan).

Cell cultures. Patient-derived neuroblastoma cell lines NBL-28, NBL-38, and NBL-40 were established from tumor tissue samples^{98,99} with written informed consent obtained for our previous research project (IGA MZCR NR/9125-4), approved by the Research Ethics Committee of the School of Medicine, Masaryk University, Brno, Czech Republic (Approval No. 23/2005). According to Czech legal and ethical regulations governing the use of human biological material for research purposes, a new ethical assessment of this study is not necessary. In brief, the tumor biopsy was disinfected, cut into ~2 mm pieces, and placed into T25 flask with 1 mL of complete medium based on DMEM (PAA Laboratories, Linz, Austria) supplemented with 20% fetal calf serum (PAA), 2 mM glutamine and 1 × penicillin/streptomycin (BioWhittaker, Inc., Walkersville, MD, USA) under 37 °C and 5% CO₂. After specimen attachment, the volume of the medium was slowly brought up to 5 ml during 48 h. Once outgrowing cells reached 60% confluency, they were passaged and maintained. The SH-SY5Y neuroblastoma cell line was purchased from ECACC cat. # 94030304. CHLA-15 and CHLA-20 neuroblastoma cell lines were obtained from Alex's Lemonade Stand Foundation Childhood Cancer Repository (cccells.org) and kindly provided by Dr. Michael D. Hogarty (Children's Hospital of Philadelphia, PA, USA). Pluripotent embryonal carcinoma cell line NTERA-2 (clone D1) was purchased from ECACC (cat. # 01071221) and served as a control of HTR3A expression. Cells were cultured in DMEM/Ham's F-12 medium mixture (1:1; all neuroblastoma cells) or DMEM (NTERA-2) supplemented with 10% (CHLA-15, CHLA-20, and NTERA-2) or 20% fetal calf serum (FCS), 2 mM l-glutamine, 100 IU/mL penicillin, and 100 µg/mL streptomycin (all from Biosera, Nuaille, France), at 37 °C with 5% CO₂. For all neuroblastoma cell lines, media were further supplemented with 1% of nonessential amino acids (Biosera) and in case of CHLA-15 and CHLA-20 also with 1 × ITS-X (Gibco). All cell lines were routinely authenticated by STR profiling.

qRT-PCR. Total RNA was extracted with the GenElute™ Mammalian Total RNA Miniprep kit including genomic DNA elimination step using the On-Column DNase I Digestion Set (both Sigma-Aldrich, St. Louis, MO, USA). For all samples, equal amounts of RNA (25 ng of RNA/1 µL of total reaction content) were reverse transcribed into cDNA using M-MLV (Top-Bio, Prague, Czech Republic) and oligo-dT (Qiagen Inc., Valencia, CA, USA) priming. Quantitative PCR was performed in 10 µL reaction volumes using the KAPA SYBR® FAST qPCR Kit (Kapa Biosystems, Wilmington, MA, USA) and 7500 Fast Real-Time PCR System and 7500 Software v.2.0.6 (both Life Technologies, Carlsbad, CA, USA). The expression of individual genes was assessed using at least three technical replicates from three

Table 2 Composition of quality control samples.

Nº	Name	NM/D/E/M/NE concentration, ng/ml
1	QCL	3/75/15/3/15
2	QCH	800/800/400/800/400

biological replicates of each cell line. The heat shock protein gene HSP90AB1 was used as the endogenous reference control. Following primers (5'→3') forward—AGGAAGCCA ACCACCGTATC; HTR3A reverse—GTCCGTGGGGATGGACAACT; HSP90AB1 (Heat shock protein 90 alpha family class B member 1) forward—CGCATGA AGGAGACACAGAA; HSP90AB1 reverse—TCCCATCAAATTCCTTGAGC.

Western blotting. Whole-cell extracts were collected using RIPA buffer and 30 µg of total proteins were resolved on 10% polyacrylamide gels and blotted onto PVDF membranes (Bio-Rad Laboratories, Munich, Germany). The membranes were blocked with 5% non-fat dry milk in Tris-buffered saline with 0.05% Tween-20 (Sigma) and incubated overnight with primary antibodies. The following antibodies were used: rabbit anti-HTR3A (1:5000, Abcam, #ab13897), rabbit anti-c-MYC (1:1000, Cell Signaling Technology, CST, #5605), rabbit anti-N-MYC (1:1000, CST, #84406), rabbit anti-SOX2 (1:1000, CST, #3579), rabbit anti-cleaved caspase-3 (1:1000; CST, #9664), rabbit anti-GADPH (1:10,000, CST, #2118), and mouse anti-α-tubulin (1:10,000, Abcam, #ab7291). The next day, the membranes were incubated for 1 h with HRP-linked secondary antibodies: goat anti-rabbit IgG (1:5000, CST, #7074) or horse anti-mouse IgG (1:5000, CST, #7076). Chemiluminescent detection was performed using Amersham ECL Prime (Cytiva, Marlborough, MA, USA) and either Azure 600 imaging system (Azure Biosystems, Dublin, CA, USA) or photosensitive film. GAPDH or α-tubulin served as loading controls. Protein band densities were quantified using ImageJ (Fiji) software (NIH, Bethesda, MD, USA), version 2.1.0/1.53c.

Neuroblastoma xenografts in NSG mice. Eight-week-old female NSG (NOD/ShiLtSz-scid/Il2r^γ null) mice were injected subcutaneously into the right flank with a suspension of 1×10^6 enzymatically dissociated cells in 100 µL of serum-free DMEM. The mice were examined every three days over the period of 4 months for the presence of subcutaneous tumors. After the development of a tumor or after 4 months, the mice were sacrificed and surgically examined. The xenograft tumors were excised and photographed, and the final tumor volume was measured using the following formula: tumor volume (mm³) = length (mm) × width (mm) × width (mm) × 1/2.

MTT cell proliferation assay. Neuroblastoma cells were seeded in 96-well plates at a density of 10^3 cells/well in a defined serum-free medium: DMEM/F12 based medium (as detailed in Cell lines) w/o FCS, supplemented with 10 ng/mL EGF (Sigma-Aldrich), 20 ng/mL FGF2 (Sigma-Aldrich), and 1× B-27 supplement w/o vitamin A (Gibco). After 24 h, cells were treated by the addition of fresh medium with the selective HTR3A receptor agonists, N-methylquinazoline dimaleate (NMQ; Tocris, cat. #0566) or SR57227 (Tocris, cat. #1205), or the HTR3A receptor antagonists, granisetron hydrochloride (Tocris, cat. #2903) and VUF 10166 (Tocris, cat. #10166). In case of HTR3A receptor antagonists, medium was further supplemented with 5HT (Merck, cat. #14927) to the final concentration of 1 µM to evaluate the effect of HTR3A receptor inhibition. The proliferation activity was analyzed after additional 5 days using 3-[4,5-dimethylthiazol-2-yl]-2,5-diphenyltetrazolium bromide (MTT) (Sigma) at a final concentration of 455 µg/ml¹⁰⁰. The medium with MTT was replaced by 200 µL of DMSO per well after a 3 h incubation under standard conditions in order to solubilize the MTT product. The absorbance was measured at 570 nm with a reference absorbance at 620 nm wavelength using a Sunrise Absorbance Reader (Tecan).

Limiting dilution sphere formation assay. Prior to sphere formation assay, cells were treated for 5 days with 75 µM NMQ or an equivalent concentration of vehicle (DMSO). Cells were then harvested and dissociated into single-cell suspension by Accutase (Biosera), re-suspended in a defined serum-free medium (detailed above) and serially diluted into ultra-low attachment 96-well plates (Corning, cat. #3474) to reach final cell densities of 200, 100, 50, 25, 5, and 1 per well. At least four technical replicates of each cell density were included per cell line and treatment group. Every three days, growth factors were replenished by addition of fresh defined medium. After a week, for each cell density, the fraction of wells containing neurospheres ≥ 50 µm in diameter was determined using an Olympus CKX41 light microscope with Lumenera Infinity 2 CCD camera and QuickPhoto Camera 2.3 system (PROMICRA, Prague, Czech Republic). Frequencies of sphere-forming cells among experimental groups were calculated and compared using ELDA software¹⁰¹.

Statistical analysis. Statistical analysis was done using GraphPad Prism 8.1.1 software. All datasets were checked for normality with Shapiro–Wilk test, as this test reliably works for small datasets. For datasets with normal distribution double-sided unpaired t-test was applied. For datasets which failed a test for normal distribution, Mann–Whitney test was applied. For comparisons between multiple groups for one variable the one-way ANOVA test was applied (Fig. 3d, Fig. 6a, c, l, Supplementary Fig. 7d, e, f). In case one-way ANOVA test was showing significant differences, Tukey's multiple comparison test was used for a robust pairwise comparison of groups with unequal size (every mean to every other mean) or Dunnett's multiple comparison test for a pairwise comparison of groups to a control group.

In the analyses of statistical significance in catecholamine measurement as well as in behavioral tests (Fig. 7, Supplementary Fig.8) we have chosen the pairwise comparison within genders. The reason for it is that the treatment with 5HTP or

1-h restrain was applied at the stage, when the sexual dimorphism is not established in the forming adrenal glands and, consequently, the treatment equally affects males and females. However, adrenal glands have sexual dimorphism at postnatal stages and therefore must be analyzed separately, since the combined analysis of these groups can mask the effects of our prenatal treatment. We do not report a quantitative difference in catecholamines and catecholamine metabolites concentration. We have calculated statistical significance with Mann–Whitney test within genders between treated and control animals as this test is applicable to small samples and can evaluate statistical significance regardless of the normality of data distribution and homoscedasticity of the data. For these experiments the analysis was performed in SigmaPlot 12.1.

One of the values of catecholamine content in plasma in female 5HTP-treated group was removed based on the τ -criterion (blunder detection techniques). The outlier value from one animal may be caused by an error when taking a blood sample. Indeed, catecholamine release from adrenals is known to be very sensitive to various factors (in particular, stressful ones, at the time of sampling).

For all violin plots, median and quartiles are shown as those values work equally good for normally and not normally distributed data points.

Reporting summary. Further information on research design is available in the Nature Research Reporting Summary linked to this article.

Data availability

The raw and processed data of single-cell transcriptomic experiments generated in this study have been deposited in the GEO database under accession codes: [GSE1180861](https://www.ncbi.nlm.nih.gov/geo/query/acc.cgi?acc=GSE1180861) (mouse), [GSE195929](https://www.ncbi.nlm.nih.gov/geo/query/acc.cgi?acc=GSE195929) (human). The single-cell RNA-seq data of mouse adrenal gland from Furlan et al. (2017) used in this study are available in the GEO database under accession code [GSE99933](https://www.ncbi.nlm.nih.gov/geo/query/acc.cgi?acc=GSE99933), mm10_ERCC genome used in this study is available in the RefSeq database under accession code [GCF_000001635.20](https://www.ncbi.nlm.nih.gov/RefSeq/assembly/GCF_000001635.20). The data other than RNA-seq data generated in this study are provided in the Source data file.

Code availability

The code for reproducing the bioinformatic analysis can be found on the following GitHub repository: [\[https://github.com/LouisFaure/Adrenal5HTP_paper\]](https://github.com/LouisFaure/Adrenal5HTP_paper) (<https://doi.org/10.5281/zenodo.6247197>).

Received: 26 June 2020; Accepted: 23 April 2022;

Published online: 25 May 2022

References

- Kastriti, M. E., Kameneva, P. & Adameyko, I. Stem cells, evolutionary aspects and pathology of the adrenal medulla: a new developmental paradigm. *Mol. Cell. Endocrinol.* **518**, 110998 (2020).
- Lin, V. T. G., Pruiett, H. C., Samant, R. S. & Shevde, L. A. Developing cures: targeting ontogenesis in cancer. *Trends Cancer* **3**, 126–136 (2017).
- Tirosh, I. et al. Single-cell RNA-seq supports a developmental hierarchy in human oligodendrogloma. *Nature* **539**, 309–313 (2016).
- Gojo, J. et al. Single-cell RNA-Seq reveals cellular hierarchies and impaired developmental trajectories in pediatric ependymoma. *Cancer Cell* **38**, 44–59.e49 (2020).
- Couturier, C. P. et al. Single-cell RNA-seq reveals that glioblastoma recapitulates a normal neurodevelopmental hierarchy. *Nat. Commun.* **11**, 3406 (2020).
- Furlan, A. et al. Multipotent peripheral glial cells generate neuroendocrine cells of the adrenal medulla. *Science* **357**, eal3753 (2017).
- La Manno, G. et al. RNA velocity of single cells. *Nature* **560**, 494–498 (2018).
- Kastriti, M. E. et al. Schwann cell precursors generate the majority of paraganglia in Zuckerkandl organ and some sympathetic neurons in paraganglia. *Front. Mol. Neurosci.* **12**, <https://doi.org/10.3389/fnmol.2019.00006> (2019).
- Kameneva, P. et al. Single-cell transcriptomics of human embryos identifies multiple sympathoblast lineages with potential implications for neuroblastoma origin. *Nat. Genet.* **53**, 694–706 (2021).
- Cote, F. et al. Maternal serotonin is crucial for murine embryonic development. *Proc. Natl Acad. Sci. USA* **104**, 329–334 (2007).
- Alenina, N. et al. Growth retardation and altered autonomic control in mice lacking brain serotonin. *Proc. Natl Acad. Sci. USA* **106**, 10332–10337 (2009).
- Narboux-Neme, N. et al. Postnatal growth defects in mice with constitutive depletion of central serotonin. *ACS Chem. Neurosci.* **4**, 171–181 (2013).
- Iwashkin, E. et al. Serotonin mediates maternal effects and directs developmental and behavioral changes in the progeny of snails. *Cell Rep.* **12**, 1144–1158 (2015).

14. Bonnin, A. et al. A transient placental source of serotonin for the fetal forebrain. *Nature* **472**, 347–350 (2011).
15. Vitalis, T., Ansorge, M. S. & Dayer, A. G. Serotonin homeostasis and serotonin receptors as actors of cortical construction: special attention to the 5-HT3A and 5-HT6 receptor subtypes. *Front Cell Neurosci.* **7**, 93 (2013).
16. Migliarini, S., Pacini, G., Pelosi, B., Lunardi, G. & Pasqualetti, M. Lack of brain serotonin affects postnatal development and serotonergic neuronal circuitry formation. *Mol. Psychiatry* **18**, 1106–1118 (2013).
17. Lv, J. & Liu, F. The role of serotonin beyond the central nervous system during embryogenesis. *Front Cell Neurosci.* **11**, 74 (2017).
18. Rauw, W. M., Johnson, A. K., Gomez-Raya, L. & Dekkers, J. C. M. A hypothesis and review of the relationship between selection for improved production efficiency, coping behavior, and domestication. *Front Genet.* **8**, 134 (2017).
19. Cagan, A. & Blass, T. Identification of genomic variants putatively targeted by selection during dog domestication. *BMC Evol. Biol.* **16**, 10 (2016).
20. Trut, L., Oskina, I. & Kharlamova, A. Animal evolution during domestication: the domesticated fox as a model. *BioEssays* **31**, 349–360 (2009).
21. Wilkins, A. S., Wrangham, R. W. & Fitch, W. T. The “domestication syndrome” in mammals: a unified explanation based on neural crest cell behavior and genetics. *Genetics* **197**, 795–808 (2014).
22. Jansky, S. et al. Single-cell transcriptomic analyses provide insights into the developmental origins of neuroblastoma. *Nat. Genet.* **53**, 683–693 (2021).
23. Munoz-Manchado, A. B. et al. Novel striatal gabaergic interneuron populations labeled in the 5HT3a(EGFP) mouse. *Cereb. Cortex* **26**, 96–105 (2016).
24. Finger, T. E., Bartel, D. L., Shultz, N., Goodson, N. B. & Greer, C. A. 5HTR3A-driven GFP labels immature olfactory sensory neurons. *J. Comp. Neurol.* **525**, 1743–1755 (2017).
25. Jessen, K. R. & Mirsky, R. The origin and development of glial cells in peripheral nerves. *Nat. Rev. Neurosci.* **6**, 671–682 (2005).
26. Schroeter, S., Levey, A. I. & Blakely, R. D. Polarized expression of the antidepressant-sensitive serotonin transporter in epinephrine-synthesizing chromaffin cells of the rat adrenal gland. *Mol. Cell Neurosci.* **9**, 170–184 (1997).
27. Brindley, R. L., Bauer, M. B., Blakely, R. D. & Currie, K. P. M. Serotonin and serotonin transporters in the adrenal medulla: a potential hub for modulation of the sympathetic stress response. *ACS Chem. Neurosci.* **8**, 943–954 (2017).
28. Delarue, C., Becquet, D., Idres, S., Hery, F. & Vaudry, H. Serotonin synthesis in adrenochromaffin cells. *Neuroscience* **46**, 495–500 (1992).
29. García-Ararrás, J. E. & Martínez, R. Developmental expression of serotonin-like immunoreactivity in the sympathoadrenal system of the chicken. *Cell Tissue Res.* **262**, 363–372 (1990).
30. Bondarenko, N. S. et al. Plasticity of central and peripheral sources of noradrenaline in rats during ontogenesis. *Biochemistry* **82**, 373–379 (2017).
31. Mitchell, J. A., Hammer, R. E. & Goldman, H. Serotonin induced disruption of implantation in rats: II. Suppression of decidualization. *Biol. Reprod.* **29**, 6 (1983).
32. Udenfriend, S., Weissbach, H. & Bordanski, D. Increase in tissue serotonin following administration of its precursor 5-hydroxytryptophan. *J. Biological Chem.* **224**, 7 (1957).
33. Bogdanski, D. F., Weissbach, H. & Udenfriend, S. Pharmacological studies with the serotonin precursor, 5-hydroxytryptophan. *J. Pharm. Exp. Ther.* **122**, 182–194 (1958).
34. Schneider, B. F. & Norton, S. Equivalent ages in rat, mouse and chick embryos. *Teratology* **19**, 273–278 (1979).
35. Le Douarin, N. M., Smith, J. & Le Lievre, C. S. From the neural crest to the ganglia of the peripheral nervous system. *Annu. Rev. Physiol.* **43**, 653–671 (1981).
36. Cheraghali, A. M., Knaus, E. E. & Wiebe, L. I. Bioavailability and pharmacokinetic parameters for 5-ethyl-2'-deoxyuridine. *Antivir. Res.* **25**, 259–267 (1994).
37. Chan, W. H. et al. Differences in CART expression and cell cycle behavior discriminate sympathetic neuroblast from chromaffin cell lineages in mouse sympathoadrenal cells. *Developmental Neurobiol.* **76**, 137–149 (2016).
38. Alexandrov, A., Colognori, D., Shu, M.-D. & Steitz, J. A. Human spliceosomal protein CWC22 plays a role in coupling splicing to exon junction complex deposition and nonsense-mediated decay. *Proc. Natl Acad. Sci. USA* **109**, 21313 (2012).
39. Steckelberg, A.-L., Boehm, V., Gromadzka, A. M. & Gehring, N. H. CWC22 connects pre-mRNA splicing and exon junction complex assembly. *Cell Rep.* **2**, 454–461 (2012).
40. Anderson, K. M. et al. Transcription of the non-coding RNA upperhand controls Hand2 expression and heart development. *Nature* **539**, 433–436 (2016).
41. Morikawa, Y., D'Autrèaux, F., Gershon, M. D. & Cserjesi, P. Hand2 determines the noradrenergic phenotype in the mouse sympathetic nervous system. *Developmental Biol.* **307**, 114–126 (2007).
42. McCann, J. L. et al. The DNA deaminase APOBEC3B interacts with the cell-cycle protein CDK4 and disrupts CDK4-mediated nuclear import of Cyclin D1. *J. Biol. Chem.* **294**, 12099–12111 (2019).
43. Martin, V. et al. Response of Htr3a knockout mice to antidepressant treatment and chronic stress. *Br. J. Pharm.* **174**, 2471–2483 (2017).
44. Zimmerman, M. W. et al. MYC drives a subset of high-risk pediatric neuroblastomas and is activated through mechanisms including enhancer hijacking and focal enhancer amplification. *Cancer Discov.* **8**, 320 (2018).
45. Wang, L. L. et al. Augmented expression of MYC and/or MYCN protein defines highly aggressive MYC-driven neuroblastoma: a Children's Oncology Group study. *Br. J. Cancer* **113**, 57–63 (2015).
46. Eisenhofer, G. et al. Plasma normetanephrine and metanephrine for detecting pheochromocytoma in von Hippel–Lindau disease and multiple endocrine neoplasia type 2. *N. Engl. J. Med.* **340**, 1872–1879 (1999).
47. Raber, W. et al. Diagnostic efficacy of unconjugated plasma metanephrines for the detection of pheochromocytoma. *Arch. Intern. Med.* **160**, 2957–2963 (2000).
48. Axelrod, J. Metabolism of epinephrine and other sympathomimetic amines. *Physiological Rev.* **39**, 751–776 (1959).
49. Axelrod, J. Noradrenaline: fate and control of its biosynthesis. *Science* **173**, 598–606 (1971).
50. Kopin, I. J. Storage and metabolism of catecholamines: the role of monoamine oxidase. *Pharm. Rev.* **16**, 179–191 (1964).
51. Parvez, H., Ismahan, G., Parvez, S. & Youdim, M. B. Developmental changes in the activity of catechol-O-methyl transferase in rat and rabbit fetuses. *J. Neural Transm.* **44**, 65–75 (1979).
52. Chen, H. J. et al. Prenatal stress causes intrauterine inflammation and serotonergic dysfunction, and long-term behavioral deficits through microbe- and CCL2-dependent mechanisms. *Transl. Psychiatry* **10**, 191 (2020).
53. Dmitriev, S. G., Zakharov, V. M. & Sheftel, B. I. Cytogenetic homeostasis and population density in red-backed voles *Clethrionomys glareolus* and *C. rutilus* in central Siberia. *Acta Theriologica Suppl.* **4**, 49–55 (1997).
54. Zakharov, V. M., Trofimov, I. E. & Sheftel, B. I. Fluctuating asymmetry and population dynamics of the common shrew, *Sorex araneus*, in Central Siberia under climate change conditions. *Symmetry* **12**, 1960 (2020).
55. Henttonen, H., McGuire, A. D. & Hansson, L. Comparisons of amplitudes and frequencies (spectral analyses) of density variations in long-term data sets of *Clethrionomys* species. *Annales Zoologici Fennici* **22**, 221–227 (1985).
56. Liu, J. et al. High housing density increases stress hormone- or disease-associated fecal microbiota in male Brandt's voles (*Lasiopodomys brandtii*). *Hormones Behav.* **126**, 104838 (2020).
57. Huber, K., Kalchheim, C. & Unsicker, K. The development of the chromaffin cell lineage from the neural crest. *Auton. Neurosci.* **151**, 10–16 (2009).
58. Furlan, A. & Adameyko, I. Schwann cell precursor: a neural crest cell in disguise? *Developmental Biol.* **444**, S25–S35 (2018).
59. Duester, G. Retinoic Acid synthesis and signaling during early organogenesis. *Cell* **134**, 921–931 (2008).
60. Nicosia, R. F., Zorzi, P., Ligresti, G., Morishita, A. & Aplin, A. C. Paracrine regulation of angiogenesis by different cell types in the aorta ring model. *Int. J. Dev. Biol.* **55**, 447–453 (2011).
61. Hockman, D. et al. Striking parallels between carotid body glomus cell and adrenal chromaffin cell development. *Dev. Biol.* **444**, S308–S324 (2018).
62. St-Pierre, J., Laurent, L., King, S. & Vaillancourt, C. Effects of prenatal maternal stress on serotonin and fetal development. *Placenta* **48**, S66–S71 (2016).
63. Nordquist, N. & Orelund, L. Serotonin, genetic variability, behaviour, and psychiatric disorders—a review. *Upsala J. Med. Sci.* **115**, 2–10 (2010).
64. Kalueff, A. V., Olivier, J. D. A., Nonkes, L. J. P. & Homberg, J. R. Conserved role for the serotonin transporter gene in rat and mouse neurobehavioral endophenotypes. *Neurosci. Biobehav. Rev.* **34**, 373–386 (2010).
65. Brindley, R. L. et al. Adrenal serotonin derives from accumulation by the antidepressant-sensitive serotonin transporter. *Pharmacol. Res.* **140**, 56–66 (2019).
66. Noorlander, C. W. et al. Modulation of serotonin transporter function during fetal development causes dilated heart cardiomyopathy and lifelong behavioral abnormalities. *PLoS ONE* **3**, e2782 (2008).
67. Gutknecht, L. et al. Impacts of brain serotonin deficiency following Tph2 inactivation on development and raphe neuron serotonergic specification. *PLoS ONE* **7**, e43157 (2012).
68. Schaefer, T. L., Vorhees, C. V. & Williams, M. T. Mouse plasmacytoma-expressed transcript 1 knock out induced 5-HT disruption results in a lack of cognitive deficits and an anxiety phenotype complicated by hypoactivity and defensiveness. *Neuroscience* **164**, 1431–1443 (2009).
69. Thiele, C. J., Reynolds, C. P. & Israel, M. A. Decreased expression of N-myc precedes retinoic acid-induced morphological differentiation of human neuroblastoma. *Nature* **313**, 404–406 (1985).
70. Hölzel, M. et al. NF1 is a tumor suppressor in neuroblastoma that determines retinoic acid response and disease outcome. *Cell* **142**, 218–229 (2010).
71. Bayeva, N., Coll, E. & Piskareva, O. Differentiating neuroblastoma: a systematic review of the retinoic acid, its derivatives, and synergistic interactions. *J. Pers. Med.* **11** (2021).
72. Dong, R. et al. Single-cell characterization of malignant phenotypes and developmental trajectories of adrenal neuroblastoma. *Cancer Cell* **38**, 716–733.e716 (2020).

73. Bedoya-Reina, O. C. et al. Single-nuclei transcriptomes from human adrenal gland reveal distinct cellular identities of low and high-risk neuroblastoma tumors. *Nat. Commun.* **12**, 5309 (2021).
74. Hanemaaijer, E. S. et al. Single-cell atlas of developing murine adrenal gland reveals relation of Schwann cell precursor signature to neuroblastoma phenotype. *Proc. Natl Acad. Sci. USA* **118**, e2022350118 (2021).
75. Kildisute, G. et al. Tumor to normal single-cell mRNA comparisons reveal a pan-neuroblastoma cancer cell. *Sci. Adv.* **7**, eabd3311 (2021).
76. Kliman, H. J. et al. Pathway of maternal serotonin to the human embryo and fetus. *Endocrinology* **159**, 1609–1629 (2018).
77. Bonnin, A. & Levitt, P. Fetal, maternal, and placental sources of serotonin and new implications for developmental programming of the brain. *Neuroscience* **197**, 1–7 (2011).
78. Goeden, N. et al. Maternal inflammation disrupts fetal neurodevelopment via increased placental output of serotonin to the fetal brain. *J. Neurosci.* **36**, 6041–6049 (2016).
79. Williams, M. et al. Maternal inflammation results in altered tryptophan metabolism in rabbit placenta and fetal brain. *Dev. Neurosci.* **39**, 399–412 (2017).
80. Ranzil, S. et al. The relationship between the placental serotonin pathway and fetal growth restriction. *Biochimie* **161**, 80–87 (2019).
81. Koolhaas, J. M. et al. The resident-intruder paradigm: a standardized test for aggression, violence and social stress. *J. Vis. Exp.* e4367, <https://doi.org/10.3791/4367> (2013).
82. de Boer, S. F., Buwalda, B. & Koolhaas, J. M. Untangling the neurobiology of coping styles in rodents: towards neural mechanisms underlying individual differences in disease susceptibility. *Neurosci. Biobehav. Rev.* **74**, 401–422 (2017).
83. Voronezhskaya, E. E., Khabarova, M. Y., Nezhlin, L. P. & Ivashkin, E. G. Delayed action of serotonin in molluscan development. *Acta Biol. Hung.* **63**, 210–216 (2012).
84. Voronezhskaya, E. E. Maternal serotonin: shaping developmental patterns and behavioral strategy on progeny in molluscs. *Front. Ecol. Evol.* **9**, <https://doi.org/10.3389/fevo.2021.739787> (2021).
85. Das, S. et al. Serotonin signaling by maternal neurons upon stress ensures progeny survival. *eLife* **9**, e55246 (2020).
86. Andreassen, H. P. et al. Population cycles and outbreaks of small rodents: ten essential questions we still need to solve. *Oecologia* **195**, 601–622 (2021).
87. Podgorny, O., Peunova, N., Park, J. H. & Enikolopov, G. Triple S-phase labeling of dividing stem cells. *Stem Cell Rep.* **10**, 615–626 (2018).
88. Stuart, T. et al. Comprehensive integration of single-cell data. *Cell* **177**, 1888–1902.e1821 (2019).
89. Picelli, S. et al. Full-length RNA-seq from single cells using Smart-seq2. *Nat. Protoc.* **9**, 171–181 (2014).
90. Becht, E. et al. Dimensionality reduction for visualizing single-cell data using UMAP. *Nat. Biotechnol.* **37**, 38–44 (2019).
91. Huang, Y. & Sanguinetti, G. BRIE: transcriptome-wide splicing quantification in single cells. *Genome Biol.* **18**, 123 (2017).
92. Huang, Y. & Sanguinetti, G. BRIE2: computational identification of splicing phenotypes from single-cell transcriptomic experiments. *Genome Biol.* **22**, 251 <https://doi.org/10.1186/s13059-021-02461-5> (2021).
93. Hao, Y. et al. Integrated analysis of multimodal single-cell data. *Cell* **184**, 3573–3587.e3529 (2021).
94. Wolock, S. L., Lopez, R. & Klein, A. M. Scrublet: computational identification of cell doublets in single-cell transcriptomic data. *Cell Syst.* **8**, 281–291.e289 (2019).
95. Blasco-Serra, A., Gonzalez-Soler, E. M., Cervera-Ferri, A., Teruel-Marti, V. & Valverde-Navarro, A. A standardization of the novelty-suppressed feeding test protocol in rats. *Neurosci. Lett.* **658**, 73–78 (2017).
96. Bali, A. & Jaggi, A. Electric foot shock stress: a useful tool in neuropsychiatric studies. *Rev. Neurosci.* **26**, 655–677 (2015).
97. Wall, P. M. & Messier, C. Methodological and conceptual issues in the use of the elevated plus-maze as a psychological measurement instrument of animal anxiety-like behavior. *Neurosci. Behav. Rev.* **25**, 12 (2001).
98. Veselska, R. et al. Nestin expression in osteosarcomas and derivation of nestin/CD133 positive osteosarcoma cell lines. *BMC Cancer* **8**, 300 (2008).
99. Veselska, R. et al. Nestin expression in the cell lines derived from glioblastoma multiforme. *BMC Cancer* **6**, 32 (2006).
100. Dobrotkova, V. et al. Prediction of neuroblastoma cell response to treatment with natural or synthetic retinoids using selected protein biomarkers. *PLoS ONE* **14**, e0218269 (2019).
101. Hu, Y. & Smyth, G. K. ELDA: extreme limiting dilution analysis for comparing depleted and enriched populations in stem cell and other assays. *J. Immunol. Methods* **347**, 70–78 (2009).

Acknowledgements

This work of J.S., P.C., L.C., L.S., and J.N. was supported by the European Regional Development Fund – Project ENOCH (No. CZ.02.1.01/0.0/0.0/16_019/0000868). J.S. acknowledges support from the Czech Science Foundation (No. GJ20-00987Y). Experiments of V.I.M., E.E.V.,

and A.K. on mice and rats describing the effects of 5HT on the developing AM, long-term effects on CAs and CA-mediated behavior, AM size, as well as experiments with wild population of red-backed voles were supported by the Russian Science Foundation grant # 17-14-01353. M.E.K. was supported by the Novo Nordisk Foundation (Postdoc fellowship in Endocrinology and Metabolism at International Elite Environments, NNF17OC0026874) and Stiftelsen Riksbankens Jubileumsfond (Erik Rönnerbergs fond stipend). M.T., T.Z., and J.K. acknowledge CzechNanoLab Research Infrastructure supported by MEYS CR (LM2018110). M.T. and L.C. were financially supported by the Brno City Municipality as Brno Ph.D. Talent Scholarship Holders. M.T. acknowledges Martina Roeselova Memorial fellowship. P.G., M.P., N.A., and M.B. were supported by the EU H2020 MSCA ITN projects “Serotonin and Beyond” (N 953327). N.A. and M.B. were supported by German Federal Ministry of Education and Research under the framework of the EU-ERA-NET NEURON project; N.A. was supported by the project 73022475 of the St. Petersburg State University and the Volkswagen Foundation. I.A. was supported by Knut and Alice Wallenberg Research Foundation, Bertil Hallsten Research Foundation, Paradifference Foundation, Swedish Research Council, Austrian Science Fund (FWF), ERC Synergy grant “KILL-OR-DIFFERENTIAT”, EMBO Young Investigator Program, Cancer Fonden. The grant support of the Ministry of Science and Higher Education of the Russian Federation (#075-15-2020-784) covered computational pipeline and corresponding analysis of single-cell data. L.F. was supported by Austrian Science Fund DOC 33-B27. I.P. was supported by the European Union’s Horizon 2020 Research and Innovation Program under Marie Skłodowska-Curie (grant agreement No. 860635, ITN NEUcrest). E.E.V., V.I.M., A.K., V.Y., and B.S. thank Director of the Yenisey ecological station “Mirmoe” Viktor Lunevsky for the organization of the field work, and the IDB RAS Core Centrum for the provided laboratory equipment. E.E.V. and A.K. thank Fedor Shkil for inspiring to visit “Mirmoe”. The human prenatal tissue was provided by the Karolinska Institutet Developmental Tissue Bank and the authors thank Erik Sundström for the help with obtaining human tissue.

Author contributions

I.A., P.K., V.I.M., E.E.V., and K.F. conceived and designed the main idea, conceptualized and drafted the manuscript. P.K., V.I.M., M.E.K., E.K., A.M., A.K., M.B., M.P., P.G., and N.A. designed and performed key experiments, analyzed the data. M.T., T.Z., and J.K. performed X-ray computed microtomography analysis and provided their expertise. T.S.K. and N.V.K. designed, performed, and analyzed the behavior tests. J.S., P.C., L.C., L.S., and J.N. designed, performed, and analyzed the neuroblastoma cell line and NSG mice experiments. V.Y., B.S., E.E.V., and A.K. collected and analyzed data for *Clethrionomys rutilus*. L.F., A.V.A., and I.P. performed computational analysis.

Funding

Open access funding provided by Karolinska Institute.

Competing interests

The authors declare no competing interests.

Additional information

Supplementary information The online version contains supplementary material available at <https://doi.org/10.1038/s41467-022-30438-w>.

Correspondence and requests for materials should be addressed to Elena E. Voronezhskaya or Igor Adameyko.

Peer review information *Nature Communications* thanks Lukas Sommer and the other anonymous reviewers for their contribution to the peer review of this work. Peer reviewer reports are available.

Reprints and permission information is available at <http://www.nature.com/reprints>

Publisher’s note Springer Nature remains neutral with regard to jurisdictional claims in published maps and institutional affiliations.



Open Access This article is licensed under a Creative Commons Attribution 4.0 International License, which permits use, sharing, adaptation, distribution and reproduction in any medium or format, as long as you give appropriate credit to the original author(s) and the source, provide a link to the Creative Commons license, and indicate if changes were made. The images or other third party material in this article are included in the article’s Creative Commons license, unless indicated otherwise in a credit line to the material. If material is not included in the article’s Creative Commons license and your intended use is not permitted by statutory regulation or exceeds the permitted use, you will need to obtain permission directly from the copyright holder. To view a copy of this license, visit <http://creativecommons.org/licenses/by/4.0/>.

© The Author(s) 2022



OPEN

Resolving complex cartilage structures in developmental biology via deep learning-based automatic segmentation of X-ray computed microtomography images

Jan Matula¹, Veronika Polakova¹, Jakub Salplachta¹, Marketa Tesarova¹, Tomas Zikmund¹, Marketa Kaucska², Igor Adameyko^{3,4} & Jozef Kaiser¹✉

The complex shape of embryonic cartilage represents a true challenge for phenotyping and basic understanding of skeletal development. X-ray computed microtomography (μ CT) enables inspecting relevant tissues in all three dimensions; however, most 3D models are still created by manual segmentation, which is a time-consuming and tedious task. In this work, we utilised a convolutional neural network (CNN) to automatically segment the most complex cartilaginous system represented by the developing nasal capsule. The main challenges of this task stem from the large size of the image data (over a thousand pixels in each dimension) and a relatively small training database, including genetically modified mouse embryos, where the phenotype of the analysed structures differs from the norm. We propose a CNN-based segmentation model optimised for the large image size that we trained using a unique manually annotated database. The segmentation model was able to segment the cartilaginous nasal capsule with a median accuracy of 84.44% (Dice coefficient). The time necessary for segmentation of new samples shortened from approximately 8 h needed for manual segmentation to mere 130 s per sample. This will greatly accelerate the throughput of μ CT analysis of cartilaginous skeletal elements in animal models of developmental diseases.

Abbreviations

μ CT	X-ray computed microtomography
CNN	Convolutional neural network
ReLU	Rectified linear unit
SELU	Scaled exponential linear unit
DSC	Dice–Sørensen coefficient
TP	True positive
TN	True negative
FP	False positive
FN	False negative
IQR	Interquartile range

To understand the complexity of embryonic development, it was essential to assess the shape and structure of tissues and organs in three-dimensional space. It also enabled us to dissect the sequential steps of their formation. Pioneering work introduced tissue contrasting techniques that enabled the detection of previously hidden

¹Central European Institute of Technology, Brno University of Technology, Purkynova 123, Brno 61200, Czech Republic. ²Max Planck Institute for Evolutionary Biology, August-Thienemann-Str.2, 24306 Ploen, Germany. ³Medical University of Vienna, Spitalgasse 23, 1090 Vienna, Austria. ⁴Department of Physiology and Pharmacology, Karolinska Institutet, 17165 Stockholm, Sweden. ✉email: jozef.kaiser@ceitec.vutbr.cz

structures such as embryonic cartilage or even their predecessor, mesenchymal condensations, using X-ray computed tomography^{1–3}. The newly generated knowledge revolutionised the field of developmental biology and enabled, among others, the detection of the onset of congenital disorders and uncovering the origin and sequential steps of complex structure formation^{4,5}. During embryogenesis, the formation of the skull is preceded by the formation of chondrocranium. This cartilaginous 3D blueprint of future skeletal elements in the head is formed quite early in embryonic development and establishes the original layout of the future facial shape⁶. The shape of the head, specifically the face, is important for many aspects of everyday life—eating, breathing, vision, communication and mutual recognition in humans. Any morphological change in chondrocranium will be maintained even after replacement by bone. Therefore, when we aim to investigate the formation of the face, it is necessary to look at the embryonic stages and the 3D shape of the cartilage. Approximately 30% of congenital syndromes are represented by craniofacial malformations⁷. Investigations of the underlying causes were performed mainly using mouse genetic models that in part uncovered the basis of selected malformations. Nevertheless, numerous genetic perturbations were embryonically lethal and did not allow researchers to analyse and understand their role in the formation and shaping of embryonic structures.^{8,9}

Historically, the investigation of head skeletal system formation relied on basic methodology such as histological staining of sections and a subsequent assembly of the 2D images into a stack¹⁰. Needless to say, this approach was prone to artifacts and time- and effort-demanding, not allowing us to unwind the 4D dynamics of face formation to the full extent or at high resolution. With the technological and contrasting advances in recent years, it has become possible to visualise nearly any structure in the developing embryo using 3D imaging techniques^{2,3} and obtain more profound insights into the mechanisms of skeletal development, shaping and origin of craniofacial malformations. X-ray computed microtomography (μ CT) is an imaging technique capable of capturing complex geometries in 3D with a high spatial resolution in the range of micrometres. This methodology became an ultimate booster in developmental biology, where the high spatial resolution allowed researchers to accurately assess the morphological properties of both hard and soft tissues of biological samples¹¹. While advanced imaging protocols currently allow the detection of even delicate structures, such as embryonic cartilage shaping the face, the subsequent image processing preceding any further analysis remains enormously time-consuming and represents the major drawback of this methodology.

An essential step before any further analysis of μ CT images is the segmentation of the structure of interest. Image segmentation is the task of assigning a class label to each pixel or, in the case of volumetric image data, the voxel of an image¹². Many image segmentation algorithms have been developed and are actively utilised to segment mineralized matrices from μ CT data. However, the low contrast of soft tissues (cartilage, peripheral nerves and others) represents a significant challenge for their application. High X-ray attenuation coefficients of hard tissues, such as bones and teeth, allow their segmentation with relative ease by applying simple segmentation algorithms, e.g., basic thresholding. Such image processing is unfeasible in the case of soft tissues¹³. The low X-ray attenuation provided by the various soft tissues present in biological samples renders them nearly transparent for X-rays with energies used in traditional laboratory μ CT systems. Tissue contrasting with substances containing elements with high atomic numbers (iodine¹⁴, osmium¹⁵, tungsten¹⁶) is frequently used to enhance the visibility of soft tissues. The contrast between various soft tissues (for instance, peripheral nerves, cartilage, muscles or parts of the brain) results from the differential uptake of the contrast solution¹⁷. However, the generated contrast is insufficient for utilising traditional fully automatic segmentation algorithms. In many cases, the desired structures must be segmented manually due to the complex shapes and uncertain borders between different tissues. This manual segmentation is a taxing and time-consuming task, especially in the case of volumetric image data containing thousands of tomographic cross-sections. One such difficult-to-segment structure is the cartilaginous nasal capsule of a developing mouse embryo. 3D models created by manual segmentation were crucial in the work of Kaucka and colleagues^{2,3}. Manual segmentation was a significant bottleneck in data processing in these publications, as the manual segmentation of cartilaginous nasal capsule in one μ CT scan of a mouse embryo required at least 8 h of an expert's time. Therefore, a fully automatic solution that could decrease the time requirement and manual work of the expert is highly sought after.

Deep learning and, specifically, convolutional neural networks (CNNs) consistently achieve state-of-the-art results in image segmentation tasks¹⁸. Therefore, they seem to be a logical candidate for automatic segmentation of the nasal capsule cartilage; however, there are several challenges. The μ CT measurement provides extremely large image data (thousands of pixels in each plane). Such a high resolution cannot be compromised, as it is crucial in studies where minor morphological differences among several samples are sought and compared^{2,3}. Furthermore, the segmented cartilage is structurally inhomogeneous, and its shape differs considerably depending on its location within the embryonic head. Additionally, subtle intraspecies differences in cartilage geometry, structure and thickness are observed among individuals. The size of the training database also plays an important role in creating a robust CNN-based segmentation model.

U-Net is a well-established convolutional neural network architecture for the segmentation of biomedical images¹². Its ability to learn from size-limited datasets stems from its fully convolutional nature with so-called skip connections and the lack of any fully connected layers. The success of the U-net architecture greatly increased the popularity of so-called encoder-decoder architectures with skip connections in segmentation of biomedical images, where the encoder is responsible for feature extraction and the decoder for the localisation and segmentation of the desired structures. U-net's power in segmentation of datasets with a limited training database stems from its fully-convolutional nature. In the work of Rytky and colleagues¹⁹ the authors propose a method for segmentation of calcified articular cartilage in μ CT images of rabbit knees, where they utilise a feature pyramid network decoder with a ResNet-18²⁰ encoder trained in the ImageNet dataset²¹. As articular cartilage is a relatively spatially homogeneous structure, the authors in¹⁹ can apply patch-based training with a relatively low input size. Similarly, the authors in the work of Léger and colleagues²² employ a 3-D U-Net CNN to segment mineralised cartilage in μ CT images of the Achilles tendon-to-bone interface and can employ patch-based

training due to the homogeneity of the segmented structure. To our knowledge, there is only one work dealing with a similar high-resolution segmentation of chondrocranium in developing mouse embryos imaged via μ CT, published by Zheng and colleagues²³. A manually annotated database is not available to the authors, and they approach the segmentation task using sparse annotation with uncertainty-guided self-training. The authors segment cartilage in the whole chondrocranium. They evaluated the performance of their method on selected, manually annotated subregions of the whole 3-D volume, as manual annotations of the whole chondrocranium were not available. This manual selection of the evaluation region may skew the final evaluation accuracy.

Here, we provide a methodology for fully automatic segmentation of highly complex cartilaginous nasal capsules in μ CT images of mouse embryos. We utilised a CNN trained in a supervised training mode on a unique database of 14 manually annotated μ CT scans of mouse embryo heads on their 17th day of embryonic development. We employed different modifications to a basic encoder-decoder CNN architecture to improve the segmentation performance of the model. We experimentally validated the proposed methodology for the particular image segmentation task. This μ CT image segmentation model can be further used to segment newly scanned mouse embryos, thus greatly reducing the time required for processing new samples. The segmentation model is ready to be trained to include additional embryonic developmental stages or used as a basis for transfer learning for other high-resolution μ CT segmentation tasks. We also show that the data provided by the proposed automatic segmentation methodology can be further quantitatively analysed in the same manner as manually segmented data.

Methods

Samples. The database for training and testing the proposed segmentation method consists of 14 micro-CT scans of mouse embryonic heads at E17.5 (developmental stage). The heads were contrasted using the PTA-staining procedure before scanning, which enabled the detection of tissues with low density (e.g., cartilage and muscle)²⁴. The staining protocol was previously described in^{2,3,25}. A subset of the dataset was published and is available for inspection in²⁶. All samples utilised in this work are summarised in Suppl. Table S1. All animal work was approved by the Local Ethical Committee on Animal Experiments (Norra Djurförsöksetiska Nämnd, ethical permit N226/15 and N5/14) and conducted according to The Swedish Animal Agency's Provisions and Guidelines for Animal Experimentation recommendations. In order to comply with the 3R strategy of animal welfare, we decided to use data generated for previous studies^{2,3}. No additional animals have been used in this study. All experiments on animals were conducted in compliance with the ARRIVE guidelines.

Multiple genetically modified embryos with altered cartilage development were included in the database to improve the generalisability of the developed method. As proper sample preparation is very important, we included an improperly stained embryo during the sample preparation procedure. The differences are further visualised in the tomographic cross-section in Fig. 1a. The changes in the cartilaginous nasal capsule geometry and morphology in genetically modified samples differ in severity from moderate to severe. The shape differences found in mutant embryos are visualised as 3-D renders in Fig. 1b.

Sample preparation. Mice were sacrificed with isoflurane (Baxter KDG9623) overdose or cervical dislocation, and embryos were dissected and collected in ice-cold PBS. Subsequently, the samples were fixed in 4% paraformaldehyde (PFA) in PBS solution for 24 h at +4 °C with slow rotation. Before contrasting, samples were dehydrated in incrementally increasing ethanol concentrations (30%, 50%, 70%), one day in each concentration to minimise the shrinkage of the tissue. Samples were transferred into 1.5% PTA (phospho-tungstic acid) in 90% methanol for tissue contrasting. The PTA-methanol solution was changed every 2–3 days. Samples were stained for seven weeks. The contrasting procedure was followed by rehydration of the samples by incubation in an ethanol series (90%, 70%, 50% and 30%).

μ CT measurement. The samples were scanned with a laboratory μ CT system GE Phoenix v|tome|x L 240 (Waygate Technologies GmbH Germany). The system was equipped with a high contrast flat panel detector DXR250 with 2048 × 2048-pixel resolution and 200 × 200 μm^2 pixel size. The embryos were fixed in polyimide tubes filled with 1% agarose gel to prevent sample movement during the μ CT stage rotation. Two thousand projections were acquired with an exposure time of 900 ms per projection. Each projection was captured three times, and an average of the signal was used to improve the signal-to-noise ratio. The acceleration voltage of the X-ray tube was 60 kV, and the tube current was 200 μA . The X-ray beam was filtered with a 0.1 mm aluminum plate. Tomographic reconstruction of the obtained set of projections was performed using the FDK reconstruction algorithm²⁷ in GE phoenix datos |x 2.0 3D computed tomography software (Waygate Technologies GmbH Germany). Output of the reconstructed CT slices was 16-bit integer. To compensate for small and smooth drift of axis (samples and detector) and focus (X-ray tube) position, scan optimiser module was applied during the reconstruction. Beam hardening correction was applied by the commercially available module in the reconstruction software with parameter 7 for different materials. The voxel size was variable depending on the sample size (see Suppl. Table S1 for complete information).

Manual segmentation. Avizo image processing software (version 7, Thermo Fisher Scientific, USA) was used to manually segment the nasal capsule cartilage in the reconstructed CT images. The data were aligned for each embryo head to have the same orientation. The manual segmentation of the cartilaginous nasal capsule tissue takes at least 8 h¹⁶, depending on the sample and operator's experience. As a result of the cartilage being segmented by multiple operators, some intraoperator variability is introduced into the manually segmented samples. It was partially avoided by the quality check performed by a single expert, but it might still affect the quality of the dataset and then further evaluation of the segmentation accuracy. To make the load of 3D seg-

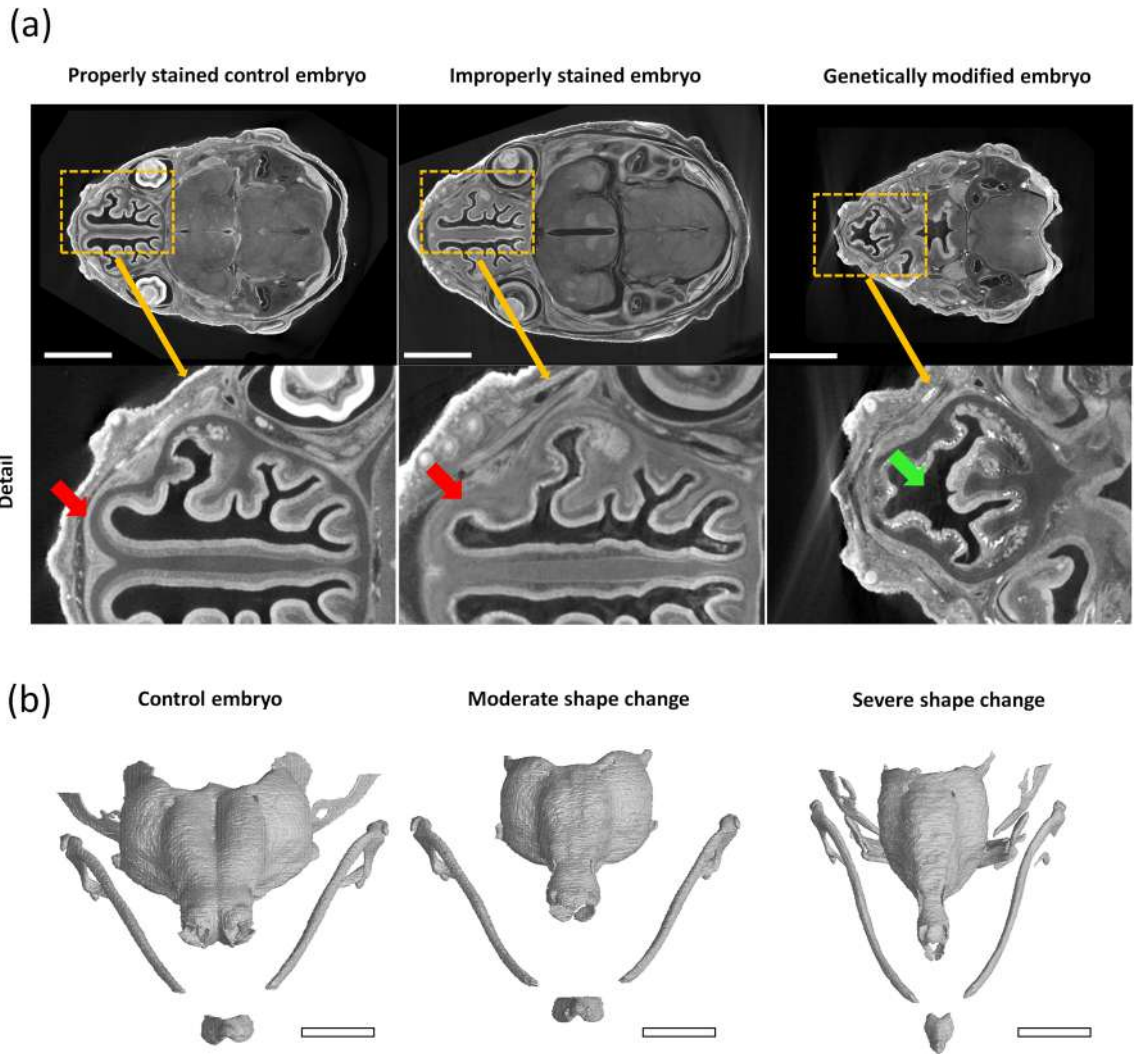


Figure 1. Visualisation of selected samples included in the database utilised in this work. **(a)** Visualisation of challenging cases compared to control mouse embryo represented in the majority of the database. The figure shows selected tomographic cross-sections of properly stained control embryos in comparison with improperly stained embryos. Red arrows indicate the difference in cartilage staining between properly stained samples and an improperly stained sample. A tomographic cross-section of genetically modified sample 10 is also shown. The green arrow shows the main phenotype difference: the underdeveloped nasal septum. Scale bar 2 mm. **(b)** Frontal view of 3-D rendering of the segmented nasal capsule cartilage of the control (Sample 8), moderate shape change in Sample 6 and severe shape change in Sample 10. Scale bar 1 mm.

mentation volume easier to handle, only every 3rd slice was manually segmented, and the remaining slices were calculated by linearly interpolating between adjacent manually segmented slices. Figure 2 depicts the segmented structure in the context of the whole head in 3-D volume.

Neural network architecture. We aimed to fully preserve the resolution provided by the μ CT imaging modality. In the CNN architecture design, we had to keep in mind the large size of the segmented images, which is over 1000 voxels in all three dimensions. Utilising a fully 3-D CNN architecture for the segmentation of image data of this size is not feasible due to memory limitations. A piecewise segmentation of patches extracted from the 3-D volume seems to be a possible solution to this problem; however, even the segmented structure is enormous for a typical segmentation via 3-D CNN (see Suppl. Table S1). The size of the segmented structure is in each case over $700 \times 1000 \times 600$ pixels. By extracting patches from the whole 3-D volume, much of the global spatial context needed for proper localisation and segmentation of the cartilage would be lost. For these reasons, a slice-by-slice approach to segmentation is the most appropriate. Manual segmentation was performed in the axial slices of the whole 3-D volume, and we thus decided to utilise the axial plane for training and subsequent inference of the developed segmentation model.

We use the basic U-Net shape; however, the input is downsampled only four times in the original implementation¹². To compensate for the large image size, two additional levels were added to the architecture. This means that the input, set to a fixed size of 1792×1280 pixels, is downsampled a total of 6 times to the size of

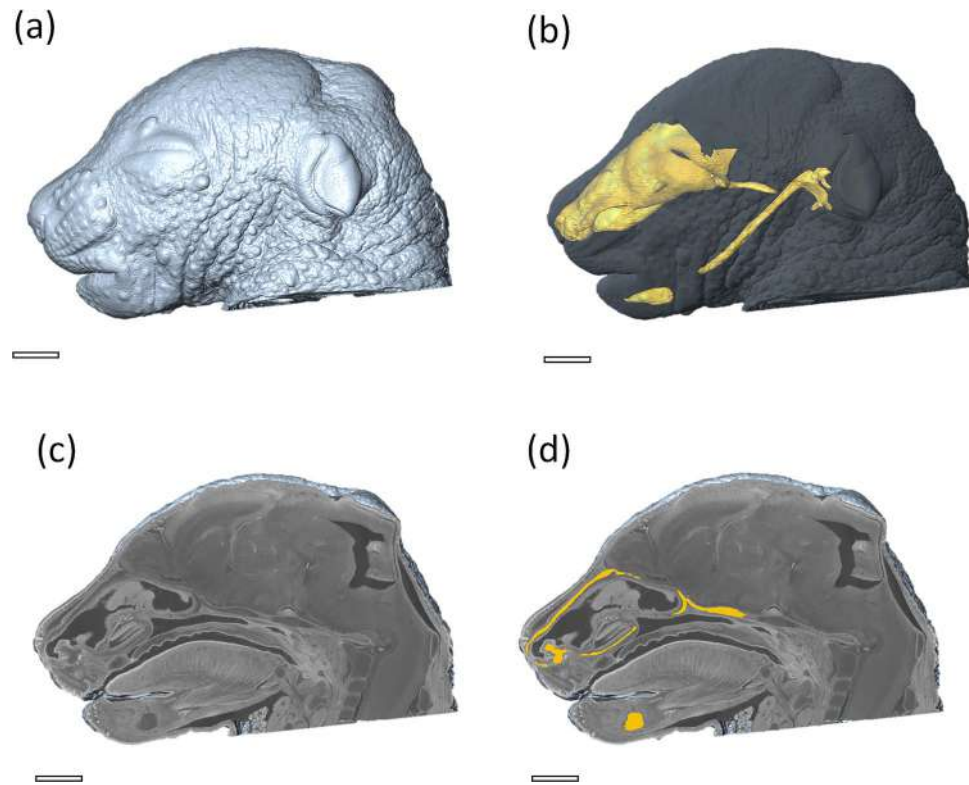


Figure 2. Visualisation of the segmented structure of interest in the context of the mouse embryo head. **(a)** 3-D rendering of the embryo head, **(b)** 3-D rendering of craniofacial cartilage tissue (yellow) in the context of the whole embryo head (grayscale), **(c)** clipping plane through the 3-D rendering showing the tomographic data, and **(d)** yellow showing the manually segmented craniofacial cartilage tissue. Scale bar 1 mm.

28 × 20 pixels in the lowest level of the network. This makes the network very deep, and issues such as the vanishing gradient could significantly hinder the training of the model. For this reason, the architecture was enhanced by utilising residual blocks that had been first proposed in²⁰. Residual blocks are a structure consisting of stacked layers utilised in CNNs. They improve the information flow through the deep network, prevent vanishing gradient problems, and improve the network's training²⁸. Three types of residual blocks are used in the architecture (see Fig. 3). A downsampling residual block implements dimensionality reduction in the encoding part of the CNN architecture. Strided convolutional layers achieve dimensionality reduction in the convolutional path of the residual block and max-pooling in the identity path of the residual block. Because in U-Net-based architectures, the number of filters increases twice with each dimension reduction level, it is also necessary to increase the number of filters in the identity part of the residual block. This is performed by a 1 × 1 convolutional layer with the required number of filters to perform the addition of the feature maps from the convolutional and identity paths. Another type of residual block in the proposed architecture is a so-called flat block that outputs feature maps with the same dimensions as the output. The third type of residual block utilised in the proposed architecture is an upsampling block. The upsampling block is a residual equivalent of the transposed convolutional layers of the decoder part of the basic U-Net architecture. The upsampling is performed by transpose convolutional layers in the convolutional path of the residual block and by nearest neighbor interpolation in the identity path. The 1 × 1 convolutional layer in the identity path ensures the correct number of feature maps for the addition with the feature maps from the convolutional path. As in any U-Net-based architecture, feature maps from the encoder are concatenated with the decoder feature maps. The overall CNN architecture is visualised in Fig. 3.

Furthermore, we used the SELU activation function²⁹ with LeCun normal weight initialisation in the proposed CNN architecture³⁰. SELU is designed by its authors to have a so-called self-normalizing property which makes the training of the network more stable implying better network's performance. A great advantage of SELU over the other normalization techniques is no need for hyperparameter tuning as well as no dependency on the mini-batch size. To support weight updates even in the deepest part of the network, additional paths were added to each upsampling block: a 1 × 1 convolution layer with a sigmoidal activation function followed by a basic upsampling layer that transforms the feature map dimension to the dimensions of the ground-truth mask. The losses were weighed by the following weights from the deepest layer to the shallowest: 0.03, 0.05, 0.08, 0.12, 0.15, 0.2, and 0.37, with the largest weights being given to the layers with the feature maps of largest dimensions.

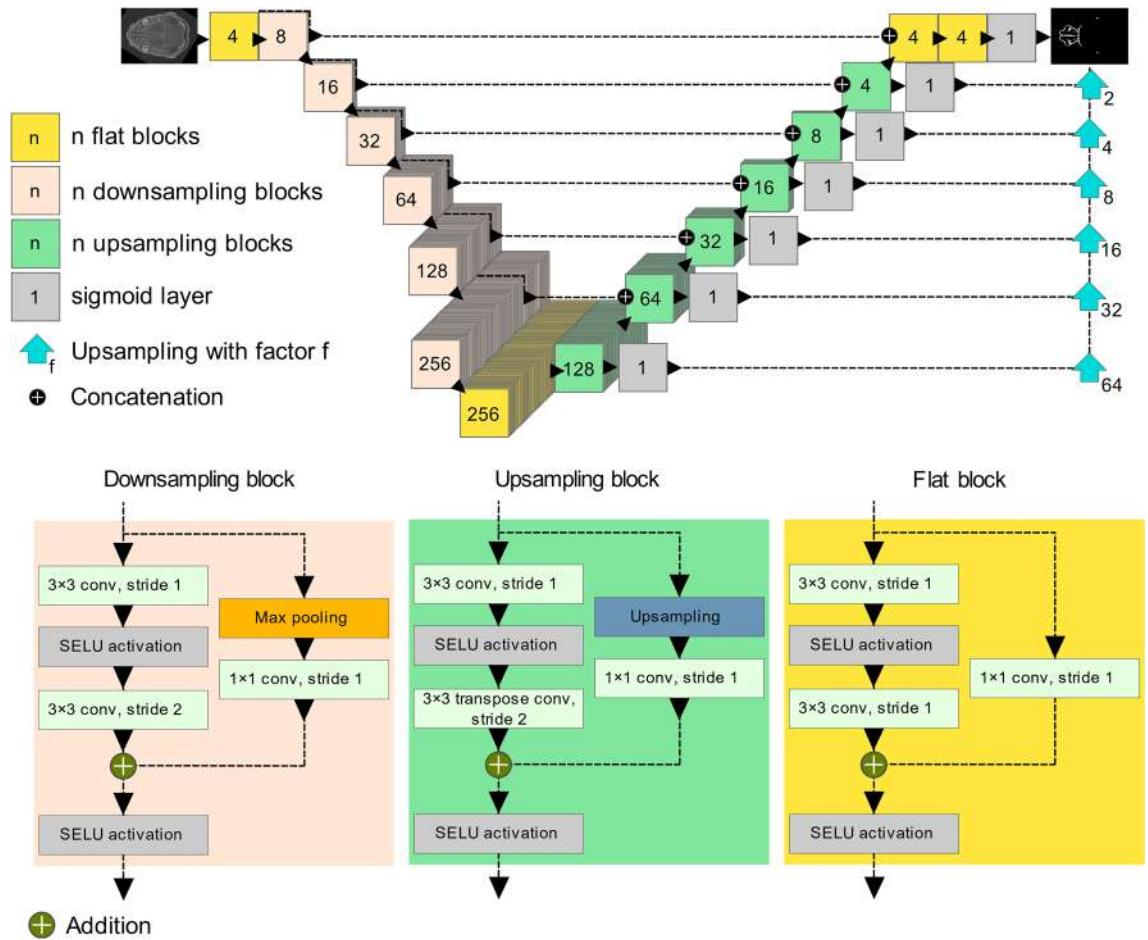


Figure 3. The proposed CNN architecture for segmentation of nasal capsule cartilage.

	Parameter range
Random rotation	- 10° to 10°
Vertical flipping	-
Random gamma transform	0.9-1.1
Random elastic	-
Random scaling	0.9-1.1

Table 1. Augmentation parameters.

Experiments

Implementation. The proposed CNN was implemented in the programming language Python (version 3.7.9) using the library Keras³¹ (version 2.3.1) with the TensorFlow backend³² (version 2.1.0). CUDA (version 10.1) and CUDnn (version 7.6.5) were used for GPU acceleration of the training and inference process. NumPy³³, scikit-image³⁴ and Pillow libraries were used for manipulating and transforming the image data.

Data preparation. As the proposed CNN architecture requires a fixed size input, the CT images' dimensions and corresponding manual segmentation masks had to be unified. First, we rescaled the data to a unified voxel size of 6 μm by bilinear interpolation. A suitable dimension size proved to be 1792 × 1280 pixels. This value allowed us to crop the tomographic cross-sections in the case of larger datasets without any loss of relevant information. In the cases where one or both dimensions of the data were smaller than this value, the image data were padded with zero-value pixels. Such prepared data were standardised to 0 mean and standard deviation 1.

Training. For better generalisation of the trained segmentation model, a custom augmentation procedure is proposed. The augmentation consists of random rotation, vertical flipping, elastic deformation, gamma transform with random parameter gamma, and random scaling (see Table 1) for the transform parameters). Each training image has a certain probability of undergoing two consecutive augmentation transforms. These prob-

Transform 1	Transform 2					
	Random rotation	Vertical flipping	Random gamma	Random elastic	Random scaling	No transform
Random rotation	0.01	0.02	0.01	0.03	0.02	0.01
Vertical flipping	0.02	0.04	0.02	0.06	0.04	0.02
Random gamma	0.01	0.02	0.01	0.03	0.02	0.01
Random elastic	0.03	0.06	0.03	0.09	0.06	0.03
Random scaling	0.02	0.04	0.02	0.06	0.04	0.02
No transform	0.01	0.02	0.01	0.03	0.02	0.01

Table 2. Augmentation transform probabilities.

abilities are shown in Table 2. The network is trained with the Adam optimisation algorithm³⁵ with an initial learning rate of $1e-4$, and AMSgrad enabled to improve convergence³⁶. Dice loss is utilised³⁷. The CNN is trained with a batch size of 4. A nVidia Quadro P5000 with 16 GB of graphical memory was utilised to train the CNN on a system equipped with 512 GB of RAM and an Intel® Xeon® Gold 6248R CPU.

Performance evaluation. The performance of the proposed segmentation method was evaluated using the Dice similarity coefficient (DSC). DSC is a generally utilised binary segmentation mask overlap measure. Its maximum value is 1, which signifies a complete overlap of the evaluated segmentation mask and the ground-truth mask³⁸. The equation for computing the Dice coefficient from true positive (TP), true negative (TN), false positive (FP) and false negative (FN) segmented pixels can be seen in Eq. 1. A sevenfold cross-validation was performed to evaluate the accuracy of segmentation with the proposed model. This means that the model was trained on 12 samples and evaluated on the remaining two.

$$DSC = \frac{2 * TP}{2 * TP + FP + FN} \quad (1)$$

Ablation experiment. To show the benefits of the proposed modifications to the base U-Net-shaped CNN architecture, we performed an ablation experiment. For each individual ablation, we eliminated one of the proposed modifications from the CNN segmentation methodology. These modifications are: residual blocks, deep supervision, SELU activation, increased depth and the proposed augmentation techniques. Visualisations of the CNN architectures used for the ablation experiment can be found in the Supplementary material S1 of this work (supplementary Figs. S1–S4). To make the ablation experiment less time demanding, only a subset of the training database is used for the experiments. Every 200th tomographic cross-section not containing cartilage and every 30th cross-section from the region containing cartilage tissue is used from each sample. Other than these modifications to the methods, the remaining hyperparameters are kept identical to the hyperparameters outlined in the Training section of this chapter. We again performed the ablation experiment as a sevenfold cross-validation, where the models were trained on 12 samples and validated on the remaining two. The model from the epoch where the lowest validation loss was achieved was used for the cross-validation.

Wall thickness analysis. Wall thickness analysis was performed using VG Studio MAX 3.5 software (Volume Graphics GmbH, Germany). The wall thickness for each voxel was calculated as the diameter of the largest inscribed sphere to the volume, which still contains the center position of the voxel.

Results and discussion

The results of the sevenfold cross-validation are summarised in Table 3. The results of the segmentation were compared with the ground-truth segmentation masks via the Dice coefficient. The results are also visualised in the form of a boxplot (Fig. 4a), where each point represents the segmentation accuracy of a 3-D segmented sample.

According to the Dice coefficient, the median segmentation accuracy is 84.44%, with the largest outlier being Sample 4, with a segmentation accuracy of merely 55.68%. As shown in Fig. 1, Sample 4 was improperly stained during the sample preparation procedure, and the proposed segmentation model could not correctly identify the necessary features for the accurate segmentation of the cartilage. It is thus essential that the staining protocol performed prior to the μ CT measurement be followed correctly for the segmentation model to perform well. Sample 10 is a severely affected mutant embryo, significantly different from the rest of the available database. It was included in the training and evaluation of CNN to show its capabilities of processing even morphologically different samples. The DSC of 71.16% is relatively low compared to the remaining database, and more scans of mutant mouse embryos should be included in the training database to improve the model segmentation accuracy of this type of sample. The moderately changed mutant embryo (Sample 6) was segmented with an above-average accuracy of 86.67%. See Fig. 5a for a visualisation of the difference in the segmentation accuracy in genetically modified embryos. Figure 5b then shows an example of both manual and automatic segmentation in a selected tomographic cross-section of Sample 8.

We also evaluated the proposed method in comparison with 100 randomly selected tomographic slices from the validation fold of the available database, segmented by a second independent operator to see if the proposed

Sample code	Dice coefficient [%]	Comment
Sample 1	82.8282	Control
Sample 2	78.8173	Control
Sample 3	79.3120	Control
Sample 4	55.6860	Improper staining
Sample 5	91.6862	Control
Sample 6	86.6735	Genetically modified
Sample 7	87.7789	Genetically modified
Sample 8	91.7748	Control
Sample 9	84.3186	Control
Sample 10	71.1617	Genetically modified
Sample 11	92.0235	Control
Sample 12	79.8854	Control
Sample 13	84.4525	Control
Sample 14	90.6867	Control

Table 3. Results of the sevenfold cross-validation.

CNN behaves similarly to an independent human operator performing the manual segmentation. The segmentation was performed the same way as the segmentation of the ground-truth data: Avizo (Thermo Fisher Scientific, USA) was used. Both the CNN segmentation and the independent operator segmentation were compared with the ground-truth segmentation masks using the Dice coefficient. The results of this experiment are summarised in Fig. 4b in the form of a boxplot, where each data point represents one segmented tomographic slice. The median accuracy of the automatic CNN segmentation with respect to the ground-truth data was 87.43%, and the accuracy of the second operator with respect to the ground-truth data was 88.14%. There was also a moderate positive correlation between the values (Spearman coefficient 0.59, $p < 0.01$). This shows that the CNN operates within the scope of the intraoperator variability. As such, the segmentation error might be caused partially by the uncertainty of the manual segmentation in some regions of the cartilage.

The performance of the trained segmentation model was also evaluated on samples from different developmental stages that were not present in the training database (specifically embryos from the 12th to 18th day of their development). The accuracy of such segmentation was 86% (DSC) for the sample on the 18th day of development (E18.5) and 72% for the scan of embryos on the 16th day of development (E16.5). We performed Theiler staging of the embryos in this external dataset.^{25,39} Theiler stages objectively evaluate the development of the embryos based on their morphology independently on their gestational age. The Theiler stages for both the 17 day old embryo and 18 day old embryo is the same (Theiler stage 26), with 16 day old embryo being only 1 stage lower (Theiler stage 25). These samples were not involved in the development of the proposed method and these results thus show, that the proposed methodology performs well even on an external test set of embryos with comparable developmental stages. When the network is applied to earlier stages, the segmentation accuracy decreases rapidly. In the developmental stages from 12 to 13 days, when the cartilage is not fully developed and mesenchymal condensations are still present, the trained CNN fails completely (see Fig. 4c). Including other developmental stages in the training database might improve the robustness of the method; however, using the same segmentation model to segment the images of embryos in earlier developmental stages than 14 days after conception, before the cartilage is formed, seems not feasible.

As a further qualitative check of the segmentation accuracy, we performed a wall thickness analysis of the segmented structure for both the 3-D model created by manual segmentation and the 3-D model created by the proposed CNN (Fig. 6). Wall thickness analysis is a routine follow-up analysis to show additional developmental changes. Figure 6 shows the wall thickness analysis of Sample 8. As the wall thickness histogram (c) in Fig. 6 shows, the results of wall thickness analysis performed on both 3-D models are very similar. This is also demonstrated by the very high positive correlation of the wall thickness distributions (Spearman coefficient 0.98, $p < 0.01$). Slight differences may be caused by the step artefact produced by the manual segmentation performed only in a single plane. Even though the CNN also performs segmentation in a single plane, its predictions are much smoother.

We performed an ablation experiment to evaluate the contribution of each proposed modification to the CNN architecture and to the training strategy towards the total nasal capsule cartilage segmentation accuracy. Here we removed the modifications from the complete architecture and one by one evaluated the segmentation accuracy of each model by sevenfold cross-validation. The results of this experiment can be seen in Fig. 7. The proposed methodology employing increased depth of the CNN, deep supervision, SELU activations, residual blocks and the proposed image augmentation strategy provides the highest median segmentation accuracy: 74.58% (DSC). Note that this number is significantly lower than the median segmentation accuracy presented in Fig. 4a. This lower segmentation accuracy is caused by training the CNNs in the ablation experiment on a reduced training set of images to make the ablation experiment less time-demanding. Deep supervision seems to provide only minor improvement to the total segmentation accuracy, as the median segmentation accuracy is lower only by ~2% (DSC) when training without deep supervision. Training models without utilising the residual blocks or the proposed augmentation procedure sees a more significant drop in the cross-validation

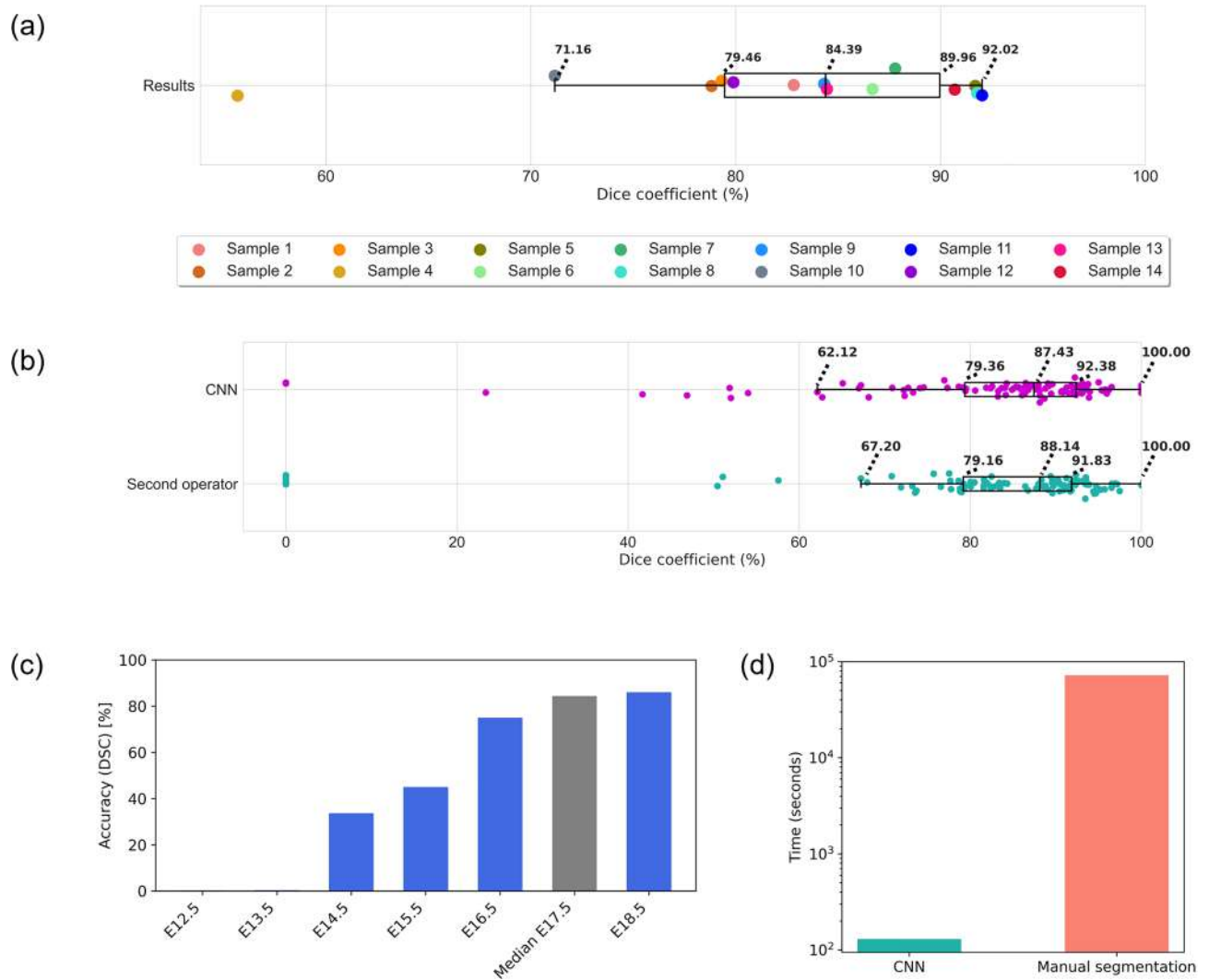


Figure 4. Evaluation of the segmentation accuracy of the proposed image segmentation model. **(a)** Segmentation accuracy boxplot. The box extends from the first quartile $Q1$ to the third quartile $Q3$, and its length represents the interquartile range ($IQR = Q3 - Q1$). The length of whiskers is the largest and smallest data point lying within the range defined by $1.5 \cdot IQR$ subtracted from $Q1$ and added to $Q3$. The line inside the box represents the median. **(b)** Time requirements comparison of the CNN and manual segmentation for segmentation of one mouse embryo scan. **(c)** The accuracy of segmentation with the CNN trained on the available database of 17-day-old embryos applied for segmentation of the nasal capsule in images of mouse embryos in other developmental stages. **(d)** Time requirements comparison of the CNN and manual segmentation for the segmentation of one mouse embryo scan.

accuracy to the median of $\sim 67\%$ (DSC). This justifies the use of residual blocks to improve the training of the CNN. The segmentation accuracy of the CNN without the increased depth drops even further to the median of 63.52% (DSC). This decrease in segmentation accuracy is expected as the shallow network has fewer trainable parameters and cannot benefit from the abstract features extracted in the deep layers of the proposed CNN. Finally, the most significant drop in accuracy is observed when not substituting the ReLU activations for SELU activations. This shows that the reported self-normalizing property of the SELU activation function dramatically improves the final segmentation accuracy and generalisability of the trained image segmentation model. This makes SELU an extremely valuable addition to the CNN architecture.

As in many supervised machine learning application tasks, the performance and generalisability of the trained model are closely tied to the distribution of the training database. In our work, the proposed CNN was trained exclusively on data originating from a single μ CT scanner with the samples measured under a unified methodology (sample staining, scanning parameters, resolution, image size). The methodology described here should be followed as closely as possible to achieve segmentation performance comparable to the results shown in this work. We artificially enlarged the training database by applying selected data augmentation techniques; however, despite this fact, a decrease in performance should be expected when deviating from the outlined data acquisition methodology. This decrease in segmentation accuracy was demonstrated in the case of Sample 4, where the staining of the sample is significantly different from the rest of the database. Expanding the training database

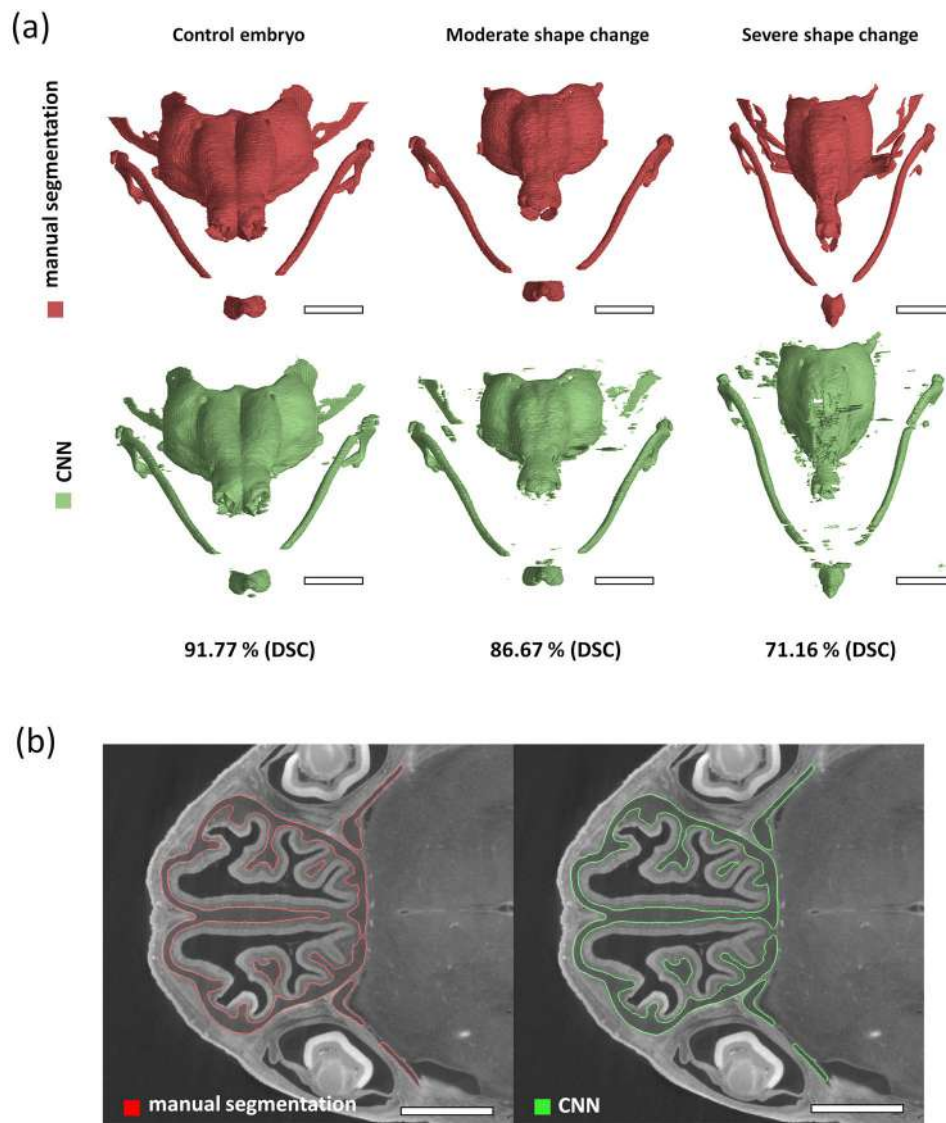


Figure 5. Visualisation of the proposed segmentation model's output together with the ground-truth data. (a) Comparison of the nasal capsule 3-D renders created by manual segmentation (red) and the CNN (green). Note the decrease in the segmentation accuracy in samples with significantly changed morphology due to genetic modifications. Scale bar 1 mm. (b) Visualisation of the proposed segmentation (green contour) in a selected tomographic cross-section of Sample 8 compared to manual segmentation (red contour). Scale bar 1 mm.

by adding a more significant number of samples coming from different CT systems and obtained under different conditions concerning sample preparation and measurement parameters could dramatically improve the generalizability of the segmentation model. Such a database is unfortunately not yet available for this particular segmentation problem. It would, however, be highly beneficial to utilise the weights of the trained CNN as a starting point for training a nasal capsule cartilage segmentation model on new data obtained with significantly different parameters, as the basic extracted features used to predict the cartilaginous nasal capsule will always be similar. This type of transfer learning could significantly improve the convergence of the segmentation model to an optimum with a lower training time.

Conclusion

In this work, we have demonstrated a highly efficient and time-saving application of a custom U-Net-based CNN for the segmentation of cartilaginous tissue in μ CT images of mouse embryos. We employed this architecture and trained it on a database of 14 3-D manually segmented μ CT scans. It has been proven that a highly accurate, fully automatic segmentation (84.44% overlap with ground truth according to the Dice coefficient) of the complex cartilaginous structures in a developing mouse head is achievable via deep learning and will be vital for accelerating research on mammalian chondrocranium. One of the primary motivations for this work was to reduce the time required to process new data by employing a fully automatic segmentation procedure

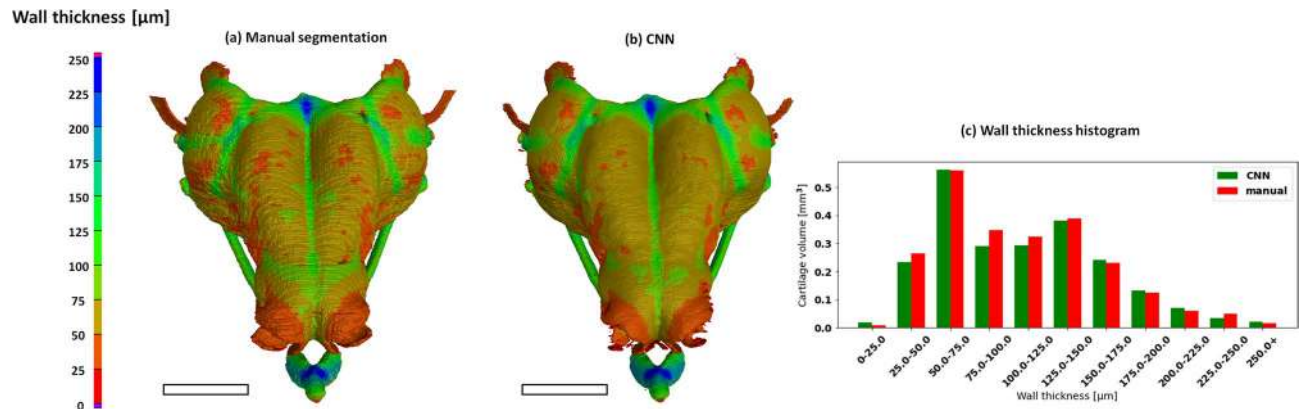


Figure 6. Visualisation of wall thickness analysis applied to the 3-D model created by manual segmentation (a) and by the proposed automatic segmentation (b). Scale bar 1 mm. (c) The histogram of the wall thickness distribution.

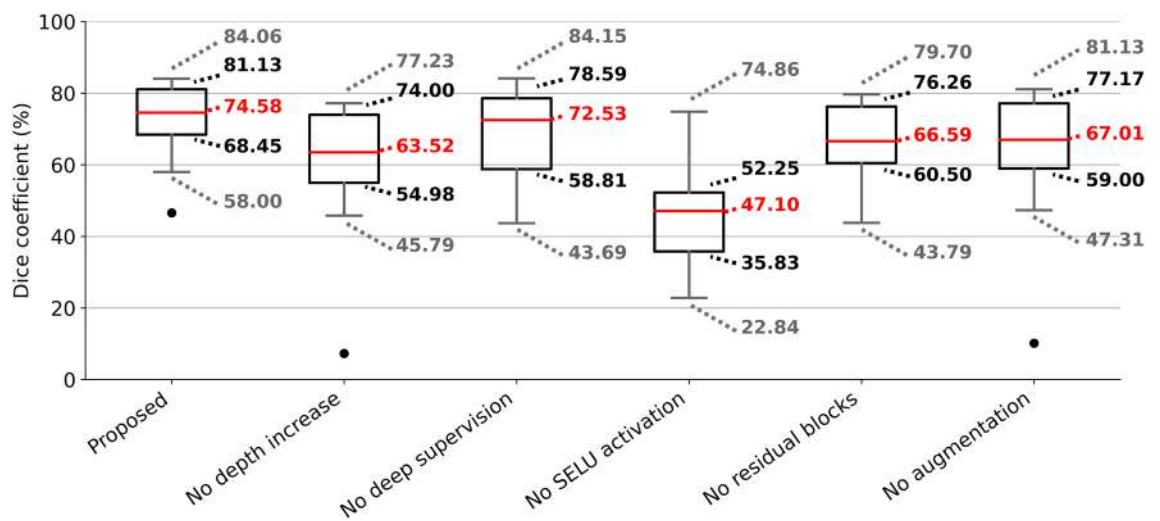


Figure 7. Results of the ablation experiment. Each box represents sevenfold cross-validation segmentation accuracy of a CNN trained without one of the modification to the architecture or training strategy employed in this work. The boxes extend from the first quartile Q1 to the third quartile Q3, and its length represents the interquartile range ($IQR = Q3 - Q1$). The length of whiskers is data largest and smallest data point lying within the range defined by $1.5 \cdot IQR$ subtracted from Q1 and added to Q3. Outliers are marked as a black dot.

instead of the time-demanding manual segmentation. Training of the model on 12 samples for 50 epochs took approximately 27 h. The model is then able to segment a new sample in approximately 130 s (Fig. 4d), depending on the number of tomographic cross-sections present and on available hardware. This segmentation model will be further used to segment new samples, including models of major congenital craniofacial and skeletal diseases. It is possible to obtain an even larger training database by manual corrections of the initial segmentation results and make the final model even more robust.

Data availability

Due to the training data coming from multiple sources and studies, it is currently not feasible to share the complete training and testing database; however, a subset of the whole database was published as an X-ray microtomography-based atlas of mouse embryo cranial development and can be accessed at²⁶. The trained models and accompanying code can be found in a public GitHub repository: <https://github.com/janmatula/deep-mouse-cartilage>.

Received: 8 December 2021; Accepted: 3 May 2022

Published online: 24 May 2022

References

1. Metscher, B. D. MicroCT for developmental biology: A versatile tool for high-contrast 3D imaging at histological resolutions. *Dev. Dyn.* <https://doi.org/10.1002/dvdy.21857> (2009).

2. Kaucka, M. *et al.* Oriented clonal cell dynamics enables accurate growth and shaping of vertebrate cartilage. *Elife* <https://doi.org/10.7554/eLife.25902> (2017).
3. Kaucka, M. *et al.* Signals from the brain and olfactory epithelium control shaping of the mammalian nasal capsule cartilage. *Elife* <https://doi.org/10.7554/eLife.34465> (2018).
4. De Bakker, B. S. *et al.* An interactive three-dimensional digital atlas and quantitative database of human development. *Science* (80-). (2016). <https://doi.org/10.1126/science.aag0053>.
5. Powell, K. A. & Wilson, D. 3-dimensional imaging modalities for phenotyping genetically engineered mice. *Vet. Pathol.* <https://doi.org/10.1177/0300985811429814> (2012).
6. Karaplis, A. C. Embryonic Development of Bone and Regulation of Intramembranous and Endochondral Bone Formation. in *Principles of Bone Biology, Two-Volume Set* (2008). <https://doi.org/10.1016/B978-0-12-373884-4.00025-2>.
7. Vanhoenacker, F. M., Van Hul, W., Gielen, J. & De Schepper, A. M. Congenital skeletal abnormalities: An introduction to the radiological semiology. *Eur. J. Radiol.* [https://doi.org/10.1016/S0720-048X\(01\)00398-9](https://doi.org/10.1016/S0720-048X(01)00398-9) (2001).
8. Neben, C. L., Roberts, R. R., Dipple, K. M., Merrill, A. E. & Klein, O. D. Modeling craniofacial and skeletal congenital birth defects to advance therapies. *Hum. Mol. Genet.* <https://doi.org/10.1093/hmg/ddw171> (2016).
9. Brommage, R. & Ohlsson, C. High fidelity of mouse models mimicking human genetic skeletal disorders. *Front. Endocrinol.* <https://doi.org/10.3389/fendo.2019.00934> (2020).
10. McBratney-Owen, B., Iseki, S., Bamforth, S. D., Olsen, B. R. & Morriss-Kay, G. M. Development and tissue origins of the mammalian cranial base. *Dev. Biol.* <https://doi.org/10.1016/j.ydbio.2008.07.016> (2008).
11. Hatt, M., Parmar, C., Qi, J. & El Naqa, I. Machine (Deep) learning methods for image processing and radiomics. *IEEE Trans. Radiat. Plasma Med. Sci.* <https://doi.org/10.1109/trpms.2019.2899538> (2019).
12. Ronneberger, O., Fischer, P. & Brox, T. U-net: Convolutional networks for biomedical image segmentation. *Lect. Notes Comput. Sci.* https://doi.org/10.1007/978-3-319-24574-4_28 (2015).
13. Dong, H., Yang, G., Liu, F., Mo, Y. & Guo, Y. Automatic brain tumor detection and segmentation using U-net based fully convolutional networks. *Commun. Comput. Inf. Sci.* https://doi.org/10.1007/978-3-319-60964-5_44 (2017).
14. Degenhardt, K., Wright, A. C., Horng, D., Padmanabhan, A. & Epstein, J. A. Rapid 3D phenotyping of cardiovascular development in mouse embryos by micro-CT with iodine staining. *Circ. Cardiovasc. Imaging* <https://doi.org/10.1161/CIRCIMAGING.109.918482> (2010).
15. Pai, V. M. *et al.* Coronary artery wall imaging in mice using osmium tetroxide and micro-computed tomography (micro-CT). *J. Anat.* <https://doi.org/10.1111/j.1469-7580.2012.01483.x> (2012).
16. Kaiser, J. *et al.* Use of micro computed-tomography and 3D printing for reverse engineering of mouse embryo nasal capsule. *J. Instrum.* **11**, C03006–C03006 (2016).
17. Norman, B., Pedito, V. & Majumdar, S. Use of 2D U-net convolutional neural networks for automated cartilage and meniscus segmentation of knee MR imaging data to determine relaxometry and morphometry. *Radiology* <https://doi.org/10.1148/radiol.2018172322> (2018).
18. Zhu, Q., Du, B., Turkbey, B., Choyke, P. L. & Yan, P. Deeply-supervised CNN for prostate segmentation. *Proc. Int. Joint Conf. Neural Netw.* <https://doi.org/10.1109/IJCNN.2017.7965852> (2017).
19. Rytky, S. J. O. *et al.* Automated analysis of rabbit knee calcified cartilage morphology using micro-computed tomography and deep learning. *J. Anat.* <https://doi.org/10.1111/joa.13435> (2021).
20. He, K., Zhang, X., Ren, S. & Sun, J. Deep residual learning for image recognition. *Proc. IEEE Comput. Soc. Conf. Comput. Vis. Pattern Recognit.* <https://doi.org/10.1109/CVPR.2016.90> (2016).
21. Jia Deng *et al.* ImageNet: A large-scale hierarchical image database. in (2009). <https://doi.org/10.1109/cvprw.2009.5206848>.
22. Léger, J., Leyssens, L., De Vleschouwer, C. & Kerckhofs, G. Deep learning-based segmentation of mineralized cartilage and bone in high-resolution micro-CT images. *Lect. Notes Comput. Vis. Biomech.* https://doi.org/10.1007/978-3-030-43195-2_12 (2020).
23. Zheng, H. *et al.* Cartilage segmentation in high-resolution 3d micro-ct images via uncertainty-guided self-training with very sparse annotation. *Lect. Notes Comput. Sci.* https://doi.org/10.1007/978-3-030-59710-8_78 (2020).
24. Metscher, B. D. Micro CT for comparative morphology: Simple staining methods allow high-contrast 3D imaging of diverse non-mineralized animal tissues. *BMC Physiol.* <https://doi.org/10.1186/1472-6793-9-11> (2009).
25. Matula, J. *et al.* X-ray microtomography-based atlas of mouse cranial development. *GigaScience* **10**, (2021).
26. Matula, J. *et al.* Supporting data for 'X-ray microtomography-based atlas of mouse cranial development'. *GigaScience Database* (2021).
27. Feldkamp, L. A., Davis, L. C. & Kress, J. W. Practical cone-beam algorithm. *J. Opt. Soc. Am. A* <https://doi.org/10.1364/josaa.1.000612> (1984).
28. Khanna, A., Londhe, N. D., Gupta, S. & Semwal, A. A deep Residual U-Net convolutional neural network for automated lung segmentation in computed tomography images. *Biocybern. Biomed. Eng.* <https://doi.org/10.1016/j.bbe.2020.07.007> (2020).
29. Klambauer, G., Unterthiner, T., Mayr, A. & Hochreiter, S. Self-normalizing neural networks. in *Advances in Neural Information Processing Systems* (2017).
30. LeCun, Y. A., Bottou, L., Orr, G. B. & Müller, K. R. Efficient backprop. *Lect. Notes Comput. Sci. (including Subser. Lect. Notes Artif. Intell. Lect. Notes Bioinformatics)* (2012). https://doi.org/10.1007/978-3-642-35289-8_3.
31. Chollet, F. Keras: The Python Deep Learning library. *Keras.Io* (2015).
32. Martin, A., Paul, B., Jianmin, C. & Zhifeng, C. TensorFlow: A system for large-scale machine learning. *OSDI* **16**, 265–283 (2016).
33. Harris, C. R. *et al.* Array programming with NumPy. *Nature* <https://doi.org/10.1038/s41586-020-2649-2> (2020).
34. Van Der Walt, S. *et al.* Scikit-image: Image processing in python. *PeerJ* <https://doi.org/10.7717/peerj.453> (2014).
35. Kingma, D. P. & Ba, J. L. Adam: A method for stochastic optimization. in *3rd International Conference on Learning Representations, ICLR 2015—Conference Track Proceedings* (2015).
36. Reddi, S. J., Kale, S. & Kumar, S. On the convergence of adam and beyond. *arXiv* (2019).
37. Milletari, F., Navab, N. & Ahmadi, S. A. V-Net: Fully convolutional neural networks for volumetric medical image segmentation. in *Proceedings—2016 4th International Conference on 3D Vision, 3DV 2016* 565–571 (2016). <https://doi.org/10.1109/3DV.2016.79>.
38. Zou, K. H. *et al.* Statistical validation of image segmentation quality based on a spatial overlap index. *Acad. Radiol.* [https://doi.org/10.1016/S1076-6332\(03\)00671-8](https://doi.org/10.1016/S1076-6332(03)00671-8) (2004).
39. Theiler, K. The house mouse. *House Mouse* <https://doi.org/10.1007/978-3-642-88418-4> (1989).

Acknowledgements

We acknowledge CzechNanoLab Research Infrastructure supported by MEYS CR (LM2018110). T.Z. thanks to Grant Agency of the Czech Republic grant 21-05146S. J.K. thanks to the support of grant FSI-S-20-6353. J.M. was financially supported by Grant CEITEC VUT-J-20-6477. M.T. acknowledges the Brno City Municipality as a Brno Ph.D. Talent Scholarship Holder and Martina Roeselova Memorial Fellowship.

Author contributions

J.M.: conceptualisation, methodology, software, formal analysis, investigation, writing—original draft, visualisation, writing—review and editing. V.P.: methodology, software, investigation. J.Š.: conceptualisation, validation. M.T.: validation, data curation, visualisation. T.Z.: conceptualisation, supervision. M.K.: writing—original draft, validation. I.A.: writing—original draft. J.K.: supervision, project administration, funding acquisition.

Funding

This article was funded by Ministerstvo Školství, Mládeže a Tělovýchovy (LM2018110), Vysoké Učení Technické v Brně, (CEITEC VUT-J-20-6477, FSI-S-20-6353) and Grantová Agentura České Republiky (21-05146S).

Competing interests

The authors declare no competing interests.

Additional information

Supplementary Information The online version contains supplementary material available at <https://doi.org/10.1038/s41598-022-12329-8>.

Correspondence and requests for materials should be addressed to J.K.

Reprints and permissions information is available at www.nature.com/reprints.

Publisher's note Springer Nature remains neutral with regard to jurisdictional claims in published maps and institutional affiliations.



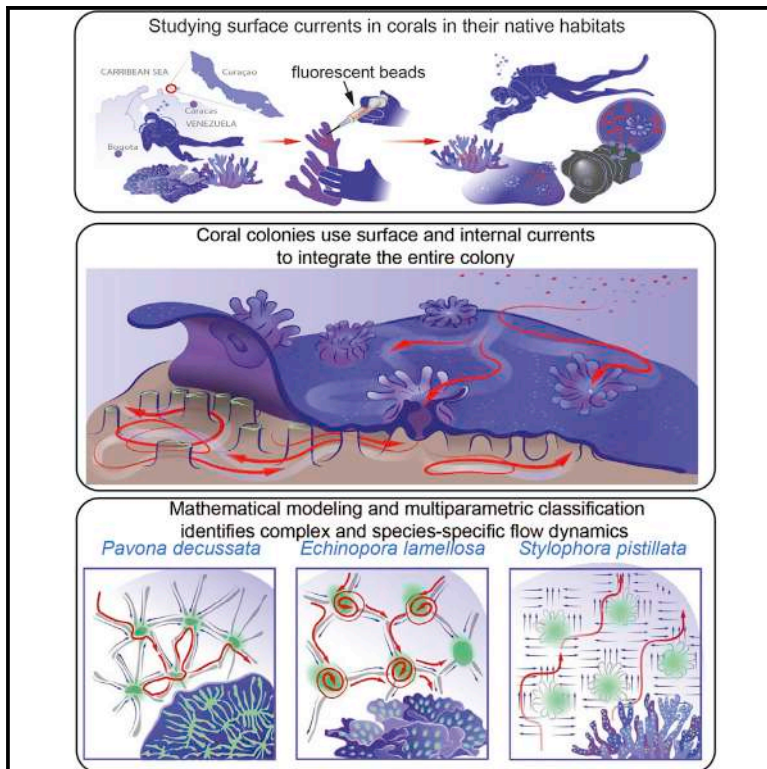
Open Access This article is licensed under a Creative Commons Attribution 4.0 International License, which permits use, sharing, adaptation, distribution and reproduction in any medium or format, as long as you give appropriate credit to the original author(s) and the source, provide a link to the Creative Commons licence, and indicate if changes were made. The images or other third party material in this article are included in the article's Creative Commons licence, unless indicated otherwise in a credit line to the material. If material is not included in the article's Creative Commons licence and your intended use is not permitted by statutory regulation or exceeds the permitted use, you will need to obtain permission directly from the copyright holder. To view a copy of this licence, visit <http://creativecommons.org/licenses/by/4.0/>.

© The Author(s) 2022

Current Biology

Surface flow for colonial integration in reef-building corals

Graphical abstract



Authors

Thibault Boudierlique, Julian Petersen, Louis Faure, ..., Andreas Hellander, John Bythell, Igor Adameyko

Correspondence

igor.adameyko@meduniwien.ac.at

In brief

Boudierlique et al. reveal a new way of integrating individual coral polyps via complex-surface-associated currents. These mucus-containing currents show species-specific patterns connecting individual polyps, removing debris to keep the surface clean and to help polyps to control individual feeding territories on the colony's surface.

Highlights

- Surface-associated currents connect individual polyps in a coral colony
- Surface currents show species-specific topography, complexity, and speed variation
- Mucus plays a role in surface currents to different extent depending on the species
- Complex flow in the gastrovascular system further integrates individual polyps

Article

Surface flow for colonial integration in reef-building corals

Thibault Boudierlique,^{1,15} Julian Petersen,^{1,2,15} Louis Faure,^{1,15} Daniel Abed-Navandi,^{3,15} Anass Bouchnita,^{4,14} Benjamin Mueller,^{5,6} Murtazo Nazarov,⁴ Lukas Englmaier,¹ Marketa Tesarova,⁷ Pedro R. Frade,⁸ Tomas Zikmund,⁷ Till Koehne,² Jozef Kaiser,⁷ Kaj Fried,⁹ Christian Wild,¹⁰ Olga Pantos,¹¹ Andreas Hellander,⁴ John Bythell,¹² and Igor Adameyko^{1,13,16,*}

¹Department of Neuroimmunology, Center for Brain Research, Medical University Vienna, 1090 Vienna, Austria

²Department of Orthodontics, University of Leipzig Medical Center, Leipzig, Germany

³Haus des Meeres, 1060 Vienna, Austria

⁴Department of Information Technology, University of Uppsala, 751 05 Uppsala, Sweden

⁵Department of Freshwater and Marine Ecology, University of Amsterdam, 1090 GE Amsterdam, the Netherlands

⁶CARMABI Foundation, Willemstad, Curaçao

⁷Central European Institute of Technology, Brno University of Technology, Brno, Czech Republic

⁸Natural History Museum Vienna, 1010 Vienna, Austria

⁹Department of Neuroscience, Karolinska Institutet, 17177 Stockholm, Sweden

¹⁰Department of Marine Ecology, Faculty of Biology & Chemistry of Bremen, 28359 Bremen, Germany

¹¹Institute of Environmental Science and Research, 27 Creyke Road, Ila, Christchurch 8041, New Zealand

¹²School of Natural and Environmental Sciences, Newcastle University, NE1 7RU Newcastle Upon Tyne, UK

¹³Department of Physiology and Pharmacology, Karolinska Institutet, 17177 Stockholm, Sweden

¹⁴Present address: Department of Integrative Biology, University of Texas at Austin, Austin, TX 78712, USA

¹⁵These authors contributed equally

¹⁶Lead contact

*Correspondence: igor.adameyko@meduniwien.ac.at

<https://doi.org/10.1016/j.cub.2022.04.054>

SUMMARY

Reef-building corals are endangered animals with a complex colonial organization. Physiological mechanisms connecting multiple polyps and integrating them into a coral colony are still enigmatic. Using live imaging, particle tracking, and mathematical modeling, we reveal how corals connect individual polyps and form integrated polyp groups via species-specific, complex, and stable networks of currents at their surface. These currents involve surface mucus of different concentrations, which regulate joint feeding of the colony. Inside the coral, within the gastrovascular system, we expose the complexity of bidirectional branching streams that connect individual polyps. This system of canals extends the surface area by 4-fold and might improve communication, nutrient supply, and symbiont transfer. Thus, individual polyps integrate via complex liquid dynamics on the surface and inside the colony.

INTRODUCTION

Reef-building corals are made up of a magnitude of individual polyps produced via fissiparity. Benefits of colonial living, in combination with the secretion of a hard calcium carbonate exoskeleton, include efficient propagation and growth, enabling them to utilize space efficiently and overtop competitors.^{1,2} Their three-dimensional framework provides habitat for a plethora of associated species, yet these “ecosystem engineers” and the functions they offer are being threatened by climate change.³ The controlled and flexible interaction between individual polyps is key to the stability and ecological success of their colonial lifestyle that underpins the coral reef ecosystem. As an example, a recent study reported food sharing between neighboring polyps via direct physical interaction.⁴ In another example of colonial integration, the response to physical damage spread through the coral colony with a constant speed, suggesting its nerve-dependent nature and the important role of the nervous system

in inter-polyp communication.^{5,6} Yet little is known about the distribution of resources among polyps within a colony and the physical mechanisms regulating its dynamics. Finally, the resilience of corals to coral bleaching, at least partly, relies on the integration of multiple polyps,⁷ which warrants further studies of the colonial integration and the means connecting individual polyps.

Recently, Shapiro et al. revealed that vertical vortices produced by the ciliated cells on the coral colony surface increase the vertical mass transfer by up to 400%, thus tremendously enhancing gas and nutrient exchange with the surrounding environment.⁸ This vertical mass transfer of water above the coral surface results from the collective activity of multiple individual polyps and likely regulates the thickness/dynamics of the diffusive boundary layer.⁹ Whereas interactions between the coral colony and the surrounding environment are mediated by hydromechanical boundary layers,^{9,10} the physical pathways linking individual polyps within the colony remain enigmatic.

Furthermore, how the vertical mass transfer occurs in relation to the previously discovered surface mucus layer¹¹ stays enigmatic. Indeed, previous studies established an important role of surface mucus in feeding, microbial gardening, defense, and surface cleaning of the coral colony.^{12–14} The previous observations of cilia-based surface-associated flows of the mucus and particles were attributed to the food capture strategies, particularly in corals with short tentacles.¹⁵ At the same time, individual particle trajectories were never evaluated or subjected to a systematic analysis. The complexity of the surface currents, their control, involvement of mucus, and species specificity remain largely unknown.

Hydrodynamics play a role not only in the fluid transport/transfer on the surface but also within the coral colony (inside of the coenosarc). The gastric cavities of individual polyps are interconnected by a system of canals lined by ciliated cells to create an internal waterflow.^{16,17} The direction, complexity, and strength of this flow in the gastrovascular system of reef-building corals remain poorly known.¹⁸

Therefore, to address questions regarding (1) the logic and mechanisms of colony integration via fluid transport in relation to surface-associated mucus and (2) the organization of the internal gastrovascular flow, we applied a new methodology combining mass tracking of fluorescent beads with state-of-the-art computational analysis. We discovered highly complex, branching, and stereotypical horizontal currents on the coral surfaces. The currents connected multiple polyps into coordinated subnetworks within a larger colony and outlined specific territories corresponding to individual polyps. These surface-associated currents appeared species specific and involved surface mucus of different concentrations, which enabled trapping particles and coordinating their movements on the coral surface toward the mouths or toward the edge of the colony. The network of mucus-coordinated horizontal “conveyor belts” assisted the feeding of colonies. Beyond the feeding role, the discovered surface currents transported seawater to the desiccating regions when corals were exposed to air in the lab, suggesting a potential important role during low tide. Finally, we revealed a highly branching and bidirectional pattern of the water flow in the gastrovascular system. The topology of this system appeared to be dependent on the corallum morphology. The modeling revealed that liquid dynamics in a gastrovascular system forms a sharp gradient of particle diffusion resulting in longer detainment of particles near the polyps, suggesting the unexpected tactics of nutrient sharing or spreading symbiont-generated O₂ and chemical signals.

RESULTS

Reef-building corals create complex horizontal currents at their surface *in situ*

Previously, some general movements of water and mucus were observed on the surfaces of corals in the lab environment (*ex situ*).^{15,19} To investigate the patterns and the integrating role of water and mucus movement at the surface of corals and validate their existence in natural conditions, we performed *in situ* experiments with four Caribbean reef-building coral species. These species present different colony morphologies, corallite diameter, and depth ranges on the fringing reef off the CARMABI research station at Curaçao, Southern Caribbean (Data S1A).

To study currents at the surface of the corals in native habitats, we added a solution of concentrated beads at their surfaces and recorded their movements during several diving sessions (Figure 1A). The concentrated beads formed visible streams on top of the coral surfaces (Figures 1B and 1G).

We recorded the spreading of beads on top of several independent *Agaricia lamarcki* (Milne Edwards and Haime, 1851) colonies and found a stereotypic pattern of surface-associated streams (Figures 1B and 1C; Video S1). Beads were moving along the valleys away from the mouths of the individual polyps to the periphery. To understand the logic of this pattern, we applied a 2D mathematical modeling approach based on these observations and in wide viscosity ranges reflecting the potential presence of mucus on the coral surface (Figures 1D and S1). The 2D nature of the model was justified by a highly ordered and symmetrical 3D structure of corallites along the valleys. This model revealed the formation of a low-pressure zone above the polyp (Figures 1D–1G). According to this coherent model, fitting the observed streams, we concluded that the surface-associated currents along the valleys generated a low-pressure zone above the center of the fossa (see Data S2A for coral nomenclature and Figures 1E and 1F for the pressure plotting). This lower pressure resulted in a centrally descending stream bringing new water to the polyp mouths.

Diploria labyrinthiformis (Linnaeus, 1758) also displayed reproducible surface-associated flows of beads within the valley, along the mouth, and numerous polyps located in there (Figure 1H; Video S1). Overall, we observed uniform horizontal flow patterns in coral *in situ*, on the reef. These patterns suggested functional integration of multiple polyps via the flow.

The other two species were *Siderastrea siderea* (Ellis and Solander, 1786) and *Orbicella faveolata* (Ellis and Solander, 1786). Their extended, closely nested polyps were shading the regions spanning between the polyps and were releasing mucus at any disturbance nearby, which precluded the reliable observations of the forming currents.

To study this surface flow phenomenon in more controlled conditions, we attended the Haus des Meeres in Vienna, where we worked with a 50-cm large, 5-year-old colony of *Echinopora lamellosa* (Esper, 1791) within its exposition tank (Figure S2A). The application of beads to several horizontal plates of *E. lamellosa* resulted in the formation of large stable networks of surface-associated streams connecting the mouths of polyps and even transporting beads against gravity within a matter of seconds (Figures S2B–S2E). This formation of surface networks was repeated on different parts of the same large colony as well as on another independently grown large colony of *E. lamellosa* (data are available in an online data repository; see the resource availability section).

Horizontal currents develop under different concentrations of mucus in the surface mucus layer

Next, we addressed how the surface-associated streams coexist with the surface mucus layer in the field. The formation of streams cleaned the surfaces of *A. lamarcki* and *Orbicella faveolata* of free-moving and mucus-coordinated beads within 50 s. The coordination of bead movement by mucus was evident by the formation of mucus strings and filaments. Only small patches

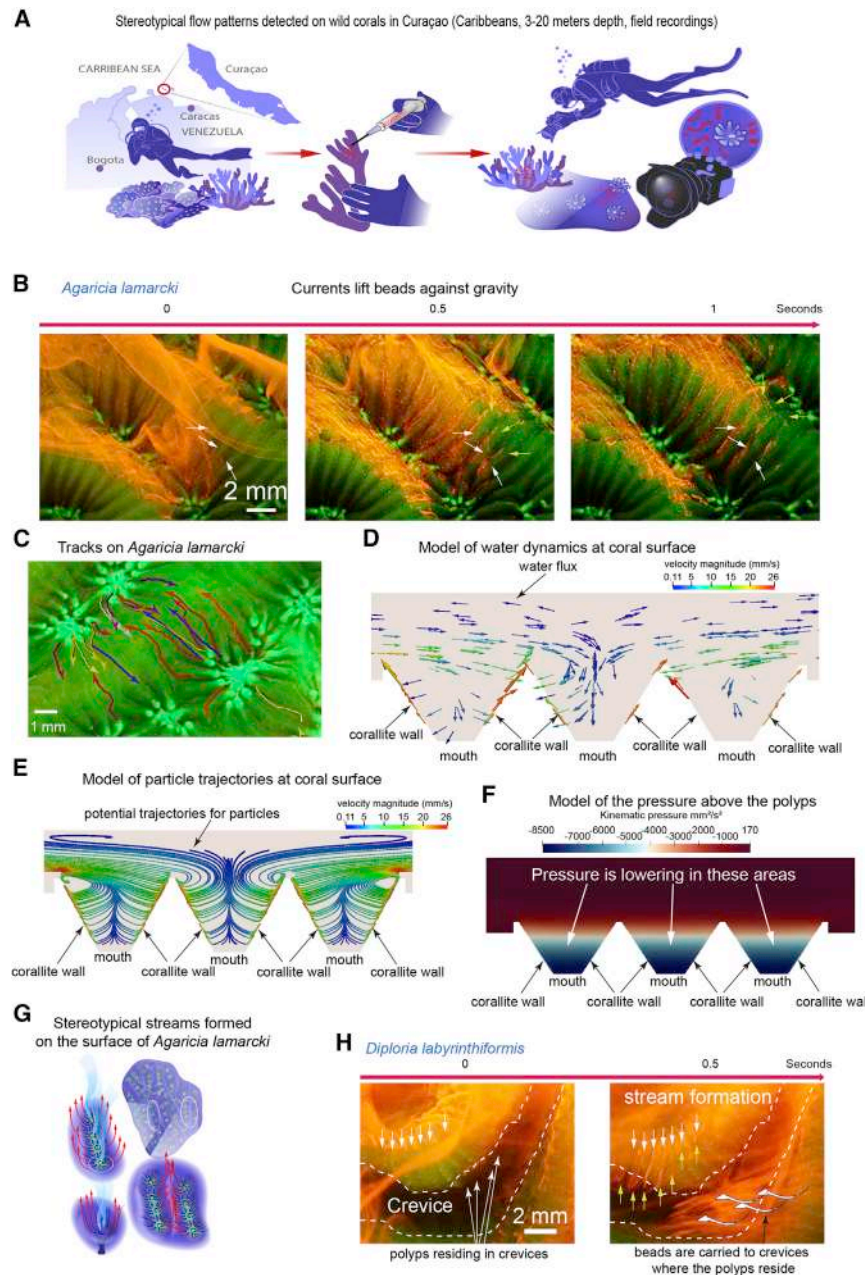


Figure 1. Scleractinian corals create intense currents at their surface

(A) Experimental design of field experiment. (B) Microbeads climb the walls surrounding the mouths of the polyps in an *A. lamarcki* ($n = 8$ colonies). White arrowheads, bead position at the beginning of the sequence; yellow arrowheads, bead position at 0.5 or 1 s. (C) Reconstruction of bead trajectories at the surface of *A. lamarcki*; each vector represents the trajectory of one bead. (D) Mathematical model of the water flux at the surface of the corals. (E) Mathematical model of the potential trajectories of particles. (F) Mathematical model of the kinematic pressure above the polyps. Colors represent the values of pressure. Note the lower pressure zones above the polyps. (G) Schematic model of the streams formed by the coral activity (red) and the resulting currents (white). (H) Creation of streams at the surface of *D. labyrinthiformis* ($n = 5$ colonies). White arrowheads, bead position at the beginning of the sequence; yellow arrowheads, bead position after 0.5 s. See also [Figures S1](#) and [S2](#), [Data S1A](#) and [S2](#) (part 1), and [Video S1](#).

E. lamellosa, *Pavona cactus* (Forskål, 1775), and *Montipora foliosa* (Pallas, 1766) colonies grown in large holding tanks ([Data S1B](#)). After lightly brushing the coral surface, we sampled the water/mucus at the brushed area (1–2 mm above the surface) before and after brushing. Before brushing, we found the presence of a mucus layer with higher protein content compared with the surrounding seawater. Brushing induced an efflux of mucus. Mucus concentration returned to the steady-state levels after 2 min ([Figures 2E–2G](#)), with the exception of *M. foliosa*, where the high mucus concentration remained elevated for more than 30 min ([Figure 2G](#)). Mathematical

of mucus-trapped beads persisted longer than a minute on the coral surfaces ([Figures 2A, 2B, and 2D](#); [Video S2](#)).

Siderastrea siderea showed a more complex pattern: in locations where most beads were applied, beads were trapped permanently by mucus (longer than 5 min), whereas in the more peripheral locations (receiving less beads), no beads were trapped and surface-associated currents efficiently cleared the surface ([Figures 2C and 2D](#); [Video S2](#)). Accompanying *ex situ* experiments provided similar findings ([Video S3](#)). These results suggest that the amount of mucus varies in different zones of a colony and is dynamically controlled.

Since mucus influenced surface currents, we studied the dynamics of mucus secretion and clearance in a controlled environment. We performed experiments on clonally propagated

modeling showed that different amounts of mucus do not impair the general directions of the flow dynamics but rather impact the speed of the flow ([Figure S1](#)).

Overall, these results show that surface-associated streams *de facto* exist in a range of species and mucus concentrations. This starts from a low mucus content unable to coordinate or trap the beads to complete trapping and immobilization, when the coral is under high stress.

Mucus concentrations and horizontal currents shape feeding strategies in different species

The species-specific stereotypical formation of surface/associated streams, particularly in the context of different mucus content, raised an important question about their functions. Here, we

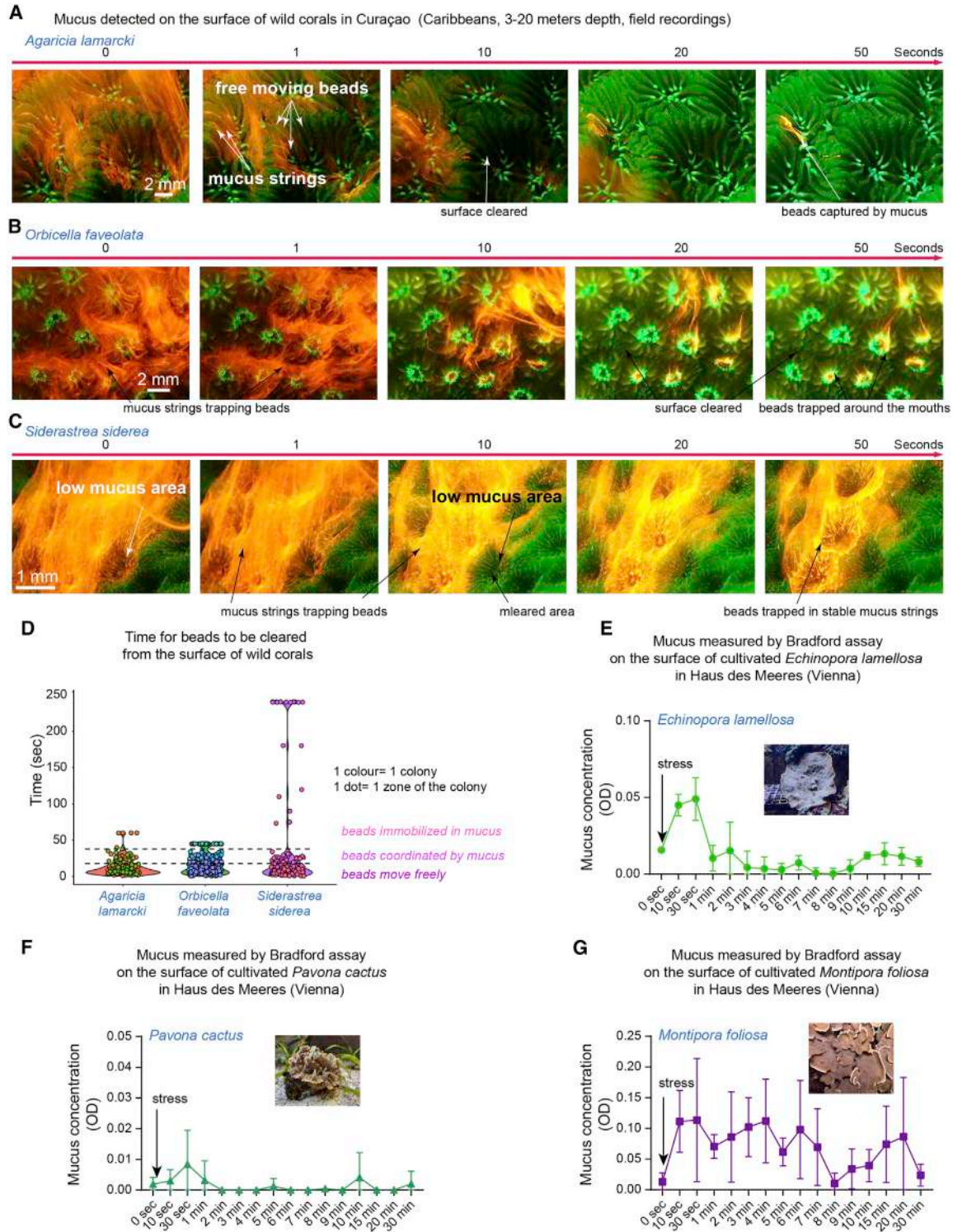


Figure 2. Beads cleared from the surface of corals despite the presence of mucus at their surface

(A) Microbeads trapped by mucus at the surface of an *A. lamarcki* ($n = 8$ colonies).

(B) Microbeads are trapped by mucus at the surface of *O. faveolata*.

(C) Microbeads are fully trapped by mucus at the surface of *S. siderea*. The white arrow shows an area devoid of mucus where the beads are cleared in a few seconds.

(legend continued on next page)

specifically observed the patterns of ingestion of particles in relation with surface mucus. In Curaçao, wild *A. lamarcki* and *O. faveolata* polyps sucked in the thick mucus filaments containing permanently immobilized beads (Figures 3A and 3B; Video S2). In contrast, *E. lamellosa* tested *ex situ* at Haus des Meeres generated surface-associated currents and vortices directing free-moving particles into the mouths of polyps (Figures 3C and 3D; Video S4). Such a way of feeding was not predicted or observed previously.

We next wanted to investigate this further on corals from the great barrier reef. Due to local authority rules “regarding microplastic contamination,” we had to switch to charcoal particles instead of the previously used fluorescent beads. These, however, had the advantage of being observable also under bright light and did not change the behavior relative to the other particles. Interestingly, the application of charcoal particles onto *Acropora muricata* (Linnaeus, 1758) (Data S1C) nubbins revealed an intermediate situation, where particles were coordinated by the surface mucus layer but were still able to move along the surface-associated currents toward the mouths of polyps (Figures 3E and 3F; Video S5). Thus, these findings indicate the existence of different feeding modalities associated with surface streams and varying amounts of mucus either allowing the free movement or coordinating the particles.

Following the concept of Lagrangian coherent structure for identifying patterns of flows from the particle tracking, we summarized the trajectories of charcoal particles at the surface of *A. muricata* into vector fields, which were then used to produce finite-time Lyapunov exponents (FTLEs) ridge visualizations (Figure 3G). FTLE enables the identification of substructures in the flow dynamics including the separation of convective cells or confined moving particles over time as used for atmospheric convections and weather forecast.^{20,21} In other words, FTLE allows the identification of diverging and converging zones from the tracked particles (Data S2A). This analysis showed that every polyp “collects” particles from a specific converging adjacent area via a system of surface streams, and the polyps compete for the particles located at the diverging borders separating the collection areas of neighboring polyps (Figure 3G, right). The dead corals (utilized as controls) did not show any dynamic movement of applied particles (Figure 3H).

This observation was validated using selected clonally propagated in-house grown species presenting diverse macro- and micro-morphology including *Stylophora pistillata* (Esper, 1792), *E. lamellosa*, *P. cactus*, *Pavona decussata* (Dana, 1846), *Montipora efflorescens* (Bernard, 1897), *M. foliosa*, *Merulina scabricula* (Dana, 1846), and *Seriatorpora caliendrum* (Ehrenberg, 1834) (Data S1B). Using multiple healthy coral colonies from 8- to 50-mm diameter, we tracked the movements of fluorescent beads applied to their surfaces under the microscope (Figure 4A; Video S6). The movements of individual beads were converted into trajectories, which were superimposed back onto the corresponding coral surface (Figure 4B; Data S2B).

Similar to the previous approach, we summarized the trajectories into vector fields and generated FTLE ridge visualizations (Figure 4B; Data S2C). The FTLE demonstrated confined flow cells with a flow connecting only one polyp or integrating a group of polyps, allowing them to collect food particles from these areas.

Stable species-specific surface currents integrate polyps into functional groups

To understand how the currents integrate several polyps into a group, we analyzed the characteristics of the trajectories of individual beads in several coral species. The analysis of particle tracking experiments established several novel important findings. First, the resulting trajectories connected multiple individual polyps within seconds. Second, the topology of the networks of currents appeared species specific and revealed a high complexity and regularity of its structure as evidenced from trajectory shapes and uniform manifold approximation and projection (UMAP) clustering based on a wide range of parameters (Figures 5A and 5B; Data S1D, S1E, and S2A [part 4]). The patterns of currents are resumed in Figure 5C. Indeed, in these experiments, independently moving beads repeated the same complex trajectory at different time points. Most importantly, these results showed the existence of generalized patterns of a coral surface tessellation with ciliated regions harboring specifically oriented beating cilia. These currents consistently connected multiple individual polyps and revealed a remarkable stability over time, as we observed in a 7-day experiment with a 15-cm *E. lamellosa* (Data S2E).

We then investigated the interconnectivity of the polyps in a foliaceous growth form (5 × 15 cm) of *E. lamellosa* by analyzing the horizontal water currents on its surface. Several networks of water currents appeared isolated from each other within a single colony, forming independent transportation units, thereby integrating multiple polyps (Figure S3; Video S4). No currents were detected on the surface of dead *E. lamellosa* colonies (Figure S3C; Video S4). Hence, we showed that, in addition to a previously characterized vertical, turbulent mass transfer,⁸ scleractinian corals direct a sophisticated large-scale horizontal mass transfer connecting polyps into regional sub-groups via oriented, surface-associated, and mucus-coordinated or non-coordinated currents.

Next, we addressed the role of the nervous system in controlling horizontal water currents. We tracked fluorescent beads and reconstructed the resulting trajectories after the addition of classical low molecular weight neurotransmitters (excluding neuropeptides) similar to experiments performed on other ciliated marine invertebrates.^{22,23} The speed of the surface currents was affected to different extents in different species upon the treatment with adrenaline, serotonin, glutamate, carbachol (cholinergic agonist of the muscarinic and nicotinic receptors), and GABA. Specifically, serotonin resulted in higher max speed of the particles on *P. decussata*, while carbachol, adrenaline,

(D) Time for beads to be cleared of the multiple point at the surface of *A. lamarcki* (n = 8 colonies), *O. faveolata* (n = 5 colonies), and *S. siderea* (n = 5 colonies). Dashed lines highlight the locations of differential movement of the beads.

(E–G) Bradford assay performed on collected liquids at the surface of *E. lamellosa* (E), *P. cactus* (F), and *M. foliosa* (G), before and after stress induction (n = 3 nubbins per species). Error bars represent the SD.

See also Figure S1 and Videos S2 and S3.

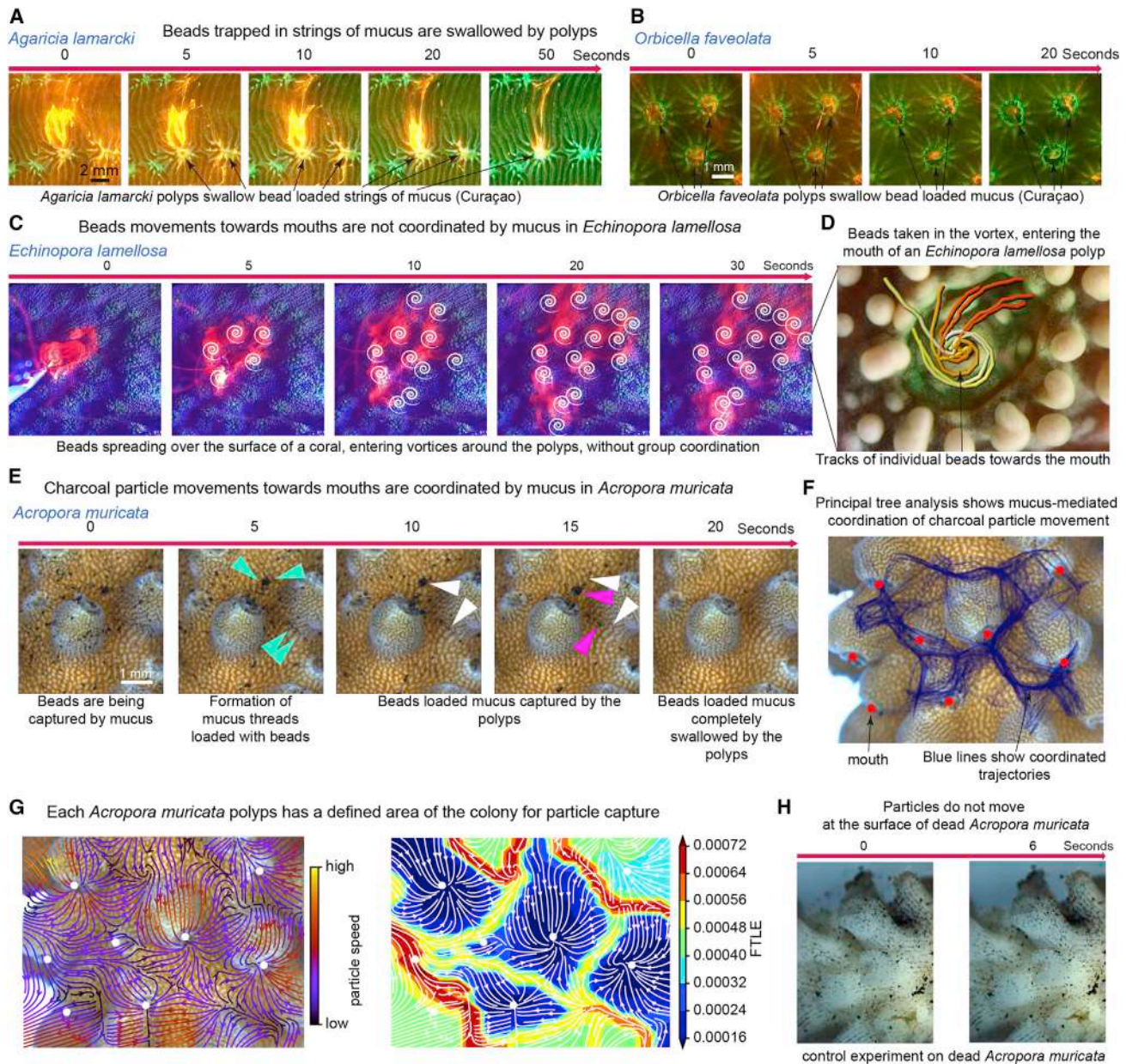


Figure 3. Corals use different strategies involving mucus or not to capture particles

(A) Beads trapped in mucus are swallowed by a polyp of *A. lamarcki* (n = 8 colonies).

(B) Beads trapped in mucus are swallowed by a polyp of *O. faveolata* (n = 5 colonies).

(C) Microbeads applied to the surface of *E. lamellosa* spread to multiple polyps over time. White vortices represent the polyps that are reached by the bead front.

(D) Bead tracking at the level of a polyp of *E. lamellosa*.

(E) Charcoal particle movement is coordinated by mucus at the surface of *A. muricata*. Turquoise arrowheads indicate mucus threads loaded with charcoal particles. White arrowheads indicate the position of charcoal particles at 10 s. Fuchsia arrowheads indicate the position of the charcoal particles at 15 s.

(F) Superposed trajectories of charcoal particles at the surface of *A. muricata*. Red dots represent the mouths of the polyps. Blue lines represent the particles' trajectories. Error bars represent the SD.

(G) Analysis of charcoal particles trajectories in *A. muricata*. Left: vectors represent the averaged trajectories of the particles, speed is color coded. Right: FTLE analysis of the particle trajectories. White dots represent the mouths.

(H) Charcoal particles movement at the surface of a dead *A. muricata*.

See also [Data S1A](#), [S1C](#), and [S2A](#) and [Videos S4](#) and [S5](#).

glutamate, and GABA modified the speed of the particles in *E. lamellosa* ([Data S1F](#)). The orientation and complexity of the currents, however, stayed largely unchanged in all cases ([Data](#)

[S2F](#)). Similarly, treatments with 5-hydroxy-L-tryptophan (5HTP) (precursor of serotonin), fluoxetine (inhibitor of serotonin reuptake), EGTA (chelator of Ca^{2+} and Mg^{2+}), and orthovanadate

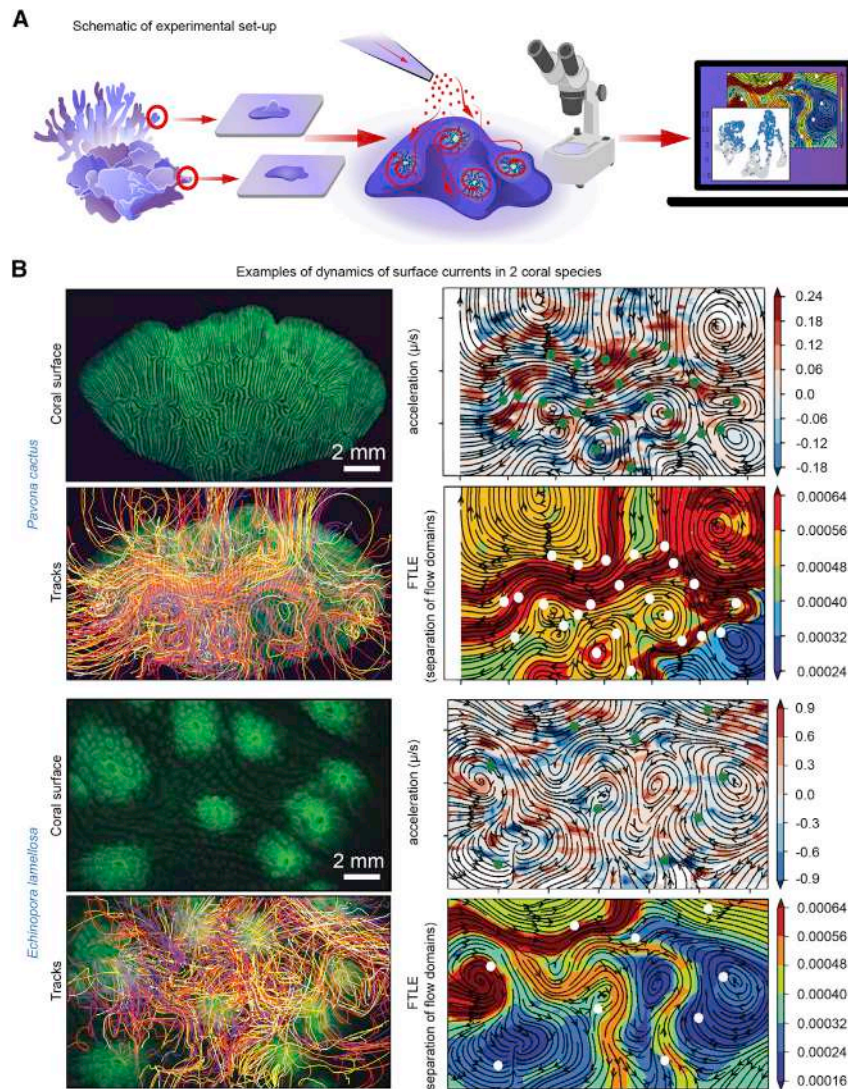


Figure 4. Formation of species-specific and stereotypical horizontal water currents at the surfaces of different coral species

(A) Scheme of the experiment: fluorescent beads are applied to the coral surface and tracked for trajectory generation, recapitulating surface currents.

(B) Analysis of bead trajectories in *P. cactus* ($n = 5$ nubbins) and *E. lamellosa* ($n = 4$ nubbins). Note that beads repeat stable trajectories over time highlighting the stable distribution of horizontal mass transfer units, currents, and areas with confined or cyclic water movements. FTLE values are proportional to the separability of two close-by points exploring the vector field over time (amount of divergence) and suggest regions of dynamically distinct flow behavior. White dots represent the polyps.

See also [Data S2B](#) and [S2C](#) and [Video S6](#).

beads were added onto the water next to the colony and their movements tracked. Beads engaged into horizontal or even surface-associated vertical streams, reaching all parts of the colony exposed to air (Figures 6C, 6D, and 6F). Even though the air-exposed surface retained a minimal layer of water, beads followed stereotypical paths forming chains and cycles according to the previously described models of horizontal currents (Figures 6C and 6E). No activity was observed at the surface of a dead *P. decussata* (Figure 6G). Thus, the oriented activity of the ciliated epithelium can sustain water exchange and, potentially, a continuous active hydration of the colony surface during air exposure, which warrants further experimentation on multiple coral species in the

(inhibitor of cilia activity) influenced the speed of the currents, without modifying the directionality of these currents (Data S2G) These suggest that the orientation of beating cilia has a developmental origin (emerging during colony growth) and is beyond the dynamic control of the nervous system.

Networks of surface currents lift water onto air-exposed surface

In several location on our planet, the reef is exposed to air at low tide.²⁴ This happens to a large extent in Indo-Pacific region and to much less extent in Caribbean, where only the strongest tides expose the corals to the atmosphere for a short while.²⁴ The robustness of horizontal water currents led us to hypothesize that cilia-induced horizontal currents have a lifting power and might hydrate the coral surface and maintain homeostasis (e.g., stable salinity) during air exposure at low tide (Figure 6A). To test the role of oriented ciliated fields in transporting water to the exposed parts of a colony, we lowered the level of seawater, leaving 2–10 mm of a *P. decussata* colony (a Caribbean species) exposed to air (Figure 6B; Video S7). Fluorescent

field to test if this mechanism truly contributes to coral survival during low tides.

Branching currents in the gastrovascular system connect individual neighboring polyps

We aimed to not only understand surface-associated flows at the coral surface but also comprehend the complexity of hydrodynamics inside the system of internal gastrovascular canals. To address the patterns of the flow within the gastrovascular system of a reef-building scleractinian coral, we mapped the inner canals and cavities in nubbins of *S. pistillata* using microcomputed tomography analysis (μ CT), light and fluorescent confocal microscopy (Figures 7A and 7B; Video S8). The results revealed a regular pattern of highly complex and adjoined cavities connecting individual polyps. The walls of the gastrovascular canals appeared shaped by the elevations and rifts forming the skeletal surface, thus recapitulating the corallite topography.

To investigate the directions of the flow in this gastrovascular tubing system, fluorescent microbeads were injected into the gastric cavities of individual polyps and tracked their movement

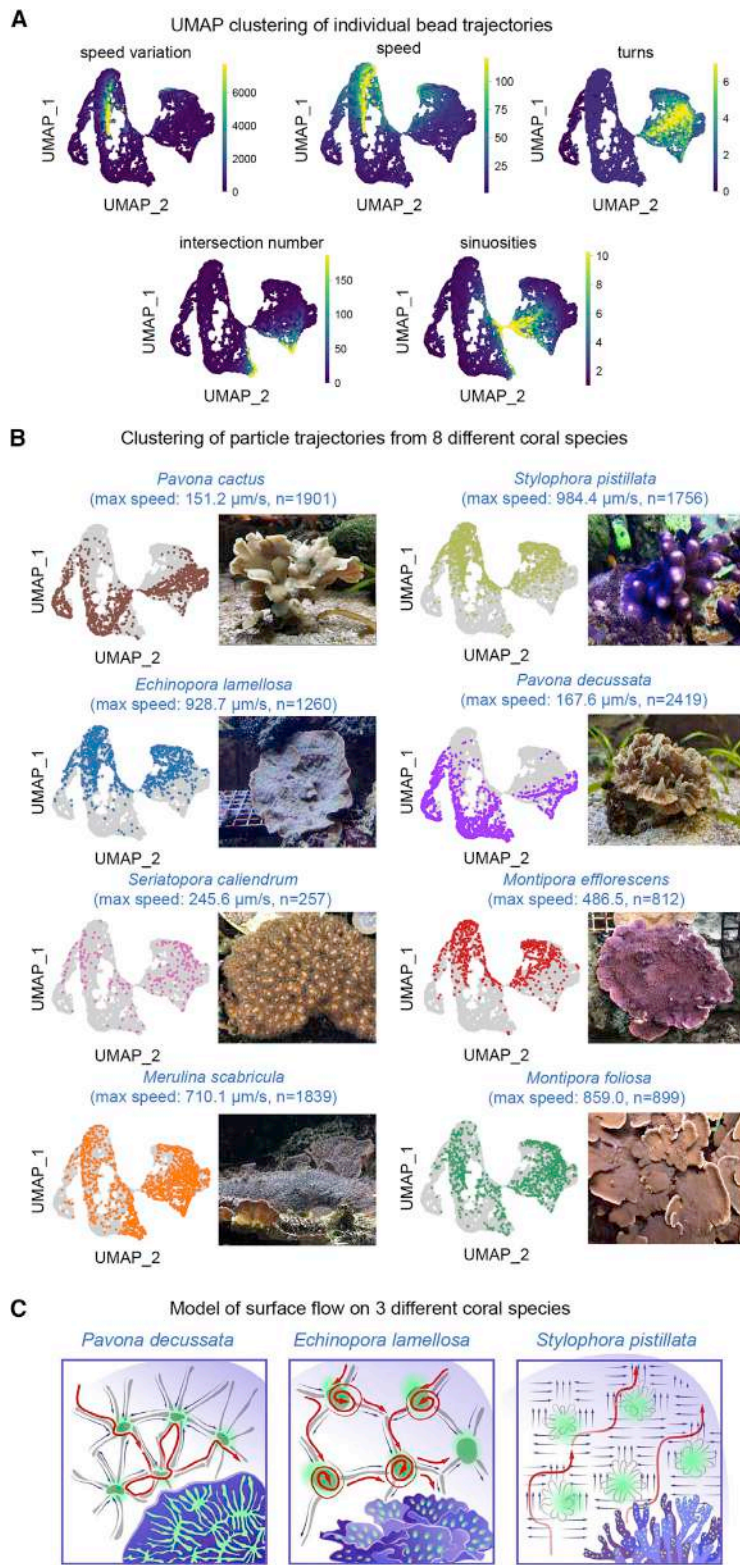


Figure 5. Multiparametric classification of the tracks at the surface of different coral species

(A) Distribution of values of measured variables plotted as densities on UMAPs.

(B) UMAP projections of multidimensional clustering of individual trajectories generated from eight coral species. We used the tracks obtained from *E. lamellosa* (n = 4 nubbins), *M. scabricula* (n = 4 nubbins), *M. efflorescens* (n = 5 nubbins), *M. foliosa* (n = 4 nubbins), *P. cactus* (n = 5 nubbins), *P. decussata* (n = 3 nubbins), *S. callendrum* (n = 4 nubbins), and *S. pistillata* (n = 6 nubbins). Note that dominating stereotypical shapes and other properties of trajectories display species specificity.

(C) Generalized schemes of oriented ciliated surface regions and major directions of horizontal water currents in three coral species.

See also [Figure S3](#) and [Data S1B, S1D, S1E, and S2D–S2G](#).

revealed that the opposite ciliated surfaces of individual canals create a bidirectional flow, creating circular currents within a linear segment of a canal. Nevertheless, these circular currents allowed microbeads to travel between interconnected segments of the gastrovascular system after being trapped in few rotation cycles within an individual segment. The resulting trajectories connected many segments and appeared as complex as branching surface currents.

To obtain better insights into the principles of fluid dynamics at a scale of several interconnected polyps, we took advantage of mathematical modeling ([Figures 7G–7I](#)). We devised a 2D structure resulting from approximating μ CT data and confocal analysis of distributed gastrovascular canals (in case of plain-growing specimens) and applied a set of rules obtained from these combined observations of moving beads. The Navier-Stokes equations were used to simulate flow dynamics inside a colony and experimentally observed currents were implemented as additional forces. Then, we introduced beads as particles inserted on random locations and simulated their motion using Newton's law of dynamics, as well as using variation of liquid viscosity in the canals (imitating the presence of mucus). The parameters of the model were calibrated to mimic the motion of beads quantitatively and qualitatively. The results of these simulations are in line with our experiments and suggest the idea of a “selfish sharing” model, where the signaling molecules or food particles have a higher chance to be retained longer in the vicinity of an individual polyp, which initially obtained or produced them ([Figures 7H–7J](#); [Data S2H](#)). When using parameters according to the experimentally observed cilia orientation, the model predicted the specific structured distribution of particles. This spatial organization of particle distribution disappeared when the parameters were changed to a chaotic orientation of ciliated areas. Simulations further suggested difference in the efficiency of keeping the particle around its source depending on its size ([Figure 7H](#)). This may define, an effective radius of nutrient sharing with neighbor polyps or the range of action of a released soluble signal.²⁵ Such chemical communication could be important for a

with live fluorescent microscopy ([Figures 7C–7F](#); [Video S9](#)). Similar gastrovascular activities were observed in *Pocillopora damicornis* (Linnaeus, 1758) ([Figure 7D](#)). These experiments

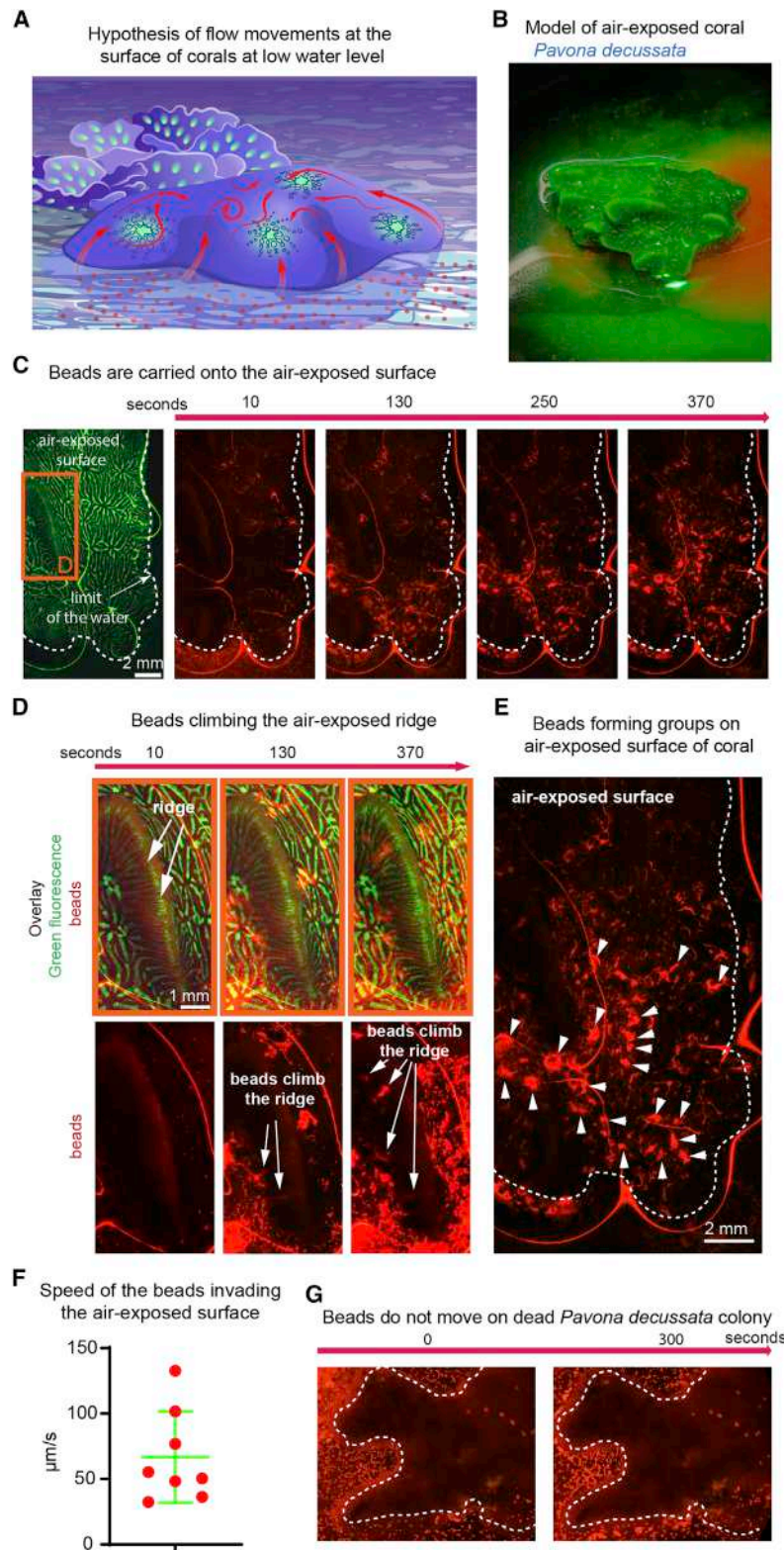


Figure 6. Active transportation of water carrying microbeads from submerged to air-exposed parts of a coral colony

(A) Hypothesis scheme showing the potential role of active oriented cilia beating in surviving the low-tide periods. (B) Picture of the air-exposed coral model. (C) Addition of red fluorescent beads to the water nearby the coral colony results in their fast transportation to areas of the coral exposed to the air. Dotted lines surround the areas above the water level. (D and E) Magnified regions show progressive distribution of engaged beads on the surfaces of air-exposed portions. Note the beads climbing the ridges on the coral surface (arrowheads, D). Note the formation of vortices induced by opposite currents in different regions (arrows, E). (F) Speed of the beads engaging on the air-exposed coral surface. Each dot represents one bead front on one analyzed nubbin. This experiment was reproduced on 3 different nubbins. (G) Dead *P. decussata* does not induce bead movement. See also [Video S7](#).

A number of studies revealed that corals consume planktonic bacterial and algal cells in addition to much larger prey caught by polyps.^{28–30} In such a case, the gastrovascular system may serve as a filter and a location where food particles can be phagocytosed by the cells within the walls of the gastrovascular canals. Our estimations based on μCT scans indicate that this system of gastrovascular canals extends the surface area for potential heterotrophic feeding nearly 4-fold as compared with the surface of gastric cavities of individual polyps ([Figure 7A](#); [Video S8](#)). This enlarged area with dynamic currents inside may not only improve organic carbon supply by stimulating the uptake of particulate organic matter (e.g., detritus, small phyto- and zooplankton) and dissolved organic matter (e.g., small carbohydrates and amino and fatty acids) but also enhance organic nitrogen and phosphorus supplies essential for coral growth.

DISCUSSION

Being sessile and colonial creatures, corals are limited in their direct coordination via active physical interaction between the individuals. Thus, other means of functional colonial integration direct the coherent living of the entire coral holobiont. Here, we revealed the astonishing complexity and scale of surface-associated currents, which span across large areas of the colony connecting dozens of polyps. Our work builds on top of earlier studies examining the general existence of surface-associated mucus

number of aspects of coral life: signaling disease or predation,²⁶ interaction with symbionts,²⁶ coordination of spawning,²⁷ and capture of food.

flows on the coral surface, as was observed in lab-based experiments.^{15,19} We attempted to take this line of previous observations^{15,19} to a principally new level.

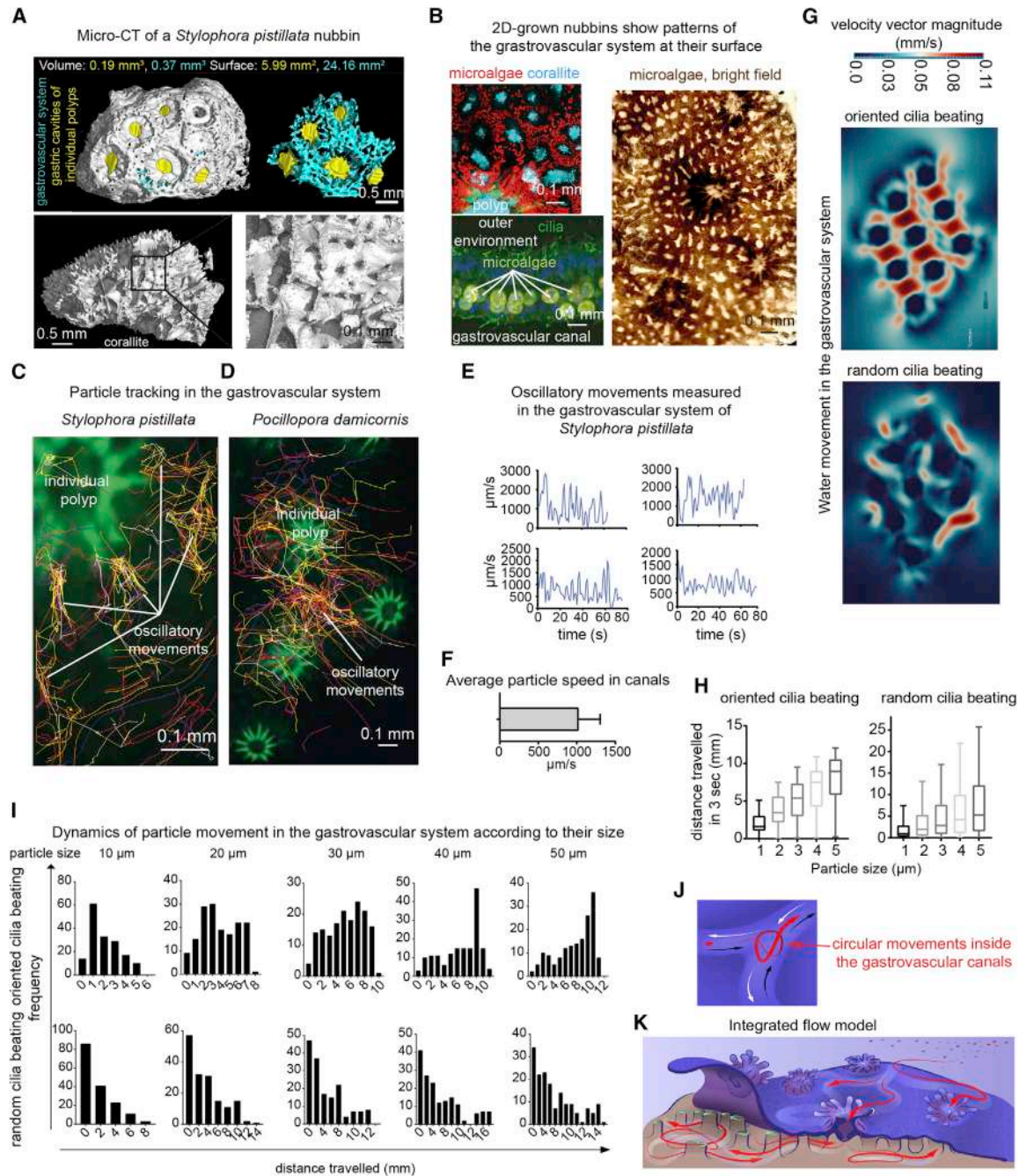


Figure 7. Complexity of the waterflow in the gastrovascular system of *S. pistillata*

(A) μ CT analysis of a PTA-contrasted nubbin of *S. pistillata* followed by 3D reconstructions of its gastrovascular system and corallite surface.
 (B) The walls of gastrovascular canals are lined up by ciliated cells containing the microalgae symbionts or neighboring the symbiont-containing cells.
 (C) Reconstruction of multiple trajectories of individual fluorescent beads injected into gastrovascular system.
 (D) Trajectories in the gastrovascular canals of *P. damicornis*.
 (E) Measurements of the cyclic/oscillating movements of fluorescent beads within the segments of the gastrovascular system before translocation to joint gastrovascular segments.
 (F) Average speed of the beads in the gastrovascular system. Error bars represent the SD.
 (G) Mathematical modeling of the water dynamics in the gastrovascular system of *S. pistillata* with oriented (top) or random (bottom) beating cilia.
 (H) Analysis of the effective translocation radius for particles with different sizes traveling in simulated gastrovascular system of *S. pistillata* with oriented (left) or random (right) beating cilia. Error bars represent the SD.
 (I) Computational analysis of the dynamics of bead movement.
 (J and K) Concluding scheme summarizing the complexity of horizontal water currents at the coral surface and inside of the coral colony.
 See also [Data S2H](#) and [Videos S8](#) and [S9](#).

Based on the application of computer-assisted particle mass tracking in numerous reproducible experiments and controls including dead corals, we addressed the complexity and species-specific features of the surface currents in multiple species, both in the wild (Curaçao, Caribbean Sea) or fully grown in-house. Furthermore, we investigated the dynamics at the surfaces of clonally propagated micro-nubbins used for reproducibility in multiple testing. We revealed that the species specificity of the surface tracks is rooted in the stereotypical cilia orientations on the surfaces of different coral species resulting in variation of sinuosity, turns, speed, intersections, orientation, and length of the tracks (clustered and shown in a UMAP plot). Furthermore, for the first time, we innovated the application of a FTLE field-based analysis to the dynamics of a surface-associated flow in corals using mass tracking. This helped to discover that individual polyps or their small groups have dedicated surface territories, from which they collect particles to feed. On the borders of such “flow cell” territories, the polyps compete with each other. In some species, the special surface-associated currents formed subnetworks connecting the polyps into larger groups within a context of a colony, thus breaking the morphological symmetry of the coral generating these asymmetric currents.

Next, we hypothesized that the modulation of the neural activity by a range of evolutionarily conserved neurotransmitters might change the orientation of the surface currents. However, the applications of a wide range of neurotransmitters and related drugs did not perturb the orientation of such surface currents, although the neurotransmitters influenced the speed of the surface flow in some cases. In line with this, the repeated daily recordings of the currents on the surface of the same coral throughout a week further showed their consistency. Thus, the oriented networks of streams are likely stable over a prolonged period, which can provide long-term adaptations to seasonal or other conditions on the timescale of weeks and months. The temporal stability of the discovered patterns at a greater scale requires further investigation.

As the majority of our experiments were carried out in the lab, it is still questionable whether the observed surface network of streams similarly exists in natural conditions, for instance, in the presence of strong external water currents. The fact that we managed to record surface streams in natural conditions supports their formation and role in natural settings, although the strength of the ambient flow at the recorded micro spots did not exceed 2 cm/s (estimated from the videos, as the marker streams of residual beads synchronously drift in the water column). The flow conditions differ during daily changes of tide direction, wind strength, shading, and many other local reasons. The surface streams are likely adapting coral to conditions when the ambient flow becomes weaker. On the other side, corals with deep corallite grooves (*A. lamarcki* forming well-like structures and especially *D. labyrinthiformis* with deep crevices) naturally shade individual polyps from a strong flow, and, despite we could not effectively record surface currents under strong ambient flow, the directional surface currents might still be present in some parts of the colonies. The reconciliation may derive from the formation of layered transport regime based on the mucus covering the coral surface,^{11,13,15} which requires further investigation in natural environments. This could explain how

the oriented surface-associated streams still operate in the changing conditions of the sea.

To understand the networks of surface streams in relation to the previously described surface mucus layer,^{11,13} we analyzed the amount and the distribution of mucus using direct video recordings after bead application and chemical tests. We found that the mucus concentration at the coral surface is dynamically regulated for all analyzed species. Despite covering the coral surface, in the majority of investigated species, the mucus layer was permitting the formation of surface currents often resulting in mucus-coordinated movements of particles and flow-based connections between polyps. To pinpoint this mucus-coordinated “conveyor belt” movement of particles, we innovated a computational analysis based on the “principal tree approach” applied to particle trajectories. According to these experiments, the mucus-coordinated particle movement within surface streams is a part of a highly integrative feeding strategy of corals, where the individual polyps control specific surface territories, from which they collect food particles. This result fits previous findings of the role of mucus in feeding and creating the layered transport regime.^{15,19} We also discovered that some coral species are covered by mucus which is not sufficient to coordinate the particle movement in the surface layer.^{15,19} It would be exciting to learn how these lower mucus concentrations are related to the properties of the diffusive boundary layer,³¹ where the particles move. The existence of groups of polyps integrated via the surface streams aids the discussion about the “individual units” in the context of the entire colony. Based on these findings, we hypothesized and validated that the structure of the coral colony is much more modular and hierarchical as compared with what we knew before this study. Furthermore, integration of polyps via streams turned out to be helpful not only in feeding but also as a potential protection against desiccation, as we observed a surface stream-based lift of seawater with mucus to the air-exposed parts of the coral in the lab. This capacity might thus be essential for the survival of corals living in regions experiencing low tides,^{24,32} which requires further open-field investigations. Furthermore, the presence of mucus forming a thicker water-retaining layer could enhance the hydration caused by the lifting power of streams.^{12,13,32}

As the water and mucus at the coral surface connect with the internal gastrovascular system via the distributed mouths, we also questioned the dynamics of the liquid flow within the system of internal gastrovascular canals. Previously, a few aspects of the active movement of fluids inside the gastrovascular system of corals were already reported.^{16,17} In stoloniferan octocorals, such flow appeared bidirectional within the individual channel at the stolon-gastrovascular junction, and the pulsations of the flow corresponded to the coordinated activity of cilia.¹⁷ Besides, the flow in the system of canals connecting individual polyps is involved in nutrient sharing in colonial hydroids.³³ Presumably, this way of transport and integration may be similarly important in reef-building corals. Interestingly, even the photoautotrophic symbionts were traveling inside such gastrovascular systems,¹⁷ also in line with our own observations. Here, we revealed the degree of complexity of a gastrovascular network and showed that all neighboring polyps were connected by the inner flow with complex characteristics and topography, such as branching and bidirectionality of streams. Our results suggest that although

the water flow within every segment is cyclic and isolated to some extent from the neighboring segments, there is an intense fluid exchange between multiple segments, as the injected microbeads could travel large distances (several centimeters) over short time (minutes) within the gastrovascular system of the entire colony. Since the walls of the interconnected gastrovascular canals are enriched in symbiotic algae, the cyclic flow could contribute to the efficient exchange of gases and nutrients needed for photosynthesis and homeostasis (e.g., removal of oxygen radicals), thus sustaining the symbiotic lifestyle of reef-building corals. In line with this, the recent findings of the role of oxygenation in coral health and bleaching^{34,35} suggest that intense currents in the gastrovascular system might facilitate redistributing O₂ from well-lit to shaded areas of a coral colony throughout the day.

Next, because the cyclic flow tended to retain the microbeads within the site of injection for a longer time, we hypothesized that the flow structure favors the spatial and temporal gradient of gas, signaling molecules, and nutrients per location. The modeling of this gastrovascular networks based on planar-grown coral nubbins suggests that the particles, metabolites, and soluble signals are preferentially retained in the vicinity of every polyp similarly to the situation described for colonial hydroids.³³ Most importantly, we connected the microgeometry of the coral skeletal surface and passages of gastrovascular canals in three dimensions, explaining the structural role that skeletal landscapes play in underpinning the overlying gastrovascular canals and hydrodynamics.

In addition to the possible roles in nutrient sharing, signaling, gas, or metabolite exchange, the gastrovascular network may serve for repopulating the colony with photoautotrophic symbiont cells (*Symbiodiniaceae*) after bleaching events and for exchanging and regulating *Symbiodiniaceae* in different parts of the colony. Consistently, while tracking the fluorescent beads, we routinely detected *Symbiodiniaceae* cells moving with the flow in gastrovascular canals, a phenomenon previously reported, but not fully understood.¹⁷ Using complex internal flow dynamics, coral colonies could¹⁷ distribute the incoming and outgoing flow between different polyps creating powerful sucking and filtering effects, which could regulate the heterotrophy of corals.²⁸ Indeed, the sucking power of interconnected gastrovascular system may facilitate entry and exit of microbial symbionts into the coral holobiont.^{36,37}

In opposition to other modes of water movement found in benthic animals known to associate with symbiotic microbes,³⁸ such as pulsation (soft corals), pumping (upside-down jellyfish *Cassiopea* sp.), and contraction (sessile colonial ciliate *Zoothamnium* sp.), this complex gastrovascular flow does not imply movement of the animal's body and may represent an adaptation to the immotile lifestyle of reef-building corals.

The future prospects resulting from this study are expected to stem from the integration of the internal and surface-associated flows, which may result in a holistic understanding of the colony coordination via liquid dynamics. The existence of polyp-integrating surface currents universally observed in multiple species in conjunction with surface mucus layer opens up multiple future research directions including the evolution of species-specific adaptations of the flow patterns in different coral species living in a wide range of environmental conditions.

Our discoveries will shift the perspective on coral biology, as we show that the colonies are modular and show previously unknown functional hierarchical organization due to the existence of polyp groups integrated by the flow. This knowledge will fundamentally affect our understanding of colonial growth, feeding, ecological strategies, and resistance to disease or other adverse conditions. Last, but not least, the understanding of how the topology of skeletal surfaces connects with the integrating coral-controlled hydrodynamics will revolutionize our vision of coral evolution and will transform the interpretation of the paleontological samples in light of paleoecology. Indeed, the evolution of coral surface structures at longer timescales as well as during faster adaptive radiation might be partly explained by the adaptations to specific feeding habits and flow regimes. Further research on modern corals will help to establish how surface geometry and skeletal micropatterns direct surface flow and coordinate the feeding of the colony. This knowledge might be translated to extinct groups to infer finer specifics of their lifestyles and evolutionary transitions controlling changes in skeletal morphology and colony shape.

STAR★METHODS

Detailed methods are provided in the online version of this paper and include the following:

- **KEY RESOURCES TABLE**
- **RESOURCE AVAILABILITY**
 - Lead contact
 - Materials availability
 - Data and code availability
- **EXPERIMENTAL MODEL AND SUBJECT DETAILS**
- **METHOD DETAILS**
 - Bead preparation
 - Field experiments
 - Laboratory experiments
- **QUANTIFICATION AND STATISTICAL ANALYSIS**
 - Evaluation of surface clearing in corals in Curaçao
 - Track creation
 - Track Analysis
 - Mathematical model
 - Computational Fluid Dynamics of the *Agaricia lamarcki* coral reef
 - Computational Fluid Dynamics of the *Agaricia lamarcki* coral reef
 - Imaging

SUPPLEMENTAL INFORMATION

Supplemental information can be found online at <https://doi.org/10.1016/j.cub.2022.04.054>.

ACKNOWLEDGMENTS

I.A. was supported by Bertil Hallsten Research Foundation, Karolinska Institutet, and Medical University of Vienna; J.P. was supported by Vetenskapsrådet (VR); T.B. was supported by a Meitner grant from the Förderung der Wissenschaftlichen Forschung (FWF, M2688-B28); L.F. was supported by the Austrian Science Fund DOC 33-B27MT; M.T., T.Z., and J.K. acknowledge Czech NanoLab Research Infrastructure supported by MEYS CR (LM2018110); M.T. acknowledges Brno City Municipality as a Brno Ph.D. Talent Scholarship

Holder and Martina Roeselova Memorial fellowship; and B.M. was supported by the European Union's Horizon 2020 research innovation program under the Marie Skłodowska-Curie actions (global fellowship grant agreement no. 894645).

AUTHOR CONTRIBUTIONS

Conceptualization, T.B., J.P., L.F., D.A.-N., J.B., A.H., and I.A.; data curation, T.B., L.F., and B.M.; formal analysis, T.B., J.P., L.F., A.B., M.N., and M.T.; investigation, T.B., J.P., L.F., D.A.-N., B.M., A.B., M.N., L.E., M.T., P.R.F., O.P., J.B., and I.A.; methodology, T.B., J.P., L.F., D.A.-N., B.M., J.B., O.P., A.H., and I.A.; software, L.F., A.B., and M.N.; supervision, K.F., C.W., A.H., J.B., and I.A.; validation, T.B. and D.A.-N.; visualization, T.B., J.P., L.F., A.B., M.T., and I.A.; writing – original draft, T.B., J.P., and I.A.; writing – review & editing, T.B., J.P., L.F., D.A.-N., A.B., B.M., M.N., L.E., M.T., P.R.F., T.Z., T.K., J.K., K.F., C.W., A.H., J.B., and I.A.; project administration, T.B., J.P., D.A.-N., and I.A.; funding acquisition, B.M., J.B., and I.A.; resources, D.A.-N., B.M., A.H., T.K., O.P., J.B., and I.A.

DECLARATION OF INTERESTS

The authors declare no competing interests.

Received: October 8, 2021

Revised: March 4, 2022

Accepted: April 20, 2022

Published: May 12, 2022

REFERENCES

1. Barbeitos, M.S., Romano, S.L., and Lasker, H.R. (2010). Repeated loss of coloniality and symbiosis in scleractinian corals. *Proc. Natl. Acad. Sci. USA* *107*, 11877–11882. <https://doi.org/10.1073/pnas.0914380107>.
2. Danchin, E., and Wagner, R.H. (1997). The evolution of coloniality: the emergence of new perspectives. *Trends Ecol. Evol.* *12*, 342–347.
3. Wild, C., Hoegh-Guldberg, O., Naumann, M.S., Colombo-Palotta, M.F., Ateweberhan, M., Fitt, W.K., Iglesias-Prieto, R., Palmer, C., Bythell, J.C., Ortiz, J., et al. (2011). Climate change impedes scleractinian corals as primary reef ecosystem engineers. *Mar. Freshw. Res.* *62*, 205–215.
4. Mullen, A.D., Treibitz, T., Roberts, P.L.D., Kelly, E.L.A., Horwitz, R., Smith, J.E., and Jaffe, J.S. (2016). Underwater microscopy for *in situ* studies of benthic ecosystems. *Nat. Commun.* *7*, 12093. <https://doi.org/10.1038/ncomms12093>.
5. Chen, E., Stiefel, K.M., Sejnowski, T.J., and Bullock, T.H. (2008). Model of traveling waves in a coral nerve network. *J. Comp. Physiol. A Neuroethol. Sens. Neural Behav. Physiol.* *194*, 195–200. <https://doi.org/10.1007/s00359-007-0305-z>.
6. Horridge, G. (1957). The co-ordination of the protective retraction of coral polyps. *Philos. Trans. R. Soc. Lond. B* *240*, 495–529.
7. Swain, T.D., Bold, E.C., Osborn, P.C., Baird, A.H., Westneat, M.W., Backman, V., and Marcelino, L.A. (2018). Physiological integration of coral colonies is correlated with bleaching resistance. *Mar. Ecol. Prog. Ser.* *586*, 1–10.
8. Shapiro, O.H., Fernandez, V.I., Garren, M., Guasto, J.S., Debailon-Vesque, F.P., Kramarsky-Winter, E., Vardi, A., and Stocker, R. (2014). Vortical ciliary flows actively enhance mass transport in reef corals. *Proc. Natl. Acad. Sci. USA* *111*, 13391–13396. <https://doi.org/10.1073/pnas.1323094111>.
9. Shashar, N., Kinane, S., Jokiel, P.L., and Patterson, M.R. (1996). Hydromechanical boundary layers over a coral reef. *J. Exp. Mar. Biol. Ecol.* *199*, 17–28. [https://doi.org/10.1016/0022-0981\(95\)00156-5](https://doi.org/10.1016/0022-0981(95)00156-5).
10. Larkum, A.W.D., Koch, E.-M.W., and Kühl, M. (2003). Diffusive boundary layers and photosynthesis of the epilithic algal community of coral reefs. *Mar. Biol.* *142*, 1073–1082. <https://doi.org/10.1007/s00227-003-1022-y>.
11. Brown, B.E., and Bythell, J.C. (2005). Perspectives on mucus secretion in reef corals. *Mar. Ecol. Prog. Ser.* *296*, 291–309. <https://doi.org/10.3354/meps296291>.
12. Glasl, B., Herndl, G.J., and Frade, P.R. (2016). The microbiome of coral surface mucus has a key role in mediating holobiont health and survival upon disturbance. *ISME J* *10*, 2280–2292. <https://doi.org/10.1038/ismej.2016.9>.
13. Bythell, J.C., and Wild, C. (2011). Biology and ecology of coral mucus release. *J. Exp. Mar. Biol. Ecol.* *408*, 88–93. <https://doi.org/10.1016/j.jembe.2011.07.028>.
14. Wild, C., Huettel, M., Klueber, A., Kremb, S.G., Rasheed, M.Y., and Jørgensen, B.B. (2004). Coral mucus functions as an energy carrier and particle trap in the reef ecosystem. *Nature* *428*, 66–70. <https://doi.org/10.1038/nature02344>.
15. Lewis, J.B., and Price, W.S. (1976). Patterns of ciliary currents in Atlantic reef corals and their functional significance. *J. Zool.* *178*, 77–89.
16. Gladfelter, E.H. (1983). Circulation of fluids in the gastrovascular system of the reef coral *Acropora cervicornis*. *Biol. Bull.* *165*, 619–636. <https://doi.org/10.2307/1541469>.
17. Parrin, A.P., Netherton, S.E., Bross, L.S., McFadden, C.S., and Blackstone, N.W. (2010). Circulation of fluids in the gastrovascular system of a stoloniferan octocoral. *Biol. Bull.* *219*, 112–121. <https://doi.org/10.1086/BBLv219n2p112>.
18. Gateño, D., Israel, A., Barki, Y., and Rinkevich, B. (1998). Gastrovascular circulation in an octocoral: evidence of significant transport of coral and symbiont cells. *Biol. Bull.* *194*, 178–186. <https://doi.org/10.2307/1543048>.
19. Duerden, J.E. (1906). The role of mucus in corals. *Q. J. Microsc. Sci.* *49*, 591–614.
20. BozorgMagham, A.E., and Ross, S.D. (2015). Atmospheric Lagrangian coherent structures considering unresolved turbulence and forecast uncertainty. *Commun. Nonlinear Sci. Numer. Simul.* *22*, 964–979. <https://doi.org/10.1016/j.cnsns.2014.07.011>.
21. Garaboa-Paz, D., Eiras-Barca, J., and Pérez-Muñizuri, V. (2017). Climatology of Lyapunov exponents: the link between atmospheric rivers and large-scale mixing variability. *Earth Syst. Dynam.* *8*, 865–873. <https://doi.org/10.5194/esd-8-865-2017>.
22. Beiras, R., and Widdows, J. (1995). Effect of the neurotransmitters dopamine, serotonin and norepinephrine on the ciliary activity of mussel (*Mytilus edulis*) larvae. *Mar. Biol.* *122*, 597–603.
23. Wada, Y., Mogami, Y., and Baba, S. (1997). Modification of ciliary beating in sea urchin larvae induced by neurotransmitters: beat-plane rotation and control of frequency fluctuation. *J. Exp. Biol.* *200*, 9–18.
24. Anthony, K.R.N., and Kerswell, A.P. (2007). Coral mortality following extreme low tides and high solar radiation. *Mar. Biol.* *151*, 1623–1631. <https://doi.org/10.1007/s00227-006-0573-0>.
25. Atema, J. (1995). Chemical signals in the marine environment: dispersal, detection, and temporal signal analysis. *Proc. Natl. Acad. Sci. USA* *92*, 62–66. <https://doi.org/10.1073/pnas.92.1.62>.
26. Dixon, D.L., Abrego, D., and Hay, M.E. (2014). Reef ecology. Chemically mediated behavior of recruiting corals and fishes: a tipping point that may limit reef recovery. *Science* *345*, 892–897. <https://doi.org/10.1126/science.1255057>.
27. Flint, M., and Than, J.T. (2016). Potential spawn induction and suppression agents in Caribbean *Acropora cervicornis* corals of the Florida Keys. *PeerJ* *4*, e1982. <https://doi.org/10.7717/peerj.1982>.
28. Houlbrèque, F., and Ferrier-Pagès, C. (2009). Heterotrophy in tropical scleractinian corals. *Biol. Rev. Camb. Philos. Soc.* *84*, 1–17. <https://doi.org/10.1111/j.1469-185X.2008.00058.x>.
29. Meunier, V., Bonnet, S., Pernice, M., Benavides, M., Lorrain, A., Grosso, O., Lambert, C., and Houlbrèque, F. (2019). Bleaching forces coral's heterotrophy on diazotrophs and *Synechococcus*. *ISME J.* *13*, 2882–2886. <https://doi.org/10.1038/s41396-019-0456-2>.

30. Bak, R.P.M., Joenje, M., de Jong, I., Lambrechts, D.Y.M., and Nieuwland, G. (1998). Bacterial suspension feeding by coral reef benthic organisms. *Mar. Ecol. Prog. Ser.* 175, 285–288. <https://doi.org/10.3354/meps175285>.
31. Jimenez, I.M., Kühl, M., Larkum, A.W.D., and Ralph, P.J. (2011). Effects of flow and colony morphology on the thermal boundary layer of corals. *J. R. Soc. Interface* 8, 1785–1795. <https://doi.org/10.1098/rsif.2011.0144>.
32. Krupp, D.A. (1984). Mucus production by corals exposed during an extreme low tide. *Pac. Sci.* 38, 1–11.
33. Buss, L.W., Anderson, C.P., Perry, E.K., Buss, E.D., and Bolton, E.W. (2015). Nutrient distribution and absorption in the colonial hydroid *Podocoryna carnea* is sequentially diffusive and directional. *PLoS One* 10, e0136814. <https://doi.org/10.1371/journal.pone.0136814>.
34. Nelson, H.R., and Altieri, A.H. (2019). Oxygen: the universal currency on coral reefs. *Coral Reefs* 38, 177–198. <https://doi.org/10.1007/s00338-019-01765-0>.
35. Alderdice, R., Suggett, D.J., Cárdenas, A., Hughes, D.J., Kühl, M., Pernice, M., and Voolstra, C.R. (2021). Divergent expression of hypoxia response systems under deoxygenation in reef-forming corals aligns with bleaching susceptibility. *Glob. Change Biol.* 27, 312–326. <https://doi.org/10.1111/gcb.15436>.
36. Hirose, M., Yamamoto, H., and Nonaka, M. (2008). Metamorphosis and acquisition of symbiotic algae in planula larvae and primary polyps of *Acropora* spp. *Coral Reefs* 27, 247–254. <https://doi.org/10.1007/s00338-007-0330-y>.
37. Davy, S.K., Allemand, D., and Weis, V.M. (2012). Cell biology of cnidarian-dinoflagellate symbiosis. *Microbiol. Mol. Biol. Rev.* 76, 229–261. <https://doi.org/10.1128/MMBR.05014-11>.
38. Wild, C., and Naumann, M.S. (2013). Effect of active water movement on energy and nutrient acquisition in coral reef-associated benthic organisms. *Proc. Natl. Acad. Sci. USA* 110, 8767–8768. <https://doi.org/10.1073/pnas.1306839110>.
39. Osinga, R., Schutter, M., Wijgerde, T., Rinkevich, B., Shafir, S., Shpigiel, M., Luna, G.M., Danovaro, R., Bongiorno, L., Deutsch, A., et al. (2012). The CORALZOO project: a synopsis of four years of public aquarium science. *J. Mar. Biol. Assoc. UK* 92, 753–768. <https://doi.org/10.1017/S0025315411001779>.
40. Stabili, L., Schirosi, R., Di Benedetto, A., Merendino, A., Villanova, L., and Giangrande, A. (2011). First insights into the biochemistry of *Sabella spallanzanii* (Annelida: Polychaeta) mucus: a potentially unexplored resource for applicative purposes. *J. Mar. Biol. Assoc. UK* 91, 199–208. <https://doi.org/10.1017/S00253154110001013>.
41. Stabili, L., Schirosi, R., Parisi, M.G., Piraino, S., and Cammarata, M. (2015). The mucus of *actinia equina* (Anthozoa, Cnidaria): an unexplored resource for potential applicative purposes. *Mar. Drugs* 13, 5276–5296.
42. Stehnach, M.R., Waisbord, N., Walkama, D.M., and Guasto, J.S. (2021). Viscophobic turning dictates microalgae transport in viscosity gradients. *Nat. Phys.* 17, 926–930. <https://doi.org/10.1038/s41567-021-01247-7>.
43. Issa, R.I. (1986). Solution of the implicitly discretised fluid flow equations by operator-splitting. *J. Comput. Phys.* 62, 40–65. [https://doi.org/10.1016/0021-9991\(86\)90099-9](https://doi.org/10.1016/0021-9991(86)90099-9).
44. Jasak, H., Jemcov, A., and Tukovic, Z. (2007). OpenFOAM: a C++ library for complex physics simulations. *International Workshop on Coupled Methods in Numerical Dynamics*.

STAR★METHODS

KEY RESOURCES TABLE

REAGENT or RESOURCE	SOURCE	IDENTIFIER
Chemicals, peptides, and recombinant proteins		
Bradford reagent	Sigma Aldrich	Ref: B6916-500ML; Lot: SLCC0151
Charcoal particles (10 μ m)	Kebo laboratories	N/A
Fluorescent Red Polyethylene Microspheres	Cospheric	Ref: 0.995g/cc 10-90-10g; Batch:150629-1
FMR-Red Fluorescent Microspheres	Cospheric	Ref: 1.3g/cc-500mg; Batch: 300-45-3511
GABA	TOCRIS	Ref: 0344; Lot: 5A/153607
Glycine	TOCRIS	Ref: 0219; Lot: 14A/147308
L-(-)-Norepinephrine	Sigma Aldrich	Ref: A9512-250MG; Lot: SLBC1882V
L-glutamic acid	TOCRIS	Ref: 0218; Lot: 12B/157431
Methanol	VWR	Ref: 20847.307; Lot: 20K034002
PBS	gibco	Ref: 14190-094 Batch:2326202
Phosphotungstic acid hydrate	Sigma Aldrich	Ref P4006-250G; Lot: SLBX2662
Serotonin hydrochloride	TOCRIS	Ref 3547; Lot: 2B/210430
Sodium chloride	Millipore	Ref: 1.06404.1000; Batch K51163304918
Sodium orthovanadate	Sigma Aldrich	Ref: S6508-250G; Batch: 0000104515
EGTA	Millipore	Ref: 324626-25GM; Lot: 3761062
Fluoxetine hydrochloride	Sigma	Ref: F132-50MG; Lot: SLCF6196
5-Hydroxy-L-tryptophan (5HTP)	Sigma	Ref: H9772-5G; Lot: BCCC7473
Tween 80	Sigma Aldrich	ref: P4780-500ML, batch: BCCB6908
Deposited data		
Raw data	Harvard Dataverse: https://doi.org/10.7910/DVN/OHPVD7 ; Harvard Dataverse: https://doi.org/10.7910/DVN/2N115F	N/A
Jupyter notebooks	GitHub: https://github.com/LouisFaure/coral_paper	N/A
track analysis tool	GitHub: https://github.com/LouisFaure/dyntrack	N/A
Experimental models: Organisms/strains		
<i>Echinopora lamelllose</i>	Haus des Meeres, Vienna	Esper, 1791
<i>Merulina scabricula</i>	Haus des Meeres, Vienna	Dana, 1846
<i>Montipora efflorescens</i>	Haus des Meeres, Vienna	Bernard, 1897
<i>Montipora foliosa</i>	Haus des Meeres, Vienna	Pallas, 1766
<i>Pavona cactus</i>	Haus des Meeres, Vienna	Forskål, 1775
<i>Pavona decussata</i>	Haus des Meeres, Vienna	Dana, 1846
<i>Pocillopora damicornis</i>	Haus des Meeres, Vienna	Linnaeus, 1758
<i>Seriatopora caliendrum</i>	Haus des Meeres, Vienna	Ehrenberg, 1834
<i>Stylophora pistillata</i>	Haus des Meeres, Vienna	Esper, 1792
Experimental models: corals in native habitats		
<i>Acropora muricata</i>	Heron Island	Linnaeus, 1758
<i>Agaricia lamarcki</i>	Curaçao	Milne Edwards and Haime, 1851
<i>Diploria labyrinthiformis</i>	Curaçao	Linnaeus, 1758
<i>Orbicella faveolata</i>	Curaçao	Ellis and Solander, 1786
<i>Siderastrea sidereal</i>	Curaçao	Ellis and Solander, 1786
Software and algorithms		
IMARIS 9.6.0	https://imaris.oxinst.com/	N/A

(Continued on next page)

Continued

REAGENT or RESOURCE	SOURCE	IDENTIFIER
R	https://cran.r-project.org/bin/windows/base/	N/A
Python	https://www.python.org/downloads/	N/A
	https://github.com/LouisFaure/coral_paper/	N/A
Python tool	https://pypi.org/project/dyntrack/	N/A
	https://dyntrack.readthedocs.io/en/latest/	N/A
Other		
Plate reader	Promega	GLOMAX MULTI+ detection system
HTEC Salzwasser Refraktometer Meerwasser	HTEC	RHS-10ATC

RESOURCE AVAILABILITY

Lead contact

Further information and requests for resources and reagents should be directed to and will be fulfilled by the lead contact, Igor Adameyko (igor.adameyko@meduniwien.ac.at).

Materials availability

This study did not generate new unique reagents.

Data and code availability

- Original videos obtained in situ and ex situ, imaris files, raw data obtained from the imaris files, track data and the scripts to extract frames from the videos are available here: <https://doi.org/10.7910/DVN/OHPVD7> and <https://doi.org/10.7910/DVN/2N115F>
- Code for reproducibility has been deposited as Jupyter notebooks on the following github repository: https://github.com/LouisFaure/coral_paper.
- We constructed a single python package for ease of reproduction for tracking analysis (<https://github.com/LouisFaure/dyntrack>).

EXPERIMENTAL MODEL AND SUBJECT DETAILS

All coral species used in this study are listed in the [key resources table](#) and in [Data S1A](#). The specific preparation as well as rearing conditions are listed in the [method details](#) section.

We started the tracking experiments with molecular dyes. However, molecular dyes diluted too fast to be tracked. The molecular dyes quickly made a cloud in the water, precluding any reliable recording of precise area with a sharp focus camera. Thus, we switched to fluorescent beads and charcoal particles of different sizes. Notably, too small beads (less than 10 microns in diameter) did not emit enough light for efficient individual mass tracking, and they appeared dim for the analysis of gastrovascular canals.

METHOD DETAILS

Bead preparation

Beads (1–5 μ m and 10–90 μ m) were coated in Tween 80 for 12 hours in a 50 ml tube (Falcon). This preparation was then diluted in PBS and centrifuged for 10 min at 1000g. Beads were then rinsed in PBS 5 more times and a further 3 times with sea water coming from the original tanks of the corals for laboratory and aquarium experiments. For field experiments, beads were diluted in deionized water and salinity was adjusted to 40PSU with NaCl. Floating beads were separated from the sinking beads during the washes and were used for the experiments studying the water currents developing at the surface of air-exposed coral specimens. Sinking beads were used for the underwater experiments.

For each bead preparation, we tuned the salinity of the presoaking solution, to achieve neutral density of the beads. This helped us to create a bead solution with a buoyancy similar to the surrounding water (with sedimentation speed less than 1 cm per min). This helped us to keep the beads on the coral surface and observed the streams without beads floating back to the surface. Small beads (1–5 μ m) were used for the analysis of the gastrovascular canals as they are less invasive. However, their light emitting was not optimal and therefore only macro-recordings were possible (see “[Internal tracking](#)” for details). Bigger beads (10–90 μ m) were used for

individual trajectory recordings as their light emitting was optimal for the identification of individual trajectory recordings over an entire coral nubbin (see “[bead tracking experiments in laboratory](#)” for more details).

Field experiments

Field experiments in Curaçao

Experiments were done during 4 dives in late March 2021, between 10AM and 4PM. The experiments were performed on the reef in front of the CARMABI research station (12° 7'18.85"N, 68°58'10.40"W) on Curaçao, Southern Caribbean. Videos were recorded between 3 and 20 meters in generally calm conditions, camera was in macro mode. We used an Olympus TG 5 in Olympus PT-059 underwater housing with Night Sea barrier filter attached for image capture and a Light & Motion Go Be Night Sea LED light as light source. We used a Sea & Sea arm 7 compact set and a Light & Motion camera tray to insure flexibility in positioning and at the same time stability during the recording. Beads were ejected to the coral surface using 5ml syringes.

Experiment in Haus des Meeres exposition tank

A colony of *Echinopora lamellosa* was grown undisturbed for 5 years with natural-like currents (3 Aqua Medic EcoDrift 15.2), in presence of other animals. The exposition tank was: 187cm x 150cm x 77cm water depth. Beads (1-5µm) were deposited above the surface of the coral with a Pasteur pipette. Videos were recorded with an iPhone X from the exposition area side of the tank.

Laboratory experiments

Creation of the laboratory specimens in Vienna

Stylophora pistillata, *Echinopora lamellosa*, *Pavona cactus*, *Pavona decussata*, *Montipora efflorescens*, *Montipora foliosa*, *Merulina scabricula* and *Seriatopora caliendrum* colonies were obtained from Haus des Meeres, a public aquarium in Vienna, Austria. Original corals colonies originated from Rotterdam Zoo as of 2012. The coral nubbins (*Stylophora pistillata*, *Montipora foliosa*, *Seriatopora caliendrum*) used for the experiments consisted of less than fifty polyps and were propagated according to Osinga et al.³⁹ on transparent PET sheets of 0,5mm width. *Echinopora lamellosa*, *Pavona cactus*, *Pavona decussata*, *Montipora efflorescens* and *Merulina scabricula* pieces were broken from the original colony and allowed to heal for at least a week at + 25°C before being transferred in the laboratory.

Creation of the laboratory specimens in Heron Island

Acropora muricata specimens were collected on the forereef of Heron Island, at 6 meters depth (23°26'50"S 151°54'46"E). They were allowed to recover and acclimate to the tank's condition for a minimum of 14 days before experiment.

Tank experiment in Heron Island

Specimens were mounted on screwcap fittings with plasticine to hold them and transfer them without handling the tissues. Then transferred immediately to the video tank (20cm x 10cm, 8 cm depth) without air exposure and recordings taken in still water within a few min of collection from the holding aquarium. Specimens were covered with 1cm of water. Videos were recorded using an Olympus SZX7 stereomicroscope, QImaging Micropublisher 3.3 camera and Q-Capture v6 imaging software.

Bead tracking experiments in laboratory

Upon collection, corals were transported to our laboratory and allowed to rest for at least 2 hours in petri dishes (Greiner bio-one, diameter: 100mm, depth: 20mm) containing water coming from their original tank. Specimens were covered with sea water (from their original tank) between 0.5cm to 1 cm above their surface. For these experiments, we analyzed 5 specimens of *P. cactus*, 4 specimens of *E. lamellosa*, 6 specimens of *S. pistillata*, 3 specimens of *P. decussata*, 4 specimens of *S. caliendrum*, 4 specimens of *M. scabricula*, 5 specimens of *M. efflorescens* and 4 specimens of *M. foliosa*.

Position of the corals in the petri dishes were recorded using a fluorescent stereomicroscope (Zeiss, Lumar.V12), mounted with a camera (AxiocamERc 5s). Concentrated beads (10-90µm, 100µl of bead suspension) suspended in sea water from the original tank of the corals were then added close to the coral surface with a micropipette. The beads were ejected at distances between 1 and 3 mm above the coral surface. Being neutral in flowability or slightly heavier as compared to the surrounding seawater, the beads successfully landed right onto the coral surface after being pushed from the pipette. The following horizontal movement of beads in streams confirmed their resulting position within DBL.

Bead movements were recorded when the water disruption induced by the experimenter was settled. Bead movements were recorded until the surface of the coral was devoid of beads (3-5 minutes). An additional picture of a ruler was taken to obtain the scale.

Bead tracking with neurotransmitter

The experimental set up was similar as the basic bead tracking. Concentrated beads (10-90µm) suspended in sea water from the original tank of the corals were then added in the petri dishes. Bead movements were recorded a first time (5-10 min), then half the sea water was replaced with a neurotransmitter solution to a final concentration of 100µM. Concentrated beads (10-90µm, 20µl of bead suspension) suspended in sea water from the original tank of the corals were then added in the petri dishes. Bead movements were recorded for 5-10 minutes. Each condition was assayed on 3 independent specimens for *P. decussata* and *E. lamellosa*. An additional picture of a ruler was taken to obtain the scale.

Bead tracking with other chemicals (5HTP, fluoxetine, EGTA, orthovanadate)

The experimental set up was similar to the bead tracking with neurotransmitters section, except that the nubbins were incubated for 2 hours with either 5HTP (100µM), fluoxetine (25µM), EGTA, (2mM) or orthovanadate (0.1mM) after the first control recording.

Experiment on *Pavona decussata* in low water

Pavona decussata specimens (live or dead) were put in petri dishes containing sea water. Only the extreme outer parts of the specimens were allowed to be partially submerged. We added a few drops of a solution containing floating beads (10 μ m–90 μ m diameter) and recorded for 5 min. These experiments were carried out on 3 specimens.

Macroscopic visualization of surface currents on *Echinopora lamellosa*

A piece of *Echinopora lamellosa* of a surface of 100 cm² was placed in an aquarium (20cm x 30cm, 20cm depth) containing sea water coming from its original tank. Specimens were covered with 15 cm of water. A concentrated solution of suspended 1–5 μ m beads was applied on the surface of the coral and the currents were recorded using an iPhone X. The tank was lit with an aqua sunspot 7x1 (Aqua Medic, Germany) bulb mounted on a JBL Temp set basic (JBL, Germany). The experiments were conducted in a 12-liter tank without detectable horizontal currents except slow vertical convection, which was checked via analyzing the bead behavior at the surfaces of analogous dead corals used for control.

Internal tracking

Stylophora pistillata and *Pocillopora damicornis* specimens were injected with 1–5 μ m beads in one polyp. We used a 30G needle mounted on a 1ml syringe to do the injection. Videos were then recorded using the same stereoscope as for the basic bead tracking. To be able to visualize the bead movements inside the coral, we used a 150X magnification.

Bradford assay on mucus

Coral specimens from *Echinopora lamellosa*, *Pavona cactus* and *Montipora foliosa* were prepared at least a week before experiment at Haus des Meeres. The day of the experiment, specimens were put in tanks containing the water of their original tank and let to rest for an hour at Haus des Meeres. We sampled the liquid at the surface of the coral with a pipette and marked it as time 0. Their surface was lightly scratched with a soft toothbrush. We then sampled the liquid at the surface of the specimens at different intervals. Liquid samples were saved at –80°C until analysis.

The day of the experiment, 100 μ l of each sample was put in a 96 well plate and covered with 100 μ l of Bradford reagent. After 30 min incubation, the plate was read at λ = 595nm. Water from the original tank was used as blank.

QUANTIFICATION AND STATISTICAL ANALYSIS

Evaluation of surface clearing in corals in Curaçao

A transparent sheet with dots equally distant (2 cm from each other) and lettered/numbered (A to I and 1 to 15) was put on a screen and each video was played on the screen. Each point was monitored from the bead application to the moment the surface was cleared from the beads. Each dot on one colony represented an individual measurement for this colony. We analysed multiple colonies for each species.

Track creation

Frames were extracted from the videos using ffmpeg (<https://www.ffmpeg.org/>) as tiff images (ffmpeg -i [name of your video] -r [frame rate of your video]/2 -pix_fmt rgb24 [name of your output]%04d.tiff). The frame rate of the video was obtained using ffmpeg (ffmpeg -i [name of your video] 2>&1 | sed -n "s/.*, \(.*) fp.*\1/p"). We provide annotated bash scripts to extract all frames of a video and one out of 2 frames of a video (see [data and code availability section](#)). These scripts require a linux/ubuntu/wsl environment to function and to install ffmpeg. The scripts need to be put in the folder containing the videos to be processed and modified to process the video with your choice of extension (see in comments in the script, can be modified in notepad). The resulting pictures can be processed with IMARIS or ImageJ. To reduce computational requirements, we extracted only half of the frames, this was taken into account to evaluate the time in our further analyses. Extracted odd frames were assembled in an IMARIS (Bitplane, Zurich, Switzerland) file using the built in Batch Converter. The resulting IMARIS files were analyzed using the IMARIS semi-automated tracking module. Raw data were extracted as excel files and analysed using our new python package (Dytracks).

Track Analysis

For each replicate, track data were exported from IMARIS and rescaled. Tracks were summarized into grid vector fields of 30 by 30 vectors using vfm tool with smoothing parameter 0.5. The resulting grid vector field was represented as a stream plot. From the grid vector field, an attempt in identifying Lagrangian Coherent Structures (LCS) was performed. LCS are separate surfaces that form the skeleton of the traced trajectories and that separate time dependent flows into regions of dynamically distinct behavior. Identifying such structures rely on generating a Finite-time Lyapunov exponent (FTLE) field from the vector grid data. First, all points from the grid are taken as starting points and each trajectory is integrated via bilinear interpolation combined with Runge-Kutta method. The integration was performed over 20000 timepoint/frames with a delta t of 5 frames. This number of 20000 is purposely greater than the number of frames captured in each experiment, since the aim is to integrate over the whole vector field. Second, the integrated trajectories were used to compute the FTLE value for each point on the grid. The scalar FTLE value is meant to be compared relatively on the same vector field, with low values indicating zones of convergence or low divergence and high values indicating zones of high divergence. Observing ridges on the FTLE field plot is an indicator of dynamically distinct regions. To identify coherent structures possibly generated by slime or currents, a principal tree was fitted to each frame of the experiment, using SimplePPT algorithm (parameters lambda=10 and sigma=10, as many nodes as tracked point on the given

frame). All previously mentioned techniques in this section have been compiled into a single python package for ease of reproduction (<https://github.com/LouisFaure/dyntrack>). This tool is applicable to any dataset containing 2D tracks. From each tracked particle were extracted the mean, maximum and variance of its speed. Sinuosity was calculated as the ratio between the distance of a track and the distance of a straight line spanning the two extremities of it. Sinuosity along the track was also computed using a moving window of 20 points that slides one point at a time, for a given data point the maximum sinuosity value calculated was retained. Number of turns on a track was estimated by counting the number of groups of points on the track with a sinuosity value higher than 1.2. Number of self-intersections was also counted.

Finally, to classify tracks, we applied scanpy python tool to a dataset generated by compiling the z scores of the number of turns, the sinuosity, the mean speed, the maximum speed, and the number of intersections. A 30 nearest neighbors graph was generated from these features using correlation distance metrics. From this nearest neighbors graph was computed a leiden clustering (resolution=0.05) and an UMAP dimensionality reduction (min_dist=0.2). Differential changes in the features between clusters were calculated using t test. Proportion of each species versus the rest for each cluster was tested using a permutation method: over 1000 repeats, a null distribution is generated by randomly separating all tracks into two groups having the same size as the original groups. For each repeat is calculated the proportional difference between the two groups for each cluster. These values are then compared to the initial observed proportional difference for each cluster. The p value is calculated by dividing the number of randomly generated proportional differences that are greater than the observed proportional difference over the total number of random generations.

For the neurotransmitter experiment, tracks were analysed in 4 separated time points: 10 to 5min before NT addition, 5 to 0min before NT addition, 0 to 5 min after NT addition and 5 to 10 min after NT addition. A vector field was generated for each time point, and maximum and mean track speed was cross compared between timepoints using the Mood median test, multiple testing correction was performed using Holm-Šidák test.

Mathematical model

Dynamics of particles in the gastrovascular system

Flow hydrodynamics. We described the hydrodynamics of the gastrovascular system using the Immersed Boundary Method (IBM). The IBM method was developed by Charles Peskin in 1972 to describe biological fluid-structure interactions problems. In this method, fluid dynamics are simulated on a Eulerian cartesian grid, while the shape of the immersed structure is tracked using Lagrangian coordinates. We used a delta function to compute the exchanged forces between the two coordinate systems. For an incompressible Newtonian fluid, fluid dynamics are governed by Navier-Stokes equations:

$$\rho \left(\frac{\partial u}{\partial t} + u \cdot \Delta u \right) = -\nabla p + \mu \Delta u + F_d - F_p, \quad (\text{Equation 1})$$

$$\nabla \cdot u = 0, \quad (\text{Equation 2})$$

where ρ and μ are the fluid density and viscosity. F_d and F_p are the drag force and the penalization force imposed by solid bodies, and μ - viscosity coefficient of water. The Navier-Stokes equations are solved in a rectangular domain discretized into 500×300 nodes and we impose periodic boundary conditions at the four sides. The drag side is described using the formula:

$$F_d(x, t) = \frac{1}{2} \rho (u_s(x, t) - u(x, t)), \quad (\text{Equation 3})$$

Where $u_s(x, t)$ is the velocity of the body interpolated to the point x of the cartesian grid. It is obtained by the interpolation of the velocities of the structure nodes (beating cilia) using the following RBF:

$$\varphi(r) = \begin{cases} 0.25(1 + \cos(\pi r/r_0)), & \text{if } r \leq r_0 \\ 0, & \text{if } r \geq r_0 \end{cases}$$

And, we consider that

$$u_s(x, t) = \int_{\Omega} u_s(x, t) \varphi(|s - x|) ds.$$

In order to prevent the penetration of fluid inside corallites, we added a Brinkman penalization term describing flow arrest as it goes through the solid. The method consists in considering the solids as porous media whose permeability tends to zero. The Brinkman force term F_p is given by the formula:

$$F_p = g(x, t) \frac{\mu}{k} u, \quad (\text{Equation 4})$$

where $g(x, t)$ denotes a function that returns the value 1 for the nodes that are inside the immersed corallite and 0 elsewhere. k is the permeability of the solid (taken too small).

The accuracy of this method was ensured by quantitatively comparing the results for flow distribution with the ones obtained using simulations with the finite element method.

Particle motion. Individual particles driven by the flow can be tracked using the Newton 2nd law of dynamics. These particles are subject to three forces: the lift action by the fluid, the viscous friction (due to mucus), and the potential force between the particles and the cylinders. The motion of each particle (x_i) can be described by:

$$\ddot{m}_i \ddot{x}_i = F_i^D + F_i^V + F_i^P, \quad (\text{Equation 5})$$

where m_i denotes the mass of the particle, F_i^D , F_i^V , and F_i^P represents the drag, viscosity, and potential forces respectively.

Drag is the hydrodynamic force exerted by the fluid on the particle. It depends on the characteristics of both the fluid and the object. When flow is laminar, it is given by the formula:

$$F_i^D = \frac{1}{2} C_d \rho A_i v_i^2, \quad (\text{Equation 6})$$

where C_d represents the drag coefficient, A_i is the surface of the particle exposed to the flow given by $A_i = \pi r_i^2$, with r the radius, in the case of spheric particles, v_i is the relative velocity of the particle which corresponds to the difference between the particle velocity and the fluid speed at the particle coordinates. The viscous resistance force corresponds to the transfer of mechanical energy into heat energy due to friction between the particle and the mucus. It is given by:

$$F_i^R = R_v \dot{x}_i, \quad (\text{Equation 7})$$

where R_v represents the fluid resistance coefficient. The last force corresponds to the potential due to contact between particles and corallite. Since both the corallites and particle have a spheric shape, then the potential force can be described as follows:

$$F_i^P = \sum_j f_{ij}^P, \quad (\text{Equation 8})$$

where

$$f_{ij}^P = \begin{cases} K_1 + K_2 \frac{r_i + r_j}{d_{ij}}, & \text{if } d_{ij} \leq (r_i + r_j), \\ 0, & \text{if } d_{ij} \geq (r_i + r_j) \end{cases}$$

Here K_1 and K_2 are two positive constants, d_{ij} is the distance between the center of the two objects, r_i and r_j are their two respective radii. We do not consider contact between particles as the potential force due to this type of interactions is too small.

Model implementation

The C++ language was used to implement the model using an object-oriented programming (OOP) structure. Since particle motion does not influence hydrodynamics, we first solved the IBM model to determine the distribution of flow velocity reached in steady-state. Then, we saved this velocity and used it to simulate the motion of particles with different sizes and initial positions. This allowed us not having to solve the computationally intensive model for flow hydrodynamics for each simulation.

Model parameters

We summarize the model parameters in [Data S1G](#).

Boundary conditions

Particle dynamics in the gastrovascular system model. Some boundary conditions were already given in the original supplementary file. We add the following information for the gastrovascular system model:

The model simulations particle dynamics in the gastrovascular system in two steps. First, we simulate flow dynamics in the absence of particle dynamics until they reach steady-state. Then, we introduce particles and simulate their movement in the system.

- Periodic boundary conditions were applied for flow velocity at the four boundaries.
- Pressure is set to zero on the four boundaries.
- Particles are removed from the simulation as soon they cross one of the four boundaries.

Computational Fluid Dynamics of the *Agaricia lamarcki* coral reef

Boundary conditions

We assume a no-slip boundary condition on the mouth and the surrounding walls of the corallites. Dirichlet boundary conditions were applied at the internal walls of the corallite and the imposed velocity was chosen such that the velocity observed above the coral reef mimics the one measured experimentally. Zero-gradient conditions were applied for flow velocity at the top and the two sides boundaries with a constant pressure equal to zero.

Parameters

In the absence of mucus, we consider water parameters for density and viscosity: $\rho = 1000 \text{ kg/m}^3$ and $\mu = 1 \text{ cP}$.

Mucus viscosity

Mucus increases viscosity as proven experimentally for different types of coral species. The values of 2 cP and 5 cP were chosen to approximate the experimentally measured mucus on coral surface.^{40–42}

Computational Fluid Dynamics of the *Agaricia lamarcki* coral reef

Water flow surrounding coral reefs can be modelled as a Newtonian laminar incompressible flow. We modeled water flow inside and around the coral polyp using the Navier-Stokes equations:

$$\rho \left(\frac{\partial u}{\partial t} + u \cdot \nabla u \right) = - \nabla p + \mu \Delta u, \quad (\text{Equation 9})$$

$$\nabla \cdot u = 0, \quad (\text{Equation 10})$$

where u and p represent the flow velocity and pressure, ρ and μ are density and viscosity of water. We imposed constant Dirichlet boundary conditions on the corallite wall such that the velocity observed above the coral reef mimics the one measured experimentally.

We used the PISO algorithm to solve the continuity equation.⁴³ The model was implemented using the OpenFOAM library.⁴⁴ We generate a mesh consisting of 431 hexahedra volumes. The solver takes approximately 21 seconds to simulate 10 seconds of the physical time on an i7, 6GB computer. Stationary solution is reached in 0.25 seconds.

Imaging

X-ray microcomputed tomography analysis (μ CT)

For the visualization of soft tissue, corals were fixed in 4% formaldehyde in PBS solution for 4 hours at +4°C with slow rotation. Subsequently, samples were dehydrated in incrementally increasing ethanol concentrations (30%, 50%, 70%), 1 day in each concentration to minimize the shrinkage of the soft tissue. Then, samples were transferred, into 1% PTA (phospho-tungstic acid) in 90% methanol for tissue contrasting. The PTA-methanol solution was changed every 2–3 days for 7 days. The contrasting procedure was followed by rehydration of the sample by incubation in ethanol series (90%, 70%, 50% and 30%) before μ CT scanning. Scanning of stained corals was performed using GE phoenix v|tome|x L 240, equipped with a 180 kV/15W maximum power nanofocus X-ray tube and high contrast flat panel detector DXR250 with 2048 × 2048 pixel, 200 × 200 μ m pixel size. The exposure time was 900 ms in 2200 positions over 360°. The μ CT scan was carried out at 60 kV acceleration voltage and with 200 μ A X-ray tube current. The beam was filtered by a 0.1 mm-thick aluminum filter. The voxel size of obtained volume was 2.8 μ m. The tomographic reconstructions were performed using GE phoenix datos|x 2.0 3D computed tomography software. Segmentation of structures was performed manually by combination of software Avizo (Thermo Fisher Scientific, USA) and VG Studio MAX 3.2 (Volume Graphics GmbH, Germany).

Microscopy

Confocal microscopy was performed using Zeiss LSM880 Airyscan CLSM instruments. Image analysis was performed using IMARIS Software (Bitplane, Zurich, Switzerland). All results were replicated at least in 3 different coral specimens.

Current Biology, Volume 32

Supplemental Information

Surface flow for colonial integration in reef-building corals

Thibault Boudier, Julian Petersen, Louis Faure, Daniel Abed-Navandi, Anass Bouchnita, Benjamin Mueller, Murtazo Nazarov, Lukas Englmaier, Marketa Tesarova, Pedro R. Frade, Tomas Zikmund, Till Koehne, Jozef Kaiser, Kaj Fried, Christian Wild, Olga Pantos, Andreas Hellander, John Bythell, and Igor Adameyko

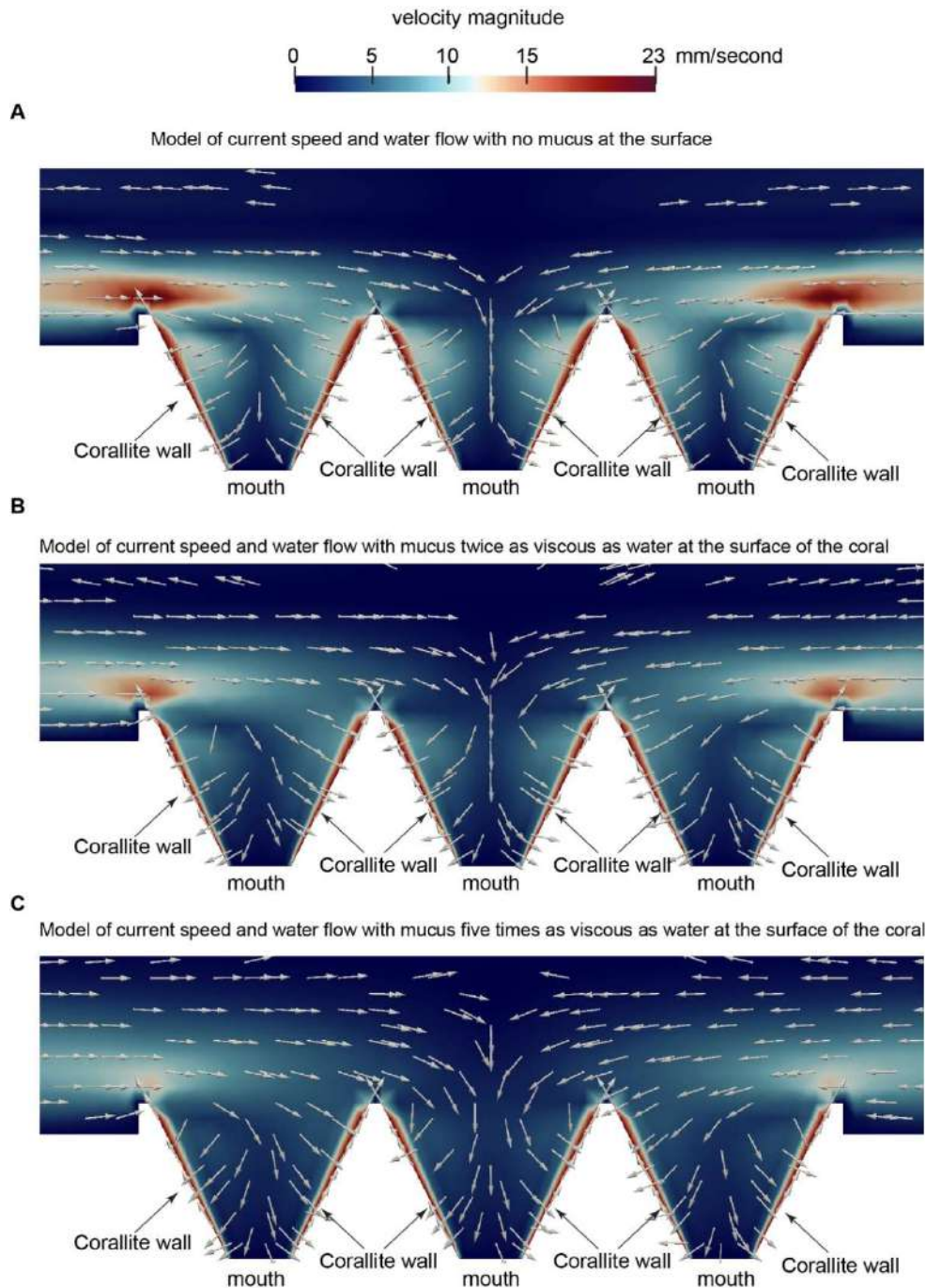


Figure S1: Mucus at the surface of *A. lamarcki* does not impair particle movement towards the mouth. Related to Figure 1, 2.

(A) Model in presence of water at the surface of the coral. (B) Model in presence of a fluid twice as viscous as water at the surface of the coral. (C) Model in presence of a fluid five times as viscous as water at the surface of the coral. Colors represent the velocity of the fluids currents; vectors represent the direction of the fluids currents.

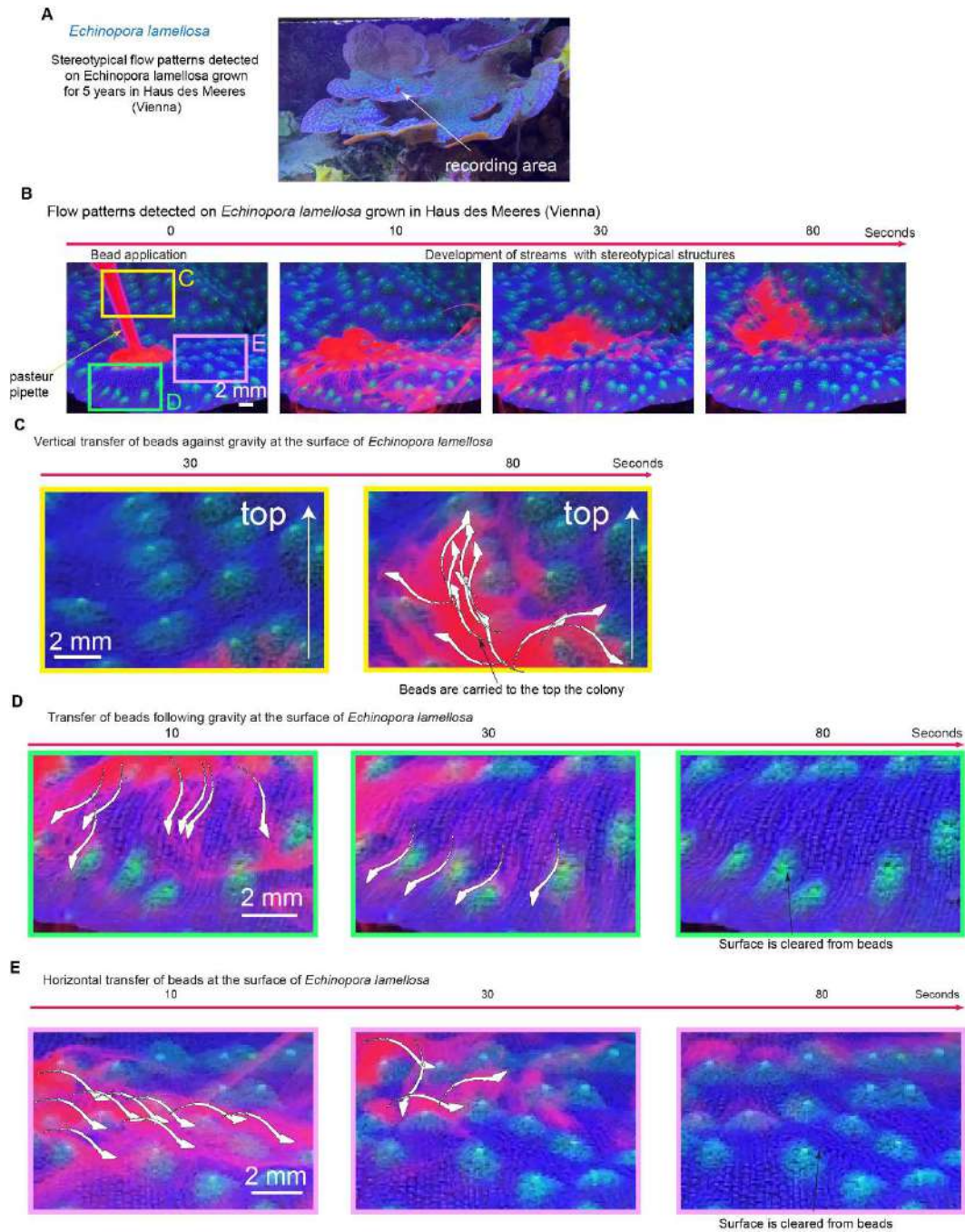


Figure S2: *E. lamellosa* can transport beads over the colony, even against gravity. Related to Figure 1.

(A) Picture of the aquarium- cultivated (5 years, Haus des Meeres, Vienna) *E. lamellosa* colony used for tracking beads. (B) Time course after bead application at the surface of the colony. The colored boxes at time 0 are the areas that are enlarged in panels C, D and E. (C) Enlarged picture of the yellow panel in B. (D) Enlarged picture of the green panel in B. (E) Enlarged picture of the pink panel in B. Arrows represent the movement of the beads.

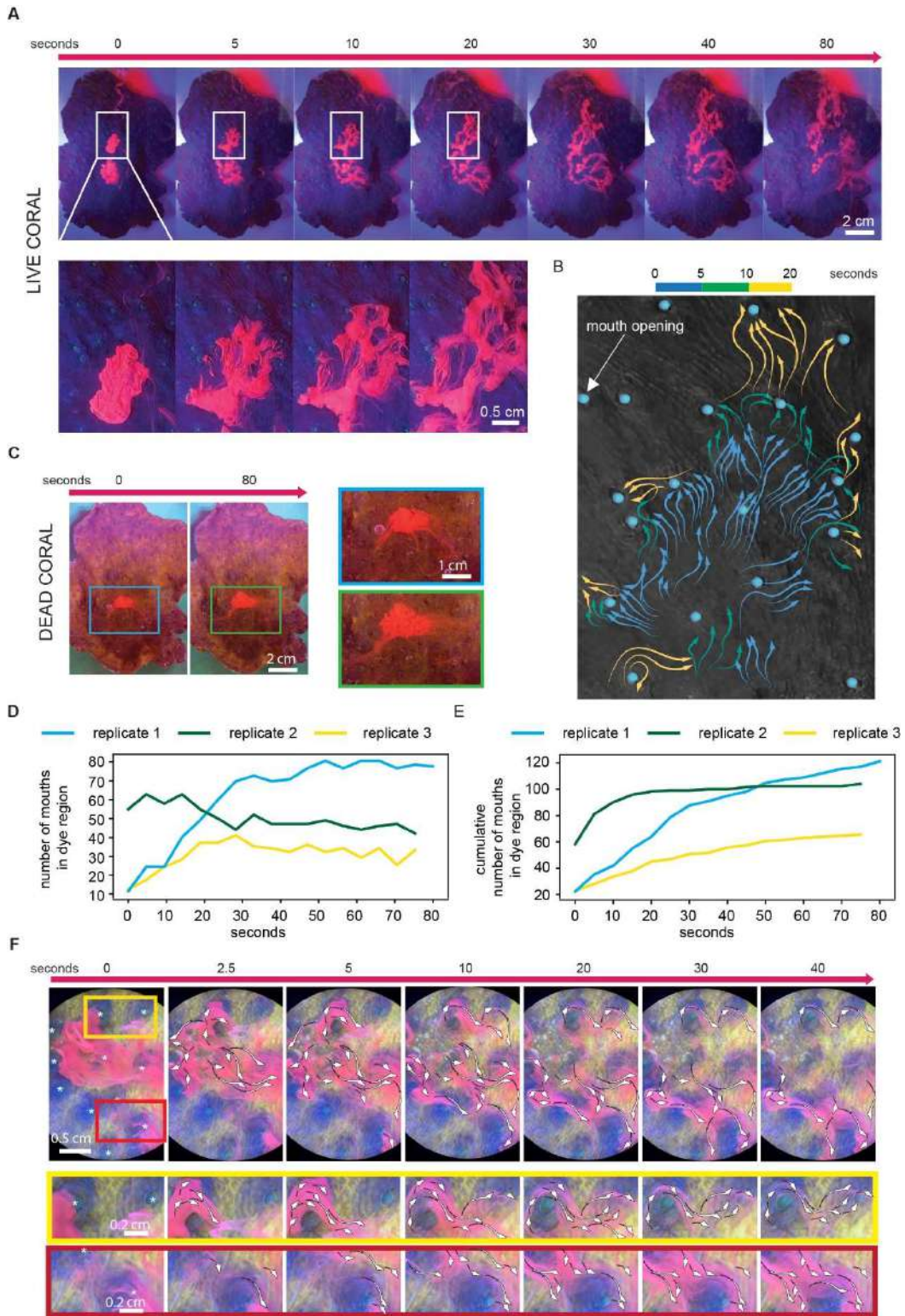


Figure S3: Formation of horizontal transportation water mass transfer units on the surface of a 15 cm-wide *E. lamellosa*. Related to Figure 5.







(A) Application of red fluorescent beads to two locations on the coral surface allows the visualization of stable currents and transportation units connecting a fraction of specifically distributed individual polyps. (B) Most of the currents are unidirectional and share the same general direction within this portion of a coral surface. (C) Control condition with the same coral after killing the colony via a 24-hour drying period. Note that oriented streams are not formed, and the beads sediment and stay in the same location. (D-E) Graph showing the absolute and cumulative numbers of individual polyps connected via the visualized water currents over time. (F) Horizontal currents engage and transport fluorescent beads until the translocation of beads is complete. During the transportation of beads, currents show high stability in terms of geometry, localization and speed. Arrows delineate the directions of the currents; stars highlight the coordinates of individual polyps or their mouths. The experiment was repeated 3 times on different colonies and produced similar results.

Supplemental references

[S1]. Jacquemin, J., Husson, P., Padua, A.A.H., and Majer, V. (2006). Density and viscosity of several pure and water-saturated ionic liquids. *Green Chemistry* 8, 172-180. 10.1039/B513231B.

DATA NOTE

X-ray microtomography-based atlas of mouse cranial development

Jan Matula ¹, Marketa Tesarova ¹, Tomas Zikmund ^{1,*},
Marketa Kaucka ^{2,3}, Igor Adameyko ³ and Jozef Kaiser ¹

¹Central European Institute of Technology, Brno University of Technology, Purkyňova 123, Brno, 61200, Czech Republic; ²Max Planck Institute for Evolutionary Biology, August-Thienemann-Str. 2, Plön, 24306, Germany and ³Medical University of Vienna, Spitalgasse 23, Vienna, 1090, Austria

*Correspondence address: Tomas Zikmund, Central European Institute of Technology, Brno University of Technology, Purkyňova 123, Brno, 61200, Czech Republic. E-mail: tomas.zikmund@ceitec.vutbr.cz  <http://orcid.org/0000-0003-2948-5198>

Abstract

Background: X-ray microtomography (μ CT) has become an invaluable tool for non-destructive analysis of biological samples in the field of developmental biology. Mouse embryos are a typical model for investigation of human developmental diseases. By obtaining 3D high-resolution scans of the mouse embryo heads, we gain valuable morphological information about the structures prominent in the development of future face, brain, and sensory organs. The development of facial skeleton tracked in these μ CT data provides a valuable background for further studies of congenital craniofacial diseases and normal development. **Findings:** In this work, reusable tomographic data from 7 full 3D scans of mouse embryo heads are presented and made publicly available. The ages of these embryos range from E12.5 to E18.5. The samples were stained by phosphotungstic acid prior to scanning, which greatly enhanced the contrast of various tissues in the reconstructed images and enabled precise segmentation. The images were obtained on a laboratory-based μ CT system. Furthermore, we provide manually segmented masks of mesenchymal condensations (for E12.5 and E13.5) and cartilage present in the nasal capsule of the scanned embryos. **Conclusion:** We present a comprehensive dataset of X-ray 3D computed tomography images of the developing mouse head with high-quality manual segmentation masks of cartilaginous nasal capsules. The provided μ CT images can be used for studying any other major structure within the developing mouse heads. The high quality of the manually segmented models of nasal capsules may be instrumental to understanding the complex process of the development of the face in a mouse model.

Keywords: X-ray; computed tomography; microtomography; mouse embryo head; tissue contrast; 3D modelling; nasal capsule

Background

The vertebrate head is considered one of the most complex parts of the body. The head is formed during embryonic development through a process known as morphogenesis, which involves hundreds of genes and non-coding regulatory sequences [1, 2]. This intricate body compartment hosts numerous cell and tissue types forming, e.g., muscles, ligaments, nerves and central nervous system, sensory organs, hair follicles, and teeth, which

are all integrated in the complexly shaped skull. There is a remarkable interspecies but in some cases (such as humans) also intraspecies variability of the craniofacial shapes [3]. Reportedly, the shape of the face (or the whole head) depends on the geometry of the skeleton, which provides protection to sensitive nervous tissues and serves as a scaffold for muscle attachment [1]. The skeleton of the head is formed by 2 types of stiff tissue—bone and cartilage. Although the majority of the head skeleton

Received: 21 September 2020; Revised: 21 December 2020; Accepted: 2 February 2021

© The Author(s) 2021. Published by Oxford University Press GigaScience. This is an Open Access article distributed under the terms of the Creative Commons Attribution License (<http://creativecommons.org/licenses/by/4.0/>), which permits unrestricted reuse, distribution, and reproduction in any medium, provided the original work is properly cited.

in mammals is formed by bones postnatally, the embryonic development of the skull relies on the cartilage. Chondrocranium is induced as 14 independent pieces that grow, acquire specific shape, and fuse later to form the skull [1]. Interestingly, the development of cartilage and bone corresponds to the progress of development of the central and peripheral nervous system and sensory organs [2]. Therefore, the exact developmental link between the emergence of nervous structures and the appearance of cartilage and bone is one of the fundamental questions in developmental biology. At the same time, understanding both the molecular basis and cellular dynamics driving the formation and shaping of the mammalian head is of utmost interest in the fields of clinical genetics and regenerative medicine, which deal with a broad spectrum of human congenital craniofacial disorders.

In our previous work, we aimed to explore the exact sequence of formation and shaping of the developing mammalian face and we used a mouse model for our investigation [1, 2]. The morphological properties of the observed structures are complex, and to fully understand their shaping, advanced imaging techniques are required. X-ray microtomography (μ CT) technique is one of the oldest imaging techniques, but in recent years it has shown its strengths in the field of developmental biology [4]. The principle of μ CT lies in acquiring 2D projections of the scanned sample at regular angle increments. A 3D view of the scene is then created by the process of tomographic reconstruction. This way we gain 3D spatial information that would be otherwise unobtainable without destroying the sample. The superior resolution of modern laboratory-based μ CT machines provides a way to visualize and analyse biological structures on the level of microns and, more importantly, in the 3D spatial context. We combined genetic tracing, gene knockout strategies, mathematical modelling, and μ CT to reconstruct craniofacial development in detail. As a result, we generated a set of μ CT scans from wild-type mouse strains, ranging from E12.5 (where the first induction of early cartilage, represented by condensation of the mesenchyme, can be observed) to E18.5 with fully formed chondrocranium.

While μ CT has been proven useful for non-destructive high-resolution imaging of high-density biological tissues (e.g., bones [5, 6], teeth [7, 8]), there are issues with the differentiation between types of soft tissues in the resulting images. The reason is an insufficient difference in their X-ray attenuation coefficients, which results in low contrast in the reconstructed tomographic images [4]. This inherent limitation of absorption-based computed tomography can be addressed by using contrast-enhancing techniques (e.g., staining the sample with contrast-enhancing chemical substances [9]). Several approaches for soft-tissue contrasting are explored in the literature, e.g., osmium tetroxide [10, 11], Lugol's iodine [12, 13], or phosphotungstic acid (PTA) [4, 9]. We used a contrast method based on differential uptake of PTA by various tissues, resulting in excellent resolution and visibility of fine structures (e.g., see tomographic slices in Fig. 1). It enabled us to differentiate between nasal capsule cartilage (and mesenchymal condensations in the images of younger embryos) and surrounding soft tissues. An operator was then able to manually segment the mesenchymal condensations and cartilage forming the nasal capsule of the embryos (Fig. 2). We provide the generated manual segmentations alongside the tomographic slices. These scans can be used by researchers interested in the development of various structures in the head.

The provided atlas of mouse cranial development (including tomographic slices and segmented nasal capsules) will be es-

sential for tracing the normal development of any tissue type within the vertebrate head. Given the excellent differential contrast and general high quality of the data, they can be reused for any investigation of normal anatomy during the developmental time course.

Methods

Sample preparation

Mouse embryonic heads were contrasted using PTA-staining procedure, followed by a μ CT measurement. The staining protocol is a modification of the protocol pioneered by Metscher [9] and has been described previously [2, 14]. Briefly, the mouse embryos were fixed with 4% formaldehyde in phosphate-buffered saline for 24 hours at 4°C. The samples were then washed with phosphate-buffered saline and subsequently dehydrated with 30%, 50%, and 70% ethanol for 1 day each to minimize shrinking of the embryonic tissue. The samples were then transferred into 0.5–1.0% PTA solution (Lach-Ner, Czech Republic) in 90% methanol. The solution was replaced every 2–3 days. The E12.5 sample was left to absorb the contrasting solution for 1 week, the E15.5 for 3 weeks, and the E18.5 for 7 weeks. After stage E15.5, the head was separated from the body at the level of the shoulders to ensure an adequate and uniform contrasting. After this staining procedure was completed, the samples were rehydrated in a methanol series of decreasing concentration (90%, 70%, 50%, and 30%). Prior to the μ CT scanning, the samples were submerged in 0.5% agarose gel (A5304, Sigma-Aldrich, St. Louis, MO, USA) and placed in polypropylene conical tubes with volume ranging from 0.5 to 15 mL. The tube volume was chosen with respect to the size of the sample to obtain images of the best possible quality. To further characterize the embryonal stages in addition to their age after fertilization, Theiler staging was performed [15]. The prepared samples are listed in Table 1. The *Mus musculus* C57BL/6NCrl samples were sourced from Charles River Laboratories, Germany (IMSR Cat# CRL.27, RRID:IMSR_CRL.27).

Image acquisition

The samples were scanned with a laboratory-based μ CT system, GE Phoenix v|tome|x L 240 (GE Sensing & Inspection Technologies GmbH, Germany). The system was equipped with a high-contrast flat-panel detector DXR250 with 2,048 × 2,048 pixel resolution. The embryos were fixed in polypropylene conical tubes with 0.5% agarose gel to prevent sample movement during the μ CT stage rotation. A total of 2,000 projections were acquired with an exposure time of 900 ms per projection. Each projection was captured 3 times, and an average of the signal was used to improve the signal-to-noise ratio. The acceleration voltage of the X-ray tube was 60 kV, and the tube current, 200 μ A. The X-ray beam was filtered with a 0.1-mm aluminium plate. The time required for scanning 1 sample was 1 hour and 30 minutes.

Software processing

Tomographic reconstruction of the obtained set of projections was performed with GE phoenix datos|x 2.0 3D computed tomography software (GE Sensing & Inspection Technologies GmbH, Germany), which allowed a 3D image of the mouse embryo head to be generated. The voxels are isotropic; voxel sizes for individual samples are listed in Table 1.

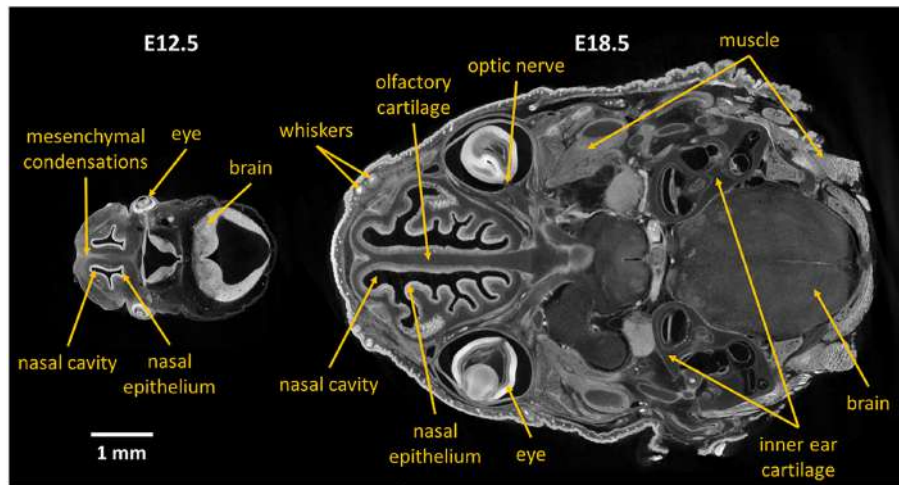


Figure 1: Examples of tomographic slices of mouse embryos 12.5 days old (E12.5) and 18.5 days old (E18.5). μ CT scanning of samples stained with PTA provides image data with excellent contrast, where even fine details are visible. Arrows indicate areas of the image that might be interesting for potential users of the provided dataset.

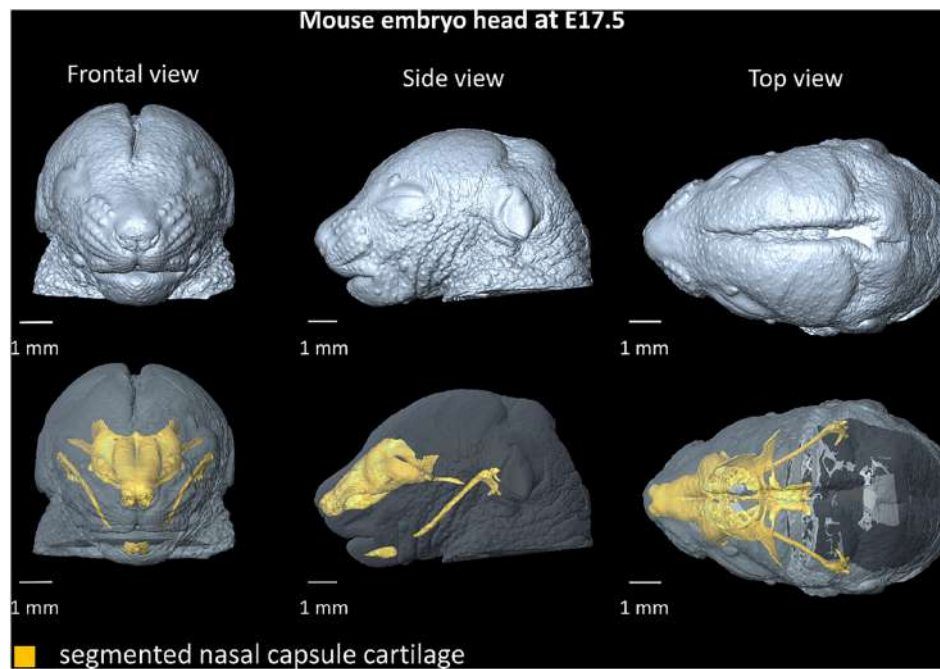


Figure 2: 3D reconstruction of a mouse embryo head at E17.5. Yellow 3D model represents segmented nasal capsule and Meckel cartilage in the head.

Table 1: List of *Mus musculus* C57BL/6NCR1 samples

Resource	Age (days)	Theiler stage	Voxel size (μ m)
Embryo 1	12.5	TS 20	2.6
Embryo 2	13.5	TS 21	3.0
Embryo 3	14.5	TS 23	5.0
Embryo 4	15.5	TS 24	6.0
Embryo 5	16.5	TS 25	6.0
Embryo 6	17.5	TS 26	5.8
Embryo 7	18.5	TS 26	5.5

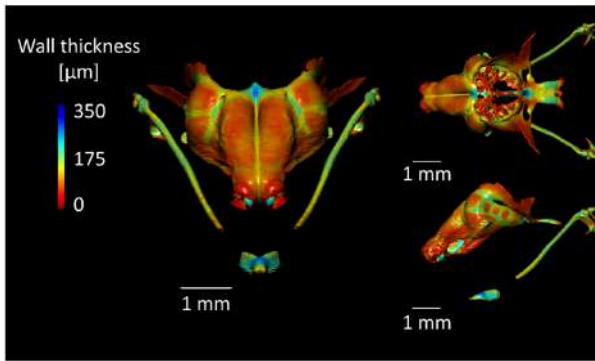


Figure 3: Wall thickness analysis of the manually segmented mouse embryonic nasal capsule (sample E17.5). The wall thickness is calculated as the diameter of a hypothetical sphere that fits within boundary points of the nasal capsule mesh. The 3D wall thickness model was created in the Dragonfly software (Object Research Systems [ORS] Inc., Canada).

Manual segmentation

Avizo (Thermo Fisher Scientific, Waltham, MA, USA) image-processing software was used for manual segmentation of the mesenchymal condensations and nasal capsule cartilage in the reconstructed CT images. Avizo is a commercial software package providing a broad range of tools for manipulating and processing 3D image data. The manual segmentation of the cartilaginous nasal capsule tissue takes ~10–20 hours depending on the size of the sample and the experience of the operator. To make the load of 3D segmentation volume smaller, only every third slice was manually segmented and the rest was calculated by linear interpolation between adjacent manually segmented slices [14]. This 3-fold increase in segmentation speed does not significantly affect the accuracy of the segmentation because the small slice width keeps differences in structures in adjacent slices to a minimum. The overlap between the segmentation performed on a slice-by-slice basis and segmentation with interslice interpolation is >98% (Dice coefficient) in the case of this type of sample. The cartilage was segmented in 2D slices of the whole 3D volume, so there is in some cases a staircase artefact present in the planes other than the plane in which the segmentation was performed.

Data validation and quality control

The segmented 3D models of nasal capsule can be subjected to various subsequent analyses that further highlight the differences between compared models from distinct samples. For instance, wall thickness analysis of the segmented nasal capsule provides valuable information outside of the general morphology assessment of the mouse embryonic anterior face. This information serves to compare multiple samples and provides quantitative information on the variability within each specimen (Fig. 3). Such an approach was instrumental in the work of Kaucza and collaborators [1, 2], where the wall thickness analysis was used to dissect the fundamental mechanisms of cartilage growth and highlighted the molecular basis of the thickness regulation. The obtained results were implemented in a mathematical model that could predict the underlying cellular dynamics of the cartilage growth. Furthermore, using this method it was possible to depict subtle differences between control and mutant embryonic samples that seemed otherwise morphologically similar [1]. Together with core measurements such as the

Table 3: Length and width measurement of the manually segmented nasal capsule performed in the Avizo (Thermo Fisher Scientific, USA) software with the Measure tool

Sample	Length (mm)	Width (mm)
Embryo 1	0.48	1.37
Embryo 2	0.90	1.41
Embryo 3	1.33	1.53
Embryo 4	1.56	1.99
Embryo 5	2.12	2.53
Embryo 6	2.34	2.83
Embryo 7	2.56	2.85

width and the length (see Table 3) of the nasal capsule and mapping the surface expansion during embryonic growth, the authors acquired a detailed understanding of the shaping and the growth of this complex structure.

Shape comparison between individual stages of development provides us with valuable information about the areas of the sample where growth is the most prominent. Figure 4 depicts such an analysis performed on the nasal capsule of embryos in developmental stages ranging from 12.5 to 17.5 days old [1]. This analysis was done in the software GOM Inspect (GOM GmbH, Germany).

By manually segmenting the nasal capsule cartilage in reconstructed images of the samples, we were able to obtain an anatomically accurate 3D-printed model of the embryonic mouse nasal capsule. This is beneficial for researchers to physically evaluate the morphology of the embryonic head. Precise visualization of the developing nasal capsule, together with the opportunity to produce a physical 3D-printed model of this complex anatomical structure, allows better understanding of the organization of single skeletal elements in the framework of the sophisticated organization of the mammalian embryonic head [14] (Fig. 5).

Reuse potential

This dataset with its high-quality manually segmented masks can be instrumental in creating a robust method for segmentation of cartilaginous structures from μ CT images of mouse embryos. The field of image processing has lately been dominated by deep learning algorithms, and specifically convolutional neural networks consistently achieve state-of-the-art results in fully automatic image segmentation tasks [16]. A segmentation model created in such way could make acquiring new samples for analysis of nasal capsule development in mouse embryos much less time consuming because the time-expensive process of manual segmentation would be eliminated. Nevertheless, high-quality scans with a sufficient tissue contrast are required for such automated segmentation. Our dataset has been validated for its suitability for such deep learning algorithm application and can be therefore used by other researchers for this purpose as well.

Biological potential

The possibilities to reuse this dataset are broad and include the analysis of developmental changes in nasal epithelium, eyes, whiskers, tongue, oral cavity, developing teeth, brain, cranial cartilage and bone, tendons, muscles, endocrine organs, vessels, and nerves. For instance, questions pertaining to the mechanisms controlling the growth and shaping of the brain or cranio-

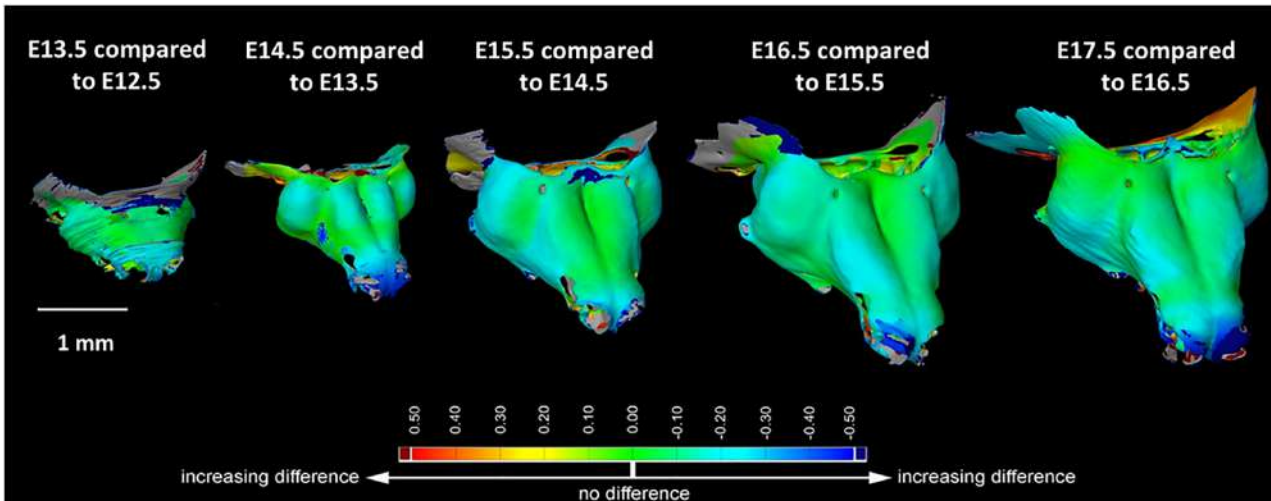


Figure 4: Manually segmented nasal capsules of developmental stages E13.5, E14.5, E15.5, E16.5, and E17.5 were compared to the previous developmental stage in the GOM Inspect software. Figure adapted from Fig. 3—figure supplement 2 from [1] under CC BY 4.0.

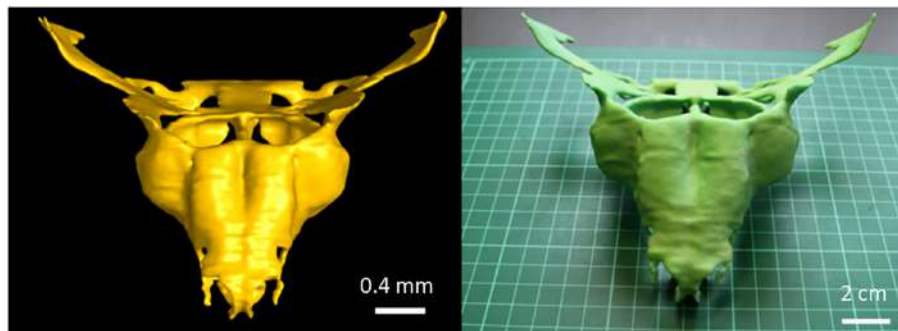


Figure 5: 3D-printed model of the mouse embryo nasal capsule (right) next to its 3D render created from manually segmented binary masks (left). Figure adapted from Fig. 7 from [14] under CC BY 3.0.

facial skeleton are still open and will benefit from the presented data. Furthermore, during development and growth, multiple tissue interactions and integration events occur at multiple morphologically distinct tissue interfaces. Such interactions at the tissue scale lead to the development of muscle attachments, correct vascularization, innervation, and many other key developmental events. This dataset embraces late stages of mouse cranial development when the definitive tissue integration events take place. Without doubt, such tomographic data will be suitable for improving our understanding of these fundamental questions.

Data Availability

The data underlying this article are available in the *GigaScience* Database repository [17]. We provide already-reconstructed μ CT data. The dataset is presented as 8-bit TIFF stacks of corresponding computed tomographic slices and manually segmented masks. The folders are structured so that each folder representing 1 sample contains 2 folders: Images and Masks. The Images folder contains reconstructed tomographic slices in TIFF format, and the folder Masks contains corresponding manually segmented masks. The naming convention is as follows: Sample_name.tif for slice and mask_Sample_name.tif for seg-

mented mask. To enable the users of the dataset to visually inspect the embryo heads in 3 dimensions, .stl files were included together with the image stacks. In addition, a text file is provided for each sample containing information about the voxel size.

As TIFF stacks, the deposited data can be opened and viewed in any basic image viewer; however, to fully take advantage of the possibilities provided by the 3D nature of the images, a specialized viewer for 3D data is recommended. Avizo (Thermo Fisher Scientific, Waltham, MA, USA) is a commercial software package providing a broad range of possibilities to visualize, manipulate, and analyse 3D μ CT image data. Another commercial software option is VG Studio MAX (Volume Graphics GmbH, Germany). We recommend the Fiji ImageJ distribution [18] as a free software option to view and manipulate the provided data. Because the manually segmented masks of the data are binary images composed of 0s (background) and 1s (mesenchymal condensations/cartilage), they can be displayed as black images. To visually inspect the data, it may be necessary to set the software display window to the range from 0 to 1 in some image viewers. The included .stl files of the embryo heads can be explored in many different 3D mesh viewers; a popular free open-source software option is MeshLab [19]. Reconstructions are also available for browsing in Sketchfab [20].

Abbreviations

μ CT: X-ray microtomography; GE: General Electric; PTA: phosphotungstic acid.

Ethics Approval and Consent to Participate

All animal work was approved and permitted by the Local Ethical Committee on Animal Experiments (North Stockholm Animal Ethics Committee) and conducted according to The Swedish Animal Agency's Provisions and Guidelines for Animal Experimentation recommendations.

Competing Interests

The authors declare that they have no competing interests.

Funding

This research was carried out under the project CEITEC 2020 (LQ1601) with financial support from the Ministry of Education, Youth and Sports of the Czech Republic under the National Sustainability Programme II and CzechNanoLab Research Infrastructure supported by MEYS CR (LM2018110). J.M. was financially supported by grant CEITEC VUT-J-20-6477. M.T. was financially supported by grant CEITEC VUT-J-20-6317 and by the Brno City Municipality as a Brno Ph.D. Talent Scholarship Holder.

Authors' Contributions

J.M.: Conceptualization, writing—original draft, visualization, writing—review and editing. M.T.: Methodology, data curation, writing—review and editing. T.Z.: Conceptualization, writing—review and editing. M.K.: Writing—original draft, writing—review and editing. I.A.: Writing—original draft. J.K.: Funding acquisition, supervision, project administration.

References

- Kaucka M, Zikmund T, Tesarova M, et al. Oriented clonal cell dynamics enables accurate growth and shaping of vertebrate cartilage. *Elife* 2017;6:e25902.
- Kaucka M, Petersen J, Tesarova M, et al. Signals from the brain and olfactory epithelium control shaping of the mammalian nasal capsule cartilage. *Elife* 2018;7:e34465.
- Zollikofer CPE, Ponce de León MS. Visualizing patterns of craniofacial shape variation in *Homo sapiens*. *Proc Biol Sci* 2002;269(1493):801–7.
- Metscher BD. MicroCT for developmental biology: A versatile tool for high-contrast 3D imaging at histological resolutions. *Dev Dyn* 2009;238:632.
- Balto K, Muller R, Carrington DC, et al. Quantification of periapical bone destruction in mice by micro-computed tomography. *J Dent Res* 2000;79:35.
- Sabolova V, Brinek A, Sladek V. The effect of hydrochloric acid on microstructure of porcine (*Sus scrofa domestica*) cortical bone tissue. *Forensic Sci Int* 2018;291:260.
- Dosedelova H, Stepankova K, Zikmund T, et al. Age-related changes in the tooth–bone interface area of acrodont dentition in the chameleon. *J Anat* 2016;229:356.
- Landova Sulcova M, Zahradnicek O, Dumkova J, et al. Developmental mechanisms driving complex tooth shape in reptiles. *Dev Dyn* 2020;249:441.
- Metscher BD. Micro CT for comparative morphology: Simple staining methods allow high-contrast 3D imaging of diverse non-mineralized animal tissues. *BMC Physiol* 2009;9:11.
- Choi JP, Foley M, Zhou Z, et al. Micro-CT imaging reveals Mekk3 heterozygosity prevents cerebral cavernous malformations in Ccm2Deficient mice. *PLoS One* 2016;11:e0160833.
- Pai VM, Kozlowski M, Donahue D, et al. Coronary artery wall imaging in mice using osmium tetroxide and micro-computed tomography (micro-CT). *J Anat* 2012;220:514.
- Degenhardt K, Wright AC, Horng D, et al. Rapid 3D phenotyping of cardiovascular development in mouse embryos by micro-CT with iodine staining. *Circ Cardiovasc Imaging* 2010;3:314–22.
- Choi JP, Yang X, Foley M, et al. Induction and micro-CT imaging of cerebral cavernous malformations in mouse model. *J Vis Exp* 2017(127),doi:10.3791/56476.
- Tesarova M, Zikmund T, Kaucka M, et al. Use of micro computed-tomography and 3D printing for reverse engineering of mouse embryo nasal capsule. *J Instrum* 2016;11, doi:10.1088/1748-0221/11/03/C03006.
- Theiler K. *The House Mouse: Atlas of Embryonic Development*. 2nd ed. Springer; 1989.
- Ronneberger O, Fischer P, Brox T. U-net: Convolutional networks for biomedical image segmentation. In: Navab M, Hornegger J, Wells W, et al., eds. *Medical Image Computing and Computer-Assisted Intervention - MICCAI*. Cham: Springer; 2015, doi:10.1007/978-3-319-24574-4_28.
- Matula J, Tesarova M, Zikmund T, et al. Supporting data for “X-ray microtomography-based atlas of mouse cranial development.” *GigaScience Database* 2021. <http://dx.doi.org/10.5524/100862>.
- Schindelin J, Arganda-Carreras I, Frise E, et al. Fiji: An open-source platform for biological-image analysis. *Nat Methods* 2012;9:6:76.
- Cignoni P, Callieri M, Corsini M, et al. MeshLab: An open-source mesh processing tool. In: 6th Eurographics Ital Chapter Conf 2008, Salerno, Italy. Eurographics Association; 2008, doi:10.2312/LocalChapterEvents/ItalChap/ItalianChapConf2008/129-136.
- Sketchfab. <https://sketchfab.com/GigaDB/collections/mouse-embryo>. Accessed 23 Feb 2021.

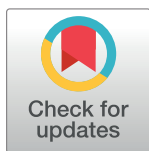
RESEARCH ARTICLE

Local retinoic acid signaling directs emergence of the extraocular muscle functional unit

Glenda Evangelina Comai^{1,2*}, Markéta Tesařová³, Valérie Dupé⁴, Muriel Rhinn⁵, Pedro Vallecillo-García⁶, Fabio da Silva^{7,8}, Betty Feret⁵, Katherine Exelby⁹, Pascal Dollé⁵, Leif Carlsson¹⁰, Brian Pryce¹¹, François Spitz¹², Sigmar Stricker⁶, Tomáš Zikmund³, Jozef Kaiser³, James Briscoe⁹, Andreas Schedl⁷, Norbert B. Ghyselinck⁵, Ronen Schweitzer¹¹, Shahragim Tajbakhsh^{1,2*}

1 Stem Cells & Development Unit, Institut Pasteur, Paris, France, **2** CNRS UMR 3738, Institut Pasteur, Paris, France, **3** Central European Institute of Technology, Brno University of Technology, Brno, Czech Republic, **4** Université de Rennes, CNRS, IGDR, Rennes, France, **5** IGBMC-Institut de Génétique et de Biologie Moléculaire et Cellulaire, Illkirch, France, **6** Institute for Chemistry and Biochemistry, Freie Universität Berlin, Berlin, Germany, **7** Université Côte d'Azur, INSERM, CNRS, iBV, Nice, France, **8** Division of Molecular Embryology, German Cancer Research Center (DKFZ), Heidelberg, Germany, **9** The Francis Crick Institute, London, United Kingdom, **10** Umeå Center for Molecular Medicine, Umeå University, Umeå, Sweden, **11** Research Division, Shriners Hospital for Children, Portland, United States of America, **12** Genomics of Animal Development Unit, Institut Pasteur, Paris, France

* comai@pasteur.fr (GEC); shaht@pasteur.fr (ST)



OPEN ACCESS

Citation: Comai GE, Tesařová M, Dupé V, Rhinn M, Vallecillo-García P, da Silva F, et al. (2020) Local retinoic acid signaling directs emergence of the extraocular muscle functional unit. *PLoS Biol* 18(11): e3000902. <https://doi.org/10.1371/journal.pbio.3000902>

Academic Editor: Simon M. Hughes, King's College London, UNITED KINGDOM

Received: January 7, 2020

Accepted: October 1, 2020

Published: November 17, 2020

Peer Review History: PLOS recognizes the benefits of transparency in the peer review process; therefore, we enable the publication of all of the content of peer review and author responses alongside final, published articles. The editorial history of this article is available here: <https://doi.org/10.1371/journal.pbio.3000902>

Copyright: © 2020 Comai et al. This is an open access article distributed under the terms of the [Creative Commons Attribution License](https://creativecommons.org/licenses/by/4.0/), which permits unrestricted use, distribution, and reproduction in any medium, provided the original author and source are credited.

Data Availability Statement: All relevant data are within the paper and its [Supporting Information](#) files.

Abstract

Coordinated development of muscles, tendons, and their attachment sites ensures emergence of functional musculoskeletal units that are adapted to diverse anatomical demands among different species. How these different tissues are patterned and functionally assembled during embryogenesis is poorly understood. Here, we investigated the morphogenesis of extraocular muscles (EOMs), an evolutionary conserved cranial muscle group that is crucial for the coordinated movement of the eyeballs and for visual acuity. By means of lineage analysis, we redefined the cellular origins of periocular connective tissues interacting with the EOMs, which do not arise exclusively from neural crest mesenchyme as previously thought. Using 3D imaging approaches, we established an integrative blueprint for the EOM functional unit. By doing so, we identified a developmental time window in which individual EOMs emerge from a unique muscle anlage and establish insertions in the sclera, which sets these muscles apart from classical muscle-to-bone type of insertions. Further, we demonstrate that the eyeballs are a source of diffusible all-trans retinoic acid (ATRA) that allow their targeting by the EOMs in a temporal and dose-dependent manner. Using genetically modified mice and inhibitor treatments, we find that endogenous local variations in the concentration of retinoids contribute to the establishment of tendon condensations and attachment sites that precede the initiation of muscle patterning. Collectively, our results highlight how global and site-specific programs are deployed for the assembly of muscle functional units with precise definition of muscle shapes and topographical wiring of their tendon attachments.

Funding: We acknowledge funding support from the Institut Pasteur, Association Française contre le Myopathies, Agence Nationale de la Recherche (Laboratoire d'Excellence Revive, Investissement d'Avenir; ANR-10-LABX-73) and the Centre National de la Recherche Scientifique. We gratefully acknowledge the UtechS Photonic Bioluminescence (Imagopole), C2RT, Institut Pasteur, supported by the French National Research Agency (France Bioluminescence; ANR-10-INSB-04; Investments for the Future). MT, TZ and JK acknowledge the project CEITEC 2020 (LQ1601) with financial support from the Ministry of Education, Youth and Sports of the Czech Republic under the National Sustainability Programme II and Ceitec Nano+ project CZ.02.01/0.0/0.0/16_013/0001728 under the program OP RDE. MT was financially supported by the Brno City Municipality as a Brno Ph.D. Talent Scholarship Holder. The funders had no role in study design, data collection and analysis, decision to publish, or preparation of the manuscript.

Competing interests: The authors have declared that no competing interests exist.

Abbreviations: ADH, alcohol dehydrogenase; ATRA, all-trans retinoic acid; ALDH1A1, Aldehyde Dehydrogenase 1 Family Member A1; ALDH1A3, Aldehyde Dehydrogenase 1 Family Member A3; E, embryonic day; EOM, extraocular muscle; GFP, green fluorescent protein; KO, knock-out; LHX2, LIM Homeobox 2; Mesp1, mesoderm posterior BHLH transcription factor 1; mGFP, membrane tagged GFP; micro-CT, micro-computed tomography; MYF5, myogenic factor 5; MYOD, myogenic differentiation 1; MYOG, Myogenin; MyHC, myosin heavy chain; NCC, neural crest cell; PAX6, Paired Box 6; PAX7, Paired Box 7; PITX2, Paired-like homeodomain transcription factor 2; POM, periocular mesenchyme; RAR, retinoic acid receptor; RARE, retinoic acid response element, RDH, retinol dehydrogenase; RPE, retinal pigmented epithelium; RXR, retinoid X receptor; Scx, scleraxis; Shh, Sonic Hedgehog; SMA, alpha smooth muscle actin; SOX9, SRY-box containing gene 9; TCF4, Transcription factor 4; Tom, tdTomato; WMIF, whole-mount immunofluorescence; Wnt1, Wnt Family Member 1.

Introduction

Acquisition of shape and pattern during development depends on the orchestrated crosstalk between a variety of tissues and cell types. Although significant knowledge on the mechanisms of differentiation and patterning within individual tissues has been attained, much less is known on how patterning of different adjacent tissues is integrated. The vertebrate musculoskeletal system serves as an ideal model to study these processes as different tissues including muscle, tendon and their attachments need to be articulated in 3D for proper function [1,2].

Among the craniofacial muscles, the morphological configuration of the extraocular muscles (EOMs) has been a longstanding challenge in comparative anatomy and evolutionary biology. Besides specialized adaptations, the basic EOM pattern is shared among all vertebrate classes [3–5] and includes 4 recti muscles (the superior rectus, the medial rectus, the inferior rectus, and the lateral rectus) and 2 oblique muscles (superior oblique and inferior oblique) for movement of the eyeball. Most vertebrates have also accessory ocular muscles that serve to retract the eye (the retractor bulbi) or control eyelid elevation (the levator palpebrae superioris) [3,6]. As such, the EOMs constitute an archetypal and autonomous functional unit for the study of how muscles, tendons, and tendon attachments are integrated with the development of the eyeball, their target organ.

Craniofacial muscles are derived from cranial paraxial and prechordal head mesoderm [3,7]. The corresponding connective tissues, i.e., tendons, bones, cartilages, and muscle connective tissue, were reported to be derived from cranial neural crest cells (NCCs) [7,8]. Although early myogenesis is NCC independent, NCCs later regulate the differentiation and segregation of muscle precursors, dictate the pattern of muscle fiber alignment, and that of associated skeletal and tendon structures [9–14]. Moreover, deletion of several genes in NCCs demonstrated their non-cell-autonomous roles in muscle morphogenesis at the level of the jaw [12,15,16], extraocular [17,18], and somitic-derived tongue muscles [19]. However, the full series of events driving morphogenesis of craniofacial musculoskeletal functional units is unexplored to date, in part because of the anatomical complexity of their configuration in the head. Moreover, understanding the developmental mechanisms that allow musculoskeletal connectivity is essential to understand the anatomical diversification that took place during the evolution of the vertebrate head. Yet, proximate factors that allow cross-tissue communication for coordinated emergence of the individual muscle masses with that of their tendons and attachment sites are poorly defined.

Much of our understanding of musculoskeletal development and integration into functional units comes from studies in the limb. Lateral plate mesoderm-derived muscle connective tissue cells and tendon primordia establish a pre-pattern that determines the sites of myogenic differentiation and participate in splitting of the muscle masses in the limb [20–22]. Tendons connect muscles to the skeleton and are formed by scleraxis (Scx)-expressing mesenchymal progenitors [23,24]. Although some features of tendon development are autonomous, key stages rely on signals emanating from muscle or cartilage, according to their positioning in the limb [2]. Bone superstructures, which provide anchoring points for tendons to the skeleton, are initiated independently of muscle, but their maintenance and growth depend on cues from both tendon and muscle [2]. Given the distinct gene regulatory networks governing cranial muscle development [25,26], and embryonic origins of connective tissues in the head [7,8], it is unclear if this logic of musculoskeletal integration is conserved in the head and how structures that do not integrate bones, such as EOMs, are established.

All-trans retinoic acid (ATRA), the biologically active metabolite of retinol (vitamin A), is a critical morphogen with widespread roles in craniofacial development [27,28]. ATRA acts as a ligand for nuclear retinoic acid receptors (RARs), which are ligand-dependent transcriptional

regulators that work as heterodimers with retinoid X receptors (RXRs) [28,29]. ATRA is synthesized from retinol through 2 oxidation steps by specific retinol/alcohol dehydrogenases (RDH/ADH) and retinaldehyde dehydrogenases (ALDH1A1, ALDH1A2, and ALDH1A3) [28,29]. ATRA is critical for early eye development in several species [30–32], in which ATRA metabolic enzymes are expressed in the early retina with tight spatiotemporal patterns [33]. As such, the developing eye acts as a signaling center nucleating anterior segment morphogenesis, with paired-like homeodomain transcription factor 2 (PITX2) being the potential major downstream ATRA effector in periocular NCCs [30,34–36]. Whether ATRA is required for morphogenesis of the EOMs and associated connective tissues remains unexplored.

Here, we reassessed the embryological origins of the connective tissues of the periocular region and present the first integrative blueprint for morphogenesis of the EOM functional unit. We provide genetic evidence for the existence of a retinoic acid signaling module that coordinates the emergence of individual EOMs, their tendons, and insertion sites. We show that the action of retinoic acid signaling in muscle patterning is mainly non-cell-autonomous, through its action on the NCC-derived periocular mesenchyme. We propose that the interactions between muscles, tendons, and their attachments are similar to those observed in the limb, yet they exhibit specific hallmarks that are characteristic of this anatomical location.

Results

Genetic fate mapping of mouse periocular tissues

Given the complex anatomical disposition of the EOMs, we first set out to map morphological landmarks and cell relationships during patterning of these muscles. The periocular mesenchyme (POM) is a heterogeneous cell population surrounding the optic cup that gives rise to specialized structures of the anterior segment of the eye and connective tissues associated with the EOMs [37]. With exception of the EOMs and endothelial lining of ocular blood vessels (choroid), all connective tissues of the POM (cartilage, muscle connective tissue, tendons) were reported to be derived from NCCs in zebrafish, chicken, and mouse embryos [38–43]. The 4 recti EOMs originate deep in the orbit, at the level of a fibrous ring called the annulus of Zinn, and insert into the scleral layer of the eye [44]. Because information on EOM tendons and attachment sites is scarce, we used genetic fate mapping to reassess the embryological origins of the tissues interacting with EOMs during their morphogenesis. We simultaneously traced the contribution of NCC (Fig 1A–1B", S1A, and S1B Fig) and mesodermal (Fig 1C–1D", S1C and S1D Fig) derivatives using *Tg:Wnt1^{Cre}* and *Mesp1^{Cre}* mice, respectively [45,46], in combination with the *R26^{Tom}* reporter [74].

As expected, connective tissues at the EOM insertion level were derived from NCCs as assessed by tdTomato expression (*Tg:Wnt1^{Cre};R26^{Tom}*, Fig 1A–1A", S1A Fig). Surprisingly, we found that lineage contributions differed in dorsal sections, where connective tissues at the EOM origin level were derived from the cranial mesoderm (*Mesp1^{Cre};R26^{Tom}*, Fig 1D–1D", S1D Fig). To characterize in more detail the cell populations arising from these derivatives, we used transcription factor 4 (TCF4) as muscle connective tissue marker [47], and a *Scx* reporter line (*Tg:Scx-GFP+*) to mark tendons and their early progenitors with green fluorescent protein (GFP) [24,48]. TCF4 was expressed robustly in muscle connective tissue fibroblasts in both NCC- and mesoderm-derived regions (S1E–S1F' Fig). Similarly, *Tg:Scx-GFP* (Fig 1A–1D", S1A–S1D Fig) strongly labeled the future EOM tendons at the origin and insertion sites residing respectively in mesoderm- and NCC-derived domains. Additionally, *Tg:Scx-GFP* (Fig 1A1, 1D1, S1G and S1H Fig) and *Scx* mRNA (S1I and S1J Fig) marked muscle connective tissue fibroblasts that were widely distributed among the muscle masses and overlapped with TCF4 (S1G and S1H Fig), as described in other regions of the early embryo [49,50]. Altogether, these

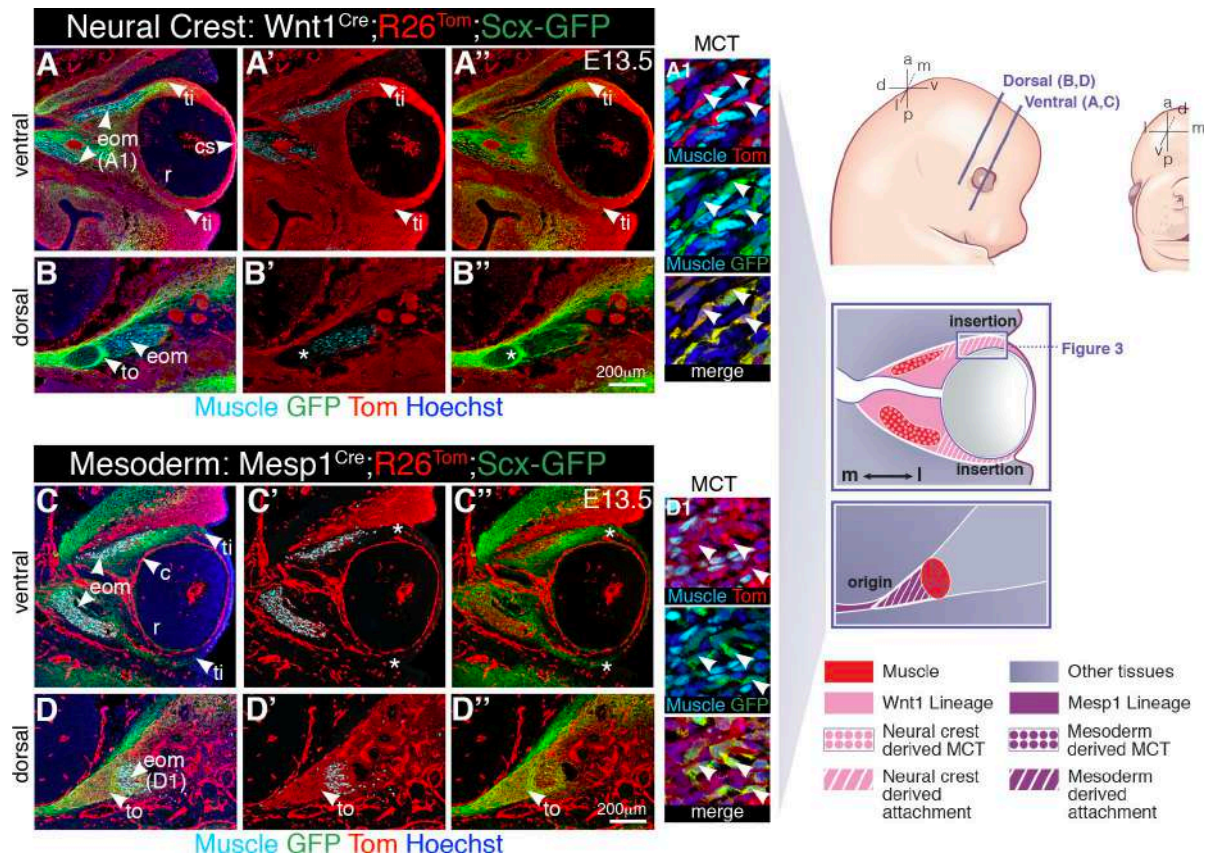


Fig 1. Lineage contributions to the EOM functional unit. (A–B'') Neural crest (*Tg:Wnt1^{Cre};R26^{Tom};Scx-GFP*) and (C–D'') mesodermal (*Mesp1^{Cre};R26^{Tom};Scx-GFP*) lineage contributions to the periocular region of E13.5 embryos, combined with immunostaining for tdTomato (Tom), GFP (*Tg:Scx-GFP* reporter), and muscle (PAX7/MYOD/MYOG, myogenic markers). Coronal sections at ventral (A–A'', C–C'') and dorsal (B–B'', D–D'') levels. Asterisks in B', B'' denote Tom negativity at the tendon origin. Asterisks in C', C'' denote Tom negativity at the tendon insertion site. (A1, D1) High-magnification views of muscle areas in panels A and D. (*n* = 3 per condition). a, anterior; c, choroid; cs, corneal stroma; d, dorsal; E, embryonic day; eom, extraocular muscle; l, lateral; m, medial; MCT, muscle connective tissue; p, posterior; r, retina; ti, tendon insertion; to, tendon origin; v, ventral.

<https://doi.org/10.1371/journal.pbio.3000902.g001>

findings indicate that the EOMs develop in close association with connective tissues of 2 distinct embryonic origins: neural crest laterally (at the EOM insertion) and mesoderm medially (at the EOM origin).

Development of the EOMs and their insertions overlap spatiotemporally

Patterning of the EOMs and their insertions is understudied because of the difficulty in interpreting a complex 3D tissue arrangement from tissue sections alone. Therefore, we established an imaging pipeline that includes whole-mount immunofluorescence (WMIF) of the periocular region, tissue clearing, confocal microscopy, and reconstructions of the obtained images into 3D objects. To visualize the developing EOMs, we used antibodies against myogenic differentiation 1 (MYOD), myogenin (MYOG), and Desmin as myogenic commitment and differentiation markers and myosin heavy chain (MyHC) to label myofibers (Fig 2A–2C' and S1 Video). At embryonic day (E)11.75, the EOMs were present as a single anlage (Fig 2A and 2A') medial to the eyeball. By E12.5, the EOM anlage split towards the eyeball into submasses corresponding to the future 4 recti, 2 oblique muscles, and the accessory retractor bulbi muscle (Fig 2B and 2B'). Fully individuated muscles were evident by E13.5 (Fig 2C and 2C'). Thus, we

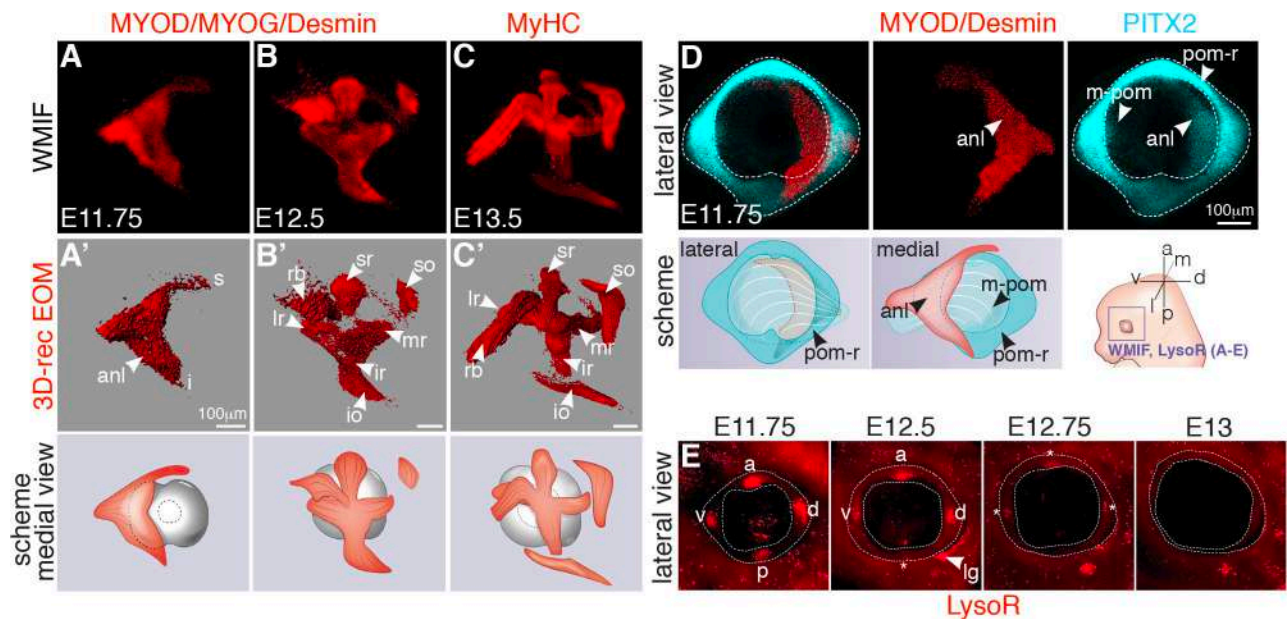


Fig 2. Developmental time course of EOM development. (A–C) WMIF for MYOD/MYOG/Desmin (myogenic differentiation markers) (A, B) and MyHC (myofibers) (C) at the indicated embryonic stages. EOMs were segmented from adjacent head structures and 3D-reconstructed in Imaris (Bitplane). (A'–C') EOMs are shown as isosurfaces for clarity of visualization. Medial views as schemes (left eye). (D) WMIF for MYOD/Desmin (labeling the EOM anlage, isosurface) and PITX2 (labeling the POM and EOM anlage) on E11.75 embryos (left eye). Lateral and medial views as schemes. (E) Whole-mount LysoTracker Red (LysoR) staining of the periocular region at the indicated stages (left eye). The POM is delimited with dashed lines. Asterisks indicate apoptotic foci with reduced intensity from E12.5 onwards. anl, anlage; a, anterior; d, dorsal; 3D-rec, 3D reconstruction; E, embryonic day; i, inferior EOM anlage projection; io, inferior oblique; ir, inferior rectus; l, lateral; lg, lacrimal gland sulcus; lr, lateral rectus; m, medial; m-pom, medial periocular mesenchyme; mr, medial rectus; p, posterior; pom, periocular mesenchyme; pom-r, periocular mesenchyme ring; rb, retractor bulbi; s, superior EOM anlage projection; so, superior oblique; sr, superior rectus; v, ventral; WMIF, whole-mount immunofluorescence.

<https://doi.org/10.1371/journal.pbio.3000902.g002>

conclude that EOM patterning in the mouse occurs by splitting from a single mass of myogenic progenitors that target the eyeball, with the most dramatic morphogenetic changes taking place between E11.75 and E12.5.

The EOMs insert into the sclera, a dense fibrous layer derived from the POM [40,44]. PITX2 is a well-established marker of both the POM and EOM progenitors ([40], S2A–S2C Fig), and foci of cell death in the POM were suggested to label the tendon attachment positions of the 4 recti muscles [51]. To better understand the development of the EOM insertions, we first performed whole-mount immunostaining for the POM marker PITX2 and LysoTracker Red staining to detect programmed cell death on live embryos [52]. WMIF for PITX2 at E11.75 revealed a ring of POM cells expressing high levels of PITX2 that formed a continuum with low-expressing cells extending towards the base of the EOM anlage (Fig 2D and S2 Video). The pattern of LysoTracker Red staining in the POM-ring was highly dynamic, where 4 foci of apoptosis were present at E11.75 at the horizons of the eye but regressed progressively from E12.5 onwards (Fig 2E). To confirm that these foci define tendon attachment positions in the POM, we performed whole-mount immunostaining for myogenic and tendon progenitors on LysoTracker-stained embryos. Surprisingly, we observed that even before muscle splitting initiated, *Scx-GFP*⁺ condensations bridged the edges of the EOM anlage and the 4 LysoTracker Red⁺ foci in the POM (E11.75, S3 Video), presaging the attachment sites of the future 4 recti muscles (E12.5, S4 Video).

We next wanted to understand the relationship between foci of apoptosis in the POM and the establishment of the tendon insertion sites per se. In the developing limb and jaw, bone superstructures or ridges, generated by a unique set of progenitors that co-express *Scx* and

SRY-box containing gene 9 (SOX9), provide a stable anchoring point for muscles via tendons [53–56]. Although EOMs insert into a non-bone NCC-derived structure, early markers of pre-committed cartilage, such as SOX9, are expressed in the POM [57]. To examine the time course of development of EOM insertions in greater detail, we immunostained *Tg:Scx-GFP* and *Tg:Wnt1^{Cre};R26^{Tom};Scx-GFP* coronal (Fig 3A–3J” and S3A–S3F” Fig) and transverse (S3G–S3H” Fig) sections for PITX2 and SOX9. Between E11.5 and E13.5, PITX2 marked all cells of the lateral-most NCC-derived POM between the surface ectoderm and retina (Fig 3B and 3F, and S2A–S2B” Fig), which corresponds to the POM-ring observed in 3D views (Fig 2D). In this region, *Scx-GFP* expression was initially detected in a salt-and-pepper pattern (Fig 3C and S3E Fig) but became progressively limited to the forming tendon tips (Fig 3G and S3F Fig). SOX9 expression overlapped with that of PITX2 (Fig 3D, 3H, S3E’ and S3F’ Fig) but became more restricted to the insertion site by E13.5 and with a pattern complementary to *Scx-GFP*+ (Fig 3G and S3F Fig). Notably, *Scx-GFP*+ SOX9+ cells could be detected between E11.5 and E13.5 at the interface between mutually exclusive *Scx-GFP*+ and SOX9+ cells (S3A–S3C” Fig), resembling what was observed during tendon-to-bone attachment formation in other regions in the embryo [53–56].

At the putative insertion site, the tdTomato staining in the NCC-derived lateral POM initially appeared as punctate (Fig 3A), and reminiscent of the apoptotic domains observed in 3D views (Fig 2E). LysoTracker Red and TUNEL staining confirmed cell death of SOX9+ PITX2 + POM cells (Fig 3I–3J””, S3E, S3E’ and S3G–S3H” Fig) that were at a higher density than the more medial POM cells (Fig 3K, S1 Data). Given that LysoTracker Red+ cells could not longer be seen at E13.5 (S3F and S3F’ Fig), these data suggest that at the insertion sites of the recti muscles in the POM, foci of apoptosis mark the places where cell compaction and refinement of the SOX9 expression pattern will take place.

Major POM remodeling events could be detected by E14.5. EOM tendons co-expressed *Scx-GFP*, Tenascin, and PITX2, but surprisingly, SOX9 expression became restricted to the thin scleral layer and retinal pigmented epithelium (RPE) (Fig 3L–N’ and S3D–S3D” Fig). Altogether, these results show that development of the EOMs, their tendons and insertion sites overlap spatiotemporally and thus, might be regulated in a coordinated manner. Moreover, similarly to other locations in the body, *Scx* and SOX9 show dynamic expression patterns at the insertion site, but additional specific hallmarks, notably the presence of cell compaction and apoptotic foci, seem to be characteristic of this anatomical location.

Abnormal EOM morphogenesis in mutants with ocular malformations

Having assessed how morphogenesis of EOMs and their insertion sites is coordinated, we set out to investigate the role of the target organ, the eyeball, on the establishment of the EOM functional unit. To this end, we performed micro-computed tomography (micro-CT) scans in mouse mutants with a spectrum of ocular perturbations. First, we examined *small eye* (Sey) *Pax6* (Paired box 6) mutant embryos (*Pax6^{Sey/Sey}*), in which eye development is arrested at the optic vesicle stage [58–60]. EOM patterning in *Pax6^{Sey/+}* embryos proceeded normally (S4A and S4B Fig), whereas in the *Pax6^{Sey/Sey}* mutant, the EOMs appeared as a single mass on top of a rudimentary optic vesicle (S4C Fig). As *Pax6* is expressed in the optic vesicle and overlying ectoderm that forms the lens and cornea [58], but not in EOMs, these observations suggest a non-cell-autonomous role in EOM patterning. Similarly, in LIM homeobox 2 (*Lhx2*) mutant embryos (*Tg:Lhx2^{Cre};Lhx2^{fl/fl}*) embryos, in which inactivation of the *Lhx2* gene in eye committed progenitor cells leads to a degeneration of the optic vesicle at E11.5 [61], EOM patterning was severely affected, and few EOM submasses were observed (S4D–S4E’ Fig). Finally, in cyclopic embryos resulting from inversion of Sonic hedgehog (*Shh*) regulatory regions, EOMs

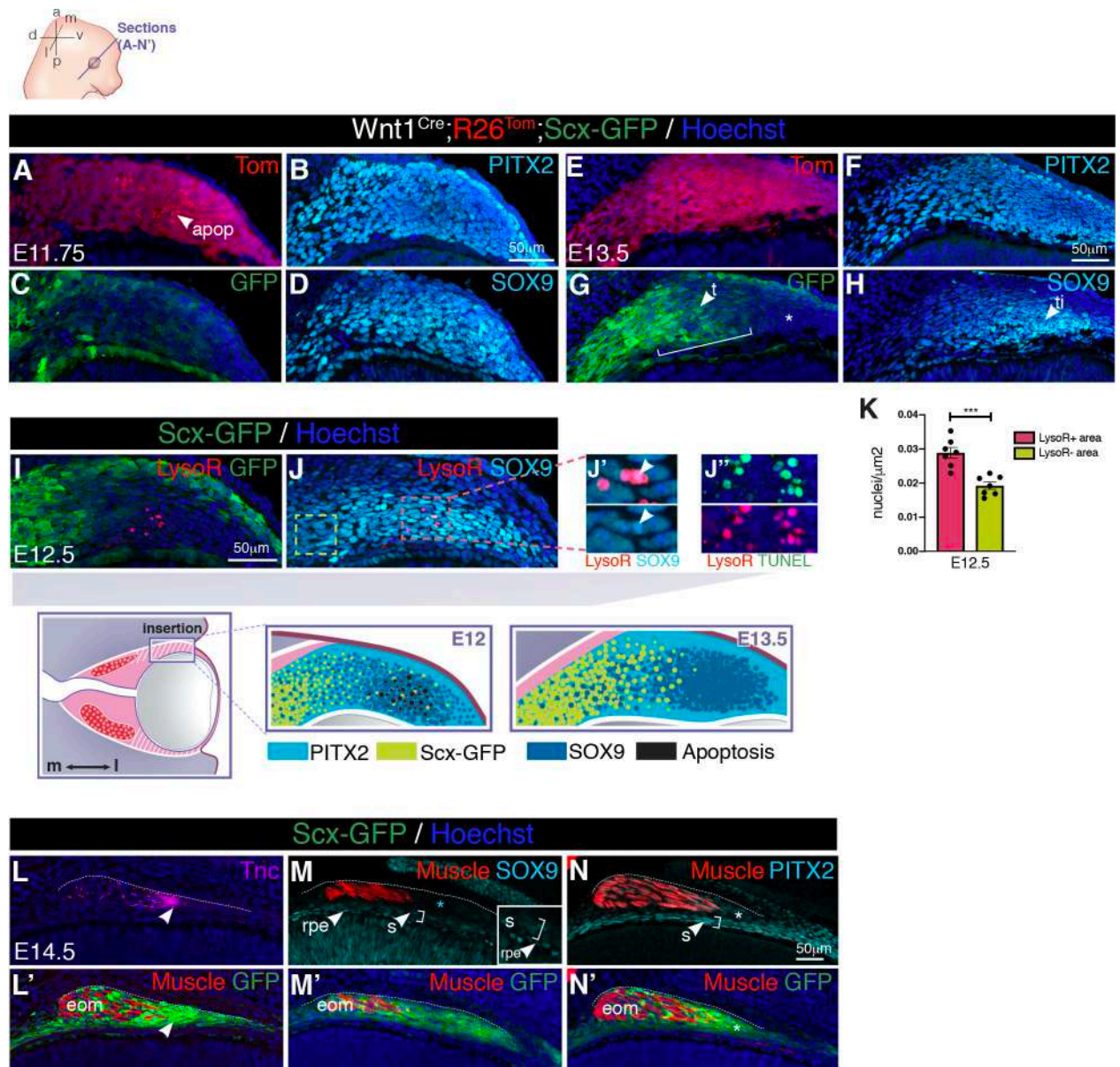


Fig 3. Developmental time course of EOM insertions in the POM. (A-D) Immunostaining of lateral POM in coronal sections of E11.75 *Tg:Wnt1^{Cre};R26^{Tom};Scx-GFP* embryos for the indicated markers. B, Immunostaining of section adjacent to the one shown in (A, C, D; channels split for clarity). (E-H) Immunostaining of lateral POM in coronal sections of E13.5 *Tg:Wnt1^{Cre};R26^{Tom};Scx-GFP* embryos for the indicated markers. G, Immunostaining of section adjacent to the one shown in (E, F, H; channels split for clarity). Bracket show overlap between *Scx-GFP* and *SOX9* expression domains (high-magnification views in S3C Fig). The asterisk in G points to *Scx-GFP*-negative *SOX9*+ lateral-most POM at the insertion site. (I, J) Immunostaining of lateral POM in coronal sections of E12.5 *Tg:Scx-GFP* embryos pretreated with LysoR. Arrowheads in J point to LysoR + *SOX9*+ cells. (J') TUNEL and LysoR staining of a section adjacent to the one shown in (I, J). (K) Quantification of the total number of *SOX9*+ cells per square-micrometer in LysoR+ regions (red square, J) and more medial LysoR-negative regions (yellow square, J). Mann-Whitney test. Cell density was 33% higher in the LysoR+ area compared with the more medial POM. See S1 Data for individual values. (L-N') Immunostaining on coronal sections of E14.5 *Tg:Scx-GFP* embryos. (L, L') *Tnc* and *Scx-GFP* co-localize in tendons at level of insertion (arrowhead). (M, M') *SOX9* expression in the POM is greatly reduced at the insertion site and no longer overlaps with *Scx-GFP* (asterisk, cyan). Low levels of *SOX9* expression in the RPE and sclera. (N, N') *PITX2* remains expressed in the POM at the insertion site overlapping with *Scx-GFP* (asterisk) and in the sclera. MyHC (L') and SMA (M-N') were used to label EOM muscle. Dashes in L-N were drawn according to GFP labeling in L'-N'. Images in A-N' correspond to insertion site of superior rectus muscle in the POM as shown in the scheme. (*n* = 3 per condition). a, anterior; apop, apoptosis spots; d, dorsal; E, embryonic day; eom, extraocular muscle; l, lateral; LysoR, LysoTracker Red; m, medial; p, posterior; POM, periorbital mesenchyme; rpe, retinal pigmented epithelium; s, sclera; t, tendon; ti, tendon insertion, v, ventral.

<https://doi.org/10.1371/journal.pbio.3000902.g003>

underwent splitting and projected towards the centrally located ectopic eye, although with an abnormal 3D arrangement as reported for human cyclopia conditions (S4F–S4F” Fig) [7]. Together with previous studies in which surgical removal of the eye at specific timepoints of development results in smaller EOMs [9,62], our observations point to the eye as a critical organizer of EOM patterning.

Muscle patterning depends on retinoic acid signaling of neural origin

To study the role of target organ derived cues in EOM patterning, we investigated the role of retinoic acid signaling, which plays multiple paracrine roles during embryonic eye development [33]. As ALDH1A1-3 are rate-limiting enzymes in the production of ATRA [63], we characterized their expression in the periocular region at the time of EOM patterning. Between E10.5 and E12.5, *Aldh1a1* was expressed strongly in the dorsal retina and lens, *Aldh1a2* was expressed in the temporal mesenchyme, and *Aldh1a3* was most strongly expressed in the ventral retina and RPE (S5A–S5A” Fig) [34,36]. At the protein level, ALDH1A3 was detected on tissue sections in the surface ectoderm, presumptive corneal epithelium, retina, and RPE (Fig 4A). Interestingly, ALDH1A3 was also expressed in the optic stalk between E10.5 and E12.5 and thus centrally positioned with respect to EOM development (Fig 4A). To target the retinoic signaling pathway (Fig 4B), we used *Aldh1a3*^{-/-} [64] and *Rdh10*^{-/-} [65] mutants. We also administered the BMS493 inhibitor (pan-RAR inverse agonist) to pregnant females every 10–12 hours between E10.5 and E11.75, i.e., preceding the initiation of muscle splitting (Fig 2A–2C), and once NCC migration to the POM was finalized [66,67]. Micro-CT analysis showed that *Aldh1a3*^{-/-} and BMS493-treated embryos displayed eye ventralization and a shortened optic nerve when compared with controls (S5B Fig), but they retained the overall organization of the nasal capsule and orbit (S5C Fig). Ventral and lateral views of the 3D-reconstructed EOMs (Fig 4C–4E), showed that *Aldh1a3*^{-/-} and BMS493-treated embryos lacked the standard 3D arrangement of 4 recti and 2 oblique muscles observed at E13.5 in control embryos. Nevertheless, in all cases, EOMs originated medially from the hypochiasmatic cartilages of the pre-sphenoid bone, indicating that the overall orientation of the EOMs was preserved (Fig 4D”). Given that the EOMs are more affected at their insertion than their origin level upon ATRA deficiency, this finding suggests that EOM patterning is, in part, modular.

To analyze EOM and tendon patterning with higher resolution, we performed whole-mount immunostainings for differentiated myofibers and tendon with MyHC and Tnc (Tenascin) antibodies (Fig 4F–4H”). On medial and lateral views of 3D-reconstructed EOMs, only the retractor bulbi and superior rectus could be clearly identified among the non-segregated muscle fibers in *Aldh1a3*^{-/-} embryos (Fig 4G and 4G”). As expected from global invalidation of retinoic acid signaling, EOM perturbation was more severe in BMS493-treated embryos (Fig 4H and 4H”). The superior oblique was absent or continuous with the anterior part of the anlage, and the medial portion of the retractor bulbi was thicker and less clearly isolated from the rest of the anlage (Fig 4H). In both conditions of ATRA deficiency, Tenascin and *Scx*-GFP+ cells were present at the tips of the individual, though mispatterned, muscles at this stage (Fig 4G’, 4H’, and S5 Video). Analysis of *Aldh1a3*^{-/-} and BMS493-treated embryos revealed, on average, a 26% reduction in the EOM volume compared with controls (Fig 4I, S2 Data). However, MyHC+ myofibers were present in *Aldh1a3*^{-/-} and BMS493-treated embryos (Fig 4G and 4H), suggesting that EOM differentiation was not overtly affected in these conditions. Instead, these observations suggest that EOM fiber alignment and segregation of the muscle masses are dependent on retinoic acid signaling.

As dose and temporal control are critical in the context of retinoic acid signaling [27,32,68], we performed other BMS493 injection regimes between E10.5 and E12.5 (S1 Table). EOM

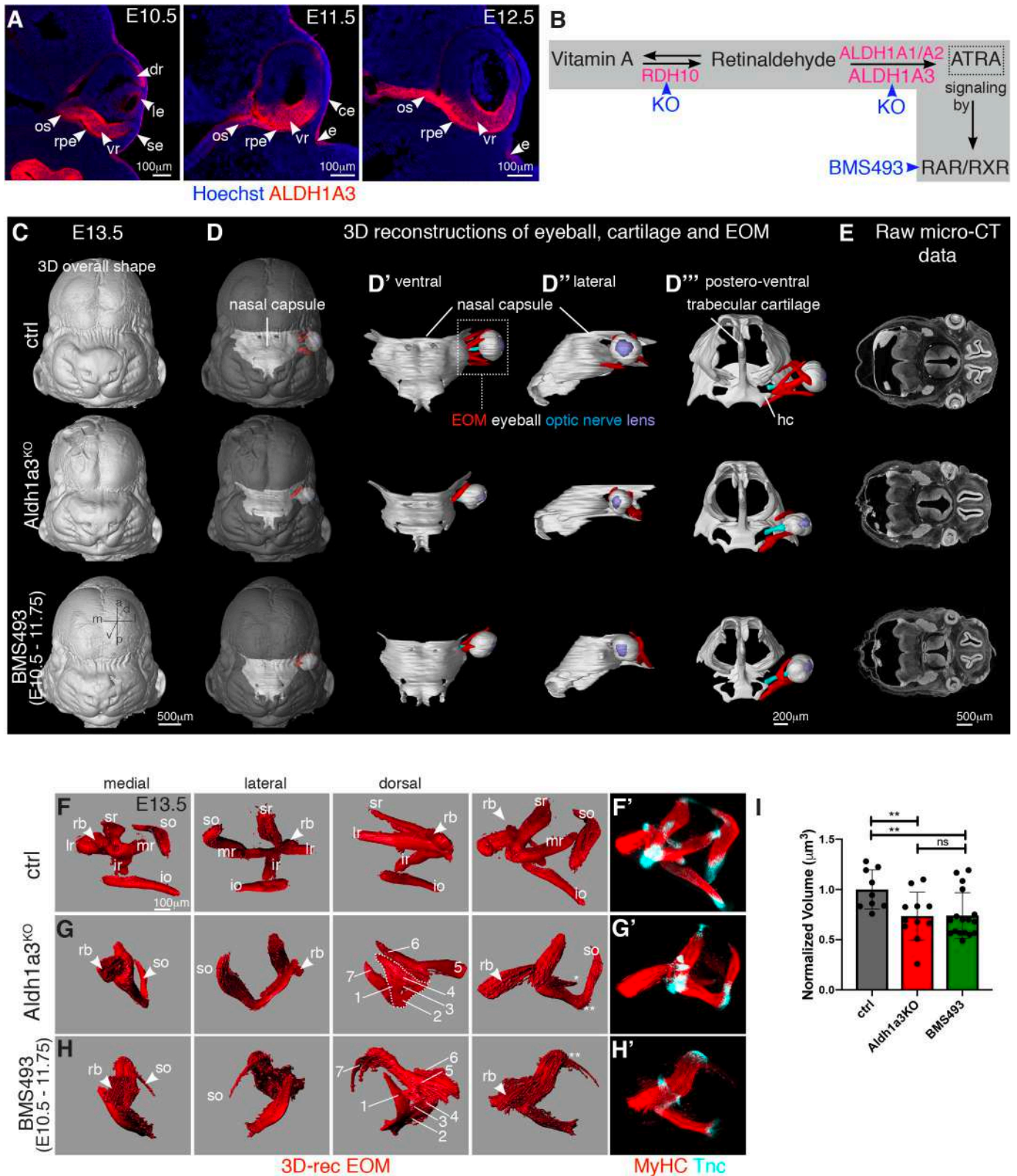


Fig 4. Extraocular muscle morphogenesis is dependent on ATRA. (A) Immunostaining for ALDH1A3 on coronal sections of E10.5, E11.5, and E12.5 control embryos ($n = 3$). (B) Scheme of retinoic acid signaling pathway with key enzymes for oxidation of retinol (Vitamin A) and retinaldehyde (pink) and mutants/inhibitors used in this study (blue). (C-D''') Micro-CT-based 3D-reconstruction of chondrogenic mesenchymal condensations of nasal capsule, trabecular

cartilage, EOM, eyeball, optic nerve, and lens in E13.5 control, *Aldh1a3*^{KO} and BMS493-treated embryos. EOM visualization in context of whole head (D), nasal capsule (D'-D''), trabecular cartilage (D'''). (E) Raw micro-CT data ($n = 2$). (F-H) 3D-reconstructions of WMIF for MyHC of E13.5 control (F), *Aldh1a3*^{KO} (G) and BMS493-treated embryos (H) ($n > 9$). EOMs were segmented from adjacent head structures and 3D-reconstructed in Imaris (Bitplane). EOMs are shown as isosurfaces for clarity of visualization. (1-7) denote non-segregated muscle masses with differential fiber orientation (see also S5D Fig). Raw immunostaining data for MyHC (myofibers) and Tnc (tendon) are shown in panels F'-H'. Double asterisk in G,H indicate fused muscle masses. Asterisk in G indicate misoriented medial rectus. (I) Relative EOM volume (compared with control) of WMIF in F-H. Each dot represents an individual embryo ($n > 9$). Mann-Whitney test. See S2 Data for individual values. a, anterior; ATRA, all-trans retinoic acid; ce, presumptive corneal epithelium; ctrl, control; d, dorsal; dr, dorsal retina; 3D-rec, 3D-reconstruction; e, eyelid groove; E, embryonic day; EOM, extraocular muscle; hc, hypochiasmatic cartilage; io, inferior oblique; ir, inferior rectus; l, lateral; le, lens; lr, lateral rectus; m, medial; mr, medial rectus; micro-CT, micro computed tomography; os, optic stalk; p, posterior; rb, retractor bulbi; rpe, retinal pigmented epithelium; RAR, retinoic acid receptor; RXR, retinoid X receptor; se, surface ectoderm; so, superior oblique; sr, superior rectus; v, ventral; vr, ventral retina.

<https://doi.org/10.1371/journal.pbio.3000902.g004>

patterning phenotypes categorized as strong or severe at E13.5 were only obtained when an E10.75 time point of injection (8 PM of day E10.5) was included in the regime (experiment type I-III, S1 Table, and S5D Fig). Surprisingly, even a single injection at this time point resulted in strong phenotypes (experiment type IV, S1 Table, and S5D Fig), whereas exclusion of this time point (experiment type V, S1 Table, and S5D Fig) resulted in only mild phenotypes at best. Therefore, we identified an early and restricted temporal window in which ATRA activity, prior to any sign of muscle splitting, impacts correct muscle patterning 36–48 hours later. Given the critical action of RDH10 in generating retinaldehyde, the intermediate metabolite in the biosynthesis of ATRA, we examined EOM development in *Rdh10* mutant embryos. *Rdh10* is normally expressed in the optic vesicle and RPE [69], and in *Rdh10*^{-/-} embryos, eyes develop intracranially, close to the diencephalon with a very short ventral retina [65]. WMIF analysis of *Rdh10* mutant EOMs revealed that the anlage was specified but lacked any sign of segmentation, in agreement with an upstream role in ATRA synthesis (S5E and S5F Fig). Taken together, our data show that retinoic acid signaling is essential for the correct myofiber alignment and segregation of EOM masses in a dose- and time dependent manner.

ATRA-responsive cells drive muscle patterning in the periocular mesenchyme

In all body regions, muscle connective tissue plays a central role in muscle patterning [22]. Moreover, this process appears to be tightly coupled to development of tendons and tendon attachment sites [15,70–72]. To determine whether the role of retinoic acid signaling in EOM patterning is direct in myogenic cells or indirect, through action in adjacent connective tissues, we tracked cells that are responsive to ATRA using a novel retinoic acid transgenic Cre reporter line [73]. This transgenic line comprises 3 retinoic acid response elements (*RARE*) from the *Rarb* gene fused to the *Hspa1b* minimal promoter driving expression of a tamoxifen-inducible *Cre-ERT2* recombinase (*Tg:RARE-Hspa1b-Cre/ERT2*, designated as *Tg:RARE-CreERT2* for simplicity). By crossing this line with the *R26*^{mTmG} or *R26*^{Tom} reporter mice [74,75] (Fig 5A), we permanently labeled ATRA-responsive cells and their descendants with membrane-tagged GFP or tdTomato. Different tamoxifen regimes showed that a greater number of responsive cells were present in the periocular region when tamoxifen was administered between E9.75–E10.5 (S6A–S6C Fig). This finding is in agreement with BMS493 treatments identifying E10.75 as a critical time point for the action of ATRA (S1 Table and S5D Fig) and the fact that maximal recombination efficiency can be achieved between 12–24 hours upon tamoxifen induction [76,77].

To assess whether myogenic cells and adjacent POM cells respond to retinoic acid signaling, we microdissected the periocular region of *Tg:RARE-CreERT2;R26*^{mTmG} embryos and subjected it to mild digestion in bulk. Cells were allowed to attach to culture dishes, immunostained, and scored for co-expression of GFP and myogenic markers (MYOD, MYOG). Notably, the great majority of reporter positive-responsive cells were not myogenic (Fig 5B and 5C,

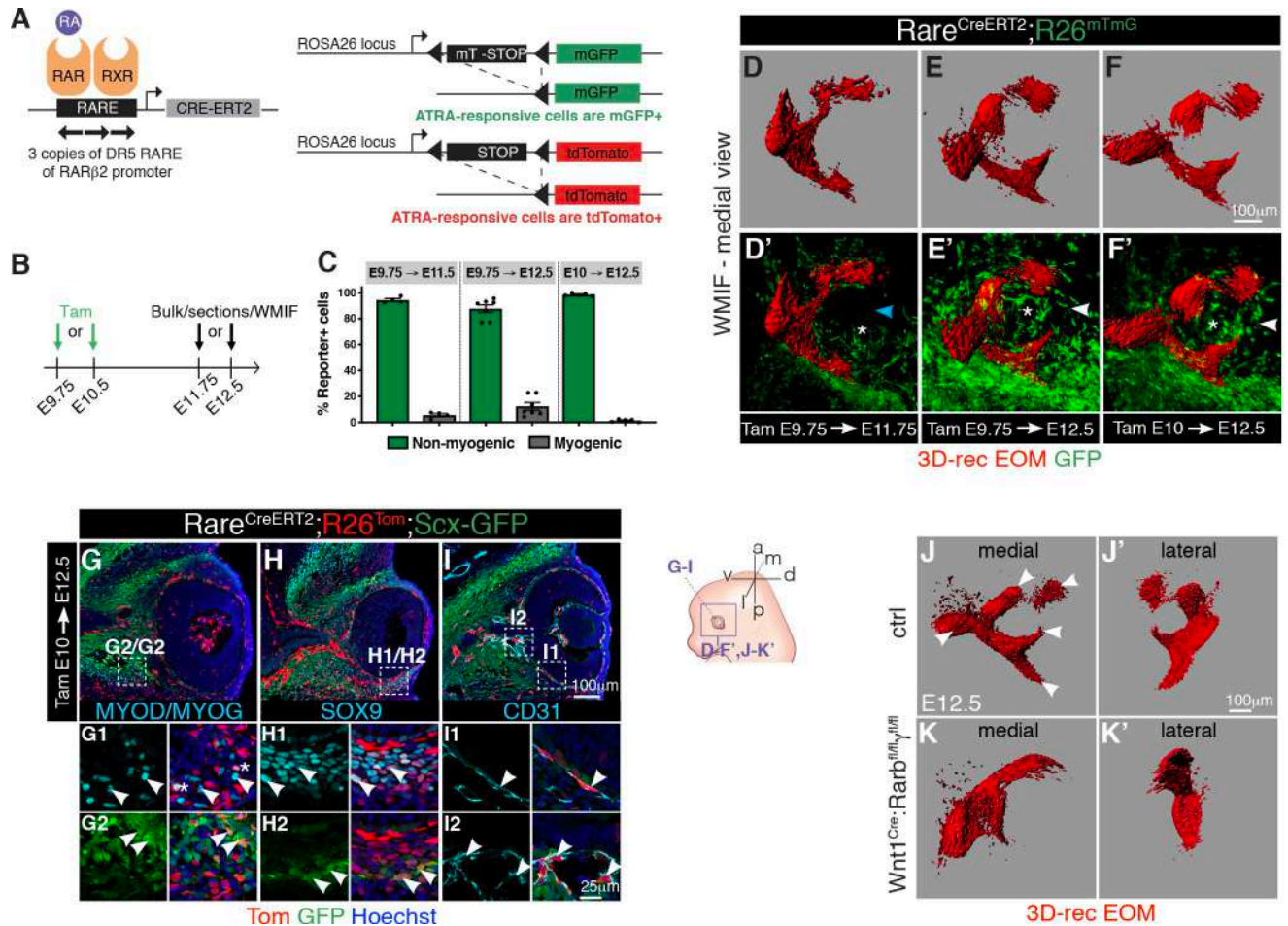


Fig 5. Periocular connective tissues are responsive to retinoic acid signaling. (A) Scheme of mouse alleles used. (B) Strategy used to determine cell types responsive to retinoic acid signaling in *Tg:RARE-CreERT2;R26^{mTmG}* embryos. Tamoxifen was injected to pregnant females at E9.75 or E10.5 and analysis performed (bulk, sections or WMIF) at E11.75 or E12.5. (C) The percentage of recombined (GFP+) cells within the non-myogenic or myogenic populations (PAX7+, MYOD+, MYOG+) was assessed by immunostaining on bulk cell preparations of the periocular region of *Tg:RARE-CreERT2;R26^{mTmG}* embryos following different tamoxifen treatments. Each dot represents an individual embryo (*n* > 4 embryos/condition). See S3 Data for individual values. (D–F) WMIF of *Tg:RARE-CreERT2;R26^{mTmG}* embryos for SMA (differentiated muscle) and GFP (ATRA-responsive cells) at the indicated embryonic stages. The number of reporter positive cells at the place where the developing medial rectus muscle will project increases from E11.75 (blue arrowhead) to E12 (white arrowheads). Asterisks mark the optic nerve (*n* = 3). (G–I) Coronal sections of E12.5 *Tg:RARE-CreERT2;R26^{mTmG};Scx-GFP* embryos immunostained for GFP, Tom (ATRA-responsive cells), MYOD/MYOG (muscle), and CD31 (endothelial cells). Higher-magnification views as insets. Asterisks in G1 indicate sporadic labeling in myogenic cells (*n* = 3). (J–K') WMIF for MyHC (myofibers) of E12.5 control (*Tg:Wnt1Cre;Rarb^{fl/+};Rarg^{fl/+}*) and mutant (*Tg:Wnt1Cre;Rarb^{fl/fl};Rarg^{fl/fl}*) EOM. Medial and lateral views are shown. Note absence of splitting in mutant EOM. Arrowheads indicate split EOM in controls (*n* = 2 per genotype). In D–F' and J–K' EOMs were segmented from adjacent head structures and 3D-reconstructed in Imaris (Bitplane). EOMs are shown as isosurfaces for clarity of visualization. a, anterior; ATRA or RA, all trans retinoic acid; ctrl, control; d, dorsal; 3D-rec, 3D-reconstruction; E, embryonic day; EOM, extraocular muscle; l, lateral; m, medial; mGFP, membrane-tagged GFP; p, posterior; RAR, retinoic acid receptor; RXR, retinoid X receptor; SMA, alpha smooth muscle actin; Tam, Tamoxifen; v, ventral; WMIF, whole-mount immunofluorescence.

<https://doi.org/10.1371/journal.pbio.3000902.g005>

S6D Fig and S3 Data). We next performed immunostaining in whole-mount to assess the spatial distribution of ATRA-responsive cells in periocular connective tissues (Fig 5D–5F'). This analysis revealed that the mesenchyme around the optic nerve in close proximity to the developing EOMs was positive for the reporter. Interestingly, the number of POM GFP+ cells increased from E11.75 to E12 (Fig 5D'–5F'), which is the temporal window corresponding to EOM splitting (Fig 2A and 2B). Inactivation of downstream retinoic acid signaling with BMS493, prior and subsequent to the induction of *Tg:RARE-CreERT2;R26^{mTmG}* mice with

tamoxifen (S6E Fig), greatly reduced the responsiveness of the reporter in the POM compared with non-treated controls (S6F–S6I Fig, S6 and S7 Videos).

As with experiments on isolated cells, the great majority of tdTomato positive-responsive cells on tissue sections of *Tg:RARE-CreERT2;R26^{Tom}* embryos were not myogenic at ventral (Fig 5G) and dorsal levels (S6J Fig). tdTomato positive-responsive cells co-expressed *Scx-GFP* (Fig 5G and 5H), Sox9 (Fig 5H) or the endothelial cell marker CD31 along the choroid (vascular layer of the eye) and ciliary arteries around the optic nerve (Fig 5I). Together, these results are in agreement with previous studies [34–36] showing that despite a sophisticated pattern of ATRA metabolism in the developing retina, retinoic acid signaling exerts its action mostly non-cell autonomously. We show that ATRA targets various connective tissue types of the POM within a temporal window that is crucial for EOM patterning.

As ATRA-responsive cells were found in NCC- (ventral POM) and mesoderm-derived cell compartments (dorsal POM, choroid, and a fraction of myogenic progenitors), we performed more selective perturbations of retinoic acid signaling with available genetic tools. Expression of a dominant negative nuclear retinoid receptor isoform in myogenic cells (*Myod^{flCre}; R26^{RAR403}*, [78,79]) did not result in noticeable EOM patterning defects (S6K–S6L' Fig). We then inactivated the RAR β and RAR γ receptors in the NCC-derived POM, which respond to ATRA synthesized by the retina [80,81], using the *Tg:Wnt1^{Cre}* driver (*Tg:Wnt1^{Cre};Rarb^{fl/fl}; Rarg^{fl/fl}*, [35]). WMIF for muscle in *Tg:Wnt1^{Cre};Rarb^{fl/fl};Rarg^{fl/fl}* embryos showed absence of muscle splitting (Fig 5J–5K'), and this was as severe as that observed in fully ATRA-deficient *Rdh10^{-/-}* embryos (S5F Fig). Altogether, these data suggest that synthesis of ATRA from neural derivatives (retina, optic nerve, RPE) is crucial for EOM patterning, through its action on NCC-derived periocular connective tissues at earlier stages.

Defective organization of EOM insertions in embryos deficient in retinoic acid signaling

Having addressed a major role of ATRA in NCC-derived cells of the POM for EOM patterning, we set out to assess which specific connective tissue subpopulations, including the EOM insertions in the POM, were affected in *Aldh1a3^{-/-}* and BMS493-treated embryos. First, we examined the distribution of Collagen XII (Fig 6A–6C'), a marker of the sclera and corneal stroma [82], on tissue sections at E12. We observed a marked reduction of Collagen XII (Col XII) at the level of the medial-POM that gives rise to the sclera, upon ATRA deficiency (Fig 6B–6C'). In addition, although PITX2 was expressed continuously in the entire POM and corneal stroma in controls (Fig 6D and 6D'), expression in the medial-POM was selectively lost upon ATRA deficiency (Fig 6E–6F'). This observation is in agreement with *Pitx2* being a retinoic acid signaling target in the NCC-derived POM [34–36] and the sclera being absent at fetal stages in *Rarb/Rarg*-NCC mutants [35]. Interestingly, POM organization was unaffected in *Myf5^{nlacZ/nlacZ}* mutants (Fig 6G and 6G'), in which the initial EOM anlage forms but myogenesis is aborted from E11.5 [83].

To understand whether the abnormal distribution of POM markers translates into EOM insertion defects and how EOM development and insertion sites are coordinated, we examined the organization of the POM-ring in control, *Aldh1a3^{-/-}*, and BMS493-treated embryos. We systematically compared E11.75 and E12 embryos to visualize the organization of these tissues prior to and during muscle splitting (Fig 6H–6P and S7A–S7N Fig). Control embryos showed the presence of overlapping SOX9 and PITX2 POM-ring domains, together with 4 foci of apoptosis labeling the prospective tendon attachment points of the 4 recti muscles (Fig 6H–6J, S7A–S7C', S7E and S7F Fig). As expected, ATRA deficiency perturbed these patterns in a dose-dependent manner. At the level of the POM-ring, *Aldh1a3^{-/-}* embryo heads displayed

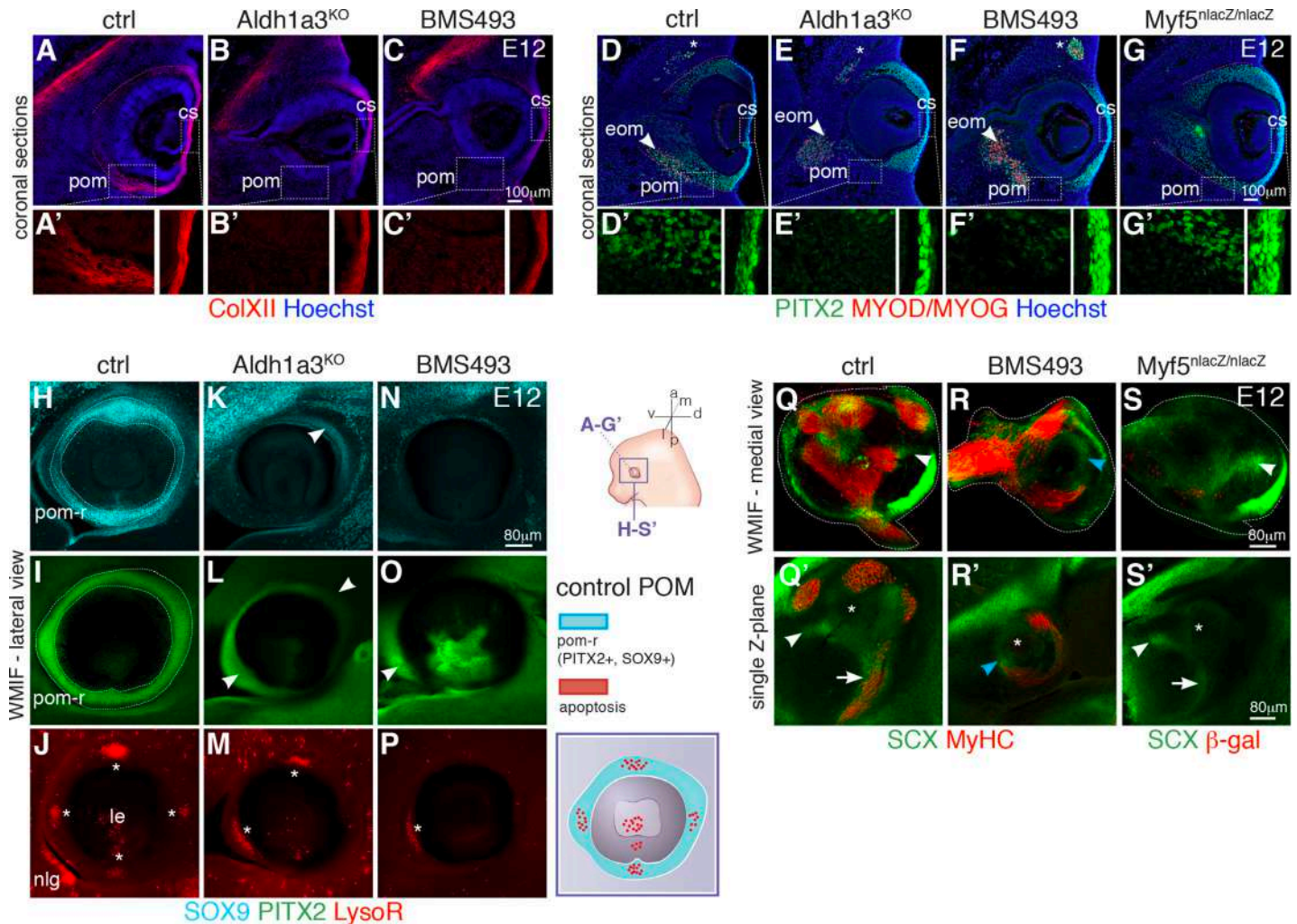


Fig 6. Altered EOM insertions in the POM upon ATRA deficiency. (A-C') Immunostaining for ColXII on E12 coronal sections. ColXII expression is lost in the medial POM (future sclera) but not in the corneal stroma of *Aldh1a3*^{KO} (B,B') and BMS493-treated embryos (C,C'). Higher magnification of ColXII staining as insets in (A'-C'). (D-G) Immunostaining for PITX2 (muscle progenitors, POM) and MYOD/MYOG (myogenic cells) on E12 coronal sections. Asterisks indicate superior oblique muscle. Red dashed lines delimitate the POM in controls (D) and *Myf5*^{nlacZ/nlacZ} (G) embryos. Higher magnification of PITX2 staining as insets in (D'-G'). Note absence of PITX2 expression in medial-POM of *Aldh1a3*^{KO} (E,E') and BMS493-treated embryos (F,F'). (H-P) WMIF for SOX9 and PITX2 of E12 control (H-J), *Aldh1a3*^{KO} (K-M) and BMS493-treated (N-P) embryos preincubated with LysoR (left eyes). *Aldh1a3*^{KO} and BMS493 embryos do not show a complete POM-ring as controls (dashed lines in H,I). Arrowheads mark remaining expression of SOX9/PITX2 in the POM of *Aldh1a3*^{KO} (K,L) or inhibitor-treated (O) embryos. Asterisks in (J, M, P) mark apoptosis spots in POM. (Q-R) WMIF for MyHC (myofibers) and GFP on E12 control (Q) and BMS493-treated *Tg:Scx-GFP* embryos (R). WMIF for β -gal (myogenic progenitors) and GFP on E12 *Tg:Scx-GFP;Myf5*^{nlacZ/nlacZ} E12 embryos (S) (left eyes). The periocular area was segmented from adjacent structures for ease on visualization (dashed lines). White arrowheads in Q and S highlight correct position of tendon condensations for medial rectus muscle. Blue arrowhead in R marks a diffuse *Scx-GFP*+ pattern at the position of the mispatterned medial rectus muscle. (Q'-S') Single Z-section of the segmented volume. White arrowheads in Q',S' show tendon tips and white arrows correct *Scx-GFP*+ connective tissue pattern along with muscle (Q') or prospective muscle masses (S'). Blue arrowhead in R' marks a *Scx-GFP*+ condensation at the muscle tip. Asterisks mark position of the optic nerve. (*n* = 3 per condition). a, anterior; ATRA, all-trans retinoic acid; cs, corneal stroma; ctrl, control; d, dorsal; eom, extraocular muscles; l, lateral; le, lens; LysoR, LysoTracker red; m, medial; nlg, nasolacrimal gland; p, posterior; pom, periocular mesenchyme; pom-r, periocular mesenchyme ring; v, ventral; WMIF, whole-mount immunofluorescence.

<https://doi.org/10.1371/journal.pbio.3000902.g006>

narrower SOX9 and PITX2 expression domains than controls (Fig 6K–6L, S7G and S7H Fig). In BMS493-treated embryos, expression of these genes in the POM-ring (Fig 6N, 6O, S7D, S7D', S7I and S7J Fig) was further reduced to a minority of cells. Accordingly, foci of apoptosis were lost or disorganized in both cases of ATRA deficiency with a single LysoTracker Red spot almost invariably present in the ventral POM in both conditions (Fig 6M, 6P, S7H and S7J Fig). In medial views of reconstructed 3D volumes, PITX2 showed continuous expression

from the POM-ring to the medial-POM in control embryos (Fig 2D, S7K Fig and S2 Video), whereas we noticed loss of PITX2 expression in both cases of ATRA deficiency (S7M and S7N Fig, blue arrowheads) as observed on tissue sections (Fig 6E' and 6F'). Consistent with these results, the *Tg:RARE-CreERT2;R26^{mTmG}* reporter showed a marked reduction of ATRA-responsive cells in the medial POM and POM-ring of *Aldh1a3^{-/-}* and BMS493-treated embryos when compared with controls (S7O–S7Q' Fig and S8–S10 Videos). Thus, as seen in other body regions, where development of muscles and bone superstructures into which they insert are tightly coordinated [70], the development of the EOMs is tightly coupled to development of their insertion sites in the soft tissues of the POM.

As tendons were present at muscle tips in E13.5 *Aldh1a3^{-/-}* and BMS493-treated embryos but located ectopically with respect to a wild-type configuration (Fig 4F'–4J'), we suspected that the initial 3D organization of *Scx-GFP+* tendon and connective tissue progenitors might also be affected. We performed WMIF for differentiated muscle (MyHC) and tendon progenitors (*Tg:Scx-GFP*) and segmented the reconstructed 3D volume. In control embryos at E12.5, *Scx-GFP+* condensations projected from the tips of the future 4 recti muscles toward the POM-ring (Fig 6Q and S11 Video), facing the 4 foci of apoptosis (Fig 6J and S4 Video). Moreover, as observed in tissue sections (Fig 1A1, 1D1, and S1G–S1H' Fig), *Scx-GFP+* and TCF4+ cells were also present in POM connective tissues presaging the final locales of the recti muscles (Fig 6Q' and S7R Fig). In BMS493-treated embryos at E12, *Scx-GFP* and TCF4 expression were less organized and diffuse (Fig 6R and 6R', and S7S Fig), yet *Scx-GFP+* condensations started to form at the tips of ectopic muscle masses (Fig 6R' and S12 Video). Altogether, these results show that ATRA is required for the proper specification/organization of NCC-derived POM connective tissues, which includes the muscle connective tissue, tendons, and their insertion sites.

In stark contrast with what we observed upon ATRA deficiency, *Scx-GFP* and TCF4 patterning in POM connective tissues was preserved in muscle-less *Myf5^{nlacZ/nlacZ}* mutants (Fig 6S and 6S', and S7T Fig). Moreover, *Scx-GFP+* tendon condensations formed at the tips of prospective (albeit absent) recti muscles (Fig 6S and 6S'). This situation is similar to the specification of individual tendons on muscle-less limbs [20,84] and branchial arches [41]. However, at later stages, tendons did not continue their maturation in the absence of EOMs (S7V and S7V' Fig, S13 and S14 Videos), reinforcing the notion that, as in most other anatomical locations [2], tendon differentiation and maintenance ultimately rely on muscle–tendon interactions.

In summary, ATRA produced by the developing eye influences the organization of the entire NCC-derived POM, allowing integration of these tissues into a musculoskeletal functional unit (S8 Fig).

Discussion

The striking differences in embryological origins, function, and susceptibility to disease among cranial and somite-derived muscles [26] provides impetus to study in detail the morphogenesis of different muscle groups and their integration as part of the musculoskeletal system. Here, we focused on EOMs, an evolutionary conserved group of muscles that are precisely engineered for fine displacement of the eyeball and thus, crucial for visual acuity. Using genetic and 3D imaging approaches, we analyzed EOM development from their emergence as a unique anlage to the establishment of a fully formed functional unit with insertions in the sclera, which sets it apart from classical muscle-to-bone insertions studied to date. We identified a spatiotemporal window in which retinoic acid signaling from the target organ is required for patterning of NCC-derived soft tissues of the POM. These findings provide insights into the deployment of site-specific programs for the establishment of anatomically

distinct muscle functional units, with precise definition of muscle shapes and topographical wiring of their tendon attachments.

Dual origin of EOM insertions

The connective tissues of the rostral cranium (bone, cartilage, tendon, and muscle connective tissue) were reported to be derived from the neural crest [3,7,8]. However, the hypochiasmatic cartilages, from which the recti muscles originate in mammals, are an exception to this rule as they are mesoderm derived [85]. Here, we found that at this location, tendon and muscle connective tissue are also of mesodermal origin. As such, EOMs originate in mesoderm-derived bone and insert in NCC-derived fibrous tissue of the sclera with muscle connective tissue following the embryonic origins of the respective attachments, as observed in other anatomical locations [86]. Taken together, our observations redefine a novel boundary for NCC contribution to the connective tissues of the periocular region and suggest that at their origin in the base of the skull, the EOMs and their associated connective tissues might have evolved neomorphically in situ from the same mesodermal source.

RA responsiveness on the POM

Previous studies showed that NCCs have a critical role in the acquisition of cranial muscle morphology [9,13–16]. Our data using the *Tg:RARE-CreERT2* reporter and following invalidation of *Rarb/Rarg* in NCC derivatives suggest that the action of retinoic acid signaling on EOM patterning is also indirect, through its action on periocular connective tissues.

The observation that BMS493 treatments to impair ATRA signaling results in a more severe phenotype than that observed in *Aldh1a3* mutants could have several explanations. First, BMS493 is not a RAR antagonist but pan-RAR inverse agonist, which is capable of repressing RAR basal activity by favoring the recruitment of corepressors and promoting chromatin compaction [87]. Second, additional sources of ATRA could signal to the POM and be inhibited by the BMS493 treatment. Candidates include *Aldh1a1* (retina), *Aldh1a2* (temporal mesenchyme), and *Cyp11B1*, a member of the cytochrome p450 family of monooxygenases that can generate ATRA in the retina in a retinaldehyde dehydrogenase-independent manner [88]. Noneless, the severe patterning phenotypes observed in the *Aldh1a3* single mutant suggest that the local synthesis of ATRA in the RPE, optic stalk, and ventral retina at early stages (around E10.5) cannot be fully compensated by the action of other retinaldehyde dehydrogenases in adjacent tissues (this study, [31,64]).

Interestingly, although the constitutive *RARE-hsp68-lacZ* transgene displays strong reporter activity in the retina and RPE [34,89], we observed a strong ATRA response in the choroid and in POM connective tissues with the *Tg:RARE-CreERT2;R26^{Tom}* reporter. However, one needs to consider that this type of reporter provides an off/on readout whose threshold level of response might depend on Cre levels, accessibility of the locus to recombination, and stochastic epigenetic mechanisms [90–93]. Given the difficulties in invalidating retinoic acid signaling in a cell-type-specific fashion and on cells perceiving a certain level of ATRA activity, it remains unclear how a gradient-like signaling system transitions to defined territories of transcription factor activity that will ultimately govern morphogenesis at a local level. We foresee that advances in single-cell transcriptomic approaches will help resolve the consecutive steps of musculoskeletal patterning in this and other anatomical locations.

EOM and tendon patterning are concerted processes under RA control

We identified a short temporal window (E10.5–E11.75) in which ATRA is essential for the precise morphogenesis of several elements of the POM, including the formation of tendon

condensations and insertion sites in the POM-ring. These phenotypes are already evident from E11.75, a stage in which the EOM still figures as a muscle anlage. Interestingly, analysis of chick and mouse limb development also identified a short time window in which limb mesenchyme perturbations result later in muscle and tendon patterning defects [71,94]. Moreover, concomitant muscle and tendon defects have been observed in the chick limb and zebrafish jaw upon retinoic acid signaling misregulation [15,95]. Altogether, these results suggest that at certain anatomical locations, including the EOMs, endogenous local variations in the concentration of retinoids contribute to the establishment of *Scx-GFP+* condensations, a critical step in muscle functional unit assembly.

Role of RA in the integration of EOM patterning and insertion site formation

The EOMs insert into the sclera, a non-bone structure in mammals. The generation of 4 attachment points that precisely mirror the position of the 4 recti muscles is a morphogenesis conundrum, as details on their specification are scarce. Four mesenchymal condensations have been described at the periphery of the developing optic cup in cat and human embryos, in positions facing the locations of the recti muscles [96,97]. In the mouse, at equivalent developmental timepoints (E11.5-E12.5) and homologous positions, apoptotic foci were observed and suggested to provide attachment for the recti muscles [51]. Using 3D imaging, we showed that at E11.75, the apoptotic foci are aligned with *Scx-GFP+* condensations that project medially, before any sign of splitting of the EOM anlage. As the apoptotic foci decrease in size from E12.5 onwards concomitant with ongoing muscle splitting and tendon formation, it is possible that they initially presage the POM for future tendon insertions but are not required for attachment per se. These foci appear in condensed SOX9+ PITX2+ cell domains of the future sclera; however, to our knowledge, their presence has not been reported in superstructures at other anatomical locations.

In agreement with the role of RA in the induction of cell death in other locations in the embryo [64], our study shows that upon perturbation of RA signaling, the apoptotic foci in the POM are absent or severely reduced. However, it is also possible that the loss of apoptotic foci upon RA inhibition is secondary to loss or mispatterning of the SOX9+ PITX2+ POM-ring. Thus, it will be of interest to determine whether null or NCC-specific mutations in PITX2 affect the patterns or amount of naturally occurring cell death in the periocular condensations. Although our work sheds light on the genetic mechanisms that regulate EOM insertion, the cellular mechanisms underlying this process remain undefined. It is tempting to speculate that the apoptotic foci are related to the disappearance of signaling centers [98,99] or compaction-mediated cell death and extrusion [100]. Future experiments directed towards modifying the amount or timing of cell death will be informative.

Few reports have demonstrated that mispatterning of specific muscles is coupled with aberrant superstructures [13,70,72] or removal of the prospective tendon attachment sites [95]. Our results are in agreement with that model, given that EOM mispatterning is concomitant with aberrant EOM insertions. As mammals do not develop a cartilage layer within the sclera [57,101], transient expression of SOX9 in the POM-ring of mouse embryos at the time of EOM patterning is intriguing. In the developing limb and jaw, tendon and bone are attached by a transitional connective tissue that develops from bipotent progenitors that co-express *Scx* and SOX9 [53–56], before progenitors are allocated to either cartilage or tendon lineages. Similarly, we observed a transient population of *Scx-GFP/SOX9* double-positive cells at the insertion sites in the POM. In this context, our data suggest that SOX9 expression may represent a redeployment of the developmental module for tendon attachment, despite the fact that there

is no definitive cartilage in the mammalian sclera. Genetic studies will be required to ultimately assess the functional relevance of this population in EOM attachment.

Finally, transcriptome analysis revealed the existence of global and regional regulatory modules for superstructure patterning in the limb bones, offering a mechanism to induce variations in attachment sites without having to rewrite the entire skeletogenic program [102]. As several markers of the POM (*Pitx2*, *Foxc1/2*) and retinoic acid signaling modulators (*Cyp26a1/b1*) were identified as part of specific limb superstructure signatures [102], it is tempting to speculate that those genes also play a conserved role in the generation of the attachment module of the EOMs.

Conclusion

The developing eye has been proposed to be key organizer of craniofacial development, independent of its role in vision [103]. This notion is based on the role of the eye for proper NCC migration to the periocular region [104], the common association of ocular and craniofacial developmental abnormalities [105] and the initial development of an eye in blind vertebrate species [103,106,107]. Moreover, as the appearance of a "camera-type" eye is a vertebrate innovation [108], and the EOM are already present in lamprey [4], it is possible that muscles and their target tissue might have co-evolved. Here, by characterizing coordinated patterning of the EOMs, their respective tendons and insertions, our findings illustrate further the role of the developing eye as a signaling center allowing integration of the EOM functional unit in the POM. Our results show that the tissue interactions during the development of this craniofacial muscle unit share features with those described in the limb but with additional regional properties (e.g., cell death, specification of attachments in the sclera) that seem to have been specifically incorporated into this group. Moreover, the capacity to instruct muscle patterning through variations in connective tissue derivatives provides a mechanism to explain the plasticity of the musculoskeletal system, at the anatomical and interspecies levels, while ensuring functional integration during evolution. These findings also imply that the generation of musculoskeletal units do not require major restructuring of the developmental programs of all the tissues implicated. Instead, co-option of a general program and simultaneous addition of local features appear to elaborate musculoskeletal diversity.

Materials and methods

Mouse strains and animal information

Animals were handled as per European Community guidelines, and the ethics committee of the Institut Pasteur (CETEA) approved protocols (Licence 2015–0008). The following strains were previously described: *Aldh1a3*^{KO} [64], *Mesp1*^{Cre} [46], *Tg(RARE-Hspa1b-cre/ERT2)*, designated here as *Tg:RARE-CreERT2* [73], *R26*^{Tom} (Ai9; [74]), *R26*^{mTmG} [75], *Tg:Scx-GFP* [48], *Myf5*^{nlacZ} [109], *Myod*^{Cre} ([79,110]), *Rarb*^{lox} [111], *Rarg*^{lox}, [112], *Rdh10*^{KO} [65], *Pax6*^{Sey/Sey} [59], and *Tg:Wnt1*^{Cre} [45]. *R26*^{RAR403} ([78]) mice contain a loxP-flanked STOP sequence upstream of a mutated human RAR alpha gene, which behaves as a dominant negative receptor for all nuclear receptors upon Cre-mediated recombination. *Rdh10*^{KO} embryos were received from the laboratory of Pascal Dollé. *Tg:Wnt1Cre;Rarb*^{fl/fl}; *Rarg*^{fl/fl} embryos were received from the laboratory of Valérie Dupé. *Pax6*^{Sey/Sey} and control embryos were received from the laboratory of James Briscoe. *Tg:Lhx2*^{Cre}; *Lhx2*^{fl/fl} [61] were received from the laboratory of Leif Carlsson. *Shh(invC-6)2* embryos were received from the laboratory of François Spitz.

To generate experimental embryos for *Mesp1*^{Cre} or *Tg:Wnt1*^{Cre} together with *Tg:Scx-GFP* and *R26*^{Tom} lineage tracings, Cre/+ males were crossed with *Tg:Scx-GFP;R26*^{Tom/Tom} females. Mice were kept on a mixed genetic background C57BL/6Jrj and DBA/2Jrj (B6D2F1, Janvier

Labs). Mouse embryos and fetuses were collected between E10 and E18.5, with noon on the day of the vaginal plug considered as E0.5. Pregnant females were euthanized by cervical dislocation.

To induce recombination with the *Tg:RARE-CreERT2;R26^{mTmG}* line, 5 mg of tamoxifen (Sigma #T5648) were administered by gavage to pregnant females. A 25 mg/ml stock solution in 5% ethanol and 95% sunflower seed oil was prepared by thorough resuspension with rocking at 4°C.

To inhibit retinoic acid signaling, pregnant females of relevant genotypes were injected intraperitoneally with 10 mg/kg of BMS493 (Tocris, 3509), a pan-RAR inverse agonist. A 5-mg/ml BMS493 stock solution in DMSO (SIGMA, D2650) was prepared and stored in single use aliquots at -20°C in tight cap tubes. At the time of injection, the aliquot was thawed, 200 µl of sterile PBS was added per 50µl aliquot and injected immediately.

Immunofluorescence, detection of cell death, and in situ hybridization

Embryos were fixed for 2.5 hours in 4% paraformaldehyde (PFA; 15710, Electron Microscopy Sciences) in PBS with 0.2–0.5% Triton X-100 (according to the embryonic stage) at 4°C and washed overnight at 4°C in PBS. For cryosectioning, embryos were equilibrated in 30% sucrose in PBS overnight at 4°C and embedded in OCT. Cryosections (16–18 µm) were allowed to dry at RT for 30 minutes and washed in PBS. Immunostaining was performed as described in [113]. An anti-DsRed antibody (rabbit) was used to enhance the *R26^{Tom}* signal except when co-staining was performed with antibodies raised in rabbit. In this case, the endogenous reporter signal was used. An anti-GFP antibody (chicken) was used to enhance the *R26^{mTmG}* and *Tg:Scx-GFP* signal in whole-mount and section immunostainings.

Scx in situ hybridization was performed as per manufacturer instructions using the RNA-scope Multiplex Fluorescent V2 Assay [113] and RNAscope Probe-Mm-Scx probe (Cat No. 439981). Sample pre-treatments were performed as described in [113]. Signal development was carried out using Opal 570 Reagent Pack (FP1488001KT, Perkin Elmer) diluted 1:1,500 in the ACD-provided TSA buffer and followed up by immunostaining.

TUNEL staining, which marks double-strand breaks, was performed with the In Situ Cell Death Detection Kit/Fluorescein (Roche, 11 684 795 910). Slides were first pretreated with a 2:1 mix of Ethanol:Acetic Acid for 5 minutes at -20°C, washed twice for 20 minutes with PBS at RT, and processed for TUNEL staining as described by the manufacturer.

For whole-mount immunostaining, embryos were fixed and washed as described here and dehydrated in 50% Methanol in PBS and twice in 100% Methanol, 30 minutes each at RT and kept at -20°C till needed. Heads were rehydrated, the periocular region was microdissected in PBS, and immunostaining performed as described in [113]. For embryos older than E13.5, the alternative pretreatment (containing 0.1% Tween-20, 0.1% TritonX100, 0.1% Deoxycholate, 0.1% NP40, 20% DMSO in PBS) and primary antibody immunolabeling steps of the idisco protocol (<https://idisco.info/idisco-protocol/>) were generally used. In all cases, secondary antibodies were applied in blocking buffer as described in [113] for >4 days at 4°C with rocking. After immunolabelling, samples washed in 0.1% Tween/PBS, dehydrated in 50% Methanol in PBS and 100% Methanol 10 minutes each at RT, cleared with a mix benzyl alcohol and benzyl benzoate (BABB), and mounted for imaging as described in [114].

LysoTracker Red staining was used for detection of cell death in whole-mount live tissues as it reveals lysosomal activity correlated with increased cell death [52,115]. Embryos were quickly dissected in HBSS (Invitrogen, 14025–092), incubated in 2-ml tubes containing 5 µM of LysoTracker Red DND-99 (Molecular Probes, L7528) 45 minutes at 37°C with rocking in

the dark, washed twice in PBS, fixed and processed for cryosections or whole-mount immunostaining as described previously.

Antibodies

Primary and secondary antibodies used in this study are listed in [S2 Table](#). To detect differentiating EOMs, we used α -smooth muscle actin (SMA), which is transiently expressed in differentiating myoblasts and myotubes [116–118]; Desmin, an early cytoskeletal muscle protein expressed in myoblasts, myotubes, and myofibers [116,119]; and myosin heavy chain (MyHC) to label sarcomeric myosin [120].

Static imaging

A Zeiss SteREO Discovery V20 microscope was used for imaging the endogenous fluorescence of whole embryos at the time of dissection. For tissue sections and whole-mount immunostaining of cleared embryos, a LSM700 and a LSM800 laser-scanning confocal microscope with ZEN software (Carl Zeiss, www.zeiss.com) were used.

All images were assembled in Adobe Photoshop and InDesign (Adobe Systems). Volume-3D rendering of the Z-stack series was performed in Imaris (version 7.2.1) software (Bitplane). For ease of EOM visualization, the Z-stack volumes were first manually segmented to define the EOM or the whole POM area using the Isosurface Imaris function. The signal outside the isosurface was set to zero, the corresponding channel duplicated, and subsequently, a new isosurface was created using automatic thresholding on the new channel. This new isosurface was used to calculate the corresponding EOM volumes.

In situ hybridization

Whole-mount in situ hybridization with digoxigenin-labeled antisense mRNA probes was performed as described previously in [90]. The Aldh1a1, Aldh1a2, and Aldh1a3 probes were previously described in [34,36].

micro-CT analysis

The tissue contrasting protocol has been adapted from the original protocol developed by [121] and applied to mouse embryos as described in [122] and [86]. For tissue contrasting, E13.5 embryos were stained in 0.5% phospho-tungstic acid (PTA) in 90% methanol for 4 days, E15.5 embryos were stained in 0.7% PTA in 90% methanol for 1 week.

The micro-CT analysis of the embryos was conducted using the GE phoenix v|tome|x L 240 (GE Sensing and Inspection Technologies GmbH, Germany), equipped with a 180 kV/15W maximum power nanofocus X-ray tube and flat panel detector DXR250 with 2048 × 2048 pixel, 200 × 200 μ m pixel size. The exposure time of the detector was 900 milliseconds in every position over 360°. Three projections were acquired and averaged in every position for reduction of the noise in micro-CT data. The acceleration voltage was set to 60 kV and tube current to 200 μ A. The radiation was filtered by 0.2 mm of aluminium plate. The voxel size of obtained volumes (depending on a size of an embryo) appeared in the range of 2–6 μ m. The tomographic reconstructions were performed using GE phoenix datos|x 2.0 3D CT software (GE Sensing and Inspection Technologies GmbH, Germany). The EOM, eye, and cartilages in the embryo head were segmented by an operator with semiautomatic tools within Avizo - 3D image data processing software (FEI, USA). The 3D segmented region was transformed to a polygonal mesh as an STL file and imported to VG Studio MAX 2.2 software (Volume Graphics GmbH, Germany) for surface smoothing and 3D visualization.

Cell isolation from the periocular region and bulk cell cultures

The periocular region of *Tg:RARE-CreERT2;R26^{mTomG}* embryos (including the eye itself) was microdissected and minced with small scissors inside a 2-ml Eppendorf tube. Samples were incubated with 1 ml of TrypLE Express (Invitrogen, 12604013) for 15 minutes at 37°C with agitation. Samples were resuspended by gently pipetting up and down 10–15 times using a P1000 pipette. Upon addition of 1 ml of culture media containing (10 µg/ml) DNaseI (Roche, 11284932001), samples were spun 15 minutes at 500g at RT, pellet resuspended in 400 µl of culture media containing of 20% fetal bovine serum (FBS, Gibco), 1% Penicillin-Streptomycin (15140, Gibco), and 2% Ultrosor G (15950–017, Pall Biosepra) in 50:50 DMEM:F12 (31966 and 31765, Gibco) and plated on individual wells of 8-well glass-bottom dishes (Ibidi, 80826) coated with 1 mg/ml of Matrigel (354234, BD Biosciences). Cells were allowed to attach for 8 hours at 37°C 5% CO₂, washed with PBS, and fixed for 15 minutes at RT with 4% PFA in PBS. After fixation, cells were washed in PBS and permeabilized with 0.5% Triton X-100 in PBS for 5 minutes at RT. After 3 washes in PBS (5 minutes each), cells were blocked with 20% goat serum in PBS 1 hour at RT. Primary antibodies were added to cells in 2% goat serum in PBS for 2 h at RT or ON at 4°C. Cells were washed 3 times with PBS, incubated with secondary antibodies for 1 hour at RT, washed in PBS, and kept in PBS for imaging.

Statistics

The number of embryos of each genotype used for analysis is indicated in the figure legends and [S1 Table](#). The graphs were plotted, and statistical analyses were performed using Prism8 (GraphPad Software, Inc). All data points are presented as mean ± SEM (error bars). Individual values can be found in S1, S2 and S3 Data files. Statistical tests used for analysis are indicated on the respective figure legends. *p*-values less than 0.05 were considered significant (**p* < 0.05; ***p* < 0.01; ****p* < 0.001).

Supporting information

S1 Fig. Lineage contributions to the EOM functional unit. (A–D) NCC (*Tg:Wnt1^{Cre};R26^{Tom};Scx-GFP*) and mesoderm (*Mesp1^{Cre};R26^{Tom};Scx-GFP*) lineage contributions to the periocular region on coronal cryosections of E17.5 embryos, combined with immunostaining for tendon (GFP) and muscle (Tnnt3, Troponin T Type 3, differentiated muscle). Sections at ventral (A, C) and dorsal (B,D) levels. Note that tendon insertions at the level of the orbit are NCC-derived (A), whereas the tendon origin (D) is mesoderm-derived. Higher-magnification views at the level of the tendon insertion (A1,C1) and origin (B1,D1) are shown as insets. Asterisk in D1 indicates *Scx-GFP*⁺ cells in the perichondrium of the hypochiasmatic cartilage. (E–F') NCC (*Tg:Wnt1^{Cre};R26^{Tom}*) and mesoderm (*Mesp1^{Cre};R26^{Tom}*) lineage contributions to the periocular region on coronal cryosections of E13.5 embryos, combined with immunostaining for TCF4 and muscle (PAX7/MYOD/MYOG, myogenic markers). Note that TCF4 is expressed robustly in connective tissue fibroblasts and at lower levels in myogenic cells. White arrowheads in (E',F') mark Tom⁺, TCF4⁺, myogenic marker-negative connective tissue cells in the NCC- and mesoderm-derived areas. Pink arrowheads in (E',F') mark myogenic cells (TCF4^{low}). (G–H') Coronal cryosections of E13.5 *Tg:Scx-GFP* embryos, combined with immunostaining for TCF4 (connective tissue, myogenic progenitors) and muscle (PAX7/MYOD/MYOG). White arrowheads in (G',H') mark Tom⁺, TCF4⁺, myogenic marker-negative connective tissue cells in the NCC and mesoderm-derived areas. Pink arrowheads in (G',H') mark myogenic cells (TCF4^{low}). (I,J) In situ hybridization on E12.5 (I) and E13.5 (J) coronal cryosections for *Scx* combined with immunofluorescence for muscle (PAX7/MYOD/MYOG). High levels of *Scx* mRNA are seen at the tendon origin and insertion but also in the bulk of the

muscle masses (I',J', insets). a, anterior; d, dorsal; l, lateral; m, medial; MCT, muscle connective tissue; E, embryonic day; eom, extraocular muscle; NCC, neural crest cell; p, posterior; ti, tendon insertion; to, tendon origin; v, ventral.

(TIF)

S2 Fig. Expression of PITX2 in the POM. (A-C) Immunostaining on E11.5 (A), E12.5 (B) and E13.5 (C) coronal sections of control embryos for PITX2 (EOM myogenic progenitors, POM) and SMA (differentiated muscle). Arrowheads mark the EOM masses and asterisks point to PITX2 expression in the medial POM. Note thinning of the lateral POM as development proceeds (brackets). ($n = 3$ per stage). E, embryonic day; EOM, extraocular muscle; POM, periocular mesenchyme.

(TIF)

S3 Fig. Developmental timing of EOM functional unit components. (A-D') Immunostaining for the indicated markers on coronal sections of E11.5 (A), E12.5 (B, E, F), E13.5 (C) and E14.5 (D) *Tg:Scx-GFP* embryos. (A'-D'') Higher-magnification views of the anterior tendon insertions (superior rectus) in the POM. White arrowheads mark SOX9+ *Scx-GFP*+ cells up to E13.5. Asterisks in A'-C'' point to SOX9+ *Scx-GFP*-negative areas. Double asterisk in D'' mark *Scx-GFP*+ SOX9-negative tendon tips at E14.5. SOX9 expression remains at the sclera. (E-F') Immunostaining for the indicated markers on coronal sections of E11.75 and E13.5 *Tg:Scx-GFP* embryos preincubated with LysoR. Arrowheads in E,E' indicate SOX9+ LysoR+ cells in the E11.75 POM. (G-H'') Immunostaining for the indicated markers on transversal sections of E12.5 *Tg:Scx-GFP* embryos. (G'-H'') Higher magnification views of the lateral tendon insertions (lateral rectus) showing SOX9+ or PITX2+ LysoR+ areas. MYOD/MYOG (myogenic markers) in A-D and MyHC (myofibers) in G-H were used to identify the EOMs. ($n = 3$ per stage). a, anterior; d, dorsal; E, embryonic day; EOM, extraocular muscle; l, lateral; LysoR, LysoTracker Red; m, medial; p, posterior; POM, periocular mesenchyme; s, sclera; v, ventral.

(TIF)

S4 Fig. EOM morphogenesis in mutants with eye defects. (A-C) Micro-CT-based 3D reconstruction of EOM, eyeball, optic nerve, and lens in E13.5 control (A), *Pax6^{Sey/+}* (B), and *Pax6^{Sey/Sey}* embryos (C). Note that in heterozygote embryos, EOM patterning proceeds normally despite having a smaller retina and lens ($n = 3$). (D-E) Micro-CT-based 3D-reconstruction of EOM and eyeball in E18.5 control (A) and *Tg:Lhx2^{Cre};Lhx2^{fl/fl}* (B) embryos. Arrowheads highlight some extent of EOM segregation in the mutant. (D'-E') Coronal sections of control (D') and mutant (E') embryos stained with MyHC (differentiated muscle). Arrowheads indicate individual EOM masses ($n = 2$). (F-F'') Analysis of EOM patterning in E15.5 embryos containing inversions of *Shh* genomic regulatory regions (Inv(6-C2)). (F) Skeletal preparation of mutant embryos displaying cyclopia. (F'-F'') Micro-CT-based 3D-reconstruction of EOM and eyeball of mutant embryos ($n = 2$). a, anterior; ctrl, control; d, dorsal; E, embryonic day; EOM, extraocular muscle; l, lateral; m, medial; micro-CT, micro-computed tomography; p, posterior; v, ventral.

(TIF)

S5 Fig. EOM morphogenesis is dependent retinoic acid signaling. (A) Whole-mount in situ hybridization for *Aldh1a1*, *Aldh1a2*, and *Aldh1a3* in E10.5, E11.5, and E12.5 wildtype embryos ($n = 3$). (A'-A'') In situ hybridization for *Aldh1a2* (A') and immunostaining for ALDH1A2 and MyHC (differentiated muscle) (A'') on E12.5 coronal sections. ALDH1A2 is expressed in the temporal mesenchyme and adjacent connective tissues ($n = 3$). (B) Micro-CT-based 3D-reconstruction of eyeball, optic nerve and lens of E13.5 control, *Aldh1a3^{KO}* and BMS493-treated embryos ($n = 2$ each genotype). The lower row is a scheme of a sphere fitting the

eyeball and lens, and a cylinder for the optic nerve. Note ventralization of the eyeball in *Aldh1a3^{KO}* and BMS493-treated embryos. (C) Micro-CT-based 3D-reconstruction of the mesenchymal condensations of the nasal capsule and trabecular cartilage of E13.5 control (white), *Aldh1a3^{KO}* (yellow) and BMS493-treated (green) embryos. (D–D') MyHC WMIF of E13.5 BMS493-treated embryos as described in S1 Table. The most severe phenotype obtained in each condition is shown as an isosurface. Two different examples of the phenotype observed upon treatment VI (a,b) are shown (most and least severe). An *Aldh1a3^{KO}* embryo is shown as comparison. Asterisk denotes ectopic duplicated SO muscle. (D') Higher-magnification views from D (dashed squares) with examples of adjacent, nonsplit muscle masses (1,2) depicted by differential fiber orientation. (E–F) MyHC WMIF of E13.5 control (E) and *Rdh10^{KO}* (F) embryos. Note total absence of muscle splitting in mutant ($n = 3$ per condition). EOMs in D–F were segmented from adjacent head structures and 3D-reconstructed in Imaris (Bitplane). ctrl, control; dr, dorsal retina; 3D-rec, 3D-reconstruction; e, eyelid groove; E, embryonic day; EOM, extraocular muscle; io, inferior oblique; ir, inferior rectus; le, lens; lgb, lacrimal gland bud; lr, lateral rectus; micro-CT, micro-computed tomography; mr, medial rectus; nlg, nasolacrimal groove; np, nasal pit; os, optic stalk; rb, retractor bulbi; rpe, retinal pigmented epithelium; so, superior oblique; sr, superior rectus; tm, temporal mesenchyme; vr, ventral retina, WMIF, whole-mount immunofluorescence. (TIF)

S6 Fig. Retinoic acid signaling responsiveness in the periocular region. (A–C) Macroscopic views of endogenous GFP fluorescence of *Tg:RARE-CreERT2;R^{26mTomG}* embryos. Tam was injected into pregnant females and embryos analyzed at indicated time points. Arroheads indicate labeling in POM ($n > 3$ per condition). (D) Immunostaining on cells isolated from the periocular region of *Tg:RARE-CreERT2;R^{26mTomG}* embryos for GFP and myogenic markers (MYOD/MYOG). (E) Strategy used to determine responsiveness of *Tg:RARE-CreERT2* reporter in presence of BMS493. BMS493 was injected to pregnant females every 10–12 hours between E10 and E11.75. Recombination was induced by tamoxifen at E10.5 (2 hours after the first BMS injection). (F–I) WMIF for MyHC (differentiated muscle) and GFP (ATRA-responsive cells) of control (F,G) and BMS493-treated embryos (H,I). BMS493 treatment before and after tamoxifen induction reveals a drastic decrease in GFP+ cells in the periocular region (I) compared with controls (G). Asterisks mark the location of the optic nerve ($n = 3$). (J) Coronal sections (dorsal, EOM origin) of E12.5 *Tg:RARE-CreERT2;R26^{Tom};Scx-GFP* embryos immunostained for GFP, Tom (ATRA-responsive cells) and MYOD/MYOG (muscle). Higher magnification views as insets. Arrowheads in J1 mark Tom-negative myogenic cells, and asterisks indicate sporadic labeling in myogenic cells. Arrowheads in J2 mark Tom+ *Scx-GFP*+ cells ($n = 3$). (K–L) WMIF for SMA (differentiated muscle) of *Myod^{iCre}* (control, K, K') and *Myod^{iCre};R26^{RAR403}* (mutant embryos, L, L') ($n = 3$). EOMs in F–I and K–L' were segmented from adjacent head structures and 3D-reconstructed in Imaris (Bitplane). a, anterior; ATRA, all-trans retinoic acid; ctrl, control; d, dorsal; E, embryonic day; EOM, extraocular muscle; l, lateral; m, medial; p, posterior; POM, periocular mesenchyme; Tam, tamoxifen; v, ventral; WMIF, whole-mount immunofluorescence. (TIF)

S7 Fig. EOM insertions in the POM are altered upon ATRA deficiency. (A–D') Immunostaining for the indicated markers on coronal E12 sections of control (A,C,C') and BMS493-treated (B,D,D') *Tg:Scx-GFP* embryos pre-incubated with LysoTracker Red (LysoR). (C',D') Higher-magnification views of the POM region. In BMS493-treated embryos, LysoR and SOX9 staining are absent in the POM (D', asterisk) and SOX9 staining also missing in the RPE (D', double asterisk). (E–N) WMIF for the indicated markers of E11.75 control (E,F,K),

Aldh1a3^{KO} (G,H,M) and BMS493-treated (I,J,N) embryos pre-incubated with LysoR (right eyes). In lateral views, neither *Aldh1a3*^{KO} or BMS493-treated embryos (H,J) show a full PITX2+ POM-ring as the controls (F). Arrowheads in (G,H) mark remaining expression of SOX9/PITX2 in the POM of mutant or inhibitor treated embryos. Asterisks in (F,H,J) mark apoptosis spots in the POM. (K-N) Segmented medial views of periocular region of control, *Aldh1a3*^{KO} or BMS493-treated embryos. Volumes were truncated in Z for clarity. Full view as schemes below. The PITX2+ POM-ring is continuous with the medial-POM in control embryos (K). In mutant and BMS493-treated embryos, residual PITX2 expression in POM is discontinuous with the medial-POM (blue arrowheads) (M,N). (O-Q') WMIF for SMA (differentiated muscle), GFP (ATRA-responsive cells) and PITX2 (muscle progenitors, POM) of *Tg:RARE-CreERT2;R26^{mTmG}* control (O,O'), *Aldh1a3*^{KO} (P,P') and BMS493-treated (Q,Q') embryos. Blue arrowheads in P and Q show reduction or loss of ATRA-responsive cells in the periocular region. (O'-Q') Single Z-planes of the segmented volume. White arrowhead in O shows correct PITX2+ connective tissue pre-pattern in the prospective muscle areas and arrow marks PITX2 expression along the muscle masses. Blue arrowheads in P' and Q' show reduction or loss of ATRA-responsive cells and PITX2 pre-pattern in the medial periocular mesenchyme. (R-T) Single cell plane of WMIF of E12 control (R), BMS493-treated (S) and *Myf5^{nlacZ/nlacZ}* embryos (T) (right eyes) for TCF4 (muscle connective tissue) and SMA (differentiated muscle). Asterisks mark position of the optic nerve. White arrowheads in R,T show correct TCF4+ connective tissue pre-pattern in the prospective muscle areas and white arrow marks TCF4 expression along the muscle masses (R). (U-V) WMIF for GFP and β -gal (myogenic progenitors) of E14.5 *Tg:Scx-GFP;Myf5^{nlacZ/+}* (U, control) and *Tg:Scx-GFP;Myf5^{nlacZ/nlacZ}* (V, mutant) embryos (left eyes). Asterisk indicates few remaining β -gal+ cells in mutant. (U', V') split GFP channel. Arrowheads in (V) indicate the correct position of tendon condensations for the 4 recti muscles although these are absent in the mutant. Lower panel, higher-magnification views. a, anterior; ATRA, all-trans retinoic acid; anl, anlage; apop, apoptosis; ctrl, control; d, dorsal; E, embryonic day; eom, extraocular muscle; l, lateral; m, medial; m-pom, medial periocular mesenchyme; l-pom, lateral periocular mesenchyme; POM, periocular mesenchyme; pom-r, periocular mesenchyme ring; p, posterior; rpe, retinal pigmented epithelium; v, ventral; WMIF, whole-mount immunofluorescence.

(TIF)

S8 Fig. Illustration depicting the timeline of EOM and POM development in relation to ATRA signaling. Summary of the most relevant genetic perturbations and drug treatments of this study. ATRA, all-trans retinoic acid; EOM, extraocular muscle; POM, periocular mesenchyme.

(TIF)

S1 Table. BMS493 injection regimes. The same BMS493 concentration (Conc BMS) was used across injection regimes, from I to VI. Pink cases mark injection time points in the morning (mo), midday (mid) or evening (eve) between E10.5 and E12.5. The number of embryos with different muscle phenotype severity at E13.5 are shown: (no), no altered phenotype; mild (+), muscle mispatterning but overall organization retained; strong (++) , strong mispatterning but with a minimum of 2 muscles split; severe (+++), no or almost absent splitting. n is the total number of embryos analyzed for a certain treatment type ($n = 38$ embryos analyzed in total); N exp, number of times the experiment was repeated. E, embryonic day; EOM, extraocular muscle.

(XLSX)

S2 Table. Antibodies and resources used in this study.

(XLSX)

S1 Data. Excel table containing individual values to generate the histogram in Fig 3K.

For each tissue section, a rectangular ROI (region of interest) was defined in Fiji (Image J) in the LysoTracker Red-positive and adjacent LysoTracker Red-negative areas. The number of SOX9+ cells was scored in each ROI. Individual values were represented by the ratio of N° cells/ROI area (μm^2).

(XLSX)

S2 Data. Excel table containing individual values to generate the histogram in Fig 4I. For each embryo, the EOM volume was calculated as described in the methods section. The normalized EOM volume is the ratio of the individual volume value/average of the control values. EOM, extraocular muscle.

(XLSX)

S3 Data. Excel table containing individual values to generate the histogram in Fig 5C. Each data point represents the percentage of myogenic and non-myogenic GFP+ cells isolated by bulk digestion of the periocular area of a single *Tg:RARE-CreERT2;R26^{mTmG}* reporter embryo.

(XLSX)

S1 Video. Temporal sequence of EOM patterning. Whole-mount immunostaining for MYOD/MYOG/Desmin (E11.5 to E12.5) or MyHC (E13.5 to E14.5) on the developing EOM of control embryos. EOMs were segmented from adjacent head structures and 3D-reconstructed in Imaris (Bitplane). E, embryonic day; EOM, extraocular muscle.

(MOV)

S2 Video. Organization of the EOM functional unit at E11.75. Whole-mount immunostaining for MyHC (myofibers, Red) and PITX2 (POM and myogenic progenitors, Cyan) on control embryo. EOMs were segmented from adjacent head structures and 3D-reconstructed in Imaris (Bitplane). E, embryonic day; EOM, extraocular muscle; POM, periocular mesenchyme.

(MOV)

S3 Video. Organization of the EOM functional unit at E11.75. Whole-mount immunostaining for MyHC (myofibers, Cyan) and GFP (tendon progenitors, Green) on *Tg:Scx-GFP* embryo. EOMs were segmented from adjacent head structures and 3D-reconstructed in Imaris (Bitplane). Apoptotic foci are visualized by LysoTracker Red staining. A clipping plane was added for clarity of visualization. Note that tendon condensations start to organize radially and towards the apoptotic foci in the POM. E, embryonic day; EOM, extraocular muscle; POM, periocular mesenchyme.

(MOV)

S4 Video. Organization of the EOM functional unit at E12.5. Whole-mount immunostaining for MyHC (myofibers, Cyan) and GFP (tendon progenitors, Green) on *Tg:Scx-GFP* embryo. EOMs were segmented from adjacent head structures and 3D-reconstructed in Imaris (Bitplane). Apoptotic foci are visualized by LysoTracker Red staining. A clipping plane was added for clarity of visualization. Note how tendon condensations of the recti muscles are more refined at this stage and project towards the apoptotic foci in the POM. E, embryonic day; EOM, extraocular muscle; POM, periocular mesenchyme.

(MOV)

S5 Video. Organization of the EOM functional unit of E13.5 BMS493-treated (E10.5 → E11.75) *Tg:Scx-GFP* embryos. Whole-mount immunostaining for MyHC (myofibers, Red) and GFP (tendon progenitors, Green). EOMs were segmented from adjacent head structures

and 3D-reconstructed in Imaris (Bitplane). Note the presence of tendon condensations at the tips of mispatterned muscle masses. E, embryonic day; EOM, extraocular muscle.

(MOV)

S6 Video. ATRA-responsiveness in the periocular region of E13.5 *Tg:RARE-CreERT2*; *R26^{mTmG}* control embryos (Tamoxifen induction at E10.5). Whole-mount immunostaining for MyHC (myofibers, Red), and GFP (ATRA-responsive cells, Green). EOMs were segmented from adjacent head structures and 3D-reconstructed in Imaris (Bitplane). EOMs are shown as isosurfaces for clarity of visualization. ATRA, all-trans retinoic acid; E, embryonic day; EOM, extraocular muscle.

(MOV)

S7 Video. ATRA-responsiveness in the periocular region of E13.5 BMS493-treated *Tg:RARE-CreERT2*; *R26^{mTmG}* embryos (BMS493 treatment: E10 → E11.75; Tamoxifen induction at E10.5). Whole-mount immunostaining for MyHC (myofibers, Red) and GFP (ATRA-responsive cells, Green). EOMs were segmented from adjacent head structures and 3D-reconstructed in Imaris (Bitplane). EOMs are shown as isosurfaces for clarity of visualization.

ATRA, all-trans retinoic acid; E, embryonic day; EOM, extraocular muscle.

(MOV)

S8 Video. ATRA-responsiveness in the periocular region of E12.5 *Tg:RARE-CreERT2*; *R26^{mTmG}* control embryos (Tamoxifen induction at E10.5). Whole-mount immunostaining for GFP (ATRA-responsive cells, Green), PITX2 (POM and myogenic progenitors, Cyan) and SMA (differentiated muscle, Red). Z-planes from medial to lateral levels. ATRA, all-trans retinoic acid; E, embryonic day; POM, periocular mesenchyme.

(MOV)

S9 Video. ATRA-responsiveness in the periocular region of E12.5 *Tg:RARE-CreERT2*; *R26^{mTmG}*; *Aldh1a3^{KO}* embryos (Tamoxifen induction at E10.5). Whole-mount immunostaining for GFP (ATRA-responsive cells, Green), PITX2 (POM and myogenic progenitors, Cyan), and SMA (differentiated muscle, Red). Z-planes from medial to lateral levels. ATRA, all-trans retinoic acid; E, embryonic day; POM, periocular mesenchyme.

(MOV)

S10 Video. ATRA-responsiveness in the periocular region of E12.5 *Tg:RARE-CreERT2*; *R26^{mTmG}* BMS493-treated embryos (BMS493 treatment: E10 → E11.75; Tamoxifen induction at E10.5). Whole-mount immunostaining for GFP (ATRA-responsive cells, Green), PITX2 (POM and myogenic progenitors, Cyan) and SMA (differentiated muscle, Red). Z-planes from medial to lateral levels. ATRA, all-trans retinoic acid; E, embryonic day; POM, periocular mesenchyme.

(MOV)

S11 Video. Organization of the EOM insertions of E12.5 *Tg:Scx-GFP* control embryos. Whole-mount immunostaining for MyHC (myofibers, Red) and GFP (tendon progenitors, Green). EOMs were segmented from adjacent head structures and 3D-reconstructed in Imaris (Bitplane). A clipping plane has been added for clarity of visualization. E, embryonic day; EOM, extraocular muscle.

(MOV)

S12 Video. Organization of the EOM insertions of E12.5 BMS493-treated (E10.5 → E11.75) *Tg:Scx-GFP* embryos. Whole-mount immunostaining for MyHC (myofibers, Red) and GFP (tendon progenitors, Green). EOMs were segmented from adjacent head structures

and 3D-reconstructed in Imaris (Bitplane). A clipping plane has been added for clarity of visualization. Note that distribution of *Scx-GFP*⁺ cells is more diffuse than for controls (Video 11), but an *Scx-GFP*⁺ condensation is present at the tip of the inferior muscle mass. E, embryonic day; EOM, extraocular muscle.

(MOV)

S13 Video. Organization of the EOM insertions of E14.5 *Tg:Scx-GFP;Myf5^{nlacZ/+}* embryos.

Whole-mount immunostaining for β -gal (myogenic progenitors, Red) and GFP (tendon, Green). EOMs were segmented from adjacent head structures and 3D-reconstructed in Imaris (Bitplane). E, embryonic day; EOM, extraocular muscle.

(MOV)

S14 Video. Organization of the EOM insertions of E14.5 *Tg:Scx-GFP;Myf5^{nlacZ/nlacZ}* embryos.

Whole-mount immunostaining for β -gal (myogenic progenitors, Red) and GFP (tendon, Green). E, embryonic day; EOM, extraocular muscle.

(MOV)

Acknowledgments

We gratefully acknowledge the UtechS Photonic BioImaging (Imagopole), C2RT, Institut Pasteur. We thank Robert Kelly (IBDM, Marseille, France) for kindly providing *R26^{RAR403}* mice.

Author Contributions

Conceptualization: Glenda Evangelina Comai, Shahragim Tajbakhsh.

Data curation: Glenda Evangelina Comai.

Formal analysis: Glenda Evangelina Comai, Markéta Tesařová.

Funding acquisition: Shahragim Tajbakhsh.

Investigation: Glenda Evangelina Comai.

Methodology: Glenda Evangelina Comai, Markéta Tesařová, Tomáš Zikmund, Jozef Kaiser.

Project administration: Glenda Evangelina Comai, Shahragim Tajbakhsh.

Resources: Glenda Evangelina Comai, Valérie Dupé, Muriel Rhinn, Pedro Vallecillo-García, Fabio da Silva, Betty Feret, Katherine Exelby, Pascal Dollé, Leif Carlsson, Brian Pryce, François Spitz, Sigmar Stricker, James Briscoe, Andreas Schedl, Norbert B. Ghyselinck, Ronen Schweitzer, Shahragim Tajbakhsh.

Supervision: Jozef Kaiser, Ronen Schweitzer, Shahragim Tajbakhsh.

Validation: Glenda Evangelina Comai.

Visualization: Glenda Evangelina Comai, Markéta Tesařová.

Writing – original draft: Glenda Evangelina Comai.

Writing – review & editing: Glenda Evangelina Comai, Markéta Tesařová, Valérie Dupé, Muriel Rhinn, Pedro Vallecillo-García, Fabio da Silva, Leif Carlsson, Sigmar Stricker, Tomáš Zikmund, Jozef Kaiser, James Briscoe, Andreas Schedl, Norbert B. Ghyselinck, Ronen Schweitzer, Shahragim Tajbakhsh.

References

1. Hasson P. "Soft" tissue patterning: muscles and tendons of the limb take their form. *Developmental dynamics: an official publication of the American Association of Anatomists*. 2011; 240(5):1100–7. <https://doi.org/10.1002/dvdy.22608> PMID: 21438070
2. Huang AH. Coordinated development of the limb musculoskeletal system: Tendon and muscle patterning and integration with the skeleton. *Developmental biology*. 2017; 429(2):420–8. <https://doi.org/10.1016/j.ydbio.2017.03.028> PMID: 28363737; PubMed Central PMCID: PMC5581688.
3. Noden DM, Francis-West P. The differentiation and morphogenesis of craniofacial muscles. *Developmental dynamics: an official publication of the American Association of Anatomists*. 2006; 235(5):1194–218. <https://doi.org/10.1002/dvdy.20697> PMID: 16502415.
4. Suzuki DG, Fukumoto Y, Yoshimura M, Yamazaki Y, Kosaka J, Kuratani S, et al. Comparative morphology and development of extra-ocular muscles in the lamprey and gnathostomes reveal the ancestral state and developmental patterns of the vertebrate head. *Zoological Lett*. 2016; 2:10. <https://doi.org/10.1186/s40851-016-0046-3> PMID: 27081572; PubMed Central PMCID: PMC4831119.
5. Young GC. Number and arrangement of extraocular muscles in primitive gnathostomes: evidence from extinct placoderm fishes. *Biology letters*. 2008; 4(1):110–4. <https://doi.org/10.1098/rsbl.2007.0545> PMID: 18077236.
6. Spencer RF, Porter JD. Biological organization of the extraocular muscles. *Progress in brain research*. 2006; 151:43–80. Epub 2005/10/14. [https://doi.org/10.1016/S0079-6123\(05\)51002-1](https://doi.org/10.1016/S0079-6123(05)51002-1) PMID: 16221585.
7. Ziermann JM, Diogo R, Noden DM. Neural crest and the patterning of vertebrate craniofacial muscles. *Genesis*. 2018; 56(6–7):e23097. <https://doi.org/10.1002/dvg.23097> PMID: 29659153.
8. Nassari S, Duprez D, Fournier-Thibault C. Non-myogenic Contribution to Muscle Development and Homeostasis: The Role of Connective Tissues. *Front Cell Dev Biol*. 2017; 5:22. <https://doi.org/10.3389/fcell.2017.00022> PMID: 28386539; PubMed Central PMCID: PMC5362625.
9. Bohnsack BL, Gallina D, Thompson H, Kasprick DS, Lucarelli MJ, Dootz G, et al. Development of extraocular muscles requires early signals from periocular neural crest and the developing eye. *Archives of ophthalmology*. 2011; 129(8):1030–41. Epub 2011/04/13. <https://doi.org/10.1001/archophthalmol.2011.75> PMID: 21482859; PubMed Central PMCID: PMC3248700.
10. Ericsson R, Cerny R, Falck P, Olsson L. Role of cranial neural crest cells in visceral arch muscle positioning and morphogenesis in the Mexican axolotl, *Ambystoma mexicanum*. *Developmental dynamics: an official publication of the American Association of Anatomists*. 2004; 231(2):237–47. <https://doi.org/10.1002/dvdy.20127> PMID: 15366001.
11. Noden DM. The role of the neural crest in patterning of avian cranial skeletal, connective, and muscle tissues. *Developmental biology*. 1983; 96(1):144–65. [https://doi.org/10.1016/0012-1606\(83\)90318-4](https://doi.org/10.1016/0012-1606(83)90318-4) PMID: 6825950.
12. Rinon A, Lazar S, Marshall H, Buchmann-Moller S, Neufeld A, Elhanany-Tamir H, et al. Cranial neural crest cells regulate head muscle patterning and differentiation during vertebrate embryogenesis. *Development*. 2007; 134(17):3065–75. <https://doi.org/10.1242/dev.002501> PMID: 17652354.
13. Tokita M, Schneider RA. Developmental origins of species-specific muscle pattern. *Developmental biology*. 2009; 331(2):311–25. <https://doi.org/10.1016/j.ydbio.2009.05.548> PMID: 19450573; PubMed Central PMCID: PMC2726847.
14. von Scheven G, Alvares LE, Mootoosamy RC, Dietrich S. Neural tube derived signals and Fgf8 act antagonistically to specify eye versus mandibular arch muscles. *Development*. 2006; 133(14):2731–45. <https://doi.org/10.1242/dev.02426> PMID: 16775000.
15. McGurk PD, Swartz ME, Chen JW, Galloway JL, Eberhart JK. In vivo zebrafish morphogenesis shows Cyp26b1 promotes tendon condensation and musculoskeletal patterning in the embryonic jaw. *PLoS Genet*. 2017; 13(12):e1007112. <https://doi.org/10.1371/journal.pgen.1007112> PMID: 29227993; PubMed Central PMCID: PMC5739505.
16. Shimizu M, Narboux-Neme N, Gitton Y, de Lombares C, Fontaine A, Alfama G, et al. Probing the origin of matching functional jaws: roles of Dlx5/6 in cranial neural crest cells. *Scientific reports*. 2018; 8(1):14975. <https://doi.org/10.1038/s41598-018-33207-2> PMID: 30297736; PubMed Central PMCID: PMC6175850.
17. Evans AL, Gage PJ. Expression of the homeobox gene Pitx2 in neural crest is required for optic stalk and ocular anterior segment development. *Human molecular genetics*. 2005; 14(22):3347–59. Epub 2005/10/06. <https://doi.org/10.1093/hmg/ddi365> PMID: 16203745.
18. Heude E, Bellessort B, Fontaine A, Hamazaki M, Treier AC, Treier M, et al. Etiology of craniofacial malformations in mouse models of blepharophimosis, ptosis and epicanthus inversus syndrome. *Human molecular genetics*. 2015; 24(6):1670–81. <https://doi.org/10.1093/hmg/ddu579> PMID: 25416281.

19. Iwata J, Suzuki A, Pelikan RC, Ho TV, Chai Y. Noncanonical transforming growth factor beta (TGFbeta) signaling in cranial neural crest cells causes tongue muscle developmental defects. *The Journal of biological chemistry*. 2013; 288(41):29760–70. <https://doi.org/10.1074/jbc.M113.493551> PMID: 23950180; PubMed Central PMCID: PMC3795273.
20. Kardon G. Muscle and tendon morphogenesis in the avian hind limb. *Development*. 1998; 125(20):4019–32. Epub 1998/09/15. PMID: 9735363.
21. Kardon G, Harfe BD, Tabin CJ. A Tcf4-positive mesodermal population provides a prepattern for vertebrate limb muscle patterning. *Developmental cell*. 2003; 5(6):937–44. [https://doi.org/10.1016/s1534-5807\(03\)00360-5](https://doi.org/10.1016/s1534-5807(03)00360-5) PMID: 14667415.
22. Sefton EM, Kardon G. Connecting muscle development, birth defects, and evolution: An essential role for muscle connective tissue. *Current topics in developmental biology*. 2019; 132:137–76. <https://doi.org/10.1016/bs.ctdb.2018.12.004> PMID: 30797508; PubMed Central PMCID: PMC6449175.
23. Murchison ND, Price BA, Conner DA, Keene DR, Olson EN, Tabin CJ, et al. Regulation of tendon differentiation by scleraxis distinguishes force-transmitting tendons from muscle-anchoring tendons. *Development*. 2007; 134(14):2697–708. <https://doi.org/10.1242/dev.001933> PMID: 17567668.
24. Schweitzer R, Chyung JH, Murtaugh LC, Brent AE, Rosen V, Olson EN, et al. Analysis of the tendon cell fate using Scleraxis, a specific marker for tendons and ligaments. *Development*. 2001; 128(19):3855–66. PMID: 11585810.
25. Diogo R, Kelly RG, Christiaen L, Levine M, Ziermann JM, Molnar JL, et al. A new heart for a new head in vertebrate cardiopharyngeal evolution. *Nature*. 2015; 520(7548):466–73. Epub 2015/04/24. <https://doi.org/10.1038/nature14435> PMID: 25903628.
26. Sambasivan R, Kuratani S, Tajbakhsh S. An eye on the head: the development and evolution of craniofacial muscles. *Development*. 2011; 138(12):2401–15. <https://doi.org/10.1242/dev.040972> PMID: 21610022.
27. Gitton Y, Heude E, Vieux-Rochas M, Benouaiche L, Fontaine A, Sato T, et al. Evolving maps in craniofacial development. *Seminars in cell & developmental biology*. 2010; 21(3):301–8. <https://doi.org/10.1016/j.semcd.2010.01.008> PMID: 20083217.
28. Rhinn M, Dolle P. Retinoic acid signalling during development. *Development*. 2012; 139(5):843–58. <https://doi.org/10.1242/dev.065938> PMID: 22318625.
29. Cunningham TJ, Duester G. Mechanisms of retinoic acid signalling and its roles in organ and limb development. *Nature reviews Molecular cell biology*. 2015; 16(2):110–23. <https://doi.org/10.1038/nrm3932> PMID: 25560970; PubMed Central PMCID: PMC4636111.
30. Bohnsack BL, Kasprick DS, Kish PE, Goldman D, Kahana A. A zebrafish model of axenfeld-rieger syndrome reveals that pitx2 regulation by retinoic acid is essential for ocular and craniofacial development. *Investigative ophthalmology & visual science*. 2012; 53(1):7–22. <https://doi.org/10.1167/iov.11-8494> PMID: 22125274; PubMed Central PMCID: PMC3292384.
31. Harding P, Moosajee M. The Molecular Basis of Human Anophthalmia and Microphthalmia. *J Dev Biol*. 2019; 7(3):16. <https://doi.org/10.3390/jdb7030016> PMID: 31416264; PubMed Central PMCID: PMC6787759.
32. See AW, Kaiser ME, White JC, Clagett-Dame M. A nutritional model of late embryonic vitamin A deficiency produces defects in organogenesis at a high penetrance and reveals new roles for the vitamin in skeletal development. *Developmental biology*. 2008; 316(2):171–90. <https://doi.org/10.1016/j.ydbio.2007.10.018> PMID: 18321479.
33. Cvekl A, Wang WL. Retinoic acid signaling in mammalian eye development. *Exp Eye Res*. 2009; 89(3):280–91. <https://doi.org/10.1016/j.exer.2009.04.012> PMID: 19427305; PubMed Central PMCID: PMC2756743.
34. Matt N, Dupe V, Garnier JM, Dennefeld C, Chambon P, Mark M, et al. Retinoic acid-dependent eye morphogenesis is orchestrated by neural crest cells. *Development*. 2005; 132(21):4789–800. Epub 2005/10/07. <https://doi.org/10.1242/dev.02031> PMID: 16207763.
35. Matt N, Ghyselinck NB, Pellerin I, Dupe V. Impairing retinoic acid signalling in the neural crest cells is sufficient to alter entire eye morphogenesis. *Developmental biology*. 2008; 320(1):140–8. Epub 2008/06/10. <https://doi.org/10.1016/j.ydbio.2008.04.039> PMID: 18539269.
36. Molotkov A, Molotkova N, Duester G. Retinoic acid guides eye morphogenetic movements via paracrine signaling but is unnecessary for retinal dorsoventral patterning. *Development*. 2006; 133(10):1901–10. Epub 2006/04/14. <https://doi.org/10.1242/dev.02328> PMID: 16611695; PubMed Central PMCID: PMC2833011.
37. Williams AL, Bohnsack BL. Neural crest derivatives in ocular development: discerning the eye of the storm. *Birth defects research Part C, Embryo today: reviews*. 2015; 105(2):87–95. <https://doi.org/10.1002/bdrc.21095> PMID: 26043871; PubMed Central PMCID: PMC5262495.

38. Couly GF, Coltey PM, Douarin NML. The developmental fate of the cephalic mesoderm in quail-chick chimeras. *Development*. 1992; 114:1–15. PMID: [1576952](#)
39. Creuzet S, Couly G, Le Douarin NM. Patterning the neural crest derivatives during development of the vertebrate head: insights from avian studies. *J Anat*. 2005; 207(5):447–59. <https://doi.org/10.1111/j.1469-7580.2005.00485.x> PMID: [16313387](#); PubMed Central PMCID: [PMC1571568](#).
40. Gage PJ, Rhoades W, Prucka SK, Hjalt T. Fate maps of neural crest and mesoderm in the mammalian eye. *Investigative ophthalmology & visual science*. 2005; 46(11):4200–8. Epub 2005/10/27. <https://doi.org/10.1167/iovs.05-0691> PMID: [16249499](#).
41. Grenier J, Teillet MA, Grifone R, Kelly RG, Duprez D. Relationship between neural crest cells and cranial mesoderm during head muscle development. *PLoS ONE*. 2009; 4(2):e4381. <https://doi.org/10.1371/journal.pone.0004381> PMID: [19198652](#).
42. Johnston MC, Noden DM, Hazelton RD, Coulombre JL, Coulombre AJ. Origins of avian ocular and periocular tissues. *Exp Eye Res*. 1979; 29(1):27–43. [https://doi.org/10.1016/0014-4835\(79\)90164-7](https://doi.org/10.1016/0014-4835(79)90164-7) PMID: [510425](#).
43. Noden DM. The embryonic origins of avian cephalic and cervical muscles and associated connective tissues. *Am J Anat*. 1983; 168:257–76. <https://doi.org/10.1002/aja.1001680302> PMID: [6650439](#)
44. Sevel D. The origins and insertions of the extraocular muscles: development, histologic features, and clinical significance. *Trans Am Ophthalmol Soc*. 1986; 84:488–526. PMID: [3590478](#); PubMed Central PMCID: [PMC1298748](#).
45. Danielian PS, Muccino D, Rowitch DH, Michael SK, McMahon AP. Modification of gene activity in mouse embryos in utero by a tamoxifen-inducible form of Cre recombinase. *Curr Biol*. 1998; 8(24):1323–6. [https://doi.org/10.1016/s0960-9822\(07\)00562-3](https://doi.org/10.1016/s0960-9822(07)00562-3) PMID: [9843687](#).
46. Saga Y, Miyagawa-Tomita S, Takagi A, Kitajima S, Miyazaki J, Inoue T. MesP1 is expressed in the heart precursor cells and required for the formation of a single heart tube. *Development*. 1999; 126(15):3437–47. PMID: [10393122](#).
47. Mathew SJ, Hansen JM, Merrell AJ, Murphy MM, Lawson JA, Hutcheson DA, et al. Connective tissue fibroblasts and Tcf4 regulate myogenesis. *Development*. 2011; 138(2):371–84. Epub 2010/12/24. <https://doi.org/10.1242/dev.057463> PMID: [21177349](#); PubMed Central PMCID: [PMC3005608](#).
48. Pryce BA, Brent AE, Murchison ND, Tabin CJ, Schweitzer R. Generation of transgenic tendon reporters, ScxGFP and ScxAP, using regulatory elements of the scleraxis gene. *Developmental dynamics: an official publication of the American Association of Anatomists*. 2007; 236(6):1677–82. Epub 2007/05/15. <https://doi.org/10.1002/dvdy.21179> PMID: [17497702](#).
49. Deries M, Schweitzer R, Duxson MJ. Developmental fate of the mammalian myotome. *Developmental dynamics: an official publication of the American Association of Anatomists*. 2010; 239(11):2898–910. <https://doi.org/10.1002/dvdy.22425> PMID: [20865781](#).
50. Stricker S, Mathia S, Haupt J, Seemann P, Meier J, Mundlos S. Odd-skipped related genes regulate differentiation of embryonic limb mesenchyme and bone marrow mesenchymal stromal cells. *Stem Cells Dev*. 2012; 21(4):623–33. <https://doi.org/10.1089/scd.2011.0154> PMID: [21671783](#).
51. Sulik KK, Dehart DB, Johnson CS, Ellis SL, Chen SY, Dunty WC Jr., et al. Programmed cell death in extraocular muscle tendon/sclera precursors. *Molecular vision*. 2001; 7:184–91. Epub 2001/08/15. PMID: [11503002](#).
52. Fogel JL, Thein TZ, Mariani FV. Use of LysoTracker to detect programmed cell death in embryos and differentiating embryonic stem cells. *J Vis Exp*. 2012; (68). <https://doi.org/10.3791/4254> PMID: [23092960](#); PubMed Central PMCID: [PMC3490301](#).
53. Blitz E, Sharir A, Akiyama H, Zelzer E. Tendon-bone attachment unit is formed modularly by a distinct pool of Scx- and Sox9-positive progenitors. *Development*. 2013; 140(13):2680–90. <https://doi.org/10.1242/dev.093906> PMID: [23720048](#).
54. Blitz E, Viukov S, Sharir A, Shwartz Y, Galloway JL, Pryce BA, et al. Bone ridge patterning during musculoskeletal assembly is mediated through SCX regulation of Bmp4 at the tendon-skeleton junction. *Developmental cell*. 2009; 17(6):861–73. <https://doi.org/10.1016/j.devcel.2009.10.010> PMID: [20059955](#); PubMed Central PMCID: [PMC3164485](#).
55. Roberts RR, Bobzin L, Teng CS, Pal D, Tuzon CT, Schweitzer R, et al. FGF signaling patterns cell fate at the interface between tendon and bone. *Development*. 2019; 146(15). <https://doi.org/10.1242/dev.170241> PMID: [31320326](#); PubMed Central PMCID: [PMC6703712](#).
56. Sugimoto Y, Takimoto A, Akiyama H, Kist R, Scherer G, Nakamura T, et al. Scx+/Sox9+ progenitors contribute to the establishment of the junction between cartilage and tendon/ligament. *Development*. 2013; 140(11):2280–8. <https://doi.org/10.1242/dev.096354> PMID: [23615282](#).
57. Thompson H, Griffiths JS, Jeffery G, McGonnell IM. The retinal pigment epithelium of the eye regulates the development of scleral cartilage. *Developmental biology*. 2010; 347(1):40–52. <https://doi.org/10.1016/j.ydbio.2010.08.006> PMID: [20707994](#); PubMed Central PMCID: [PMC2977850](#).

58. Grindley JC, Davidson DR, Hill RE. The role of Pax-6 in eye and nasal development. *Development*. 1995; 121(5):1433–42. PMID: [7789273](#).
59. Roberts RC. Small eyes—a new dominant eye mutant in the mouse. *Genet Res, Cam*. 1967; 9:121–2. <https://doi.org/10.1017/S0016672300010387>
60. Kaufman MH, Chang HH, Shaw JP. Craniofacial abnormalities in homozygous Small eye (Sey/Sey) embryos and newborn mice. *J Anat*. 1995; 186(Pt 3):607–17. PMID: [7559133](#); PubMed Central PMCID: PMC1167018.
61. Hagglund AC, Dahl L, Carlsson L. Lhx2 is required for patterning and expansion of a distinct progenitor cell population committed to eye development. *PLoS ONE*. 2011; 6(8):e23387. <https://doi.org/10.1371/journal.pone.0023387> PMID: [21886788](#); PubMed Central PMCID: PMC3158764.
62. Twitty VC. Influence of the eye on the growth of its associated structures, studied by means of heteroplastic transplantation. *Journal of Experimental Zoology*. 1932; 61:333–74. <https://doi.org/10.1002/jez.1400610302>
63. Duester G. Keeping an eye on retinoic acid signaling during eye development. *Chem Biol Interact*. 2009; 178(1–3):178–81. <https://doi.org/10.1016/j.cbi.2008.09.004> PMID: [18831967](#); PubMed Central PMCID: PMC2646828.
64. Dupe V, Matt N, Garnier JM, Chambon P, Mark M, Ghyselinck NB. A newborn lethal defect due to inactivation of retinaldehyde dehydrogenase type 3 is prevented by maternal retinoic acid treatment. *Proceedings of the National Academy of Sciences of the United States of America*. 2003; 100(24):14036–41. <https://doi.org/10.1073/pnas.2336223100> PMID: [14623956](#); PubMed Central PMCID: PMC283541.
65. Rhinn M, Schuhbauer B, Niederreither K, Dolle P. Involvement of retinol dehydrogenase 10 in embryonic patterning and rescue of its loss of function by maternal retinaldehyde treatment. *Proceedings of the National Academy of Sciences of the United States of America*. 2011; 108(40):16687–92. <https://doi.org/10.1073/pnas.1103877108> PMID: [21930923](#); PubMed Central PMCID: PMC3189044.
66. Osumi-Yamashita N, Ninomiya Y, Doi H, Eto K. The contribution of both forebrain and midbrain crest cells to the mesenchyme in the frontonasal mass of mouse embryos. *Developmental biology*. 1994; 164(2):409–19. <https://doi.org/10.1006/dbio.1994.1211> PMID: [8045344](#).
67. Serbedzija GN, Bronner-Fraser M, Fraser SE. Vital dye analysis of cranial neural crest cell migration in the mouse embryo. *Development*. 1992; 116(2):297–307. PMID: [1283734](#).
68. Chawla B, Schley E, Williams AL, Bohnsack BL. Retinoic Acid and Pitx2 Regulate Early Neural Crest Survival and Migration in Craniofacial and Ocular Development. *Birth Defects Res B Dev Reprod Toxicol*. 2016; 107(3):126–35. <https://doi.org/10.1002/bdrb.21177> PMID: [27175943](#).
69. Sandell LL, Sanderson BW, Moiseyev G, Johnson T, Mushegian A, Young K, et al. RDH10 is essential for synthesis of embryonic retinoic acid and is required for limb, craniofacial, and organ development. *Genes & development*. 2007; 21(9):1113–24. <https://doi.org/10.1101/gad.1533407> PMID: [17473173](#); PubMed Central PMCID: PMC1855236.
70. Colasanto MP, Eyal S, Mohassel P, Bamshad M, Bonnemann CG, Zelzer E, et al. Development of a subset of forelimb muscles and their attachment sites requires the ulnar-mammary syndrome gene Tbx3. *Dis Model Mech*. 2016; 9(11):1257–69. <https://doi.org/10.1242/dmm.025874> PMID: [27491074](#); PubMed Central PMCID: PMC5117227.
71. Hasson P, DeLaurier A, Bennett M, Grigorieva E, Naiche LA, Papaioannou VE, et al. Tbx4 and tbx5 acting in connective tissue are required for limb muscle and tendon patterning. *Developmental cell*. 2010; 18(1):148–56. <https://doi.org/10.1016/j.devcel.2009.11.013> PMID: [20152185](#); PubMed Central PMCID: PMC3034643.
72. Swinehart IT, Schlientz AJ, Quintanilla CA, Mortlock DP, Wellik DM. Hox11 genes are required for regional patterning and integration of muscle, tendon and bone. *Development*. 2013; 140(22):4574–82. <https://doi.org/10.1242/dev.096693> PMID: [24154528](#); PubMed Central PMCID: PMC3817943.
73. Chassot AA, Le Rolle M, Jolivet G, Stevant I, Guignon JM, Da Silva F, et al. Retinoic acid synthesis by ALDH1A proteins is dispensable for meiosis initiation in the mouse fetal ovary. *Sci Adv*. 2020; 6(21):eaaz1261. Epub 2020/06/05. <https://doi.org/10.1126/sciadv.aaz1261> PMID: [32494737](#); PubMed Central PMCID: PMC7244317.
74. Madisen L, Zwingman TA, Sunkin SM, Oh SW, Zariwala HA, Gu H, et al. A robust and high-throughput Cre reporting and characterization system for the whole mouse brain. *Nature neuroscience*. 2010; 13(1):133–40. Epub 2009/12/22. <https://doi.org/10.1038/nn.2467> PMID: [20023653](#); PubMed Central PMCID: PMC2840225.
75. Muzumdar MD, Tasic B, Miyamichi K, Li L, Luo L. A global double-fluorescent Cre reporter mouse. *Genesis*. 2007; 45(9):593–605. <https://doi.org/10.1002/dvg.20335> PMID: [17868096](#).
76. Nakamura E, Nguyen MT, Mackem S. Kinetics of tamoxifen-regulated Cre activity in mice using a cartilage-specific CreER(T) to assay temporal activity windows along the proximodistal limb skeleton.

- Developmental dynamics: an official publication of the American Association of Anatomists. 2006; 235(9):2603–12. <https://doi.org/10.1002/dvdy.20892> PMID: 16894608.
77. Nguyen MT, Zhu J, Nakamura E, Bao X, Mackem S. Tamoxifen-dependent, inducible Hoxb6CreERT recombinase function in lateral plate and limb mesoderm, CNS isthmic organizer, posterior trunk neural crest, hindgut, and tailbud. *Developmental dynamics: an official publication of the American Association of Anatomists*. 2009; 238(2):467–74. <https://doi.org/10.1002/dvdy.21846> PMID: 19161221; PubMed Central PMCID: PMC3483870.
 78. Rajaii F, Bitzer ZT, Xu Q, Sockanathan S. Expression of the dominant negative retinoid receptor, RAR403, alters telencephalic progenitor proliferation, survival, and cell fate specification. *Developmental biology*. 2008; 316(2):371–82. <https://doi.org/10.1016/j.ydbio.2008.01.041> PMID: 18329011.
 79. Wood WM, Etemad S, Yamamoto M, Goldhamer DJ. MyoD-expressing progenitors are essential for skeletal myogenesis and satellite cell development. *Developmental biology*. 2013; 384(1):114–27. Epub 2013/09/24. <https://doi.org/10.1016/j.ydbio.2013.09.012> PMID: 24055173; PubMed Central PMCID: PMC3838901.
 80. Kastner P, Grondona JM, Mark M, Gansmuller A, LeMeur M, Decimo D, et al. Genetic analysis of RXR alpha developmental function: convergence of RXR and RAR signaling pathways in heart and eye morphogenesis. *Cell*. 1994; 78(6):987–1003. [https://doi.org/10.1016/0092-8674\(94\)90274-7](https://doi.org/10.1016/0092-8674(94)90274-7) PMID: 7923367.
 81. Mori M, Ghyselinck NB, Chambon P, Mark M. Systematic immunolocalization of retinoid receptors in developing and adult mouse eyes. *Investigative ophthalmology & visual science*. 2001; 42(6):1312–8. PMID: 11328745.
 82. Oh SP, Griffith CM, Hay ED, Olsen BR. Tissue-specific expression of type XII collagen during mouse embryonic development. *Developmental dynamics: an official publication of the American Association of Anatomists*. 1993; 196(1):37–46. <https://doi.org/10.1002/aja.1001960105> PMID: 8334298.
 83. Sambasivan R, Gayraud-Morel B, Dumas G, Cimper C, Paisant S, Kelly R, et al. Distinct regulatory cascades govern extraocular and pharyngeal arch muscle progenitor cell fates. *Developmental cell*. 2009; 16(6):810–21. <https://doi.org/10.1016/j.devcel.2009.05.008> PMID: 19531352.
 84. Huang AH, Riordan TJ, Pryce B, Weibel JL, Watson SS, Long F, et al. Musculoskeletal integration at the wrist underlies the modular development of limb tendons. *Development*. 2015; 142(14):2431–41. <https://doi.org/10.1242/dev.122374> PMID: 26062940; PubMed Central PMCID: PMC4510863.
 85. McBratney-Owen B, Iseki S, Bamforth SD, Olsen BR, Morriss-Kay GM. Development and tissue origins of the mammalian cranial base. *Developmental biology*. 2008; 322(1):121–32. <https://doi.org/10.1016/j.ydbio.2008.07.016> PMID: 18680740; PubMed Central PMCID: PMC2847450.
 86. Heude E, Tesarova M, Sefton EM, Jullian E, Adachi N, Grimaldi A, et al. Unique morphogenetic signatures define mammalian neck muscles and associated connective tissues. *Elife*. 2018;7. <https://doi.org/10.7554/eLife.40179> PMID: 30451684; PubMed Central PMCID: PMC6310459.
 87. Germain P, Gaudon C, Pogenberg V, Sanglier S, Van Dorsselaer A, Royer CA, et al. Differential action on coregulator interaction defines inverse retinoid agonists and neutral antagonists. *Chem Biol*. 2009; 16(5):479–89. <https://doi.org/10.1016/j.chembiol.2009.03.008> PMID: 19477412.
 88. Chambers D, Wilson L, Maden M, Lumsden A. RALDH-independent generation of retinoic acid during vertebrate embryogenesis by CYP1B1. *Development*. 2007; 134(7):1369–83. <https://doi.org/10.1242/dev.02815> PMID: 17329364.
 89. Rossant J, Zirngibl R, Cado D, Shago M, Giguere V. Expression of a retinoic acid response element-hsplacZ transgene defines specific domains of transcriptional activity during mouse embryogenesis. *Genes & development*. 1991; 5(8):1333–44. <https://doi.org/10.1101/gad.5.8.1333> PMID: 1907940.
 90. Comai G, Sambasivan R, Gopalakrishnan S, Tajbakhsh S. Variations in the efficiency of lineage marking and ablation confound distinctions between myogenic cell populations. *Developmental cell*. 2014; 31(5):654–67. Epub 2014/12/10. <https://doi.org/10.1016/j.devcel.2014.11.005> PMID: 25490270.
 91. Liu J, Willet SG, Bankaitis ED, Xu Y, Wright CV, Gu G. Non-parallel recombination limits Cre-LoxP-based reporters as precise indicators of conditional genetic manipulation. *Genesis*. 2013; 51(6):436–42. Epub 2013/02/27. <https://doi.org/10.1002/dvg.22384> PMID: 23441020; PubMed Central PMCID: PMC3696028.
 92. Long MA, Rossi FM. Silencing inhibits Cre-mediated recombination of the Z/AP and Z/EG reporters in adult cells. *PLoS ONE*. 2009; 4(5):e5435. <https://doi.org/10.1371/journal.pone.0005435> PMID: 19415111; PubMed Central PMCID: PMC2672169.
 93. Ma Q, Zhou B, Pu WT. Reassessment of Isl1 and Nkx2-5 cardiac fate maps using a Gata4-based reporter of Cre activity. *Developmental biology*. 2008; 323(1):98–104. Epub 2008/09/09. <https://doi.org/10.1016/j.ydbio.2008.08.013> PMID: 18775691; PubMed Central PMCID: PMC2655699.
 94. Chevallier A, Kieny M. On the role of the connective tissue in the patterning of the chick limb musculature. *Wilehm Roux Arch Dev Biol*. 1982; 191(4):277–80. <https://doi.org/10.1007/BF00848416> PMID: 28305059.

95. Rodriguez-Guzman M, Montero JA, Santesteban E, Ganan Y, Macias D, Hurle JM. Tendon-muscle crosstalk controls muscle bellies morphogenesis, which is mediated by cell death and retinoic acid signaling. *Developmental biology*. 2007; 302(1):267–80. <https://doi.org/10.1016/j.ydbio.2006.09.034> PMID: 17070795.
96. Gilbert P. The origin and development of the human extrinsic ocular muscles. 1957. Carnegie Inst. Wash. Publ. 611, Contrib. Embryol. 36: 59–78.
97. Gilbert PW. The origin and development of the extrinsic ocular muscles in the domestic cat. *Journal of morphology*. 1947; 81(2):151–93. Epub 1947/09/01. PMID: 20258884.
98. Jernvall J, Aberg T, Kettunen P, Keranen S, Thesleff I. The life history of an embryonic signaling center: BMP-4 induces p21 and is associated with apoptosis in the mouse tooth enamel knot. *Development*. 1998; 125(2):161–9. PMID: 9486790.
99. Nonomura K, Yamaguchi Y, Hamachi M, Koike M, Uchiyama Y, Nakazato K, et al. Local apoptosis modulates early mammalian brain development through the elimination of morphogen-producing cells. *Developmental cell*. 2013; 27(6):621–34. <https://doi.org/10.1016/j.devcel.2013.11.015> PMID: 24369835.
100. Moreno E, Valon L, Levillayer F, Levayer R. Competition for Space Induces Cell Elimination through Compaction-Driven ERK Downregulation. *Curr Biol*. 2019; 29(1):23–34 e8. <https://doi.org/10.1016/j.cub.2018.11.007> PMID: 30554899; PubMed Central PMCID: PMC6331351.
101. Franz-Odenaal TA, Vickaryous MK. Skeletal elements in the vertebrate eye and adnexa: morphological and developmental perspectives. *Developmental dynamics: an official publication of the American Association of Anatomists*. 2006; 235(5):1244–55. <https://doi.org/10.1002/dvdy.20718> PMID: 16496288.
102. Eyal S, Kult S, Rubin S, Krief S, Felsenthal N, Pineault KM, et al. Bone morphology is regulated modularly by global and regional genetic programs. *Development*. 2019; 146(14). <https://doi.org/10.1242/dev.167882> PMID: 31221640; PubMed Central PMCID: PMC6679367.
103. Kish PE, Bohnsack BL, Gallina D, Kasprick DS, Kahana A. The eye as an organizer of craniofacial development. *Genesis*. 2011; 49(4):222–30. Epub 2011/02/11. <https://doi.org/10.1002/dvg.20716> PMID: 21309065; PubMed Central PMCID: PMC3690320.
104. Langenberg T, Kahana A, Wszalek JA, Halloran MC. The eye organizes neural crest cell migration. *Developmental dynamics: an official publication of the American Association of Anatomists*. 2008; 237(6):1645–52. <https://doi.org/10.1002/dvdy.21577> PMID: 18498099; PubMed Central PMCID: PMC2762319.
105. Zein WM, Lewanda AF, Traboulsi EI, Jabs EW. Ocular Manifestations of Syndromes with Craniofacial Abnormalities. In: Traboulsi EI, editor. *Genetic Diseases of the Eye* (2nd ed). New York: Oxford University Press; 2012. p. 174–89
106. Durand JP. Ocular development and involution in the European cave salamander, *Proteus anguinus laurenti*. *Biol Bull*. 1976; 151(3):450–66. <https://doi.org/10.2307/1540499> PMID: 1016662.
107. Yamamoto Y, Stock DW, Jeffery WR. Hedgehog signalling controls eye degeneration in blind cavefish. *Nature*. 2004; 431(7010):844–7. <https://doi.org/10.1038/nature02864> PMID: 15483612.
108. Lamb TD, Collin SP, Pugh EN Jr. Evolution of the vertebrate eye: opsins, photoreceptors, retina and eye cup. *Nature reviews Neuroscience*. 2007; 8(12):960–76. <https://doi.org/10.1038/nrn2283> PMID: 18026166; PubMed Central PMCID: PMC3143066.
109. Tajbakhsh S, Rocancourt D, Buckingham M. Muscle progenitor cells failing to respond to positional cues adopt non-myogenic fates in myf-5 null mice. *Nature*. 1996; 384:266–70. <https://doi.org/10.1038/384266a0> PMID: 8918877
110. Yamamoto M, Shook NA, Kanisicak O, Yamamoto S, Wosczyzna MN, Camp JR, et al. A multifunctional reporter mouse line for Cre- and FLP-dependent lineage analysis. *Genesis*. 2009; 47(2):107–14. <https://doi.org/10.1002/dvg.20474> PMID: 19165827.
111. Chapellier B, Mark M, Bastien J, Dierich A, LeMeur M, Chambon P, et al. A conditional floxed (loxP-flanked) allele for the retinoic acid receptor beta (RARbeta) gene. *Genesis*. 2002; 32(2):91–4. <https://doi.org/10.1002/gene.10073> PMID: 11857787.
112. Chapellier B, Mark M, Garnier JM, Dierich A, Chambon P, Ghyselinck NB. A conditional floxed (loxP-flanked) allele for the retinoic acid receptor gamma (RARgamma) gene. *Genesis*. 2002; 32(2):95–8. <https://doi.org/10.1002/gene.10072> PMID: 11857788.
113. Comai G, Heude E, Mella S, Paisant S, Pala F, Gallardo M, et al. A distinct cardiopharyngeal mesoderm genetic hierarchy establishes antero-posterior patterning of esophagus striated muscle. *Elife*. 2019;8. <https://doi.org/10.7554/eLife.47460> PMID: 31535973; PubMed Central PMCID: PMC6752947.
114. Yokomizo T, Yamada-Inagawa T, Yzaguirre AD, Chen MJ, Speck NA, Dzierzak E. Whole-mount three-dimensional imaging of internally localized immunostained cells within mouse embryos. *Nat*

- Protoc. 2012; 7(3):421–31. <https://doi.org/10.1038/nprot.2011.441> PMID: 22322215; PubMed Central PMCID: PMC3629302.
115. Zucker RM, Hunter ES, 3rd, Rogers JM. Apoptosis and morphology in mouse embryos by confocal laser scanning microscopy. *Methods*. 1999; 18(4):473–80. <https://doi.org/10.1006/meth.1999.0815> PMID: 10491277.
 116. Babai F, Musevi-Aghdam J, Schurch W, Royal A, Gabbiani G. Coexpression of alpha-sarcomeric actin, alpha-smooth muscle actin and desmin during myogenesis in rat and mouse embryos I. *Skeletal muscle*. *Differentiation*. 1990; 44(2):132–42. <https://doi.org/10.1111/j.1432-0436.1990.tb00546.x> PMID: 2283002.
 117. Li L, Miano JM, Cserjesi P, Olson EN. SM22 alpha, a marker of adult smooth muscle, is expressed in multiple myogenic lineages during embryogenesis. *Circulation research*. 1996; 78(2):188–95. <https://doi.org/10.1161/01.res.78.2.188> PMID: 8575061.
 118. Sawtell NM, Lessard JL. Cellular distribution of smooth muscle actins during mammalian embryogenesis: expression of the alpha-vascular but not the gamma-enteric isoform in differentiating striated myocytes. *The Journal of cell biology*. 1989; 109(6 Pt 1):2929–37. <https://doi.org/10.1083/jcb.109.6.2929> PMID: 2687290; PubMed Central PMCID: PMC2115902.
 119. Li Z, Marchand P, Humbert J, Babinet C, Paulin D. Desmin sequence elements regulating skeletal muscle-specific expression in transgenic mice. *Development*. 1993; 117(3):947–59. PMID: 8325245.
 120. Bader D, Masaki T, Fischman DA. Immunochemical analysis of myosin heavy chain during avian myogenesis in vivo and in vitro. *The Journal of cell biology*. 1982; 95(3):763–70. <https://doi.org/10.1083/jcb.95.3.763> PMID: 6185504; PubMed Central PMCID: PMC2112936.
 121. Metscher BD. MicroCT for developmental biology: a versatile tool for high-contrast 3D imaging at histological resolutions. *Developmental dynamics: an official publication of the American Association of Anatomists*. 2009; 238(3):632–40. <https://doi.org/10.1002/dvdy.21857> PMID: 19235724.
 122. Kaucka M, Petersen J, Tesarova M, Szarowska B, Kastriti ME, Xie M, et al. Signals from the brain and olfactory epithelium control shaping of the mammalian nasal capsule cartilage. *Elife*. 2018;7. <https://doi.org/10.7554/eLife.34465> PMID: 29897331; PubMed Central PMCID: PMC6019068.

Signals from the brain and olfactory epithelium control shaping of the mammalian nasal capsule cartilage

Marketa Kaucka^{1,2†}, Julian Petersen^{1,2†}, Marketa Tesarova³, Bara Szarowska², Maria Eleni Kastriti^{1,2}, Meng Xie¹, Anna Kicheva⁴, Karl Annusver^{5,6}, Maria Kasper^{5,6}, Orsolya Symmons⁷, Leslie Pan⁸, Francois Spitz^{8,9}, Jozef Kaiser³, Maria Hovorakova¹⁰, Tomas Zikmund³, Kazunori Sunadome¹, Michael P Matise¹¹, Hui Wang¹¹, Ulrika Marklund¹², Hind Abdo¹², Patrik Ernfors¹², Pascal Maire¹³, Maud Wurmser¹³, Andrei S Chagin^{1,14}, Kaj Fried¹⁵, Igor Adameyko^{1,2*}

¹Department of Physiology and Pharmacology, Karolinska Institutet, Stockholm, Sweden; ²Department of Molecular Neurosciences, Medical University Vienna, Vienna, Austria; ³Central European Institute of Technology, Brno University of Technology, Brno, Czech Republic; ⁴Institute of Science and Technology IST Austria, Klosterneuburg, Austria; ⁵Department of Biosciences and Nutrition, Karolinska Institutet, Stockholm, Sweden; ⁶Center for Innovative Medicine, Karolinska Institutet, Huddinge, Sweden; ⁷Department of Bioengineering, University of Pennsylvania, Philadelphia, United States; ⁸Developmental Biology Unit, European Molecular Biology Laboratory, Heidelberg, Germany; ⁹Genomics of Animal Development Unit, Institut Pasteur, Paris, France; ¹⁰Department of Developmental Biology, Institute of Experimental Medicine, The Czech Academy of Sciences, Prague, Czech Republic; ¹¹Department of Neuroscience & Cell Biology, Rutgers-Robert Wood Johnson Medical School, Piscataway, United States; ¹²Department of Medical Biochemistry and Biophysics, Karolinska Institutet, Stockholm, Sweden; ¹³Department of Development, Reproduction and Cancer, Institute Cochin, Paris, France; ¹⁴Institute for Regenerative Medicine, Sechenov First Moscow State Medical University, Moscow, Russia; ¹⁵Department of Neuroscience, Karolinska Institutet, Stockholm, Sweden

*For correspondence:
igor.adameyko@ki.se

†These authors contributed
equally to this work

Competing interests: The
authors declare that no
competing interests exist.

Funding: See page 22

Received: 19 December 2017

Accepted: 12 June 2018

Published: 13 June 2018

Reviewing editor: Richard M
White, Memorial Sloan Kettering
Cancer Center, United States

© Copyright Kaucka et al. This
article is distributed under the
terms of the [Creative Commons
Attribution License](#), which
permits unrestricted use and
redistribution provided that the
original author and source are
credited.

Abstract Facial shape is the basis for facial recognition and categorization. Facial features reflect the underlying geometry of the skeletal structures. Here, we reveal that cartilaginous nasal capsule (corresponding to upper jaw and face) is shaped by signals generated by neural structures: brain and olfactory epithelium. Brain-derived Sonic Hedgehog (SHH) enables the induction of nasal septum and posterior nasal capsule, whereas the formation of a capsule roof is controlled by signals from the olfactory epithelium. Unexpectedly, the cartilage of the nasal capsule turned out to be important for shaping membranous facial bones during development. This suggests that conserved neurosensory structures could benefit from protection and have evolved signals inducing cranial cartilages encasing them. Experiments with mutant mice revealed that the genomic regulatory regions controlling production of SHH in the nervous system contribute to facial cartilage morphogenesis, which might be a mechanism responsible for the adaptive evolution of animal faces and snouts.

DOI: <https://doi.org/10.7554/eLife.34465.001>

Introduction

The shape of a face strongly depends on the geometry of skeletal elements directly under the skin, adipose tissue and muscles. Our adult cranial and, in particular, facial skeleton consists mostly of bony elements. Cartilaginous parts are rather minor. However, during embryonic development bone forms after the cartilage, and the initial phases of facial and skull shaping proceed with the cartilaginous skeleton only. The entire functional and evolutionary meaning of the chondrocranium, that is, the early cartilaginous elements of the embryonic skull, is not clear. Some parts of the chondrocranium will undergo endochondral ossification (for example, pre-sphenoid and basisphenoid, cribriform plate, Meckel's cartilage, olfactory septum, nasal concha, labyrinth of ethmoid, vomer and tympanic bulla). However, the majority of the bones, especially in a facial compartment, will form in a close spatial association with the chondrocranium independently through dermal membranous ossifications (Carson, 1999). Many questions, including how and from where molecular signals control the complex chondrocranial shape, and whether the geometry of the chondrocranium directs the shape of facial bones, are still unanswered.

Achondroplasia, a rare disease due to cartilage insufficiency, includes craniofacial malformations such as protruding forehead, low nasal bridge, maxillary hypoplasia, problems in the otolaryngeal system and macrocephaly as well as foramen magnum stenosis (Shirley and Ain, 2009). Prominent human and mouse achondroplasia phenotypes based on *Fgfr3* mutations suggest that a correctly shaped chondrocranium is essential for proper facial bone geometry and general facial outgrowth. However, *Fgfr3* is expressed also at membranous ossification sites (please see *Fgfr3*(mRNA) expression at E15, <http://developingmouse.brain-map.org/>), as well as in sutural osteogenic fronts (Ornitz and Marie, 2002). Therefore, models involving *Fgfr3* do not allow for precise discrimination of cartilage or bone-dependent parts of the phenotype in affected subjects. Still, these effects strongly suggest that chondrocranium shape might be truly important for producing initial facial geometry and for influencing the formation of membranous bone on top of the cartilaginous template.

The facial chondrocranium is built by neural crest cells that populate the frontal part of the head and undergo multilineage differentiation. They give rise to cartilage, bone, fascia, adipose tissue, smooth muscle, pericytes, glia and neurons (Snider and Mishina, 2014; Baggiolini et al., 2015). Paraxial mesoderm also contributes to the chondrocranium in posterior basicranial and occipital locations. Collective behavior and differentiation of the neural crest and neural crest-derived ectomesenchyme is largely responsible for the future shape of the face (Minoux and Rijli, 2010). However, the precise mechanisms governing this collective behavior, cartilage induction and shape-making are not fully understood, despite significant progress in the research field of cartilage and bone formation.

McBratney-Owen and Morris-Key with coworkers demonstrated that the complete chondrocranium (including the base of the skull) develops from 14 pairs of independently induced large cartilaginous elements that fuse together during later development (McBratney-Owen et al., 2008). Sculpting perfect geometries of such cartilaginous elements is a key developmental and regenerative process that accounts for the shape and integrity of our body. Current opinion holds that cartilage forms from condensing mesenchymal cells that are destined to become chondrocytes (Ornitz and Marie, 2002). Mesenchymal condensations emerge in specific locations. Here, they somehow become shaped, grow and turn into cartilage that later expands until the initiation of endochondral or membranous ossification.

The frontonasal prominence and other facial regions are enriched in signaling systems. Activity in these systems leads to progressive induction and shaping of craniofacial structures, including chondrogenic mesenchymal condensations that turn into cartilage (Minoux and Rijli, 2010). The signaling center located in the most anterior face, the so called FEZ (Frontonasal Ectodermal Zone), produces Sonic Hedgehog (SHH) and Fibroblast growth factor 8 (FGF8), which play important roles in facial shaping. FGF8, SHH and Bone Morphogenetic Proteins (BMPs) produced by FEZ regulate the behavior of ectomesenchymal tissue and participate in positioning of chondrogenic condensations inside of the embryonic face (Foppiano et al., 2007; Hu et al., 2015b; Young et al., 2014). The mechanisms of facial cartilage induction that involve these molecules have received particular attention during recent years (Gros and Tabin, 2014; Abzhanov and Tabin, 2004; Bhullar et al., 2015; Griffin et al., 2013).

Another recent breakthrough brought up the fact that the brain itself can emit signals that influence facial shaping. Expression of *Shh* in the forebrain turned out to be important for the correct formation of FEZ and early steps of facial shaping in general (Hu et al., 2015a; Chong et al., 2012).

Still, how these and other signaling centers synchronize in order to build the 3D shape of facial cartilaginous elements is not understood. The cartilaginous nasal capsule is the most anterior part of the chondrocranium. Together with Meckel's cartilage in the lower jaw, it constitutes an excellent model system to address questions concerning cartilage induction and shaping.

Here, using mild ablations of cartilage with tightly controlled genetic tools, we revealed that the shape of the nasal capsule is a key for the geometry and positioning of the facial bones and overall facial shape. Subsequently, with the help of numerous mouse mutants, specific contrasting techniques and micro-CT, we demonstrated that signaling centers in the developing brain and olfactory epithelium jointly and independently enable the induction of the nasal capsule in the embryonic face. Various genomic regulatory regions that direct the expression of *Shh* to the developing nervous system participate in the fine-tuning of the shape of the facial cartilaginous skeleton.

Results

Taking into account known achondroplasia facial phenotypes, we hypothesized that even minor changes in the facial cartilaginous template may lead to significant or even major changes in the overlying membranous bone geometry and the overall facial shape. Thus, we performed mild time-controlled genetic ablation of early chondrocytes employing *Col2a1-CreERT2/R26DTA* mice and analyzed their facial development (Figure 1). We used a dose of 2.5 mg of tamoxifen administered at E12.5 and, in an alternative experiment, double injection at E13.5-E14.5 to avoid a strong phenotype with dramatic face shortening and brain shape distortion, and we analyzed the mutant embryos at E17.5 and E15.5 correspondingly (Figure 1). *Col2a1-CreERT2* is a well-established tool to target facial chondrocytes and their immediate progenitors. Tamoxifen was administered at early stages of facial development where no bone is present. Also, this *CreERT2* line does not recombine in osteoblasts or their progenitors in membranous ossification sites and, thus, cannot directly impinge on them (Figure 1A–D). Despite only mild cartilage reduction (mean 30,7% of the cartilage surface decrease at E15.5 and mean 35,2% at E17.5), the facial compartment of the *Col2a1-CreERT2^{+/-}/R26DTA^{+/-}* embryos appeared massively affected with short snout and distorted membranous ossifications (Figure 1E–R). Interestingly, the forming mandibular bone appeared shortened and widened at the same time, which cannot be explained only by the shortening of Meckel's cartilage (Figure 1—figure supplement 1). This fact suggests an interplay between cartilage and membranous bone that might involve signal-guided rearrangements in skeletogenic tissues. Thus, genetic ablations of COL2A1-producing pre-chondrocytes and chondrocytes revealed a different degree of cartilage loss in the nasal capsule and Meckel's cartilage, together with corresponding incremental dysmorphologies of membranous bones and face in general. These slight differences in the strength of the phenotype are likely attributed to the fine diversity of developmental stages within one litter receiving tamoxifen during a single injection into a mother (Figure 1Q–R and Figure 1—figure supplement 1). Thus, the geometry of the face and corresponding bony structures depend on the correct induction and shaping of a facial cartilage. This, in turn, is largely established at the level of chondrogenic mesenchymal condensations, as we recently demonstrated (Kaucka et al., 2017). It is worth emphasizing that according to our previous study, the chondrogenic condensations are induced being pre-shaped (Kaucka et al., 2017).

Consequently, we decided to analyze the molecular signals and their sources that induce these geometrically complex condensations. Several molecules were reported to have an impact on the cartilage induction, either on the condensation placement or on proper timing of cartilage-forming events (Goldring et al., 2006). Among those, SHH was shown to play a key role in the spatio-temporal induction of chondrogenic mesenchymal condensations (Abzhanov and Tabin, 2004; Billmyre and Klingensmith, 2015; Park et al., 2010). We analyzed the expression of *Shh* in early and late developing mouse face with the help of the *Shh-Cre/GFP* (*B6.Cg-Shhtm1(EGFP/cre)Cjt/J*) model, and found that *Shh* is expressed in very discrete regions of the face between E11.5 and E14.5 at the time of induction of facial cartilages (Figure 2 and Figure 2—figure supplement 1). At the early stages (E11.5 and E12.5, see Figure 2A–B), the SHH + regions included forming olfactory epithelium (magenta), dental and oral epithelium (red), eyes (cyan) and brain (yellow). Interestingly,

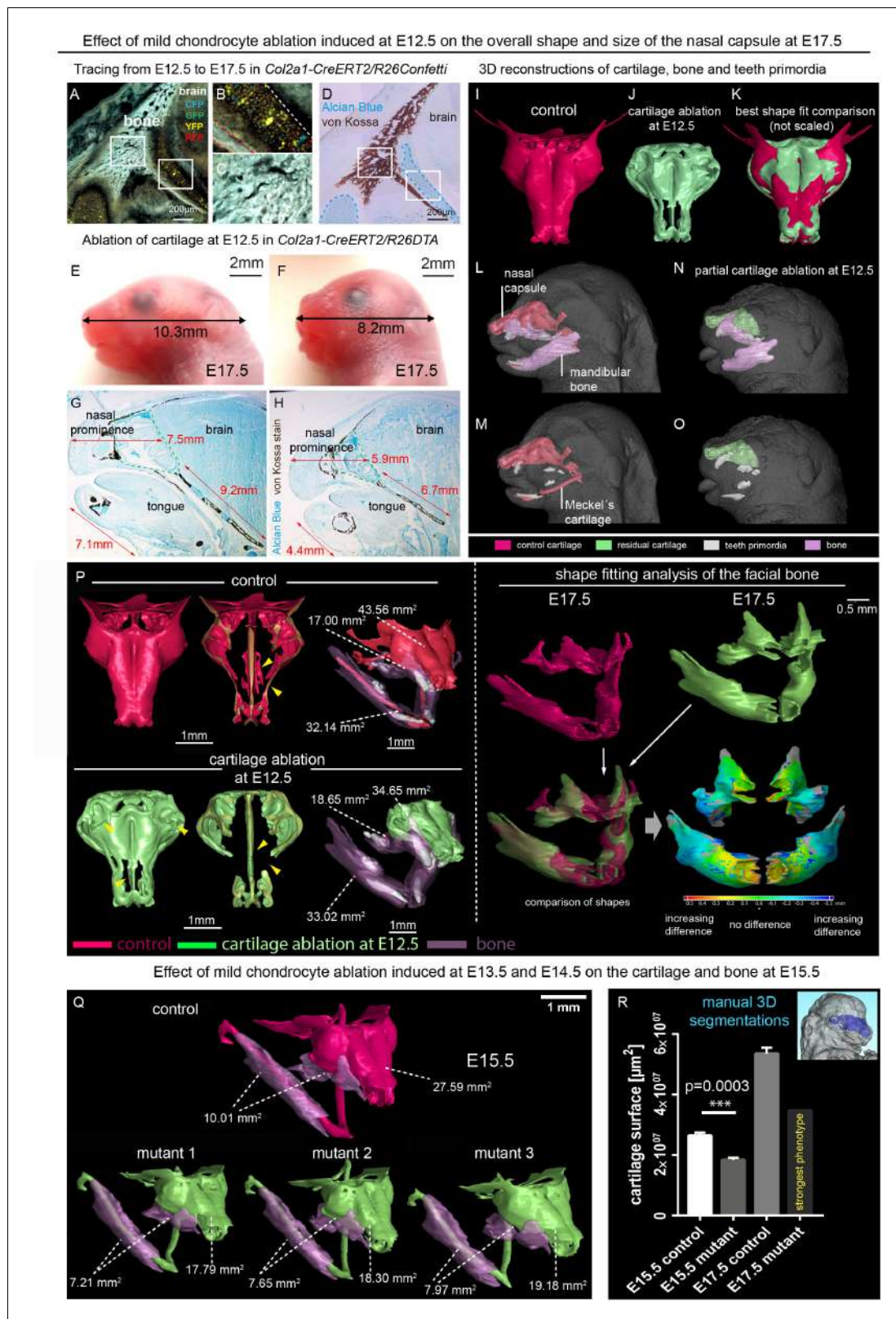


Figure 1. Correct chondrocranium development is essential for shaping the embryonic face. (A–C) Genetic tracing induced at E12.5 in *Col2a1-CreERT2/R26Confetti* shows recombination in chondrocytes (B) only and not in a lineage of membranous bone osteoblasts and their progenitors (C), 25 μm cryo-sections (A–D, G–H) were imaged with a confocal microscope (A–C) or phase contrast microscope (D, G–H). (D) Traced sections have been stained using Alcian Blue (cartilage, blue) and von Kossa (brown, mineralized tissue). (E–F) Wild type (E) and *Col2a1-CreERT2/R26DTA* (F) embryos with Figure 1 continued on next page

Figure 1 continued

cartilage being partially ablated as a result of tamoxifen injection (2.5 mg) at E12.5, both analyzed at E17.5. (G–H) Sagittal sections of the anterior head from wild type (G) and *Col2a1-CreERT2/R26DTA* (H) embryos stained with Alcian Blue (blue, stains for cartilage) and von Kossa staining (black, stains for mineralized bone tissue). Olfactory system is outlined by green dashed line for better orientation. Note that physiological growth of the cartilage sets the proper size of the facial compartment. (I–O) 3D-reconstructions of frontal chondrocranium together with bone and teeth primordia in control (I, L, M) and cartilage-ablated (J, N, O) embryos. (K) Best fit comparison of control (red) and cartilage-ablated (light green) 3D chondrocranium models. (P) 3D-reconstruction of frontal chondrocranium and formed cartilage including GOM Inspect software analysis of the mutant bone (Q) overview of analyzed mutants (injected with low dose of tamoxifen (2.5 mg) at both E13.5 and E14.5 and analyzed at E15.5) and formed bone in one representative control and three mutants (R) Bar-graphs showing the manual 3D segmentation of the surface area of cartilage. Data are obtained from three control samples and three mutant mice for (E15.5) and three control samples and one mutant sample with the most pronounced phenotype for (E17.5). The error bars show mean and standard deviation (SD). For the comparison, we used unpaired Student t-test (95% confidence interval –9974138 to –6056665). Raw data are available in **Figure 1—source data 1**.

DOI: <https://doi.org/10.7554/eLife.34465.002>

The following source data and figure supplement are available for figure 1:

Source data 1. Raw values of cartilage surface measurements corresponding to Graph in **Figure 1R**.

DOI: <https://doi.org/10.7554/eLife.34465.004>

Figure supplement 1. Mild ablation of cartilage using *Col2a1-CreERT2/R26DTA*.

DOI: <https://doi.org/10.7554/eLife.34465.003>

only certain regions of olfactory epithelium were SHH+ (see stained cryosections under the 3D models in **Figure 2**). Later on (at E13.5 and E14.5 – **Figure 2—figure supplement 1**), we detected additional SHH-producing structures such as whiskers (blue-green), tongue (not segmented) and salivary

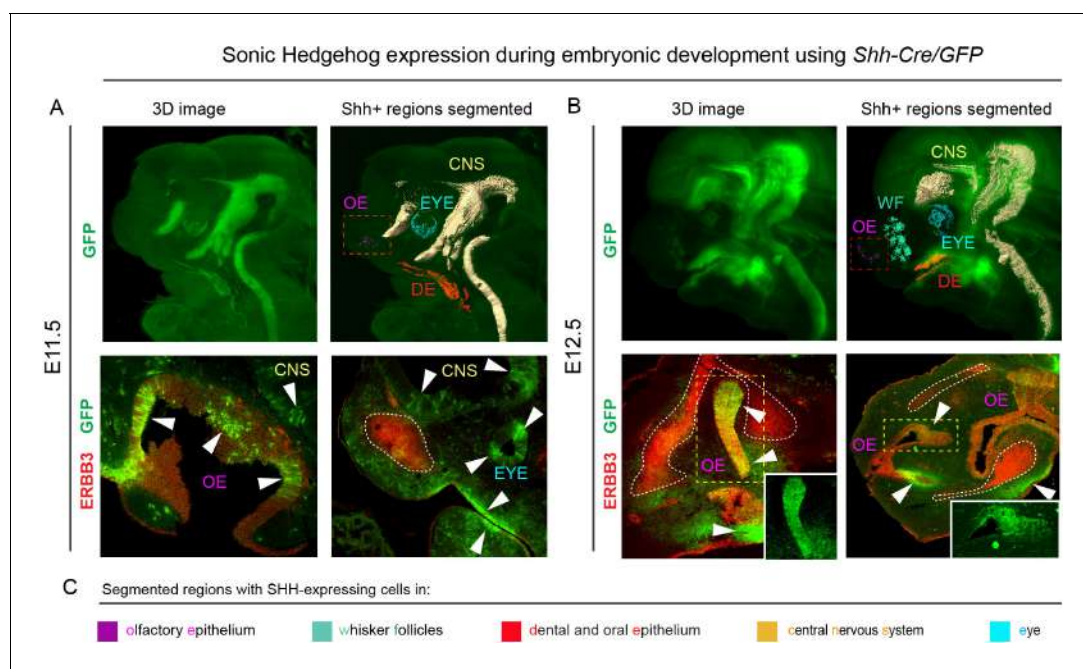


Figure 2. *Shh* is expressed through the early facial development in distinct regions of the head. The expression pattern of *Shh* during developmental stages E11.5 (A) and E12.5 (B) in *B6.Cg-Shhtm1(EGFP/cre)Cjt/J*, segmented *Shh*-expression regions are color-coded and clarified in legend (C).

Immunohistochemical (IHC) staining shows olfactory neuroepithelium and newly formed mesenchymal condensation as ERBB3 positive. White arrows point at GFP-expressing parts of various tissues. Red rectangle in (A) and (B) upper panel mark the olfactory neuroepithelium, yellow rectangle in (B) shows area magnified in the right bottom corner. White dotted line outlines the shape of mesenchymal condensation. IHC staining was performed on 20 μ m cryosections and imaged using a confocal microscope.

DOI: <https://doi.org/10.7554/eLife.34465.005>

The following figure supplement is available for figure 2:

Figure supplement 1. *Shh* is expressed through the later facial development in distinct regions of the head.

DOI: <https://doi.org/10.7554/eLife.34465.006>

gland (blue). We assumed that there is a prerequisite for a certain minimal distance between *Shh*-expressing structures and forming cartilage of nasal capsule that enables the secreted molecule to reach the target and impose chondrogenic stimuli on mesenchymal cells. According to our results, the most probable pro-chondrogenic SHH-emitting structures in the face were the olfactory epithelium and the forebrain.

To test if SHH emitted by these structures controls nasal capsule induction or influences its geometrical features, we analyzed a series of mouse mutants with a micro-CT-based 3D-visualization approach. To perform these 3D visualizations of the mesenchymal chondrogenic condensations, cartilage and bone, we utilized a soft tissue contrasting with phosphotungstic acid (PTA) followed by micro-CT scanning. Chelation of tungsten is uneven in various cell types and creates reliable contrast highlighting different tissues.

Firstly, to address whether the induction of distinct elements of the facial chondrocranium is not only timely regulated, but also has a discrete spatial aspect related to various sources of inductive signals, we genetically ablated *Shh* in the brain to test its role in facial cartilage induction. For this, we took advantage of *Nkx2.2-Cre/Shh^{floxed/floxed}* animals to delete *Shh* in the floor plate cells since the beginning of central nervous system (CNS) development and patterning. We analyzed two different stages: E12.5 as a stage of condensations of cartilaginous mesenchyme (**Figure 3** and **Figure 3—figure supplement 1** 'Interactive PDF') and E15.5 as a later stage of nearly fully formed chondrocranium with its rather final shape (**Figure 3** and **Figure 3—figure supplement 1** 'Interactive PDF'). This experiment resulted in an unexpected phenotype. It included a selective loss of a nasal septum together with heavily affected posterior part of the nasal capsule as detected at E12.5 (**Figure 3B–C, E–F**). The chondrogenic condensation corresponding to a forming septum failed completely, whereas the condensation of the posterior part of nasal capsule appeared incompletely induced. Additional changes were detected in the facial cartilage at E15.5, mainly represented by the missing midline groove (**Figure 3G–H**) and the absence of the very anterior part of nasal cartilage (**Figure 3H**). Additional changes included various malpositioned parts, fused nerve foramina and variations in shaping and bending of cartilage elements, as summarized in **Figure 3**. Notably, the mutant embryos analyzed at E12.5 and E15.5 presented with cleft palate. This could indicate that some clinical cleft palate cases might have their origin in disturbed brain-derived signaling (**Figure 3—figure supplement 2**).

At the same time, the general geometry of the frontal part of facial chondrocranium remained almost unperturbed, thus, supporting the spatial modularity of cartilage induction in the face. The microstructure of the cartilage stayed normal, with fine borders defining bent cartilaginous sheets forming the major structure of the nasal capsule. The thickness of the cartilaginous sheets forming the capsule also remained comparable to that found in littermate controls (**Figure 3J**). These observations strongly suggested that the early stages of cartilage induction must be affected.

We also investigated bone formation in the area of the nasal capsule at E15.5 (**Figure 3I**). We observed missing parts in maxillary bones from mutants, and malpositioned incisors that were found more posteriorly on top of instead of being in the anterior part of the maxilla. At this stage and in this particular location, there was no endochondral ossification ongoing. However, according to micro-CT data, the bone was forming in the proximity and on top of the existing cartilaginous shape template. Thus, the facial chondrocranium is important for the correct formation of the membranous facial bones.

Recently it has been shown that the brain can influence facial shaping via *Shh*, acting presumably on the frontonasal ectodermal signaling zone (abbreviated as FEZ) (**Hu et al., 2015a; Chong et al., 2012**). It is currently believed that FGF8, SHH and BMPs produced by FEZ regulate the behavior of ectomesenchymal tissue and participate in positioning of chondrogenic condensations inside of the embryonic face (**Foppiano et al., 2007; Hu et al., 2015b; Young et al., 2014**). However, our data show that SHH emitted from the forebrain mostly affects the basicranial, posterior and septal parts of the facial chondrocranium without strong effects on the most anterior nasal capsule (including other soft tissues in general), which could be expected if the effects of a brain-derived SHH are entirely mediated by FEZ. Importantly, the major geometric structure of the mutant brain stays largely unchanged although it appears reduced in size. Thus, changes in brain shape are not likely to cause very selective influences on forming facial structures due to mere mechanical interactions (**Figure 3—figure supplement 3**).

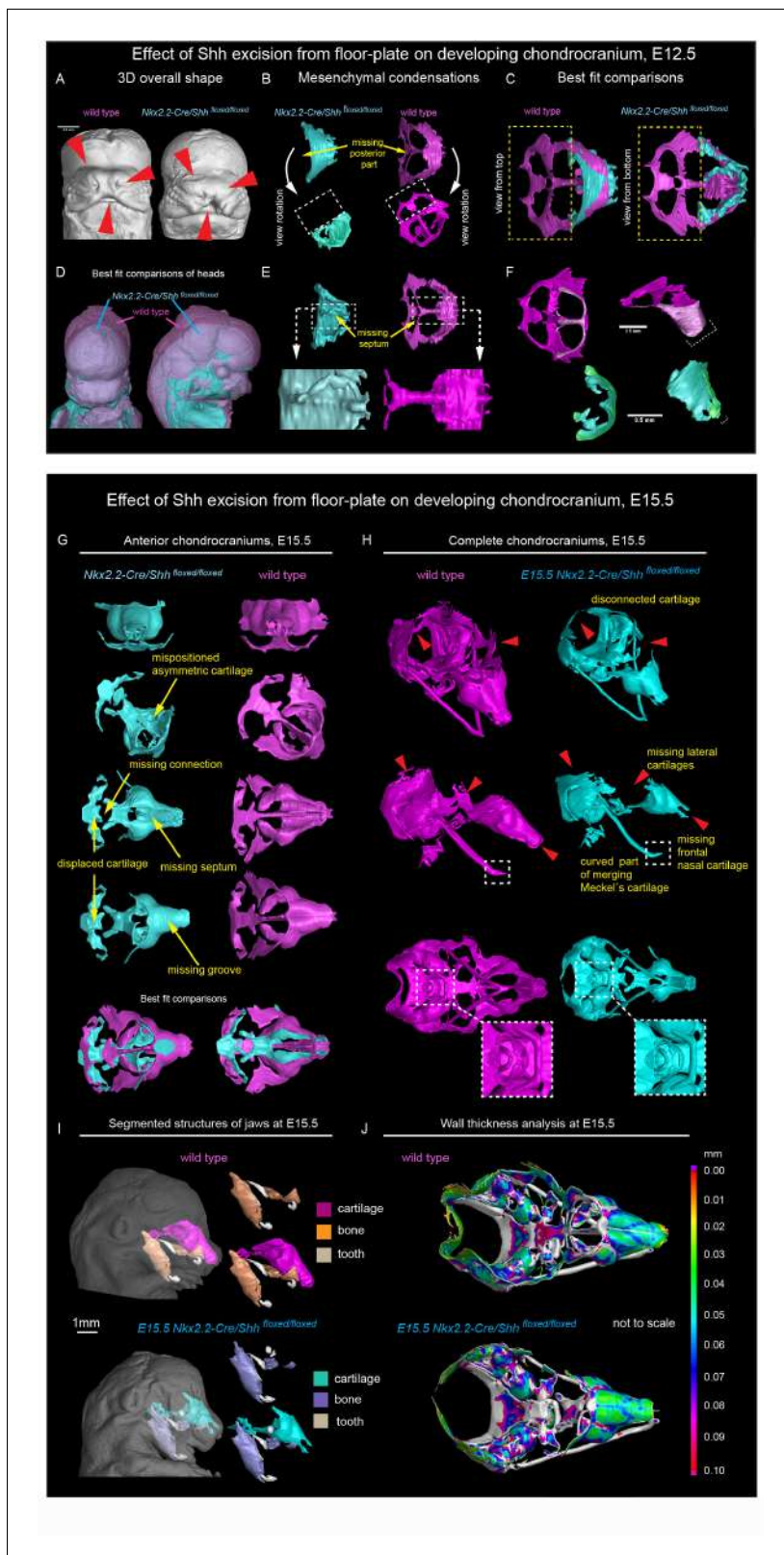


Figure 3. *Shh* signal from the brain induces a posterior part of a nasal capsule. (A) Model of overall shape resulting from the excision of *Shh* from the floor plate using *Nkx2.2-Cre/Shh^{flxed/flxed}* shows visible phenotype in the E12.5 mutant embryo comprising, for instance, from the cleft of upper lip, non-prominent or missing nasal vestibule and diminished curvature of the snout. (B–C, E–F) micro-CT scans-based 3D reconstructions of chondrogenic mesenchymal condensations in E12.5 mutant and control embryos. Note the missing posterior part of the developing nasal capsule and the missing Figure 3 continued on next page

Figure 3 continued

septum in the mutant. (D) best-fit computed comparison of the overall shape and size of mutant and control embryo. (G–H) 3D models of chondrocrania of mutant (*Nkx2.2-Cre/Shh^{floxexd/floxexd}*) and control embryo, analyzed at E15.5. Among the main differences are missing frontal part of nasal cartilage, missing lateral parts of developing nasal capsule, malpositioned asymmetric cartilage, not fully closed foramina for pervading nerves and vasculature and various disconnected cartilaginous segments. (I) Segmented cartilage and bones projected in the overall shape of the head of mutant (bottom) and control (upper) embryo. Note the malpositioned incisors in the maxilla of the mutant and missing part of the frontal nasal capsule formed by the bone. (J) Wall thickness analysis of the cartilages in the E15.5 head of mutant (bottom) and control (upper) embryo show no evident differences in the thickness of formed cartilage.

DOI: <https://doi.org/10.7554/eLife.34465.007>

The following figure supplements are available for figure 3:

Figure supplement 1. 'Interactive PDF'.

DOI: <https://doi.org/10.7554/eLife.34465.008>

Figure supplement 2. Ablation of *Shh* from the floor plate results in the cleft palate.

DOI: <https://doi.org/10.7554/eLife.34465.009>

Figure supplement 3. Brain volume and overall anatomy in mutants with *Shh* genetically deleted from the floor plate of the developing CNS.

DOI: <https://doi.org/10.7554/eLife.34465.010>

Figure supplement 4. Phenotypic manifestation of *Shh* genetic ablation from the floor-plate, analyzed at E15.5 upper part of spine.

DOI: <https://doi.org/10.7554/eLife.34465.011>

Finally, we analyzed the spinal column of the mutants and control embryos and found localized shape defects in the cervical vertebrae represented by incomplete transverse foramina (*foramina transversariae*) (**Figure 3—figure supplement 4**). Notably, the defects in the nasal septum stayed confined only to the cartilage as a tissue. The septal chondrogenic condensations and cartilage were missing as apparent E12.5 and E15.5, whereas the soft tissues of the septum stayed in place (**Figure 3—figure supplement 4**). Similarly, despite the cartilage defects clearly identified in spinal column, the other tissue types that were in close proximity to the defects did not show any difference from control. For instance, the vertebral arteries traversing the distorted cartilage of the transverse foramina appeared unaffected in *Nkx2.2-Cre/Shh^{floxexd/floxexd}* animals (**Figure 3—figure supplement 4**).

Next, we determined the *Shh* expression in the forming olfactory epithelium and tested the role of the forming olfactory epithelium and olfactory neurons in the process of nasal capsule induction. The possibility that olfactory epithelium controls cartilage shaping is supported by the fact that the conchae of nasal labyrinth geometrically correlate with the folded structure of the olfactory epithelium, which they mechanically support.

A desired experimental setup that would allow us to target and genetically delete *Shh* from the olfactory epithelium does not exist. To define the importance of any signal derived from the olfactory epithelium we utilized *Six1* and *Six4* double knockout to specifically ablate the development of the olfactory epithelium (*Ikeda et al., 2007; Kobayashi et al., 2007*). We analyzed *Six1/4* double mutant embryos at E18.5, that showed no olfactory structures, using the micro-CT method and performed a thorough comparison to wildtype littermates (**Figure 4** and **Figure 3—figure supplement 1** 'Interactive PDF'). In these mutants which had markedly shortened noses, the roof of the nasal capsule was entirely missing. However, the septum and the posterior part of the capsule were relatively well-preserved (**Figure 4B–D**). An earlier analysis at E12.5, a stage when the majority of facial chondrogenic condensations come into place, showed that in double knockouts, the chondrogenic condensation corresponding to the nasal capsule roof is missing. The chondrogenic condensation corresponding to the nasal septum appeared non-fused at this stage and fused only later, as evident from E17.5 reconstructions. At the same time, the roof of the nasal capsule was never induced (**Figure 4—figure supplement 1A–D**). This is consistent with the prediction that a lack of the olfactory epithelium will prevent the induction of olfactory cartilages. Analyses of the bones showed a major change in the overall geometry, with prominent shortening along the anterior-posterior axis (brachycephalic-like appearance). Furthermore, we noticed a lack of mandibular incisors and an obvious asymmetry between left and right parts of the maxilla (**Figure 4E,J**).

In addition to the expression in olfactory placodes, *Six1* and *Six4* are expressed in different parts of early facial mesenchyme (*Kobayashi et al., 2007; Grifone et al., 2005*). The full knockout of *Six4* does not show any phenotype according to previously published data (*Ozaki et al., 2001*). We

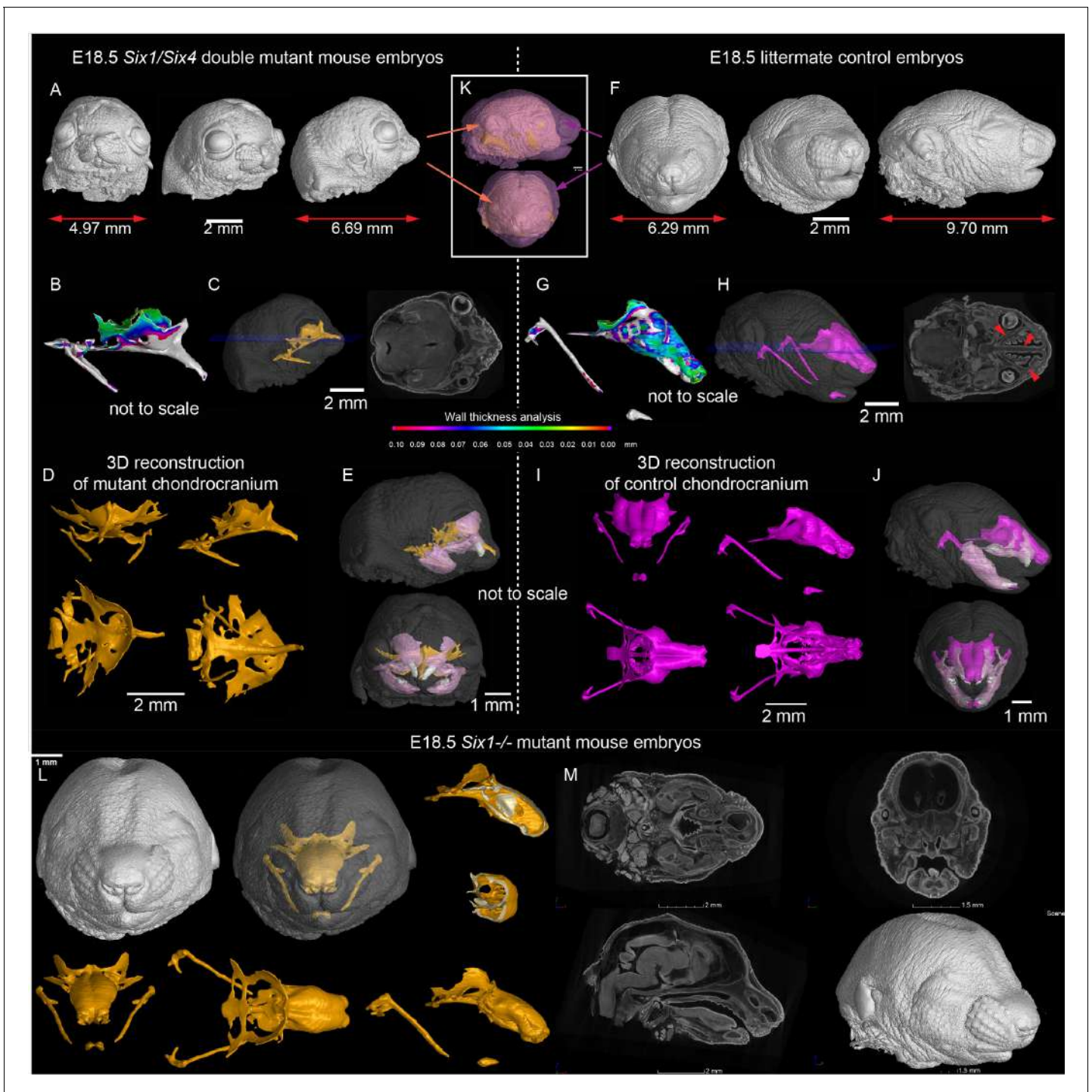


Figure 4. Signals from the olfactory epithelium induce the anterior part of the nasal capsule. (A–J) *Six1/Six4* double knock out mouse embryo compared to littermate control and analyzed at E18.5 using micro-CT and 3D-reconstruction. (A, E, K) overall shape and size of the mutant head is different from the control head, showing brachycephalic phenotype, bulging eyes, misshaped earlobes positioned more frontal and lower than the control embryo (F, J, K). Note also the left-right asymmetry of the snout of the mutant. (B, G) Wall thickness analysis of mutant (B) and control (G) embryo. (C, H) single plane from raw CT data shows missing olfactory neuroepithelium in the *Six1/Six4* double mutant and control. Note also missing nasal capsule but retained septum in the mutant. (D–E, I–J) various views on segmented 3D model of chondrocranium of mutant (D–E) and control (I–J) embryo. Among the obvious differences are missing roof and lateral parts of nasal capsule while the septum is preserved. (L) *Six1* single knock out mouse embryo analyzed at E18.5 using micro-CT 3D reconstruction (M) single plane cross-sections from raw CT of *Six1* single knock out E18.5 embryo. DOI: <https://doi.org/10.7554/eLife.34465.012>

Figure 4 continued on next page

Figure 4 continued

The following figure supplements are available for figure 4:

Figure supplement 1. Analysis of mesenchymal condensations in *Six1/Six4* double knock out embryos at E12.5.

DOI: <https://doi.org/10.7554/eLife.34465.013>

Figure supplement 2. *Ascl1* knockout embryo analyzed at E16.5 does not show any significant changes in formed nasal capsule.

DOI: <https://doi.org/10.7554/eLife.34465.014>

therefore analyzed the full knockout of *Six1*, in which the olfactory epithelium is present, to see whether it will show a mesenchyme-driven phenotype in the nasal capsule roof. The analysis of E18.5 *Six1*^{-/-} embryos demonstrated the presence of the nasal capsule roof as well as a septum. The phenotype in *Six1*^{-/-} embryos mostly included a narrowing of the posterior nasal capsule with mild septal defects (**Figure 4L–M** and **Figure 4—figure supplement 1E**).

This experiment provided a complementary, non-overlapping phenotype to the one with a nasal capsule resulting from the excision of *Shh* from the floor plate (*Nkx2.2-Cre/Shh*^{floxed/floxed}). This suggests that solid cartilage elements in the forming face depend on joint activities of multiple regulatory zones (sources of SHH) during their induction and shaping.

To investigate if sensory neurons in the olfactory neuro-epithelium might be potential sources of SHH, we utilized *Ascl1* (*Mash1*) knock-out embryos (**Figure 4—figure supplement 2**). In these animals, major neurogenic transcriptional factor essential for olfactory neuron formation are missing, and very few olfactory sensory neurons are generated (*Guillemot et al., 1993; Cau et al., 1997*). We analyzed craniofacial structures in these mutants and found out that they did not demonstrate any gross abnormality despite their inability to develop large amounts of olfactory neurons. Hence, the sensory olfactory neurons are not critical cartilage-inducing sources, while the early olfactory epithelium, before the neurogenesis, is important for the formation of chondrogenic mesenchymal condensations.

To check if SHH from the brain and presumably from the olfactory epithelium acts directly on facial mesenchyme inducing chondrogenic differentiation or during cartilage growth, we analyzed embryos carrying a SHH-activity reporter *GBS-GFP* (*Balaskas et al., 2012*) at different developmental stages ranging from E9 to E14.5. The GFP signal was detectable as expected in the forming palate, brain, spinal cord and tissues that are known to receive SHH input. However, we did not observe *GBS-GFP* activity in the chondrogenic mesenchymal condensations from the earliest chondrogenic stages E11.5–E12.5 onwards (**Figure 5A**). Consistently with this, lineage tracing in *Gli1-CreERT2/R26Tomato* mice injected with tamoxifen at E11.5 and analyzed at E17.5 showed sporadic patches of traced chondrocytes in the facial cartilages (**Figure 5B**). If the injection of tamoxifen was performed at E12.5 or later, these sporadic patches of labeled chondrocytes disappeared; that is we observed only very rarely scattered chondrocytes in other locations (**Figure 5B–C**). Analysis of the rare individual clones of chondrocytes resulting from labeling at E11.5 in *Gli1-CreERT2/R26Confetti* demonstrated that mesenchymal cells turn into chondroprogenitors that divide several times to generate clonal clusters of mature chondrocytes (**Figure 5C–D**). At later stages of tamoxifen administration, this was not observed, which is consistent with analysis of *Gli1-LacZ* embryos at E12.5, where the X-gal staining was confined to whisker pads and other peripheral locations. In situ hybridization (RNAscope) for other components of the Hedgehog pathway (including *Ptch1*(mRNA), *Ptch2* (mRNA), *Gli1*(mRNA), *Gli2*(mRNA)) showed no enrichment within potential and actual chondrogenic areas (**Figure 5—figure supplement 1**). To functionally test if inhibition of SHH at chondrogenic stages will affect the development of facial cartilage, we administered SHH-inhibitor vismodegib (*LoRusso et al., 2011*) at either E11.5, E12.5, or E13.5 and analyzed the embryos at E15.5. In line with predictions from expression analysis and SHH-activity reporter, we did not find striking abnormalities in nasal and Meckel's cartilages from all treated and analyzed embryos (n = 4) (**Figure 6A**). At the same time, we observed the absence of palate and concomitant abnormalities in whiskers distributions in E11.5-to-E15.5 and E12.5-to-E15.5 stages of treatment, but not in E13.5-to-E15.5 stages. Indeed, in embryos treated between E11.5 and E12.5, the palatal shelves were severely reduced or missing (**Figure 6A–C**). This showed that SHH signaling in these embryos was inhibited to significant extents and also suggested that the action of SHH on patterning of the nasal capsule precedes the stage of chondrogenic condensations.

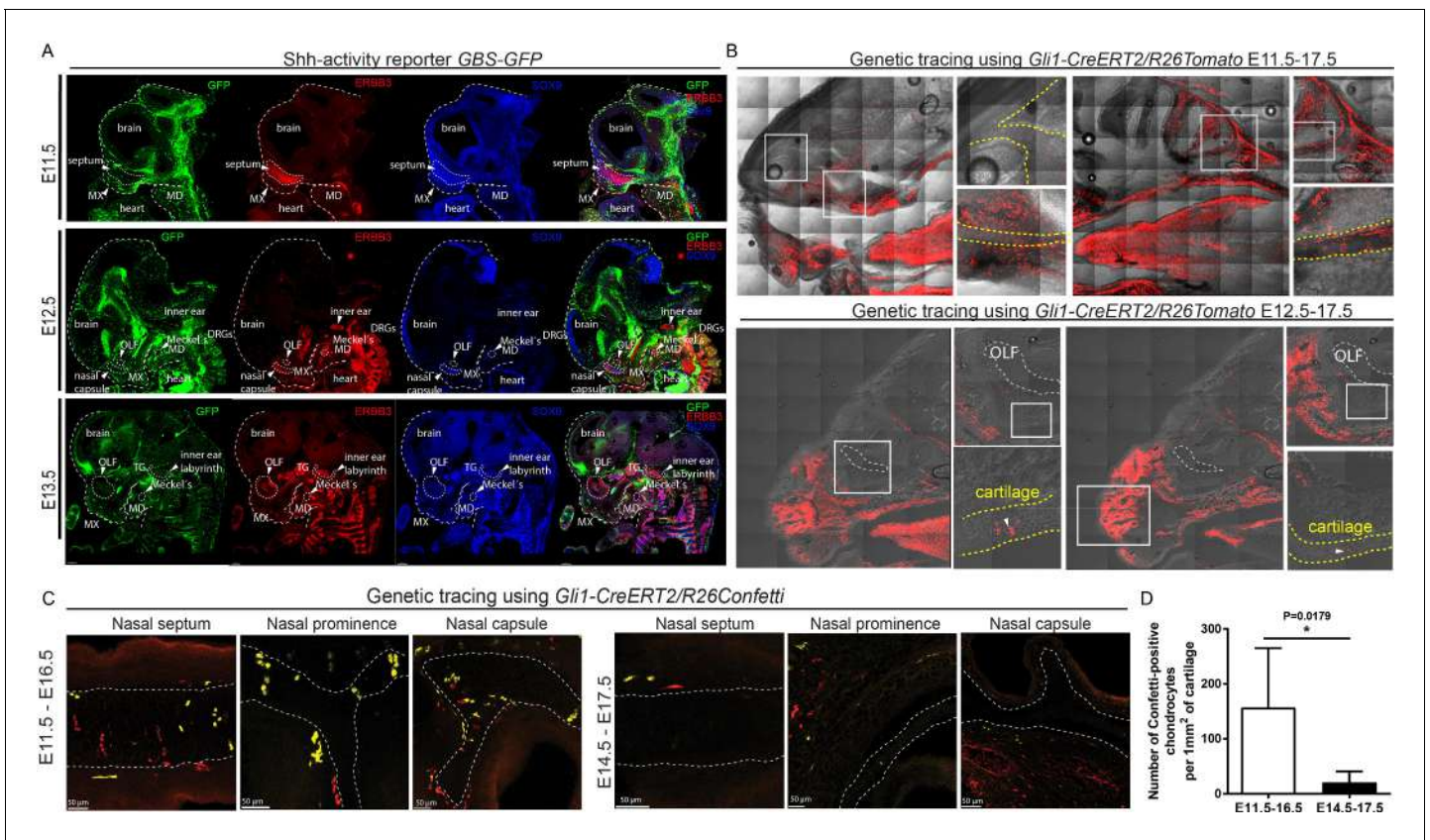


Figure 5. Mapping of the expression of *Gli1* and *Shh* signaling activity in mouse embryonic head. (A) Mapping of the activity of the SHH signaling in mouse embryonic head at E11.5, E12.5 and E13.5 prechondrogenic and early chondrogenic stages using *GBS-GFP* activity reporter. (B) Genetic tracing using *Gli1-CreERT2/R26Tomato* induced at E11.5 (upper panel) and E12.5 (bottom panel) and analyzed at E17.5. Dotted line outlines cartilaginous structures within the nasal capsule. White squares outline the magnified area. DRG = dorsal root ganglion, OLF = Olfactory system, MX = maxillary prominence, MD = mandibular prominence. TG = trigeminal ganglion. (C) Genetic tracing using *Gli1-CreERT2/R26Confetti*, induced at E11.5 and analyzed at E16.5 (left panel) and induced at E14.5 and analyzed at E17.5 (right panel) shows the contribution of *Gli1*-traced positive cells to the cartilaginous structures in the embryonic head. (D) Quantification of the contribution of *Gli1*-traced positive cells to the cartilage. (A–C) 20 μ m cryosections were used for the IHC staining and analysis. A confocal microscope has been used for imaging.

DOI: <https://doi.org/10.7554/eLife.34465.015>

The following figure supplement is available for figure 5:

Figure supplement 1. Mapping of the presence of major SHH signaling components in the E12.5 embryo.

DOI: <https://doi.org/10.7554/eLife.34465.016>

Consistent with these results, which suggest an early pre-chondrogenic role of SHH signaling on nasal capsule patterning, the analysis of embryos homozygous for a hypomorphic *Shh* allele (*Shh-GFP*, here referred to as *Shh^{HyPO}*), in which SHH signaling is constitutively reduced (Zagorski et al., 2017; Chamberlain et al., 2008), revealed severe abnormalities in the facial cartilage (Figure 6D and Figure 6—figure supplement 3). The results of all genetic perturbations and treatments with drugs as well as their comparative phenotypes are summarized in Figure 7. Taken together, the effects of SHH on chondrogenic differentiation in the facial region are early and precede the first wave of chondrocyte differentiation that occurs between E11.5 and E14.5. These results are also consistent with the phenotype of *Six1/Six4* double knockout embryos at E12.5 (Figure 4), and corroborate the notion of an early pre-cartilage onset of the phenotype.

Tissue-specific expression of *Shh* is known to be controlled by multiple enhancers. Some, which may regulate *Shh* expression in the cranial region, have been characterized (Yao et al., 2016; Jeong et al., 2006; Sagai et al., 2009). To modulate *Shh* expression in different craniofacial regions, we analyzed mutant mice carrying different rearrangements (deletions or inversions) with impacts on the distal regulatory landscape of *Shh* (Symmons et al., 2016). We paid specific attention to

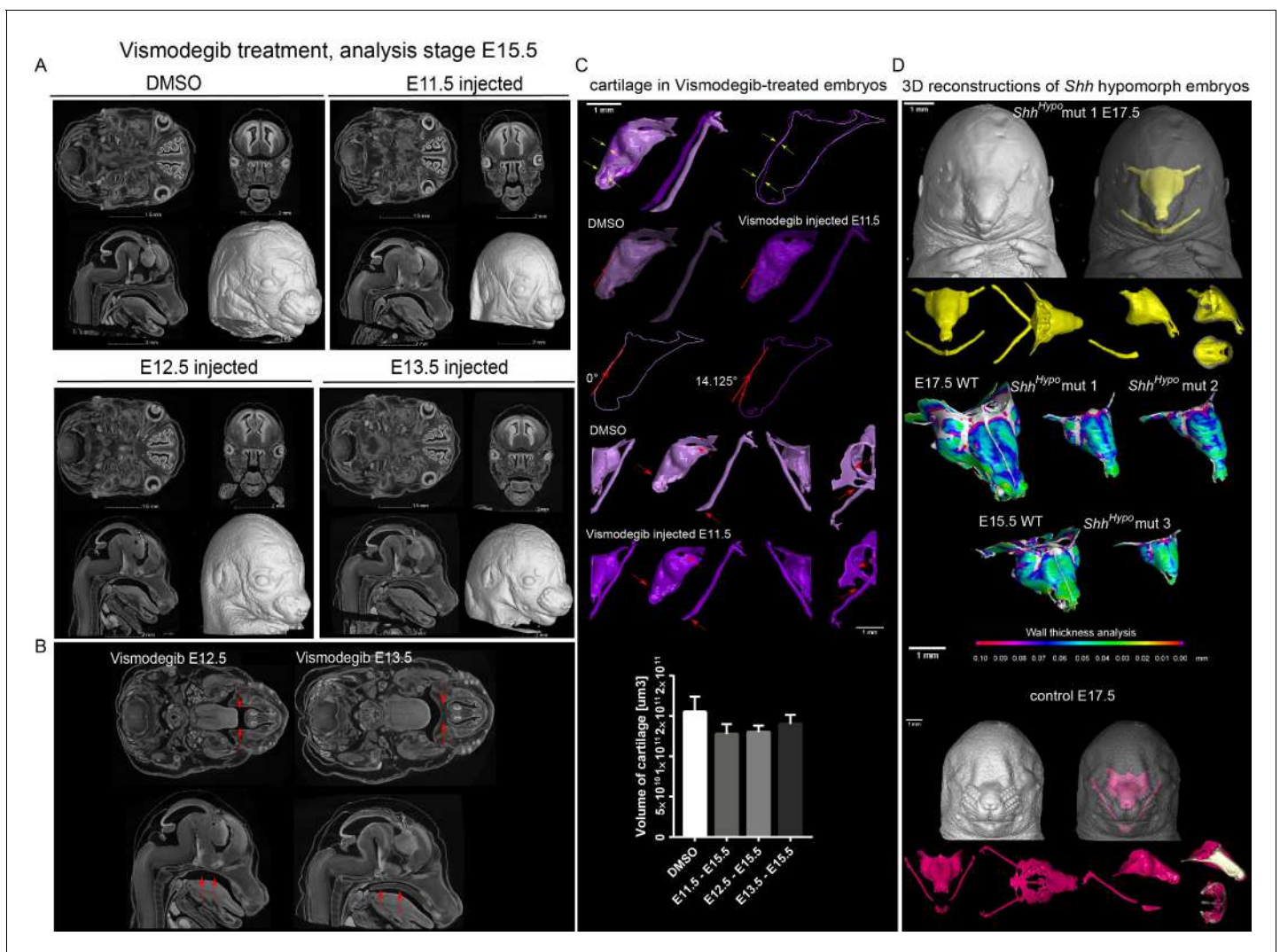


Figure 6. Effect of Vismodegib treatment on the size and structure of nasal cartilage. (A) Panel shows raw CT data, cross-sections from various planes from DMSO (control treatment), Vismodegib inhibitor administered at E11.5, E12.5 or E13.5, all analyzed at E15.5 (B) Raw CT cross-sections show absent/disrupted cartilaginous structures in Vismodegib-treated embryos (C) 3D reconstruction and comparison of inhibitor-treated (Vismodegib E11.5-E15.5) and control (DMSO-treated) embryos and their nasal capsules. Arrows point at differences in anatomy and overall geometry of the nasal capsule. Graph representation of overall cartilage change of inhibitor-treated embryos. Raw data are available in **Figure 6—source data 1**. (D) 3D-reconstruction of the nasal capsule of *Shh* hypomorph (analyzed at E15.5 and E17.5) including wall thickness analysis.

DOI: <https://doi.org/10.7554/eLife.34465.017>

The following source data and figure supplements are available for figure 6:

Source data 1. Raw values of cartilage measurements corresponding to Graph in **Figure 6C**.

DOI: <https://doi.org/10.7554/eLife.34465.021>

Figure supplement 1. Mutations of various regulatory regions controlling expression of *Shh*, their positions and effect on chondrogenesis.

DOI: <https://doi.org/10.7554/eLife.34465.018>

Figure supplement 2. Mutated genomic regions containing regulatory sequences controlling expression of *Shh* show a variety of similar and dissimilar phenotypes.

DOI: <https://doi.org/10.7554/eLife.34465.019>

Figure supplement 3. The effect of reduced SHH signaling on chondrogenesis at E15.5 and E17.5.

DOI: <https://doi.org/10.7554/eLife.34465.020>

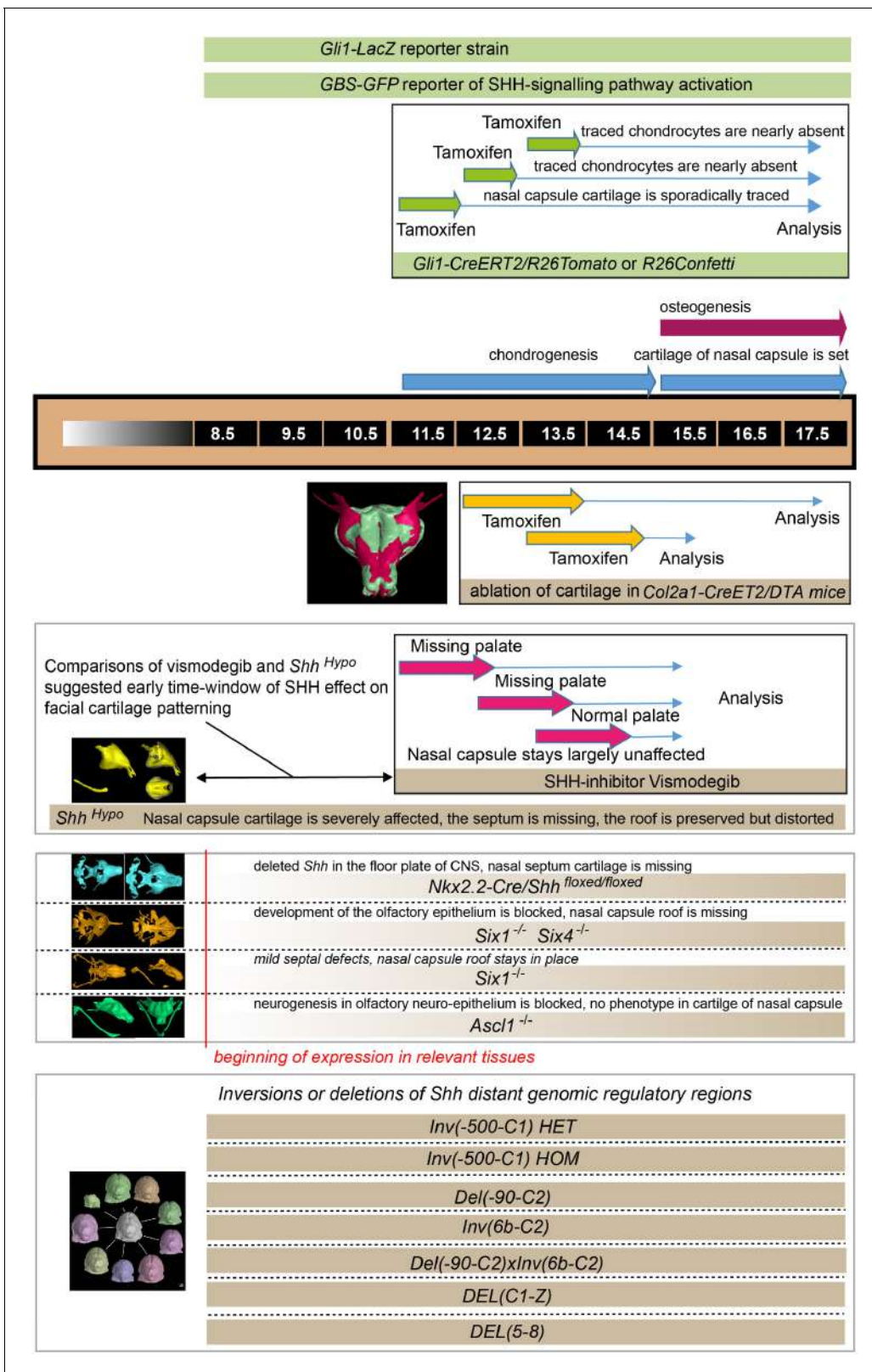


Figure 7. Illustration depicting the timeline of all experiments and the beginning of effects. The results of all genetic perturbations and treatments with drugs as well as their comparative phenotypes are summarized.

DOI: <https://doi.org/10.7554/eLife.34465.022>

genomic regions where known and potentially unknown brain-specific enhancers (SBE, Shh Brain Enhancers) are located (Jeong et al., 2006; Sagai et al., 2009). Currently known SBEs (SBE2, SBE3, SBE4) localize between the *Shh* coding region and *mark 6b* (Irimia et al., 2012) (see scheme in **Figure 6—figure supplement 1**). Animals carrying an allele with the inversion of a large genomic region including known SBEs, *INV(–500 C1)*, demonstrated selectively localized mild defects in the nasal septum and also in the tips of Meckel’s cartilage, but not in the roof of nasal capsule. This septum-specific phenotype appeared more pronounced in a homozygous *INV(–500 C1)* as compared to the heterozygous genotype. Interestingly, this allele does not change the relative position to *Shh* of most known enhancers that could be responsible for SHH-dependent facial skeletal development. The phenotype observed in this experiment showed that septal cartilage is sensitive to minor changes in SHH patterning signals that result from either removal of regulatory sequences distal to the C1 position, or indirect effects affecting distant enhancer-promoter-communications.

INV(6b-C2), which removes additional enhancers required for ventral forebrain expression of *Shh* in E10.5 embryos (**Figure 6—figure supplement 1A–C**), showed much stronger phenotypes.

Such strong phenotypes are most likely due to disruption of the *Shh* TAD (Topologically Associating Domain), and displacement of major regulatory elements at a position which prevent their interaction with *Shh* (Symmons et al., 2016). Accordingly, *Shh* expression is much reduced in the forebrain of mutant embryos at E10.5 as evident from the results of in situ hybridization for *Shh* (**Figure 6—figure supplement 1A–C**).

Heterozygote *INV(6b-C2)* did cause minor defects in septum, while the same inversion over a full *Shh* deficiency (*DEL(–90 C2)*) led to a strong holoprosencephaly similar to *Shh*^{Hyp^o} (**Figure 6 and Figure 6—figure supplement 2**). However, it was not as strong as a full *Shh* knockout, where only a proscis is left.

In the mutants *INV(6b-C2) x DEL(–90 C2)*, the nasal septum did not develop at all, and the rest of the nasal capsule (roof) was present although severely disturbed in shape. The gradual increase in severity of the malformations from *INV(–500 C1)* to *INV(6b-C2)* may indicate the presence of several distinct enhancers related to face morphology distal to position 6b (which likely includes yet uncharacterized enhancers). It could also mean that the efficiency of the interactions of the known enhancers (SBE2-4) with the *Shh* promoter is modulated by the presence of distal elements, which may contribute to organize the *Shh* TAD (Symmons et al., 2016). Both scenarios suggest the existence of other regulatory regions important for facial development including new potential SBEs based on the reduction of the LacZ-based *Shh*-expression reporter signal in the forebrain of mutant embryos at E10.5 (**Figure 6—figure supplement 1**).

DEL(5-8) showed a powerful phenotype similar to the homozygous *INV(6b-C2)*. This, in a combination with previous phenotypes, reveals that the key regulatory regions essential for the facial cartilage patterning are located between marks 6b and C1. These regulatory regions are likely SBEs since the LacZ expression disappears from the forebrain of reporter embryos at E12.5 according to previous results (Symmons et al., 2016). *DEL(C1-Z)* did not show any gross abnormalities in the nasal capsule cartilage. Embryos carrying this mutation showed abnormal Meckel’s cartilage and a generally affected mandible.

Taken together, local tuning of SHH expression by various enhancers (including brain-specific regulatory elements) seemingly controls discrete steps of chondrocranial patterning, which may represent a key evolutionary mechanism shaping animal snouts and faces.

Discussion

In addition to the obvious functional aspects, facial shape is important in many ways. For example, recognition of individual facial features assists social interaction and affects numerous important aspects of our everyday life (Vernon et al., 2014). Pathological conditions include a very wide spectrum of deficiencies, and may involve eating, breathing and speech impairments, emotional problems and low quality of life in general (Forbes, 2010). Here, we demonstrated that even fine and selective manipulations of a facial cartilage geometry and size (performed in *Col2-CreERT2^{+/-}/R26DTA⁺* embryos) result in significant changes of adjacent membranous bones and facial shape. In turn, the facial cartilage geometry is controlled by the signals coming from neurosensory structures such as brain and olfactory epithelium. Altogether, these results might provide a new explanatory

framework revealing how the integrated development of neural and non-neural tissues results in the precise and evolutionary adapted shape of the bony cranium and corresponding facial appearance.

Previously, Marcucio and Hallgrímsson laboratories demonstrated the co-variation of brain and face as well as the impact of brain-emitted SHH on avian facial development (*Hu and Marcucio, 2009; Marcucio et al., 2011; Parsons et al., 2011; Petryk et al., 2015*). Yet, the role of such brain-derived signals in cartilage and bone shaping has not been extensively investigated. According to our results, SHH, a key signal enabling cartilage induction, arrives from the floorplate of the brain, and the selective ablation of *Shh* in that area by non-inducible *Nkx2.2-Cre* causes a highly selective loss of the nasal septum cartilage. The soft non-cartilaginous tissue of the nasal septum, however, remains intact, rendering this part of the phenotype highly cartilage-specific. The roof of the nasal capsule stays nearly unaffected. The analysis at E12.5 stage suggested that this phenotype must be related to pre-chondrogenic, early SHH-dependent patterning signals enabling cartilage formation.

This reasoning is further supported by the line of experiments involving 'early on action' *Shh^{HypO}* embryos, which demonstrated a profound phenotype in the nasal capsule cartilage. This was in contrast to wild type embryos treated with the SHH-inhibitor Vismodegib strictly between chondrogenic stages (E11.5-E13.5). These embryos showed no significant phenotype in the nasal capsule cartilage. Correspondingly, lineage tracing with *Gli1-CreERT2* and expression analysis of SHH pathway members starting from E11.5 did not show any association with development of facial cartilages.

These cartilage-related results, where SHH-activity was not associated with facial chondrogenic differentiation, were dramatically different from those observed in palate-forming mesenchymal cells in the same experimental embryos. Unlike cartilage, the developing palate showed strong activity of the SHH-signaling reporter *GBS-GFP*. We also found high expression levels of SHH pathway members, including numerous traced progeny in *Gli1-CreERT2/R26Tomato* animals. As expected, in embryos treated with Vismodegib between E11.5-E12.5, the palate was almost missing, in contrast to contrary to the nasal capsule cartilage that stayed virtually intact. The presence of abnormal palate clefts in Vismodegib-treated and also in *Nkx2.2-Cre/Shh^{floxex/floxex}* embryos agrees with previous findings, which have established a general role of SHH in the patterning of the face and in development of pathological midfacial clefts (*Hu and Helms, 1999*). Accordingly, ciliopathies and their animal models often demonstrate similar defects (*Brugmann et al., 2010; Chang et al., 2016*).

Thus, according to our results, SHH is not involved into facial chondrogenesis at stages when chondrogenic condensations form and convert into mature cartilage. Hence, the role of SHH is most likely indirect. Presumably, it is involved in the early patterning of facial ectomesenchyme, to create proper conditions for the sophisticated facial chondrogenesis that will start at later developmental stages. In line with this reasoning, the mode of action of SHH on chondrogenesis in non-facial locations, for example, during the development of axial skeleton, is indirect and based on SHH-dependent alterations of cell responses to BMPs in potentially pre-chondrogenic mesenchymal cells. Murtaugh et al. demonstrated that even a transient SHH signal was able to ensure the competent chondrogenic response of mesenchymal cells to BMPs (*Murtaugh et al., 1999*). In the case of the axial skeleton, such competence-changing action of SHH depends on the initiated and sustained expression of the transcriptional repressor *Nkx3.2*, which renders cells responsive to pro-chondrogenic actions of BMPs (*Murtaugh et al., 2001*). As shown by Zeng et al., expression of *Nkx3.2* is sufficient to induce SOX9, a major chondrogenic master regulator, and in the presence of BMPs, *NKX3.2* and SOX9 could induce the expression of each other (*Zeng et al., 2002*). Finally, the sequential action of SHH and BMPs could induce SOX9. According to the public in situ database Allen Developmental Mouse Brain Atlas (<http://developingmouse.brain-map.org>), *Nkx3.2* shows distinct expression in a range of cranial cartilages or their future locations at pre-chondrogenic (E11.5) and chondrogenic (E13.5) stages. The knockout of *Nkx3.1* and *Nkx3.2* yields changes in the facial shape, as evident from **Figure 1** in Herbrand et al. (*Herbrand et al., 2002*). Similar patterning effects of SHH in relation to chondrogenesis have previously been demonstrated during the development of serial tracheal rings reinforced with cartilage. SHH inactivation in ventral trachea resulted in a lack of tracheal segmentation which coincided with the loss of cartilage, while the upregulation of *Shh* resulted in cartilage overproduction and similar segmentation defects (*Sala et al., 2011*). Altogether, this may suggest an analogous or similar mechanism of an indirect action of SHH on craniofacial chondrogenesis, especially in light of our results showing only minor and sporadic activity of SHH-signaling reporter in facial chondrogenic condensations or cartilage. Determination of the mechanisms behind SHH action in facial chondrogenesis, with a special focus on the position of the SHH-

signal in the hierarchy of events leading to chondrogenic differentiation, is a key future direction. We anticipate that Single cell transcriptomics approaches (Picelli et al., 2013) will be applied to facial mesenchymal populations prior and during chondrogenesis. This should resolve cell signaling cascades with high precision along the developmental timeline, in similarity to pioneering studies utilizing this methodology in other tissue types (Furlan et al., 2017).

Complementary to the ablation of *Shh* by *Nkx2.2-Cre*, the loss of the olfactory epithelium in *Six1/Six4* double knockout mutants leads to the absence of the nasal capsule roof, while the nasal septum cartilage stays largely in place. Our data indicate that the loss of a nasal capsule roof in the double knockout condition is driven by the loss of nasal placodes (requiring both *SIX1* and *SIX4*), which causes a collapse of olfactory epithelium. Despite the specific loss of nasal capsule roof, other cartilages appeared intact in locations corresponding to the expression sites of *Six1* and *Six4* (including Meckel's cartilage). The perfect match between the shape of cartilaginous olfactory turbines and the epithelium, as well as the coordinated time course of their development (Kaucka et al., 2017), additionally support the notion that signals from the developing olfactory epithelium might enable the induction of adjacent cartilage. Still, these arguments cannot completely rule out the possibility that co-expressed *Six1* and *Six4* may have early roles during neural crest migration and early post-neural crest stages that might be important for the nasal roof formation. Taken together, our results provide strong support for the idea that a single solid cartilaginous element such as the nasal capsule can be induced by the combinatorial action of signals derived from several, in the present case, neural and neurosensory, locations. Notably, facial chondrogenic condensations are induced being 'pre-shaped'. Already at the earliest steps, they are laid down as highly complex 3D-geometries (Kaucka et al., 2017). The induction of such 3D-shapes is unlikely to be achieved by signals from a single site and might require more sources including spatially opposed brain and olfactory structures. Since we were unable to validate that SHH from the olfactory placode or epithelium is the key factor that induces a nasal capsule roof, we cannot exclude that other signaling molecules participate during critical steps of facial cartilage induction. This will require further investigations.

During evolution of vertebrates, cartilages forming the neurocranium and the future upper jaw appear before Meckel's cartilage attains a function of a lower jaw skeleton, and the animals acquire articulated hinged jaws (Shimeld and Donoghue, 2012). Therefore, one of the primeval functions of the neurocranial and frontal cartilages could be the encasement and protection of the neural and sensory compartments such as brain, eyes, ears and olfactory neurons. If that is the case, it is logical to reason that these neurosensory structures could emit cartilage-inducing signals and coordinate cartilage growth and shaping. Our experimental results reveal the key role of SHH from the developing brain in enabling the induction of a nasal capsule and basicranial cartilages, and, thus, support the aforementioned evolutionary hypothesis. The capacity of the developing olfactory epithelium to shape the cartilaginous support also favors this reasoning. Genetics-based prevention of neuronal differentiation in the olfactory epithelium (via *Ascl1* knockout) does not interfere with shaping of the nasal capsule and confines the shaping role of presumably olfactory progenitors to the developmental period before their differentiation into the mature olfactory neurons. Alternatively, other cell types in the olfactory epithelium may play a cartilage-inducing role (olfactory glia, non-neurogenic epithelium).

In addition to the evolutionary aspect, the role of different neurosensory structures (mainly the brain) in coordinated cartilage induction may suggest a new connection between neurological and craniofacial symptoms in numerous genetic syndromes. Examples of such conditions are Williams syndrome, Down syndrome and others that are manifested by behavioral and morphological abnormalities in the central nervous system (Starbuck et al., 2017; Weisman et al., 2017; Vincent et al., 2014; Antshel et al., 2008) (and reviewed by [Marcucio et al., 2011]). Based on this reasoning, it is possible to envision a mechanistic connection between the fine aspects of a facial geometry and individual features of the human brain. An enormous facial variability is found among humans, which poses a question regarding the molecular and cellular mechanisms that underlie this variability. In difference to humans, non-human primates generally use variations in colored facial hairs to express their species, social status and sex in addition to body movements, voice expressions and scent (Santana et al., 2012; Allen and Higham, 2015). This brings us to speculate whether the loss of dense facial hairs during evolution of humans led to the development of a very broad range of various facial tissue-related features in order to compensate for the loss of facial hair-related communication and individual recognition. We hypothesize that one of those shape-tuning mechanisms could

include flexible and individual modulation of SHH, an important patterning and shaping agent during the embryonic development that comes from different spatial sources including the developing brain.

Previous research has established the existence and position of some of the specific regulatory elements that direct the expression of *Shh* in the craniofacial epithelial linings (*MRC51* and *MFCS4*, see (Sagai et al., 2009) for details) as well as in the floor plate and anterior forebrain (*SBE2* ((*Shh* Brain Enhancer 2)), *SBE3* and *SBE4* [Yao et al., 2016; Jeong et al., 2006]). In order to find out fine effects in facial cartilages as a result of activity by site-specific enhancers, we analyzed a variety of mutants with deleted and inverted genomic regions containing such regulatory elements (mutants created by François Spitz' laboratory [Symmons et al., 2016]). The inversion of the -500 C1 genomic region including known CBEs showed localized defects within the nasal septum that incrementally increased from heterozygous to homozygous state without influencing nasal capsule roof shape. Similarly, the inversion of (*6b-C2*) region in a heterozygous state caused minor defects in septum, whereas the same inversion on the background of deletion of the entire regulatory region (-90 C2) appeared similar to *Shh*^{HypO} or even *Shh* knock out. This is explained by the translocation of TAD (see (Symmons et al., 2016) for details) and resulting 'isolation' of *Shh* coding part from head-specific regulatory regions located between positions six and C2. In this latter case (*INV(6b-C2)*), *Shh* expression was dramatically reduced in the anterior forebrain as compared to the control (Symmons et al., 2016).

Further analysis of more restricted *Shh* regulatory regions revealed that brain-specific and facial cartilage-related enhancers are confined within the region (5-8) and are at least partly responsible for the expression of *Shh* in the forebrain according to the loss of in situ hybridization signal in the forebrain of (*DEL(5-8)*) compared to controls. The deletion of this (*DEL(5-8)*) region resulted in severe facial malformation and collapse of the nasal capsule shape to the state resembling *Shh*^{HypO}. Despite that we clearly observed the misshaped nasal capsule roof in these embryos, the septum was completely gone similarly to (*DEL(-90 C2) x INV(6b-C2)*) mutants. Taken together, these results provide strong support to the discrete role of genomic regulatory regions directing the expression of *Shh* to the forebrain and, through this, affecting the patterning of septal, basicranial and other cartilages in the head.

Importantly, all analyzed embryos carrying mutated regulatory regions never demonstrated missing nasal capsule roof including severe (*DEL(-90 C2) x INV(6b-C2)*), (*DEL(5-8) HOMO*) and *Shh*^{HypO}. This might mean that we still do not know about the position of the corresponding regulatory regions targeting the expression of *Shh* to the olfactory epithelium or FEZ in the frontal face. The loss or inversion of regulatory regions resulting in mild septal defects did not affect the anterior nasal capsule, which might be independently patterned by FEZ. Similarly, the morphology of the anterior nasal capsule stayed relatively stable when septal cartilage disappeared in *Nkx2.2-Cre/Shh^{floxed/floxed}* animals. This suggests that the most anterior face including frontal facial cartilages might be indeed patterned by FEZ together with olfactory placodes independently from brain-derived signals. These results point towards the possibility that mouse FEZ can form and act independently of the CNS signaling center contrary to chick embryonic development (Hu and Marcucio, 2009).

To summarize, it is possible that enhancer-dependent spatial and temporal regulations of *Shh* expression could be evolutionary tools to achieve the impressive variety of facial cartilage shapes in humans - a basis for facial individuality. Indeed, much attention has been focused on the role of enhancers in craniofacial evolution. Recently, by applying a combination of morphometry, molecular biology and mouse genetics, Attanasio et al. described numerous enhancers that are differentially active and take part in the development of a facial shape (Attanasio et al., 2013). In line with this, mutations in the enhancers that control the expression of *Fgf8*, another cartilage-inducing factor (Abzhanov and Tabin, 2004), also result in geometrical abnormalities of the nasal capsule (Marinić et al., 2013). It seems that many genes and pathways are involved in shaping the face (Young et al., 2014; Hu et al., 2015a; Foppiano et al., 2007; Hu et al., 2015b). This is not surprising, since the facial shaping includes many stages that are pre-chondrogenic, chondrogenic (including induction, growth, remodeling of the cartilage) and osteogenic. Processes of isotropic and anisotropic growth of the skeletal structures also play important roles in achieving the final geometry of the facial region (Kaucka et al., 2017). Despite such complexity and the enormous degree of spatio-temporal integration, the initial induction of cartilage guided by the brain and olfactory epithelium represents a key moment of facial skeleton formation. It may well also be an evolutionary

substrate driving the diversity of faces and snouts. Consequently, the fine-tuning of patterning and cartilage-inducing signals in neurosensory structures deserves further attention, including explorations of the diversity of corresponding genetic regulatory regions in human and animal genomes.

Materials and methods

Key resources table

Reagent type species or resource	Designation	Source or reference	Identifiers	Additional information
Strain	<i>Col2a1-CreERT2</i>	Nakamura et al. (2006)		Received from S. Mackem
Strain	<i>R26Confetti</i>	https://www.jax.org/strain/013731		Received from H. Clevers
Strain	<i>R26DTA</i>	Voehringer et al. (2008)		Received from Jackson
Strain	<i>Six1 KO</i>	Grifone et al. (2005)		Received from P. Maire
Strain	<i>Six1/4 double KO</i>	Grifone et al. (2005)		Received from P. Maire
Strain	<i>Nkx2.2-Cre/Shhflx/flx</i>	Yu et al., 2013		Received from M. Matisse
Strain	<i>Ascl1 (Mash1)</i>	Cau et al. (1997)		Received from U. Marklund
Strain	<i>B6.Cg-Shhtm1EGFP/creCjt/J</i>	Harfe et al. (2004)		Received from M. Hovorakova
Strain	<i>Gli1-CreERT2</i>	https://www.jax.org/strain/007913		Received from M.Kasper
Strain	<i>Gli1-lacZ</i>	https://www.jax.org/strain/008211		Received from M.Kasper
Strain	<i>Shh-GFP</i>	https://www.jax.org/strain/008466 (Chamberlain et al., 2008)		Received from Jackson
Strain	<i>TgGBS-GFP</i>	Balaskas et al. (2012)		Received from A. Kicheva
Strain	<i>Rosa-CAG-LSL-tdTomato-WPRE</i>	https://www.jax.org/strain/007914		Received from M. Kasper
Strain	<i>INV-500-C1</i>	F. Spitz (Symmons et al., 2016)		Received from F. Spitz
Strain	<i>INV6b-C2</i>	F. Spitz (Symmons et al., 2016)		Received from F. Spitz
Strain	<i>Del-90-C2</i>	F. Spitz (Symmons et al., 2016)		Received from F. Spitz
Strain	<i>DEL1-Z</i>	F. Spitz (Symmons et al., 2016)		Received from F. Spitz
Strain	<i>DEL5-8</i>	F. Spitz (Symmons et al., 2016)		Received from F. Spitz
Antibody	SOX9	Sigma Aldrich, HPA001758		one to 1000 in PBS-T over night at RT
Antibody	ERBB3	RnD Systems, AF4518		one to 500 in PBS-T over night at RT
Drug	Vismodegib	LoRusso et al. (2011)		0.1 mg/kg
Software	IMARIS	http://www.bitplane.com/		
Software	GOM Inspect	https://www.gom.com/de/3d-software/gom-inspect.html		
Software	VGStudio Max	https://www.volumegraphics.com/en/products/vgstudio-max.html		

Continued on next page

Continued

Reagent type species or resource	Designation	Source or reference	Identifiers	Additional information
RNAScope probes	Gli1 (311001), Gli2 (405771), Gli3 (445511), Smo (318411), Ptch1 (402811) and Ptch2 (435131)	https://acdbio.com/rnascope%C2%AE-technology-novel-rna-situ-hybridization-research-platform		

Mouse strains and animal information

All animal work were approved and permitted by the Local Ethical Committee on Animal Experiments (North Stockholm Animal Ethics Committee) and conducted according to The Swedish Animal Agency's Provisions and Guidelines for Animal Experimentation recommendations. Genetic tracing mouse strain *Nkx2.2-Cre* was described previously (Yu et al., 2013). *Col2a1-CreERT2* (Ozaki et al., 2001) (obtained from the laboratory of S. Mackem, NIH) strains (Nakamura et al., 2006) were coupled to *R26Confetti* mice that were received from the laboratory of Professor H. Clevers (Snippert et al., 2010). *DTA* strain (Voehringer et al., 2008) (*B6.129P2-Gt(ROSA)26Sortm1(DTA)Lky/J*, The Jackson Laboratory) was coupled to *Col2a1-CreERT2*. *Six1* and *Six1/4* double KO embryos were generated as described already (Grifone et al., 2005; Laclef et al., 2003). *Nkx2.2-Cre/Shh^{flx/flx}* embryos were received from the laboratory of Michael Matisse. *Ascl1* (*Mash1*) KO embryos were received from the laboratory of Ulrika Marklund. *B6.Cg-Shhtm1(EGFP/cre)Cjt/J* (Harfe et al., 2004) embryos were received from the laboratory of Maria Hovorakova (CAS). *Gli1-CreERT2* and *Gli1-lacZ* strains were obtained from the laboratory of Maria Kasper (Karolinska Institutet). *Gli1-CreERT2* was coupled with *R26Confetti* and *R26Tomato*.

The following strains were previously described: *Tg(GBS-GFP)* (Balaskas et al., 2012), *Shh-GFP* (JAX stock #008466 (Chamberlain et al., 2008)). *Shh^{Hypo}* embryos are homozygous for *Shh-GFP* and their morphological phenotypes are not affected by the presence or absence of the *Tg(GBS-GFP)* transgene. Strains were bred and maintained on 129/Sv background, in accordance with license BMWFW-66.018/0006-WF/V/3b/2016 granted by the Austrian BMWFW.

Gli1-LacZ (<https://www.jax.org/strain/008211>), *Gli1-CreERT2* (<https://www.jax.org/strain/007913>) and *Rosa-CAG-LSL-tdTomato-WPRE* (<https://www.jax.org/strain/007914>) were used under the ethical permit: number S40/13, granted by South Stockholm Animal Ethics Committee.

Mice of the relevant genotype were mated overnight, and noon of the day of the plug was considered as E0.5. To induce genetic recombination of adequate efficiency, pregnant females of relevant couplings were injected intraperitoneally with tamoxifen (Sigma T5648) dissolved in corn oil (Sigma C8267). Tamoxifen concentration ranged from 1.5 to 5.0 mg per animal to obtain a range of recombination efficiency. Mice were sacrificed with isoflurane (Baxter KDG9623) overdose or cervical dislocation, and embryos were dissected out and collected into ice-cold PBS. Subsequently, the samples were placed into freshly prepared 4% paraformaldehyde (PFA) and depending on the developmental stage and the application they were fixed for 3–24 hr at 4°C on a roller. Subsequently, for the purpose of microscopy analysis, the embryos were cryopreserved in 30% sucrose (VWR C27480) overnight at 4°C, embedded in OCT media (HistoLab 45830) and cut into 18 µm to 30 µm sections on a cryostat (Microm). Embryos designated for CT analysis were then stained according to the protocol described beneath.

Inhibition of hedgehog signaling

In order to inhibit SHH during embryonic development (stages E11.5 to E13.5), the pharmacological inhibitor Vismodegib (LoRusso et al., 2011) was injected intraperitoneally at a dosage of 0.1 mg per g of bodyweight of the pregnant mouse. Embryos were collected at E15.5 and fixed in 4% formaldehyde in PBS solution for 24 hr at +4°C with slow rotation.

Histological staining

Slides were stained for mineral deposition using von Kossa calcium staining: 5% silver nitrate solution was added to the sections at a room temperature and exposed to strong light for 30 min. After that the silver nitrate solution was removed, and slides were washed with distilled water for 3 times during 2 min. 2.5% sodium thiosulphate solution (w/v) was added to the sections and incubated for five

mins. Slides were again rinsed for 3 times during 2 min in distilled water. The sections were then counterstained using Alcian blue. Alcian blue solution (0.1% alcian blue 8GX (w/v) in 0.1 M HCl) was added to the tissue for 3 min at room temperature and then rinsed for 3 times during 2 min in distilled water. Slides were then transferred rapidly into incrementally increasing ethanol concentrations (20%, 40%, 80%, 100%) and incubated in 100% ethanol for 2 min. Finally, the slides were incubated in two xylene baths (for 2 min and then for 5 min) before mounting and analysis.

Immunohistochemistry, histological staining and EdU analysis

Frozen samples were sectioned at 18–30 μm depending on specific experiment. If needed, sections were stored at -20°C after drying 1 hr at room temperature, or processed immediately after sectioning. Primary antibodies used were: chicken anti-GFP (Abcam, 1:500, ab13970), rabbit anti-SOX9 (Sigma Aldrich, 1:1000, HPA001758), sheep anti-ERBB3 (RnD Systems, 1:500, AF4518). For detection of above-mentioned primary antibodies, we utilized 405, 488, 555 or 647-conjugated Alexa secondary antibodies produced in donkey (Invitrogen, 1:1000). Slices were mounted with 87% glycerol mounting media (Merck).

Fluorescent in situ hybridization (RNAscope)

E12.5 and E13.5 embryos were collected, embedded immediately in OCT and snap frozen on dry ice. Tissue blocks were stored at -20°C until further use. 8- μm -thick cryosections were collected on Superfrost Plus slides and stored at -20°C until further use. Fluorescent in situ hybridization was performed for the genes *Gli1* (311001), *Gli2* (405771), *Gli3* (445511), *Smo* (318411), *Ptch1* (402811) and *Ptch2* (435131) using the RNAscope 2.0 Assay, reagents and probes according to manufacturer's instructions (Wang *et al.*, 2012). RNAscope probes were designed commercially by the manufacturer and are available from Advanced Cell Diagnostics, Inc. being protected by patent.

X-gal staining

E11.5, E12.5 and E13.5 embryos were fixed in 4% formaldehyde in PBS solution for 2–3 hr at $+4^{\circ}\text{C}$ with slow rotation. Following washes with PBS, embryos were incubated in X-gal staining solution (1 mg/ml X-gal; 2 mM MgCl_2 ; 0.5 M potassium ferrocyanide; 0.5 M potassium ferricyanide in PBS) at 37°C , overnight, with gentle agitation. Samples were washed twice, 20 min each time at room temperature in PBS and imaged whole mount. When necessary, we proceeded to cryoprotection in 30% sucrose in PBS and embedding in OCT medium.

Microscopy, volume rendering, image analysis and quantifications

Confocal microscopy was performed using Zeiss LSM880 Airyscan CLSM instruments. The settings for the imaging of Confetti fluorescent proteins were previously described (Snippert *et al.*, 2010). Image analysis has been performed using IMARIS Software (Bitplane, Zurich, Switzerland). Before performing manual segmentations of cartilages and mesenchymal chondrogenic condensations on all representative samples, we assessed the phenotype and the stability of the phenotype using analysis of multiple embryos (typically 3–5 per condition) on histological sections as well as whole-mount assessments of facial morphology and including usage of tomographic slices. In case the phenotype was stable, the representative embryos underwent 3D segmentation process, otherwise we manually segmented facial cartilage and bone from all experimental embryos (in case of *Col2a1-CreERT2/R26DTA* or *Shh^{Hypo}*, please see Figure 1—figure supplement 1 and Figure 6—figure supplement 3). For embryonic day E17.5 *Col2a1-CreERT2/R26DTA*, we performed segmentations of the most affected embryo from the litter (Figure 1I–P and graph in R). Other litter mates were analyzed using cryo-sections only (Figure 1E–H). Since we did not investigate fine differences in shape of the nasal capsule and rather concentrated on missing structures (septum or nasal capsule roof), we did not analyze fine shape differences morphometrically in a quantitative way. In special cases, where relevant, we utilized shape fitting analysis using GOM Inspect tool. We did not use any special randomization or masking of embryos during experimental and control group allocations.

Tissue contrasting for $\mu\text{-CT}$ scanning

Staining protocol has been adapted and modified from the original protocol developed by Brian Metscher laboratory (Metscher, 2009). After embryo dissection in ice-cold PBS, the samples were

fixed in 4% formaldehyde in PBS solution for 24 hr at +4°C with slow rotation. Subsequently, samples were dehydrated in incrementally increasing ethanol concentrations (30%, 50%, 70%), 1 day in each concentration to minimize the shrinkage of the tissue. Samples were transferred, depending on the embryonic stage, into 1.0–1.5% PTA (phospho-tungstic acid) in 90% methanol for tissue contrasting. The PTA-methanol solution was changed every 2–3 days. E12.5 embryos were stained for 7 days, E15.5 embryos for 3 weeks and E18.5 embryos for 7 weeks. The contrasting procedure was followed by rehydration of the samples by incubation in ethanol series (90%, 70%, 50% and 30%) and shipped to the CT-laboratory for scanning. There the rehydrated embryos were embedded in 0.5% agarose gel (A5304, Sigma-Aldrich) and placed in polypropylene conical tubes (0.5, 1.5 or 15 ml depending on the sample size to minimize the amount of medium surrounding it) and to avoid the movement artifacts during X-ray computer tomography scanning.

μ-CT analysis (micro computed tomography analysis) and 3D analysis

The μ-CT analysis of the embryos was conducted using the laboratory system GE phoenix v|tome|x L 240 (GE Sensing and Inspection Technologies GmbH, Germany), equipped with a 180 kV/15W maximum power nanofocus X-ray tube and flat panel detector DXR250 with 2048 × 2048 pixel, 200 × 200 μm pixel size. The embryos were fixed in polyimide tubes by 1% agarose gel to prevent tomographic movement artifacts. The exposure time of the detector was 900 ms in every of 2000 positions. Three projections were acquired and averaged for reduction of the noise in μ-CT data. The utilized power of the tube was 11 W given by acceleration voltage of 60 kV and tube current of 200 μA. X-ray spectrum was filtered by 0.1 mm of aluminium plate. The voxel size of obtained volumes (depending on a size of an embryo head) appeared in the range of 5 μm - 7 μm. The tomographic reconstructions were performed using GE phoenix datos|x 2.0 3D computed tomography software (GE Sensing and Inspection Technologies GmbH, Germany). The cartilage in the embryo head was segmented by an operator with semi-automatic tools within Avizo - 3D image data processing software (FEI, USA). The 3D segmented region was transformed to a polygonal mesh as a STL file. The mesh of the embryo head was imported to VG Studio MAX 2.2 software (Volume Graphics GmbH, Germany) for consequent modification of the mesh, like a surface smoothing, and 3D visualization. The software GOM Inspect V8 (GOM, Braunschweig, Germany) was implemented for comparisons of full shapes of the head. The triangular meshes of the surface of the heads represented by STL models were imported into the software, aligned and compared with parameters of maximum searching distance 1 mm and maximum opening angle 30°. All raw STL files are freely accessible via the following Dryad link: <https://doi.org/10.5061/dryad.f1s76f2>

The STL format can be opened with Paint 3D or Print 3D software.

Light sheet microscopy and sample clearing

Whole heads from *Shh-GFP* embryos at E11.5, E12.5, E13.5 and E14.5 were cleared using a modified CUBIC protocol (Susaki et al., 2014). In brief, embryos were fixed by using 4% PFA in PBS for 4 hr at four degrees before incubating in CUBIC one solution (25% urea, 25% N,N,N',N'-tetrakis-(2-hydroxypropyl) ethylenediamine and 15% Triton X-100) at 37°C under shaking conditions for 3 days. Subsequently, the samples were washed in PBS at RT. Next, samples were immersed in CUBIC two solution (50% sucrose, 25% urea, 10% 2,2',2''-nitrilotriethanol, and 0.1% Triton X-100) and left shaking at RT for an additional 2–3 days before image acquisition.

Whole embryo head (E11.5–E14.5) GFP fluorescence images were acquired on a Light sheet Z.1 microscope (Zeiss) using a × 5 (EC Plan Neofluar 5×/0.16) detection objective, ×5/0.1 illumination optics, and laser excitation at 488 nm. Samples were imaged in CUBIC two solution with a measured refractory index of 1.45. Each plane was illuminated from a single side of the sample. Whole images were obtained through tile scanning. 3D-rendered images were visualized with Arivis Vision4D for Zeiss (v. 2.11) or Imaris (v. 7.4.2, Bitplane).

Bitplane IMARIS software was subsequently used for 3D visualization and analysis of the light sheet tiles. By using the surface option in IMARIS the different parts of *Shh-GFP* have been highlighted.

Acknowledgements

We would like to thank to Prof. Susan Mackem for the *Col2a1-CreERT2* mouse strain. MKau was supported by the SSMF fellowship (Svenska sällskapet för medicinsk forskning). IA was supported by Bertil Hållsten Research Foundation, Åke Wiberg Foundation, Vetenskapsrådet (VR), ERC Consolidator grant (STEMMING-FROM-NERVE, Project ID: 647844; ERC-2014-CoG), EMBO Young Investigator Program and Karolinska Institutet. JP was supported by a VR grant. KF was supported by VR MT, JK and TZ have been financially supported by the Ministry of Education, Youth and Sports of the Czech Republic under the project CEITEC 2020 (LQ1601) and by the project CEITEC Nano Research Infrastructure (MEYS CR, 2016–2019). MKas was supported by Cancerfonden, Swedish Foundation for Strategic Research and Ragnar Söderberg Foundation. KA was supported by Karolinska Institutet. FS lab was supported by EMBL. MEK was supported by the NovoNordisk Fonden Postdoctoral Stipend (Ref No NNF17OC0026874). MH was supported by Grant Agency of Czech Republic (14–37368G). Work in the AK lab is supported by the European Research Council under European Union Horizon 2020 research and innovation program grant 680037.

Additional information

Funding

Funder	Grant reference number	Author
Vetenskapsrådet		Julian Petersen Andrei S Chagin Igor Adameyko
Svenska Sällskapet för Medicinsk Forskning		Marketa Kaucka
Bertil Hållstens Forskningsstiftelse		Igor Adameyko
Åke Wibergs Stiftelse		Igor Adameyko
Karolinska Institutet		Ulrika Marklund Andrei S Chagin Kaj Fried Igor Adameyko
Ministerstvo Vnitřní České republiky		Marketa Tesarova Tomas Zikmund
Central European Institute of Technology		Marketa Tesarova Tomas Zikmund
Grantová Agentura České republiky		Maria Hovorakova
H2020 European Research Council	680037	Anna Kicheva

The funders had no role in study design, data collection and interpretation, or the decision to submit the work for publication.

Author contributions

Marketa Kaucka, Julian Petersen, Conceptualization, Data curation, Supervision, Validation, Investigation, Visualization, Methodology, Writing—original draft, Writing—review and editing; Marketa Tesarova, Data curation, Supervision, Investigation, Visualization, Methodology, Writing—review and editing; Bara Szarowska, Maria Eleni Kastriiti, Jozef Kaiser, Resources, Data curation, Supervision, Methodology, Writing—review and editing; Meng Xie, Data curation, Writing—review and editing; Anna Kicheva, Conceptualization, Resources, Data curation, Supervision, Writing—original draft, Writing—review and editing; Karl Annusver, Data curation, Investigation, Methodology, Writing—review and editing; Maria Kasper, Resources, Data curation, Supervision, Methodology, Writing—original draft, Writing—review and editing; Orsolya Symmons, Resources, Data curation, Investigation; Leslie Pan, Resources, Data curation, Investigation, Writing—original draft, Writing—review and editing; Francois Spitz, Data curation, Supervision, Methodology, Writing—review and editing; Maria

Hovorakova, Conceptualization, Resources, Data curation, Supervision, Investigation, Writing—review and editing; Tomas Zikmund, Resources, Investigation, Methodology, Writing—review and editing; Kazunori Sunadome, Resources, Data curation, Investigation, Methodology, Writing—original draft, Writing—review and editing; Michael P Matise, Conceptualization, Resources, Data curation, Investigation, Methodology, Writing—original draft, Writing—review and editing; Hui Wang, Pascal Maire, Conceptualization, Resources, Data curation, Investigation, Methodology, Writing—review and editing; Ulrika Marklund, Hind Abdo, Patrik Ernfors, Andrei S Chagin, Kaj Fried, Igor Adameyko, Conceptualization, Resources, Data curation, Formal analysis, Supervision, Funding acquisition, Investigation, Methodology, Writing—original draft, Writing—review and editing; Maud Wurmser, Conceptualization, Resources, Data curation, Supervision, Investigation, Methodology, Writing—original draft, Writing—review and editing

Author ORCIDs

Marketa Kaucka  <https://orcid.org/0000-0002-8781-9769>

Julian Petersen  <http://orcid.org/0000-0002-7444-0610>

Ulrika Marklund  <https://orcid.org/0000-0003-1426-1271>

Andrei S Chagin  <https://orcid.org/0000-0002-2696-5850>

Igor Adameyko  <https://orcid.org/0000-0001-5471-0356>

Ethics

Animal experimentation: All animal work was approved and permitted by the Local Ethical Committee on Animal Experiments (North Stockholm Animal Ethics Committee) and conducted according to The Swedish Animal Agency's Provisions and Guidelines for Animal Experimentation recommendations. Permit numbers S40/13 and N226/15, granted by South Stockholm Animal Ethics Committee. The part, which was done in Austria at the Medical University of Vienna and IST was performed in accordance with license BMWFW-66.018/0006-WF/V/3b/2016 and BMWFW-66.009/0163-WF/V/3b/2016 granted by the Austrian BMWFW.

Decision letter and Author response

Decision letter <https://doi.org/10.7554/eLife.34465.027>

Author response <https://doi.org/10.7554/eLife.34465.028>

Additional files

Supplementary files

- Transparent reporting form

DOI: <https://doi.org/10.7554/eLife.34465.023>

Data availability

All data obtained including tomographic reconstructions will be freely available upon request since some datasets are considerably large (1TB and more) and depositing the full data is unfeasible. We have made a subset of the datasets available on the Dryad Digital Repository (<http://dx.doi.org/10.5061/dryad.f1s76f2>).

The following dataset was generated:

Author(s)	Year	Dataset title	Dataset URL	Database, license, and accessibility information
Kaucka M, Petersen J, Tesarova M, Szarowska B, Kas-triti ME, Xie M, Kicheva A, Annus-ver K, Kasper M, Symmons O, Pan L, Spitz F, Kaiser J, Hovorakova M, Zik-	2018	Data from: Signals from the brain and olfactory epithelium control shaping of the mammalian nasal capsule cartilage	http://dx.doi.org/10.5061/dryad.f1s76f2	Available at Dryad Digital Repository under a CC0 Public Domain Dedication

mund T, Sunadome K, Matisse MP, Wang H, Marklund U, Abdo H, Ernfors P, Maire P, Wurmser M, Chagin AS, Fried K, Adameyko I

References

- Abzhanov A**, Tabin CJ. 2004. Shh and Fgf8 act synergistically to drive cartilage outgrowth during cranial development. *Developmental Biology* **273**:134–148. DOI: <https://doi.org/10.1016/j.ydbio.2004.05.028>, PMID: 15302603
- Allen WL**, Higham JP. 2015. Assessing the potential information content of multicomponent visual signals: a machine learning approach. *Proceedings of the Royal Society B: Biological Sciences* **282**:20142284. DOI: <https://doi.org/10.1098/rspb.2014.2284>, PMID: 25652832
- Antshel KM**, Fremont W, Kates WR. 2008. The neurocognitive phenotype in velo-cardio-facial syndrome: a developmental perspective. *Developmental Disabilities Research Reviews* **14**:43–51. DOI: <https://doi.org/10.1002/ddr.7>, PMID: 18636636
- Attanasio C**, Nord AS, Zhu Y, Blow MJ, Li Z, Liberton DK, Morrison H, Plajzer-Frick I, Holt A, Hosseini R, Phouanavong S, Akiyama JA, Shoukry M, Afzal V, Rubin EM, FitzPatrick DR, Ren B, Hallgrímsson B, Pennacchio LA, Visel A. 2013. Fine tuning of craniofacial morphology by distant-acting enhancers. *Science* **342**:1241006. DOI: <https://doi.org/10.1126/science.1241006>, PMID: 24159046
- Baggiolini A**, Varum S, Mateos JM, Bettosini D, John N, Bonalli M, Ziegler U, Dimou L, Clevers H, Furrer R, Sommer L. 2015. Premigratory and migratory neural crest cells are multipotent in vivo. *Cell Stem Cell* **16**:314–322. DOI: <https://doi.org/10.1016/j.stem.2015.02.017>, PMID: 25748934
- Balaskas N**, Ribeiro A, Panovska J, Dessaud E, Sasai N, Page KM, Briscoe J, Ribes V. 2012. Gene regulatory logic for reading the Sonic Hedgehog signaling gradient in the vertebrate neural tube. *Cell* **148**:273–284. DOI: <https://doi.org/10.1016/j.cell.2011.10.047>, PMID: 22265416
- Bhullar BA**, Morris ZS, Sefton EM, Tok A, Tokita M, Namkoong B, Camacho J, Burnham DA, Abzhanov A. 2015. A molecular mechanism for the origin of a key evolutionary innovation, the bird beak and palate, revealed by an integrative approach to Major transitions in vertebrate history. *Evolution* **69**:1665–1677. DOI: <https://doi.org/10.1111/evo.12684>, PMID: 25964090
- Billmyre KK**, Klingensmith J. 2015. Sonic hedgehog from pharyngeal arch 1 epithelium is necessary for early mandibular arch cell survival and later cartilage condensation differentiation. *Developmental Dynamics* **244**:564–576. DOI: <https://doi.org/10.1002/dvdy.24256>, PMID: 25626636
- Brugmann SA**, Powder KE, Young NM, Goodnough LH, Hahn SM, James AW, Helms JA, Lovett M. 2010. Comparative gene expression analysis of avian embryonic facial structures reveals new candidates for human craniofacial disorders. *Human Molecular Genetics* **19**:920–930. DOI: <https://doi.org/10.1093/hmg/ddp559>, PMID: 20015954
- Carson B**. 1999. *Human Embryology & Developmental Biology*. Mosby.
- Cau E**, Gradwohl G, Fode C, Guillemot F. 1997. Mash1 activates a cascade of bHLH regulators in olfactory neuron progenitors. *Development* **124**:1611–1621. PMID: 9108377
- Chamberlain CE**, Jeong J, Guo C, Allen BL, McMahon AP. 2008. Notochord-derived Shh concentrates in close association with the apically positioned basal body in neural target cells and forms a dynamic gradient during neural patterning. *Development* **135**:1097–1106. DOI: <https://doi.org/10.1242/dev.013086>, PMID: 18272593
- Chang CF**, Chang YT, Millington G, Brugmann SA. 2016. Craniofacial ciliopathies reveal specific requirements for GLI proteins during development of the facial midline. *PLoS Genetics* **12**:e1006351. DOI: <https://doi.org/10.1371/journal.pgen.1006351>, PMID: 27802276
- Chong HJ**, Young NM, Hu D, Jeong J, McMahon AP, Hallgrímsson B, Marcucio RS. 2012. Signaling by SHH rescues facial defects following blockade in the brain. *Developmental dynamics : an official publication of the American Association of Anatomists* **241**:247–256. DOI: <https://doi.org/10.1002/dvdy.23726>, PMID: 22275045
- Foppiano S**, Hu D, Marcucio RS. 2007. Signaling by bone morphogenetic proteins directs formation of an ectodermal signaling center that regulates craniofacial development. *Developmental Biology* **312**:103–114. DOI: <https://doi.org/10.1016/j.ydbio.2007.09.016>, PMID: 18028903
- Forbes BJ**. 2010. Congenital craniofacial anomalies. *Current Opinion in Ophthalmology* **21**:367–374. DOI: <https://doi.org/10.1097/ICU.0b013e32833cd422>, PMID: 20634697
- Furlan A**, Dyachuk V, Kastriti ME, Calvo-Enrique L, Abdo H, Hadjab S, Chontorotzea T, Akkuratova N, Usoskin D, Kamenev D, Petersen J, Sunadome K, Memic F, Marklund U, Fried K, Topilko P, Lallemand F, Kharchenko PV, Ernfors P, Adameyko I. 2017. Multipotent peripheral glial cells generate neuroendocrine cells of the adrenal medulla. *Science* **357**. DOI: <https://doi.org/10.1126/science.aal3753>, PMID: 28684471
- Goldring MB**, Tsuchimochi K, Ijiri K. 2006. The control of chondrogenesis. *Journal of Cellular Biochemistry* **97**:33–44. DOI: <https://doi.org/10.1002/jcb.20652>, PMID: 16215986

- Griffin JN**, Compagnucci C, Hu D, Fish J, Klein O, Marcucio R, Depew MJ. 2013. Fgf8 dosage determines midfacial integration and polarity within the nasal and optic capsules. *Developmental Biology* **374**:185–197. DOI: <https://doi.org/10.1016/j.ydbio.2012.11.014>, PMID: 23201021
- Grifone R**, Demignon J, Houbron C, Souil E, Niro C, Seller MJ, Hamard G, Maire P. 2005. Six1 and Six4 homeoproteins are required for Pax3 and Mrf expression during myogenesis in the mouse embryo. *Development* **132**:2235–2249. DOI: <https://doi.org/10.1242/dev.01773>, PMID: 15788460
- Gros J**, Tabin CJ. 2014. Vertebrate limb bud formation is initiated by localized epithelial-to-mesenchymal transition. *Science* **343**:1253–1256. DOI: <https://doi.org/10.1126/science.1248228>, PMID: 24626928
- Guillemot F**, Lo LC, Johnson JE, Auerbach A, Anderson DJ, Joyner AL. 1993. Mammalian achaete-scute homolog 1 is required for the early development of olfactory and autonomic neurons. *Cell* **75**:463–476. DOI: [https://doi.org/10.1016/0092-8674\(93\)90381-Y](https://doi.org/10.1016/0092-8674(93)90381-Y), PMID: 8221886
- Harfe BD**, Scherz PJ, Nissim S, Tian H, McMahon AP, Tabin CJ. 2004. Evidence for an expansion-based temporal Shh gradient in specifying vertebrate digit identities. *Cell* **118**:517–528. DOI: <https://doi.org/10.1016/j.cell.2004.07.024>, PMID: 15315763
- Herbrand H**, Pabst O, Hill R, Arnold HH. 2002. Transcription factors Nkx3.1 and Nkx3.2 (Bapx1) play an overlapping role in sclerotomal development of the mouse. *Mechanisms of Development* **117**:217–224. DOI: [https://doi.org/10.1016/S0925-4773\(02\)00207-1](https://doi.org/10.1016/S0925-4773(02)00207-1), PMID: 12204261
- Hu D**, Helms JA. 1999. The role of sonic hedgehog in normal and abnormal craniofacial morphogenesis. *Development* **126**:4873–4884. PMID: 10518503
- Hu D**, Marcucio RS. 2009. A SHH-responsive signaling center in the forebrain regulates craniofacial morphogenesis via the facial ectoderm. *Development* **136**:107–116. DOI: <https://doi.org/10.1242/dev.026583>, PMID: 19036802
- Hu D**, Young NM, Li X, Xu Y, Hallgrímsson B, Marcucio RS. 2015b. A dynamic shh expression pattern, regulated by SHH and BMP signaling, coordinates fusion of primordia in the amniote face. *Development* **142**:567–574. DOI: <https://doi.org/10.1242/dev.114835>, PMID: 25605783
- Hu D**, Young NM, Xu Q, Jamniczky H, Green RM, Mio W, Marcucio RS, Hallgrímsson B. 2015a. Signals from the brain induce variation in avian facial shape. *Developmental dynamics : an official publication of the American Association of Anatomists*. DOI: <https://doi.org/10.1002/dvdy.24284>, PMID: 25903813
- Ikeda K**, Ookawara S, Sato S, Ando Z, Kageyama R, Kawakami K. 2007. Six1 is essential for early neurogenesis in the development of olfactory epithelium. *Developmental Biology* **311**:53–68. DOI: <https://doi.org/10.1016/j.ydbio.2007.08.020>, PMID: 17880938
- Irimia M**, Royo JL, Burguera D, Maeso I, Gómez-Skarmeta JL, Garcia-Fernandez J. 2012. Comparative genomics of the hedgehog loci in chordates and the origins of shh regulatory novelties. *Scientific Reports* **2**:433. DOI: <https://doi.org/10.1038/srep00433>, PMID: 22666536
- Jeong Y**, El-Jaick K, Roessler E, Muenke M, Epstein DJ. 2006. A functional screen for sonic hedgehog regulatory elements across a 1 Mb interval identifies long-range ventral forebrain enhancers. *Development* **133**:761–772. DOI: <https://doi.org/10.1242/dev.02239>, PMID: 16407397
- Kauka M**, Zikmund T, Tesarova M, Gyllborg D, Hellander A, Jaros J, Kaiser J, Petersen J, Szarowska B, Newton PT, Dyachuk V, Li L, Qian H, Johansson AS, Mishina Y, Currie JD, Tanaka EM, Erickson A, Dudley A, Brismar H, et al. 2017. Oriented clonal cell dynamics enables accurate growth and shaping of vertebrate cartilage. *eLife* **6**:e25902. DOI: <https://doi.org/10.7554/eLife.25902>, PMID: 28414273
- Kobayashi H**, Kawakami K, Asashima M, Nishinakamura R. 2007. Six1 and Six4 are essential for gdnf expression in the metanephric mesenchyme and ureteric bud formation, while Six1 deficiency alone causes mesonephric-tubule defects. *Mechanisms of Development* **124**:290–303. DOI: <https://doi.org/10.1016/j.mod.2007.01.002>, PMID: 17300925
- Laclef C**, Hamard G, Demignon J, Souil E, Houbron C, Maire P. 2003. Altered myogenesis in Six1-deficient mice. *Development* **130**:2239–2252. DOI: <https://doi.org/10.1242/dev.00440>, PMID: 12668636
- LoRusso PM**, Rudin CM, Reddy JC, Tibes R, Weiss GJ, Borad MJ, Hann CL, Brahmer JR, Chang I, Darbonne WC, Graham RA, Zerivitz KL, Low JA, Von Hoff DD. 2011. Phase I trial of hedgehog pathway inhibitor vismodegib (GDC-0449) in patients with refractory, locally advanced or metastatic solid tumors. *Clinical Cancer Research* **17**:2502–2511. DOI: <https://doi.org/10.1158/1078-0432.CCR-10-2745>, PMID: 21300762
- Marcucio RS**, Young NM, Hu D, Hallgrímsson B. 2011. Mechanisms that underlie co-variation of the brain and face. *Genesis* **49**:177–189. DOI: <https://doi.org/10.1002/dvg.20710>, PMID: 21381182
- Marinić M**, Aktas T, Ruf S, Spitz F. 2013. An integrated holo-enhancer unit defines tissue and gene specificity of the Fgf8 regulatory landscape. *Developmental Cell* **24**:530–542. DOI: <https://doi.org/10.1016/j.devcel.2013.01.025>, PMID: 23453598
- McBratney-Owen B**, Iseki S, Bamforth SD, Olsen BR, Morriss-Kay GM. 2008. Development and tissue origins of the mammalian cranial base. *Developmental Biology* **322**:121–132. DOI: <https://doi.org/10.1016/j.ydbio.2008.07.016>, PMID: 18680740
- Metscher BD**. 2009. MicroCT for comparative morphology: simple staining methods allow high-contrast 3D imaging of diverse non-mineralized animal tissues. *BMC Physiology* **9**:11. DOI: <https://doi.org/10.1186/1472-6793-9-11>, PMID: 19545439
- Minoux M**, Rijli FM. 2010. Molecular mechanisms of cranial neural crest cell migration and patterning in craniofacial development. *Development* **137**:2605–2621. DOI: <https://doi.org/10.1242/dev.040048>, PMID: 20663816

- Murtaugh LC**, Chyung JH, Lassar AB. 1999. Sonic hedgehog promotes somitic chondrogenesis by altering the cellular response to BMP signaling. *Genes & Development* **13**:225–237. DOI: <https://doi.org/10.1101/gad.13.2.225>, PMID: 9925646
- Murtaugh LC**, Zeng L, Chyung JH, Lassar AB. 2001. The chick transcriptional repressor Nkx3.2 acts downstream of Shh to promote BMP-dependent axial chondrogenesis. *Developmental Cell* **1**:411–422. DOI: [https://doi.org/10.1016/S1534-5807\(01\)00039-9](https://doi.org/10.1016/S1534-5807(01)00039-9), PMID: 11702952
- Nakamura E**, Nguyen MT, Mackem S. 2006. Kinetics of tamoxifen-regulated Cre activity in mice using a cartilage-specific CreER(T) to assay temporal activity windows along the proximodistal limb skeleton. *Developmental dynamics : an official publication of the American Association of Anatomists* **235**:2603–2612. DOI: <https://doi.org/10.1002/dvdy.20892>, PMID: 16894608
- Ornitz DM**, Marie PJ. 2002. FGF signaling pathways in endochondral and intramembranous bone development and human genetic disease. *Genes & Development* **16**:1446–1465. DOI: <https://doi.org/10.1101/gad.990702>, PMID: 12080084
- Ozaki H**, Watanabe Y, Takahashi K, Kitamura K, Tanaka A, Urase K, Momoi T, Sudo K, Sakagami J, Asano M, Iwakura Y, Kawakami K. 2001. Six4, a putative myogenin gene regulator, is not essential for mouse embryonal development. *Molecular and Cellular Biology* **21**:3343–3350. DOI: <https://doi.org/10.1128/MCB.21.10.3343-3350.2001>, PMID: 11313460
- Park J**, Zhang JJ, Moro A, Kushida M, Wegner M, Kim PC. 2010. Regulation of Sox9 by sonic hedgehog (Shh) is essential for patterning and formation of tracheal cartilage. *Developmental Dynamics* **239**:514–526. DOI: <https://doi.org/10.1002/dvdy.22192>, PMID: 20034104
- Parsons TE**, Schmidt EJ, Boughner JC, Jamniczky HA, Marcucio RS, Hallgrímsson B. 2011. Epigenetic integration of the developing brain and face. *Developmental Dynamics* **240**:2233–2244. DOI: <https://doi.org/10.1002/dvdy.22729>, PMID: 21901785
- Petryk A**, Graf D, Marcucio R. 2015. Holoprosencephaly: signaling interactions between the brain and the face, the environment and the genes, and the phenotypic variability in animal models and humans. *Wiley Interdisciplinary Reviews: Developmental Biology* **4**:17–32. DOI: <https://doi.org/10.1002/wdev.161>, PMID: 25339593
- Picelli S**, Björklund ÅK, Faridani OR, Sagasser S, Winberg G, Sandberg R. 2013. Smart-seq2 for sensitive full-length transcriptome profiling in single cells. *Nature Methods* **10**:1096–1098. DOI: <https://doi.org/10.1038/nmeth.2639>, PMID: 24056875
- Sagai T**, Amano T, Tamura M, Mizushima Y, Sumiyama K, Shiroishi T. 2009. A cluster of three long-range enhancers directs regional Shh expression in the epithelial linings. *Development* **136**:1665–1674. DOI: <https://doi.org/10.1242/dev.032714>, PMID: 19369396
- Sala FG**, Del Moral PM, Tiozzo C, Alam DA, Warburton D, Grikscheit T, Veltmaat JM, Bellusci S. 2011. FGF10 controls the patterning of the tracheal cartilage rings via Shh. *Development* **138**:273–282. DOI: <https://doi.org/10.1242/dev.051680>, PMID: 21148187
- Santana SE**, Lynch Alfaro J, Alfaro ME. 2012. Adaptive evolution of facial colour patterns in neotropical primates. *Proceedings of the Royal Society B: Biological Sciences* **279**:2204–2211. DOI: <https://doi.org/10.1098/rspb.2011.2326>
- Shimeld SM**, Donoghue PC. 2012. Evolutionary crossroads in developmental biology: cyclostomes (lamprey and hagfish). *Development* **139**:2091–2099. DOI: <https://doi.org/10.1242/dev.074716>, PMID: 22619386
- Shirley ED**, Ain MC. 2009. Achondroplasia: manifestations and treatment. *The Journal of the American Academy of Orthopaedic Surgeons* **17**:231–241. DOI: <https://doi.org/10.5435/00124635-200904000-00004>, PMID: 19307672
- Snider TN**, Mishina Y. 2014. Cranial neural crest cell contribution to craniofacial formation, pathology, and future directions in tissue engineering. *Birth Defects Research Part C: Embryo Today: Reviews* **102**:324–332. DOI: <https://doi.org/10.1002/bdrc.21075>, PMID: 25227212
- Snippert HJ**, van der Flier LG, Sato T, van Es JH, van den Born M, Kroon-Veenboer C, Barker N, Klein AM, van Rheenen J, Simons BD, Clevers H. 2010. Intestinal crypt homeostasis results from neutral competition between symmetrically dividing Lgr5 stem cells. *Cell* **143**:134–144. DOI: <https://doi.org/10.1016/j.cell.2010.09.016>, PMID: 20887898
- Starbuck JM**, Cole TM, Reeves RH, Richtsmeier JT. 2017. The influence of trisomy 21 on facial form and variability. *American Journal of Medical Genetics Part A* **173**:2861–2872. DOI: <https://doi.org/10.1002/ajmg.a.38464>, PMID: 28941128
- Susaki EA**, Tainaka K, Perrin D, Kishino F, Tawara T, Watanabe TM, Yokoyama C, Onoe H, Eguchi M, Yamaguchi S, Abe T, Kiyonari H, Shimizu Y, Miyawaki A, Yokota H, Ueda HR. 2014. Whole-brain imaging with single-cell resolution using chemical cocktails and computational analysis. *Cell* **157**:726–739. DOI: <https://doi.org/10.1016/j.cell.2014.03.042>, PMID: 24746791
- Symmons O**, Pan L, Remeseiro S, Aktas T, Klein F, Huber W, Spitz F. 2016. The shh topological domain facilitates the action of remote enhancers by reducing the effects of genomic distances. *Developmental Cell* **39**:529–543. DOI: <https://doi.org/10.1016/j.devcel.2016.10.015>, PMID: 27867070
- Vernon RJ**, Sutherland CA, Young AW, Hartley T. 2014. Modeling first impressions from highly variable facial images. *PNAS* **111**:E3353–E3361. DOI: <https://doi.org/10.1073/pnas.1409860111>, PMID: 25071197
- Vincent M**, Collet C, Verloes A, Lambert L, Herlin C, Blanchet C, Sanchez E, Drunat S, Vigneron J, Laplanche JL, Puechberty J, Sarda P, Geneviève D. 2014. Large deletions encompassing the TCOF1 and CAMK2A genes are responsible for Treacher Collins syndrome with intellectual disability. *European journal of human genetics : EJHG* **22**:52–56. DOI: <https://doi.org/10.1038/ejhg.2013.98>, PMID: 23695276

- Voehringer D**, Liang HE, Locksley RM. 2008. Homeostasis and effector function of lymphopenia-induced "memory-like" T cells in constitutively T cell-depleted mice. *The Journal of Immunology* **180**:4742–4753. DOI: <https://doi.org/10.4049/jimmunol.180.7.4742>, PMID: 18354198
- Wang F**, Flanagan J, Su N, Wang LC, Bui S, Nielson A, Wu X, Vo HT, Ma XJ, Luo Y. 2012. RNAscope: a novel in situ RNA analysis platform for formalin-fixed, paraffin-embedded tissues. *The Journal of Molecular Diagnostics* : **JMD** **14**:22–29. DOI: <https://doi.org/10.1016/j.jmoldx.2011.08.002>, PMID: 22166544
- Weisman O**, Feldman R, Burg-Malki M, Keren M, Geva R, Diesendruck G, Gothelf D. 2017. Comparing the broad socio-cognitive profile of youth with williams syndrome and 22q11.2 deletion syndrome. *Journal of Intellectual Disability Research* **61**:1083–1093. DOI: <https://doi.org/10.1111/jir.12424>, PMID: 28990288
- Yao Y**, Minor PJ, Zhao YT, Jeong Y, Pani AM, King AN, Symmons O, Gan L, Cardoso WV, Spitz F, Lowe CJ, Epstein DJ. 2016. Cis-regulatory architecture of a brain signaling center predates the origin of chordates. *Nature Genetics* **48**:575–580. DOI: <https://doi.org/10.1038/ng.3542>, PMID: 27064252
- Young NM**, Hu D, Lainoff AJ, Smith FJ, Diaz R, Tucker AS, Trainor PA, Schneider RA, Hallgrímsson B, Marcucio RS. 2014. Embryonic bauplans and the developmental origins of facial diversity and constraint. *Development* **141**:1059–1063. DOI: <https://doi.org/10.1242/dev.099994>, PMID: 24550113
- Yu K**, McGlynn S, Matise MP. 2013. Floor plate-derived sonic hedgehog regulates glial and ependymal cell fates in the developing spinal cord. *Development* **140**:1594–1604. DOI: <https://doi.org/10.1242/dev.090845>, PMID: 23482494
- Zagorski M**, Tabata Y, Brandenberg N, Lutolf MP, Tkačik G, Bollenbach T, Briscoe J, Kicheva A. 2017. Decoding of position in the developing neural tube from antiparallel morphogen gradients. *Science* **356**:1379–1383. DOI: <https://doi.org/10.1126/science.aam5887>, PMID: 28663499
- Zeng L**, Kempf H, Murtaugh LC, Sato ME, Lassar AB. 2002. Shh establishes an Nkx3.2/Sox9 autoregulatory loop that is maintained by BMP signals to induce somitic chondrogenesis. *Genes & Development* **16**:1990–2005. DOI: <https://doi.org/10.1101/gad.1008002>, PMID: 12154128

Unique morphogenetic signatures define mammalian neck muscles and associated connective tissues

Eglantine Heude^{1,2}, Marketa Tesarova³, Elizabeth M Sefton⁴, Estelle Jullian⁵, Noritaka Adachi⁵, Alexandre Grimaldi^{1,2}, Tomas Zikmund³, Jozef Kaiser³, Gabrielle Kardon⁴, Robert G Kelly⁵, Shahragim Tajbakhsh^{1,2*}

¹Department of Developmental and Stem Cell Biology, Institut Pasteur, Paris, France; ²CNRS UMR 3738, Paris, France; ³Central European Institute of Technology, Brno University of Technology, Brno, Czech Republic; ⁴Department of Human Genetics, University of Utah, Salt Lake City, United States; ⁵Aix-Marseille Université, CNRS UMR 7288, IBDM, Marseille, France

Abstract In vertebrates, head and trunk muscles develop from different mesodermal populations and are regulated by distinct genetic networks. Neck muscles at the head-trunk interface remain poorly defined due to their complex morphogenesis and dual mesodermal origins. Here, we use genetically modified mice to establish a 3D model that integrates regulatory genes, cell populations and morphogenetic events that define this transition zone. We show that the evolutionarily conserved cucullaris-derived muscles originate from posterior cardiopharyngeal mesoderm, not lateral plate mesoderm, and we define new boundaries for neural crest and mesodermal contributions to neck connective tissue. Furthermore, lineage studies and functional analysis of *Tbx1*- and *Pax3*-null mice reveal a unique developmental program for somitic neck muscles that is distinct from that of somitic trunk muscles. Our findings unveil the embryological and developmental requirements underlying tetrapod neck myogenesis and provide a blueprint to investigate how muscle subsets are selectively affected in some human myopathies.

DOI: <https://doi.org/10.7554/eLife.40179.001>

Competing interests: The authors declare that no competing interests exist.

Funding: See page 20

Received: 17 July 2018

Accepted: 17 November 2018

Published: 19 November 2018

Reviewing editor: Clare Blackburn, MRC Centre for Regenerative Medicine, University of Edinburgh, United Kingdom

© Copyright Heude et al. This article is distributed under the terms of the [Creative Commons Attribution License](https://creativecommons.org/licenses/by/4.0/), which permits unrestricted use and redistribution provided that the original author and source are credited.

Introduction

The neck is composed of approximately 80 skeletal muscles in humans that allow head mobility, respiration, swallowing and vocalization processes, containing essential elements such as the trachea, esophagus, larynx, and cervical vertebrae. These processes are ensured by a robust network of muscles at the head-trunk interface, a transition zone subjected to a spectrum of human muscle diseases such as dropped head syndrome, oculopharyngeal myopathy, myotonic dystrophy, Duchenne-type dystrophy and congenital muscular disorders (*Emery, 2002; Martin et al., 2011; Randolph and Pavlath, 2015*). Defining the embryology of these distinct muscle groups is critical to understand the mechanisms underlying the susceptibility of specific muscles to muscular dystrophies. While myogenesis at the cranial and trunk levels has been studied extensively, the developmental mechanisms at the basis of neck muscle formation are poorly documented and often debated (*Ericsson et al., 2013*).

In vertebrates, head and trunk muscles arise from different mesodermal origins and their development depends on distinct myogenic programs. At the cranial level, the cardiopharyngeal mesoderm (CPM) resides in pharyngeal arches and gives rise to branchiomeric muscles and the second heart field. CPM specification is initiated by the activation of genes such as *Mesp1*, *Islet1* and *Tbx1*, while *Pax7* subsequently marks muscle stem cells (*Diogo et al., 2015; Kelly et al., 2004; Nathan et al.,*

2008; Saga et al., 1996; Sambasivan et al., 2009). In contrast, *Pax3* and *Pax7* are expressed in somitic mesoderm giving rise to trunk and limb muscles, with *Pax3* then being downregulated in most muscles during fetal stages, while *Pax7* maintains the stem cell pool (Kassar-Duchossoy et al., 2005; Relaix et al., 2005; Tajbakhsh et al., 1997). After the differential specification of cranial and trunk progenitors, the bHLH myogenic regulatory factors (MRFs) Myf5, Mrf4, Myod and Myog regulate myogenic cell fate and differentiation (reviewed in [Comai and Tajbakhsh, 2014; Noden and Francis-West, 2006]).

In early embryos, *Tbx1* is required for robust activation of MRF genes and proper branchiomic muscle formation (Grifone et al., 2008; Kelly et al., 2004; Kong et al., 2014; Sambasivan et al., 2009). In *Tbx1* mutant embryos, the first pharyngeal arch is hypoplastic and posterior pharyngeal arches do not form resulting in variably penetrant defects of masticatory muscles and absence of muscles derived from more posterior arches (Kelly et al., 2004; Lescroart et al., 2015; Theis et al., 2010). In humans, *TBX1* is a major gene involved in 22q11.2 deletion syndrome (DiGeorge/velo-cardio-facial syndrome), a congenital disease characterized by cardiovascular defects and craniofacial malformations (Papangeli and Scambler, 2013). In contrast, *Pax3* acts upstream of MRF genes in somites and *Pax3* mutants have defects of epaxial and hypaxial muscle formation while double *Pax3/Pax7*-null embryos lack trunk/limb muscles (Brown et al., 2005; Relaix et al., 2005; Tajbakhsh et al., 1997; Tremblay et al., 1998).

The neck constitutes a transition zone characterizing land vertebrates (tetrapods). The major muscle groups in the neck consist of: epaxial back muscles; ventral hypaxial musculature; pharyngeal, laryngeal and esophagus striated muscles located medioventrally; and cucullaris-derived muscles. The cucullaris is a generic term defining putative homologous muscles that are evolutionarily conserved and connect the head and trunk in jawed vertebrates (gnathostomes). In amniotes, the cucullaris represents the embryonic anlage that gives rise to trapezius and sternocleidomastoid muscles which are innervated by the accessory nerve XI (Diogo, 2010; Edgeworth, 1935; Ericsson et al., 2013; Kuratani, 2008; Kuratani et al., 2018; Lubosch, 1938; Tada and Kuratani, 2015).

While the somitic origin of epaxial/hypaxial neck muscles and CPM origin of pharyngeal, laryngeal and esophagus striated muscles are well defined (Gopalakrishnan et al., 2015; Noden, 1983; Tabler et al., 2017), the embryological origin of cucullaris-derived muscles has remained a subject of controversy (Couly et al., 1993; Edgeworth, 1935; Greil, 1913; Huang et al., 1997; Huang et al., 2000; Matsuoka et al., 2005; Noden, 1983; Piatt, 1938; Piekarski and Olsson, 2007). This muscle group was reported to originate either from lateral plate mesoderm (LPM) or CPM populations adjacent to the first three somites in chick and axolotl (Nagashima et al., 2016; Sefton et al., 2016; Theis et al., 2010). However, retrospective lineage analysis indicated that the murine trapezius and sternocleidomastoid muscles are clonally related to second heart-field-derived myocardium and laryngeal muscles, consistent with a CPM origin (Lescroart et al., 2015). Moreover, cucullaris development follows a branchiomic program and cucullaris-derived muscles were shown to be absent in *Tbx1*-null mice (Kelly et al., 2004; Lescroart et al., 2015; Sefton et al., 2016; Theis et al., 2010). Nevertheless, the source of the cucullaris is still equivocal due to the location of its embryonic anlagen at the interface of cranial, somitic and lateral plate mesodermal populations.

Skeletal elements and muscle-associated connective tissue (MCT) also have distinct embryological origins along the rostro-caudal axis. The connective tissue of branchiomic and tongue muscles originate from neural crest cells (NCCs) of cranial origin (Evans and Noden, 2006; Köntges and Lumsden, 1996; Noden, 1983; Noden, 1988; Ziermann et al., 2018b). Cranial NCCs also give rise to skeletal components and tendons in the head. In contrast, the skeleton and connective tissue originate from somitic mesoderm in the trunk and from LPM in limbs (Nassari et al., 2017). The neck and shoulder girdle contain skeletal elements and connective tissues of distinct NCC, LPM or somitic origins (Durland et al., 2008; Matsuoka et al., 2005; McGonnell et al., 2001; Nagashima et al., 2016; Tabler et al., 2017; Valasek et al., 2010). It has been suggested that NCCs form both connective tissue and endochondral cells at the attachment sites of neck muscles to shoulders in mouse (Matsuoka et al., 2005). However, studies in non-mammalian animals have contested a NCC contribution to the pectoral girdle (Epperlein et al., 2012; Kague et al., 2012; Ponomartsev et al., 2017).

Therefore, the neck region consists of muscle, skeletal and connective tissue elements of mixed cellular origins, underscoring the difficulty in assigning embryonic identities for these structures. In addition, the genetic requirements for the formation of non-somitic and somitic neck muscles remain

to be defined. To resolve these issues, we used genetic lineage and loss-of-function mice combined with histology, μ CT and 3D reconstructions to map the embryological origins of all neck muscles and associated connective tissues. In doing so, we show that cucullaris-derived muscles originate from a posterior CPM population and are differentially affected in *Tbx1*-null mice. Moreover, we identify a unique genetic network involving both *Mesp1* and *Pax3* genes for somite-derived neck muscles and we define a new limit of neural crest contribution to neck connective tissue and shoulder components.

Results

Distinct myogenic programs define neck muscle morphogenesis

To investigate the embryological origin of neck muscles in the mouse, we mapped CPM- and somite-derived myogenic cells using lineage-specific *Cre* drivers including *Mef2c-AHF*, *Islet1*, *Mesp1* and *Pax3* (Figure 1). The *Mef2c-AHF* (anterior heart field) enhancer is activated in the second heart field and myogenic progenitors of CPM origin (Lescroart et al., 2010; Verzi et al., 2005). *Islet1* and *Mesp1* genes are both expressed in early CPM and are essential for cardiac development. The *Mesp1* lineage also marks some anterior somitic derivatives (Cai et al., 2003; Harel et al., 2009; Saga et al., 2000; Saga et al., 1999). In contrast, *Pax3* is activated in all somitic progenitors and is a key actor during trunk and limb muscle formation (Relaix et al., 2005; Tajbakhsh et al., 1997; Tremblay et al., 1998). Given that the majority of *Mef2c-AHF* derivatives are myogenic cells (Lescroart et al., 2015; Lescroart et al., 2010; Verzi et al., 2005), we analyzed this lineage using *Rosa26^{R-lacZ/+}* (*R26R*) reporter mice. *Islet1*, *Mesp1* and *Pax3* genes are also expressed in cells contributing to skeletal components, connective tissues or neurons. To focus on the myogenic lineage, we used *Pax7^{nGFP-stop/nlacZ}* (*Pax7^{GPL}*) reporter mice, which mark cells with nuclear β -galactosidase (β -gal) activity following *Cre* recombination (Sambasivan et al., 2013).

We first examined embryos after myogenic specification (E10.5 and E11.75), and fetuses when muscles are patterned (E18.5). In *Mef2c-AHF^{Cre};R26R* embryos, β -gal-positive cells were observed in the mesodermal core of pharyngeal arches at the origin of branchiomeric muscles, in second heart field derivatives, and in the cucullaris anlage (Figure 1A,E). A spatiotemporal analysis of the cucullaris using *Myf5^{Cre};Pax7^{GPL}* and *Myf5^{Cre};R26^{mTmG}* embryos (Figure 1—figure supplement 1) showed that *Myf5*-derived muscle progenitors located at the level of the posterior pharyngeal arches, and adjacent to somites S1-S3 (Figure 1—figure supplement 1A'), were innervated by the accessory nerve XI (Figure 1—figure supplement 1G-G'). These cells gave rise to the trapezius and sternocleidomastoid muscles (Figure 1—figure supplement 1A-F') thus confirming the identity of the cucullaris anlage in mouse (Tada and Kuratani, 2015).

In *Islet1^{Cre};Pax7^{GPL}* and *Mesp1^{Cre};Pax7^{GPL}* embryos, labeling was also observed in pharyngeal arch derivatives and the cucullaris (Figure 1B-C,F-G), the latter showing less contribution from the *Islet1* lineage. On sections, a subset of the Myod-positive cells in the cucullaris originated from *Islet1*-derived cells (Figure 1—figure supplement 2A). Surprisingly, *Pax3^{Cre};Pax7^{GPL}* embryos also showed *lacZ* expression in the cucullaris at E11.75, although no expression was detected at E10.5 (Figure 1D,H). Given that *Pax3* and *Pax7* are also expressed in neural crest cells (Relaix et al., 2004), and that these *Pax3/Pax7*-derived cells were excluded from the Myod-positive myogenic population at E12.5 after muscle specification (Figure 1—figure supplement 2B), they are likely to be of NCC origin. As expected, *Pax3* lineage tracing also labeled the somite-derived myotomes, hypaxial migrating progenitors that form the hypoglossal cord (origin of tongue and infrahyoid muscles), and limb muscle progenitors. Furthermore, the hypaxial anlage, which is located at the proximal limb bud and gives rise to the cutaneous maximus and latissimus dorsi muscles, was *Pax3*-derived (Figure 1D,H; Figure 1—figure supplement 1D') (Prunotto et al., 2004; Tremblay et al., 1998). Unexpectedly, this anlage and the latissimus dorsi muscle were also labeled in *Islet1^{Cre};Pax7^{GPL}* but not in *Mesp1^{Cre};Pax7^{GPL}* embryos (Figure 1F-G,J-K). On sections at E12.5, *Islet1* expression was observed in *Pax3*-derived cells after the emergence of myogenic cells from the proximal limb bud (Figure 1—figure supplement 2C). In addition, the *Mesp1* lineage contributed to anterior somitic derivatives during early embryonic development as previously reported (Loebel et al., 2012; Saga et al., 1999); strong *lacZ* expression was observed in the hypoglossal

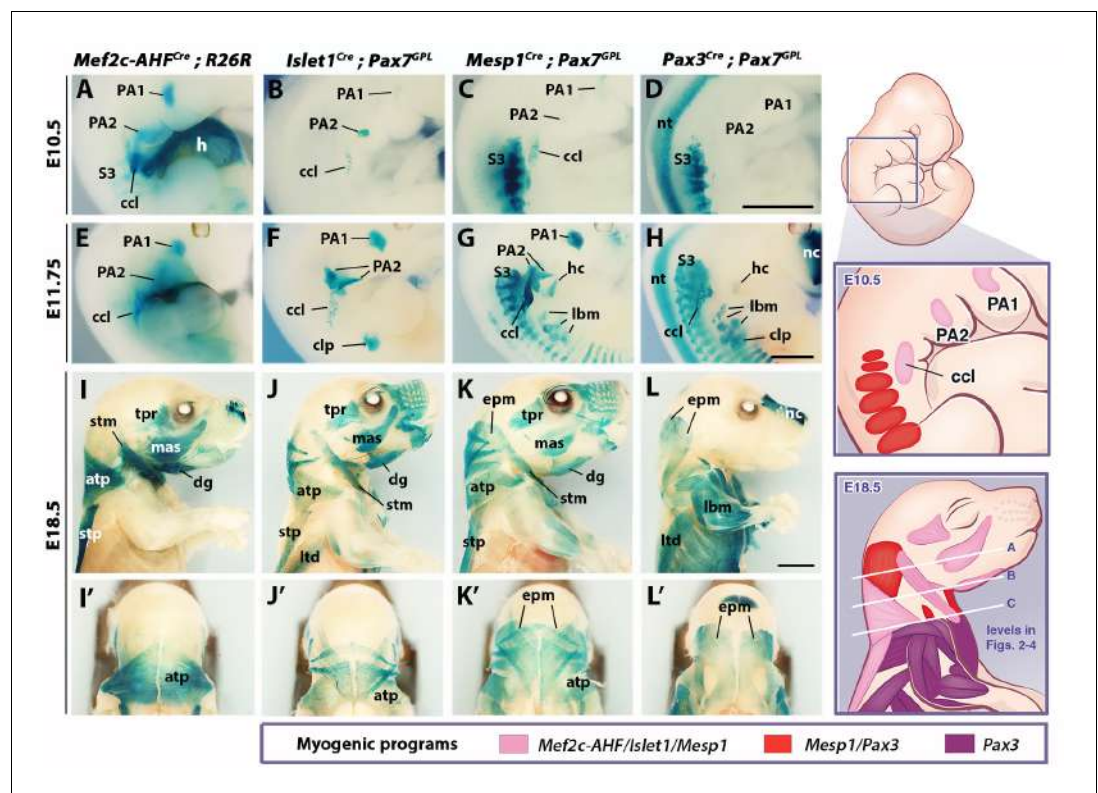


Figure 1. Genetic lineage tracing of neck muscle progenitors. Whole-mount X-gal stainings of *Mef2c-AHF^{Cre}; R26R*, *Islet1^{Cre}; Pax7^{GFP}*, *Mesp1^{Cre}; Pax7^{GFP}* and *Pax3^{Cre}; Pax7^{GFP}* mice at E10.5 (A–D), E11.75 (E–H) and E18.5 (I–L') (n = 3 for each condition). See associated **Figure 1—supplements 1–3**. (A–H) Note labeling of mesodermal core of pharyngeal arches (PAs) and cucullaris anlage (ccl) by *Mef2c-AHF*, *Islet1* and *Mesp1* lineage reporters; β -gal⁺ cells in anterior somites of *Mesp1^{Cre}* embryos and in the *clp* anlagen of *Islet1^{Cre}* embryos. *Pax3* lineage marked somitic mesoderm. (I–L') *Mef2c-AHF*, *Islet1* and *Mesp1* lineages marked branchiomeric (mas, tpr, dg) and cucullaris muscles (stm, atp and stp). *Pax3^{Cre}* and *Mesp1^{Cre}* labeled somitic epaxial neck muscles (epm) and cucullaris anlage; ccl, cucullaris anlage; clp, cutaneous maximus/latissimus dorsi precursor; dg, digastric; epm, epaxial musculature; h, heart; hc, hypoglossal cord; lbm, limb muscle anlagen and limb muscles; ltd, latissimus dorsi; mas, masseter; nc, nasal capsule; nt, neural tube; PA1–2, pharyngeal arches 1–2; S3, somite 3; stm, sternocleidomastoid; stp, spinothrapezius; tpr, temporal. Scale bars: in D for A–D and in H for E–H, 1000 μ m; in L for I–L', 2000 μ m.

DOI: <https://doi.org/10.7554/eLife.40179.002>

The following figure supplements are available for figure 1:

Figure supplement 1. Ontogenetic analysis of *Myf5* muscle progenitors at the head-trunk interface.

DOI: <https://doi.org/10.7554/eLife.40179.003>

Figure supplement 2. *Mef2c-AHF*, *Islet1*, *Mesp1* and *Pax3* lineage tracings using *lacZ* reporters.

DOI: <https://doi.org/10.7554/eLife.40179.004>

Figure supplement 3. *Mesp1* and *Pax3* lineage tracings in somitic neck muscles using the *Pax7^{GFP}* reporter.

DOI: <https://doi.org/10.7554/eLife.40179.005>

cord and somites S1–S6. Labeling decreased in more posterior myotomes and in forelimb muscle progenitors compared to *Pax3^{Cre}; Pax7^{GFP}* embryos (**Figure 1C–D,G–H**).

Lineage tracings with *Mef2c-AHF^{Cre}*, *Islet1^{Cre}* and *Mesp1^{Cre}* marked branchiomeric (temporal, masseter, digastric, mylohyoid and pharyngeal) and cucullaris-derived neck muscles (acromiortrapezius, spinothrapezius and sternocleidomastoid), all of which were excluded from the *Pax3* lineage (**Figure 1I–L**, **Figure 1—figure supplement 2D–G**). These findings support previous studies showing that cucullaris muscle development is controlled by a branchiomeric myogenic program (Kelly et al., 2004; Lescroart et al., 2015; Sefton et al., 2016; Theis et al., 2010). In addition, both

Mesp1 and *Pax3* lineages labeled somitic neck muscles (**Figure 1K–L'**, **Figure 1—figure supplement 2F–G'**).

Analysis of different somite-derived neck muscles on sections showed that *Mesp1* and *Pax3* lineages gave rise to the great majority of the Pax7-positive myogenic population (**Figure 1—figure supplement 3**), demonstrating the high recombination efficiency obtained with the *Cre* lines. The results indicate that neck somitic muscles originate from myogenic cells that have expressed both *Mesp1* and *Pax3* genes.

To further investigate the contributions of *Mesp1* and *Pax3* lineages to neck muscles, we examined sections using the *R26^{tdTomato}* reporter co-immunostained with the myofibre marker Tnnt3 at three representative levels (A, B and C levels in **Figure 1**; see also **Figure 2—figure supplement 1**). At anterior levels, while *Pax3* lineage contribution was limited to somite-derived neck muscles, the *Mesp1* lineage marked branchiomic muscles (mylohyoid, pharyngeal, laryngeal, esophagus), cucullaris-derived muscles (acromiotrapezius and sternocleidomastoid) and somite-derived neck muscles (**Figure 2A–H**, **Figure 1—figure supplement 2F–G'**, **Figure 2—figure supplement 2A–H'**). The epaxial and hypaxial neck muscles showed equivalent Tomato expression in both *Mesp1^{Cre};R26^{tdTomato}* and *Pax3^{Cre};R26^{tdTomato}* mice. These observations further indicate that *Mesp1* and *Pax3* lineages contribute equivalently to neck muscles derived from anterior somites.

At the shoulder level, we observed less *Mesp1* contribution to more posterior somitic muscles (**Figure 2I–J**). In contrast to that observed at anterior levels, little or no Tomato expression was detected in myofibres of scapular muscles in *Mesp1^{Cre};R26^{tdTomato}* mice (**Figure 2—figure supplement 2I–J'**). Therefore, *Mesp1* lineage contribution was restricted to epaxial and hypaxial neck muscles, in contrast to pectoral and trunk muscles that originate from the *Pax3* lineage (**Figures 1–2**) (**Table 1**). These observations lead us to propose that three distinct myogenic programs are involved in the formation of neck and pectoral musculature at the head-trunk interface. The branchiomic and cucullaris-derived muscles depend on a common myogenic program involving *Mef2c-AHF*, *Islet1* and *Mesp1* lineages; the somitic neck muscles that originate from anterior somites derive from both *Mesp1* and *Pax3* lineages; the pectoral muscles derived from more posterior somites depend on the activation of *Pax3* only (**Table 1**).

Dual neural crest and mesodermal origins of neck connective tissues

To define the cellular origin of neck muscle-associated connective tissue (MCT), we traced the contribution of different embryonic populations using *Mesp1^{Cre};R26^{tdTomato}* and *Pax3^{Cre};R26^{tdTomato}* mice as well as *Wnt1^{Cre}* and *Prx1^{Cre}* reporters that label NCC and postcranial LPM derivatives, respectively (**Burke and Nowicki, 2003**; **Danielian et al., 1998**; **Durland et al., 2008**). Both NCC and LPM populations were reported to contribute to trapezius MCT (**Durland et al., 2008**; **Matsuoka et al., 2005**). Moreover, it was suggested that the postcranial LPM is a source for cucullaris-derived muscles (**Theis et al., 2010**). A direct comparison of NCC and LPM derivatives allowed us to clarify the contribution of these two populations to cucullaris formation (**Figures 3–4**).

We first investigated the distribution of neck muscles and NCCs using *Myf5^{nlacZ/+}*, *Mef2c-AHF^{Cre};R26R*, *Pax3^{Cre};R26R* and *Wnt1^{Cre};R26R* embryos (**Figure 3—figure supplement 1**). At E10.5, the cucullaris anlage was positioned at the level of posterior pharyngeal arches where *Wnt1*-derived positive cells were detectable (**Figure 1A–C**, **Figure 1—figure supplement 1A'**, **Figure 3—figure supplement 1A–B**). Subsequently, the cucullaris progenitors expanded caudally from E11.5 to E13.5. The posterior limit of the cranial NCC domain also extended posteriorly; however, the *Wnt1*-labeled cells did not cover the posterior portion of cucullaris-derived muscles (**Figure 3—figure supplement 1C–H**). At E14.5, the acromiotrapezius and spinotrapezius attained their definitive position in *Myf5^{nlacZ/+}* and *Mef2c-AHF^{Cre};R26R* embryos (**Figure 3—figure supplement 1I–J**). *Wnt1*-derived cells were observed in the anterior acromiotrapezius muscle, but not in the spinotrapezius that was situated in a *Pax3*-derived domain (**Figure 3—figure supplement 1K–L**). Analysis of whole-mount embryos indicated that the cranial NCCs did not contribute to connective tissue of posterior cucullaris derivatives, in contrast to what was reported previously (**Matsuoka et al., 2005**).

To further analyze NCC contribution to the cervical region at the cellular level, we performed immunostainings on sections for Tomato and Tnnt3 in E18.5 *Wnt1^{Cre};R26^{tdTomato}* fetuses (**Figure 3**, **Figure 3—figure supplement 2**). Given that the *Wnt1* lineage is a source of both neuronal and connective tissue derivatives, we associated Tomato immunostaining with Tuj1 that marks neuronal cells and with Tcf4 that labels MCT fibroblasts (**Figure 3**, **Figure 3—figure supplements 2–3**). At the

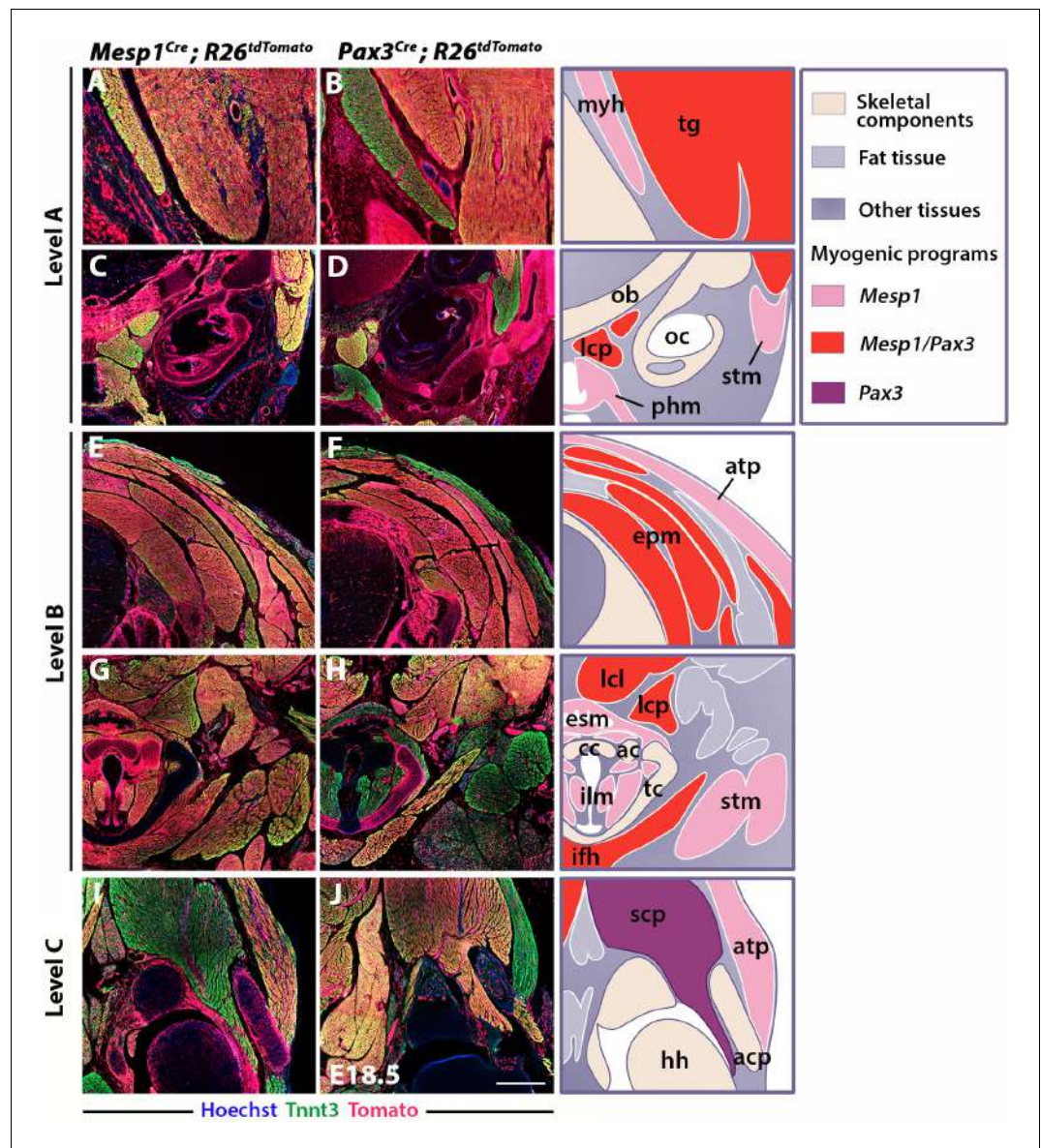


Figure 2. Differential contributions of *Mesp1* and *Pax3* lineages to neck and shoulders. Immunostainings on coronal cryosections of E18.5 *Mesp1^{Cre};R26^{tdTomato}* and *Pax3^{Cre};R26^{tdTomato}* mice for the myofibre Tntt3 and Tomato markers at levels indicated in **Figure 1**. Higher magnifications of selected areas in (A–J) are shown in **Figure 2—figure supplement 2**; (n = 2 for each condition). See also the atlas of neck musculature in **Figure 2—figure supplement 1**. (A–H) *Mesp1^{Cre}* labeled all neck muscles including branchiomeric (myh, esm, phm and ilm), cucullaris (stm, atp), somitic epaxial (epm) and hypaxial (tg, lcp, lcl, ifh) muscles. *Pax3^{Cre}* marked somitic muscles. (I–J) At shoulder level, *Mesp1*-derived cells did not contribute to posterior somitic myofibres including scapular muscles (scp) compared to that observed in *Pax3^{Cre}* embryos. ac, arytenoid cartilage; acp, scapular acromion process; atp, acromiotrapezius; cc, cricoid cartilage; epm, epaxial musculature; esm, esophagus striated muscle; hh, humeral head; ifh, infrahyoid muscles; ilm, intrinsic laryngeal muscles; lcl, longus colli; lcp, longus capitis; myh, mylohyoid; ob, occipital bone; oc, otic capsule; phm, pharyngeal muscles; stm, sternocleidomastoid; scp, scapular musculature; tc, thyroid cartilage; tg, tongue. Scale bars: in J for A–B 200 μ m, for C–J 400 μ m.

DOI: <https://doi.org/10.7554/eLife.40179.006>

The following figure supplements are available for figure 2:

Figure supplement 1. Atlas of neck musculature in mouse.

DOI: <https://doi.org/10.7554/eLife.40179.007>

Figure supplement 2. *Mesp1* and *Pax3* lineage contributions to neck and shoulder muscles.

DOI: <https://doi.org/10.7554/eLife.40179.008>

Table 1. Contribution of *Mef2c-AHF*, *Islet1*, *Mesp1* and *Pax3* lineages to neck and pectoral musculature.

<i>Mef2c/Islet1/Mesp1</i> -derived muscles	<i>Mesp1/Pax3</i> -derived muscles	<i>Pax3</i> -derived muscles
Mylohyoid Digastric muscles	Epaxial neck muscles (splenius, semispinalis, levator scapula, rhomboid occipitalis, suboccipital and postvertebral muscles)	Scapular muscles (supraspinatus, Infraspinatus, subscapularis)
Pharyngeal muscles Intrinsic laryngeal muscles Esophagus striated muscle	Hypaxial neck muscles (tongue muscles*, infrahyoid muscles, longus capitis, longus colli)	Pectoralis Latissimus dorsi [†] Cutaneous maximus [†]
Sternocleidomastoid Acromiotrapezius Spinotrapezius		
Branchiomic myogenic program	Anterior-most somite myogenic program	More posterior somite myogenic program

*Including intrinsic and extrinsic tongue muscles of somitic origin

[†]Also derived from an *Islet1* lineage

DOI: <https://doi.org/10.7554/eLife.40179.009>

cranial level, the MCT of branchiomic (masseter, mylohyoid), tongue and acromiotrapezius muscles was derived from *Wnt1*- and *Pax3*-lineages but not from the mesodermal *Mesp1* lineage (**Figure 3—figure supplement 2A–B'**, **Figure 3—figure supplement 3A,F**, **Figure 3—figure supplement 4A–D,G**). The acromiotrapezius showed a high contribution from *Wnt1*-derived cells while the underlying epaxial muscles had considerably less labeled cells that were limited to the neuronal Tuj1-positive population (**Figure 3A–A'**). The *Wnt1* lineage gave rise to Tcf4-positive fibroblasts in the acromiotrapezius, but not in epaxial neck muscles, where fibroblasts were derived from the *Mesp1* lineage (**Figure 3—figure supplements 3B–C** and **4E**). These observations are in accordance with a NCC origin of branchiomic, anterior trapezius and tongue connective tissue as reported previously (**Matsuoka et al., 2005**).

However, the NCC contribution to connective tissue in the sternocleidomastoid subset of cucullaris-derived muscles appeared more heterogeneous than that observed in the acromiotrapezius. In rodents, the sternocleidomastoid is composed of three individual muscles (cleidomastoid, sternomastoid and cleido-occipitalis portions); a differential NCC contribution to MCT was observed in these muscles. While *Wnt1*-derived NCCs were widely present in the sternomastoid and cleido-occipitalis, the NCC contribution was limited in the cleidomastoid (**Figure 3B–B'**). Indeed, Tcf4-positive fibroblasts in the cleido-occipitalis originated from the *Wnt1* lineage, whereas the majority of MCT fibroblasts in the cleidomastoid were derived from the *Mesp1* lineage (**Figure 3—figure supplements 3D–E** and **4F**).

A differential contribution of NCCs to connective tissue was also seen within the laryngeal and infrahyoid musculature. Extensive *Wnt1* lineage contributions to MCT was observed in laryngeal muscles (thyroarytenoid and cricothyroid) that connect to the thyroid cartilage, which is of NCC origin (**Figure 3C–C'**) (**Tabler et al., 2017**). In contrast, the laryngeal muscles (cricoarytenoid and vocal muscles) that link mesoderm-derived laryngeal cartilages (cricoid, arytenoid and medio-caudal portion of the thyroid) did not contain NCC-derived connective tissue (**Figures 2G–H** and **3C–C'**) (**Tabler et al., 2017**). In these muscles, the *Wnt1*-derived cells were neuronal, as observed in the esophagus, whereas the MCT fibroblasts were derived from the *Mesp1* lineage (**Figure 3C–C'**, **Figure 3—figure supplements 2D–D'** and **4H**). As another example, *Wnt1*-derived cells contributed to a greater extent to MCT in infrahyoid muscles (thyrohyoid muscles) that connect the hyoid and thyroid cartilage that are of NCC origin, compared to infrahyoid muscles (omohyoid and sternohyoid muscles) that link posteriorly pectoral structures of mesodermal origin (**Figure 3—figure supplement 2C,C', H**; **Figure 3—figure supplement 3G–H**). These observations suggest that MCT composition within laryngeal and infrahyoid muscles correlates in part with the embryonic origin of the skeletal components to which they attach (**Figure 2G–H**, **Figure 3C–C'**, **Figure 3—figure supplement 2C–C', H**).

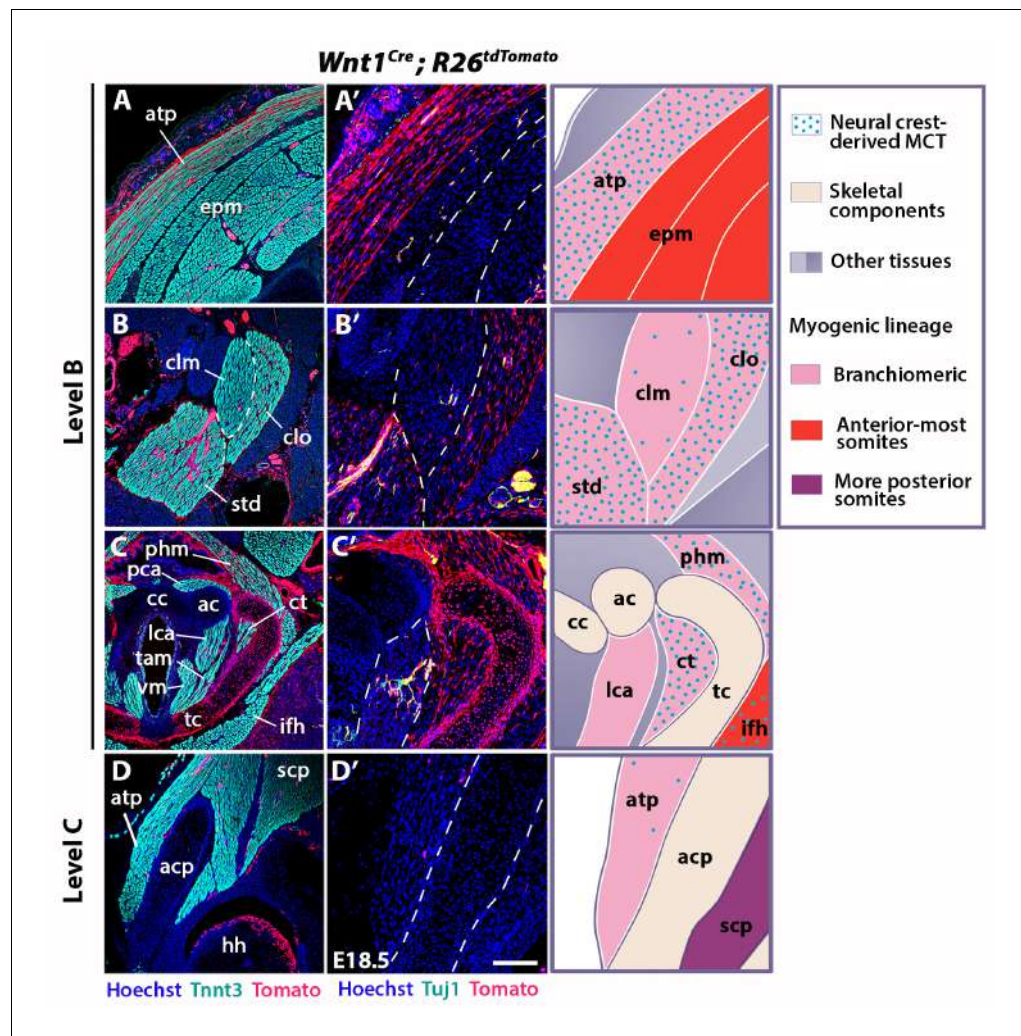


Figure 3. Neural crest contribution to neck muscle-associated tissue. Immunostainings on coronal cryosections of E18.5 *Wnt1^{Cre};R26^{tdTomato}* mice at levels indicated in **Figure 1**. Tnnt3/Tomato immunostainings are shown in (A–D) and immunostainings for Tuj1/Tomato on selected areas of (A–D) are shown with higher magnifications in (A'–D'). See associated **Figure 3—figure supplement 1–4**; (n = 2). (A–A') Note high *Wnt1* contribution in the acromiotrapezius but not in epaxial muscles where *Wnt1*-derived cells marked neuronal cells. (B–C') *Wnt1*-derived cells marked differentially the distinct muscles composing the sternocleidomastoid and laryngeal musculatures. (D–D') At shoulder level, the *Wnt1* cells did not contribute to attachment of acromiotrapezius to scapula. ac, arytenoid cartilage; acp, scapular acromion process; atp, acromiotrapezius; cc, cricoid cartilage; clm, cleidomastoid; clo, cleido-occipitalis; ct, cricothyroid; epm, epaxial musculature; hh, humeral head; ifh, infrahyoid muscles; lca, lateral cricoarytenoid; MCT, muscle-associated connective tissue; pca, posterior cricoarytenoid; phm, pharyngeal muscles; scp, scapular musculature; std, sternomastoid; tam, thyroarytenoid muscle; tc, thyroid cartilage; vm, vocal muscle. Scale bars: in D' for A–D 400 μ m for A'–D' 200 μ m.

DOI: <https://doi.org/10.7554/eLife.40179.010>

The following figure supplements are available for figure 3:

Figure supplement 1. Distribution of developing neck muscles and neural crest cells.

DOI: <https://doi.org/10.7554/eLife.40179.011>

Figure supplement 2. Neural crest contribution to neck and pectoral structures.

DOI: <https://doi.org/10.7554/eLife.40179.012>

Figure supplement 3. *Wnt1* lineage contribution to connective tissue fibroblasts.

DOI: <https://doi.org/10.7554/eLife.40179.013>

Figure supplement 4. Contribution of *Pax3* and *Mesp1* lineages to connective tissue fibroblasts.

DOI: <https://doi.org/10.7554/eLife.40179.014>

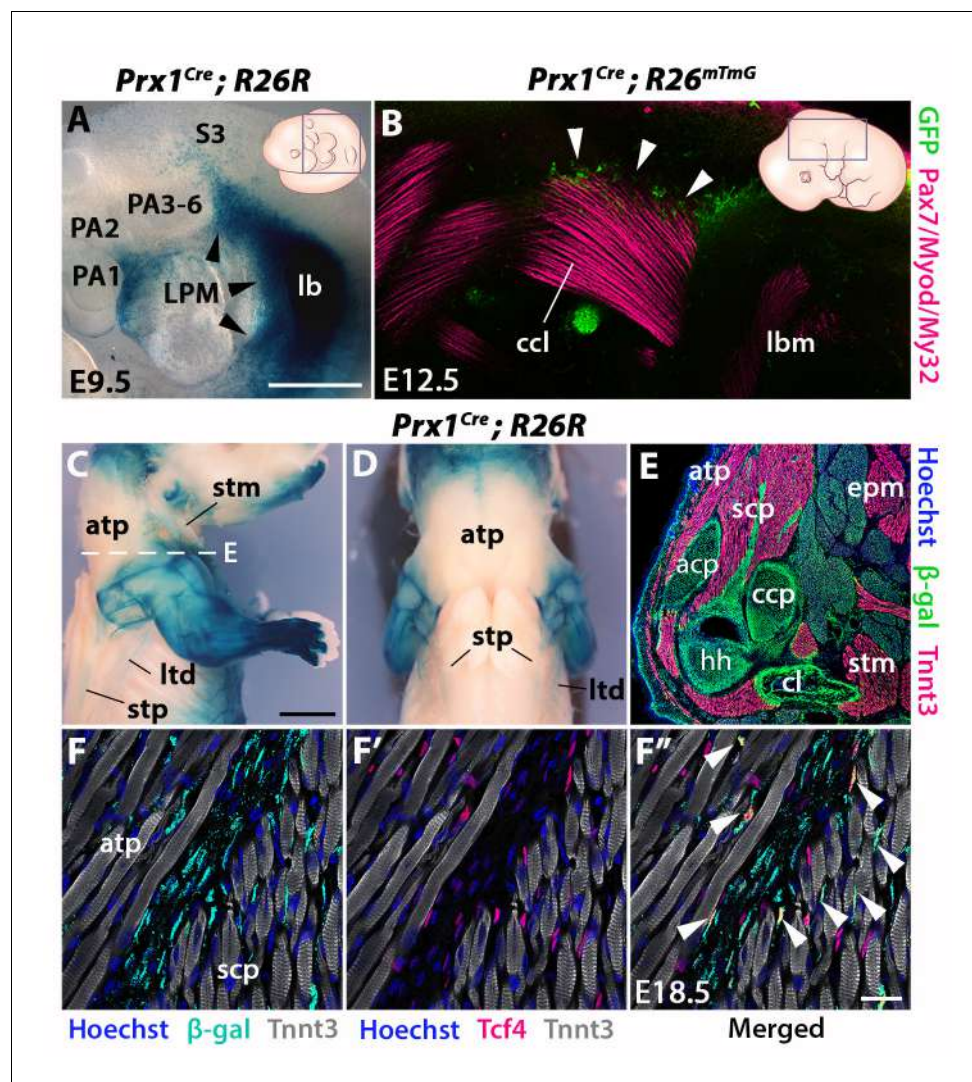


Figure 4. *Prx1*-LPM lineage contribution to neck and pectoral girdle. See also **Figure 4—figure supplement 1, 2.** (A–D) X-gal stainings of *Prx1^{Cre};R26R* reporter mice at E9.5 (n = 3) (A) and E18.5 (n = 3) (C–D), and immunostaining for GFP and the Pax7/Myod/My32 myogenic markers in *Prx1^{Cre};R26^{mTmG}* E12.5 embryo (n = 2) (B). Note *Prx1*-derived cells in postcranial LPM (A, black arrowheads) and *Prx1*-derived cells among, but not in, cucullaris myofibres (B–D). (E–F'') Immunostaining for β -gal, Tnnt3 and Tcf4 on coronal cryosections of E18.5 *Prx1^{Cre};R26R* mice (n = 2) showed β -gal⁺ cells constituting the pectoral girdle (E, level C in **Figure 1**) and in MCT fibroblasts (F–F'', white arrowheads), but not in trapezius myofibres. acp, scapular acromion process; atp, acromiotrapezius; ccl, cucullaris anlage; ccp, scapular coracoid process; cl, clavicle; epm, epaxial musculature; hh, humeral head; lb, forelimb bud; lbm, limb muscle anlagen; LPM, lateral plate mesoderm; ltd, latissimus dorsi; PA1–6, pharyngeal arches 1–6; S3, somite 3; scp, scapular muscles; stm, sternocleidomastoid; stp, spinotrapezius. Scale bars: in A for A, B 500 μ m; in C for C–D 2000 μ m, for E 500 μ m; in F'' for F–F'' 20 μ m.

DOI: <https://doi.org/10.7554/eLife.40179.015>

The following figure supplements are available for figure 4:

Figure supplement 1. Comparison of the *Myf5* and *Prx1* lineage tracings.

DOI: <https://doi.org/10.7554/eLife.40179.016>

Figure supplement 2. *Prx1* lineage contribution to neck and limbs.

DOI: <https://doi.org/10.7554/eLife.40179.017>

Given our findings that connective tissues of neck muscles have differential contributions of NCC and mesodermal populations, we analyzed the caudal connections of the cucullaris-derived muscles to the pectoral girdle (**Figure 3D**, **Figure 3—figure supplement 2E–H**). The acromiotrapezius

attaches dorsally to the nuchal ligament and ventrally to the scapular acromion process in continuity with the scapular spine. While *Wnt1*-derived cells were present dorsally (**Figure 3A**, **Figure 3—figure supplement 2E**), this contribution diminished gradually and was undetectable at the insertion on the scapula (**Figure 3D–D'**, **Figure 3—figure supplement 2F**). Similarly, the sternocleidomastoid muscle showed limited NCC contribution to the attachment sites of the clavicle and sternum (**Figure 3—figure supplement 2G–H**). In contrast to what was previously described (*Matsuoka et al., 2005*), we did not observe NCC contribution to the shoulder endochondral tissue nor to the nuchal ligament (**Figure 3—figure supplement 2E–H**). Taken together, these observations define a novel boundary for neural crest contribution to neck/pectoral components. The posterior contribution limit of neural crest to branchiomic MCT occurs at the level of laryngeal muscles that connect to NCC skeletal derivatives. Moreover, NCCs do not participate in connecting posterior cucullaris and infrahyoid muscles to their skeletal elements.

To assess the cellular origin of cucullaris connective tissue at posterior attachment sites, we next traced the contribution of lateral plate mesoderm (LPM) to the neck/shoulder region using *Prx1^{Cre}* reporter mice (*Durland et al., 2008*; *Logan et al., 2002*) (**Figure 4**, **Figure 4—figure supplements 1–2**). Analysis of E9.5 embryos showed that *Prx1*-derived cells contribute to the forelimb bud and cells adjacent to the anterior-most somites, but not to pharyngeal arches (**Figure 4A**). At E12.5, the postcranial *Prx1*-derived domain clearly defined the lateral somitic frontier along the rostrocaudal axis (*Durland et al., 2008*) and did not include the cucullaris anlage (**Figure 4—figure supplement 1**, white arrowheads). Whole-mount immunostainings for the myogenic markers Pax7/Myod/My32 and for GFP in *Prx1^{Cre};R26^{mTmG}* embryos showed that *Prx1*-derived cells were present in the dorsal part of the cucullaris but did not contribute to myofibres (**Figure 4B**, white arrowheads). At E18.5, the *Prx1* lineage marked the limb, scapular and abdominal regions, whereas only a few *Prx1*-derived cells were detected in the cucullaris-derived sternocleidomastoid, acromiotrapezius and spinotrapezius muscles (**Figure 4C–D**). On sections, immunostaining for β -gal and Tnnt3 showed that *Prx1*-derived LPM contributed to limb/shoulder MCT and to skeletal components of the pectoral girdle (**Figure 4E**, **Figure 4—figure supplement 2A–B**). In contrast, fewer *Prx1*-derived cells were detected in the acromiotrapezius and little or no contribution was observed in the epaxial muscles (**Figure 4E**, **Figure 4—figure supplement 2B–C**). In addition, only a limited number of *Prx1*-derived cells gave rise to Tcf4-positive fibroblasts in the trapezius muscles, but they contributed more extensively to the fibroblast population in scapular muscles (**Figure 4F–F''**, white arrowheads, **Figure 4—figure supplement 2D–D''**). Notably, β -gal expression for this lineage was not detected in trapezius myofibres thereby confirming the results obtained at E12.5 (**Figure 4B–F''**, **Figure 4—figure supplements 1–2**).

Therefore, these observations reveal a dual NCC/LPM origin of trapezius connective tissue, with a decrease of NCC contribution at posterior attachment sites. Moreover, our analysis shows that the postcranial LPM does not give rise to cucullaris myofibres in contrast to what was suggested previously (*Theis et al., 2010*), thus providing further evidence for a branchiomic origin of the cucullaris.

Divergent functions of *Tbx1* and *Pax3* in neck development

Given the key role for *Tbx1* and *Pax3* genes in the specification of the CPM and somites respectively, we analyzed the effect of inactivation of these genes on neck muscle formation, compared to the muscle phenotypes observed at cranial and trunk levels.

Analysis has been performed by immunostainings on sections and 3D reconstructions of the neck and pectoral girdle using high-resolution micro-computed tomographic (μ CT) scans of control, *Tbx1^{-/-}* and *Pax3^{-/-}* fetuses (**Figures 5–6**).

In the early embryo, *Tbx1* is expressed in pharyngeal mesoderm and is required for proper branchiomic muscle formation (*Grifone et al., 2008*; *Kelly et al., 2004*). While *Tbx1* is expressed in other cranial populations including the pharyngeal ectoderm and endoderm (*Arnold et al., 2006*; *Huynh et al., 2007*), the gene is known to be required cell autonomously during CPM myogenesis (*Kong et al., 2014*; *Zhang et al., 2006*). Analysis of *Tbx1* mutants revealed unexpected features in cucullaris and hypaxial neck muscle formation. As previously described (*Gopalakrishnan et al., 2015*; *Kelly et al., 2004*), anterior branchiomic muscles (digastric and mylohyoid) showed phenotypic variations, whereas posterior branchiomic muscles (esophagus and intrinsic laryngeal muscles) and the acromiotrapezius were severely affected or undetectable (**Figure 5B,E,H**;

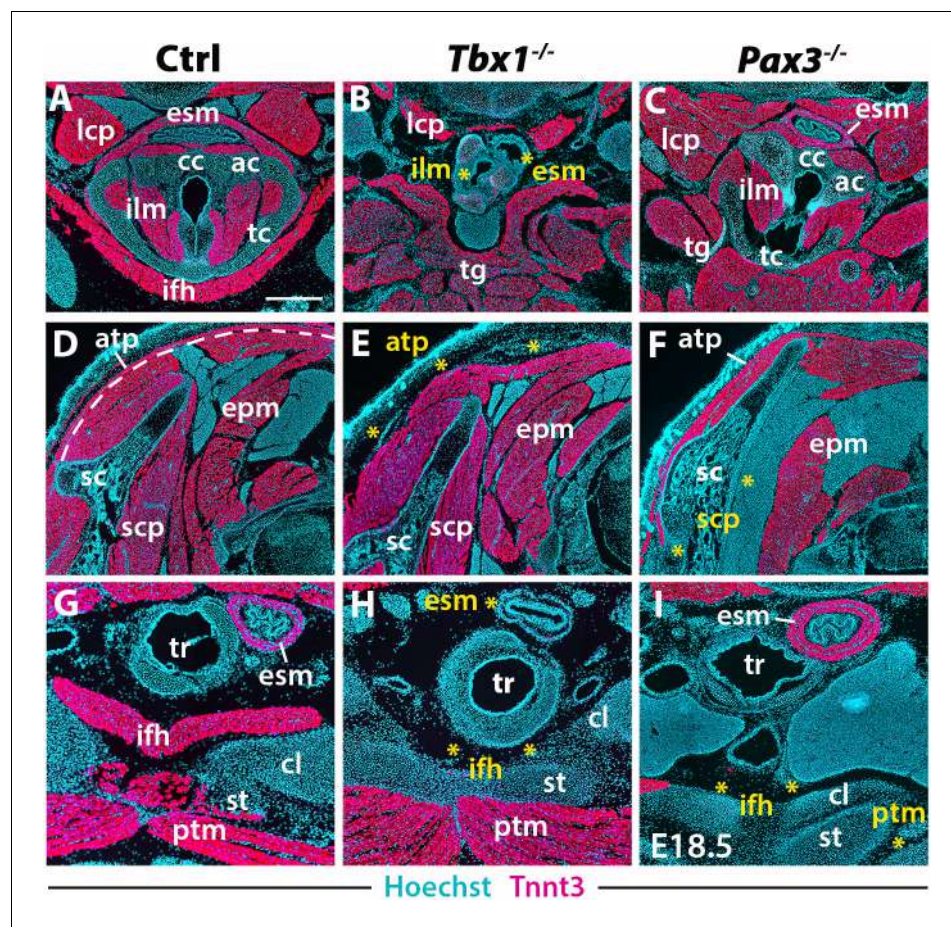


Figure 5. Neck muscle phenotypes in *Tbx1* and *Pax3* mutants. (A–I) Immunostainings for Tnnt3 on coronal cryosections of control, *Tbx1*-null and *Pax3*-null fetuses at E18.5 (n = 3 each condition). Yellow asterisks indicate missing muscles. Note absence of branchiomeric laryngeal (ilm), esophagus (esm) and trapezius (atp) muscles and severe alteration of somitic infrahyoid muscles (ifh) in *Tbx1* mutants. Scapular (scp) and pectoral (ptm) muscles are missing in *Pax3* mutants. ac, arytenoid cartilage; atp, acromiotrapezium; cc, cricoid cartilage; cl, clavicle; epm, epaxial musculature; esm, esophagus striated muscle; ifh, infrahyoid muscles; ilm, intrinsic laryngeal muscles; lcp, longus capitis; ptm, pectoralis muscles; sc, scapula; scp, scapular muscles; st, sternum; tc, thyroid cartilage; tg, tongue. Scale bars: in A for A–I 500 μ m.

DOI: <https://doi.org/10.7554/eLife.40179.018>

Figure 6B) (Table 2). However, detailed examination of the cucullaris-derived muscles revealed a heterogeneous dependence on *Tbx1* function that was not reported previously (Lescoart et al., 2015; Theis et al., 2010). Unexpectedly, the sternocleidomastoid muscle was present bilaterally but smaller (Figure 6B); the different portions (cleido-occipitalis, cleidomastoid and sternomastoid) were unilaterally or bilaterally affected in a stochastic manner. Moreover, while the epaxial neck and scapular muscles were unaffected (Figure 5E, Figure 6E–H), the hypaxial neck muscles derived from anterior somites were altered. Indeed, the tongue and longus capitis were reduced and the infrahyoid and longus colli muscles were severely affected or undetectable (Figure 5B,H, Figure 6E,H; see interactive 3D PDFs in Supplementary file 1–2).

Analysis of *Pax3* mutants showed that the neck and pectoral muscles were differentially affected. As expected, branchiomeric and epaxial muscles developed normally but displayed morphological differences adapted to malformations noted in some skeletal components (Figure 5C,F; Figure 6C, I). However, whereas hypaxial trunk/limb muscles were severely affected or undetectable in *Pax3* mutants (Figure 5F,I; Figure 6F,I) (Tajbakhsh et al., 1997; Tremblay et al., 1998), surprisingly the majority of hypaxial neck muscles derived from both *Mesp1* and *Pax3* lineages were present. Tongue muscles were reduced in size but patterned, the infrahyoid were hypoplastic, whereas the longus

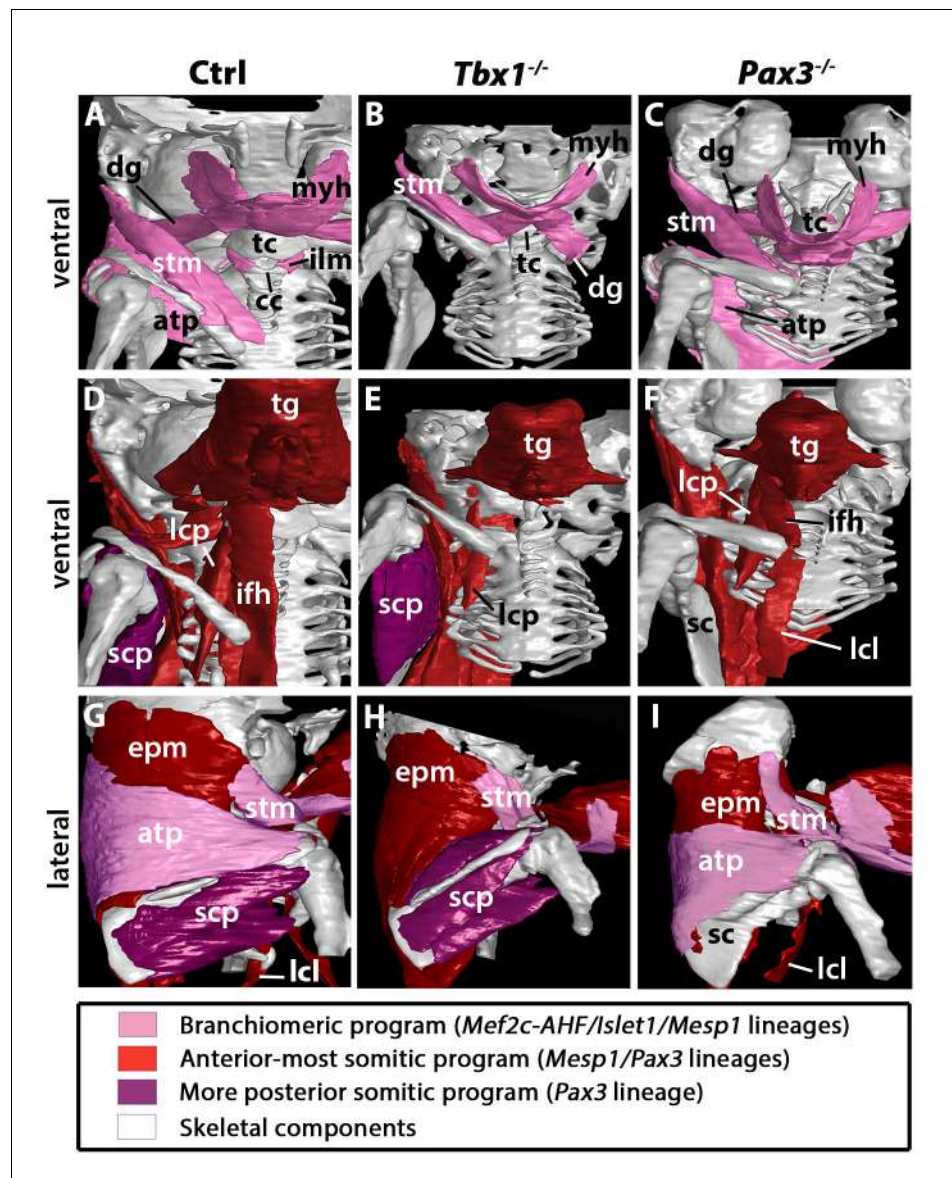


Figure 6. 3D reconstructions of neck musculoskeletal system in *Tbx1* and *Pax3* mutants. See interactive 3D PDFs in **Supplementary file 1–3**; control n = 1; mutants n = 2. (A–C) Branchiomic and cucullaris-derived muscles marked by *Mef2c-AHF/Islet1/Mesp1* lineages are indicated in pink. (D–F) Anterior somitic muscles (*Mesp1*, *Pax3* lineages), in red. (G–I) Scapular muscles from more posterior somites (*Pax3* lineage), in violet. atp, acromiotrapezius; cc, cricoid cartilage; dg, digastric muscles; epm, epaxial musculature; ifh, infrahyoid muscles; ilm, intrinsic laryngeal muscles; lcl, longus colli; lcp, longus capitis; myh, mylohyoid; sc, scapula; scp, scapular muscles; stm, sternocleidomastoid; tc, thyroid cartilage; tg, tongue.

DOI: <https://doi.org/10.7554/eLife.40179.019>

capitis and longus colli were unaffected (**Figure 5C**; **Figure 6F,I**; see interactive 3D PDF in **Supplementary file 3**). The phenotypes of the different muscle groups observed in *Tbx1* and *Pax3* mutants are summarized in **Table 2** (see also **Figure 7—figure supplement 1**).

Taken together, these observations revealed that hypaxial muscles in the neck were less affected in *Pax3* mutants than more posterior hypaxial muscles, pointing to distinct requirements for *Pax3* function during neck and trunk muscle formation. In addition, *Tbx1* mutants exhibited more severe phenotypes in hypaxial neck muscles, thus highlighting distinct roles for this gene in branchiomic and hypaxial neck myogenesis.

Table 2. Summary of the neck muscle phenotype observed in *Tbx1*- and *Pax3*-null fetuses.

	<i>Tbx1</i> -null	<i>Pax3</i> -null
Branchiomeric muscles (<i>Mef2c-AHF/Islet1/Mesp1</i> lineage)		
Mylohyoid	+/-	++
Digastric muscles	+/-	++
Intrinsic laryngeal muscles	–	+
Esophagus striated muscle	–	++
Sternocleidomastoid	+/-	+
Acromiotrapezius	–	+
Anterior-most somite muscles (<i>Mesp1/Pax3</i> lineage)		
Epaxial musculature	++	+
Longus capitis	+/-	++
Longus colli	–	++
Infrahyoid muscles	–	+/-
Tongue muscles*	+	+
More posterior somite muscles (<i>Pax3</i> lineage)		
Scapular muscles	++	–
Pectoralis	++	–

++, normal; +, altered morphology; +/-, affected; –, severely affected or undetectable

*Including intrinsic and extrinsic tongue muscles of somitic origin

DOI: <https://doi.org/10.7554/eLife.40179.020>

Discussion

The embryological origins of neck muscles and connective tissues at the head-trunk interface have been poorly defined largely due to their localization at a transition zone that involves multiple embryonic populations. Using a combination of complementary genetically modified mice and 3D analysis that identifies muscles in the context of their bone attachments, we provide a detailed map of neck tissue morphogenesis and reveal some unexpected features regarding the muscle and connective tissue network.

Branchiomeric origin of cucullaris-derived muscles

The mammalian neck consists of somitic epaxial/hypaxial muscles, branchiomeric muscles and cucullaris-derived muscles (**Table 1**). The latter constitute a major innovation in vertebrate history, connecting the head to the pectoral girdle in gnathostomes and allowing head mobility in tetrapods (**Ericsson et al., 2013**). Recent studies in different organisms including shark, lungfish and amphibians suggest that the cucullaris develops in series with posterior branchial muscles and that its developmental origin and innervation is conserved among gnathostomes (**Diogo, 2010; Ericsson et al., 2013; Naumann et al., 2017; Noda et al., 2017; Sefton et al., 2016; Tada and Kuratani, 2015; Ziermann et al., 2018a; Ziermann et al., 2017**). However, multiple embryological origins including CPM, LPM and somites have been reported for the cucullaris, underscoring the difficulty in deciphering the morphogenesis of this and other muscles in the head-trunk transition zone (**Huang et al., 2000; Nagashima et al., 2016; Sefton et al., 2016; Theis et al., 2010**).

Our study shows that the cucullaris anlage is innervated by the accessory nerve XI and develops contiguously with the mesodermal core of posterior arches and anterior-most somites 1–3. Our lineage analysis reveals that cucullaris development depends on a branchiomeric myogenic program involving *Mef2c-AHF*, *Islet1* and *Mesp1* lineages in keeping with previous results (**Table 1**) (**Lescroart et al., 2015; Sefton et al., 2016; Theis et al., 2010**). However, our detailed functional analysis and 3D reconstructions lead us to modify the view of the genetic requirements of cucullaris-derived muscles (**Lescroart et al., 2015; Theis et al., 2010**). Notably, these muscles are differentially affected in *Tbx1*-null fetuses; the acromiotrapezius does not form while the sternocleidomastoid is present but reduced. Therefore, *Tbx1* is differentially required for sternocleidomastoid and trapezius formation, suggesting that distinct subprograms regulate cucullaris development.

We also demonstrate that the cucullaris anlage is excluded from the postcranial *Prx1*-derived expression domain, which delineates the trunk LPM field (**Figure 4**). The *Prx1* lineage instead gives rise to connective tissue, thereby excluding a contribution from LPM to cucullaris-derived myofibres. Thus, our results, combined with innervation studies, retrospective clonal analyses and grafting experiments in chick and axolotl (**Lescroart et al., 2015; Nagashima et al., 2016; Sefton et al.,**

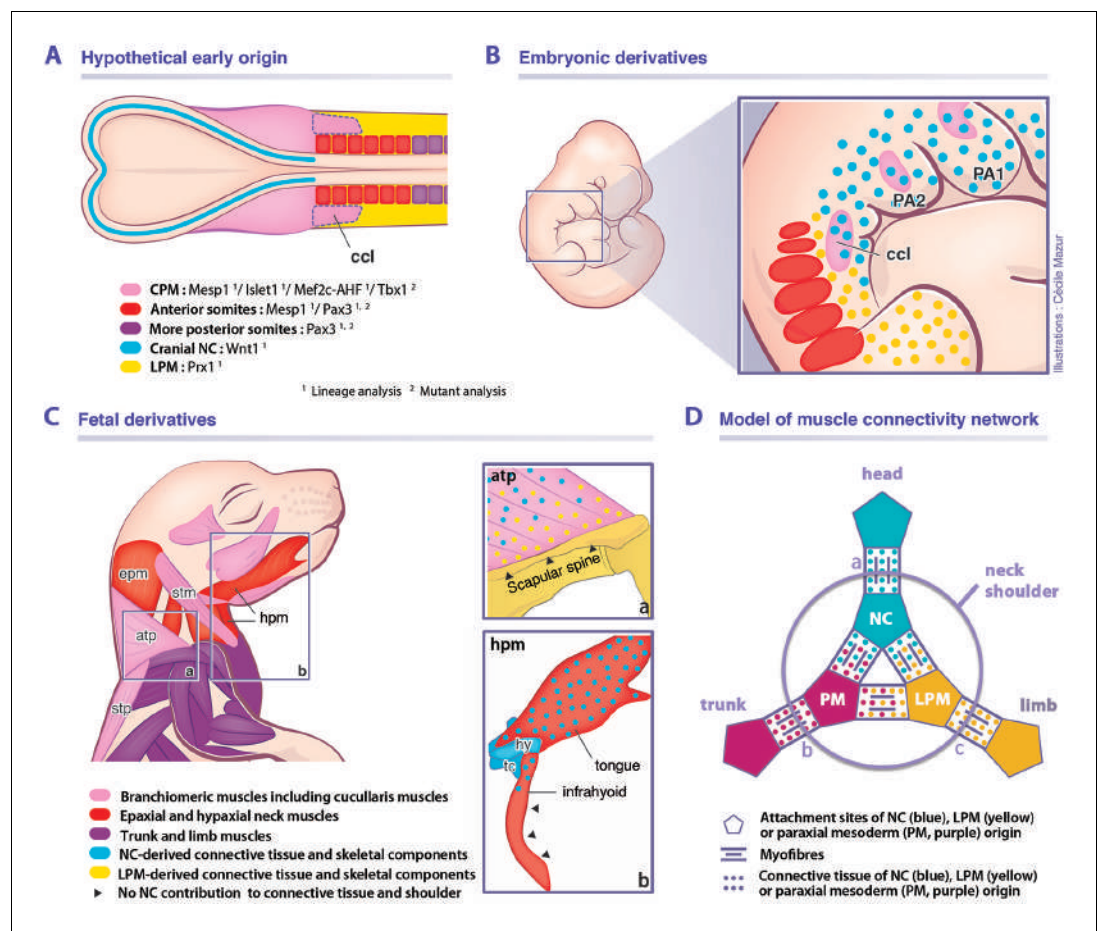


Figure 7. Model for musculoskeletal and connective tissue relationships during murine neck development. See also **Figure 7—figure supplement 1**. (A, C) CPM (pink), anterior somites (red) and more posterior somites (violet) muscles are defined by three distinct myogenic programs. (B) Note that the cucullaris develops in a NC domain (blue dots), but is excluded from the postcranial LPM (yellow dots). (C) Dual NC/LPM origin of trapezius connective tissue is indicated in (a). NC contribution to connective tissue extends to tongue and anterior infrahyoid musculature (b). (D) Mixed origins of muscle connective tissues at the head-trunk-limb interface. Example of representative muscles: (a) masseter, (b) spinalis dorsi, (c) deltoid. atp, acromiotrapezius; ccl, cucullaris; CPM, cardiopharyngeal mesoderm; epm, epaxial neck musculature; hpm, hypaxial neck musculature; hy, hyoid bone; LPM, postcranial lateral plate mesoderm; NC, neural crest; PA1-2, pharyngeal arches 1–2; PM, paraxial mesoderm; stm, sternocleidomastoid; stp, spinotrapezius; tc, thyroid cartilage.

DOI: <https://doi.org/10.7554/eLife.40179.021>

The following figure supplement is available for figure 7:

Figure supplement 1. Muscles affected in *Tbx1* and *Pax3* mutants.

DOI: <https://doi.org/10.7554/eLife.40179.022>

2016; Tada and Kuratani, 2015), suggest that the postcranial extension of the CPM lateral to the first three somites in tetrapod embryos is a source of cucullaris myogenic cells (**Figure 7A**). The discordance with previous studies regarding the origin of the cucullaris is likely due to its proximity to both anterior somites and LPM (**Figure 7A–B**), and consequently, to potential contamination of embryonic sources in grafting experiments (Couly et al., 1993; Huang et al., 1997; Huang et al., 2000; Noden, 1983; Piekarski and Olsson, 2007; Theis et al., 2010).

A unique genetic program for somite-derived neck muscles

Our study also points to a unique *Mesp1/Pax3* genetic program in anterior somites for epaxial/hypaxial neck muscle formation (**Table 1**). While it was shown that the *Mesp1* lineage gives rise to tongue muscles (Harel et al., 2009), we demonstrate that it also contributes to all neck muscles. In

chordates, *Mesp* genes appear to play a conserved role in cardiogenesis and axis segmentation. In mouse, *Mesp1* inactivation causes early embryonic death from abnormal heart development, and *Mesp1/Mesp2* double-knockout embryos lack non-axial mesoderm (Moreno et al., 2008; Saga, 1998; Saga et al., 2000; Satou et al., 2004; Sawada et al., 2000). During early murine development, *Mesp1* shows two waves of activation; initially in the nascent mesoderm destined for extra-embryonic, cranial and cardiac mesoderm at the onset of gastrulation; later during somitogenesis, transient *Mesp1* expression is limited to anterior presomitic mesoderm (Saga, 1998; Saga et al., 1996; Saga et al., 2000; Saga et al., 1999). Our lineage analysis shows that *Mesp1* extensively labels the anterior mesoderm, including the CPM and anterior somites 1–6, while contribution decreases in more posterior somites (Figure 1) (Loebel et al., 2012; Saga et al., 2000; Saga et al., 1999). Previous fate mapping experiments have shown that the mesoderm of late-streak stage embryos contributes to both CPM and anterior somites (Parameswaran and Tam, 1995). It appears that the first wave of *Mesp1* expression defines not only the CPM field but also includes the mesoderm destined for anterior somites. In contrast, the *Mesp1*-labeled cells observed in more posterior somites using the sensitive *Pax7^{GPL}* reporter may result from the transient wave of *Mesp1* expression in the presomitic mesoderm during axis segmentation. Furthermore, we show that *Mesp1*-derived anterior somites give rise to all epaxial/hypaxial neck muscles in contrast to trunk/limb muscles originating from more posterior somites marked by *Pax3*. The boundary of *Mesp1* lineage contribution to muscles corresponds to the neck/pectoral interface. Our findings indicate that the anterior somitic mesoderm employs a specific transition program for neck muscle formation involving both *Mesp1* and *Pax3* genes implicated in CPM and somitic myogenesis, respectively (Figure 7A–C).

Whereas little is known about the function of *Mesp* genes in chordates, there is evidence that *Mesp1* might be differentially required during anterior versus posterior somitic formation. In mouse, different *Mesp1* enhancer activities have been observed between CPM/anterior somites and posterior somites indicating that the regulation of *Mesp1* expression might differ in the two embryonic compartments (Haraguchi et al., 2001). In zebrafish, quadruple mutants of *Mesp* genes (*Mesp-aa/-ab/-ba/-bb*) lack anterior somite segmentation while the positioning of posterior somite boundaries is unaffected, suggesting distinct requirements for *Mesp* genes in anterior and posterior somites (Yabe et al., 2016). Interestingly, during early ascidian development, *Mesp* is expressed in B7.5 founder cells that give rise to both CPM and anterior tail muscles (ATM) (Satou et al., 2004). In *Ciona*, the CPM precursors at the origin of heart and atrial siphon (pharyngeal) muscles depend on the ascidian homologs of *Mesp1*, *Islet1* and *Tbx1* (reviewed in [Diogo et al., 2015]), indicating that a conserved genetic network promotes chordate myogenesis in the anterior embryonic domain.

Our lineage analysis also reveals an unexpected contribution of *Islet1*-derived cells to the formation of cutaneous maximus and latissimus dorsi muscle progenitors (Table 1) (Prunotto et al., 2004; Tremblay et al., 1998). *Islet1* is activated in a subset of CPM progenitors giving rise to branchiomeric muscles and second heart field myocardium (Cai et al., 2003; Harel et al., 2009; Nathan et al., 2008). At the trunk level, while *Islet1* is widely expressed in the nervous system and in the LPM forming the hindlimb bud (Cai et al., 2003; Yang et al., 2006), to our knowledge its expression in somitic myogenic cells has not been reported. The cutaneous maximus and latissimus dorsi muscles are missing in both *Pax3* and *Met* mutants (Prunotto et al., 2004; Tajbakhsh et al., 1997; Tremblay et al., 1998). Therefore, the formation of the latissimus dorsi and cutaneous maximus muscles depends on a specific developmental program implicating *Pax3*, *Islet1* and *Met* genes. Given that the latissimus dorsi and cutaneous maximus participated in the gain in mobility of the forelimbs towards the shoulder girdle in tetrapods, our findings provide insights into their genetic and evolutionary origins.

Our detailed analysis of *Tbx1*- and *Pax3*-null mice on sections and in 3D reconstructions now provides a clarified view of neck muscle morphogenesis (Table 2). In both *Tbx1* and *Pax3* mutants, whereas the epaxial neck musculature is unaffected, the hypaxial muscles originating from anterior somites are perturbed with a more severe phenotype observed in *Tbx1* mutants (Table 2). Whereas no *Tbx1* expression has been reported in early myotomes in somites, *Tbx1* transcripts appear in hypaxial limb and tongue precursors after myogenic specification (Grifone et al., 2008; Kelly et al., 2004; Zoupa et al., 2006). *Tbx1*-null embryos show normal myotomal and limb muscle morphology while the hypoglossal cord is hypoplastic, resulting in reduced tongue musculature (Table 2) (Grifone et al., 2008; Kelly et al., 2004). Therefore, we cannot exclude the possibility that *Tbx1* is activated and plays a role after specification of neck hypaxial muscles (Okano et al., 2008;

Zoupa et al., 2006). The hypaxial muscle defects might also be secondary to a failure of caudal pharyngeal outgrowth (*Kelly et al., 2004*). While *Tbx1* acts cell autonomously in mesodermal progenitors (*Kong et al., 2014; Zhang et al., 2006*), its expression in pharyngeal endoderm might imply an indirect role in CPM myogenesis (*Arnold et al., 2006*). Defects in signaling from pharyngeal endoderm may explain the hypoglossal cord deficiency and the potential non-autonomous role for *Tbx1* in neck hypaxial myogenesis. Detailed analysis of muscle formation in conditional *Tbx1* mutants is needed to resolve the relative roles of *Tbx1* in neck myogenesis.

It has been shown that hypaxial muscles are perturbed to a greater extent than epaxial muscles in *Pax3* mutants (*Tajbakhsh et al., 1997; Tremblay et al., 1998*), suggesting a different requirement for *Pax3* in these muscle groups, possibly through differential gene regulation (*Brown et al., 2005*). An unexpected outcome of our analysis was that hypaxial neck muscles (derived from *Mesp1* and *Pax3* lineages) are less perturbed in *Pax3*-null mutants than hypaxial trunk/limb muscles (*Pax3* lineage only) that are severely altered or undetectable (**Table 2**). Our results indicate that *Pax3* is not essential for the formation of neck muscles derived from anterior somites in contrast to hypaxial muscles originating from more posterior somites. These observations support our model that a distinct genetic program governs somitic neck muscles compared to more posterior trunk muscles.

Connectivity network of the neck and shoulders

Assessing the non-muscle contribution to the neck region is a major challenge due to the extensive participation of diverse cell types from different embryological origins. Previous studies in amphibians, chick and mouse reported that branchiomeric and hypobranchial connective tissue originates from NCCs (*Hanken and Gross, 2005; Köntges and Lumsden, 1996; Matsuoka et al., 2005; Noden, 1983; Olsson et al., 2001; Ziermann et al., 2018b*). It has been shown that the neural crest provides connective tissue for muscles that link the head and shoulders, whereas mesodermal cells give rise to connective tissue for muscles connecting the trunk and limbs (*Matsuoka et al., 2005*).

Our findings demonstrate that not all branchiomeric muscles are composed of neural crest-derived connective tissue, thereby redefining a new limit for NCC contribution to the neck and shoulders. Unexpectedly, we noted that the contribution of the neural crest lineage is limited in infrahyoid and posterior branchiomeric muscles that connect skeletal components of mesodermal origin. Indeed, it appears that the connective tissue of muscles that link exclusively mesodermal skeletal derivatives is of mesodermal origin. In contrast, the connective tissue of cucullaris-derived muscles is of a mixed origin, first developing in a cranial NCC domain at early stages, then expanding to incorporate connective tissue from both neural crest and LPM populations (**Figure 7B**). While NCCs are present in the anterior acromiotrapezius, sternocleidomastoid and infrahyoid muscles, contribution gradually decreases at posterior attachment sites and is undetectable at scapular level. In parallel, the LPM gives rise to shoulder skeletal components and to connective tissue at the attachment sites of associated musculature including trapezius muscles (**Figure 7C**). Therefore, the dual NCC/LPM origin of the trapezius connective tissue correlates with the embryonic origin of skeletal components to which it is connected.

Wnt1^{Cre} and *Sox10^{Cre}* NCC reporter mice were used to show that endochondral cells connecting the cucullaris-derived muscles on the scapula, clavicle and sternum share a common NCC origin with the connective tissue (*Matsuoka et al., 2005*). However, NCCs are not found in pectoral components of fish, axolotl and chick, while contribution to neurocranium is conserved, suggesting that NCC involvement in shoulder formation would be specific to mammals (*Epperlein et al., 2012; Kague et al., 2012; Piekarski et al., 2014; Ponomartsev et al., 2017*). In contrast to this view, our lineage analysis reveals that the neural crest lineage shows limited contribution to cucullaris connective tissue and does not form endochondral cells at the posterior attachment sites (**Figure 7C**). Differences in genetic lineage tracers and reagents might explain these discordant results (*Matsuoka et al., 2005*).

Taken together, our findings indicate that the gradient of neural crest and mesodermal contributions to neck connective tissue depends on the embryonic source of attachment sites. Therefore, it reveals that connective tissue composition in the neck region correlates with the cellular origin of associated skeletal components, independently of the myogenic source or ossification mode, forming a strong link between muscles and bones of the head, trunk and limb fields (**Figure 7D**).

Evolutionary and clinical perspectives

Our findings demonstrate that the hybrid origin of the skeletal, connective tissue and muscle components of the neck is defined during early embryogenesis. The close proximity of neural crest, CPM, LPM and somitic populations is unique along the body plan and underscores the difficulty in defining their relative contributions to structures in the neck (**Figure 7A–B**). Our results refine the relative contributions of the neural crest and mesodermal derivatives in mouse, thereby providing a coherent view of embryonic components at the head-trunk interface in gnathostomes. Our study highlights the limited NCC contribution to posterior branchiomic and infrahyoid muscle connective tissue, that is instead of mesodermal origin. This reinforces recent notions suggesting that the cranial NCCs and the postcranial rearrangement of mesodermal populations at the head-trunk interface had been central for the establishment of the neck during gnathostome evolution (**Adachi et al., 2018; Kuratani et al., 2018; Lours-Calet et al., 2014; Nagashima et al., 2016; Sefton et al., 2016**). The contribution of anterior mesoderm in the origin of the neck needs to be elucidated in future studies of gnathostomes.

Our study reveals that neck muscles develop in a complex domain that is distinct from the head and trunk (**Figure 7A–D**), and that might be a contributing factor to pathologies that affect subsets of neck muscles in specific myopathies (**Emery, 2002; Randolph and Pavlath, 2015**). In human, *TBX1* has been identified as a major candidate gene for 22q11.2 deletion syndrome (**Papangeli and Scambler, 2013**). Laryngeal malformations, esophageal dysmotility and shortened neck are frequent in patients. Moreover, the neck deficiencies might not be exclusively due to cervical spine abnormalities but also to neck muscle defects (**Hamidi et al., 2014; Leopold et al., 2012; Marom et al., 2012**). Therefore, our analysis of *Tbx1*-null mutants provides a better understanding of the etiology of the 22q11.2 deletion syndrome and has direct implications in establishing clinical diagnosis in cases where patients present failure in neck-associated functions.

Materials and methods

Key resources table

Reagent type (species) or resource	Designation	Source or reference	Identifiers	Additional information
Strain, strain background (<i>Mus musculus</i>)	B6D2F1/JRj	Janvier		
Genetic reagent (<i>M. musculus</i>)	<i>Mef2c-AHF^{Cre}</i>	PMID:16188249	MGI:3639735	Dr. Brian L Black (Cardiovascular Research Institute, University of California, USA)
Genetic reagent (<i>M. musculus</i>)	<i>Islet1^{Cre}</i>	PMID:11299042	MGI:2447758	Dr. Thomas M Jessell (Howard Hughes Medical Institute, Columbia University, USA)
Genetic reagent (<i>M. musculus</i>)	<i>Mesp1^{Cre}</i>	PMID:10393122	MGI:2176467	Pr. Yumiko Saga (National Institute of Genetics, Japan)
Genetic reagent (<i>M. musculus</i>)	<i>Pax3^{Cre}</i>	PMID:22394517	MGI:3573783	Dr. Jonathan A. Epstein (Perelman School of Medicine, University of Pennsylvania, USA)
Genetic reagent (<i>M. musculus</i>)	<i>Myf5^{Cre}</i>	PMID:17418413	MGI:3710099	Dr. Mario R Capecchi (Institute of Human Genetics, University of Utah, USA)
Genetic reagent (<i>M. musculus</i>)	<i>Wnt1^{Cre}</i>	PMID:9843687	MGI:J:69326	Pr. Andrew P. McMahon (Keck School of Medicine of the University of Southern California, USA)

Continued on next page

Continued

Reagent type (species) or resource	Designation	Source or reference	Identifiers	Additional information
Genetic reagent (<i>M. musculus</i>)	<i>Prx1^{Cre}</i>	PMID:12112875	MGI: J:77872	Dr. Clifford J Tabin (Department of genetics, Harvard Medical School, USA)
Genetic reagent (<i>M. musculus</i>)	<i>Pax7^{GPL}</i>	PMID:19531352	MGI:3850147	Dr. Shahragim Tajbakhsh (Department of Developmental and Stem Cell Biology, Institut Pasteur, France)
Genetic reagent (<i>M. musculus</i>)	<i>Rosa26^{R-lacZ}</i>	PMID:9916792	MGI:1861932	Pr. Philippe Soriano (Icahn School of Medicine at Mt. Sinai, USA)
Genetic reagent (<i>M. musculus</i>)	<i>R26^{mTmG}</i>	PMID:17868096	MGI:3716464	Pr. Philippe Soriano (Icahn School of Medicine at Mt. Sinai, USA)
Genetic reagent (<i>M. musculus</i>)	<i>R26^{tdTomato}</i>	PMID:20023653	MGI:3809524	Dr. Hongkui Zeng (Allen Institute for Brain Science, USA)
Genetic reagent (<i>M. musculus</i>)	<i>Myf5^{nIacZ/+}</i>	PMID:8918877	MGI:1857973	Dr. Shahragim Tajbakhsh (Department of Developmental and Stem Cell Biology, Institut Pasteur, France)
Genetic reagent (<i>M. musculus</i>)	<i>Tbx1-null</i>	PMID:11242110	MGI:2179190	Dr. Virginia Papaioannou (Department of Genetics and Development, Columbia University Medical Center, USA)
Antibody	Chicken polyclonal anti- β -gal	Abcam	Cat. #: ab9361	IF (1:1000)
Antibody	Rabbit polyclonal anti- β -gal	MP Biomedicals	Cat. #: MP 559761	IF (1:750)
Antibody	Chicken polyclonal anti-GFP	Aves Labs	Cat. #: 1020	IF (1:500)
Antibody	Chicken polyclonal anti-GFP	Abcam	Cat. #: 13970	IF (1:1000)
Antibody	Mouse monoclonal IgG1 anti-Islet1	DSHB	Cat. #: 40.2D6	IF (1:1000)
Antibody	Mouse monoclonal IgG1 anti-My32	Sigma	Cat. #: M4276	IF (1:400)
Antibody	Mouse monoclonal IgG1 anti-Myod	Dako	Cat. #: M3512	IF (1:100)
Antibody	Mouse monoclonal IgG1 anti-Pax7	DSHB	Cat. #: AB_528428	IF (1:20)
Antibody	Rabbit polyclonal anti-Tcf4	Cell Signalling	Cat. #: C48H11	IF (1:150)
Antibody	Mouse monoclonal IgG1 anti-Tnnt3	Sigma	Cat. #: T6277	IF (1:200)
Antibody	Rabbit polyclonal anti-Tomato	Clontech	Cat. #: 632496	IF (1:500)
Antibody	Mouse monoclonal IgG2a anti-Pax7	Ozyme	Cat. #: BLE801202	IF (1:1000)
Software, algorithm	GE phoenix datosx 2.0	GE Sensing and Inspection Technologies GmbH		
Software, algorithm	3D PDF maker	SolidWorks Corporation		
Software, algorithm	Zen	Zeiss		

Continued on next page

Continued

Reagent type (species) or resource	Designation	Source or reference	Identifiers	Additional information
Chemical compound, drug	X-gal	Fisher	Cat. #: 10554973	
Chemical compound, drug	paraformaldehyde	Electron Microscopy Sciences	Cat. #: 15710	
Chemical compound, drug	Triton X-100	Sigma	Cat. #: T8787	
Chemical compound, drug	Tween 20	Sigma	Cat. #: P1379	
Chemical compound, drug	Histoclear II	National Diagnostics	Cat. #: HS-202	

Animals

Animals were handled as per European Community guidelines and the ethics committee of the Institut Pasteur (CTEA) approved protocols (APAFIS#6354–20160809 I2028839). Males carrying the Cre driver gene, *Mef2c-AHF^{Cre}* (Verzi et al., 2005), *Islet1^{Cre}* (Srinivas et al., 2001), *Mesp1^{Cre}* (Saga et al., 1999), *Pax3^{Cre}* (Engleka et al., 2005), *Myf5^{Cre}* (Haldar et al., 2007), *Wnt1^{Cre}* (Danielian et al., 1998), *Prx1^{Cre}* (Logan et al., 2002), were crossed to reporter females from previously described lines including *Pax7^{GPL}* (Sambasivan et al., 2013), *Rosa26^{R-lacZ}* (R26R) (Soriano, 1999), *R26^{mTmG}* (Muzumdar et al., 2007) and *R26^{tdTomato}* (Madisen et al., 2010). *Myf5^{nlacZ/+}* KI mice and mice carrying the *Tbx1^{tm1pa}* allele (referred to as *Tbx1*-null) were previously described (Jerome and Papaioannou, 2001; Kelly et al., 2004; Tajbakhsh et al., 1996). To generate experimental *Pax3*-null fetuses, *Pax3^{WT/Cre}* males and females were intercrossed (Engleka et al., 2005) ($n = 5$ *Tbx1* and *Pax3* mutants analysed including $n = 2$ by μ CT scanning). Mice were crossed and maintained on a B6D2F1/JRj background and genotyped by PCR. Mouse embryos and fetuses were collected between E9.5 and E18.5, with noon on the day of the vaginal plug considered as E0.5.

X-gal and immunofluorescence stainings

Whole-mount samples were analysed for beta-galactosidase activity with X-gal (0.6 mg/ml) in 1X PBS buffer (D1408, Sigma, St. Louis, MO) containing 4 mM potassium ferricyanide, 4 mM potassium ferrocyanide, 0.02% NP-40 and 2 mM MgCl₂ as previously described (Comai et al., 2014). For immunostaining on cryosections, foetuses were fixed 3 hr in 4% paraformaldehyde (PFA) (15710, Electron Microscopy Sciences, Hatfield, PA) 0.5% Triton X-100 (T8787, Sigma) at 4°C, washed overnight at 4°C in PBS 0.1% Tween 20 (P1379, Sigma), cryopreserved in 30% sucrose in PBS and embedded in OCT for 12–16 μ m sectioning with a Leica cryostat (CM3050 S, Leica, Wetzlar, Germany). Cryosections were dried for 30 min and washed in PBS. For immunostaining on paraffin sections, samples were fixed overnight in 4% PFA, dehydrated in graded ethanol series and penetrated with Histoclear II (HS-202, National Diagnostics, Atlanta, GA), embedded in paraffin and oriented in blocks. Paraffin blocks were sectioned at 10–12 μ m using a Leica microtome (Reichert-Jung 2035). Sections were then deparaffinized and rehydrated by successive immersions in Histoclear, ethanol and PBS. Samples were then subjected to antigen retrieval with 10 mM Citrate buffer (pH 6.0) using a 2100 Retriever (Aptum Biologics, Rownhams, UK).

Rehydrated sections were blocked for 1 hr in 10% normal goat serum, 3% BSA, 0.5% Triton X-100 in PBS. Primary antibodies were diluted in blocking solution and incubated overnight at 4°C. Primary antibodies included the following: β -gal (1/1000, chicken polyclonal, ab9361, Abcam, Cambridge, UK; 1/750, rabbit polyclonal, MP 559761, MP Biomedicals, Illkirch, France), GFP (1/500, chick polyclonal, 1020, Aves Labs, Tigard, OR; 1/1000, chick polyclonal, 13970, Abcam), *Islet1* (1/1000, mouse monoclonal IgG1, 40.2D6, DSHB), *My32* (1/400, mouse monoclonal IgG1, M4276, Sigma), *Myod* (1/100, mouse monoclonal IgG1, M3512, Dako, Santa Clara, CA), *Pax7* (1/20, mouse monoclonal IgG1, AB_528428), *Tcf4* (1/150, rabbit polyclonal, C48H11, Cell Signalling, Leiden, Netherlands), *Tnnt3* (1/200, monoclonal mouse IgG1, T6277, Sigma), *Tomato* (1/500, rabbit polyclonal, 632496, Clontech, Shiga, Japan; 1/250, chick polyclonal, 600-901-379, Rockland, Pottstown, PA) and *Tuj1* (1/1000, monoclonal mouse IgG2a, BLE801202, Ozyme, Montigny-le-Bretonneux, France). After 3 rounds of

15 min washes in PBS 0.1% Tween 20, secondary antibodies were incubated in blocking solution 2 hr at RT together with 1 $\mu\text{g}/\text{ml}$ Hoechst 33342 to visualize nuclei. Secondary antibodies consisted of Alexa 488, 555 or 633 goat anti-rabbit, anti-chicken or anti-mouse isotype specific (1/500, Jackson ImmunoResearch, Cambridgeshire, UK). After 3 rounds of 15 min washes in PBS 0.1% Tween 20, slides were mounted in 70% glycerol for analysis.

For whole-mount immunofluorescence staining, embryos were dissected in PBS, fixed in 4% PFA, washed in PBS and stored at -20°C in 100% methanol. After rehydration in PBS, whole mount immunostainings were performed incubating the primary and secondary antibodies for 3 days each. Samples were cleared using benzyl alcohol/benzyl benzoate (BABB) clarification method (Yokomizo *et al.*, 2012).

μCT scan analysis

For μCT scan analysis, the fetuses were treated with the phosphotungstic acid (PTA) contrast agent to well reveal skeletal and muscle structures. After dissection of the cervical region (including the mandible and scapular components, see **Figure 2—figure supplement 1**), the fetuses were fixed in 4% PFA for 24 hr at 4°C . Samples were then additionally fixed and dehydrated by exchanging the fixative and washing solutions to incrementally increasing ethanol concentrations (30%, 50%, 70%) with 2 days in each concentration to minimize the shrinkage of tissues. To start the contrasting procedure, the embryos were firstly incubated in ethanol-methanol-water mixture (4:4:3) for 1 hr and then transferred for 1 hr into 80% and 90% methanol solution. The staining procedure was then performed for 10 days in 90% methanol 1.5% PTA solution (changed every day with fresh solution) to ensure optimal penetration of the contrast agent. Staining was followed by rehydration of the samples in methanol-grade series (90%, 80%, 70%, 50% and 30%) and stored in sterile distilled water. The samples were placed in polypropylene tubes and embedded in 1% agarose gel to avoid movement artefacts during measurements. μCT scanning was performed using laboratory system GE Phoenix v|tome|x L 240 (GE Sensing and Inspection Technologies GmbH, Hamburg, Germany), equipped with a nanofocus X-ray tube with maximum power of 180 kV/15 W and a flat panel detector DXR250 with 2048×2048 pixel², 200×200 μm^2 pixel size. The μCT scan was carried out at 60 kV acceleration voltage and 200 μA tube current with voxel size of 5.7 μm for all samples. The beam was filtered by a 0.2 mm aluminium filter. The 2200 projections were taken over 360° with exposure time of 900 ms. The tomographic reconstructions were done using the software GE phoenix datos|x 2.0 (GE Sensing and Inspection Technologies GmbH) and data segmentations and visualizations were performed by combination of software VG Studio MAX 2.2 (Volume Graphics GmbH, Heidelberg, Germany) and Avizo 7.1 (Thermo Fisher Scientific, Waltham, MA) according to (Tesařová *et al.*, 2016). The interactive 3D PDFs were set up using 3D PDF maker software.

Imaging

Images were acquired using the following systems: a Zeiss Axio-plan equipped with an Apotome, a Zeiss stereo zoom microscope V16 or a Zeiss LSM 700 laser-scanning confocal microscope with ZEN software (Carl Zeiss, Oberkochen, Germany). For whole-mount rendering, acquired Z-stacks were 3D reconstructed using Imaris software. All images were assembled in Adobe Photoshop (Adobe Systems, San Jose, CA).

Acknowledgements

We thank Drs. Claudio Cortes and Françoise Helmbacher for providing transgenic mice and Mirialys Gallardo for technical assistance. We also thank Cécile Mazur for illustrations.

Additional information

Funding

Funder	Grant reference number	Author
Institut Pasteur		Eglantine Heude Alexandre Grimaldi Shahragim Tajbakhsh

Agence Nationale de la Recherche	Eglantine Heude Alexandre Grimaldi Shahragim Tajbakhsh
Centre National de la Recherche Scientifique	Eglantine Heude Estelle Jullian Noritaka Adachi Alexandre Grimaldi Robert G Kelly Shahragim Tajbakhsh
French Muscular Dystrophy Association	Eglantine Heude Alexandre Grimaldi Robert G Kelly Shahragim Tajbakhsh
Central European Institute of Technology	Marketa Tesarova Tomas Zikmund Jozef Kaiser
March of Dimes Foundation	Elizabeth M Sefton Gabrielle Kardon
National Institutes of Health	Elizabeth M Sefton Gabrielle Kardon
Fondation pour la Recherche Médicale	Estelle Jullian Noritaka Adachi Robert G Kelly
Fondation Leducq	Estelle Jullian Noritaka Adachi Robert G Kelly
Yamada Science Foundation	Noritaka Adachi Robert G Kelly
Bourses du Gouvernement Français	Noritaka Adachi
project CEITEC 2020	Marketa Tesarova Tomas Zikmund Jozef Kaiser
The Ministry of Education, Youth and Sports of the Czech Republic under the National Sustainability Programme II	Marketa Tesarova Tomas Zikmund Jozef Kaiser
CEITEC Nano Research Infrastructure MEYS CR, 2016–2019	Marketa Tesarova Tomas Zikmund Jozef Kaiser

The funders had no role in study design, data collection and interpretation, or the decision to submit the work for publication.

Author contributions

Eglantine Heude, Conceptualization, Validation, Investigation, Visualization, Methodology, Writing—original draft, Writing—review and editing; Marketa Tesarova, Resources, Data curation, Formal analysis, Investigation, Visualization, Methodology; Elizabeth M Sefton, Validation, Investigation, Writing—review and editing; Estelle Jullian, Validation, Investigation; Noritaka Adachi, Alexandre Grimaldi, Investigation, Writing—review and editing; Tomas Zikmund, Resources, Supervision; Jozef Kaiser, Resources, Supervision, Funding acquisition, Project administration; Gabrielle Kardon, Robert G Kelly, Resources, Supervision, Funding acquisition, Project administration, Writing—review and editing; Shahragim Tajbakhsh, Conceptualization, Resources, Supervision, Funding acquisition, Validation, Visualization, Methodology, Project administration, Writing—review and editing

Author ORCIDs

Elizabeth M Sefton  <http://orcid.org/0000-0001-6481-612X>

Noritaka Adachi  <http://orcid.org/0000-0002-9482-8436>

Shahragim Tajbakhsh  <http://orcid.org/0000-0003-1809-7202>

Ethics

Animal experimentation: Animals were handled as per European Community guidelines and the ethics committee of the Institut Pasteur (CTEA) approved protocols. (APAFIS#6354-20160809I2028839)

Decision letter and Author response

Decision letter <https://doi.org/10.7554/eLife.40179.028>

Author response <https://doi.org/10.7554/eLife.40179.029>

Additional files

Supplementary files

- Supplementary file 1. Interactive 3D neck reconstruction of a E18.5 control fetus. Download PDF for full details.

DOI: <https://doi.org/10.7554/eLife.40179.023>

- Supplementary file 2. Interactive 3D neck reconstruction of a E18.5 *Tbx1*-null fetus. Download PDF for full details.

DOI: <https://doi.org/10.7554/eLife.40179.024>

- Supplementary file 3. Interactive 3D neck reconstruction of a E18.5 *Pax3*-null fetus. Download PDF for full details.

DOI: <https://doi.org/10.7554/eLife.40179.025>

- Transparent reporting form

DOI: <https://doi.org/10.7554/eLife.40179.026>

Data availability

All data generated or analysed during this study are included in the manuscript and supporting files.

References

- Adachi N**, Pascual-Anaya J, Hirai T, Higuchi S, Kuratani S. 2018. Development of hypobranchial muscles with special reference to the evolution of the vertebrate neck. *Zoological Letters* **4**:5. DOI: <https://doi.org/10.1186/s40851-018-0087-x>, PMID: 29468087
- Arnold JS**, Werling U, Braunstein EM, Liao J, Nowotschin S, Edelmann W, Hebert JM, Morrow BE. 2006. Inactivation of *Tbx1* in the pharyngeal endoderm results in 22q11DS malformations. *Development* **133**:977–987. DOI: <https://doi.org/10.1242/dev.02264>, PMID: 16452092
- Brown CB**, Engleka KA, Wenning J, Min Lu M, Epstein JA. 2005. Identification of a hypaxial somite enhancer element regulating *Pax3* expression in migrating myoblasts and characterization of hypaxial muscle Cre transgenic mice. *Genesis* **41**:202–209. DOI: <https://doi.org/10.1002/gene.20116>, PMID: 15789408
- Burke AC**, Nowicki JL. 2003. A new view of patterning domains in the vertebrate mesoderm. *Developmental Cell* **4**:159–165. DOI: [https://doi.org/10.1016/S1534-5807\(03\)00033-9](https://doi.org/10.1016/S1534-5807(03)00033-9), PMID: 12586060
- Cai CL**, Liang X, Shi Y, Chu PH, Pfaff SL, Chen J, Evans S. 2003. *Isl1* identifies a cardiac progenitor population that proliferates prior to differentiation and contributes a majority of cells to the heart. *Developmental Cell* **5**:877–889. DOI: [https://doi.org/10.1016/S1534-5807\(03\)00363-0](https://doi.org/10.1016/S1534-5807(03)00363-0), PMID: 14667410
- Comai G**, Sambasivan R, Gopalakrishnan S, Tajbakhsh S. 2014. Variations in the efficiency of lineage marking and ablation confound distinctions between myogenic cell populations. *Developmental Cell* **31**:654–667. DOI: <https://doi.org/10.1016/j.devcel.2014.11.005>, PMID: 25490270
- Comai G**, Tajbakhsh S. 2014. Molecular and cellular regulation of skeletal myogenesis. *Current Topics in Developmental Biology* **110**:1–73. DOI: <https://doi.org/10.1016/B978-0-12-405943-6.00001-4>, PMID: 25248473
- Couly GF**, Coltey PM, Le Douarin NM. 1993. The triple origin of skull in higher vertebrates: a study in quail-chick chimeras. *Development* **117**:409–429. PMID: 8330517
- Danielian PS**, Muccino D, Rowitch DH, Michael SK, McMahon AP. 1998. Modification of gene activity in mouse embryos in utero by a tamoxifen-inducible form of Cre recombinase. *Current Biology* **8**:1323–S2. DOI: [https://doi.org/10.1016/S0960-9822\(07\)00562-3](https://doi.org/10.1016/S0960-9822(07)00562-3)
- Diogo RA**. 2010. *Muscles of Vertebrates - Comparative Anatomy, Evolution, Homologies and Development*. Enfield, New Hampshire: Science Publishers. DOI: <https://doi.org/10.1201/9781439845622>
- Diogo R**, Kelly RG, Christiaen L, Levine M, Ziermann JM, Molnar JL, Noden DM, Tzahor E. 2015. A new heart for a new head in vertebrate cardiopharyngeal evolution. *Nature* **520**:466–473. DOI: <https://doi.org/10.1038/nature14435>, PMID: 25903628

- Durland JL**, Sferlazzo M, Logan M, Burke AC. 2008. Visualizing the lateral somitic frontier in the Prx1Cre transgenic mouse. *Journal of Anatomy* **212**:590–602. DOI: <https://doi.org/10.1111/j.1469-7580.2008.00879.x>, PMID: 18430087
- Edgeworth FH**. 1935. *The Cranial Muscles of Vertebrates*. Cambridge University Press.
- Emery AEH**. 2002. The muscular dystrophies. *The Lancet* **359**:687–695. DOI: [https://doi.org/10.1016/S0140-6736\(02\)07815-7](https://doi.org/10.1016/S0140-6736(02)07815-7)
- Engleka KA**, Gitler AD, Zhang M, Zhou DD, High FA, Epstein JA. 2005. Insertion of Cre into the Pax3 locus creates a new allele of Splotch and identifies unexpected Pax3 derivatives. *Developmental Biology* **280**:396–406. DOI: <https://doi.org/10.1016/j.ydbio.2005.02.002>, PMID: 15882581
- Epperlein HH**, Khattak S, Knapp D, Tanaka EM, Malashichev YB. 2012. Neural crest does not contribute to the neck and shoulder in the axolotl (*Ambystoma mexicanum*). *PLOS ONE* **7**:e52244. DOI: <https://doi.org/10.1371/journal.pone.0052244>, PMID: 23300623
- Ericsson R**, Knight R, Johanson Z. 2013. Evolution and development of the vertebrate neck. *Journal of Anatomy* **222**:67–78. DOI: <https://doi.org/10.1111/j.1469-7580.2012.01530.x>, PMID: 22697305
- Evans DJ**, Noden DM. 2006. Spatial relations between avian craniofacial neural crest and paraxial mesoderm cells. *Developmental Dynamics* **235**:1310–1325. DOI: <https://doi.org/10.1002/dvdy.20663>, PMID: 16395689
- Gopalakrishnan S**, Comai G, Sambasivan R, Francou A, Kelly RG, Tajbakhsh S. 2015. A Cranial Mesoderm Origin for Esophagus Striated Muscles. *Developmental Cell* **34**:694–704. DOI: <https://doi.org/10.1016/j.devcel.2015.07.003>, PMID: 26387456
- Greil A**. 1913. Entwicklungsgeschichte des Kopfes und des Blutgefäßsystems von *Ceratodus forsteri*. II. Die epigenetischen Erwerbungen während der Stadien 39–48. Denkschr Med-Naturwiss Ges Jena. *Denkschriften Der Medicinisch-Naturwissenschaftlichen Gesellschaft Zu Jena* **9**:935–1492.
- Grifone R**, Jarry T, Dandonneau M, Grenier J, Duprez D, Kelly RG. 2008. Properties of branchiomeric and somite-derived muscle development in Tbx1 mutant embryos. *Developmental Dynamics* **237**:3071–3078. DOI: <https://doi.org/10.1002/dvdy.21718>, PMID: 18816853
- Haldar M**, Hancock JD, Coffin CM, Lessnick SL, Capecchi MR. 2007. A conditional mouse model of synovial sarcoma: insights into a myogenic origin. *Cancer Cell* **11**:375–388. DOI: <https://doi.org/10.1016/j.ccr.2007.01.016>, PMID: 17418413
- Hamidi M**, Nabi S, Husein M, Mohamed ME, Tay KY, McKillop S. 2014. Cervical spine abnormalities in 22q11.2 deletion syndrome. *The Cleft Palate-Craniofacial Journal* **51**:230–233. DOI: <https://doi.org/10.1597/12-318>, PMID: 24003836
- Hanken J**, Gross JB. 2005. Evolution of cranial development and the role of neural crest: insights from amphibians. *Journal of Anatomy* **207**:437–446. DOI: <https://doi.org/10.1111/j.1469-7580.2005.00481.x>, PMID: 16313386
- Haraguchi S**, Kitajima S, Takagi A, Takeda H, Inoue T, Saga Y. 2001. Transcriptional regulation of Mesp1 and Mesp2 genes: differential usage of enhancers during development. *Mechanisms of Development* **108**:59–69. DOI: [https://doi.org/10.1016/S0925-4773\(01\)00478-6](https://doi.org/10.1016/S0925-4773(01)00478-6), PMID: 11578861
- Harel I**, Nathan E, Tirosh-Finkel L, Zigdon H, Guimarães-Camboa N, Evans SM, Tzahor E. 2009. Distinct origins and genetic programs of head muscle satellite cells. *Developmental Cell* **16**:822–832. DOI: <https://doi.org/10.1016/j.devcel.2009.05.007>, PMID: 19531353
- Huang R**, Zhi Q, Ordahl CP, Christ B. 1997. The fate of the first avian somite. *Anatomy and Embryology* **195**:435–449. DOI: <https://doi.org/10.1007/s004290050063>, PMID: 9176666
- Huang R**, Zhi Q, Patel K, Wilting J, Christ B. 2000. Contribution of single somites to the skeleton and muscles of the occipital and cervical regions in avian embryos. *Anatomy and Embryology* **202**:375–383. DOI: <https://doi.org/10.1007/s004290000131>, PMID: 11089929
- Huynh T**, Chen L, Terrell P, Baldini A. 2007. A fate map of Tbx1 expressing cells reveals heterogeneity in the second cardiac field. *Genesis* **45**:470–475. DOI: <https://doi.org/10.1002/dvg.20317>, PMID: 17610275
- Jerome LA**, Papaioannou VE. 2001. DiGeorge syndrome phenotype in mice mutant for the T-box gene, Tbx1. *Nature Genetics* **27**:286–291. DOI: <https://doi.org/10.1038/85845>, PMID: 11242110
- Kague E**, Gallagher M, Burke S, Parsons M, Franz-Odenaal T, Fisher S. 2012. Skeletogenic fate of zebrafish cranial and trunk neural crest. *PLOS ONE* **7**:e47394. DOI: <https://doi.org/10.1371/journal.pone.0047394>, PMID: 23155370
- Kassar-Duchossoy L**, Giacone E, Gayraud-Morel B, Jory A, Gomès D, Tajbakhsh S. 2005. Pax3/Pax7 mark a novel population of primitive myogenic cells during development. *Genes & Development* **19**:1426–1431. DOI: <https://doi.org/10.1101/gad.345505>, PMID: 15964993
- Kelly RG**, Jerome-Majewska LA, Papaioannou VE. 2004. The del22q11.2 candidate gene Tbx1 regulates branchiomeric myogenesis. *Human Molecular Genetics* **13**:2829–2840. DOI: <https://doi.org/10.1093/hmg/ddh304>, PMID: 15385444
- Kong P**, Racedo SE, Macchiarulo S, Hu Z, Carpenter C, Guo T, Wang T, Zheng D, Morrow BE. 2014. Tbx1 is required autonomously for cell survival and fate in the pharyngeal core mesoderm to form the muscles of mastication. *Human Molecular Genetics* **23**:4215–4231. DOI: <https://doi.org/10.1093/hmg/ddu140>, PMID: 24705356
- Köntges G**, Lumsden A. 1996. Rhombencephalic neural crest segmentation is preserved throughout craniofacial ontogeny. *Development* **122**:3229–3242. PMID: 8898235
- Kuratani S**. 2008. Evolutionary developmental studies of cyclostomes and the origin of the vertebrate neck. *Development, Growth & Differentiation* **50**:S189–S194. DOI: <https://doi.org/10.1111/j.1440-169X.2008.00985.x>, PMID: 18430164

- Kuratani S**, Kusakabe R, Hirasawa T. 2018. The neural crest and evolution of the head/trunk interface in vertebrates. *Developmental Biology*. DOI: <https://doi.org/10.1016/j.ydbio.2018.01.017>, PMID: 29408469
- Leopold C**, De Barros A, Cellier C, Drouin-Garraud V, Dehesdin D, Marie JP. 2012. Laryngeal abnormalities are frequent in the 22q11 deletion syndrome. *International Journal of Pediatric Otorhinolaryngology* **76**:36–40. DOI: <https://doi.org/10.1016/j.ijporl.2011.09.025>, PMID: 22019154
- Lescroart F**, Kelly RG, Le Garrec JF, Nicolas JF, Meilhac SM, Buckingham M. 2010. Clonal analysis reveals common lineage relationships between head muscles and second heart field derivatives in the mouse embryo. *Development* **137**:3269–3279. DOI: <https://doi.org/10.1242/dev.050674>, PMID: 20823066
- Lescroart F**, Hamou W, Francou A, Théveniau-Ruissy M, Kelly RG, Buckingham M. 2015. Clonal analysis reveals a common origin between nonsomite-derived neck muscles and heart myocardium. *PNAS* **112**:1446–1451. DOI: <https://doi.org/10.1073/pnas.1424538112>, PMID: 25605943
- Loebel DA**, Hor AC, Bildsoe H, Jones V, Chen YT, Behringer RR, Tam PP. 2012. Regionalized Twist1 activity in the forelimb bud drives the morphogenesis of the proximal and preaxial skeleton. *Developmental Biology* **362**:132–140. DOI: <https://doi.org/10.1016/j.ydbio.2011.11.020>, PMID: 22178153
- Logan M**, Martin JF, Nagy A, Lobe C, Olson EN, Tabin CJ. 2002. Expression of Cre Recombinase in the developing mouse limb bud driven by a Pxl enhancer. *Genesis* **33**:77–80. DOI: <https://doi.org/10.1002/gene.10092>, PMID: 12112875
- Lours-Calet C**, Alvares LE, El-Hanfy AS, Gandesha S, Walters EH, Sobreira DR, Wotton KR, Jorge EC, Lawson JA, Kelsey Lewis A, Tada M, Sharpe C, Kardon G, Dietrich S. 2014. Evolutionarily conserved morphogenetic movements at the vertebrate head-trunk interface coordinate the transport and assembly of hypopharyngeal structures. *Developmental Biology* **390**:231–246. DOI: <https://doi.org/10.1016/j.ydbio.2014.03.003>, PMID: 24662046
- Lubosch W**. 1938. Muskeln des Kopfes: Viscerale Muskulatur. In: Bolk L, Göppert E, Kallius E, Lubosch W (Eds). *Handbuch Der Vergleichenden Anatomie Der Wirbeltiere*. Berlin: Urban & Schwarzenberg.
- Madisen L**, Zwingman TA, Sunkin SM, Oh SW, Zariwala HA, Gu H, Ng LL, Palmiter RD, Hawrylycz MJ, Jones AR, Lein ES, Zeng H. 2010. A robust and high-throughput Cre reporting and characterization system for the whole mouse brain. *Nature Neuroscience* **13**:133–140. DOI: <https://doi.org/10.1038/nn.2467>, PMID: 20023653
- Marom T**, Roth Y, Goldfarb A, Cinamon U. 2012. Head and neck manifestations of 22q11.2 deletion syndromes. *European Archives of Oto-Rhino-Laryngology* **269**:381–387. DOI: <https://doi.org/10.1007/s00405-011-1745-1>, PMID: 21861138
- Martin AR**, Reddy R, Fehlings MG. 2011. Dropped head syndrome: diagnosis and management. *Evidence-Based Spine-Care Journal* **2**:41–47. DOI: <https://doi.org/10.1055/s-0030-1267104>, PMID: 23637681
- Matsuoka T**, Ahlberg PE, Kessar N, Iannarelli P, Dennehy U, Richardson WD, McMahon AP, Koentges G. 2005. Neural crest origins of the neck and shoulder. *Nature* **436**:347–355. DOI: <https://doi.org/10.1038/nature03837>, PMID: 16034409
- McGonnell IM**, McKay IJ, Graham A. 2001. A population of caudally migrating cranial neural crest cells: functional and evolutionary implications. *Developmental Biology* **236**:354–363. DOI: <https://doi.org/10.1006/dbio.2001.0330>, PMID: 11476577
- Moreno TA**, Jappelli R, Izpisua Belmonte JC, Kintner C. 2008. Retinoic acid regulation of the Mesp-Ripply feedback loop during vertebrate segmental patterning. *Developmental Biology* **315**:317–330. DOI: <https://doi.org/10.1016/j.ydbio.2007.12.038>, PMID: 18261720
- Muzumdar MD**, Tasic B, Miyamichi K, Li L, Luo L. 2007. A global double-fluorescent Cre reporter mouse. *Genesis* **45**:593–605. DOI: <https://doi.org/10.1002/dvg.20335>, PMID: 17868096
- Nagashima H**, Sugahara F, Watanabe K, Shibata M, Chiba A, Sato N. 2016. Developmental origin of the clavicle, and its implications for the evolution of the neck and the paired appendages in vertebrates. *Journal of Anatomy* **229**:536–548. DOI: <https://doi.org/10.1111/joa.12502>, PMID: 27279028
- Nassari S**, Duprez D, Fournier-Thibault C. 2017. Non-myogenic Contribution to Muscle Development and Homeostasis: The Role of Connective Tissues. *Frontiers in Cell and Developmental Biology* **5**:22. DOI: <https://doi.org/10.3389/fcell.2017.00022>, PMID: 28386539
- Nathan E**, Monovich A, Tirosh-Finkel L, Harrelson Z, Rousso T, Rinon A, Harel I, Evans SM, Tzahor E. 2008. The contribution of Islet1-expressing splanchnic mesoderm cells to distinct branchiomeric muscles reveals significant heterogeneity in head muscle development. *Development* **135**:647–657. DOI: <https://doi.org/10.1242/dev.007989>, PMID: 18184728
- Naumann B**, Warth P, Olsson L, Konstantinidis P. 2017. The development of the cucullaris muscle and the branchial musculature in the Longnose Gar, (*Lepisosteus osseus*, Lepisosteiformes, Actinopterygii) and its implications for the evolution and development of the head/trunk interface in vertebrates. *Evolution & Development* **19**:263–276. DOI: <https://doi.org/10.1111/ede.12239>, PMID: 29027738
- Noda M**, Miyake T, Okabe M. 2017. Development of cranial muscles in the actinopterygian fish Senegal bichir, *Polypterus senegalus* Cuvier, 1829. *Journal of Morphology* **278**:450–463. DOI: <https://doi.org/10.1002/jmor.20636>, PMID: 28182295
- Noden DM**. 1983. The embryonic origins of avian cephalic and cervical muscles and associated connective tissues. *American Journal of Anatomy* **168**:257–276. DOI: <https://doi.org/10.1002/aja.1001680302>, PMID: 6650439
- Noden DM**. 1988. Interactions and fates of avian craniofacial mesenchyme. *Development* **103**:121–140. PMID: 3074905
- Noden DM**, Francis-West P. 2006. The differentiation and morphogenesis of craniofacial muscles. *Developmental Dynamics* **235**:1194–1218. DOI: <https://doi.org/10.1002/dvdy.20697>, PMID: 16502415

- Okano J, Sakai Y, Shiota K.** 2008. Retinoic acid down-regulates Tbx1 expression and induces abnormal differentiation of tongue muscles in fetal mice. *Developmental Dynamics* **237**:3059–3070. DOI: <https://doi.org/10.1002/dvdy.21715>, PMID: 18816858
- Olsson L, Falck P, Lopez K, Cobb J, Hanken J.** 2001. Cranial neural crest cells contribute to connective tissue in cranial muscles in the anuran amphibian, *Bombina orientalis*. *Developmental Biology* **237**:354–367. DOI: <https://doi.org/10.1006/dbio.2001.0377>, PMID: 11543620
- Papangeli I, Scambler P.** 2013. The 22q11 deletion: DiGeorge and velocardiofacial syndromes and the role of *TBX1*. *Wiley Interdisciplinary Reviews: Developmental Biology* **2**:393–403. DOI: <https://doi.org/10.1002/wdev.75>, PMID: 23799583
- Parameswaran M, Tam PP.** 1995. Regionalisation of cell fate and morphogenetic movement of the mesoderm during mouse gastrulation. *Developmental Genetics* **17**:16–28. DOI: <https://doi.org/10.1002/dvg.1020170104>, PMID: 7554492
- Piatt J.** 1938. Morphogenesis of the cranial muscles of *Amblystoma punctatum*. *Journal of Morphology* **63**:531–587. DOI: <https://doi.org/10.1002/jmor.1050630306>
- Piekarski N, Gross JB, Hanken J.** 2014. Evolutionary innovation and conservation in the embryonic derivation of the vertebrate skull. *Nature Communications* **5**:5661. DOI: <https://doi.org/10.1038/ncomms6661>, PMID: 25434971
- Piekarski N, Olsson L.** 2007. Muscular derivatives of the cranialmost somites revealed by long-term fate mapping in the Mexican axolotl (*Amblystoma mexicanum*). *Evolution & Development* **9**:566–578. DOI: <https://doi.org/10.1111/j.1525-142X.2007.00197.x>, PMID: 17976053
- Ponomartsev S, Valasek P, Patel K, Malashichev Y.** 2017. Neural crest contribution to the avian shoulder girdle and implications to girdle evolution in vertebrates. *Biological Communications* **62**:26–37. DOI: <https://doi.org/10.21638/11701/spbu03.2017.104>
- Prunotto C, Crepaldi T, Forni PE, Ieraci A, Kelly RG, Tajbakhsh S, Buckingham M, Ponzetto C.** 2004. Analysis of Mlc-lacZ Met mutants highlights the essential function of Met for migratory precursors of hypaxial muscles and reveals a role for Met in the development of hyoid arch-derived facial muscles. *Developmental Dynamics* **231**:582–591. DOI: <https://doi.org/10.1002/dvdy.20177>, PMID: 15376315
- Randolph ME, Pavlath GK.** 2015. A muscle stem cell for every muscle: variability of satellite cell biology among different muscle groups. *Frontiers in Aging Neuroscience* **7**:190. DOI: <https://doi.org/10.3389/fnagi.2015.00190>, PMID: 26500547
- Relaix F, Rocancourt D, Mansouri A, Buckingham M.** 2004. Divergent functions of murine Pax3 and Pax7 in limb muscle development. *Genes & Development* **18**:1088–1105. DOI: <https://doi.org/10.1101/gad.301004>, PMID: 15132998
- Relaix F, Rocancourt D, Mansouri A, Buckingham M.** 2005. A Pax3/Pax7-dependent population of skeletal muscle progenitor cells. *Nature* **435**:948–953. DOI: <https://doi.org/10.1038/nature03594>, PMID: 15843801
- Saga Y, Hata N, Kobayashi S, Magnuson T, Seldin MF, Taketo MM.** 1996. MesP1: a novel basic helix-loop-helix protein expressed in the nascent mesodermal cells during mouse gastrulation. *Development* **122**:2769–2778. PMID: 8787751
- Saga Y.** 1998. Genetic rescue of segmentation defect in MesP2-deficient mice by MesP1 gene replacement. *Mechanisms of Development* **75**:53–66. DOI: [https://doi.org/10.1016/S0925-4773\(98\)00077-X](https://doi.org/10.1016/S0925-4773(98)00077-X), PMID: 9739106
- Saga Y, Miyagawa-Tomita S, Takagi A, Kitajima S, Miyazaki J, Inoue T.** 1999. MesP1 is expressed in the heart precursor cells and required for the formation of a single heart tube. *Development* **126**:3437–3447. PMID: 10393122
- Saga Y, Kitajima S, Miyagawa-Tomita S.** 2000. Mesp1 expression is the earliest sign of cardiovascular development. *Trends in Cardiovascular Medicine* **10**:345–352. DOI: [https://doi.org/10.1016/S1050-1738\(01\)00069-X](https://doi.org/10.1016/S1050-1738(01)00069-X), PMID: 11369261
- Sambasivan R, Gayraud-Morel B, Dumas G, Cimper C, Paisant S, Kelly RG, Kelly R, Tajbakhsh S.** 2009. Distinct regulatory cascades govern extraocular and pharyngeal arch muscle progenitor cell fates. *Developmental Cell* **16**:810–821. DOI: <https://doi.org/10.1016/j.devcel.2009.05.008>, PMID: 19531352
- Sambasivan R, Comai G, Le Roux I, Gomès D, Konge J, Dumas G, Cimper C, Tajbakhsh S.** 2013. Embryonic founders of adult muscle stem cells are primed by the determination gene Mrf4. *Developmental Biology* **381**:241–255. DOI: <https://doi.org/10.1016/j.ydbio.2013.04.018>, PMID: 23623977
- Satou Y, Imai KS, Satoh N.** 2004. The ascidian Mesp gene specifies heart precursor cells. *Development* **131**:2533–2541. DOI: <https://doi.org/10.1242/dev.01145>, PMID: 15115756
- Sawada A, Fritz A, Jiang YJ, Yamamoto A, Yamasu K, Kuroiwa A, Saga Y, Takeda H.** 2000. Zebrafish Mesp family genes, mesp-a and mesp-b are segmentally expressed in the presomitic mesoderm, and Mesp-b confers the anterior identity to the developing somites. *Development* **127**:1691–1702. PMID: 10725245
- Sefton EM, Bhullar BA, Mohaddes Z, Hanken J.** 2016. Evolution of the head-trunk interface in tetrapod vertebrates. *eLife* **5**:e09972. DOI: <https://doi.org/10.7554/eLife.09972>, PMID: 27090084
- Soriano P.** 1999. Generalized lacZ expression with the ROSA26 Cre reporter strain. *Nature Genetics* **21**:70–71. DOI: <https://doi.org/10.1038/5007>, PMID: 9916792
- Srinivas S, Watanabe T, Lin CS, Williams CM, Tanabe Y, Jessell TM, Costantini F.** 2001. Cre reporter strains produced by targeted insertion of EYFP and ECFP into the ROSA26 locus. *BMC Developmental Biology* **1**:4. PMID: 11299042
- Tabler JM, Rigney MM, Berman GJ, Gopalakrishnan S, Heude E, Al-Lami HA, Yannakoudakis BZ, Fitch RD, Carter C, Vokes S, Liu KJ, Tajbakhsh S, Egnor SR, Wallingford JB.** 2017. Cilia-mediated Hedgehog signaling controls

- form and function in the mammalian larynx. *eLife* **6**:e19153. DOI: <https://doi.org/10.7554/eLife.19153>, PMID: 28177282
- Tada MN, Kuratani S. 2015. Evolutionary and developmental understanding of the spinal accessory nerve. *Zoological Letters* **1**:4. DOI: <https://doi.org/10.1186/s40851-014-0006-8>, PMID: 26605049
- Tajbakhsh S, Rocancourt D, Buckingham M. 1996. Muscle progenitor cells failing to respond to positional cues adopt non-myogenic fates in myf-5 null mice. *Nature* **384**:266–270. DOI: <https://doi.org/10.1038/384266a0>, PMID: 8918877
- Tajbakhsh S, Rocancourt D, Cossu G, Buckingham M. 1997. Redefining the genetic hierarchies controlling skeletal myogenesis: Pax-3 and Myf-5 act upstream of MyoD. *Cell* **89**:127–138. DOI: [https://doi.org/10.1016/S0092-8674\(00\)80189-0](https://doi.org/10.1016/S0092-8674(00)80189-0), PMID: 9094721
- Tesařová M, Zikmund T, Kaucká M, Adameyko I, Jaroš J, Paloušek D, Škaroupka D, Kaiser J. 2016. Use of micro computed-tomography and 3D printing for reverse engineering of mouse embryo nasal capsule. *Journal of Instrumentation* **11**:C03006. DOI: <https://doi.org/10.1088/1748-0221/11/03/C03006>
- Theis S, Patel K, Valasek P, Otto A, Pu Q, Harel I, Tzahor E, Tajbakhsh S, Christ B, Huang R. 2010. The occipital lateral plate mesoderm is a novel source for vertebrate neck musculature. *Development* **137**:2961–2971. DOI: <https://doi.org/10.1242/dev.049726>, PMID: 20699298
- Tremblay P, Dietrich S, Mericskay M, Schubert FR, Li Z, Paulin D. 1998. A crucial role for Pax3 in the development of the hypaxial musculature and the long-range migration of muscle precursors. *Developmental Biology* **203**:49–61. DOI: <https://doi.org/10.1006/dbio.1998.9041>, PMID: 9806772
- Valasek P, Theis S, Krejci E, Grim M, Maina F, Shwartz Y, Otto A, Huang R, Patel K. 2010. Somitic origin of the medial border of the mammalian scapula and its homology to the avian scapula blade. *Journal of Anatomy* **216**:482–488. DOI: <https://doi.org/10.1111/j.1469-7580.2009.01200.x>, PMID: 20136669
- Verzi MP, McCulley DJ, De Val S, Dodou E, Black BL. 2005. The right ventricle, outflow tract, and ventricular septum comprise a restricted expression domain within the secondary/anterior heart field. *Developmental Biology* **287**:134–145. DOI: <https://doi.org/10.1016/j.ydbio.2005.08.041>, PMID: 16188249
- Yabe T, Hoshijima K, Yamamoto T, Takada S. 2016. Quadruple zebrafish mutant reveals different roles of Mesp genes in somite segmentation between mouse and zebrafish. *Development* **143**:2842–2852. DOI: <https://doi.org/10.1242/dev.133173>, PMID: 27385009
- Yang L, Cai CL, Lin L, Qyang Y, Chung C, Monteiro RM, Mummery CL, Fishman GI, Cogen A, Evans S. 2006. Isl1Cre reveals a common Bmp pathway in heart and limb development. *Development* **133**:1575–1585. DOI: <https://doi.org/10.1242/dev.02322>, PMID: 16556916
- Yokomizo T, Yamada-Inagawa T, Yzaguirre AD, Chen MJ, Speck NA, Dzierzak E. 2012. Whole-mount three-dimensional imaging of internally localized immunostained cells within mouse embryos. *Nature Protocols* **7**:421–431. DOI: <https://doi.org/10.1038/nprot.2011.441>, PMID: 22322215
- Zhang Z, Huynh T, Baldini A. 2006. Mesodermal expression of Tbx1 is necessary and sufficient for pharyngeal arch and cardiac outflow tract development. *Development* **133**:3587–3595. DOI: <https://doi.org/10.1242/dev.02539>, PMID: 16914493
- Ziermann JM, Freitas R, Diogo R. 2017. Muscle development in the shark *Scyliorhinus canicula*: implications for the evolution of the gnathostome head and paired appendage musculature. *Frontiers in Zoology* **14**:31. DOI: <https://doi.org/10.1186/s12983-017-0216-y>, PMID: 28649268
- Ziermann JM, Clement AM, Ericsson R, Olsson L. 2018a. Cephalic muscle development in the Australian lungfish, *Neoceratodus forsteri*. *Journal of Morphology* **279**:494–516. DOI: <https://doi.org/10.1002/jmor.20784>, PMID: 29214665
- Ziermann JM, Diogo R, Noden DM. 2018b. Neural crest and the patterning of vertebrate craniofacial muscles. *Genesis* **56**:e23097. DOI: <https://doi.org/10.1002/dvg.23097>, PMID: 29659153
- Zoupa M, Seppala M, Mitsiadis T, Cobourne MT. 2006. Tbx1 is expressed at multiple sites of epithelial-mesenchymal interaction during early development of the facial complex. *The International Journal of Developmental Biology* **50**:504–510. DOI: <https://doi.org/10.1387/ijdb.052116mz>, PMID: 16586352

INTERNATIONAL WORKSHOP ON IMAGING II
4–8 SEPTEMBER 2017
VARENNA, ITALY

High-contrast differentiation resolution 3D imaging of rodent brain by X-ray computed microtomography

T. Zikmund,^a M. Novotná,^a M. Kavková,^a M. Tesařová,^a M. Kaucká,^{b,c} B. Szarowská,^c I. Adameyko,^{b,c} E. Hrubá,^d M. Buchtová,^d E. Dražanová,^e Z. Starčuk^e and J. Kaiser^{a,1}

^aCentral European Institute of Technology, Brno University of Technology, CEITEC - BUT, Purkyňova 123, 612 00 Brno, Czech Republic

^bDepartment of Physiology and Pharmacology, Karolinska Institutet, Nanna Svartz väg 2, Stockholm 17177, Sweden

^cDepartment of Molecular Neurosciences, Center for Brain Research, Medical University of Vienna, Spitalgasse 4, Vienna, Austria 1090

^dLaboratory of Molecular Morphogenesis, Institute of Animal Physiology and Genetics AS CR, v. v. i., Brno, Czech Republic

^eInstitute of Scientific Instruments of the CAS, v. v. i., Brno, Czech Republic

E-mail: jozef.kaiser@ceitec.vutbr.cz

ABSTRACT: The biomedically focused brain research is largely performed on laboratory mice considering a high homology between the human and mouse genomes. A brain has an intricate and highly complex geometrical structure that is hard to display and analyse using only 2D methods. Applying some fast and efficient methods of brain visualization in 3D will be crucial for the neurobiology in the future. A post-mortem analysis of experimental animals' brains usually involves techniques such as magnetic resonance and computed tomography. These techniques are employed to visualize abnormalities in the brains' morphology or reparation processes. The X-ray computed microtomography (micro CT) plays an important role in the 3D imaging of internal structures of a large variety of soft and hard tissues. This non-destructive technique is applied in biological studies because the lab-based CT devices enable to obtain a several-micrometer resolution. However, this technique is always used along with some visualization methods, which are based on the tissue staining and thus differentiate soft tissues in biological samples. Here, a modified chemical contrasting protocol of tissues for a micro CT usage is introduced as the best tool for *ex vivo* 3D imaging of a post-mortem mouse brain. This way, the micro CT provides a high spatial resolution

¹Corresponding author.

of the brain microscopic anatomy together with a high tissue differentiation contrast enabling to identify more anatomical details in the brain. As the micro CT allows a consequent reconstruction of the brain structures into a coherent 3D model, some small morphological changes can be given into context of their mutual spatial relationships.

KEYWORDS: Computerized Tomography (CT) and Computed Radiography (CR); MRI (whole body, cardiovascular, breast, others), MR-angiography (MRA)

Contents

1	Introduction	1
2	Materials and methods	2
2.1	Sample preparation for micro CT measurement	2
2.2	Micro CT measurement and data processing	2
2.3	MRI measurement	3
3	Results and discussion	3
4	Conclusion	9

1 Introduction

Computed tomography is widely applied in the human medicine especially to monitor bone injuries, to diagnose head, lung and chest conditions or to detect cancer. In the last decades, this non-destructive imaging technique has been evolved and therefore is able to provide high-resolution *ex vivo* analyses of biological samples. The micro CT brings unique possibilities concerning the imaging of complex biological systems, such as the following cases: a description of a mouse knee cartilage development [1]; a formation of 3D models of mouse chondrocranium, an analysis of the ossification onset and morphological changes in various transgenic mice [2–4]; a noninvasive observation of a human embryo [5].

The principle of the X-ray micro CT imaging is based on taking series of 2D projection radiographs from different angles and their subsequent processing. In each projection, the information about radiographic density is recorded. A mathematical process called tomographic reconstruction forms a 3D matrix which represents a map of volume density. The spatial resolution of the system is determined by the geometry of a cone beam. The achievable resolution is down to 1 μm for lab-based machines. This method has proven to be an effective tool for imaging of native bone tissues [6, 7], since the hydroxyapatite is dense enough to be easily detected. In the case of biological samples and soft tissues *ex vivo*, the micro CT imaging requires an application of some X-ray absorbing contrast agents, e. g. phosphotungstic acid (PTA), iodine or osmium [8]. If the contrast is sufficient, it is possible to segment different structures within the 3D tomographic data by using an appropriate software.

The major advantage of the CT method is the ability to image a bone, soft tissues and blood vessels at the same time. In some cases, it is advantageous to combine the CT method with some other techniques for *in vivo* imaging to visualize better various soft tissues. Especially in the case of cancer diagnosis, the computed tomography is combined with the positron emission tomography (PET/CT) [9].

In biomedical research, the rodent brain attracts a lot of attention because of some human-related pathologies that can be modelled in transgenic animals and also because of the high homology between the human and mouse genome, which causes numerous fundamental neurobiological questions [10]. To take advantage of the information gained from mouse brain research, it is necessary to systematically collect the phenotype information at all biological levels. Conventionally used 2D analysis methods — histology, immunocytochemistry or transmission electron microscopy — show a high resolution within the plane in which the tissue is sectioned. However, these methods are destructive and two dimensional in their nature.

In the case of post-mortem 3D imaging of mouse brain, the micro CT is not the only method that could be applied. The magnetic resonance imaging (MRI) could be used for a similar purpose as well. In the past, the micro CT was used as an accessory technique to MRI for the imaging of the mouse brain. The micro CT was employed for the imaging of the skull [6, 7] or for the visualization of vascular system of mouse brain filled with radio-opaque silicone rubber Microfil [11–17]. With the recent progress in development of chemical contrasting protocols for brain tissue [6, 18–22] or application of micro CT imaging as a tool for location of cerebral ischemia [22, 23] or brain tumors [21, 24], micro CT imaging is becoming a vital research tool for mouse brain imaging in general.

In this article, we will focus on the mouse brain 3D imaging with a high-resolution laboratory micro CT system combined with an optimization of sample staining. We use different staining protocols based on iodine solution and phosphotungstic acid. The benefits of such approaches will be specified. We will summarize the comparison of the different staining procedures and we will also compare the gained data with the corresponding magnetic resonance data. Furthermore, the power of presented method will be demonstrated by a number of 3D models of selected brain structures with specifically complex 3D geometries that we have reconstructed and analyzed.

2 Materials and methods

2.1 Sample preparation for micro CT measurement

An adult mouse was sacrificed with isoflurane overdose. The brain was dissected from skull and collected into ice-cold PBS. Subsequently, the sample was fixed in freshly prepared 4% paraformaldehyde (PFA). The sample was dehydrated in ethanol grade (12 h) and stained in 1% iodine solution in 90% methanol. After 24 hours in the solution, the sample was rinsed in ethanol rehydration series to end up in sterile distilled water. For the sake of micro CT measurement, the brain was embedded in 1% agarose gel and placed in a plastic tube. All animal (mouse) concerned work had been approved and permitted by the Ethical Committee on Animal Experiments (Norra Djurförsöksetiska Nämnd, ethical permit N226/15 and N5/14) and was conducted according to The Swedish Animal Agency's Provisions and Guidelines for Animal Experimentation recommendations.

2.2 Micro CT measurement and data processing

Micro CT measurement was performed with a GE Phoenix v|tome|x L 240 (GE Sensing & Inspection Technologies GmbH, Germany), equipped with a nanofocus X-ray tube with maximum power of 180 kV/15 W. The data were acquired using a high contrast flat panel detector DXR250 with 2048 px × 2048 px, 200 μm × 200 μm pixel size. The micro CT scan was carried out in an air-conditioned cabinet (21°C) at 60 kV acceleration voltage and 200 μA tube current. Exposure

time was 900 ms and 3 images were averaged for reducing the noise. Two different measurement procedures were performed. The first one was used for the evaluation of staining protocol. The brains contrasted by various techniques were scanned with a voxel resolution of $18\ \mu\text{m}$. After the evaluation, the second measurement procedure was applied for one brain with a voxel resolution of $6.5\ \mu\text{m}$. 2200 projections were taken over 360° in this case. A tomographic reconstruction was realized by software GE phoenix datavision 2.0 (GE Sensing & Inspection Technologies GmbH, Germany). Reconstructed slices were imported into a VG Studio MAX 3.1 (Volume Graphics GmbH, Germany). In this software, the 3D data were aligned so that orthogonal slices matched the horizontal (xy), coronal (yz) and sagittal plane (xz) resulting in series of 1700 coronal, 1090 sagittal and 680 horizontal tomographic sections of the brain. These data were compared with an anatomical atlas, and 3D models of anatomical structures were obtained by a segmentation based on the global thresholding.

2.3 MRI measurement

The post-mortem mouse brain within the skull was measured by a high-resolution MRI scanner Bruker Avance 9.4 T (Bruker Biospin MRI, Ettlingen, Germany). The resolution of the obtained data was $0.027 \times 0.027\ \text{mm}$ (matrix 512×512 pixels). T_1 -weighted anatomical images of 25 parallel 2D slices were taken using the FLASH sequence with slice thickness 0.5 mm, interslice distance 0.5 mm, repetition time (TR) 461.3 ms, effective echo time (TE) 6.1 ms, 50 averages, flip angle 35.0° , echo spacing 6.1 ms. The total measurement time was 9 hours and 25 images were obtained.

3 Results and discussion

For a comprehensive visualization of the mouse brain structures done by a conventional micro CT, a chemical contrasting step is usually required. The differentiation of soft tissues by an imaging method delivers the biologically-relevant information only if the contrasting is sufficient. Our priority in this research was achieving the ultimate differential contrast enabling the identification of all major cell types or the tissue modes.

Inorganic iodine and phosphotungstic acid (PTA) are the most broadly used agents in the field of post-mortem tissue contrasting for the following X-ray investigation [25]. Previously, it was suggested to use alcohol solutions containing these compounds to enable a rapid diffusion into the sample [8]. If iodine is compared to PTA, PTA appears as a larger molecule with much slower tissue penetration rates [8]. Ten different staining protocols were tested to visualize mouse brain structures by micro CT imaging (table 1). Samples were stained in PTA, iodine or combination of both of solutions for various periods of time.

In order to compare the contrast among these samples, we analyzed all of them in the same condition. The voxel resolution of obtained CT data was $18\ \mu\text{m}$, which turned out to be enough to compare the quality of different contrasting protocols (figure 1). In summary, the staining in iodine exhibited more clear contours of fibres than in the case of PTA-stained samples. Fixation of samples in 4% PFA demonstrated higher contrast to tissues fixed in 10% PFA. The best resolution was obtained in 1% iodine in 90% methanol solution. As this staining showed the most contrastive and sharp edges of anatomical structures at coronal brain sections, we selected the sample stained with this protocol for further analysis.

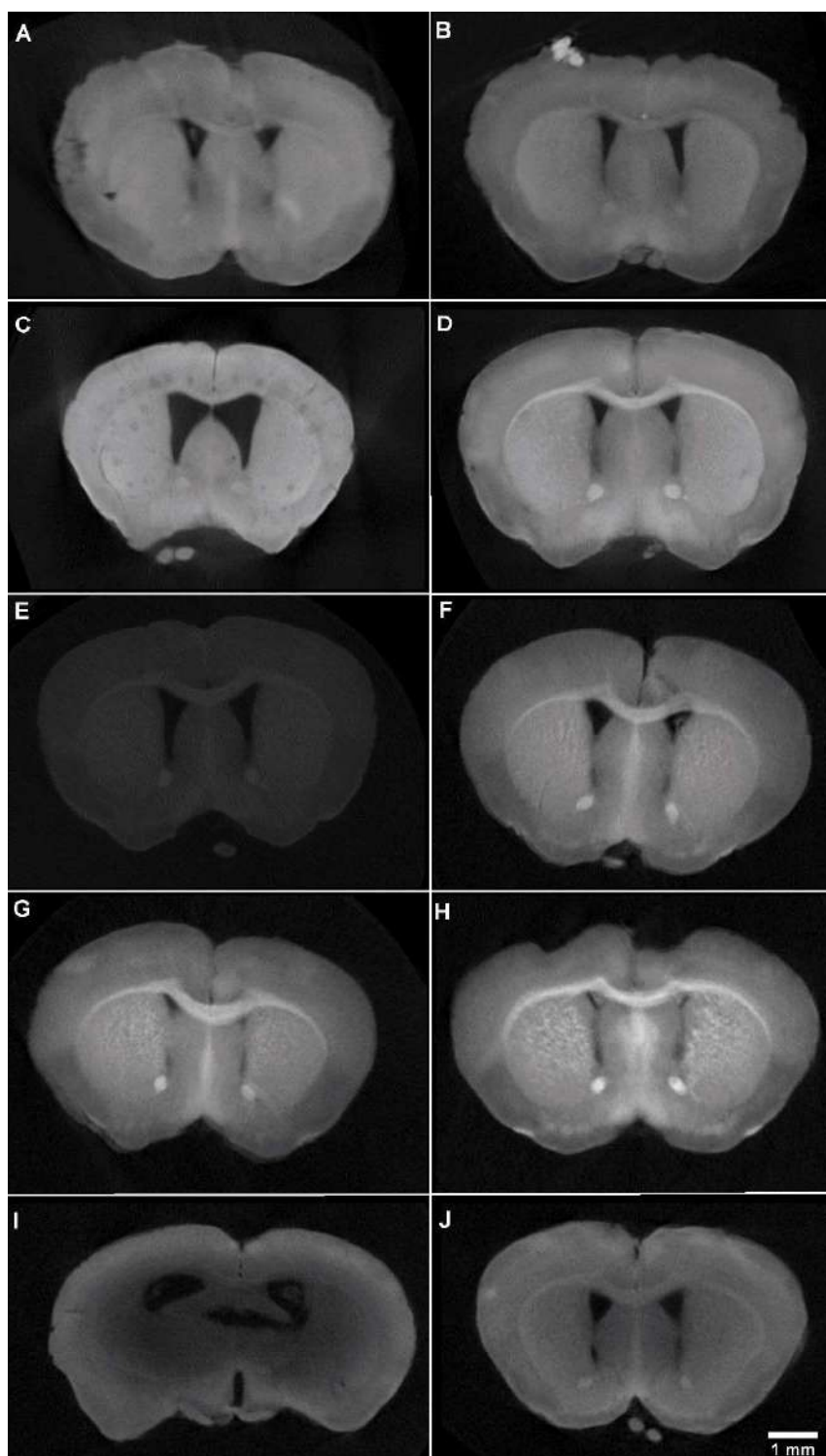


Figure 1. Comparison of the coronal sections of samples following different staining protocols. (A) 1% PTA in 90% MeOH for 21 days, (B) 1% PTA in 90% MeOH for 14 days, (C) 1% PTA in 100% MeOH for 16 days, (D) 1% PTA for 10 days + 1% iodine in 90% MeOH for additional 24h, (E) 1% iodine in 100% EtOH for 24h, (F) 1% iodine in 100% EtOH for 48h, (G) 1% iodine in 100% EtOH for 7 days, (H) 1% iodine in 90% MeOH for 24h, (I) 1% iodine in 100% EtOH overnight, (J) 1% iodine in 100% EtOH for 24h.

Table 1. List of different processing and staining protocols for brain visualization in micro CT.

	Pre-fixation	Post-fixation	Dehydration	Staining	Time
A	4% PFA	4% PFA (24h)	EtOH / 12h	1% PTA in 90% MeOH	21 days
B	/	4% PFA (24h)	EtOH / 12h	1% PTA in 90% MeOH	14 days
C	10% PFA	10% PFA (24h)	EtOH / 12h	1% PTA in 100% MeOH	16 days
D	4% PFA	4% PFA (24h)	EtOH / 12h	1% PTA + 1% iodine in 90% MeOH	10 days PTA/24h iodine
E	4% PFA	4% PFA (24h)	EtOH / 12h	1% iodine in 100% EtOH	24h
F	4% PFA	4% PFA (24h)	EtOH / 12h	1% iodine in 100% EtOH	48h
G	4% PFA	4% PFA (24h)	EtOH / 12h	1% iodine in 100% EtOH	7 days
H	4% PFA	4% PFA (24h)	EtOH / 12h	1% iodine in 90% MeOH	24h
I	10% PFA	10% PFA (12h)	EtOH / 2h	1% iodine in 100% EtOH	overnight
J	10% PFA	10% PFA (12h)	EtOH / 2h	1% iodine in 100% EtOH	24h

Four coronal sections (figure 2) from different parts of the mouse brain demonstrate the extent of resolution quality of contrasting protocol as captured by a micro CT scan. Identification of the

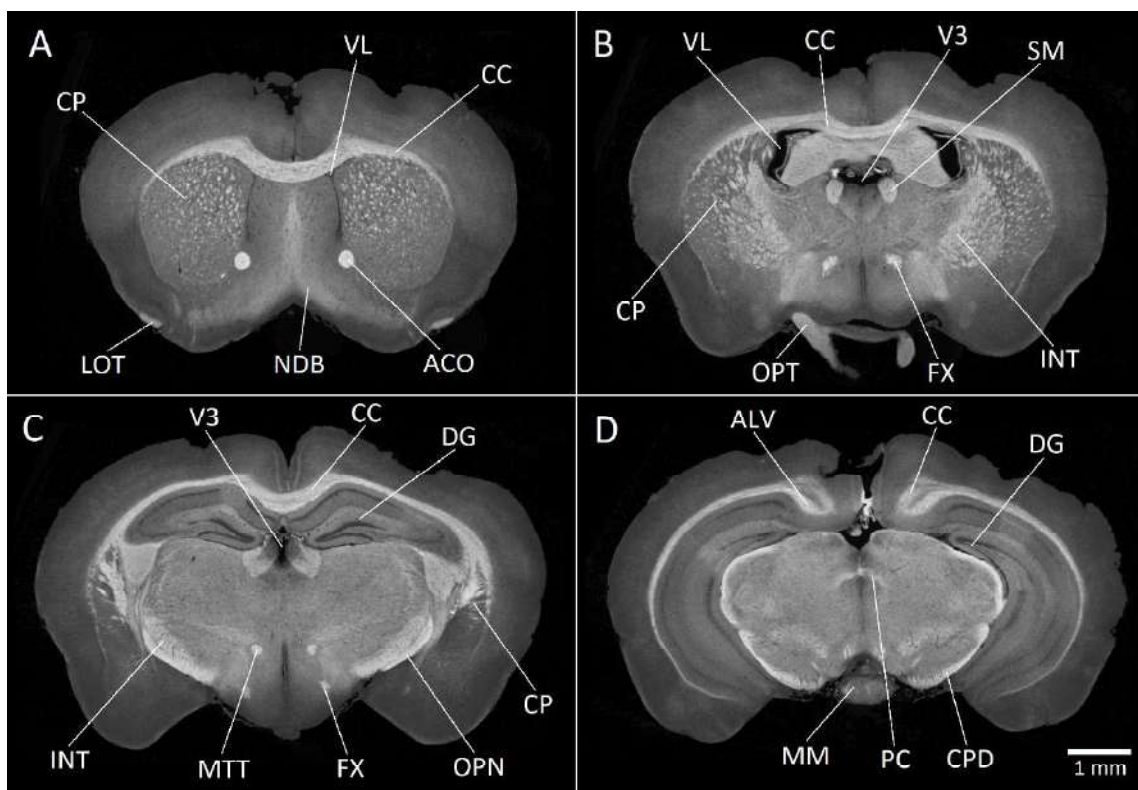


Figure 2. Visualization of the internal brain structures as shown on CT images in the coronal sections. (A) ACO anterior commissure, CC corpus callosum, CP caudoputamen, LOT lateral olfactory tract, NDB nucleus of diagonal band, VL lateral ventricle. (B) CC corpus callosum, CP caudoputamen, FX fornix, INT internal capsule, OPT optic tract, SM stria medullaris (thalamus), V3 third ventricle, VL lateral ventricle. (C) CC corpus callosum, CP caudoputamen, DG dentate gyrus, FX fornix, INT internal capsule, MTT mamillothalamic tract, OPN olivary pretectal nucleus, V3 third ventricle. (D) ALV alveus, CC corpus callosum, CPD cerebral crus, DG dentate gyrus, MM medial mammillary nucleus, PC posterior commissure.

described structures in the coronal sections was based on the annotation from Allen Mouse Brain Atlas [26]. For instance, corpus callosum, cerebral peduncle and anterior commissure appeared among the most contrasted and easily identifiable structures. Furthermore, the smaller and finer structures such as mamillothalamic tract, column of the fornix or caudoputamen were successfully recognized as well. Because of the grey matter's high contrast, the ventricles (e.g. lateral ventricle and third ventricle) were also evident.

Although both micro CT and MRI belong to the category of methods providing 3D imaging of the internal structures, the character of the output data including the resolution quality is rather different. The geometry of the data element called voxel has a cubic shape (the same dimensions in all three axes) in the CT and a rectangular cuboid shape in the MRI. The MRI data voxel is defined by the pixel size and slice thickness, which is typically significantly larger than pixel dimensions, i.e. the lateral and axial resolution are different. Isotropic 3D imaging is feasible by both methods, however the length of such experiments needed for achieving a good signal-to-noise ratio is limiting. Consequently, the brain structures were analyzed in detail on 1900 coronal CT slices (with voxel size $6.5 \mu\text{m} \times 6.5 \mu\text{m} \times 6.5 \mu\text{m}$) and 25 coronal MRI slices (with voxel size $27 \mu\text{m} \times 27 \mu\text{m} \times 500 \mu\text{m}$). From this point of view, CT data provided enhanced opportunities to study the arbitrary cross-sections within one dataset and also demonstrated an accurate 3D modelling of internal structures.

The voxel values are defined by greyscale values depending on different properties of the material. CT greyscale values are defined by the X-ray absorption properties in relation to the atomic number of the sample material and to the accelerated voltage of the X-ray source [27, 28]. Based on this fact, brighter tissues refer to denser materials. In the case of anatomical T1 weighted MRI, the amount of the obtained signal depends on the time needed for realigning proton spins in main magnetic field (realigned to Boltzmann equilibrium) [29, 30]. For instance, the fat realigns its spins quickly, and therefore it appears bright on a T_1 weighted image [29, 30]. Water realigns much slower, and therefore it has a lower signal and is represented by darker values.

As for the measurement time, it depends on the particular method. Considering *ex vivo* approach plus the highest possible resolution of both systems, the typical brain measurement took approx. 9 hours for the MRI and 2 hours for the CT.

To compare corresponding MRI and micro CT data (figure 3, table 2), we selected four pairs of corresponding coronal slices of the adult mouse brain. Corpus callosum, anterior commissure, medial mammillary nucleus, posterior commissure and cerebral peduncle were clearly recognizable on both micro CT and MRI images. All the mentioned structures demonstrated well-defined edges in micro CT data. Lateral ventricle, lateral olfactory bulb, optic tract, stria medullaris, internal capsule and cerebral peduncle were also detectable in both micro CT and MRI data. However, unlike the micro CT images, MRI pictures did not display a clear identification of above mentioned structures. The structures such as myelinated fibres in caudoputamen, third ventricle, column of the fornix, dentate gyrus, mamillothalamic tract and other locations were clearly distinguished in the micro CT. Moreover, the compartmentation of dorsal hippocampal commissure from corpus callosum and alveus was possible only in micro CT images.

As the next step, we selected several structures for segmentation to demonstrate possible outputs from micro CT data (figure 4, figure 5, figure 6). Tissue segmentation and construction of accurate

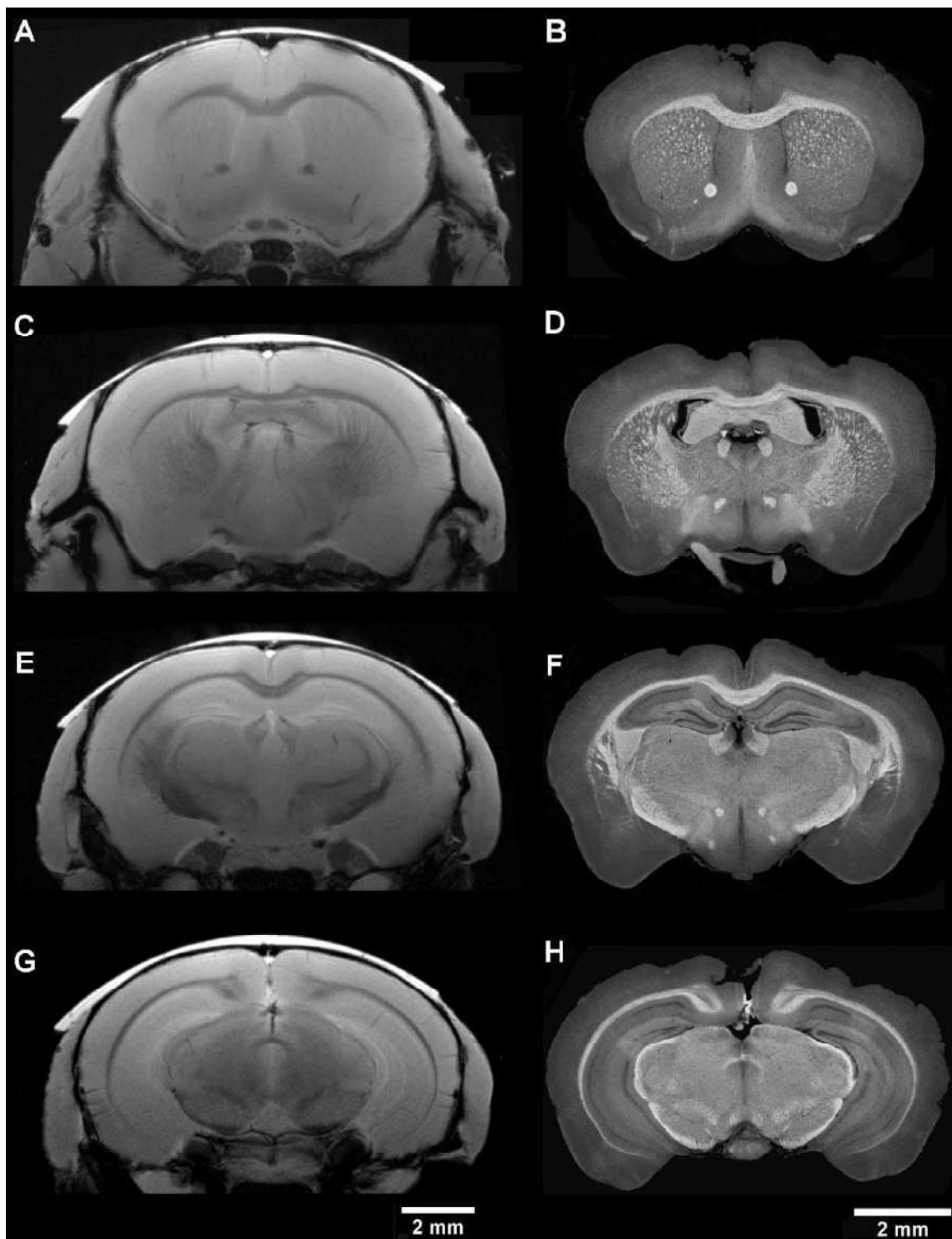


Figure 3. Comparison between corresponding coronal sections in MRI (A, C, E, G) and contrasted (1% iodine in 90% methanol) micro CT (B, D, F, H) of mouse brain.

Table 2. Identification of anatomical structures in mouse brain in micro CT and MRI images (*not suitable for segmentation, hard to detect).

structure	micro CT	MRI
corpus callosum	✓	✓
anterior commissure	✓	✓
medial mammillary nucleus	✓	✓
posterior commissure	✓	✓
cerebral peduncle	✓	✓
lateral ventricle	✓	✓*
lateral olfactory bulb	✓	✓*
optic tract	✓	✓*
stria medullaris	✓	✓*
internal capsule	✓	✓*
cerebral peduncle	✓	✓*
myelinated fibres in caudoputamen	✓	×
third ventricle	✓	×
column of the fornix	✓	×
dentate gyrus	✓	×
mamillothalamic tract	✓	×

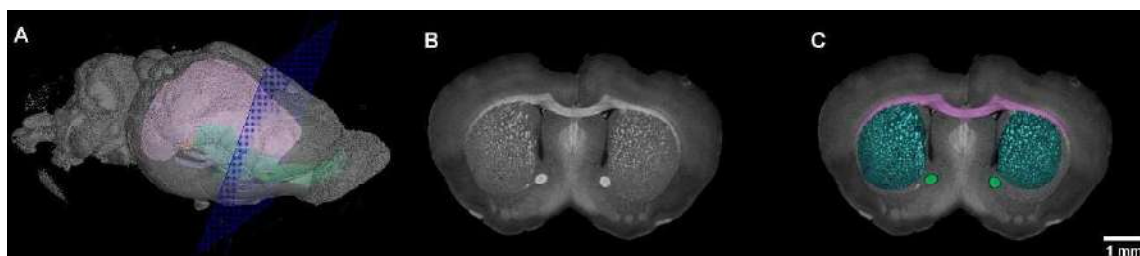


Figure 4. Visualization of steps during segmentation. (A) Area of the coronal section in the 3D model of the adult mouse brain, (B) Unmarked tomographic section, (C) Tomographic section with manually segmented corpus callosum (pink), myelinated fibres in caudoputamen (light blue) and anterior commissure (green).

3D models was possible thanks to high-resolution tomographic sections in all coronal, sagittal and horizontal planes and also, a fine contrast was implied by the improved staining protocol. Such a precise 3D visualization could be useful in future for variety of structural analyses in developmental biology and pathological studies. Above that, such data can be used for the educational purposes as they may be utilized for a subsequent 3D printing [31].

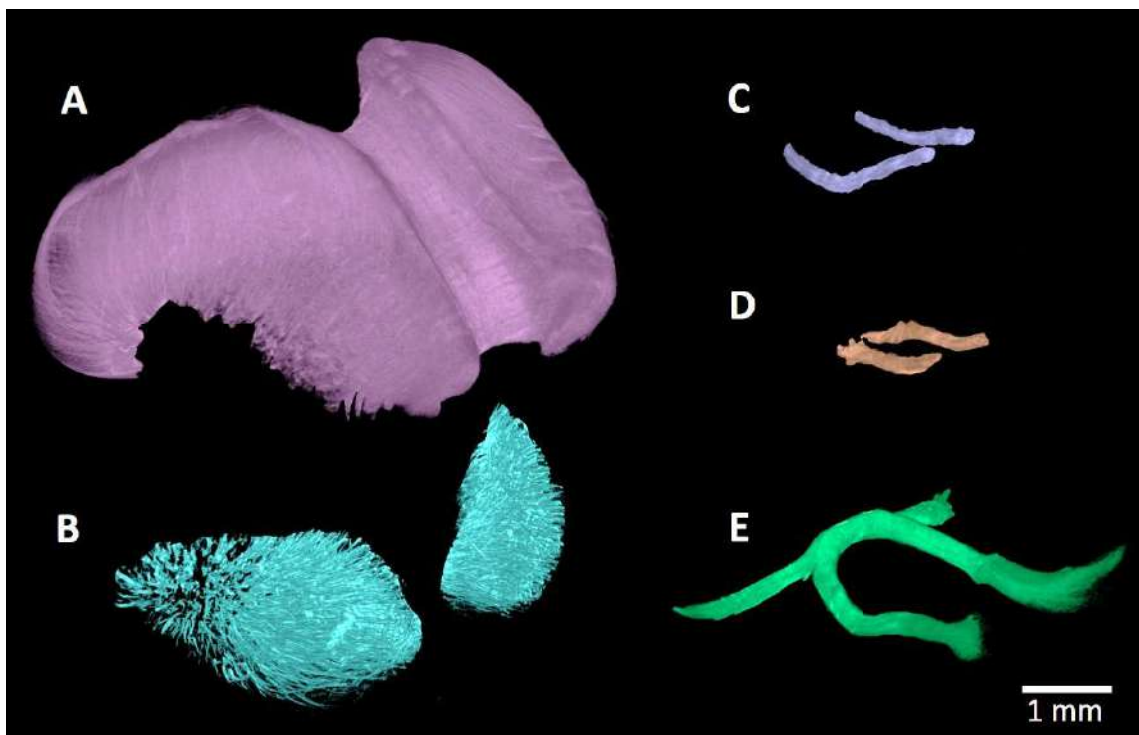


Figure 5. Structures segmented from micro CT images. (A) Complex of corpus callosum, dorsal hippocampal commissure and alveus (pink), (B) Myelinated fibres in caudoputamen (light blue), (C) Column of the fornix (purple), (D) Mamillothalamic tract (orange), (E) Anterior commissure (green).

4 Conclusion

Three-dimensional imaging of the rodent brain plays an important role in modern neurobiology and biomedicine research. This kind of imaging enables a precise analysis of developmental changes, tissue damage and tumor recognition with a focus on fine morphological modifications. We worked with several chemical contrasting protocols and compared their ability to visualize brain tissues by a laboratory micro CT device. Our results proved this method to be a powerful tool for a high-resolution *ex vivo* 3D imaging of the rodent soft tissues. The state of the art of the laboratory CT systems together with a staining protocol based on iodine solution enabled to reveal an intricate and geometrically complex internal brain structures in a high resolution. Tissue contrast was found to be considerably stronger in the micro CT images in comparison to the commonly used post-mortem MRI. Consequently, CT data enabled an easier segmentation and 3D reconstruction of internal brain structures. Generally, the 24 hours sample processing together with a two-hour-long CT measurement can provide a quick and complete visualization of the brain's internal and external morphology with a simultaneous and semi-automated identification of the major neural tracks, nuclei and other delicate details. Thanks to all these benefits, the micro CT systems have their place in a routine use in various types of neurobiological experiments.

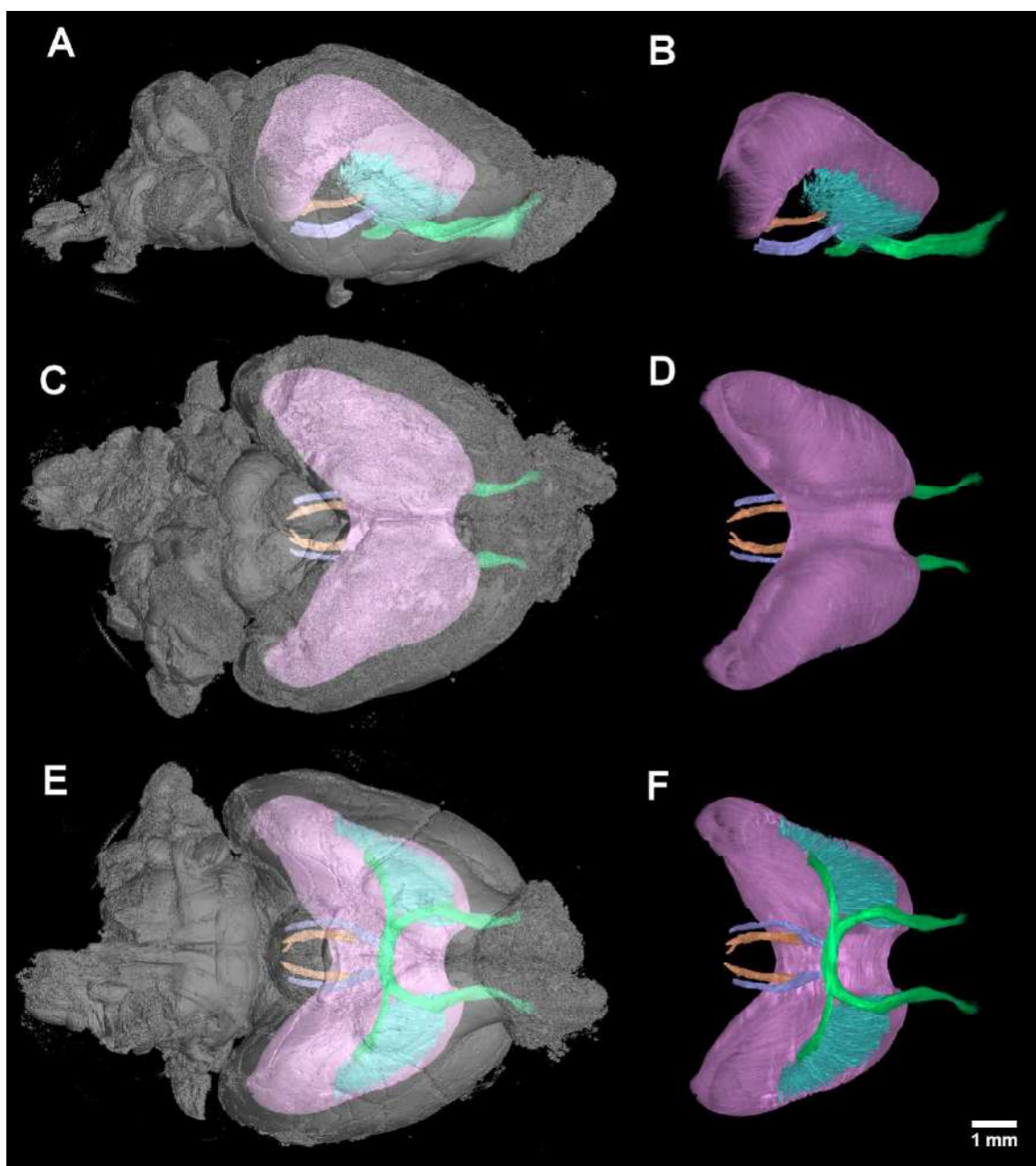


Figure 6. Segmented brain structures micro CT images. (A, B) Sagittal view, (C, D) dorsal view, (E, F) ventral views on dorsal hippocampal commissure and alveus (pink), column of the fornix (purple), mamillothalamic tract (orange), myelinated fibres in caudoputamen (light blue), anterior commissure (green) and complex of corpus callosum, dorsal hippocampal commissure and alveus (pink), in context of the whole adult mouse brain.

Acknowledgments

This research was carried out under the project CEITEC 2020 (LQ1601) with financial support from the Ministry of Education, Youth and Sports of the Czech Republic under the National

Sustainability Programme II and CEITEC Nano Research Infrastructure (MEYS CR, 2016–2019). JK acknowledges the support of the Brno University of Technology on the frame of grant FSI-S-17-4506 (Application of Advanced Optical Methods II). The MR part was supported by the Czech-BioImaging infrastructure grant LM2015062 (MEYS CR, 2016-2019) and NSP II grant LO1212 (MEYS CR, 2014–2018). MB lab was supported by the Ministry of Education, Youth and Sports of the Czech Republic (CZ.02.1.01/0.0/0.0/15_003/0000460) and Czech Science Foundation (14-37368G). MK was supported by SSMF fellowship.

References

- [1] L. Li, P. T. Newton, T. Boudierlique, M. Sejnohova, T. Zikmund, E. Kozhemyakina et al., *Superficial cells are self-renewing chondrocyte progenitors, which form the articular cartilage in juvenile mice*, *The FASEB Journal* **31** (2017) 1067.
- [2] M. Kaucka, T. Zikmund, M. Tesarova, D. Gyllborg, A. Hellander, J. Jaros et al., *Oriented clonal cell dynamics enables accurate growth and shaping of vertebrate cartilage*, *eLife* **6** (apr, 2017) e25902.
- [3] M. Kaucka, E. Ivashkin, D. Gyllborg, T. Zikmund, M. Tesarova, J. Kaiser et al., *Analysis of neural crest-derived clones reveals novel aspects of facial development*, *Sci. Adv.* **2** (2016) e1600060.
- [4] P. Cela, M. Hampl, N. Shylo, K. Christopher, M. Kavkova, M. Landova et al., *Ciliopathy protein *tmem107* plays multiple roles in craniofacial development*, *J. Dent. Res.* **97** (2017) 108.
- [5] K. Vymazalová, L. Vargová, T. Zikmund and J. Kaiser, *The possibilities of studying human embryos and fetuses using micro-CT: a technical note*, *Anat. Sci. Int.* **92** (2016) 299.
- [6] B.J. Nieman, A.M. Flenniken, S.L. Adamson, R.M. Henkelman and J.G. Sled, *Anatomical phenotyping in the brain and skull of a mutant mouse by magnetic resonance imaging and computed tomography*, *Physiol. Genom.* **24** (2006) 154.
- [7] M. Aggarwal, J. Zhang, M. Miller, R. Sidman and S. Mori, *Magnetic resonance imaging and micro-computed tomography combined atlas of developing and adult mouse brains for stereotaxic surgery*, *Neuroscience* **162** (2009) 1339.
- [8] B.D. Metscher, *MicroCT for comparative morphology: simple staining methods allow high-contrast 3d imaging of diverse non-mineralized animal tissues*, *BMC Physiol.* **9** (2009) 11.
- [9] R. Bar-Shalom et al., *Clinical performance of PET/CT in evaluation of cancer: additional value for diagnostic imaging and patient management*, *J. Nucl. Med.* **44** (2003) 1200.
- [10] W.W. Wasserman, M. Palumbo, W. Thompson, J.W. Fickett and C.E. Lawrence, *Human-mouse genome comparisons to locate regulatory sites*, *Nat. Genet.* **26** (2000) 225.
- [11] E. Stolz, M. Yeniguen, M. Kreisel, M. Kampschulte, S. Doenges, D. Sedding et al., *Angioarchitectural changes in subacute cerebral venous thrombosis. a synchrotron-based micro- and nano-CT study*, *NeuroImage* **54** (2011) 1881.
- [12] S. Heinzer, T. Krucker, M. Stampanoni, R. Abela, E. P. Meyer, A. Schuler et al., *Hierarchical microimaging for multiscale analysis of large vascular networks*, *NeuroImage* **32** (2006) 626.
- [13] S. Ghanavati, L.X. Yu, J.P. Lerch and J.G. Sled, *A perfusion procedure for imaging of the mouse cerebral vasculature by x-ray micro-CT*, *J. Neurosci. Meth.* **221** (2014) 70.
- [14] A.C. Langheinrich, M. Yeniguen, A. Ostendorf, S. Marhoffer, M. Kampschulte, G. Bachmann et al., *Evaluation of the middle cerebral artery occlusion techniques in the rat by in-vitro 3-dimensional micro- and nano computed tomography*, *BMC Neurol.* **10** (2010) .

- [15] B.P. Chugh, J.P. Lerch, L.X. Yu, M. Pienkowski, R.V. Harrison, R.M. Henkelman et al., *Measurement of cerebral blood volume in mouse brain regions using micro-computed tomography*, *NeuroImage* **47** (2009) 1312.
- [16] B. Xie, P. Miao, Y. Sun, Y. Wang and G.-Y. Yang, *Micro-computed tomography for hemorrhage disruption of mouse brain vasculature*, *Transl. Stroke Res.* **3** (2012) 174.
- [17] A. Dorr, J. Sled and N. Kabani, *Three-dimensional cerebral vasculature of the CBA mouse brain: A magnetic resonance imaging and micro computed tomography study*, *NeuroImage* **35** (2007) 1409.
- [18] R. Anderson and A.M. Maga, *A novel procedure for rapid imaging of adult mouse brains with MicroCT using iodine-based contrast*, *PLOS ONE* **10** (2015) e0142974.
- [19] A. de Crespigny, H. Bou-Reslan, M.C. Nishimura, H. Phillips, R.A. Carano and H.E. D’Arceuil, *3d micro-CT imaging of the postmortem brain*, *J. Neurosci. Meth.* **171** (2008) 207.
- [20] S. Saito and K. Murase, *Ex vivo imaging of mouse brain using micro-CT with non-ionic iodinated contrast agent: a comparison with myelin staining*, *Br. J. Radiol.* **85** (2012) e973.
- [21] N.S. Bautista, A. Martínez-Dávalos, M. Rodríguez-Villafuerte, T. Murrieta-Rodríguez, J. Manjarrez-Marmolejo, J. Franco-Pérez et al., *Ex vivo micro-CT imaging of murine brain models using non-ionic iodinated contrast*, *AIP Conf. Proc.* **1626** (2014) 19.
- [22] M. Dobrivojević, I. Boháček, I. Erjavec, D. Gorup and S. Gajović, *Computed microtomography visualization and quantification of mouse ischemic brain lesion by nonionic radio contrast agents*, *Croat. Med. J.* **54** (2013) 3.
- [23] N. Hayasaka, N. Nagai, N. Kawao, A. Niwa, Y. Yoshioka, Y. Mori et al., *In vivo diagnostic imaging using micro-CT: Sequential and comparative evaluation of rodent models for hepatic/brain ischemia and stroke*, *PLoS ONE* **7** (2012) e32342.
- [24] J.F. Hainfeld, H.M. Smilowitz, M.J. O’Connor, F.A. Dilmanian and D.N. Slatkin, *Gold nanoparticle imaging and radiotherapy of brain tumors in mice*, *Nanomedicine* **8** (2013) 1601.
- [25] B.D. Metscher, *MicroCT for developmental biology: A versatile tool for high-contrast 3d imaging at histological resolutions*, *Dev. Dynam.* **238** (2009) 632.
- [26] *Allen Mouse Brain Atlas*, Allen Institute for Brain Science © 2004, <http://mouse.brain-map.org/static/atlas>.
- [27] J. Hsieh, *Computed tomography: principles, design, artifacts, and recent advances*, SPIE, Bellingham, WA (2009).
- [28] A.C. Kak and M. Slaney, *Principles of computerized tomographic imaging*, Society for Industrial and Applied Mathematics (2001).
- [29] B.M. Dale, M.A. Brown and R.C. Semelka, *MRI: basic principles and applications*, John Wiley & Sons (2015).
- [30] P. Tofts ed., *Quantitative MRI of the brain: measuring changes caused by disease*, John Wiley & Sons (2005).
- [31] M. Tesařová et al., *Use of micro computed-tomography and 3D printing for reverse engineering of mouse embryo nasal capsule*, *2016 JINST* **11** C03006.

Oriented clonal cell dynamics enables accurate growth and shaping of vertebrate cartilage

Marketa Kaucka^{1,2}, Tomas Zikmund³, Marketa Tesarova³, Daniel Gyllborg⁴, Andreas Hellander⁵, Josef Jaros⁶, Jozef Kaiser³, Julian Petersen², Bara Szarowska², Phillip T Newton¹, Vyacheslav Dyachuk⁷, Lei Li¹, Hong Qian⁸, Anne-Sofie Johansson⁸, Yuji Mishina⁹, Joshua D Currie¹⁰, Elly M Tanaka¹⁰, Alek Erickson¹¹, Andrew Dudley¹¹, Hjalmar Brismar¹², Paul Southam¹³, Enrico Coen¹³, Min Chen¹⁴, Lee S Weinstein¹⁴, Ales Hampl⁶, Ernest Arenas⁴, Andrei S Chagin^{1,15}, Kaj Fried^{7*}, Igor Adameyko^{1,2*}

¹Department of Physiology and Pharmacology, Karolinska Institutet, Stockholm, Sweden; ²Center for Brain Research, Medical University Vienna, Vienna, Austria; ³Central European Institute of Technology, Brno University of Technology, Brno, Czech Republic; ⁴Unit of Molecular Neurobiology, Department of Medical Biochemistry and Biophysics, Karolinska Institutet, Stockholm, Sweden; ⁵Department of Information Technology, Uppsala University, Uppsala, Sweden; ⁶Department of Histology and Embryology, Medical Faculty, Masaryk University, Brno, Czech Republic; ⁷Department of Neuroscience, Karolinska Institutet, Stockholm, Sweden; ⁸Department of Medicine, Karolinska Institutet, Stockholm, Sweden; ⁹Department of Biologic and Materials Sciences, University of Michigan School of Dentistry, Ann Arbor, United States; ¹⁰Center for Regenerative Therapies, Technische Universität Dresden, Dresden, Germany; ¹¹Department of Genetics, Cell Biology and Anatomy, University of Nebraska Medical Center, Omaha, United States; ¹²Science for Life Laboratory, Royal Institute of Technology, Solna, Sweden; ¹³John Innes Centre, Norwich, United Kingdom; ¹⁴National Institute of Diabetes and Digestive and Kidney Diseases, National Institutes of Health, Bethesda, United States; ¹⁵Institute for Regenerative Medicine, Sechenov First Moscow State Medical University, Moscow, Russia

*For correspondence: kaj.fried@ki.se (KF); igor.adameyko@ki.se (IA)

Competing interests: The authors declare that no competing interests exist.

Funding: See page 28

Received: 09 February 2017

Accepted: 16 April 2017

Published: 17 April 2017

Reviewing editor: Marianne Bronner, California Institute of Technology, United States

© This is an open-access article, free of all copyright, and may be freely reproduced, distributed, transmitted, modified, built upon, or otherwise used by anyone for any lawful purpose. The work is made available under the [Creative Commons CC0 public domain dedication](https://creativecommons.org/licenses/by/4.0/).

Abstract Cartilaginous structures are at the core of embryo growth and shaping before the bone forms. Here we report a novel principle of vertebrate cartilage growth that is based on introducing transversally-oriented clones into pre-existing cartilage. This mechanism of growth uncouples the lateral expansion of curved cartilaginous sheets from the control of cartilage thickness, a process which might be the evolutionary mechanism underlying adaptations of facial shape. In rod-shaped cartilage structures (Meckel, ribs and skeletal elements in developing limbs), the transverse integration of clonal columns determines the well-defined diameter and resulting rod-like morphology. We were able to alter cartilage shape by experimentally manipulating clonal geometries. Using in silico modeling, we discovered that anisotropic proliferation might explain cartilage bending and groove formation at the macro-scale.

DOI: [10.7554/eLife.25902.001](https://doi.org/10.7554/eLife.25902.001)

Introduction

Cartilage is an essential skeletal and supportive tissue in our body. The shape and size of each cartilage element results from complex developmental processes; mesenchymal cells initially condensate, differentiate into chondrocytes, and then an orchestrated growth of the entire structure occurs (*Goldring et al., 2006*). Often, cartilage plays an important role as a developmental intermediate, such as during the endochondral growth of the long-bones (*Mackie et al., 2008*). Cartilage elements vary widely in their shapes: they may be simple shapes like rods or bars (Meckel, cartilage templates of the future long bones and ribs) or sheet-like structures (in the head), but can be extremely complicated with a huge number of irregular shapes (for instance, in the inner ear or pelvis). The geometrical properties of cartilage elements must be fine-tuned during the growth because cartilage provides indispensable structural support to the body during development. Yet, how this is achieved despite drastic changes in size is unclear.

After early cartilage forms from mesenchymal condensations, growth typically occurs in all dimensions. However, the diversity of cell dynamics controlling precise early growth and shaping is not well studied. At the same time, the late growth of long rod-shaped cartilage elements in limbs is achieved through a mechanism of endochondral ossification that includes oriented cell dynamics in growth plate-like zones (*Vortkamp et al., 1996*). In the germinal zone of a growth plate, chondrocytes proliferate and produce progenies that form long streams oriented along the main axis of the forming skeletal element. Inside such streams, chondrocytes undergo flattening, oriented cell divisions and hypertrophy before dissipating and giving place to the forming bone (*Nilsson et al., 2005*), a process which is controlled by many signals (*Kronenberg, 2003*). This cell dynamic enables efficient extension of the skeletal element in a specific direction that coincides with the orientation of cell divisions in the proliferative zone (*Abad et al., 2002*). Growth plate disorders may result in dwarfism and other illnesses (*De Luca, 2006*).

Some parts of the cartilaginous skull (e.g. the basisphenoid of the chondrocranium) also undergo endochondral ossification in synchondroses, and significant growth of the cranial base is achieved through a similar mechanism (*Hari et al., 2012; Wealhall and Herring, 2006*).

Synchondroses are mirror-image growth plates arising in the cranial base, which primarily facilitate growth in the antero-posterior direction (*Kettunen et al., 2006; Laurita et al., 2011; Nagayama et al., 2008; Young et al., 2006*). Disorders in the development of synchondroses severely impact the elongation of the cranial base and often result in short-faced mutants and a general decrease of the cranial length (*Ford-Hutchinson et al., 2007; Ma and Lozanoff, 1999*). Insufficient or abnormal development of a cartilage element is one of the reasons for human craniofacial pathologies, providing a connection between the chondrocranium and facial bone geometry, size and placement (*Wang et al., 1999*).

The growth mechanism operating in growth plates and synchondroses involves the transformation of the cartilage into the bone. Since growth plates or synchondroses are oriented towards a specific direction, the expansion of a cartilage in other dimensions is not clear from the mechanistic point of view and requires further investigation. For example, although it is well known that the mouse chondrocranium develops as 14 independent pairs of cartilage elements that form one united structure, the logic behind further shaping and scaling remains unclear (*Hari et al., 2012*). How these initially separated large cartilaginous elements form, grow and fine-tune their geometry, thickness and smoothness during development is still not completely understood. We hypothesized that accurate cartilage growth might require alternative cell dynamics that do not involve hypertrophy, ossification or growth plates.

Such alternative cell dynamics may also contribute to the accuracy of scaling during cartilage growth. Scaling is a process of growth that maintains both the shape and the proportions of the overall structure. In nature, scaling often involves sophisticated principles of directional growth and a number of feedback mechanisms (*Green et al., 2010*). For instance, during bird development, the diversity in beak shape is constrained by the dynamics of proliferative zones in the anterior face (*Fritz et al., 2014*). Furthermore, scaling variations of beaks with the same basic shape result from signaling that controls the growth of the pre-nasal cartilage and the pre-maxillary bone (*Mallarino et al., 2012*). Indeed, in order to accurately scale a pre-shaped 3D-cartilaginous template both local isotropic and anisotropic cell dynamics may be required.

To assess changes in the complete 3D anatomy of the face following cellular-level mechanistic studies we used a variety of approaches including micro-computed tomography (μ -CT), genetic tracing with multicolor reporter mouse strains, multiple mutants and mathematical modelling.

Most importantly, we reveal here how oriented clonal behavior in the chondrogenic lineage controls the overall geometry of the cartilage elements, and show that this geometry can be manipulated with molecular tools at various levels.

Results

Cartilage elements form and grow in all parts of the vertebrate body. The developing face provides a remarkable variety of cartilage geometries and sizes and, therefore, may serve as a sophisticated model system to study the induction of complex cartilaginous structures.

The developing cartilaginous skull, the chondrocranium, displays a very complex geometry of mostly sheet-like cartilages that result from coordinated anisotropic growth in all dimensions. Such expansion of sheet-like cartilaginous tissue during embryonic development involves several mechanisms that were proposed in the past, including the formation and growth of cartilage at synchondroses, as well as at the apical growth zone.

To understand the changes in dimensions of chondrocranium growth at major developmental stages, we took advantage of 3D reconstructions using μ -CT enhanced with soft tissue contrasting (**Figure 1**). This approach enables the identification of various tissues and cell types in the embryo based on differential uptake of tungsten ions. We validated the μ -CT visualization of embryonic cartilage by directly aligning stained histological sections with the 3D models (**Figure 1—figure supplements 1 and 2**).

We analyzed the expansion of the chondrocranium due to synchondroses and found that despite a significant antero-posterior elongation, synchondroses cannot entirely explain the growth dynamics in all directions: antero-posterior, latero-medial and dorso-ventral vectors of growth (**Figure 1A–C**). Specifically, we found a complete absence of synchondroses and other endochondrial ossifications in the growing nasal capsule, even at the earliest postnatal stages, while membranous ossifications appeared well developed. The stereotypical clonal cell dynamics found in synchondroses (**Figure 1D–I**) did not appear during the development of the nasal capsule. Therefore, during the entire embryonic development, chondrocranium growth and shaping is largely aided by additional and unknown mechanisms of growth.

To investigate another possible mechanism of growth, we examined the apical growth zone of the nasal capsule. To understand growth dynamics there, we birth-dated different regions of the facial cartilage using genetic tracing in *Col2a1-CreERT2/R26Confetti* and *Sox10-CreERT2/R26Confetti* embryos (**Figure 2—figure supplement 1**). Both *Col2a1-CreERT2* and *Sox10-CreERT2* lines recombine in committed chondrocyte progenitors and in mature chondrocytes. 3D analysis following tamoxifen injections at different developmental stages allowed us to identify the parts of the cartilage that develop from pre-existing chondrocytes and the regions generated from other cellular sources (**Figure 2, Figure 2—figure supplement 1**). As an example, after genetic recombination induced at E12.5, locations with high amount of traced cells show structures that come from pre-existing cartilage, whereas areas comprising from non-traced cells present structures originating from de novo mesenchymal condensations. We discovered that important and relatively large geometrical features are produced from waves of fresh mesenchymal condensations induced directly adjacent to larger pre-laid cartilage elements between E13.5 and E17.5: this includes the frontal nasal cartilage, nasal concha, labyrinth of ethmoid and, consistent with previous suggestions, cribriform plate (**Figure 2C and Figure 2—figure supplement 1A–K**). These results cannot be safely inferred from 2D traditional histological atlases because of the complex geometry. Our results are complementary to the findings of McBratney-Owen and Morris-Key with coworkers, who demonstrated that the complete chondrocranium (including skull base) develops from 14 pairs of early independently induced large cartilaginous elements that fuse together during later development (**McBratney-Owen et al., 2008**). Here, we demonstrated how new adjacent mesenchymal condensation can increase the geometrical complexity of a single solid cartilaginous element.

To substantiate our results, we took advantage of *Ebf2-CreERT2/R26Tomato* transgenic mouse line that can genetically label only a few selected patches of early mesenchyme in the cranial region. We wanted to test if some of these labelled mesenchymal patches can undergo chondrogenesis

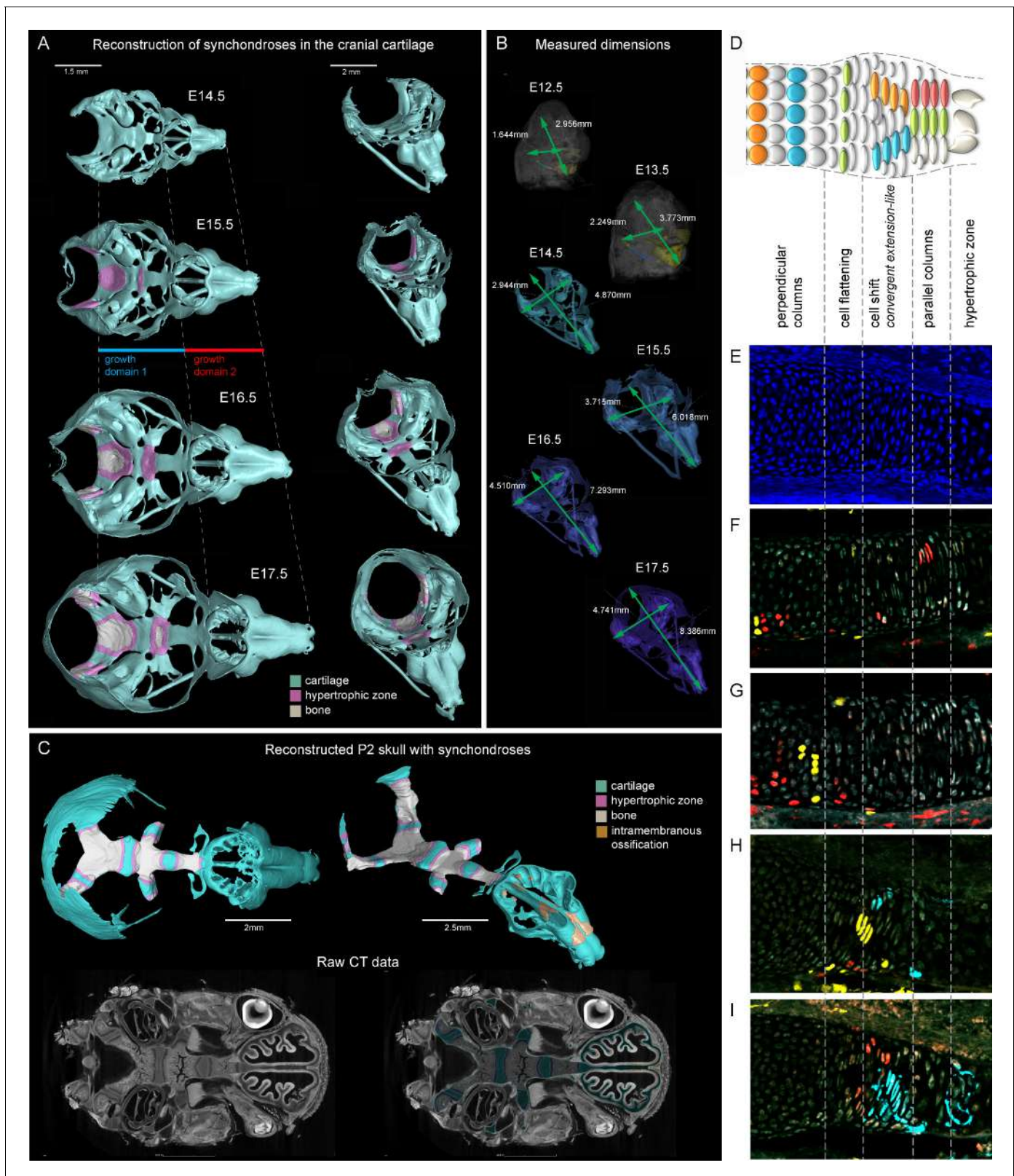


Figure 1. Visualizations of endochondrial ossifications in the chondrocranium during development. (A) 3D models of chondrocrania with visualized bone and hypertrophic cartilage. Note the absence of endochondrial ossifications in the nasal capsule between E14.5–17.5. Intramembraneous ossifications are not shown. (B) Width and length of the chondrocranium in E12.5–17.5 stages. (C) P2 stage model with visualized bone formation, hypertrophic zones and intramembraneous ossification in the nasal capsule. Clipping planes are applied for better visualizations of synchondroses. *Figure 1 continued on next page*

Figure 1 continued

Corresponding raw CT data are presented in the lower part. (D–I) Clonal genetic tracing in synchondroses with *Sox10CreERT2/R26Confetti*; injected at E12.5 and collected at E17.5. (D) Schematic of synchondroses, (E) DAPI stained nuclei, (F–I) different clonal arrangements in various zones of progressing synchondroses.

DOI: [10.7554/eLife.25902.002](https://doi.org/10.7554/eLife.25902.002)

The following figure supplements are available for figure 1:

Figure supplement 1. Histological confirmation of μ -CT results.

DOI: [10.7554/eLife.25902.003](https://doi.org/10.7554/eLife.25902.003)

Figure supplement 2. Immuno- and histological validation of cartilage contrasting obtained from μ -CT analysis and subsequent 3D modelling.

DOI: [10.7554/eLife.25902.004](https://doi.org/10.7554/eLife.25902.004)

independently and much later than most of the chondrocranium structure. If that would be the case, we could expect the formation of very sharp borders between the labelled and non-labelled cartilage due to the fusion of newly produced labelled cartilage with the old unlabeled one. If the local cartilage would form from labelled and unlabeled mesenchyme at the same time, the border would not form due to mesenchymal clone mixing that we observe when we label early neural crest. We injected *Ebf2-CreERT2/R26Tomato* animals with tamoxifen at E12.5 and analyzed the embryos at E17.5 (**Figure 2—figure supplement 2**). As a result, we discovered that the cartilage element connecting the inner ear with the basisphenoid was genetically traced, and demonstrated a very sharp border with non-traced cartilage (**Figure 2—figure supplement 2C–D**). μ -CT data confirmed that this element develops entirely after E14.5 from newly formed mesenchymal condensations adjoining the chondrocranium (**Figure 2—figure supplement 2A–B**), and this might be related to differential regulation at the neural crest-mesodermal border (McBratney-Owen et al., 2008; Thompson et al., 2012). At the same time, the main structure of the chondrocranium is expanded in a very precise and symmetrical way due to unknown cellular and molecular mechanisms that cannot be explained by the freshly induced condensations, the apical growth zone, or even cell dynamics in synchondroses. Our μ -CT results (**Figure 2**) show that various parts of the chondrocranium develop due to the growth of pre-existing cartilage not involving ossifications, while only additional features are induced in waves as de novo mesenchymal condensations that fuse with the main element during their maturation or expand in the process of ossification.

We further focused on the developing nasal capsule because its growth does not involve synchondroses while the apical growth zone and adjoining mesenchymal condensation only partly provide for the growth and shaping modifications.

The results obtained from comparisons of cartilaginous nasal capsules from different developmental stages showed that the shape of the structure is generally established by E14.5 (**Figure 3, Figure 3—figure supplement 1, Figure 3—figure supplement 2, Video 1**). Nevertheless, from E14.5 until E17.5 the cartilaginous nasal capsule is accurately scaled up with significant geometrical tuning (**Figure 3A–B**). Previous knowledge suggests that the underlying growth mechanism should be based on appositional growth of the cartilage during its transition to bone (Hayes et al., 2001; Li et al., 2017), however, numerous facial cartilages never ossify, but continue to grow.

Tomographic reconstructions of sheet-shaped cartilage elements in the nasal capsule revealed extensive expansion of the cartilage surface area and overall volume (**Figure 3E–F**). Surprisingly, the thickness of the cartilaginous sheets did not change as much as the other dimensions during nasal capsule growth (**Figure 3C–F, Figure 3—figure supplement 1, Video 1**). Thus, the sheet-shaped cartilage expands mostly laterally (within the plane) during directional growth. Therefore, we expected that clonal analysis of the neural crest progeny (with *Plp1-CreERT2/R26Confetti*) and of early chondrocytes (with *Col2a1-CreERT2/R26Confetti* or *Sox10-CreERT2/R26Confetti*) would reveal clonal units (so called clonal envelopes) oriented longitudinally along the axis of the lateral expansion of the cartilage. Surprisingly, and contrary to this, clonal color-coding and genetic tracing demonstrated transversely oriented clones represented by mostly perpendicular cell columns or clusters formed by traced chondrocytes (**Figure 4, especially A–C, Figure 4—figure supplement 1**).

To understand this process more in depth, we started with genetic tracing of the neural crest cells and their progeny in the facial cartilage with *Plp1-CreERT2/R26Confetti* (tamoxifen injected at E8.5). Clonal analysis and color-coding of neural crest-derived chondrogenic and non-chondrogenic ectomesenchyme showed intense mixing of neural crest-derived clones in any given location (**Figure 4A–**

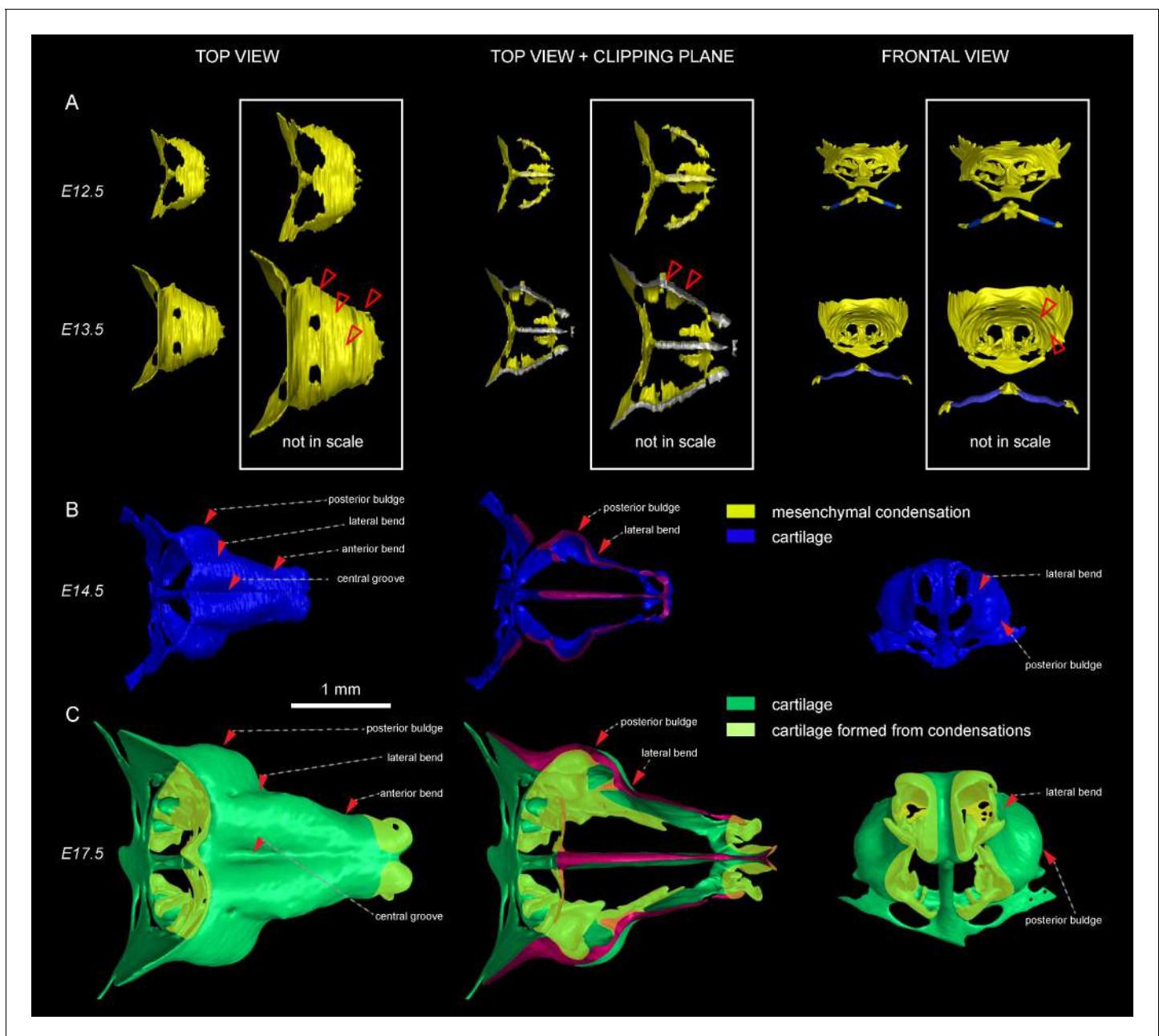


Figure 2. Induction of initial shape and geometrical transformations of the facial chondrocranium. (A–C) μ -CT-based 3D reconstruction of chondrogenic mesenchymal condensations and cartilage in the face of E12.5, E13.5, E14.5 and E17.5 embryos. (A) Mesenchymal condensations (yellow) segmented from E12.5 and E13.5 embryos and presented in frontal and top projections. Note that the basics of the facial chondrocranium are already established at the stage of mesenchymal condensations during the early development, while general geometry and fine details are tuned during further transformations. (B–C) Top, clipping plane + top and frontal projections of E14.5 (B) and E17.5 (C) developing facial chondrocranium. (C) Yellow color highlights the results of cartilage birth-dating experiments and shows the areas produced from de novo mesenchymal condensations that appear in successional waves after the primary cartilage (shown in green) is produced at previous stages (E14.5). Note that the shape of the facial chondrocranium develops as a result of incremental formation and additive fusion of new mesenchymal condensation with pre-existing cartilage. Red arrows indicate areas of cartilage which bend at later developmental stages (B,C) and red-outlined arrows indicate the same areas within the mesenchymal condensations at E13.5, prior to bending (A, bottom).

DOI: [10.7554/eLife.25902.005](https://doi.org/10.7554/eLife.25902.005)

The following figure supplements are available for figure 2:

Figure supplement 1. Genetic tracing serves as a tool for birth-dating of the cartilage during the embryonic development.

DOI: [10.7554/eLife.25902.006](https://doi.org/10.7554/eLife.25902.006)

Figure 2 continued on next page

Figure 2 continued

Figure supplement 2. Genetic tracing based on Ebf2-CreERT2/R26Tomato serves as an indicator for structures developed from late mesenchymal condensations.

DOI: [10.7554/eLife.25902.007](https://doi.org/10.7554/eLife.25902.007)

C, **Figure 4—figure supplement 1D–G** (Kaucka et al., 2016). At the same time, chondrogenic ectomesenchyme demonstrated the presence of transversely oriented doublets of genetically traced and also EdU-labeled cells already at E13.5 (**Figure 4—figure supplement 1G** (inserts) and H). Next, analysis of neural crest progeny in established cartilage highlighted the presence of perpendicularly oriented clonal doublets and columns (**Figure 4A–C**). Further analysis of EdU incorporation and genetic tracing with chondrocyte-specific *Col2a1-CreERT2/R26Confetti* and *Sox10-CreERT2/R26Confetti* lines confirmed the existence of transversely oriented products of cell proliferation in the mature (E14.5–E17.5) cartilage (**Figure 4D–F** for EdU, **Figure 4G,H–L** and **Figure 4—figure supplement 2** for lineage tracing). These results imply that cells in the sheet-shaped cartilage do not allocate daughter cells in lateral (longitudinal) dimensions as would be intuitively expected.

Thus, simple lateral or unidirectional proliferation cannot account for the accurate scaling of the sheet-shaped cartilage in the face. Instead, the cartilage development from chondrogenic condensations is achieved by a cellular mechanism that involves intercalation of columnar clonal units.

It was unclear to us why column-like structures, and no other shapes, are integrated into the sheet-shaped cartilage and how the fine surface is maintained during this mechanism of growth. To better understand possible mechanisms of accurate sheet-shaped cartilage surface development we modelled individual cell dynamics, in silico in 4D (3D + time) (**Figure 5**) (Hellander, 2015). We used this modelling to address two questions: firstly, under what conditions are clonal columns observed? Secondly, how is the sheet-like shape achieved by polarized or non-polarized cell divisions of single-cell thick layers and what are the controlling mechanisms? We tested a group of variables including: cell division speed, allocation of daughter cells in random- or defined directions, orientation cues in the tissue (equivalent to molecule gradients), as well as pushing/intercalating of the daughter cells during proliferation. We qualitatively compared the results from in silico simulations to our experimental clonal analysis from various genetic tracing experiments, in order to identify conditions in the model that were compatible with patterns observed in vivo.

The results of the mathematical modelling suggested that the clonal dynamics observed in natural conditions requires polarity cues in the system, specifically, a two-sided gradient of signals would be required to precisely fine-tune cartilage thickness (**Figure 5A–J**). At the same time, some yet to be identified mechanism controls the average number of cell divisions in a column, further controlling columnar height and undoubtedly regulating the local thickness of the cartilage. Combined with the observed introduction of the transverse clonal columns, oriented cell proliferation can provide fine surface generation and scaling (**Figure 4—figure supplement 2**). Moreover, the model highlighted the elegance of cartilage design involving transverse columnar clones in the sheet-shaped elements: this logic enables the uncoupling of thickness control (depends on cell numbers within a clone) and lateral expansion (depends on the number of initiated clones), which are likely two molecularly unrelated processes in vivo. The absence of a gradient during in silico simulations led to the generation of 3D asymmetrical clusters instead of straight columns (even in conditions of highly synchronized cell divisions, and starting from a laterally space-constrained initial configuration - suggesting the promotion of vertical growth due to space-exclusion in the lateral direction) (**Figure 5I,J**). This, in turn, led to the formation of surface irregularities in the cartilage with subsequent loss of local flatness (heat-map diagram in **Figure 5I,J**).

Importantly, lineage tracing also showed that for cartilaginous structures in the head with asymmetrical or complex irregular geometries, such as areas where several sheet-shaped cartilage elements were merged, clones were not constructed to perpendicular columns. In such locations, we identified irregular clonal clusters or randomly oriented clonal doublets, in accordance with the modelling results (**Figure 6A–J**). Thus, the shape and orientation of clones corresponds to the local geometry of the cartilage element.

Next, we attempted to target a molecular mechanism that controls the flatness and sheet-like shape of the facial cartilaginous sheets. We discovered that activation of ACVR1 (BMP type one receptor, ALK2) in developing cartilage leads to a phenotype with targeted clonal micro-geometries

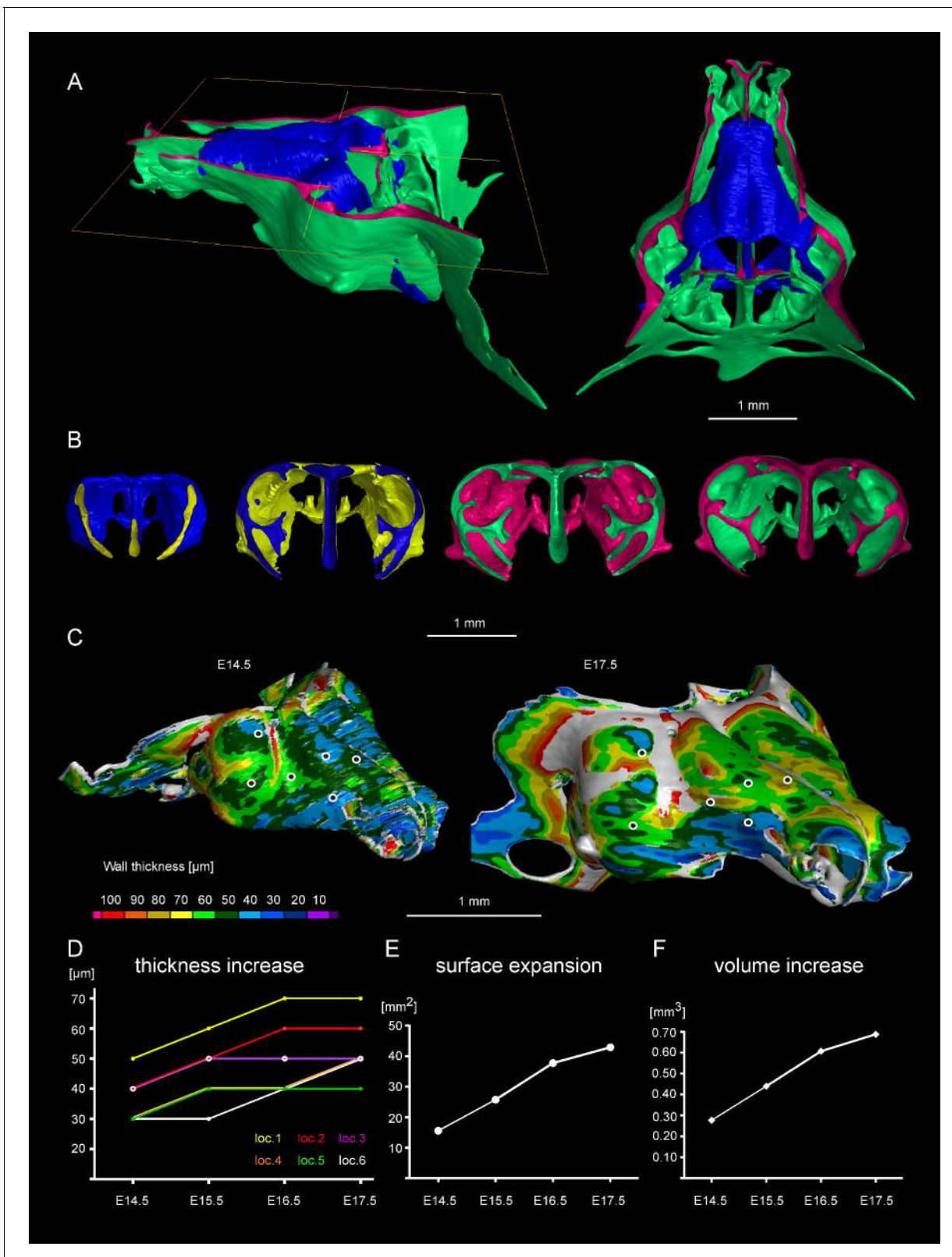


Figure 3. Facial chondrocranium undergoes major lateral expansion without extensive thickening during growth. (A) The 3D-model of E14.5 nasal capsule (blue) is placed onto the E17.5 model (green) for better presentation of growth-related changes. (B) Frontal clipping planes of 3D-models of nasal capsules at E14.5, E15.5, E16.5 and E17.5 (from left to right). Notice the mild changes in cartilage thickness as compared to the lateral expansion of the whole structure during growth. (C) Cartilage thickness heat-maps at E14.5 and E17.5 developmental stages. Less thick locations (color-coded in Figure 3 continued on next page

Figure 3 continued

blue) correspond to intense growth zones shown in **Figure 11**. Dots show individual positions selected for precise measurements and demonstration on the graph shown in (D). Note that after E16.5 cartilage thickness remains relatively stable. (E–F) Cartilage surface area (E) and volume (F) expansion has been measured and compared between above mentioned stages. Note that there is a much greater increase in surface and volume (approximately 3-fold) than in thickness of the cartilage (less than 50%).

DOI: [10.7554/eLife.25902.008](https://doi.org/10.7554/eLife.25902.008)

The following figure supplements are available for figure 3:

Figure supplement 1. 3D models and wall thickness analysis of chondrocraniums at different developmental stages.

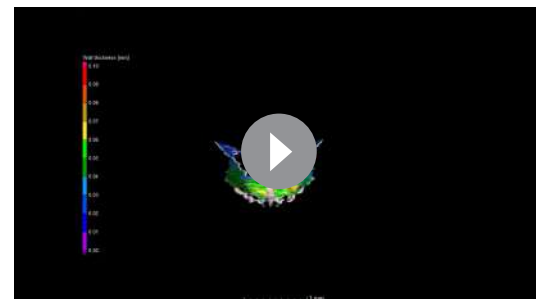
DOI: [10.7554/eLife.25902.009](https://doi.org/10.7554/eLife.25902.009)

Figure supplement 2. Comparisons of the shape and size differences between developmental stages and Wnt/PCP mutants.

DOI: [10.7554/eLife.25902.010](https://doi.org/10.7554/eLife.25902.010)

(**Figure 6K–P,R**). We utilized a constitutively activated caALK2 transgene (*Fukuda et al., 2006*) together with genetic tracing in a way that every GFP-expressing cell is carrying constitutively active ACVR1. This experiment revealed a dramatic change of the shape of clonal envelopes, changing from straight perpendicular columns to disorganized spherical clusters inside the sheet-shaped cartilages of transgenic *Sox10-CreERT2/R26caALK2-IRES-GFP* embryos (**Figure 6K–N**). The ectopically activated ACVR1 resulted in the presence of clonal spherical clusters that interfered with the cartilage borders and caused the formation of ectopic bumps, swellings and other abnormal local shapes - in accordance with the mathematical modelling predictions (substantially resembling the condition with no gradient, see **Figure 5I**) (**Figure 6O–P**). All recombined cells in this caALK2 experiment became Sox9⁺ chondrocytes. There were no other cell types found to be GFP⁺, including perichondrial cells. This result indicates that BMP family ligands either produce the gradient that directs the orientated behavior of chondrocytes inside of the cartilage or, alternatively, that an experimental increase of BMP signaling renders the cells insensitive to the gradient established by other molecules. In any case, ACVR1 mutation can be used as a tool to change columnar arrangements into clusters (**Figure 6N,R**). The activation of ACVR1 by *Sox10-CreERT2* starting from E12.5 occurred both in perichondrial cells and in chondrocytes (based on our genetic tracing results using *Sox10-CreERT2/R26Confetti*). This later coincided with clonal bumps and bulging regions positioned mainly at the surface of sheet-shaped cartilaginous sheets (**Figure 6L,N,P**). These data also support the hypothesis that integration of clonal chondrocyte clusters into existing cartilaginous sheets likely depends on clonal shape and originates from the periphery of the cartilage. When this column-inserting process fails, the progeny of cells at the periphery of the cartilage forms ectopic bumps outside of the normal cartilage borders, and disrupts the flatness and straightness of cartilage surfaces.

Next, we attempted to block the planar cell polarity (PCP) pathway to challenge the system and disrupt the formation of perpendicular columns in the flat or curved cartilaginous sheets. To do this we performed μ -CT and EdU-incorporation analysis on Wnt/PCP mutants. Wnt/PCP pathway is well known for driving the cell and tissue polarity, and distinct facial phenotypes have appeared in *Ror2*, *Vangl2* and *Wnt5a* homozygous mutants (**Figure 7A**). When EdU was administered 24 hr before embryo harvest, subsequent analysis showed no differences in the EdU-positive perpendicular clonal columns which formed within sheet-shaped facial cartilage of



Video 1. 3D-models based on segmentation of mesenchymal condensations and mature cartilage from μ -CT tomographic data. The first sequence illustrates wall thickness analysis results represented as a heat-map, starting from E12.5 (facial mesenchymal condensation) until E17.5 (facial cartilage). Cartilages and other soft tissues shrink during contrasting with phosphotungstic acid, and, thus, the reported metrics cannot be directly compared with biological samples treated in a different way. The following sequence shows facial chondrocranium models of Wnt/PCP mutants in comparison to the wild type. The last sequence shows the full chondrocranium at different embryonic stages, followed by 3D models of both the control embryo and *Wnt5a* mutant embryo at E17.5. DOI: [10.7554/eLife.25902.011](https://doi.org/10.7554/eLife.25902.011)

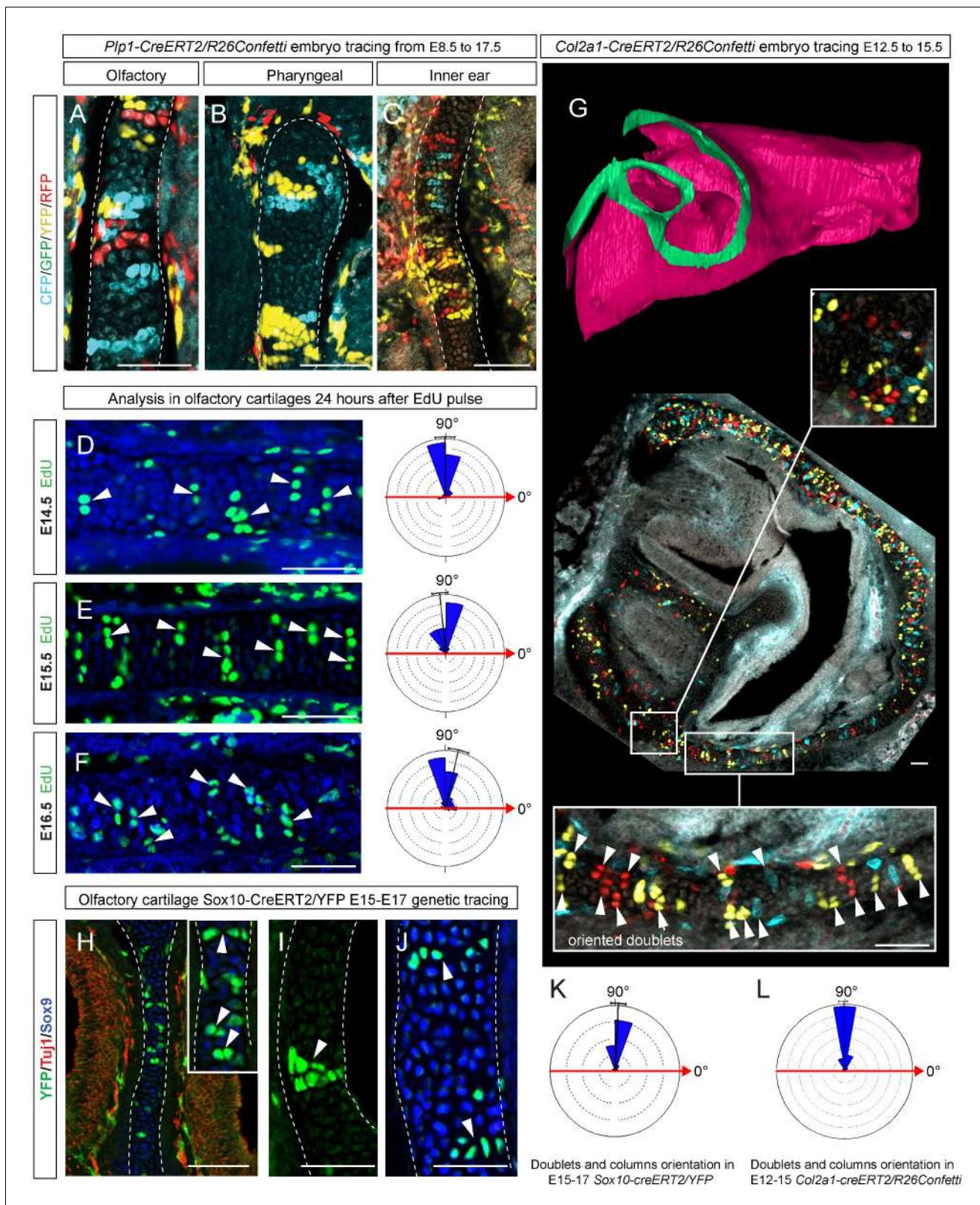


Figure 4. Clones of chondrocytes show transversely oriented columnar structure in sheet-shaped facial cartilage. (A–C) Chondrocyte clones at E17.5 were genetically traced from neural crest cells (E8.5), sagittal sections. The cartilage is outlined with white dashed line. (D–F) Analysis of EdU incorporation (24 hr after the pulse) into growing cartilage at different stages. Arrowheads indicate sparse columnar arrangements of EdU⁺ cells. Rose diagrams show orientation of EdU⁺ clusters in the cartilage of embryos at E14.5 (D), E15.5 (E) and E16.5 (F). (G) Genetic tracing of chondrocytes

Figure 4 continued on next page

Figure 4 continued

initiated at 12.5 and analyzed at 15.5. The clipping plane of a 3D-model (side projection) is shown for better orientation in the analyzed region. Note the transverse orientation of clonal doublets and columns (arrowheads). (H–J) Genetic tracing induced at E15.5 and analyzed two days later in embryos of *Sox10-CreERT2/R26YFP* mouse strain. Arrowheads indicate clonal columns of chondrocytes that formed inside of the growing cartilage between E15.5 and E17.5. The orientations of clonal arrangements are shown in the rose diagram in (K). (L) Orientation of clonal doublets and columns in genetically traced cartilage (from E12 to E15) of *Col2a1-CreERT2/R26Confetti* embryos. Scale bars = 100 μm .

DOI: [10.7554/eLife.25902.012](https://doi.org/10.7554/eLife.25902.012)

The following figure supplements are available for figure 4:

Figure supplement 1. Oriented clonal dynamics in chondrogenic mesenchymal condensations.

DOI: [10.7554/eLife.25902.013](https://doi.org/10.7554/eLife.25902.013)

Figure supplement 2. Clonal oriented clusters of chondrocytes contain closely associated perichondrial cell in flat facial cartilages.

DOI: [10.7554/eLife.25902.014](https://doi.org/10.7554/eLife.25902.014)

Wnt5a knockout mutants or wild type controls (**Figure 7B–D**). μ -CT analysis at early developmental stages showed that as early as at E12.5, Wnt5a mutants had abnormal shape and placement of the mesenchymal condensations that create a template for future cartilaginous structures (**Figure 7E–F**). Although μ -CT analysis of Wnt5a, Ror2 and Vangl2 homozygous mutants at later developmental stages confirmed that chondrocranium shape was heavily affected (with generally shortened nasal capsules as compared to both wild-type and heterozygous controls) (**Figure 7A**), we did not detect any defects in cartilage micro-geometry, including thickness or surface organization. Altogether, these results indicate that Wnt5a, Ror2 and Vangl2 do not control cartilage growth and shaping per se (via the insertion of perpendicular columns). Instead, they influence the position and shape of chondrogenic condensations, which define the future geometry of the facial chondrocranium (**Figure 7E,F**).

Following the prediction from our mathematical model that the thickness of the cartilage can be controlled by the number of cells in the inserted clonal column, we searched for the molecular mechanisms which control this. Knowing from our results that proliferation rate drops in the mature cartilage, we hypothesized that chondrocyte maturation speed may influence the number of cell divisions within a column. To test this suggestion, we analyzed G-protein stimulatory α -subunit ($Gs\alpha$) knockout embryos (**Figure 8**). Inactivation of $Gs\alpha$, encoded by *Gnas*, is known to lead to accelerated differentiation of columnar chondrocytes, without affecting other aspects of cartilage biology (**Chagin et al., 2014**). We analyzed three different locations in the developing chondrocrania, and observed a significant reduction of cartilage thickness in absolute metrics (**Figure 8A,B,J**), as well as in terms of the number of cells within each column (**Figure 8B–H**). Thus, the $Gs\alpha$ knockout is a perfect tool to test whether the modulation of differentiation speed can be used to create a variation of local cartilage thickness. The result of this experiment demonstrated that sheet-shaped cartilages in $Gs\alpha$ knockout embryos are thinner than that of littermate controls, while other parameters (including general size and shape of nasal capsule and other locations in the head together with the transverse orientation of chondrocyte columns) remain largely unaffected (**Figure 8A,B,I**). Thus, these data experimentally validated mathematical predictions and confirmed that the thickness of cartilage is determined by the number of cell divisions within a transverse clone, and that this is uncoupled from lateral expansion.

Next, we wanted to know how clonal cell dynamics accounts for the shape development in rod-shaped cartilages. For this we investigated the clonal dynamics in Meckel, rib and limb cartilages with the help of Confetti-based genetic tracing as well as EdU incorporation. The clonal arrangements appeared highly oriented and strongly resembled the clonal columns we observed in the facial cartilage. The columnar clones were oriented mostly transversally in the plane of a rod diameter and could not explain the early growth along the main axis of the skeletal element (**Figure 9**). These tracing results suggested that longitudinal extension is based on continuous development of chondrogenic mesenchymal condensations on the distal tip and is followed by the transverse proliferation of chondrocytes, which accounts for the proper diameter of a cartilaginous rod. The logic of oriented cell dynamics in sheet-shaped and rod-shaped cartilages is summarized in **Figure 10**.

Since the integration of clonal units is likely to be uneven in the cartilage, we questioned how the anisotropy of local proliferation can impact the shaping processes on a macro-scale. Starting from E14.5, the olfactory capsule is already formed of mature chondrocytes. Indeed, in this structure,

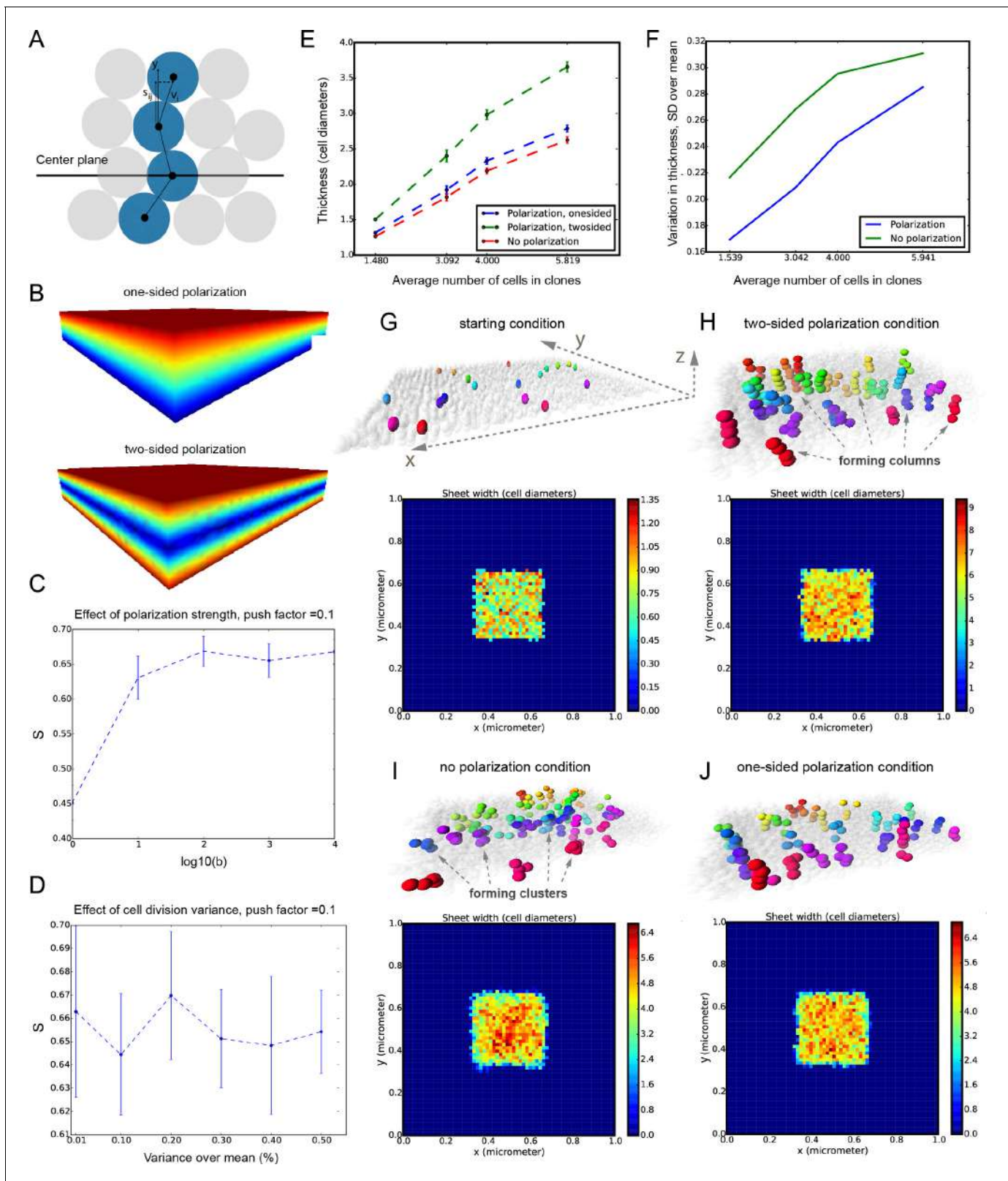


Figure 5. Mathematical model of cell dynamics during sheet-shaped cartilage development and growth. (A) Transversal (along z-axis) clipping plane showing conceptual arrangements of modelled cells within the layer as a result of a typical simulation. The degree of microstructure order, S , is measured by the sum of orthogonal projections on the unit vector in the z-direction, normalized by the number of cells. (B) Visualized and modelled one- and two-sided gradients used to direct oppositional growth of the clonal columns during computer simulations. (C) The degree of determinacy in Figure 5 continued on next page

Figure 5 continued

the response to the external gradient is modeled by a parameter, b , where a high value results in near perfectly polarized cell divisions (pushing may still introduce randomness in the eventually chosen site) and where the limit b tends to zero results in completely random division directions. As can be seen, the degree of microstructure order, and hence columnar growth, increases with the strength of the polarization response. (D) For a strongly polarized cell, the model predicts that even a large variation in the individual cell division times results in only a moderate decrease in the columnar order. (E) Graph showing the dependence of cartilage thickness on the absence or presence of one- and two-sided polarizing gradients. (F) Graph showing how the regularity of the thickness depends on the presence of a polarizing gradient. Note that, based on (E–F), the conditions with polarization demonstrate higher regularity and thickness over multiple locations. (G–I) Snapshots of typical *in silico* simulations of cell dynamics during sheet-shaped cartilage development: layers of chondrogenic cells demonstrated in 3D before (G) or after simulations (H–J) shown together with 2D heatmap diagrams of cell layer thickness irregularity (below) represented as a view from above (x,y dimensions). Clonal progeny is represented as individually color-coded cellular clusters or columns in 3D visualizations. Note the high degree of thickness irregularity that corresponds to the variety of differently oriented clonal shapes in condition with no polarizing gradient (I). The highest geometrical regularity of the modelled cartilaginous sheet together with stereotypical columnar clonal arrangement is achieved in the condition with two-sided polarizing gradient (H).

DOI: [10.7554/eLife.25902.015](https://doi.org/10.7554/eLife.25902.015)

proliferation was localized to specific regions, but remained generally low elsewhere (Figure 11A–B) according to the analysis of EdU incorporation. As we demonstrated above, proliferative regions expand due to the active integration of new clonal columns and clusters. We projected the low- and high proliferative zones onto the 3D structure of the nasal capsule at E13.5–E15.5 to understand not only the dynamics of lateral expansion, but also to see how the local expansion of cartilage may influence bending and geometrical changes on a large scale (Figure 11C–F). Since proliferative zones in nasal capsule are restricted and have defined edges, they inevitably induce tension and bending of the surrounding cartilage sheet.

In order to address the logic of distributed proliferative zones and its role in shape transitions between stages we took advantage of the mathematical model developed by the Enrico Coen and Andrew Bangham laboratories. This model has been efficiently validated and applied for advanced simulations of complex 4D plant organ development (Green *et al.*, 2010; Kennaway *et al.*, 2011). To simulate *in silico* nasal capsule shape transition from E13.5 to E14.5, we generated a basic E13.5-like shape by converting a sheet-shaped growing trapezoid into a corresponding 3D structure (Figure 12A, central part and Video 2). The result was considered as a simplified starting condition for further simulations. Next, two lateral zones with a low rate of proliferation were introduced according to their original position in E13.5 nasal capsule. Further simulations of the growth showed that these low proliferative zones impose a characteristic bending on the sides of the simulated structure. This bending corresponds to the lateral transformations observed in embryonic development of the nasal capsule between E13.5 and E14.5 (Figure 12B–C). This characteristic lateral bending did not depend on antero-posterior polarity in the cartilage or formation of the groove at the midline (Figure 12D). According to the model, the polarity only affected the potential for the anterior elongation due to the anisotropic growth of the entire cartilaginous structure. Our results also suggested that the nasal septum functions as a slower proliferating anchoring point to the roof of the nasal capsule, which is necessary for the formation of the midline groove at E14.5. A simulated groove at the midline provided for the general bend and flattened shape of the *in silico* cartilage, similar to the native E14.5 nasal capsule and contrary to the model without the simulated midline groove (Figure 12C–D).

To validate the general rules of *in silico* transformations, we performed material modelling using plastic film to simulate anisotropic expansion and bending due to integration of local growing zones with attached borders. This simple material modeling demonstrated that growth zones/local expansions in the flat planes generate mechanical tensions which bend the structure (Figure 12E). We then performed another material modelling experiment using isotropic thermal expansion/constriction of a plastic film. For this purpose, we drew black regions (analogous to the lateral low proliferative zones in E13.5 nasal capsule) onto white plastic film that was cut in a shape of a trapezoid capable of transforming into a nasal capsule-like dome. Under the heating provided by a thermal infrared lamp, the black zones received more heat and isotropically shrunk. Shrinkage of the black zones created physical tensions that eventually bent the structure in a way similar to the original nasal capsule geometry at E14.5 (Figure 12F). The model with shrinking zones is comparable to the real growth conditions as the nasal capsule expands faster than spatially distributed slow

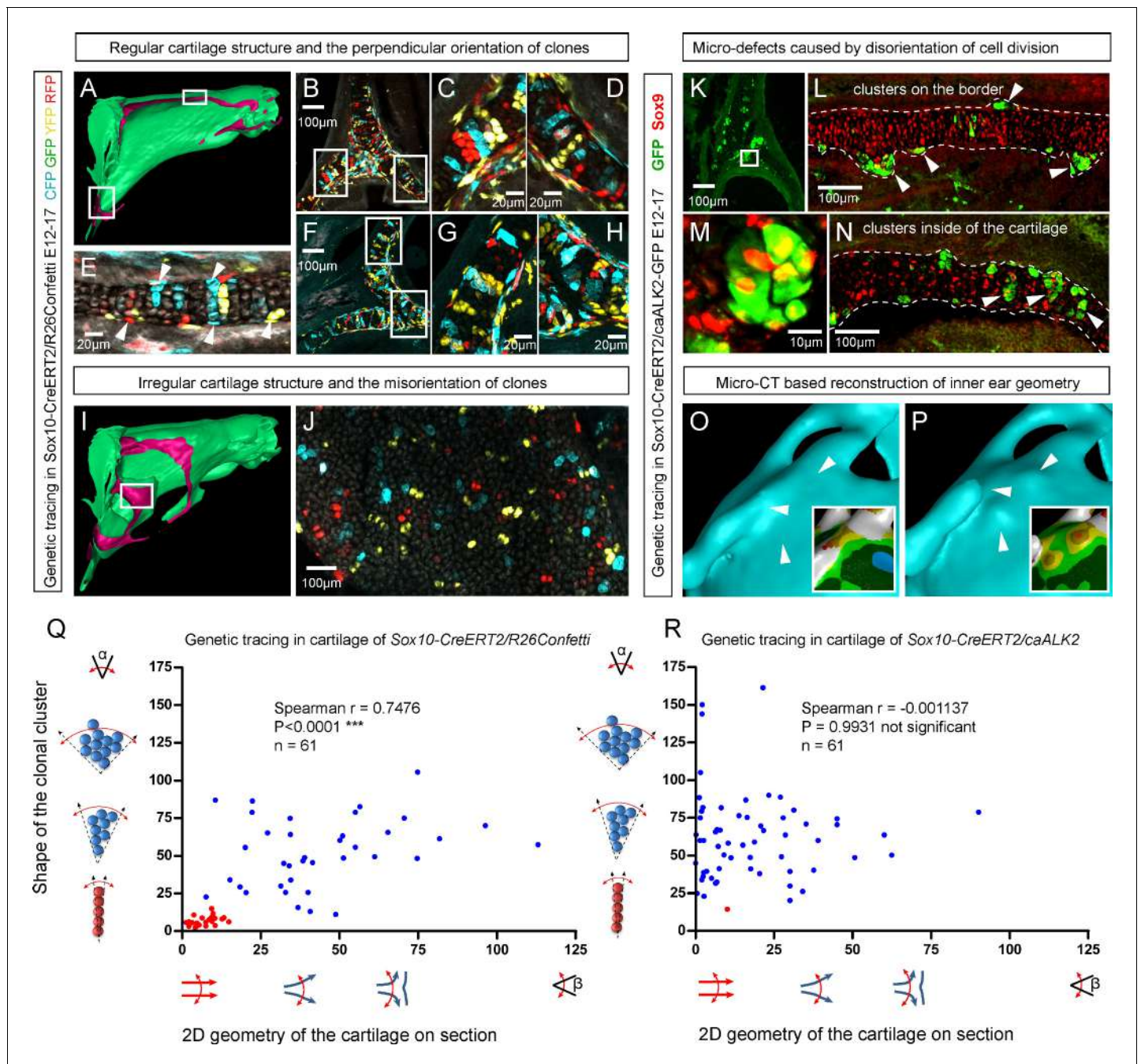


Figure 6. Clonal arrangements of chondrocytes influence local geometry and cartilage surface. (A–H) Columnar clonal arrangements in sheet-shaped cartilages of facial chondrocranium visualized with genetic tracing in *Sox10-CreERT2/R26Confetti* embryos. (A) 3D-model with a clipping plane shown as a side projection. White frames show locations analyzed in (B–H). Panels (C,D) and (G,H) represent magnified areas outlined in (B) and (F), respectively. (E) Traced perichondrial cells at the base of chondrocyte columns that share a clonal origin and are indicated by arrowheads. Note that rich tracing in the perichondrium correlates with highly efficient tracing in the cartilage (compare, for example, (B–D and E)). (I–J) Clonal clusters show no columnar structure in geometrically irregular elements such as junctions and fusion points of several cartilaginous elements (highlighted in 3D-model with frame). (K–P) Cre-based activation of ACVR1 in facial sheet-shaped cartilage elements of *Sox10-CreERT2/stop^{flxed/flxed}caAlk2-IRES-GFP* embryos induced at E12.5 and analyzed at E17.5. Locations are the same as highlighted in (A). (K–N) Green clusters are sparse and clonal and show successful activation of ACVR1. Note the formation of spherical clusters of chondrocytes instead of transversely oriented columns. Spherical clusters bulging from the sheet-shaped cartilage are indicated by arrowheads in (L). Amorphous clusters caught inside of the structure are indicated by arrowheads in (N). The cartilage surface is outlined with a dotted line. (O–P) Despite low efficiency of Cre-based ACVR1 activation, the local disruptions of cartilage 3D geometry (analyzed with μ -CT) take place: the inner ear capsule is affected by bulges and the connecting junction is destroyed as indicated by arrowheads. Thickness heatmaps of analyzed location show local thickening of the cartilage as a result of non-oriented placement of chondrocytes with disrupted

Figure 6 continued on next page

Figure 6 continued

BMP signaling. (Q–R) Graphs showing how the regularity of the cartilage (flatness) correlates with orientation of clonal envelopes in the cartilage of *Sox10-CreERT2/R26Confetti* (Q) and *Sox10-CreERT2/stop^{floxed/floxed}caAlk2-IRES-GFP* (R) embryos. The angle α characterizes the elongation of a clonal cluster consisting of multiple cells, as shown in a legend of a corresponding graph axis. Small values of α correspond to highly oriented clonal envelopes such as vertical clonal columns. Angle β is the angle between two opposite cartilage surfaces framing cartilage tissue in this locality. Sheet-shaped cartilages have almost parallel surfaces and angle β values are normally set between zero and 20 degrees. Note that the population of clonal columns (red dots) is almost completely eradicated from the cartilage when ACVR1 is activated in (R).

DOI: 10.7554/eLife.25902.016

proliferative regions (simulated as shrinking zones inside of the non-expanding plastic material). These results, combined with analysis of proliferation and 3D visualizations, strongly suggest that the distribution of uneven proliferative zones plays an important role in the shaping of the facial chondrocranium during embryonic development.

Taken together, we reveal a set of principles contributing to the accurate scaling and shaping of cartilage tissue during growth. The reverse engineering of this process highlights the involvement of highly specialized systems that control the directional growth at the levels of micro- (clonal shapes) and macro-geometries (proliferative regions in nasal capsule). Our results show that allometric growth of complex 3D cartilage elements is not achieved by simple, evenly distributed and/or unidirectional proliferation, but is sculpted by precisely localized proliferation.

Discussion

Here we report the discovery of how oriented cell behavior and molecular signals control cartilage growth and shaping. Previously, the use of chimeric avian embryos demonstrated the competence of facial mesenchyme in producing species-specific shapes and sizes of cartilage elements (Eames and Schneider, 2008), while facial epithelium and brain provided the instructive signals guiding generalized shaping of the face (Chong et al., 2012; Foppiano et al., 2007; Hu et al., 2015). Knowledge of how the facial cartilaginous elements are shaped has been rather restricted, and mainly concerned with the correct formation of chondrogenic mesenchymal condensations.

The accurate expansion of the chondrogenic condensation or cartilage during growth is no trivial matter. The general shape should be both preserved and modified at the same time. We show that anisotropic proliferation and oriented clonal cell dynamics are implemented to achieve the necessary outcome. The reverse engineering of this process highlighted the involvement of highly specialized systems that control the directional growth at the levels of micro- (clonal shapes) and macrogeometries (proliferative regions).

Allometric growth of complex 3D structures requires certain cellular logics and cannot efficiently proceed with equally distributed and/or unidirectional proliferation inside of the mesenchymal condensation or cartilage element. On the other hand, we did not observe the formation of growth plate-like zones in early sheet-shaped (nasal capsule) or rod-shaped cartilages, nor uniform expansion of cartilage in all directions. Thus, the underlying growth and shaping mechanisms required an explanation.

To test various strategies of cellular behavior during cartilage growth we devised a model simulating different aspects of multicellular dynamics in 3D together with lineage tracing of individual clones. Most of the currently existing models of cell dynamics and tracing operate in 2D space, which often limits the predictions (Jarjour et al., 2014). Our model suggested that a gradient-controlled orientation of clonal expansion can explain the biological observations (i.e. it is consistent with ordered columnar growth and its disruption results in spherical microdomains rather than columns), and showed the relation between the geometries of clonal domains (envelopes), the overall shape and the fineness of the surface. We confirmed the predictions from the model in a series of experiments involving tracing with multicolor reporters and manipulating the cartilage with mutations. Our results showed that the formation of oriented clones of chondrocytes with clonal envelope shape corresponds to the geometry of the analyzed locality. The sheet-shaped cartilage elements consisted of transversely oriented clonal columns, while asymmetric complex geometries revealed a variety of clonal shapes ranging from spherical to particularly oriented.

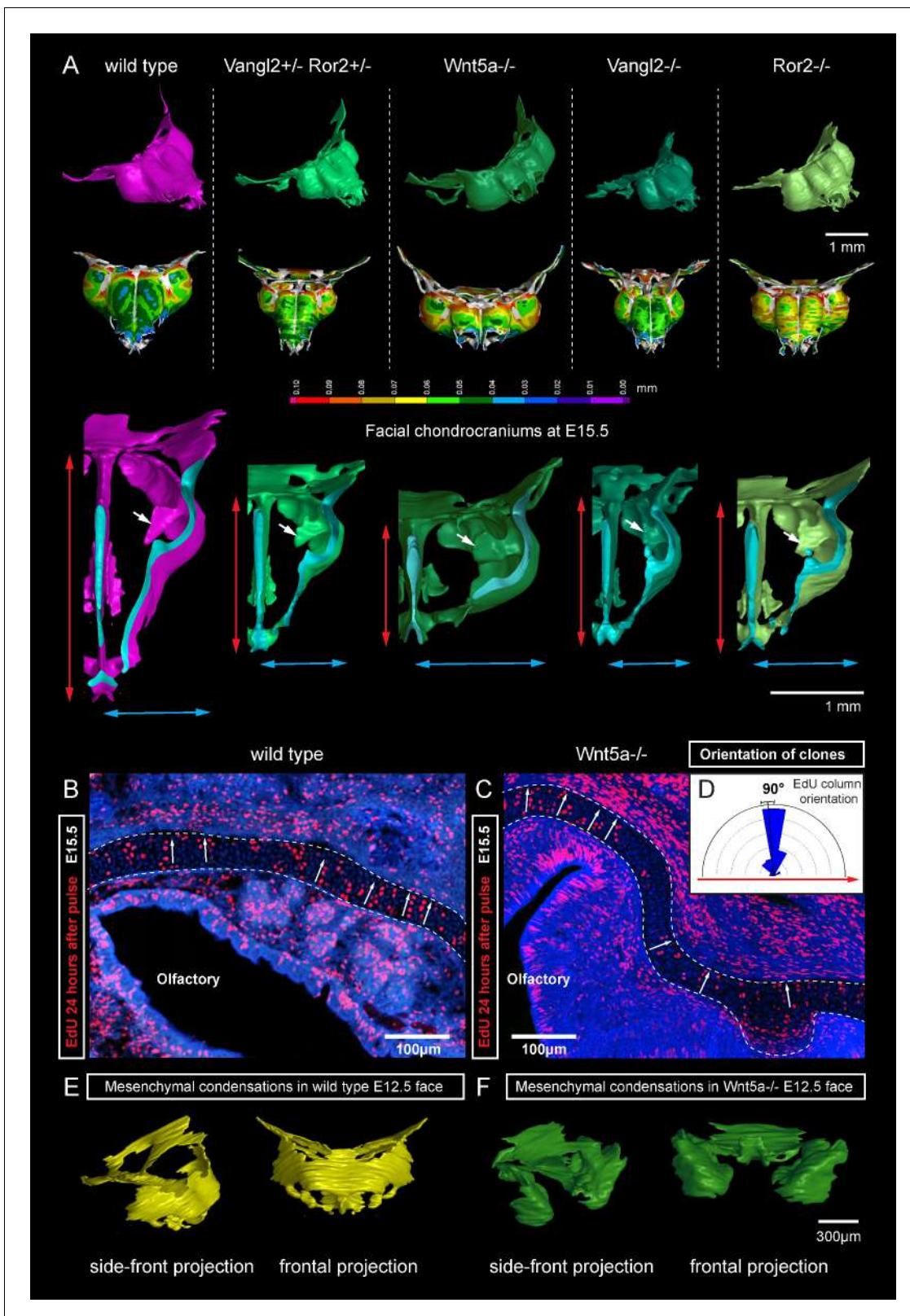


Figure 7. Deficiencies in Wnt/PCP pathway reshape the chondrocranium. (A) μ -CT-based reconstructions of the facial chondrocranium of wild type control, $Wnt5a^{-/-}$, $Vangl2^{-/-}$, $Ror2^{-/-}$ and $Vangl2^{+/-}/Ror2^{+/-}$ embryos at E15.5, with wall-thickness analysis (the row below). Clipping planes in the top projections show that all major- and fine structures (indicated by white arrows) are in place in the Wnt/PCP mutants. Red and blue arrows help to compare the width and the length of the chondrocranium. (B–D) Analysis of EdU incorporation in the facial sheet-shaped cartilage, 24 hr after the

Figure 7 continued on next page

Figure 7 continued

pulse: control (B) and *Wnt5a*^{-/-} mutant (C) embryos. Sparse clusters and columns of EdU⁺ cells correspond to clonal arrangements previously shown with genetic tracing in the same locations. Note that the orientation of chondrocyte placement in the cartilage is not affected in the mutant embryos. Quantification is presented in a rose diagram in (D). For control, we refer to the rose diagrams in Figure 3. (E, F) μ -CT-based 3D reconstruction of mesenchymal condensations at the developmental stage E12.5 in control (E) and *Wnt5a*^{-/-} mutant (F) embryos shows their misplacement in a mutant. DOI: 10.7554/eLife.25902.017

Genetic tracing initiated during transition of condensations into cartilage resulted in clonal columns within both sheet- and rod-shaped cartilage elements. This confirms that chondrogenic condensations undergo complex oriented cell dynamics during their development. Importantly, tracing of chondrocranium cartilage showed formation of transverse clonal columns as growth proceeded. Intercalation of newly born columns into pre-existing cartilage provided for the expansion potential in the sheet-shaped cartilage. This growth mechanism is very original and is not reported elsewhere so far.

A few studies have demonstrated how clonal envelopes form in accordance with the general shape of the structure. These were mainly conducted on *Drosophila* imaginal wing disc or growing flower petals. In all cases the authors highlighted that the shape of clonal geometries correlates with the major vector of expansion in the growing structure (Green et al., 2010; Repiso et al., 2013; Strutt, 2005). This implies the presence of polarized activity that directs the shaping of the tissue. Here, we provided the first experimental evidence of how the control of the directional clonal expansion influences the shape of a vertebrate tissue on a large scale. Moreover, in the sheet-shaped cartilage the orientation of clonal domains, i.e. the columns, does not correspond to the vectors of major expansion, but rather serves for uncoupling lateral expansion control and thickness tuning. In line with that, the number of chondrocytes comprising the clonal column or cluster depends on Gs α -mediated signals. Variations in this number do not significantly affect the lateral dimensions of the whole sheet-shaped cartilage structure: the thickness of the cartilage becomes less while the general geometry and size stay preserved. Additionally, the shape and orientation of clonal envelopes in cartilage is partially controlled by BMP signaling, since micro-geometries of clones depend on activation of ACVR1. Based on these results, we assume that BMP ligands (because of cAlk2/ACVR1 phenotype affected clonal orientation) expressed around the regularly shaped cartilages may play a role similar to the in silico predicted gradients. Indeed, the expression of INHBA, BMP5 and BMP3 fit this expression profile quite well (according to Allen Developing Mouse Brain Atlas (<http://developingmouse.brain-map.org>) and Eurexpress (<http://www.eurexpress.org>) in situ public databases). At least, BMP5 is clearly expressed at the cartilage periphery and has been shown to affect the cartilage shape by David Kingsley lab (Guenther et al., 2008).

Our experimental manipulations of planar cell polarity (PCP) pathway did not affect microgeometries and clonal domains, but strongly affected the chondrocranium shape on the macroscopical scale in several different ways. These phenotypes appeared to be rooted in pre-chondrogenic or early chondrogenic stages, and are based on distorted placement of mesenchymal condensations in the very early head. These experiments with *Wnt*/PCP mutants may potentially provide a better understanding of species-specific mechanisms of control and evolution of the facial shape on a macro scale.

Regular shapes require regular cellular arrangements and clonal cell dynamics. It is not only sheet-shaped cartilage in the head that demonstrate geometric regularity; rod-shaped cartilage (Meckel, embryonic ribs and long cartilages in limbs) also has a regular shape. Regular clonal patterns, conceptually similar to those found in sheet-shaped cartilage, explain conservative tissue dynamics during formation and growth of cartilaginous rods. Indeed, genetic tracing experiments suggested that formation of clonal columns is important for the diameter control, while chondrogenic condensations at the very tip of the rod-shaped growing structures enable elongation. Similar to the cell dynamics in the sheet-shaped cartilage, this mechanism may provide for uncoupling of length versus diameter control. Such uncoupling may generally enable developmental and evolutionary plasticity of cartilage size and shape.

The mechanism controlling the thickness or diameter of sheet-shaped and rod-shaped cartilage elements not only includes spatially orientated behavior, but also involves the regulation of cell number within each chondrogenic clone. Immature chondrocytes are proliferatively active, while more

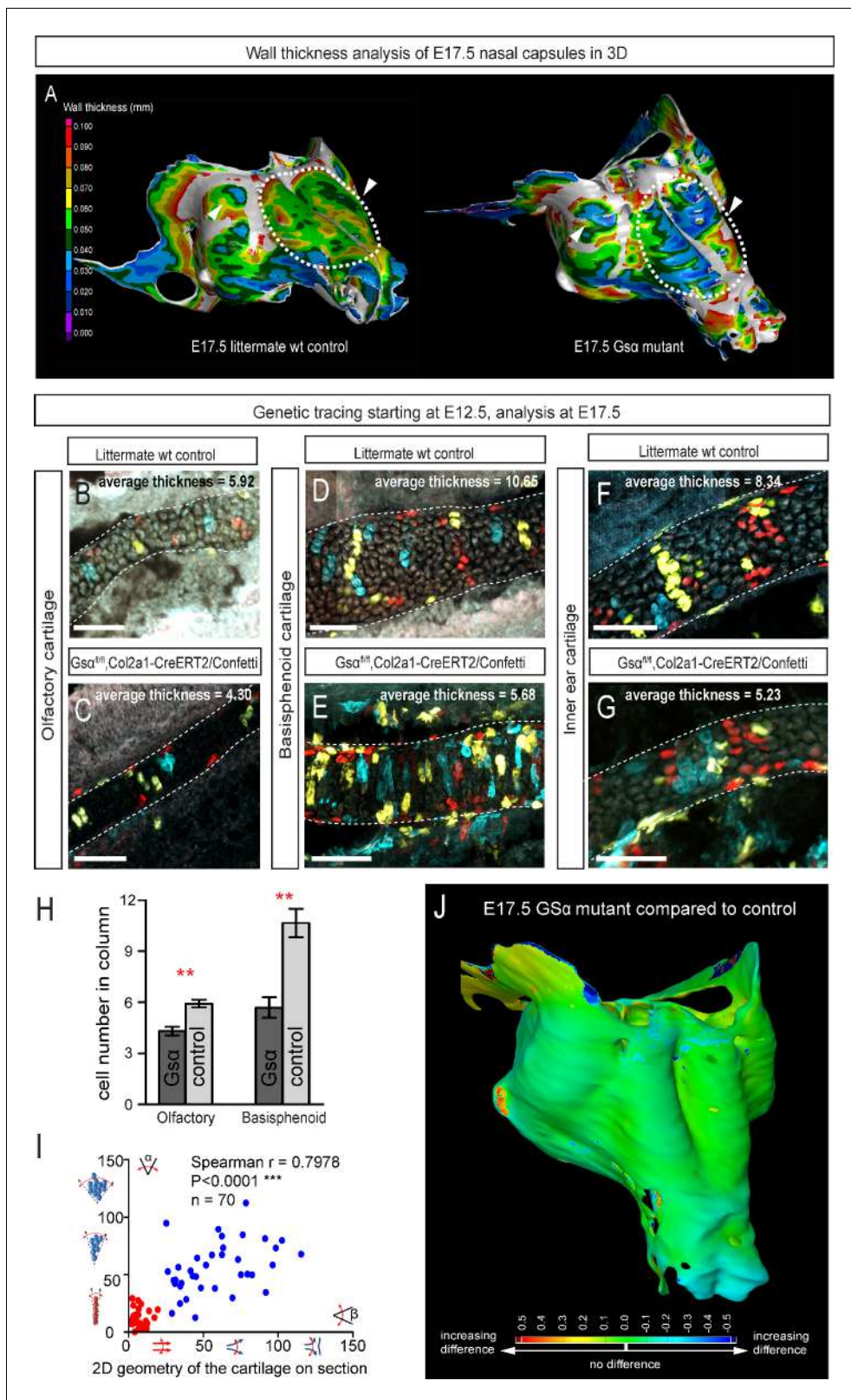


Figure 8. Manipulation of cartilage thickness in *GSα* mutant embryos. (A) Wall thickness was analysed in the μ -CT segmented olfactory system of control (left) and *GSα* (*G*-protein subunit alpha) mutant (right). Large areas with decreased cartilage thickness are highlighted with a dashed line and white arrows. (B–G) Clonal genetic tracing of chondrocyte progenitors and chondrocytes induced by tamoxifen injection at E12.5 in *Col2a1-CreERT2/R26Confetti/GSα^{fl/fl}* embryos (C,E,G) and littermate controls (B,D,F) at E17.5. (H) Quantification of cartilage thickness in the olfactory system and

Figure 8 continued on next page

Figure 8 continued

basisphenoid from three independent experiments. Note the significant decrease of cartilage thickness in all analyzed locations. Oriented organization of the chondrocyte clones was not affected by $GS\alpha$ ablation. The difference between control (mean = 5.9, sem = ± 0.23 , n = 4) and mutant (mean = 4.3, sem = ± 0.25 , n = 3) olfactory cartilage thickness is significant ($p=0.0053$). The difference between control (mean = 10.6, sem = ± 0.83 , n = 3) and mutant (mean = 5.7, sem = ± 0.61 , n = 3) basisphenoid cartilage thickness is significant ($p=0.0087$). Scale bars = 100 μm . (I) Graph showing that the regularity (straightness) of the cartilage correlates with the orientation of chondrocyte clones in the cartilage of *Col2a1-CreERT2/R26Confetti/GS α ^{floxed/floxed}* embryos. Angle α characterizes the orientation of chondrocyte clones consisting of multiple cells as shown in a legend of a corresponding graph axis (y). Small values of α correspond to highly oriented chondrocyte clones such as transverse clonal columns. Angle β is the angle between two opposite cartilage surfaces. Since sheet-shaped cartilage elements have almost parallel surfaces the angle β was normally set between zero and 20 degrees. (J) GOM Inspect software was used to compare the shape of the nasal capsule between $GS\alpha$ mutant and control embryo at E17.5.

DOI: 10.7554/eLife.25902.018

mature chondrocytes show decreased proliferation. Therefore, differentiation speed emerges as a concept which could regulate the organ shape by impinging on clone size, thereby altering the thickness or diameter of the cartilage. This concept is known to operate in the brain and other tissues with classical stem cell/transiently amplifying cell arrangements (*Díaz-Flores et al., 2006*).

Clonal genetic tracing and EdU labeling experiments suggested that the origin of clonal columns and clusters might be represented by the cells located at the periphery of forming cartilage. The spherical clusters of chondrocytes forming at the periphery of the cartilage in *cALK2* mutant mice may suggest that the cell source is also located at the periphery and might be a perichondrial cell. Clonal relationships between perichondrial cells and columns of chondrocytes also support the hypothesis of perichondrial cells acting as a stem population during cartilage expansion. In general, the heterogeneity and multipotency of perichondrial cells is still unclear, although there are multiple studies showing the perichondrium as a source of chondrocytes and osteoblasts (*Kobayashi et al., 2011; Li et al., 2017; Maes et al., 2010*).

In addition to this, the perichondrium might mediate non-autonomous effects in the cartilage in case of *cALK2* and $GS\alpha$ experiments. Genetic tracing shows that some perichondrial cells always recombine with *Sox10-*, *Plp1-* and *Col2a1-CreERT2* lines, and, in case of functional experiments, may indirectly control some evens in more mature layers. Also, it is not clear how the fine border of the cartilage is set, and whether the perichondrial layer may play a key border-setting role during development and regeneration. This should be investigated further.

Next, our results show that tuning of macro-geometries on a large scale can be achieved through a stage-specific placement of proliferative hot zones where new clonal domains intercalate into the main cartilage structure. Anisotropic heterogeneous proliferation is a powerful tool, which, together with polarity in the tissue and local patterning, can drive the organ shape development (*Ben Amar and Jia, 2013; Campinho and Heisenberg, 2013*). The localized growth zones provide for the general expansion and also bend the cartilage by creating local tensions that require mechanical relaxation and influence further development of the overall shape (*Schötz et al., 2013*). For probing such transformations of the sheet-shaped facial cartilage we applied an *in silico* model that was already successfully validated in a number of growth, shaping and scaling tasks (*Green et al., 2010; Kennaway et al., 2011*). Such a model was necessary to understand why the high and low proliferation zones are positioned in such a specific way. Indeed, the discovered distribution of proliferative zones in the whole nasal capsule did not help us *per se* with intuitive explanations of geometrical changes on the macro-scale. Despite this counter-intuitive dataset, the mathematical model provided an insight into the logic of the high and low proliferation zones in relation to a transition between investigated cartilage shapes.

For example, it turned out that the position of lateral slow proliferation zones enables the generation of the symmetrical bends at the sides of the nasal capsule during transition from E13.5 to E14.5 developmental shapes. Furthermore, real material modelling confirmed the results predicted by the mathematical model, and generated lateral bends similarly to the native structure. The molecular mechanism controlling the dynamic distribution (patterning) of fast/slow proliferative zones in the cartilage is still unknown. It is likely linked to developmental signals from other tissues such as the olfactory epithelium or the mesenchyme surrounding the cartilage. Identification and validation of these signals will be essential in future studies and would involve a substantial combination of screening and functional approaches with transgenic animal models.

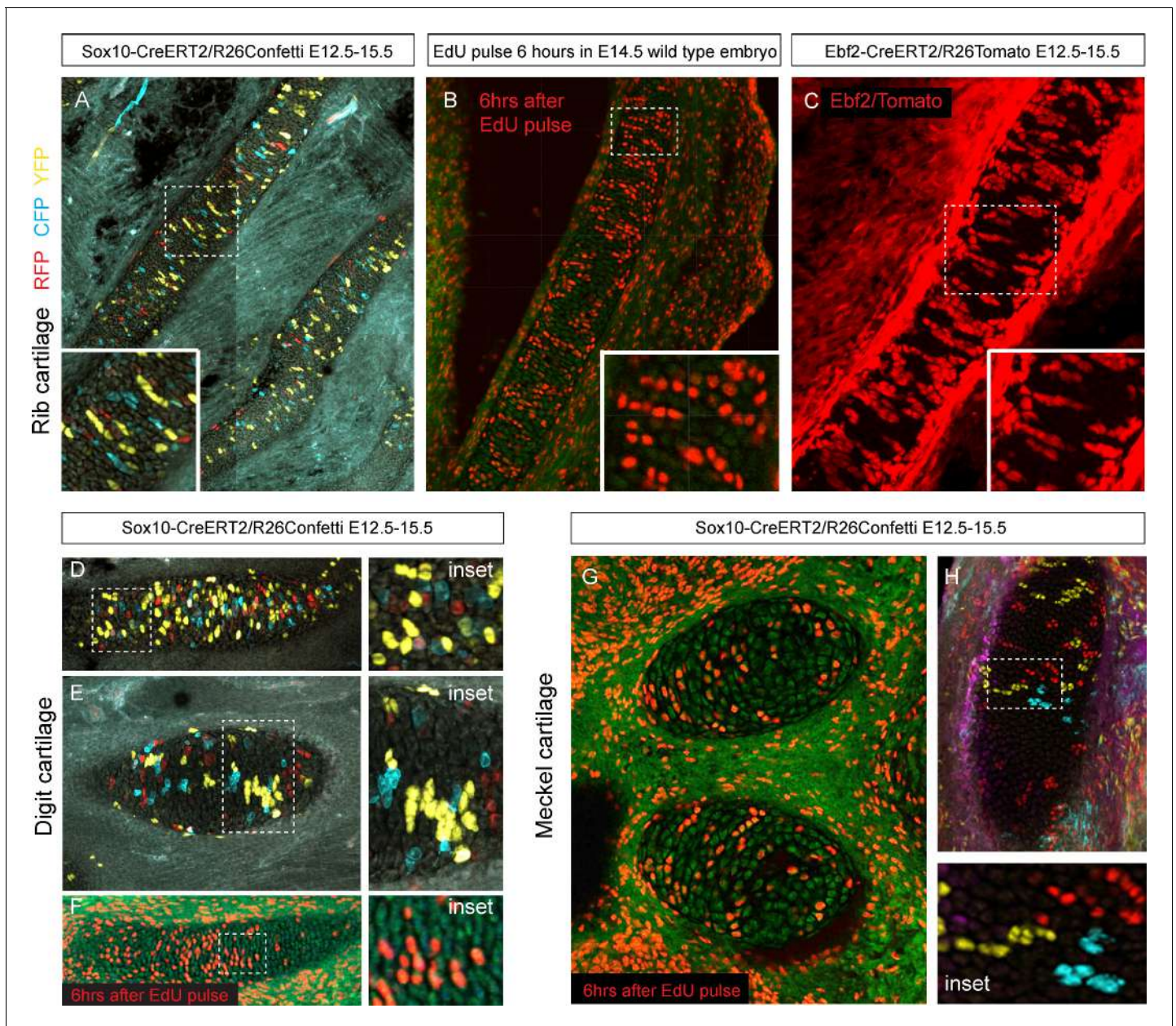


Figure 9. Oriented cell dynamics during development of rod-shaped cartilage elements. (A) Genetic tracing in developing rib cartilage. Note the transverse pattern of chondrocyte clones. Dotted rectangle shows the area of magnified inset on bottom left. (B) 6 hr after EdU pulse in E14.5 embryo, transverse patterns were observed in ribs. Dotted rectangle shows the areas of magnified inset in bottom right corner. (C) Genetic tracing in developing rib cartilage shows transverse patterns. Dotted line represents area magnified in inset on the bottom right. (D–F) Genetic tracing (D,E) and 6 hr after EdU pulse (F) in developing digit cartilage of the upper limb. The areas of magnified insets (located on the right side) are outlined by dotted lines. (G) Transverse patterns in developing Meckel cartilage resulting from EdU pulse and analysis 6 hr after administration. (H) Genetic tracing shows transverse orientation of clonal chondrocytic columns in the Meckel cartilage. Dotted line shows the area magnified in the inset on the right.

DOI: [10.7554/eLife.25902.019](https://doi.org/10.7554/eLife.25902.019)

The anisotropic proliferation can be an important evolutionary mechanism that is directly responsible for the differences in snout geometry in a variety of phylogenetic groups. Additionally, it might be important for understanding the development of the facial shape variation in humans (Sheehan and Nachman, 2014) as well as numerous pathologies (Afsharpaiman et al., 2013).

One alternative way to fine-tune macro-geometry of a cartilage element is to continuously add on pre-shaped chondrogenic mesenchymal condensations from the pool of competent progenitors that

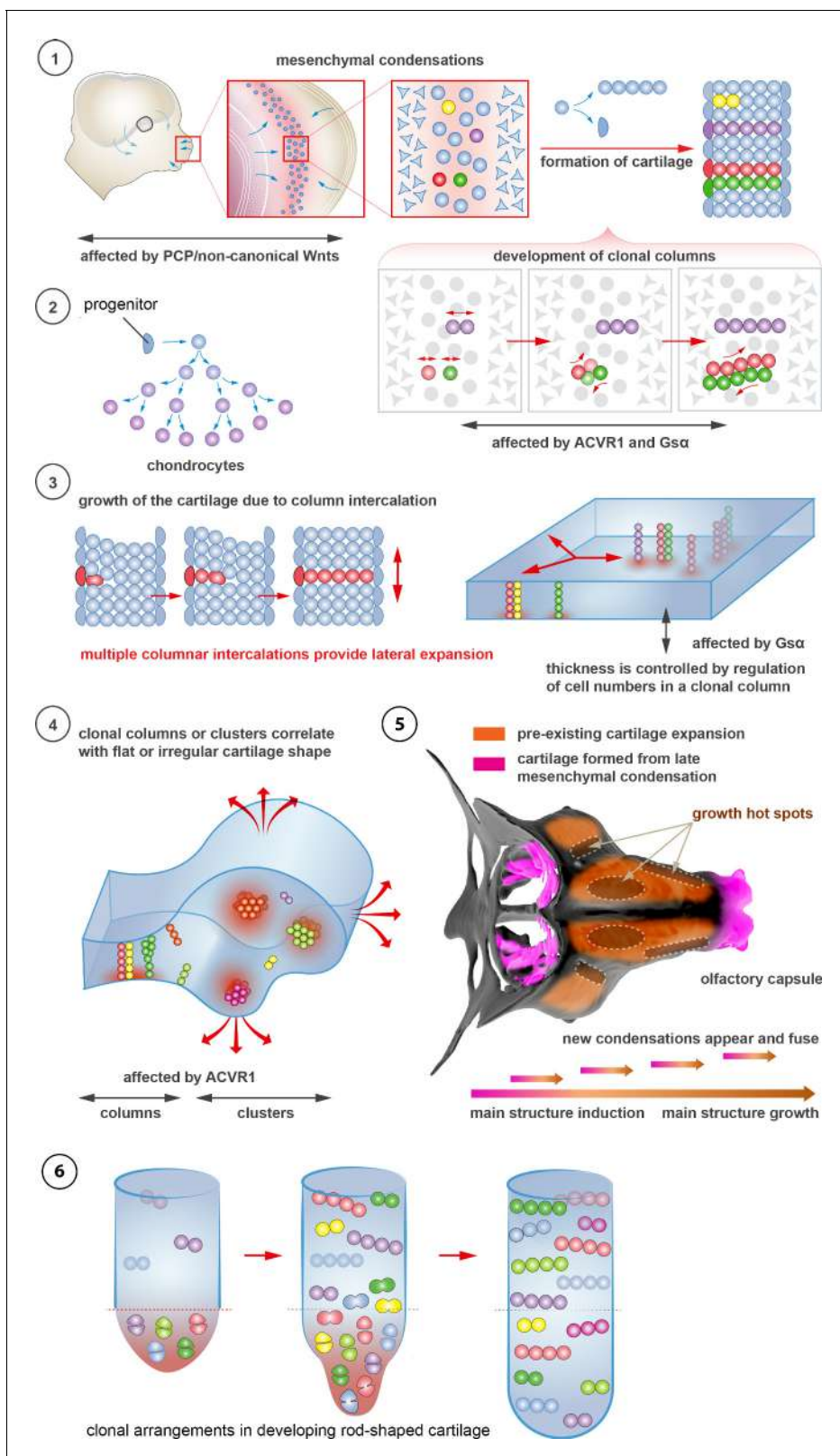


Figure 10. Schematic overview of cartilage shaping and scaling processes. (1) Oriented cell divisions in the mesenchymal condensations give rise to the transverse columnar clones of chondrocytes. (2) Perichondrial cells may potentially give rise to chondrocytes. (3) Formation of new clonal columns and their integration into pre-existing cartilage leads to directed lateral expansion of the cartilage. The thickness of the sheet-shaped cartilage depends on the number of cells comprising the column, while the lateral expansion depends on the number of clonal columnar units engaged. (4) Geometry of the

Figure 10 continued on next page

Figure 10 continued

clonal unit corresponds to the overall macro-geometry of the cartilage. Regular clonal units correspond to regular shapes of the cartilage.

(5) Chondrogenic mesenchymal condensations are sequentially induced to provide fine details and shape modifications during chondrocranium growth. Upon their maturation, they fuse with the main structure of the chondrocranium. Anisotropic proliferation and specifically positioned proliferative zones further assist the shaping process by imposing physical tensions and curves. (6) Rod-shaped cartilage elements also show the regular clonal patterns that result from the transverse orientation of cell divisions and daughter cell allocations that account for the diameter regulation.

DOI: 10.7554/eLife.25902.020

are retained until late developmental stages. As we demonstrated, the formation of adjoining mesenchymal condensations occurs in sheet-shaped cranial cartilage. In the developing face, new chondrogenic condensations are responsible for introducing geometrically complicated fine details. Such mechanisms may also operate during amphibian metamorphosis, when most of the postmetamorphic cranial cartilage develops *de novo* and not from the pre-metamorphic cartilaginous elements (Kerney *et al.*, 2012).

Taken together, we discovered important novel principles explaining the growth and shaping of cartilaginous structures. Further studies should focus, amongst other things, on the soluble signals emanating from other embryonic structures which influence the oriented behavior or proliferation of chondrogenic clones.

Materials and methods

Mouse strains and animal information

All animal (mouse) work has been approved and permitted by the Ethical Committee on Animal Experiments (Norra Djurförsöksetiska Nämnd, ethical permit N226/15 and N5/14) and conducted according to The Swedish Animal Agency's Provisions and Guidelines for Animal Experimentation recommendations. Genetic tracing mouse strains *Plp1-CreERT2* (RRID:MGI:4837112) and *Sox10-CreERT2* were previously described (Laranjeira *et al.*, 2011; Leone *et al.*, 2003; Yu *et al.*, 2013). *Plp1-creERT2*, *Sox10-creERT2* and *Col2a1-CreERT2* (RRID:IMSR_JAX:006774) (Nakamura *et al.*, 2006) (obtained from laboratory of S. Mackem, NIH) strains were coupled to *R26Confetti* (RRID:IMSR_JAX:017492) mice that were received from the laboratory of Professor H. Clevers (Snippert *et al.*, 2010). The *Stop^{flxed/flxed}caAlk2-IRES-GFP* strain from the laboratory of Y. Mishina (Fukuda *et al.*, 2006) was coupled to *Sox10-CreERT2*. The *Ebf2-CreERT2* (RRID:MGI:4421811) strain was obtained from the laboratory of H. Qian, KI, and was coupled to *R26Tomato*. The *Gsα^{flxed/flxed}* strain was obtained from the laboratory of L. Weinstein (Sakamoto *et al.*, 2005). Female mice which were homozygous for the reporter allele [*Gt(ROSA)26Sortm4(ACTB-tdTomato,-EGFP)Luo/J*; Jackson Laboratories] (Muzumdar *et al.*, 2007) were coupled to homozygous *Col2a1::creER^T* males [FVB-Tg (*Col2a1-cre/ERT*)KA3Smac/J; Jackson Laboratories] (Feil *et al.*, 1997; Nakamura *et al.*, 2006). To induce genetic recombination to adequate efficiency, pregnant females were injected intraperitoneally with tamoxifen (Sigma Aldrich, St.Louis, MO, T5648) dissolved in corn oil (Sigma Aldrich, C8267). Tamoxifen concentration ranged from 1.5 to 5.0 mg per animal in order to obtain a range of recombination efficiencies. *Wnt5a*, *Vangl2* and *Ror2* full knock-out embryos were obtained from heterozygous parents (Gao *et al.*, 2011; Yamaguchi *et al.*, 1999) at the expected Mendelian proportions.

Immunohistochemistry

For embryo analyses, heterozygous mice of the relevant genotype were mated overnight, and noon of the day of plug detection was considered E0.5. Mice were sacrificed with isoflurane (Baxter, Deerfield, IL, KDG9623) overdose, and embryos were dissected out and collected into ice-cold PBS. Subsequently, the samples were placed into freshly prepared 4% paraformaldehyde (PFA) and depending on the developmental stage they were fixed for 3–6 hr at +4°C on a roller. Embryos were subsequently cryopreserved in 30% sucrose (VWR, Radnor, PA, C27480) overnight at +4°C, embedded in OCT media (HistoLab, Serbia, 45830) and sections cut of between 14 μm to 200 μm on a cryostat (Microm International, Germany), depending on the following application. If needed, sections were stored at –20°C after drying for 1 hr at room temperature, or processed immediately

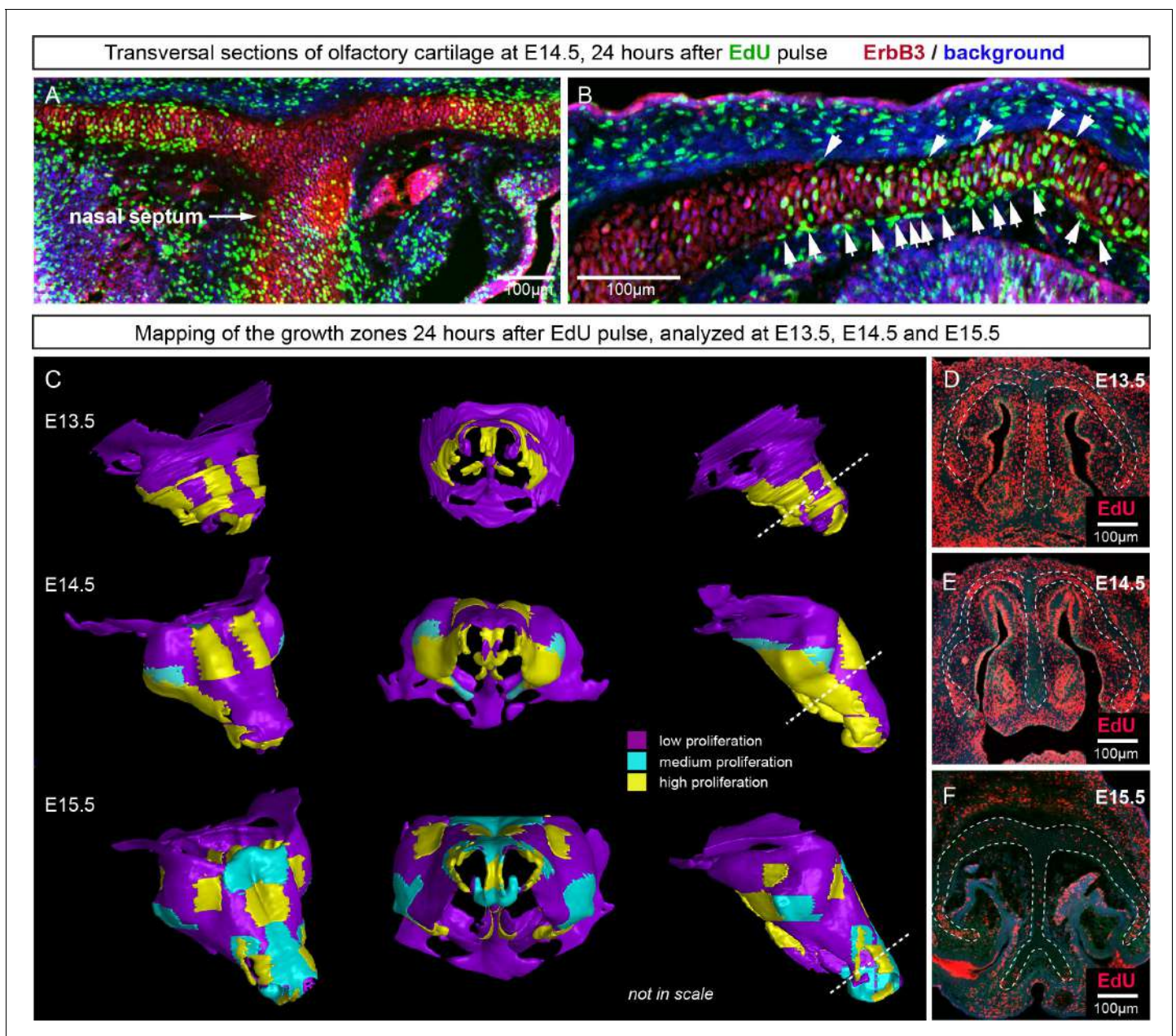


Figure 11. Analysis of proliferation identifies specific proliferative regions in nasal capsule. (A–B) Analysis of EdU incorporation 24 hr after the pulse on a transversal section of the facial chondrocranium at E14.5. Notice the distinct proliferative zones in the cartilage that correlate with intense EdU labelling in perichondrial locations shown by arrowheads in (B). (C) Mapping of distinct growth zones onto 3D models of mesenchymal condensations (E13.5) and cartilage (E14.5–E15.5) in the developing face. (D–F) Frontal transversal sections at different developmental stages include proliferative zones within the chondrocranium with EdU incorporation. Scale bars = 100 μm.
DOI: [10.7554/eLife.25902.021](https://doi.org/10.7554/eLife.25902.021)

after sectioning. Primary antibodies used were: goat anti-GFP (FITC) (Abcam, UK, 1:500, RRID:AB_305635), rabbit anti-Sox9 (Sigma Aldrich, 1:1000, RRID:AB_1080067), rabbit anti-Sox5 (Abcam, 1:500, RRID:AB_10859923), sheep anti-ErbB3 (RnD Systems, Minneapolis, MN, 1:500, RRID:AB_2099728). For detection of the above-mentioned primary antibodies we utilized 405, 488, 555 or 647-conjugated Alexa-fluor secondary antibodies produced in donkey (Invitrogen, Carlsbad, CA, 1:1000, RRID:AB_162543, RRID:AB_141788, RRID:AB_141708, RRID:AB_142672, RRID:AB_2536183, RRID:AB_141844,). Sections were mounted with 87% glycerol mounting media

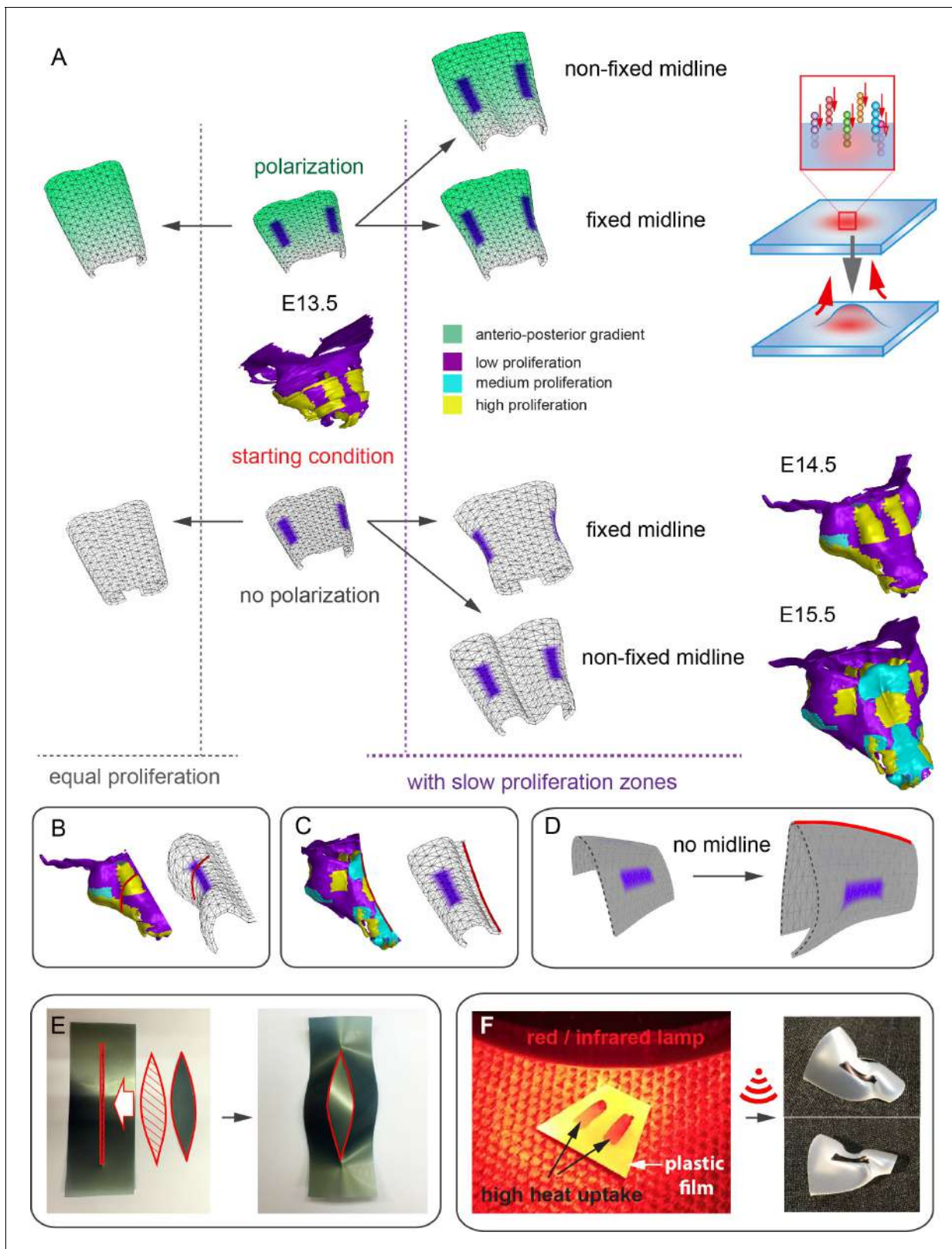


Figure 12. Modeling of uneven growth in the shaping of the nasal capsule. (A) In silico geometrical transformations of the nasal capsule-like anlage at E13.5 following various scenarios including: anisotropic oriented growth (following polarization introduced by the antero-posterior gradient shown in green), non-polarized isotropic growth (no antero-posterior gradient), the presence of fixed midline (simulation of septum and central groove), condition with the unfixed midline (only central groove), conditions with or without slowly growing lateral regions (shown in purple). Note that in *Figure 12 continued on next page*

Figure 12 continued

condition with polarized antero-posterior growth the anterior elongation of the structure is more prominent and faster as compared to the condition with non-polarized isotropic growth. The lateral bends are induced by slow proliferating lateral regions. In the center and on the right, the real nasal capsules are shown with mapped fast and slow growing regions. (B) In the condition with isotropic growth and introduced slowly growing regions, we observe the formation of lateral bends (red line) analogous to the lateral bends in the real nasal capsule at E14.5 (shown on the left). In this condition the midline is fixed, and the ventral groove forms straight. (C) In conditions with no fixed midline we observe the formation of the central groove, correct bending of the central groove (red line) and overall flattening of the simulated structure similar to the real object (on the left). (D) Simulation with no midline and central groove. Note the inverted bend (red line) and the absence of the correct flattening of the structure. Despite the absence of the midline, the lateral bends are successfully induced by the slow growing regions (purple), analogous to the real nasal capsule. (E) Material elastic modelling shows how the third dimension (bending) emerges from changes and tensions in plain 2D structure during imitated anisotropic growth. (E, left panel) Initial modelling conditions: completely flat X-ray film with the cut slot in the middle for fitting the imitated flat growth zone, which is also made from X-ray film. (E, right panel) When the growth zone is inserted into the slit, the whole structure bends to accommodate the tensions. (F) Real material (plastic film)-based simulation of isotropic growth was based on uneven shrinking during intense heating. Black painted regions uptake heat more efficiently and shrink faster. The attached edges of the shrinking zone cause bending of the entire structure. Two lateral black stripes were painted on top of the trapezoid as an analog to lateral slowly proliferating zones in nasal capsule. Note the similarity of resulting bends to the lateral bends in real nasal capsule at E14.5.

DOI: [10.7554/eLife.25902.022](https://doi.org/10.7554/eLife.25902.022)

(Merck, Germany) or in Vectashield Antifade Mounting Medium with DAPI (Vector Laboratories, Burlingame, CA, RRID:AB_2336790).

EdU incorporation analysis

EdU (Life Technologies, Carlsbad, CA) was injected intraperitoneally into the pregnant females (65 μg per gram of body mass) either 6- or 24 hr before the embryos were harvested. Cells with incorporated EdU were visualized using Click-iT EdU Alexa Fluor 647 Imaging Kit (Life Technologies) according to the manufacturer's instructions.

Microscopy, volume rendering, image analysis and quantifications

Confocal microscopy was performed using Zeiss LSM710 CLSM, Zeiss LSM780 CLSM and Zeiss LSM880 Airyscan CLSM instruments. The settings for the imaging of Confetti fluorescent proteins were previously described (*Snippert et al., 2010*). The imaging of the confocal stack was done with a Zeiss LSM780 CLSM, Plan-Apochromat 3 10x/0.45 M27 Zeiss air objective.

Histological staining

Slides were stained for mineral deposition using von Kossa calcium staining: 5% silver nitrate solution was added to the sections at a room temperature and exposed to strong light for 30 min. After that the silver nitrate solution was removed, and slides were washed with distilled water for three times during 2 min. 2.5% sodium thiosulphate solution (w/v) was added to the sections and incubated for 5 min. Slides were again rinsed for three times during 2 min in distilled water. The sections were then counterstained using Alcian blue. Alcian blue solution (0.1% alcian blue 8GX (w/v) in 0.1 M HCl) was added to the tissue for 3 min at room temperature and then rinsed for three times during 2 min in distilled water. Slides were then transferred rapidly into incrementally increasing ethanol concentrations (20%, 40%, 80%, 100%) and incubated in 100% ethanol for 2 min. Finally, the slides were incubated in two xylene baths (for 2 min and then for 5 min) before mounting and analysis.



Video 2. Simulations of shape transitions of the nasal capsule-like 3D object under different growth conditions. Notice the formation of the lateral bends corresponding to the real nasal capsule shape development from E13.5 to E14.5 occur only in the condition with slow growing purple zones. These bends form independently from isotropic or anisotropic modality of growth.

DOI: [10.7554/eLife.25902.023](https://doi.org/10.7554/eLife.25902.023)

Statistics

Statistical data are represented as mean \pm s.e.m. Unpaired version of Student's t-test was used to calculate the statistics (*P* value). All results were replicated at least in three different animals. Statistical analysis and graphs were produced in GraphPad Prism (La Jolla, CA, RRID:SCR_002798) or Oriana Software (Kovach Computing Services, UK). Spearman coefficient was used for correlation assessment of microgeometries corresponding to different locations in the cartilage.

In **Figure 8** the difference between control (mean = 5.9, sem = \pm 0.23, n = 4) and mutant (mean = 4.3, sem = \pm 0.25, n = 3) olfactory cartilage thickness is significant ($p=0.0053$). The difference between control (mean = 10.6, sem = \pm 0.83, n = 3) and mutant (mean = 5.7, sem = \pm 0.61, n = 3) basisphenoid cartilage thickness is significant ($p=0.0087$).

Tissue contrasting for μ -CT scanning

Our staining protocol has been modified from the original protocol developed by Brian Metscher laboratory (University of Vienna, Austria). After dissection, the embryos were fixed with 4% aqueous solution of formaldehyde in PBS for 24 hr at +4°C, with slow rotation. Samples were then dehydrated by incubation in incrementally increasing concentrations of ethanol in PBS (30%, 50%, 70%); samples were incubated at +4°C for two days in each concentration to minimize the tissue shrinkage.

We found that the best signal to noise ratio on scans results from contrasting the samples with 0.5–1.0% PTA (Phosphotungstic acid, Sigma Aldrich) in 90% methanol. After sample dehydration, the tissue-contrasting PTA solution was added to the samples and then changed every day with the fresh solution. E12.5 embryos were contrasted with 0.5% PTA for four days while E15.5 embryos were stained in 0.7% PTA for six days. E16.5 and E17.5 embryos were decapitated, and the contrasting procedure was extended to 9–15 days in 1% PTA to ensure the best penetration of the contrasting agent. Subsequently, tissues were rehydrated through a methanol gradient (90%, 80%, 70%, 50% and 30%), to sterile distilled water. After that, rehydrated embryos were embedded in 0.5% agarose gel (A5304, Sigma-Aldrich) and placed in polypropylene conical tubes (0.5, 1.5 or 15 ml depending on the sample size) to minimize the amount of surrounding agarose gel, and to avoid movement artifacts during X-ray computed tomography scanning.

μ -CT analysis (micro computed tomography analysis)

The μ -CT analysis of the embryos was performed using laboratory system GE phoenix v|tome|x L 240, equipped with a 180 kV/15W maximum power nanofocus X-ray tube and high contrast flat panel detector DXR250 with 2048 \times 2048 pixel, 200 \times 200 μ m pixel size. The exposure time was 900 ms in all 2000 positions. The μ -CT scan was carried out at 60 kV acceleration voltage and with 200 μ A X-ray tube current. The voxel size of obtained volumes appeared in the range of 4 μ m - 6 μ m depending on a size of an embryo. The tomographic reconstructions were performed using GE phoenix datos|x 2.0 3D computed tomography software.

The cartilage of the olfactory system was segmented manually using Avizo - 3D image data processing software (FEI, Hillsboro, OR). The volumetric data of a segmented region were transformed to a polygonal mesh that describes the outer boundary of the region. The polygonal mesh consisting of triangles is a digital geometrical representation of the real object. The polygonal mesh of the olfactory system was imported to VG Studio MAX 2.2 software (Volume Graphics, Germany) for surface smoothing. The analysis of wall thickness at different embryonic stages was performed in order to show the differences or similarities in the thickness of the cartilage structures (Tesařová *et al.*, 2016). The results are shown on the polygonal mesh by a colour map. The growth zones in facial chondrocranium at different stages were outlined on top of the 3D polygonal mesh based on the EdU analysis and confocal microscopy results.

Computer simulations of shape transitions of nasal capsule structure

Models were developed using the growing polarised tissue (GPT) framework and implemented in the MATLAB application GFtbox (Kennaway *et al.*, 2011; Kuchen *et al.*, 2012) (RRID:SCR_001622). In this method, an initial finite element mesh, also termed the canvas, is deformed during growth. The pattern of deformation depends on growth-modulating factors, whose initial distribution was established during setup. Factors have one value for each vertex and values between vertices are linearly interpolated across each finite element. In the models described here, the initial canvas is

oriented with regard to the external xy-coordinate system such that the canvas base is parallel to the x-axis and the midline is parallel to the y-axis. The initial nasal capsule-line canvas consists of 1800 elements. Elements were not subdivided during the simulations.

Each model has two interconnected networks: the Polarity Regulatory Network (PRN) specifies tissue polarity and hence specified orientations of growth, and the Growth-rate Regulatory Network (KRN) determines how factors influence specified growth rates. In total, growth interactions are specified by three equations, one for the PRN and two for the KRN. These networks determine the specified polarity and growth fields across the canvas. Growth rates are influenced by factors distributed across the canvas. Growth can be promoted in a region by the pro function or inhibited by the inh function as follows:

$$\text{pro}(n, x) = 1 + nx$$

$$\text{inh}(n, x) = 1/(1 + nx)$$

Due to the connectedness of the canvas, this specified growth differs from the resultant growth by which the system is deformed.

Fixed midline models

These models question how the structure can transform given that the septum actively anchors the midline and the central groove.

Setup

The initial set-up phase runs from 0 to 12 time steps and during this phase the canvas deforms from a square sheet into the starting shape for the nasal capsule-like structure. Factor MID is expressed along the proximal-distal midline and used to anchor the midline vertices in the z-plane. Factor CHEEKS is expressed either side of the midline.

PRN

A proximo-distal polarity field is set up and used to define the orientations of growth. This field is specified as being oriented parallel to the midline throughout growth by the gradient of a polarity factor, POLARISER (POL). POL has a linear gradient across the canvas with the highest level of one at the proximal base and zero at the distal tip.

KRN

The growth phase occurs after the initial setup phase at time step 13. During this phase there are options for specifying either isotropic growth or anisotropic growth.

During isotropic growth, the growth rate K was set to:

$$K = 0.05 \cdot \text{inh}(100, \text{iCHEEKS})$$

During anisotropic growth the specified growth rate parallel to the polarity field, K_{par} , was defined as:

$$K_{\text{par}} = 0.05 \cdot \text{inh}(100, \text{iCHEEKS})$$

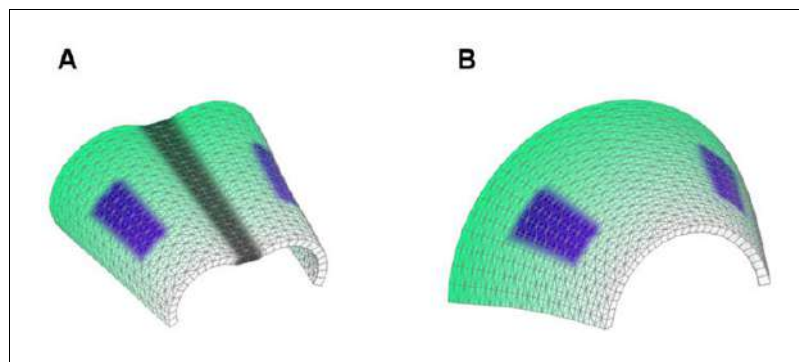
while growth perpendicular to the polarity field, K_{per} , was set to zero.

Non - Fixed midline models

These models are aiming to simulate what happens to the shape transition when the midline and corresponding central groove are not fixed in space (and can bend or change in any other way) following tensions in the whole simulated structure. We used this approach to question how much the roof of the nasal capsule is anchored by the nasal septum.

Setup

As with the Fixed-midline model, an initial setup phase runs for 0–12 time-steps in which a square sheet is deformed into an alternative starting shape for the nasal capsule-like structure. In this model the proximo-distal midline was allowed to deform in the z-plane. Factor CHEEKS is expressed either side of the midline and offset slightly distally.



Scheme 1. Starting shapes for the Fixed mid-ridge model (A) and Non-Fixed mid-ridge model (B). Green colour indicates the values of POL which is highest at the proximal end. CHEEKS are shown in purple and MID is shown in grey.

DOI: [10.7554/eLife.25902.024](https://doi.org/10.7554/eLife.25902.024)

PRN

A proximo-distal polarity field is set up as in the Fixed mid-ridge model.

KRN

The growth regulatory network is defined as in the Fixed mid-ridge model.

Mathematical model

For detailed description, please see the Appendix, **Appendix 1—figure 1** and **2** and also (Kaucka et al., 2016)

Acknowledgements

We would like to thank to Olga Kharchenko for illustrations. We are grateful to Prof. Susan Mackem from NIH for the *Col2a1-CreERT2* strain and to Prof. Hans Clevers for the *R26Confetti* strain. M K was supported by EMBO Long-term Fellowship and SSMF (Svenska Sällskapet för Medicinsk Forskning) fellowship. IA and KF were supported by grants from the Swedish Research Council and Karolinska Institutet. IA received support from The Hållsten Research Foundation and Åke Wiberg Foundation. T Z and J K were supported by the Ministry of Education, Youth and Sports of the Czech Republic under the project CEITEC 2020 (LQ1601). J J and A Ha. were supported by the Ministry of Education, Youth and Sports of the Czech Republic (project LQ1605). A He. was supported by the Swedish strategic research programme eSENCE, the Swedish Research Council (grant #2015–03964) and National Institute of Health under Award Number 1R01EB014877-01. ASC, and PN were supported by the Swedish Research Council (grant # 2016–02835) and Karolinska Institutet. A Deo lumen, ab amicis auxilium. The contents are solely the responsibility of the authors and do not necessarily represent the official views of the National Institute of Health. All authors declare no conflict of interest.

Additional information

Funding

Funder	Grant reference number	Author
European Molecular Biology Organization	ALTF 216-2013	Marketa Kaucka
Svenska Sällskapet för Medicinsk Forskning		Marketa Kaucka
National Institutes of Health		Andreas Hellander

Svenska Forskningsrådet For- mas	Phillip T Newton Andrei S Chagin Kaj Fried Igor Adameyko
Karolinska Institutet	Phillip T Newton Andrei S Chagin Kaj Fried Igor Adameyko
Bertil Hållstens Forskningsstif- telse	Igor Adameyko
Åke Wiberg Stiftelse	Igor Adameyko

The funders had no role in study design, data collection and interpretation, or the decision to submit the work for publication.

Author contributions

MK, Conceptualization, Data curation, Formal analysis, Supervision, Validation, Investigation, Visualization, Methodology, Writing—original draft, Project administration, Writing—review and editing; TZ, Software, Formal analysis, Visualization, Methodology, Writing—review and editing; MT, Software, Formal analysis, Validation, Visualization, Methodology, Writing—review and editing; DG, Investigation, Methodology, Writing—review and editing, Responsible for obtaining all Wnt/PCP mutants, sample preparation and help with their analysis; AHe, Resources, Software, Supervision, Validation, Investigation, Methodology, Writing—original draft, Writing—review and editing; JJ, Methodology, JJ has been responsible for tissue contrasting and preparation of the samples for uCT. JJ participated on the review and editing of the manuscript; JK, Supervision, Funding acquisition, Investigation, Writing—original draft, Project administration; JP, PS, Software, Validation, Investigation, Methodology, Writing—review and editing; BS, Validation, Methodology, Project administration, Writing—review and editing, BS has been responsible for preparation of the samples for uCT (tissue contrasting). Participated on data acquiring (confocal microscopy, cryosectioning, staining); PTN, Investigation, Writing—original draft, Writing—review and editing, PTN has been responsible for EdU pulse embryos and for the GSalph mouse strain. Made very significant contribution to the editing of manuscript (language correction); VD, Investigation, Writing—review and editing, Has been responsible for the production, preparation and analysis of caALK2 embryos; LL, Methodology, Has been responsible for sample preparation, cryosectioning and confocal microscopy; HQ, Conceptualization, Resources, Supervision, Methodology, Writing—review and editing, Preparation of EBF2-GFP/Tomato embryos; A-SJ, Investigation, Methodology, ASJ was responsible for the EBF2-GFP/Tomato strain, injections and sample preparation; YM, Resources, Supervision, Investigation, Writing—review and editing, Responsible for Sox10CreERT2 mouse line; JDC, Data curation, Software, Investigation, Visualization, Methodology, Writing—review and editing; EMT, Resources, Supervision, Funding acquisition, Investigation, Project administration, Writing—review and editing; AE, Software, Investigation, Visualization, Methodology, Writing—review and editing; AD, Software, Supervision, Funding acquisition, Validation, Investigation, Methodology, Writing—review and editing; HB, Resources, Supervision, Funding acquisition, Methodology, Project administration, Writing—review and editing; EC, Resources, Software, Supervision, Funding acquisition, Validation, Investigation, Methodology, Writing—review and editing; MC, Investigation, Methodology, Created and validated the GSa mouse strain; LSW, Resources, Supervision, Project administration, Writing—review and editing; AHa, Resources, Validation, Methodology; EA, Resources, Supervision, Investigation, Writing—review and editing; ASC, Conceptualization, Resources, Formal analysis, Supervision, Investigation, Writing—original draft, Writing—review and editing; KF, Conceptualization, Resources, Supervision, Investigation, Writing—original draft, Writing—review and editing; IA, Conceptualization, Resources, Formal analysis, Supervision, Funding acquisition, Investigation, Writing—original draft, Project administration, Writing—review and editing

Author ORCIDs

Marketa Kaucka, <http://orcid.org/0000-0002-8781-9769>

Hjalmar Brismar, <http://orcid.org/0000-0003-0578-4003>

Enrico Coen, <http://orcid.org/0000-0001-8454-8767>

Andrei S Chagin, <http://orcid.org/0000-0002-2696-5850>

Igor Adameyko, <http://orcid.org/0000-0001-5471-0356>

Ethics

Animal experimentation: All animal (mouse) work has been approved and permitted by the Ethical Committee on Animal Experiments (Norra Djurförsöksetiska Nämnd, ethical permit N226/15 and N5/14) and conducted according to The Swedish Animal Agency's Provisions and Guidelines for Animal Experimentation recommendations.

References

- Abad V, Meyers JL, Weise M, Gafni RI, Barnes KM, Nilsson O, Bacher JD, Baron J. 2002. The role of the resting zone in growth plate chondrogenesis. *Endocrinology* **143**:1851–1857. doi: [10.1210/endo.143.5.8776](https://doi.org/10.1210/endo.143.5.8776), PMID: [11956168](https://pubmed.ncbi.nlm.nih.gov/11956168/)
- Afsharpaiman S, Saburi A, Waters KA. 2013. Respiratory difficulties and breathing disorders in achondroplasia. *Paediatric Respiratory Reviews* **14**:250–255. doi: [10.1016/j.prrv.2013.02.009](https://doi.org/10.1016/j.prrv.2013.02.009), PMID: [23523391](https://pubmed.ncbi.nlm.nih.gov/23523391/)
- Ben Amar M, Jia F. 2013. Anisotropic growth shapes intestinal tissues during embryogenesis. *PNAS* **110**:10525–10530. doi: [10.1073/pnas.1217391110](https://doi.org/10.1073/pnas.1217391110), PMID: [23754398](https://pubmed.ncbi.nlm.nih.gov/23754398/)
- Campinho P, Heisenberg CP. 2013. The force and effect of cell proliferation. *The EMBO Journal* **32**:2783–2784. doi: [10.1038/emboj.2013.225](https://doi.org/10.1038/emboj.2013.225), PMID: [24097062](https://pubmed.ncbi.nlm.nih.gov/24097062/)
- Chagin AS, Vuppapalapati KK, Kobayashi T, Guo J, Hirai T, Chen M, Offermanns S, Weinstein LS, Kronenberg HM. 2014. G-protein stimulatory subunit alpha and $gq/11\alpha$ G-proteins are both required to maintain quiescent stem-like chondrocytes. *Nature Communications* **5**:3673. doi: [10.1038/ncomms4673](https://doi.org/10.1038/ncomms4673), PMID: [24781502](https://pubmed.ncbi.nlm.nih.gov/24781502/)
- Chong HJ, Young NM, Hu D, Jeong J, McMahon AP, Hallgrímsson B, Marcucio RS. 2012. Signaling by SHH rescues facial defects following blockade in the brain. *Developmental Dynamics* **241**:247–256. doi: [10.1002/dvdy.23726](https://doi.org/10.1002/dvdy.23726), PMID: [22275045](https://pubmed.ncbi.nlm.nih.gov/22275045/)
- De Luca F. 2006. Impaired growth plate chondrogenesis in children with chronic illnesses. *Pediatric Research* **59**:625–629. doi: [10.1203/01.pdr.0000214966.60416.1b](https://doi.org/10.1203/01.pdr.0000214966.60416.1b), PMID: [16627871](https://pubmed.ncbi.nlm.nih.gov/16627871/)
- Díaz-Flores L, Madrid JF, Gutiérrez R, Varela H, Valladares F, Alvarez-Argüelles H, Díaz-Flores L. 2006. Adult stem and transit-amplifying cell location. *Histology and Histopathology* **21**:995–1027. doi: [10.14670/HH-21.995](https://doi.org/10.14670/HH-21.995), PMID: [16763950](https://pubmed.ncbi.nlm.nih.gov/16763950/)
- Eames BF, Schneider RA. 2008. The genesis of cartilage size and shape during development and evolution. *Development* **135**:3947–3958. doi: [10.1242/dev.023309](https://doi.org/10.1242/dev.023309), PMID: [18987028](https://pubmed.ncbi.nlm.nih.gov/18987028/)
- Feil R, Wagner J, Metzger D, Chambon P. 1997. Regulation of cre recombinase activity by mutated estrogen receptor ligand-binding domains. *Biochemical and Biophysical Research Communications* **237**:752–757. doi: [10.1006/bbrc.1997.7124](https://doi.org/10.1006/bbrc.1997.7124), PMID: [9299439](https://pubmed.ncbi.nlm.nih.gov/9299439/)
- Fletcher AG, Osborne JM, Maini PK, Gavaghan DJ. 2013. Implementing vertex dynamics models of cell populations in biology within a consistent computational framework. *Progress in Biophysics and Molecular Biology* **113**:299–326. doi: [10.1016/j.pbiomolbio.2013.09.003](https://doi.org/10.1016/j.pbiomolbio.2013.09.003), PMID: [24120733](https://pubmed.ncbi.nlm.nih.gov/24120733/)
- Foppiano S, Hu D, Marcucio RS. 2007. Signaling by bone morphogenetic proteins directs formation of an ectodermal signaling center that regulates craniofacial development. *Developmental Biology* **312**:103–114. doi: [10.1016/j.ydbio.2007.09.016](https://doi.org/10.1016/j.ydbio.2007.09.016), PMID: [18028903](https://pubmed.ncbi.nlm.nih.gov/18028903/)
- Ford-Hutchinson AF, Ali Z, Lines SE, Hallgrímsson B, Boyd SK, Jirik FR. 2007. Inactivation of Pten in osteochondroprogenitor cells leads to epiphyseal growth plate abnormalities and skeletal overgrowth. *Journal of Bone and Mineral Research* **22**:1245–1259. doi: [10.1359/jbmr.070420](https://doi.org/10.1359/jbmr.070420), PMID: [17456009](https://pubmed.ncbi.nlm.nih.gov/17456009/)
- Fritz JA, Brancale J, Tokita M, Burns KJ, Hawkins MB, Abzhanov A, Brenner MP. 2014. Shared developmental programme strongly constrains beak shape diversity in songbirds. *Nature Communications* **5**:3700. doi: [10.1038/ncomms4700](https://doi.org/10.1038/ncomms4700), PMID: [24739280](https://pubmed.ncbi.nlm.nih.gov/24739280/)
- Fukuda T, Scott G, Komatsu Y, Araya R, Kawano M, Ray MK, Yamada M, Mishina Y. 2006. Generation of a mouse with conditionally activated signaling through the BMP receptor, ALK2. *Genesis* **44**:159–167. doi: [10.1002/dvg.20201](https://doi.org/10.1002/dvg.20201), PMID: [16604518](https://pubmed.ncbi.nlm.nih.gov/16604518/)
- Gao B, Song H, Bishop K, Elliot G, Garrett L, English MA, Andre P, Robinson J, Sood R, Minami Y, Economides AN, Yang Y. 2011. Wnt signaling gradients establish planar cell polarity by inducing Vangl2 phosphorylation through Ror2. *Developmental Cell* **20**:163–176. doi: [10.1016/j.devcel.2011.01.001](https://doi.org/10.1016/j.devcel.2011.01.001), PMID: [21316585](https://pubmed.ncbi.nlm.nih.gov/21316585/)
- Golding MB, Tsuchimochi K, Ijiri K. 2006. The control of chondrogenesis. *Journal of Cellular Biochemistry* **97**:33–44. doi: [10.1002/jcb.20652](https://doi.org/10.1002/jcb.20652), PMID: [16215986](https://pubmed.ncbi.nlm.nih.gov/16215986/)
- Graner F, Glazier JA. 1992. Simulation of biological cell sorting using a two-dimensional extended Potts model. *Physical Review Letters* **69**:2013–2016. doi: [10.1103/PhysRevLett.69.2013](https://doi.org/10.1103/PhysRevLett.69.2013), PMID: [10046374](https://pubmed.ncbi.nlm.nih.gov/10046374/)
- Green AA, Kennaway JR, Hanna AI, Bangham JA, Coen E. 2010. Genetic control of organ shape and tissue polarity. *PLoS Biology* **8**:e1000537. doi: [10.1371/journal.pbio.1000537](https://doi.org/10.1371/journal.pbio.1000537), PMID: [21085690](https://pubmed.ncbi.nlm.nih.gov/21085690/)
- Guenther C, Pantalena-Filho L, Kingsley DM. 2008. Shaping skeletal growth by modular regulatory elements in the Bmp5 gene. *PLoS Genetics* **4**:e1000308. doi: [10.1371/journal.pgen.1000308](https://doi.org/10.1371/journal.pgen.1000308), PMID: [19096511](https://pubmed.ncbi.nlm.nih.gov/19096511/)

- Hari L**, Miescher I, Shakhova O, Suter U, Chin L, Taketo M, Richardson WD, Kessar N, Sommer L. 2012. Temporal control of neural crest lineage generation by wnt/ β -catenin signaling. *Development* **139**:2107–2117. doi: [10.1242/dev.073064](https://doi.org/10.1242/dev.073064), PMID: [22573620](https://pubmed.ncbi.nlm.nih.gov/22573620/)
- Hayes AJ**, MacPherson S, Morrison H, Dowthwaite G, Archer CW. 2001. The development of articular cartilage: evidence for an appositional growth mechanism. *Anatomy and Embryology* **203**:469–479. doi: [10.1007/s004290100178](https://doi.org/10.1007/s004290100178), PMID: [11453164](https://pubmed.ncbi.nlm.nih.gov/11453164/)
- Hellander A**. 2015. multicell. *Github*. e7edeef. <https://github.com/ahellander/multicell>
- Hu D**, Young NM, Xu Q, Jamniczky H, Green RM, Mio W, Marcucio RS, Hallgrímsson B. 2015. Signals from the brain induce variation in avian facial shape. *Developmental Dynamics : An Official Publication of the American Association of Anatomists*. doi: [10.1002/dvdy.24284](https://doi.org/10.1002/dvdy.24284), PMID: [25903813](https://pubmed.ncbi.nlm.nih.gov/25903813/)
- Jarjour M**, Jorquera A, Mondor I, Wienert S, Narang P, Coles MC, Klauschen F, Bajénoff M. 2014. Fate mapping reveals origin and dynamics of lymph node follicular dendritic cells. *The Journal of Experimental Medicine* **211**: 1109–1122. doi: [10.1084/jem.20132409](https://doi.org/10.1084/jem.20132409), PMID: [24863064](https://pubmed.ncbi.nlm.nih.gov/24863064/)
- Kaucka M**, Ivashkin E, Gyllborg D, Zikmund T, Tesarova M, Kaiser J, Xie M, Petersen J, Pachnis V, Nicolis SK, Yu T, Sharpe P, Arenas E, Brismar H, Blom H, Clevers H, Suter U, Chagin AS, Fried K, Hellander A, et al. 2016. Analysis of neural crest-derived clones reveals novel aspects of facial development. *Science Advances* **2**: e1600060. doi: [10.1126/sciadv.1600060](https://doi.org/10.1126/sciadv.1600060), PMID: [27493992](https://pubmed.ncbi.nlm.nih.gov/27493992/)
- Kennaway R**, Coen E, Green A, Bangham A. 2011. Generation of diverse biological forms through combinatorial interactions between tissue polarity and growth. *PLoS Computational Biology* **7**:e1002071. doi: [10.1371/journal.pcbi.1002071](https://doi.org/10.1371/journal.pcbi.1002071), PMID: [21698124](https://pubmed.ncbi.nlm.nih.gov/21698124/)
- Kerney RR**, Brittain AL, Hall BK, Buchholz DR. 2012. Cartilage on the move: cartilage lineage tracing during tadpole metamorphosis. *Development, Growth & Differentiation* **54**:739–752. doi: [10.1111/dgd.12002](https://doi.org/10.1111/dgd.12002), PMID: [23036161](https://pubmed.ncbi.nlm.nih.gov/23036161/)
- Kettunen P**, Nie X, Kvinnsland IH, Luukko K. 2006. Histological development and dynamic expression of Bmp2-6 mRNAs in the embryonic and postnatal mouse cranial base. *The Anatomical Record. Part A, Discoveries in Molecular, Cellular, and Evolutionary Biology* **288**:1250–1258. doi: [10.1002/ar.a.20402](https://doi.org/10.1002/ar.a.20402), PMID: [17066377](https://pubmed.ncbi.nlm.nih.gov/17066377/)
- Kobayashi S**, Takebe T, Zheng YW, Mizuno M, Yabuki Y, Maegawa J, Taniguchi H. 2011. Presence of cartilage stem/progenitor cells in adult mice auricular perichondrium. *PLoS One* **6**:e26393. doi: [10.1371/journal.pone.0026393](https://doi.org/10.1371/journal.pone.0026393), PMID: [22039478](https://pubmed.ncbi.nlm.nih.gov/22039478/)
- Kronenberg HM**. 2003. Developmental regulation of the growth plate. *Nature* **423**:332–336. doi: [10.1038/nature01657](https://doi.org/10.1038/nature01657), PMID: [12748651](https://pubmed.ncbi.nlm.nih.gov/12748651/)
- Kuchen EE**, Fox S, de Reuille PB, Kennaway R, Bensmihen S, Avondo J, Calder GM, Southam P, Robinson S, Bangham A, Coen E. 2012. Generation of leaf shape through early patterns of growth and tissue polarity. *Science* **335**:1092–1096. doi: [10.1126/science.1214678](https://doi.org/10.1126/science.1214678), PMID: [22383846](https://pubmed.ncbi.nlm.nih.gov/22383846/)
- Laranjeira C**, Sandgren K, Kessar N, Richardson W, Potocnik A, Vanden Berghe P, Pachnis V. 2011. Glial cells in the mouse enteric nervous system can undergo neurogenesis in response to injury. *Journal of Clinical Investigation* **121**:3412–3424. doi: [10.1172/JCI58200](https://doi.org/10.1172/JCI58200), PMID: [21865647](https://pubmed.ncbi.nlm.nih.gov/21865647/)
- Laurita J**, Koyama E, Chin B, Taylor JA, Lakin GE, Hankenson KD, Bartlett SP, Nah HD. 2011. The Muenke syndrome mutation (Fgfr3P244R) causes cranial base shortening associated with growth plate dysfunction and premature perichondrial ossification in murine basicranial synchondroses. *Developmental Dynamics* **240**:2584–2596. doi: [10.1002/dvdy.22752](https://doi.org/10.1002/dvdy.22752), PMID: [22016144](https://pubmed.ncbi.nlm.nih.gov/22016144/)
- Leone DP**, Genoud S, Atanasoski S, Grausenburger R, Berger P, Metzger D, Macklin WB, Chambon P, Suter U. 2003. Tamoxifen-inducible glia-specific cre mice for somatic mutagenesis in oligodendrocytes and schwann cells. *Molecular and Cellular Neuroscience* **22**:430–440. doi: [10.1016/S1044-7431\(03\)00029-0](https://doi.org/10.1016/S1044-7431(03)00029-0), PMID: [12727441](https://pubmed.ncbi.nlm.nih.gov/12727441/)
- Li L**, Newton PT, Boudierlique T, Sejnohova M, Zikmund T, Kozhemyakina E, Xie M, Krivanek J, Kaiser J, Qian H, Dyachuk V, Lassar AB, Warman ML, Barenus B, Adameyko I, Chagin AS. 2017. Superficial cells are self-renewing chondrocyte progenitors, which form the articular cartilage in juvenile mice. *The FASEB Journal* **31**: 1067–1084. doi: [10.1096/fj.201600918R](https://doi.org/10.1096/fj.201600918R)
- Ma W**, Lozanoff S. 1999. Spatial and temporal distribution of cellular proliferation in the cranial base of normal and midfacially retrusive mice. *Clinical Anatomy* **12**:315–325. doi: [10.1002/\(SICI\)1098-2353\(1999\)12:5<315::AID-CA2>3.0.CO;2-2](https://doi.org/10.1002/(SICI)1098-2353(1999)12:5<315::AID-CA2>3.0.CO;2-2), PMID: [10462729](https://pubmed.ncbi.nlm.nih.gov/10462729/)
- Mackie EJ**, Ahmed YA, Tatarczuch L, Chen KS, Mirams M. 2008. Endochondral ossification: how cartilage is converted into bone in the developing skeleton. *The International Journal of Biochemistry & Cell Biology* **40**: 46–62. doi: [10.1016/j.biocel.2007.06.009](https://doi.org/10.1016/j.biocel.2007.06.009), PMID: [17659995](https://pubmed.ncbi.nlm.nih.gov/17659995/)
- Maes C**, Kobayashi T, Selig MK, Torrekens S, Roth SI, Mackem S, Carmeliet G, Kronenberg HM. 2010. Osteoblast precursors, but not mature osteoblasts, move into developing and fractured bones along with invading blood vessels. *Developmental Cell* **19**:329–344. doi: [10.1016/j.devcel.2010.07.010](https://doi.org/10.1016/j.devcel.2010.07.010), PMID: [20708594](https://pubmed.ncbi.nlm.nih.gov/20708594/)
- Mallarino R**, Campàs O, Fritz JA, Burns KJ, Weeks OG, Brenner MP, Abzhanov A. 2012. Closely related bird species demonstrate flexibility between beak morphology and underlying developmental programs. *PNAS* **109**:16222–16227. doi: [10.1073/pnas.1206205109](https://doi.org/10.1073/pnas.1206205109), PMID: [22988109](https://pubmed.ncbi.nlm.nih.gov/22988109/)
- McBratney-Owen B**, Iseki S, Bamforth SD, Olsen BR, Morriss-Kay GM. 2008. Development and tissue origins of the mammalian cranial base. *Developmental Biology* **322**:121–132. doi: [10.1016/j.ydbio.2008.07.016](https://doi.org/10.1016/j.ydbio.2008.07.016), PMID: [18680740](https://pubmed.ncbi.nlm.nih.gov/18680740/)
- Muzumdar MD**, Tasic B, Miyamichi K, Li L, Luo L. 2007. A global double-fluorescent cre reporter mouse. *Genesis* **45**:593–605. doi: [10.1002/dvg.20335](https://doi.org/10.1002/dvg.20335), PMID: [17868096](https://pubmed.ncbi.nlm.nih.gov/17868096/)

- Nagayama M**, Iwamoto M, Hargett A, Kamiya N, Tamamura Y, Young B, Morrison T, Takeuchi H, Pacifici M, Enomoto-Iwamoto M, Koyama E. 2008. Wnt/beta-catenin signaling regulates cranial base development and growth. *Journal of Dental Research* **87**:244–249. doi: [10.1177/154405910808700309](https://doi.org/10.1177/154405910808700309), PMID: [18296608](https://pubmed.ncbi.nlm.nih.gov/18296608/)
- Nakamura E**, Nguyen MT, Mackem S. 2006. Kinetics of tamoxifen-regulated cre activity in mice using a cartilage-specific CreER(T) to assay temporal activity windows along the proximodistal limb skeleton. *Developmental Dynamics* **235**:2603–2612. doi: [10.1002/dvdy.20892](https://doi.org/10.1002/dvdy.20892), PMID: [16894608](https://pubmed.ncbi.nlm.nih.gov/16894608/)
- Nilsson O**, Marino R, De Luca F, Phillip M, Baron J. 2005. Endocrine regulation of the growth plate. *Hormone Research in Paediatrics* **64**:157–165. doi: [10.1159/000088791](https://doi.org/10.1159/000088791), PMID: [16205094](https://pubmed.ncbi.nlm.nih.gov/16205094/)
- Radszweit M**, Block M, Hengstler JG, Schöll E, Drasdo D. 2009. Comparing the growth kinetics of cell populations in two and three dimensions. *Physical Review E* **79**:051907. doi: [10.1103/PhysRevE.79.051907](https://doi.org/10.1103/PhysRevE.79.051907)
- Repiso A**, Bergantiños C, Serras F. 2013. Cell fate respecification and cell division orientation drive intercalary regeneration in *Drosophila* wing discs. *Development* **140**:3541–3551. doi: [10.1242/dev.095760](https://doi.org/10.1242/dev.095760), PMID: [23903186](https://pubmed.ncbi.nlm.nih.gov/23903186/)
- Sakamoto A**, Chen M, Kobayashi T, Kronenberg HM, Weinstein LS. 2005. Chondrocyte-specific knockout of the G protein G(s)alpha leads to epiphyseal and growth plate abnormalities and ectopic chondrocyte formation. *Journal of Bone and Mineral Research* **20**:663–671. doi: [10.1359/JBMR.041210](https://doi.org/10.1359/JBMR.041210), PMID: [15765186](https://pubmed.ncbi.nlm.nih.gov/15765186/)
- Schötz EM**, Lanio M, Talbot JA, Manning ML. 2013. Glassy dynamics in three-dimensional embryonic tissues. *Journal of the Royal Society Interface* **10**:20130726. doi: [10.1098/rsif.2013.0726](https://doi.org/10.1098/rsif.2013.0726), PMID: [24068179](https://pubmed.ncbi.nlm.nih.gov/24068179/)
- Sheehan MJ**, Nachman MW. 2014. Morphological and population genomic evidence that human faces have evolved to signal individual identity. *Nature Communications* **5**:4800. doi: [10.1038/ncomms5800](https://doi.org/10.1038/ncomms5800), PMID: [25226282](https://pubmed.ncbi.nlm.nih.gov/25226282/)
- Snippert HJ**, van der Flier LG, Sato T, van Es JH, van den Born M, Kroon-Veenboer C, Barker N, Klein AM, van Rheenen J, Simons BD, Clevers H. 2010. Intestinal crypt homeostasis results from neutral competition between symmetrically dividing Lgr5 stem cells. *Cell* **143**:134–144. doi: [10.1016/j.cell.2010.09.016](https://doi.org/10.1016/j.cell.2010.09.016), PMID: [20887898](https://pubmed.ncbi.nlm.nih.gov/20887898/)
- Strutt D**. 2005. Organ shape: controlling oriented cell division. *Current Biology* **15**:R758–R759. doi: [10.1016/j.cub.2005.08.053](https://doi.org/10.1016/j.cub.2005.08.053), PMID: [16169474](https://pubmed.ncbi.nlm.nih.gov/16169474/)
- Tesařová M**, Zikmund T, Kaucká M, Adameyko I, Jaroš J, Paloušek D, Škaroupka D, Kaiser J. 2016. Use of micro computed-tomography and 3D printing for reverse engineering of mouse embryo nasal capsule. *Journal of Instrumentation* **11**:C03006. doi: [10.1088/1748-0221/11/03/C03006](https://doi.org/10.1088/1748-0221/11/03/C03006)
- Thompson H**, Ohazama A, Sharpe PT, Tucker AS. 2012. The origin of the stapes and relationship to the otic capsule and oval window. *Developmental Dynamics* **241**:1396–1404. doi: [10.1002/dvdy.23831](https://doi.org/10.1002/dvdy.23831), PMID: [22778034](https://pubmed.ncbi.nlm.nih.gov/22778034/)
- Van Liedekerke P**, Palm MM, Jagiella N, Drasdo D. 2015. Simulating tissue mechanics with agent-based models: concepts, perspectives and some novel results. *Computational Particle Mechanics* **2**:401–444. doi: [10.1007/s40571-015-0082-3](https://doi.org/10.1007/s40571-015-0082-3)
- Vortkamp A**, Lee K, Lanske B, Segre GV, Kronenberg HM, Tabin CJ. 1996. Regulation of rate of cartilage differentiation by indian hedgehog and PTH-related protein. *Science* **273**:613–622. doi: [10.1126/science.273.5275.613](https://doi.org/10.1126/science.273.5275.613), PMID: [8662546](https://pubmed.ncbi.nlm.nih.gov/8662546/)
- Wang Y**, Spatz MK, Kannan K, Hayk H, Avivi A, Gorivodsky M, Pines M, Yayon A, Lonai P, Givol D. 1999. A mouse model for achondroplasia produced by targeting fibroblast growth factor receptor 3. *PNAS* **96**:4455–4460. doi: [10.1073/pnas.96.8.4455](https://doi.org/10.1073/pnas.96.8.4455), PMID: [10200283](https://pubmed.ncbi.nlm.nih.gov/10200283/)
- Wealthall RJ**, Herring SW. 2006. Endochondral ossification of the mouse nasal septum. *The Anatomical Record Part A: Discoveries in Molecular, Cellular, and Evolutionary Biology* **288**:1163–1172. doi: [10.1002/ar.a.20385](https://doi.org/10.1002/ar.a.20385), PMID: [17031811](https://pubmed.ncbi.nlm.nih.gov/17031811/)
- Yamaguchi TP**, Bradley A, McMahon AP, Jones S. 1999. A Wnt5a pathway underlies outgrowth of multiple structures in the vertebrate embryo. *Development* **126**:1211–1223. PMID: [10021340](https://pubmed.ncbi.nlm.nih.gov/10021340/)
- Young B**, Minugh-Purvis N, Shimo T, St-Jacques B, Iwamoto M, Enomoto-Iwamoto M, Koyama E, Pacifici M. 2006. Indian and sonic hedgehogs regulate synchondrosis growth plate and cranial base development and function. *Developmental Biology* **299**:272–282. doi: [10.1016/j.ydbio.2006.07.028](https://doi.org/10.1016/j.ydbio.2006.07.028), PMID: [16935278](https://pubmed.ncbi.nlm.nih.gov/16935278/)
- Yu K**, McGlynn S, Matisse MP. 2013. Floor plate-derived sonic hedgehog regulates glial and ependymal cell fates in the developing spinal cord. *Development* **140**:1594–1604. doi: [10.1242/dev.090845](https://doi.org/10.1242/dev.090845), PMID: [23482494](https://pubmed.ncbi.nlm.nih.gov/23482494/)

Appendix 1

Individual based model (IBM) for cartilage dynamics

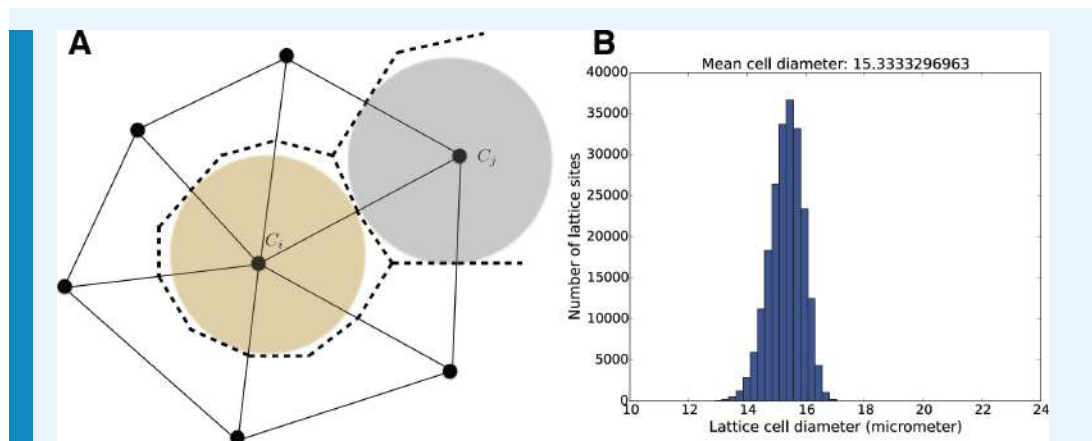
In order to model and illustrate the growth of the cartilage on the cellular level, we developed an individual-based model incorporating cell proliferation (including displacement of surrounding cells via pushing) (Hellander, 2015). The model is stochastic because we want to be able to capture effects of e.g. synchronicity in cell division and the degree of determinism needed to achieve an ordered columnar growth of the structure. We do this by letting the cell division times, direction of allocation of daughter cells after cell division, etc., be random variables. This document describes the details of the model and its implementation.

There are several popular modeling frameworks for simulating interacting cells. In the cellular potts model (Graner and Glazier, 1992) a single biological cell can be composed of multiple lattice sites making it possible to use a more detailed description of cell shape and include more detailed description of more mechanical properties. In off-lattice center based models cells are often modeled as spheres with pair-wise interactions and a force-based description to evolve the system dynamics, for an overview see (Van Liedekerke et al., 2015). Vertex models can offer even more realistic models of cell mechanics (Fletcher et al., 2013) but become expensive and complicated in three space dimensions.

Rather than these more comprehensive mechanical models, we use a simplistic rule-based, on-lattice stochastic cellular automaton (CA). In the language of a recent review (Van Liedekerke et al., 2015) our model falls into the category of a Type B CA. These types of models are widely used in e.g. cancer tumor modeling and for simulation of monolayers and spheroids (Radszweit et al., 2009). The simulation code is written in Python, relies on the PyURDME package for spatial stochastic simulations (www.pyurdme.org) and it is freely available for download from [www.github.com/ahellander/multicell](https://github.com/ahellander/multicell) (Hellander, 2015) under the GPLv3 license. A copy is archived at <https://github.com/elifesciences-publications/multicell>.

The basic entities in our simulation are Agents and Events. An Agent is a model (implemented as a Python class) of an individual (cell). Events simulate discrete state changes involving one or several agents. They occur at a certain time (assuming no other event involving the same agents occurs first). They rely on rules that specify how and under what conditions the event is to be executed. A simulation is initialized by creating the initial population of agents and events, and then creating a priority queue (in our case implemented using a heap data structure using the Python module 'heapq'). In each iteration of the algorithm, the event with the shortest time is popped from the queue and executed (assuming that all of its rules and conditions can be satisfied), the system time updated, new events derived from any newly created agents are created and inserted into the queue, and all existing events affected by changes in the agents or the system state are updated.

Each agent occupies one voxel of a tessellation of 2D or 3D space, and each lattice site can only accommodate one agent. Following the recommendation in (Radszweit et al., 2009) a Delaunay triangulation is used. The mesh resolution is chosen such that the average voxel size is close to the desired cell size (~7 μm radius) taken from the experiments. Being a lattice model, the shape and volume of the cells are a lattice property and are given by the dual grid (Voronoi cells in the case of a Delaunay triangulation). This is illustrated in **Appendix 1—figure 1A**. The interpretation is that individual agents occupy the dual elements (dashed lines) of an unstructured triangular (2D) or tetrahedral primal mesh (3D) (solid lines).



Appendix 1—figure 1. (A) Individual cells are modeled by a number of properties such as their color and distributions for cell division times. The positions of cells in space are tracked on an underlying unstructured lattice, or grid. The edges in the primary mesh (solid lines) connect vertices (black dots). A biological cell is modeled by the volume made up of the dual elements (dashed lines), connecting triangle (2D) or tetrahedral (3D) centers and edge or face centers. For visualization purposes, in 3D space, we plot cell individuals as colored spheres with radius equal to the sphere with equal volume as the dual element. (B) Size distribution for the mesh elements for the geometry and mesh used in the simulations in the **Figure 5**.

DOI: [10.7554/eLife.25902.025](https://doi.org/10.7554/eLife.25902.025)

The individual agents – colored coded cells

Each individual cell is modeled as an individual agent with the following properties:

- Color (a label used to track the lineage).
- Mean cell division time, μ_p .
- Variance in cell division time, σ_p^2 .

When visualized in 2D, we draw cells as polygons (the actual dual cells) and in 3D for practical reasons we visualize them as spheres centered on the vertices of the primal mesh, with radius chosen such that the volume corresponds to the volume of the corresponding dual element. On the unstructured mesh, there will be a size distribution for the mesh elements, i.e. there will be a small variation in the size associated with each lattice site, see **Appendix 1— figure 1B**.

Cell proliferation

Cell division time

The time until a cell, or individual, divides, is assumed to be a random variable. Although a multi-stage model of cell division can give rise to an Erlang distribution (**Radszuweit et al., 2009**) which is found to match experimental data for another system, we are not calibrating our model to experimental data on cell division time distributions. The dividing cell (referred to as the mother cell) create a daughter cell after a normally distributed waiting time τ_D .

$$\tau_D \sim N(\mu_d, \sigma_d^2) \quad (1)$$

where the mean division time m and the variance σ^2 are parameters of the model to be supplied as input to the simulation. As a measure of the degree of variability in cell division times, we use the standard deviation over the mean,

$$f = \frac{\sigma_d}{\mu_d} \quad (2)$$

The smaller value of f , the more deterministic and synchronized the cell cycles of individual cells are. The way our model is set up, there are no events that leads to the recalculation of a cell's division time. A cell gets assigned a time to division at creation and each cell then divide according to its internal clock irrespective of if it gets pushed etc.

After division, the daughter cell needs to be deposited on the grid. The division direction, or receiving voxel, is sampled according to a discrete distribution. In the simplest case, all directions of division are equally probable and the direction distribution is uniform. In the general case, weights are assigned according to an external, deterministic gradient.

Cell division direction

The division direction is also a random variable and the number of possible directions are given by the connections to the neighbors on the grid. Each individual has a property that sets its polarization, represented by a normalized vector p pointing in the preferred direction of division. With no polarization, each possible division direction is equally probable. With polarization, the probability to divide in a certain direction is biased by the gradient. The weights for sampling the division direction are taken to be

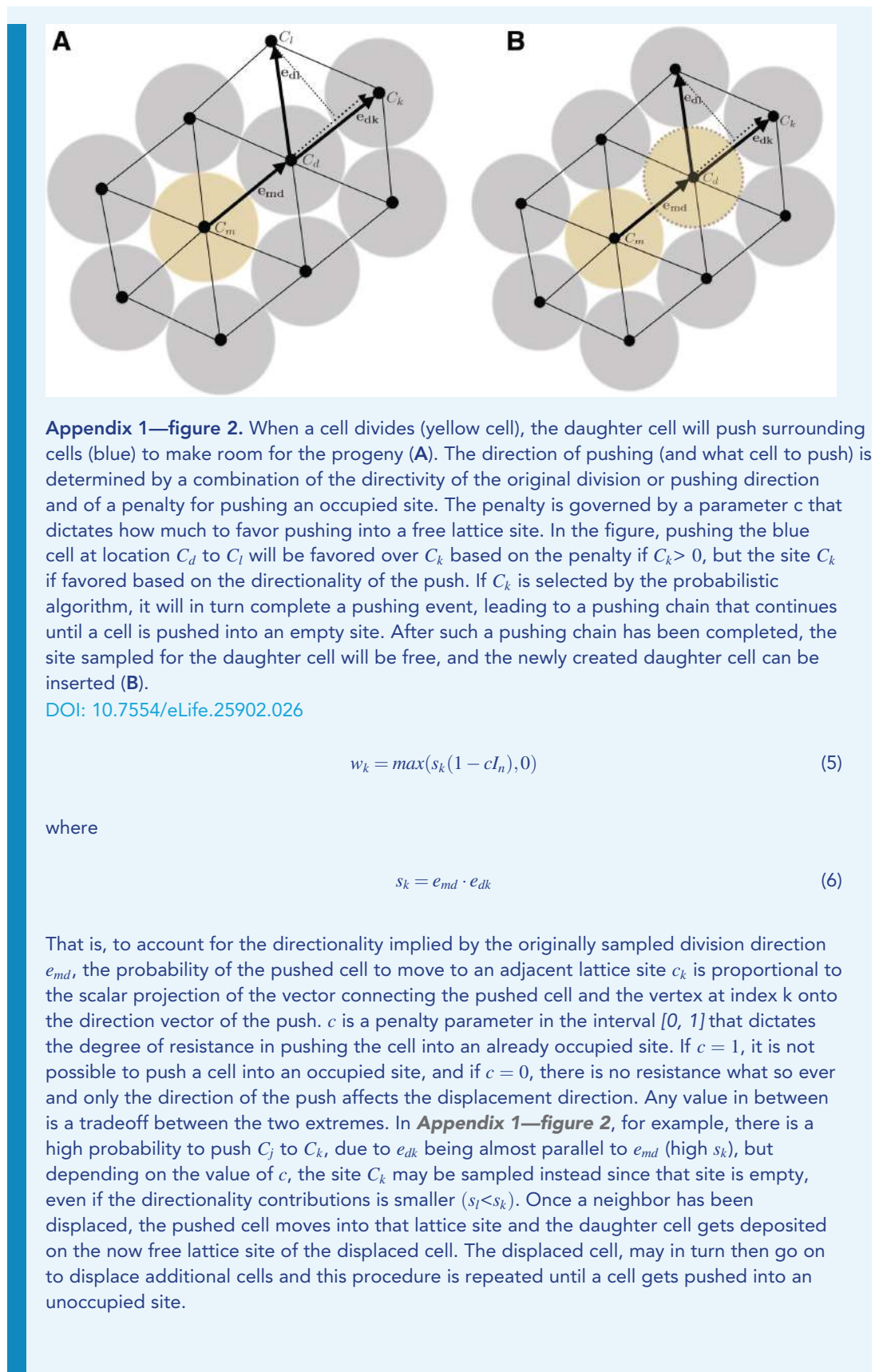
$$w_{ij} = \left(\frac{d_{ij}}{\max_j(d_{ij})} \right)^b, \quad (3)$$

$$d_{ij} = \frac{g(x_j) - g(x_i)}{h_{ij}} \quad (4)$$

where x_i is the position of the vertex in the grid for which the agent resides, and h_{ij} is the length of the edge connecting grid points x_i and x_j and $g(x)$ is a given concentration profile. The parameter $b \geq 0$ dictates how perfectly the cells become polarized by the concentration profile $g(x)$. A value $b = 0$ leads to equal probabilities for all directions, and very large value of b means that the division direction will always be in the direction of the maximal value of the gradient (the division direction becomes deterministic in the direction of the maximal gradient in the limit $b \rightarrow \infty$). Values in between the extremes describes an increasing precision in polarization axis alignment with the gradient field.

Cell pushing

If the receiving lattice for the daughter cell site is empty (i.e. occupied by matrix), it is simply deposited there. When the daughter cell cannot be placed on a free lattice site, there is an attempt to reorganize the structure by pushing neighboring cells to make room for it. The procedure is illustrated in **Appendix 1—figure 2**. The probability for the displaced cell to move to a given neighboring grid point depends on the direction of pushing. Let e_{md} be the vector along the edge connecting the mother cell C_m and the daughter cell C_d , pointing towards the daughter cell. Let e_{dk} be the unit vector along the edge connecting the daughter cell C_d and one of its neighbors, C_k . The weight for moving the displaced cell to the neighbor with index n is given by



Measure of order in the cartilage model

We are interested in assessing what factors are the main determinants to the degree of ordered columnar growth in the cartilage sheet patches. To that end, we postulate that a perfectly ordered structure consists of clonal columns growing straight and directed along the axis perpendicular to the initial condition starting plane (**Figure 5G**). We then use the following metric to quantify the degree of order in the structure

$$S = \frac{1}{C} \sum_{j=1}^C \frac{1}{N_j} \sum_{i=1}^{N_j} s_{ij} \quad (7)$$

with s_{ij}

$$s_{ij} = |v_i \bullet y| \quad (8)$$

where y is a unit vector perpendicular to the initial condition plane, and v_i are normalized vectors joining two consecutive points (sorted by y -coordinate) in clones with the same color. N_j is the number of cells of a given color minus one (the number of vectors), and C is the number of unique clones tracked. This is illustrated graphically in **Figure 5A**. With this metric, a score of $S = 1$ would mean that all columns are perfectly aligned to the main growth axis and a score of $S = 0$ would mean that they are all perpendicular to it. We use this metric to score realizations of the process either in the absence of a gradient, or when the gradient is uniform in planes parallel to the center plane, so that in the case of a perfect polarization, cells should all deposit their daughter cells perpendicular to the center plane.

Analysis of neural crest–derived clones reveals novel aspects of facial development

Marketa Kaucka,^{1*} Evgeny Ivashkin,^{1,2*} Daniel Gyllborg,³ Tomas Zikmund,⁴ Marketa Tesarova,⁴ Jozef Kaiser,⁴ Meng Xie,¹ Julian Petersen,⁵ Vassilis Pachnis,⁶ Silvia K. Nicolis,⁷ Tian Yu,⁸ Paul Sharpe,⁸ Ernest Arenas,³ Hjalmar Brismar,⁹ Hans Blom,⁹ Hans Clevers,¹⁰ Ueli Suter,¹¹ Andrei S. Chagin,¹ Kaj Fried,¹² Andreas Hellander,^{13†‡} Igor Adameyko^{1,5†‡}

2016 © The Authors, some rights reserved; exclusive licensee American Association for the Advancement of Science. Distributed under a Creative Commons Attribution NonCommercial License 4.0 (CC BY-NC). 10.1126/sciadv.1600060

Cranial neural crest cells populate the future facial region and produce ectomesenchyme-derived tissues, such as cartilage, bone, dermis, smooth muscle, adipocytes, and many others. However, the contribution of individual neural crest cells to certain facial locations and the general spatial clonal organization of the ectomesenchyme have not been determined. We investigated how neural crest cells give rise to clonally organized ectomesenchyme and how this early ectomesenchyme behaves during the developmental processes that shape the face. Using a combination of mouse and zebrafish models, we analyzed individual migration, cell crowd movement, oriented cell division, clonal spatial overlapping, and multilineage differentiation. The early face appears to be built from multiple spatially defined overlapping ectomesenchymal clones. During early face development, these clones remain oligopotent and generate various tissues in a given location. By combining clonal analysis, computer simulations, mouse mutants, and live imaging, we show that facial shaping results from an array of local cellular activities in the ectomesenchyme. These activities mostly involve oriented divisions and crowd movements of cells during morphogenetic events. Cellular behavior that can be recognized as individual cell migration is very limited and short-ranged and likely results from cellular mixing due to the proliferation activity of the tissue. These cellular mechanisms resemble the strategy behind limb bud morphogenesis, suggesting the possibility of common principles and deep homology between facial and limb outgrowth.

INTRODUCTION

The facial compartment is arguably the most sophisticated and heterogeneous part of our body. Despite the keen attention to the biology of facial development, the functional and adaptive placement and spatial integration of sensory organs, skeletal structures, nervous system, and feeding apparatus are still not well understood. Numerous congenital craniofacial abnormalities affect the form and function of the face. These may result in, for instance, deformities, distractions, elongations, shortenings, asymmetries, and generally aberrant structures. Explanations to these malformations still await the fundamental understanding of the underlying failure of morphogenesis (1). Cells of the facial compartment arise from four main sources: neural crest stem cells, paraxial mesoderm, epidermis, and endoderm. The nonepithelial tissues in the facial region originate from migratory neural crest stem cells and the paraxial mesoderm

(2). Embryonic epidermis and endoderm generate epithelialized structures, including covering tissues, various glands, epithelial compartments of the hair follicles, and teeth (3, 4). The paraxial mesoderm produces progenitors of striated muscles and endothelial cells and forms the vascular tree in the face and the head in general (5, 6). The neural crest, the largest contributor to the developing face, gives rise to cartilage, bone, dentin and pulp of the teeth, dermal papillae of hair follicles, smooth muscles of the vessel walls, ligaments, fascia, adipose tissue, dermis, pericytes in the forebrain, epithelial cells in the ear, pigment cells, peripheral glial cells, subpopulation of sensory neurons in trigeminal ganglia, sympathetic and parasympathetic neurons, and some other cell types found in the head (7). Neural crest cells have long been considered to be multipotent within the neural tube and later during their active migration (8–11). However, current evidence has suggested that early cell fate restrictions in the neural crest may already exist at the level of the neural tube (12, 13). Still, a very recently performed clonal analysis of neural crest populations in the trunk has supported the concept of multipotency of the premigratory and migratory neural crest (14). Despite this, questions concerning neural crest heterogeneity, multipotency, and progressive specification are far from resolved. This is especially evident when considering the intrinsic differences between neural crest populations that delaminate from different parts along the anterioposterior axis and also along the time scale. For example, only cranial neural crest cells give rise to the ectomesenchyme as an intermediate embryonic cell type that, in turn, will produce most of the structures in a developing face (7, 15). These neural crest–derived early ectomesenchymal cells are the main focus of this study. Little is known about their behavior before the formation of bones, cartilages, and other tissues in the face.

¹Department of Physiology and Pharmacology, Karolinska Institutet, Stockholm SE-171 77, Sweden. ²Research Center of Neurology, 125367 Moscow, Russia. ³Unit of Molecular Neurobiology, Department of Medical Biochemistry and Biophysics, Karolinska Institutet, Stockholm SE-171 77, Sweden. ⁴Central European Institute of Technology, Brno University of Technology, 616 00 Brno, Czech Republic. ⁵Department of Molecular Neurosciences, Medical University of Vienna, Vienna 1190, Austria. ⁶Division of Molecular Neurobiology, Medical Research Council National Institute for Medical Research, London NW7 1AA, UK. ⁷Department of Biotechnology and Biosciences, University of Milano-Bicocca, 20126 Milano, Italy. ⁸Department of Craniofacial Development and Stem Cell Biology, King's College London Dental Institute, Guy's Hospital, London SE1 9RT, UK. ⁹Science for Life Laboratory, Royal Institute of Technology, Solna 17121, Sweden. ¹⁰Hubrecht Institute of the Royal Netherlands Academy of Arts and Sciences, Princess Maxima Centre and University Medical Centre Utrecht, 3584 Utrecht, Netherlands. ¹¹Department of Biology, Institute of Molecular Health Sciences, ETH Zurich, Zurich CH-8093, Switzerland. ¹²Department of Neuroscience, Karolinska Institutet, Stockholm SE-171 77, Sweden. ¹³Department of Information Technology, Uppsala University, Uppsala SE-751 05, Sweden.

*These authors contributed equally to this work.

†Co-senior authors.

‡Corresponding author. Email: igor.adameyko@ki.se (I.A.); andreas.hellander@it.uu.se (A.H.)

In the limb bud, similar mesenchymal cells of a different origin also play a major role in tissue morphogenesis and shape development (16). Previous studies have demonstrated that elongation and shape formation of the embryonic limb are achieved mostly as a result of directional cell activities that include oriented cell divisions, cell allocation, and migration. The shaping largely results from orientation signals and their interpretation in the tissue, rather than only from local differences in proliferation speed (17, 18). The directional activities are regulated by Wnt5a/JNK (c-Jun N-terminal kinase), whereas continuous rearrangements of mesenchymal cells are controlled by the FGF (fibroblast growth factor)/MAPK (mitogen-activated protein kinase) pathway (17). Planar cell polarity (PCP) pathway members (including Wnt5a) are well known to control orientation of cells (19) and are heavily involved in coordinated outgrowth and shape development of multiple embryonic structures (20). As an example, knockout and overexpression of Wnt5a result in the shortening and widening of both the limbs and the face (21–23).

After the arrival of neural crest cells to the face, the embryo is still very small, and significant growth and expansion of the cranial structures will follow. Very little is known about the role of clonal dynamics and the coordinated and directional cell behavior in the ectomesenchyme that eventually shape the face. Here, we attempted to address questions concerning the process of face morphogenesis after the stage of migratory neural crest: How do the newly arrived individual neural crest cells occupy and build different regions of the face? Are there any defined regions occupied by unique clones? Is there a somatotopical mapping at the level of the dorsal neural tube, and what is the degree of cell and tissue polarization, clonal mixing, and migratory behavior of ectomesenchymal cells? Using a variety of methods, we demonstrated that the early outgrowth and shaping of the face are driven by oriented cell divisions and allocations of daughter cells, as well as organized relocations of large cellular groups with minimal individual migration. These are features shown to be of utmost importance in limb shaping, and our findings might support the concept of conserved programs in limb and facial outgrowth.

RESULTS

The early face is organized by well-defined overlapping ectomesenchymal clones

To understand clonal arrangements in relation to facial shape and outgrowth, we took advantage of genetic tracing with the help of *Sox10-CreERT2* and *PLP-CreERT2* mouse strains coupled to an *R26Confetti* reporter (24). Both *Sox10-CreERT2* (25) and *PLP-CreERT2* (26, 27) recombine in the cranial neural crest when the pregnant females are injected with tamoxifen at embryonic day 8.5 (E8.5), whereas the *R26Confetti* reporter enables efficient color coding of individual cells by 10 individual color combinations suitable for clonal analysis. There are unequal chances of activating different color combinations (14). For example, clones with activated yellow fluorescent protein (YFP) + red fluorescent protein (RFP), RFP + cyan fluorescent protein (CFP), RFP + YFP, and green fluorescent protein (GFP) are rare compared to clones expressing only YFP, RFP, or CFP and are always significantly underrepresented as compared to these single-color clones. Clones carrying GFP together with another fluorescent protein were never detected. For details about proportions of recombined color combinations, see Baggiolini *et al.* (14). *Sox10-*

CreERT2 and *PLP-CreERT2* demonstrate different recombination efficiencies and can be selectively used to achieve the desired tracing outcomes and to confirm the specificity of neural crest recombination in cross-comparisons.

With the help of the *Sox10-CreERT2* line, we focused on single-color solitary clones in the whole head, which we successfully achieved by titrating the amount of the injected tamoxifen (28). First, we induced genetic recombination in the neural crest at E8.5 and analyzed the progeny 24 to 36 hours later, using three-dimensional (3D) imaging and analysis. The results showed that genetically traced neural crest cells give rise to spatially defined clonal patches of early ectomesenchyme (“clonal envelopes”) after arrival to the facial region (Figs. 1, A and B, and 2A). A clonal envelope can be strictly defined as a region of 3D space demarcated by a graph connecting all cells belonging to one neural crest–derived clone. Such a clonal envelope occupies only a local portion of the face. Together with the identification of clonal envelopes, we could assess the amount of mixing or overlapping of several clones in a particular location that was analyzed. In cases of rare recombination events, we observed a single compact group of cells in one solitary facial location. We termed this an ectomesenchymal neural crest–derived clone (Fig. 1A). Such single clones, from multiple embryos, were analyzed in detail for cell number, occupied volume, clonal density, and variation of distances between individual cells comprising the clone (Figs. 1 and 2). Observations of such single compact clones in the whole embryo head allowed us to rule out the possibility of a long-range migration of individual early ectomesenchymal cells.

For clonal analysis, with the help of the *PLP-CreERT2* line, we focused on the rare double color combination–labeled clones in the front part of the head to clearly distinguish individual regions occupied by single clones (fig. S1). Results obtained from rare double-colored and GFP⁺ clones in *PLP-CreERT2/R26Confetti* embryos and from clonally titrated recombination events in *Sox10-CreERT2/R26Confetti* were in agreement with each other.

The cells inside the defined clonal envelopes appeared sparse at all investigated developmental stages and, as a result, we observed a high degree of clonal overlapping between the progenies of individual neural crest cells in any given location (Fig. 1, C and E to H). Despite such an extensive overlapping of the clones, all clones appeared to be spatially distinct with recognizable borders (Fig. 1, A to I).

Next, we looked into the cellular structure of ectomesenchyme clones at E10 to address their compactness, spatial heterogeneity, and size. The results showed that the cellular density in a typical clone drops from the center to the periphery of the clone. This was analyzed through measuring minimum and maximum distances between all neighboring cells of the same clone and plotting such distances in 3D space as attributes of every cell (Fig. 2). In terms of compactness, we observed a natural variation within clones. Still, they were rather similar to each other in wild-type embryos (Fig. 2, A to C and F). However, we managed to challenge the clonal arrangements, compactness, and heterogeneity by treating the embryos with cyclopamine 1 day before analysis. Facial development is known to be affected by cyclopamine, and the effects have been extensively studied in the past (29). In treated embryos, the clones were smaller and often dissimilar from each other, especially when compared to the control (Fig. 2, D to E and G). We often observed spatially distinct or even connected rare clonal patches of the same color code located in close proximity to each other in E9.5 to E10 embryonic heads (see Fig. 1B,

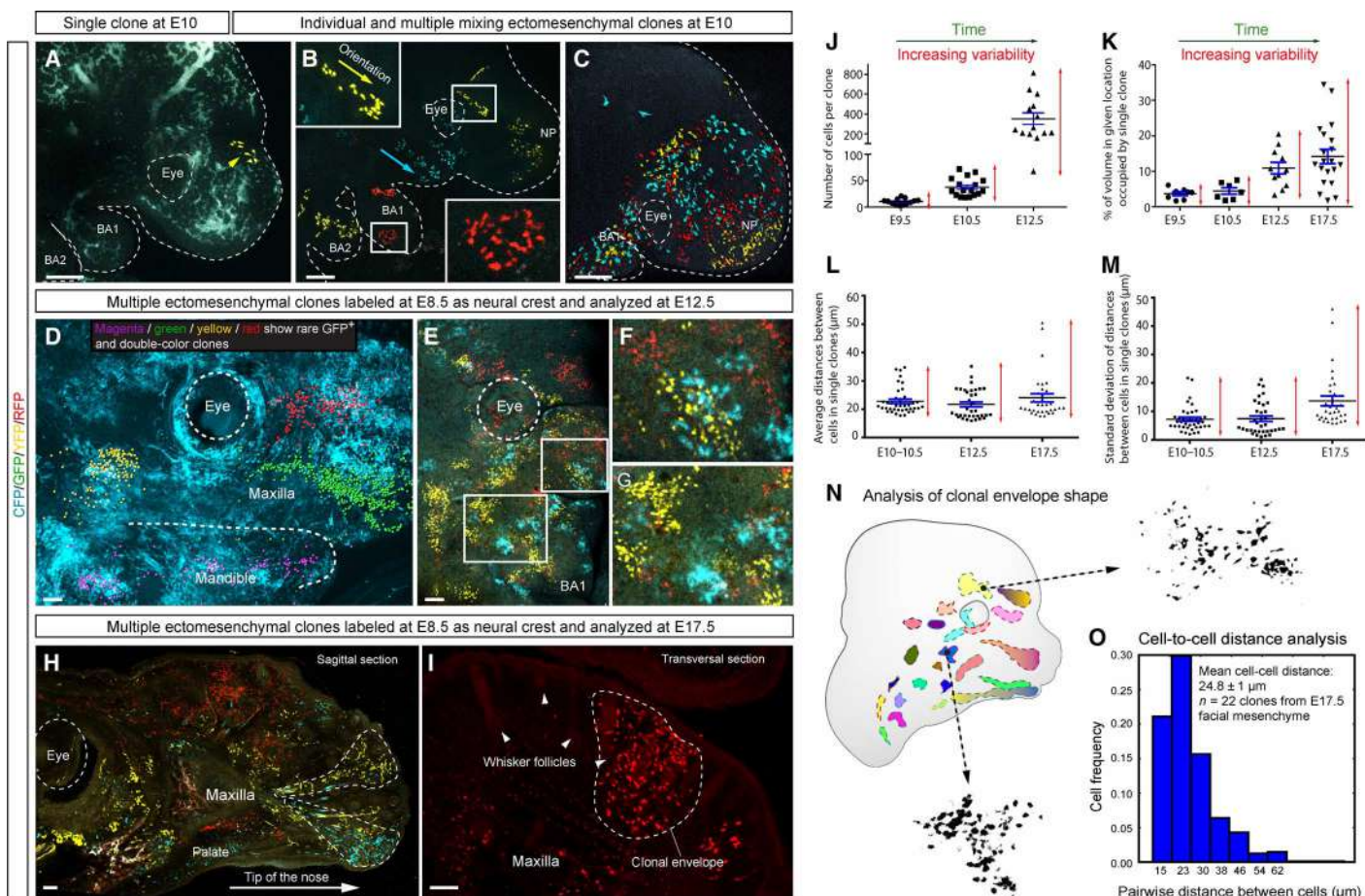


Fig. 1. Size, shape, and distribution of neural crest–derived ectomesenchymal clones. (A to C) Genetic tracing of neural crest cells and their progenies induced at E8.5 in *Sox10-CreERT2/R26Confetti* embryos and analyzed at E9.5 to E10. (A) Head of the E10 embryo with single YFP⁺ ectomesenchymal clone. Note the compact structure of the clone. (B) Multiple separated clones in different regions of embryo face. Yellow and blue arrowheads show the orientation of cellular groups. (C) Example of multiple overlapping clones in the early developing face. Note the intense local clonal mixing. (D to I) Genetic tracing of neural crest cells and their progenies induced at E8.5 in *PLP-CreERT2/R26Confetti* embryos and analyzed at E12.5. (D) Reconstruction of rare (RFP+CFP, YFP+CFP, RFP+YFP, and GFP-expressing) individual clones in the facial region of an E12.5 embryo. Note that some clones are markedly stretched in the anterior facial region. (E to G) Distribution of ectomesenchymal single-color–labeled clones in the periocular posterior maxillary region. Note the irregular geometry of clonal envelopes and their well-defined borders. (F and G) Magnified regions outlined in (E). (H) Sagittal section through the head of a genetically traced embryo starting from E8.5 and analyzed at E17.5. Area of the maxilla and frontonasal prominence with individual traced clones acquiring conical shape (dotted line) in the anterioposterior direction. (I) Transversal section through the upper jaw of the genetically traced E17.5 embryo. Note the compact shape and defined borders of the RFP⁺ clone (outlined by the dotted line). Arrowheads point at whisker follicles. (J) Graph showing the increasing size and variability of individual ectomesenchymal clones during facial development. (K) Graph showing the proportional occupied clonal volume and related variability of individual ectomesenchymal clones at different developmental stages. (L and M) Graphs visualizing developmental dynamics of clonal density (L) and its heterogeneity (M) measured as an average distance between cells of one clone (closest-neighbor approach) and SD of this parameter per clone, respectively. Bars show mean (black) and SEM (blue). (N) Examples of ectomesenchymal clonal envelopes from an E12.5 embryo with traced neural crest–derived progenies. Note the isotropic structure of clones and well-defined borders with irregular curvature. (O) Histogram showing spatial isotropy based on pairwise distances between cells sharing a common clonal origin in experimentally obtained ectomesenchymal clones at E17.5. All images are maximum-intensity projections of confocal stacks, except (C) and (D) with volume rendering of isosurfaces. BA1 and BA2, the first and the second branchial arches; NP, nasal prominence. The eye is outlined by the dashed line. Scale bars, 200 μm (A to C and E to O) and 30 μm (D).

next to the arrows). This suggests the presence of a dividing migratory neural crest cell producing progenies in a few neighboring locations within a restricted facial region.

In contrast to the arrangements in the face, migrating neural crest in the trunk did not show a similar clonal compact clustering with resolvable clonal borders (fig. S2, A to C). This suggests extensive mixing due to intense migration of individual cells.

Regardless of the significant increase in the number of cells in each clone in the growing face (Fig. 1J), the borders of the clonal envelopes remained visually defined (Fig. 1, A, I, and N), and the average distances between cells in the clone remained largely stable (Fig. 1L). However, 4 days after tamoxifen-induced genetic tracing of neural crest progenies, at E12.5 and onward, we observed an increasing variability in the size of the analyzed clones and in the proportional volume occupied by the

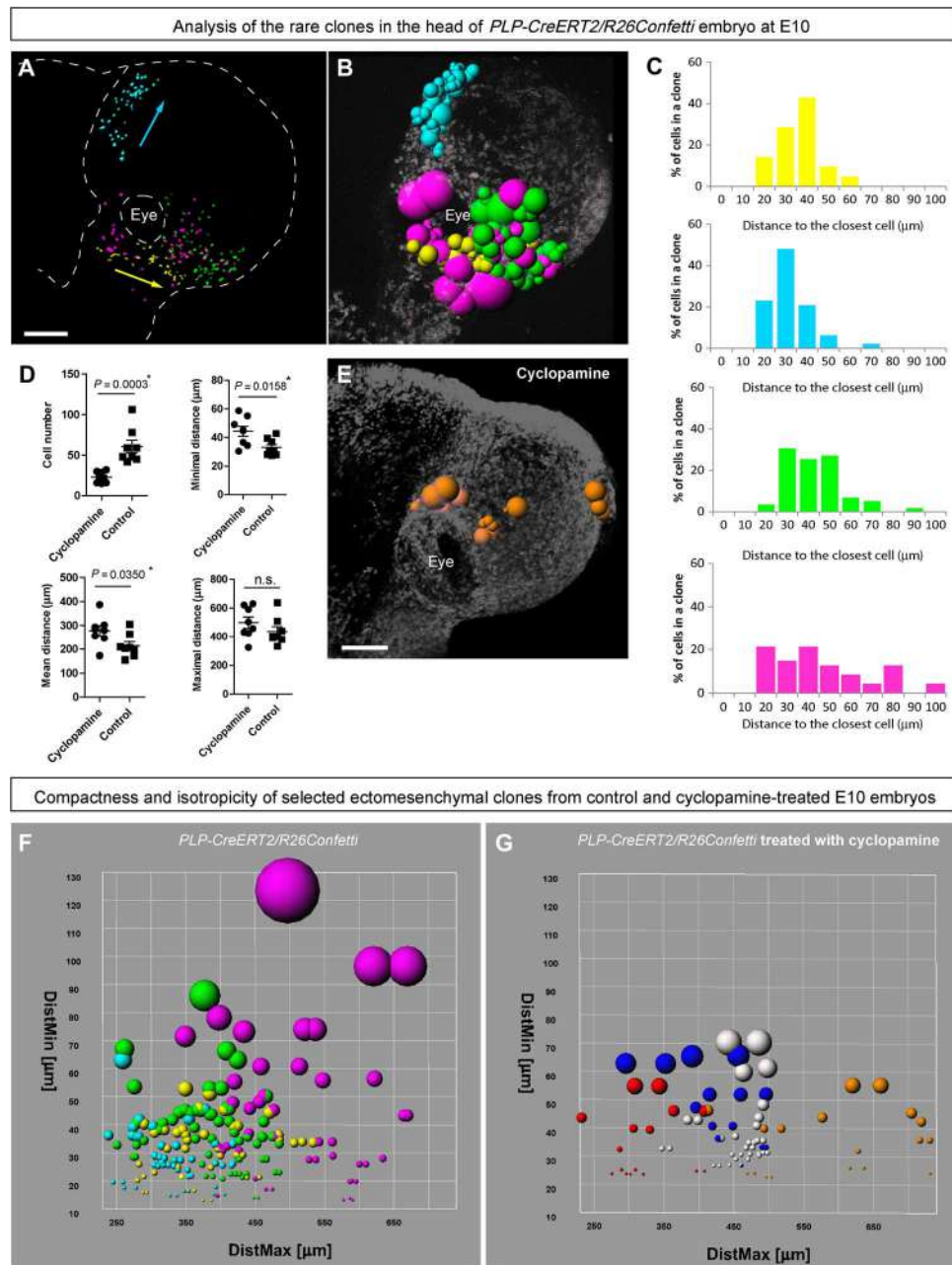


Fig. 2. Analysis of clonal structure in the faces of E10 control and cyclopamine-treated embryos. (A) Distribution of analyzed clones from *PLP-CreERT2/R26Confetti* head. Purple, yellow, and green colors mark different rare dual-color clones, whereas cyan represents the rare GFP⁺ clone. (B) Spatial structure of clones: Radiuses of colored spheres (representing single cells) correspond to minimal distances to the closest neighbors. When all cells in a clone are analyzed, this parameter reflects the compactness of the clone. (C) Histograms showing distances to the closest neighbor for every cell in the clone. (D) Graphs showing differences between wild-type and cyclopamine-treated ectomesenchymal clones in the faces of E10 embryos. Each point represents the average of the following parameters determined for each cell within a single clone: minimal distance, distance to the closest cell; mean distance, mean distance between one cell and all other cells in the clone; and maximal distance, distance to the furthest cell in the same clone. (E) Spatial structure of a clone from a cyclopamine-treated embryo. Radiuses of colored spheres (representing single cells) correspond to minimal distances to the closest neighbors. (F and G) Plots reflecting the compactness and clonal structure of analyzed clones from control (left) and cyclopamine-treated (right) E10 embryos. Colored spheres on these plots correspond to individual cells. Color defines a clone. The radius of spheres reflects the distance to the most proximal neighbor cell (DistMin) in a clone. DistMax is the maximal distance between a given cell and the most distal cell from the same clone. When the entire clone is analyzed, this parameter describes the spatial dimension of the clone. Scale bars, 200 μm (A and E). n.s., not significant.

cells of the clone within the clonal envelope (showing proportional contribution of this clone to the location) (Fig. 1, J and K). We also observed an increase in dispersion of the individual intercellular distances within a clone over time (Fig. 1M). Furthermore, the clones tended to attain a stretched asymmetric shape in regions with extensive growth in the head, which suggests a mechanism of directional clonal expansion in such locations (Fig. 1, D, H, and N). Surprisingly, the clonal progenies of labeled neural crest cells retained a compact structure even at later developmental stages, such as E17.5, as visualized on sagittal and transversal sections (Fig. 1, H, I, and O).

Clonal arrangements in the branchial arches did not differ from the nasal prominence and other facial locations in terms of defined clonal envelopes and clonal overlapping (fig. S2, D to F). Analysis of heart neural crest also showed a high degree of clonal overlapping that simultaneously occurs with clonal clustering of individual neural crest progenies (fig. S2, E and F, arrowheads).

Coexistence of neural crest–derived ectomesenchyme and mesodermal derivatives in the early face

The existence of well-defined clonal envelopes is supported by the manifestation of the border between neural crest– and mesoderm-derived mesenchymal derivatives that persists to postnatal stages. To visualize this border at postnatal stages, we used conditional knockout of Sox2 (30) in neural crest cells, using Wnt1-Cre (31).

The results of this experiment showed that only facial follicles corresponding to Sox2-deficient areas demonstrated a change in hair color shade—instead of black, it became brownish, which highlighted the border between neural crest– and mesoderm-derived dermis in young postnatal animals (fig. S3, A to Q). This border between neural crest– and mesoderm-derived mesenchyme was also observed during embryonic stages (fig. S3, R to T). Expression of dopachrome tautomerase (DCT) showed that melanocytes survived well in the targeted tissue and that the pigment-producing pathway was in place in both wild-type and Sox2-deficient melanocytes. The melanocytes did not express Sox2, as opposed to dermal papilla cells (fig. S3, B to Q). This is in line with the fact that expression of Sox2 is generally incompatible with melanocyte fate (32). Therefore, the outcome of Sox2 deficiency in skin must result from an interplay between melanocytes and dermal papilla cells. Indeed, melanocytes communicate with dermal papilla cells to adjust the amounts and the ratio of different pigments (33), which involves the Agouti pathway and explains how animals dynamically change pigmentation patterns (34). Because dermal papilla cells in the head are produced from neural crest cells and the mesoderm, and loss of Sox2 affected only the neural crest–derived dermal papillae, we were able to detect the border between numerous ectomesenchyme (NCC)– and mesoderm-derived dermal papillae in head skin. We suggest that the presence of such visual border is an interesting and important observation, especially because the dermis is organized by fibroblast-like cells that presumably are capable of long-range migration during late embryonic development and afterward.

Both neural crest and paraxial head mesoderm contribute to a range of mesenchyme-derived structures, including skeletal elements that fuse without signs of different cellular origin. This indicates that clonal behavior and morphogenetic cell dynamics in paraxial mesoderm derivatives are similar to the clonal dynamics in neural crest–derived tissues. We used *Mesp1-Cre/R26Confetti* animals in 2D and 3D imaging to trace the progeny of paraxial mesoderm in the face (35). Mesoderm-derived mesenchyme showed a high degree of clonal overlapping not only in

branchial arches but also in the dorsolateral aspects of maxillary and occipital regions (fig. S4, A to I). Additionally, local angiogenic progenitors in multiple places demonstrated an impressive diversity of clonal origins based on their color code (fig. S4, J and K). Numerous mesoderm-derived mesenchymal domains sharing the same color code appeared compact and local, similar to ectomesenchymal clones in the face (fig. S4, E to I; see arrowheads). These data point toward the possibility that similar morphogenetic mechanisms operate in neural crest– and mesoderm-derived mesenchymal tissues.

Next, we wanted to investigate the volume proportions occupied by the mesoderm and the neural crest, respectively, in different localities in the developing face. We also wanted to calculate the number of neural crest–derived clones that contribute to a given location within selected regions of interest (ROIs). For this, we made 3D analyses of the traced mesodermal (high efficiency of recombination) and neural crest (low efficiency) progenies in various facial regions, including the nasal prominence and branchial arches. The analyses showed that mesodermal derivatives occupied $21.01 \pm 3.46\%$ of ROI volume (mean and SEM; $n = 9$) in the face at E10.5 (fig. S4, L to P). Furthermore, we calculated that single neural crest–derived clones contributed to $4.465 \pm 0.8844\%$ of ROI volume (mean and SEM; $n = 7$) at the same stage (see Fig. 1K). Thus, we concluded that up to 17 neural crest clones may contribute to one ROI location.

Modeling ectomesenchymal cell dynamics in 2D and 3D confirms the minimal role of individual cell migration in clonal overlapping

As seen from above, most of the observed ectomesenchyme-derived clones in the face show complex clonal envelope shapes (Fig. 1N), with the borders representing sharp drops of cellular density at the periphery of the clone (Figs. 1O and 2C). Highly variable and complex shapes of the clonal envelopes cannot be explained without the assumption that complex morphogenetic processes operate in the tissue.

Given that the ectomesenchyme is a potentially migratory tissue, we asked whether migratory behavior contributes to the development of facial shape and, if this is the case, how the selectivity and directionality of cell migration can be achieved. On the basis of our previous results, we wanted to understand how the experimentally observed sharp borders of clonal envelopes can be maintained in the case of migratory behavior of facial neural crest–derived cells. To address this issue, we devised a mathematical model that operates virtual cells in 3D space plus time. We tested a group of variables, such as cell division speed, migration, and allocation of daughter cells in random or defined directions, as well as pushing of newborn mitotic products during proliferation. We compared the readouts from the series of *in silico* simulations to the results of our experimental clonal analyses. We looked for parameter combinations in the model that gave rise to dynamics with degrees of overlapping and clonal shapes that were compatible with those observed in the experiments. Unexpectedly, the 2D version of the model showed that proliferation-driven cell pushing/place-exchanging and related short-distance movements are sufficient to achieve efficient clonal overlapping over time (Fig. 3, A and B). In this model, we assumed (based on the biological data including live imaging experiments described below) that products of cell divisions would push neighboring cells to obtain space. Alternatively, they could intermingle with close neighboring cells by exchanging positions with them, as a way of accommodating the pushing forces in the growing tissue. Such short-ranged spatial rearrangements require some dynamics of

cell shape. This can be rendered as a very short range migratory behavior. Indeed, simulations in 3D space confirmed that clonal overlapping is compatible with zero or minimal individual migratory behavior, whereas proliferation appeared to be the main driving force for the mixing of the cell division products. Moreover, well-defined clonal envelopes were maintained only when individual migration (in relation to neighboring cells) was minimal in the simulated system. An *in silico* model, while showing defined clonal patches, also demonstrated a drop in clonal compactness from the center of the clone to the periphery in agreement with experimental data (Fig. 2, B, C, and F). Together, this strongly suggests that clonal overlap in authentic facial development may occur owing to the spatial allocations and mingling of daughter cells that result from cell divisions exclusively. In such a case, the products of mitoses will push and blend in the directions of surrounding domains, and through this, the clonal progenies will intermix.

Oriented divisions and crowd movements of ectomesenchymal cells participate in facial shaping

The modeling of fine borders of clonal envelopes remained imperfect as compared to the experimental data, unless the concept of polarizing morphogen gradients was considered. Therefore, we introduced a local radial gradient that affects the directionality of cell division and allocation of daughter cells in 3D space into the *in silico* model. The results of these simulations demonstrated that the oriented cell divisions (or controlled allocations of the progeny after mitosis) together with minimal individual migratory behavior are the keys to achieving the distribution of virtual clonal progenies that resemble the actual clonal patterns in facial development (Figs. 3, C to H, and 4). Experimental data on the stretched geometry of clonal envelopes in the most outgrowing parts of the face additionally point toward oriented cell divisions during progressive shape development (consistent with Fig. 1, D and H). At the same time, the distribution

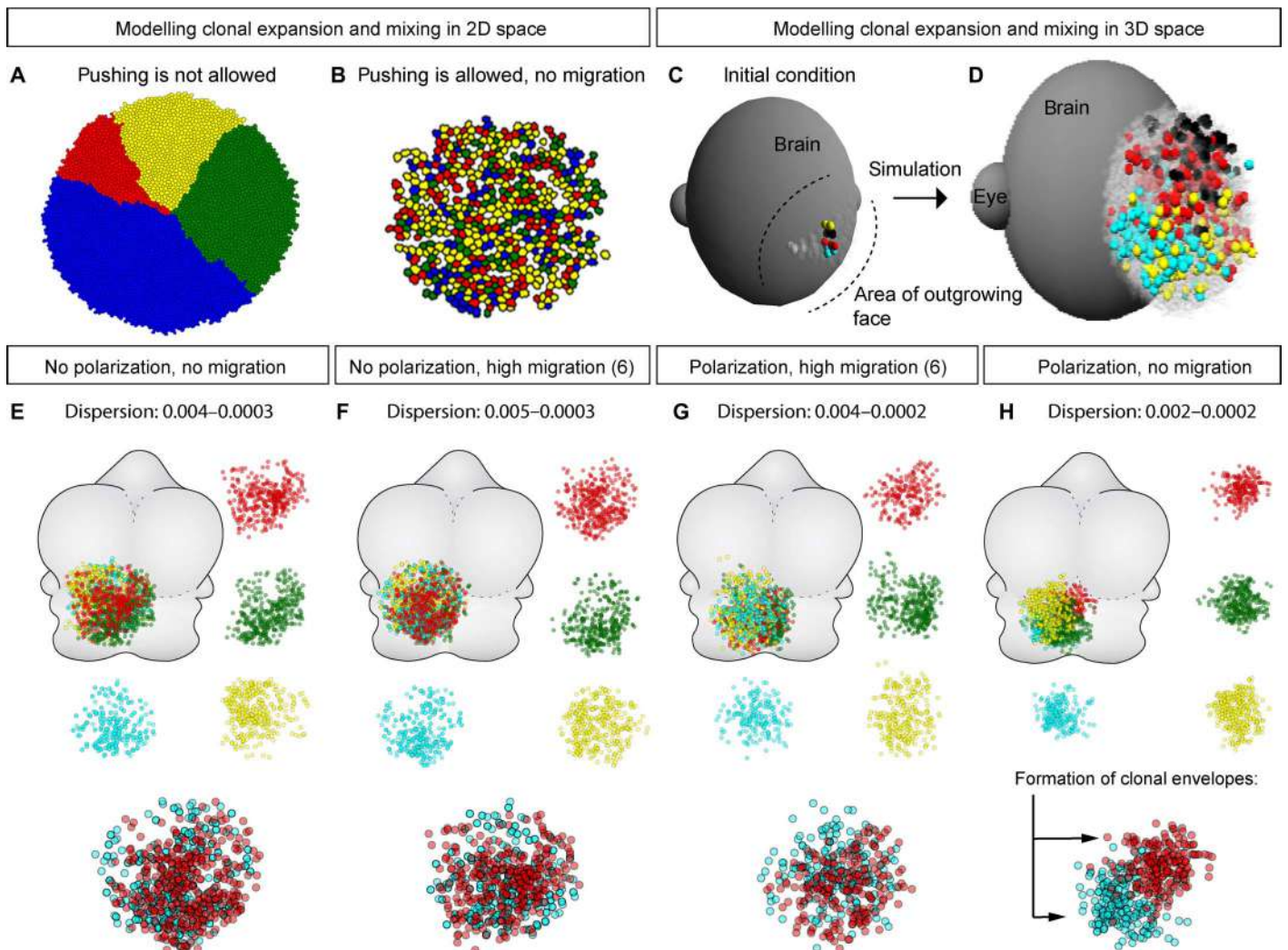


Fig. 3. Mathematical modeling of clonal expansion and overlapping in 3D space. (A and B) 2D modeling of cell dynamics; initially traced clones are labeled by different colors. Note that in the condition where cell pushing is allowed (B), clonal overlapping is efficiently achieved without any migratory behavior. (C and D) Visualization of initial conditions and example of *in silico* cell dynamics simulation in 3D space. (E to H) Results of *in silico* cell dynamics simulation in 3D space performed with different settings. Note the formation of defined clonal envelopes under the condition where polarization probabilistically directs oriented cell divisions with minimal individual cell migration (H).

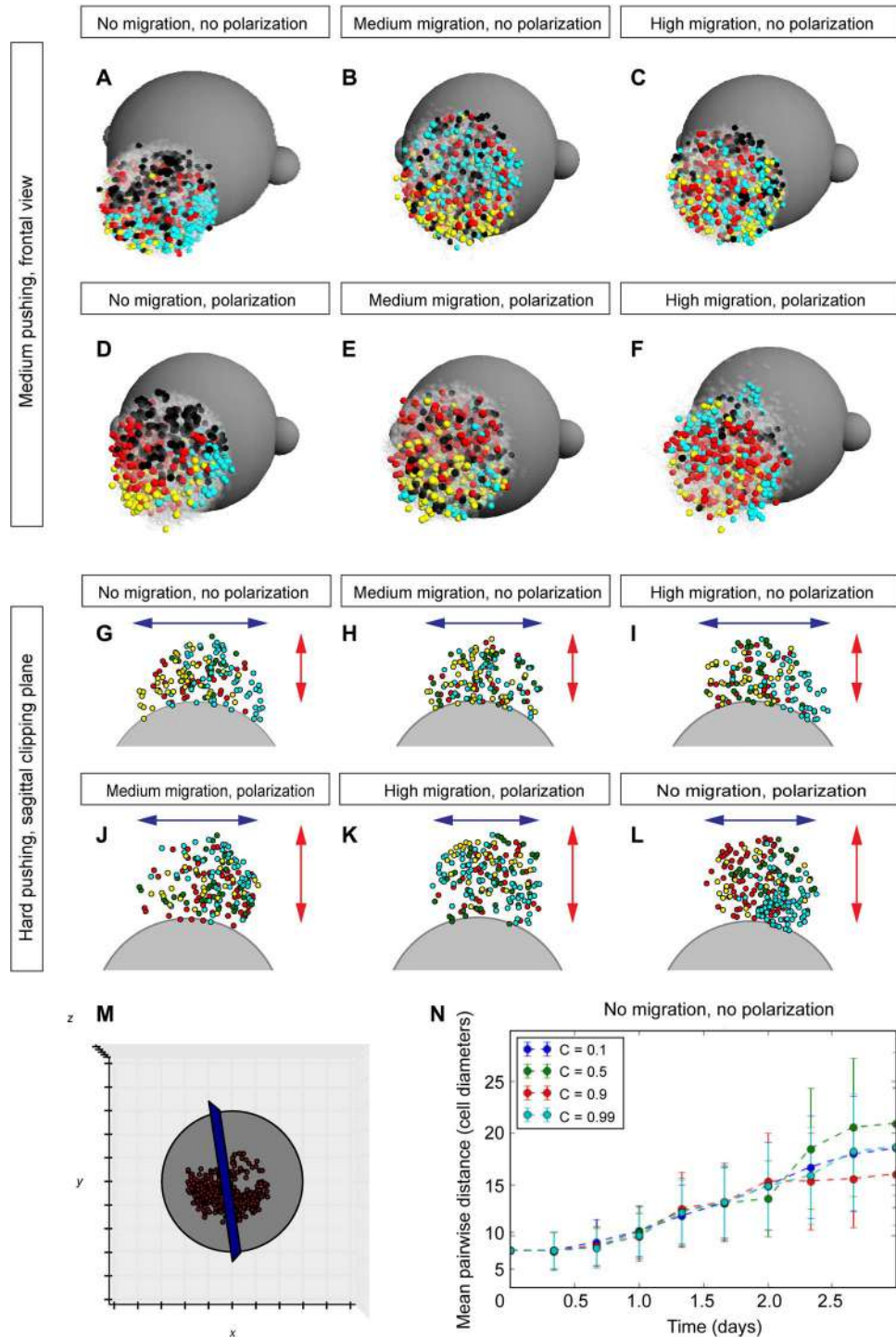


Fig. 4. Mathematical model predicts widening versus elongation strategies of in silico facial development depending on the conditions. (A to F) Simulations of cell dynamics in a 3D environment with medium pushing power (technical value in a model $c = 0.5$). **(G to L)** Clipping planes, view from the top on simulations of facial development. Note how different conditions lead to widening or elongation of the cellular cluster with clonal envelopes. The technical value for high pushing power in a model was $c = 0.9$. **(M)** Example of the clipping plane, frontal view. **(N)** Graph showing the changes in the spatial homogeneity (isotropicity) of simulated clones during rounds of simulation.

of cells within the analyzed clonal envelope appeared to be relatively uniform as defined by variation in individual cell-to-cell distances (measured as a distance to the closest neighbor) (Figs. 1O and 2C).

This was similar to the *in silico* simulations, where we found that polarization (and no migration) was characterized by the lowest dispersion of distances between the cells (Fig. 3H). *In silico* simulations demonstrated a clear difference in elongation versus widening of the modeled facial structure, depending on the presence of an anterioposterior polarizing gradient (Fig. 4, G to L).

To conclude, the mathematical model predictions pointed toward the likelihood of locally controlled allocations of daughter cells after mitosis. Such allocations can result from oriented cell divisions and controlled spindle orientation following anterioposterior polarization cues in the tissue.

In such a case, most of the allocations of newborn cells occur predominantly in one direction. This reduces the “lateral” clonal mixing because the pushing power of clonal mitotic products that invade lateral clonal domains during proliferation is eased. This should lead to reduced clonal blending and to the efficient maintenance of defined clonal envelope borders while having an impact on the resulting shape in terms of widening versus elongation (Fig. 4, especially G to L).

To directly test the predictions from the model, we analyzed *Wnt5a* knockout mouse embryos (36). *Wnt5a* is a noncanonical Wnt and a member of the PCP pathway that is involved in polarizing epithelial and mesenchymal tissues. Indeed, the knockout of *Wnt5a* leads to massive shortening and widening of the face, starting from preskeletogenic time points (Fig. 5, A to J). The lower jaw appeared much shorter and wider. At the same time, our data showed that the volume of the lower jaw was not reduced as compared to the control (Fig. 5, F and H). This indicates that there was no deficit in proliferation and in the number of cells that formed the face. This is similar to the modeling predictions shown in Fig. 4 (G to L). Moreover, this phenotype does not influence the induction of all necessary facial structures, including cartilages, bones, sensory compartments, muscles, glands, and developing teeth, as monitored by x-ray micro-computed tomography (μ -CT) scans and visualizations (Fig. 5, E to P). Additionally, we did not observe any changes in the general position of major anisotropic proliferative zones, as analyzed with ethynyl deoxyuridine (EdU) incorporation assay at E12.5 (Fig. 6, Q and R). Strikingly, when we examined the orientation of cell divisions using an antibody against phospho-histone 3 (PH3; commonly used to visualize metaphase plate) in the anterior face, we found that the predominant anterioposterior orientations of mitotic products were no longer prevalent in *Wnt5a* mutants at E12.5 (Fig. 5, S to V). This result is in full accordance with the *in silico* simulations (Figs. 3 and 4, G to L).

Live imaging in zebrafish reveals oriented crowd movements of large cellular groups

To directly observe the dynamics of early shape development in the facial region, and to connect it with individual cellular behavior, we used live imaging of genetically traced zebrafish larvae. For this, we took advantage of the *Sox10-CreERT2/Ubi:zebrabow* fish line, which is suitable for clonal color coding and inducible lineage tracing in neural crest cells. The nonrecombined cells express RFP, whereas cells after recombination can acquire stable YFP or CFP expression in the lineage. Because of imaging constraints, we followed mostly YFP⁺ neural crest-derived clones during early craniofacial development.

First, the results of this experiment demonstrated that neural crest cells labeled at clonal density give rise to spatially separate and compact groups of cells. These groups are analogous to the ectomesenchymal clones that we observed in mouse embryos (fig. S5, A to D, arrows). Second, live imaging clearly demonstrated that individual ectomesenchymal cells do not migrate significant distances but rather rearrange their shape and accommodate their position within their local microdomain (Fig. 6 and movies S1 to S4). This complies with the theoretical prediction from the mathematical model (see Fig. 4). As a result, the labeled cellular clusters change their shape over time (Fig. 6A) but do not alter their basic cellular structure. This structure includes cell density and coordinated orientation of cell divisions that may change over time (Fig. 6, B to L, and especially E).

The progenies of dividing ectomesenchymal cells remain in close proximity to each other in most of the cases (see tracks of the progeny in Fig. 6, J to L). In agreement with the inference from the mathematical model, these ectomesenchymal cells mostly divide in certain orientations within spatial microdomains, as observed in live imaging (Fig. 6, B to E). This, too, is consistent with the results obtained in the mouse model (see Fig. 5, S to V).

At the same time, ectomesenchymal cells relocate to new distant positions in the embryonic head in synchronized crowd movements (Fig. 6, J to L, and fig. S5, E to P). These movements stem from pushing activities in major proliferative centers, located in, for example, branchial arches, as evident from EdU analysis (Fig. 6, M to Q, and movie S5) and direct live observations (movies S1 to S4). Anisotropic proliferation is apparent in larval ectomesenchyme. This is reflected in results from an acute EdU incorporation experiment (Fig. 6, M and N) as well as in EdU label-retaining analysis in ectomesenchyme-derived cranial cartilage (Fig. 6, O to Q). Application of EdU for 15 min at 48 hours and analysis at 4 dpf showed an uneven, symmetrical, and specific pattern of EdU incorporation and retention in skeletal structures that form after 48 hours of development from ectomesenchymal cells. Note that the translocating groups of ectomesenchymal cells behave similarly to viscous liquid (fig. S5, E to P, and movies S1 to S4). Such morphogenetic movements may account for specific distortions and complex geometries of clonal envelopes, as shown in Fig. 1N.

To sum up, these results agree with computer simulations and are consistent with observations of clonal patterns in mouse embryos. Together, they suggest that crowd movements, anisotropic proliferation, and cell divisions with natural-like variation of the cell cycle length and phase play a significant role in facial morphogenesis, whereas long-range individual migration is limited in the face after neural crest cells transform into neuroglial and ectomesenchymal components.

Early ectomesenchymal cells are oligopotent within a given locality

The establishment of facial structures by ectomesenchymal clones raises the question whether each clone displays restricted and defined competence to generate only specific cell types. Hypothetically, overlapping clones may have committed to distinct fates and later give rise to different derivatives within a single locality. We tested this assumption using lineage tracing and fate analysis of rare double-colored and single-colored clones (Fig. 7). The results instead demonstrated that multiple fates are often generated within one compact clone. Thus, an individual clone may contribute to, for example, local mesenchyme and to dermal papillae of whisker follicles (Fig. 7, A and B). In other

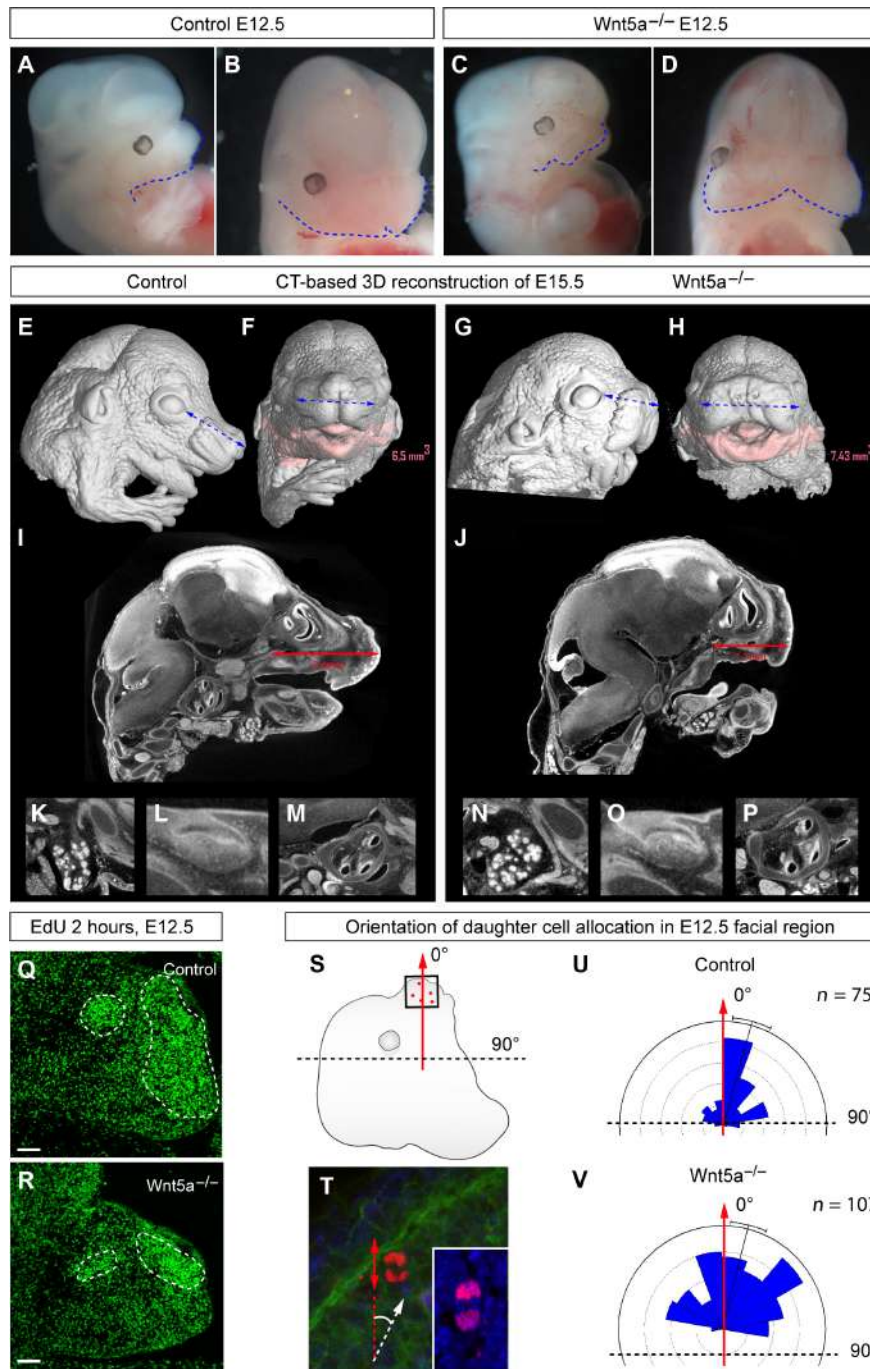


Fig. 5. Disruption of Wnt/PCP-driven cell polarization and subsequent changes in facial shape. (A to D) Representative images of E12.5 embryos: littermate controls (A and B) and *Wnt5a* full knockout embryos (C and D). (E to H) μ -CT-based 3D reconstructions of the E15.5 embryonic heads: littermate controls (E and F) and *Wnt5a* full knockout (G and H). Note the short snout and wider face of the mutant embryos as compared to the control littermates. Pink color code shows the mandible and its volume calculated for control and mutant embryos. (I to P) μ -CT-based sagittal section through the head of the control (I and K to M) and mutant (J and N to P) embryos with the measurements of the length between the posterior part of the olfactory system and the anterior tip of the snout. (K to P) Tomographic slices through the salivary gland, developing the molar and the inner ear from control (K to M) and *Wnt5a* mutant (N to P) embryos. (Q and R) Distribution of high proliferation zones in control (Q) and *Wnt5a* knockout mutant (R) E12.5 embryonic mandibles that were treated with EdU for 2 hours before analysis. Dotted lines outline stereotypic, highly proliferative zones. (S) Scheme of the ROIs where the oriented cell divisions were quantified in the head of E12.5 embryos. (T) Example of chromosome PH3-based staining on the section of an E12.5 embryonic head; the white arrow points toward the outgrowing part of nasal prominence, whereas the red arrows show the orientation of cell division and the allocation of daughter cells. (U and V) Rose diagram of quantified orientations of cell divisions in the anterior face of E12.5 control (U) and *Wnt5a* knockout mutant (V) embryos. Note the disruption of the directionality of cell divisions in the mutant embryo as compared to the control littermate. Scale bars, 200 μ m (Q and R).

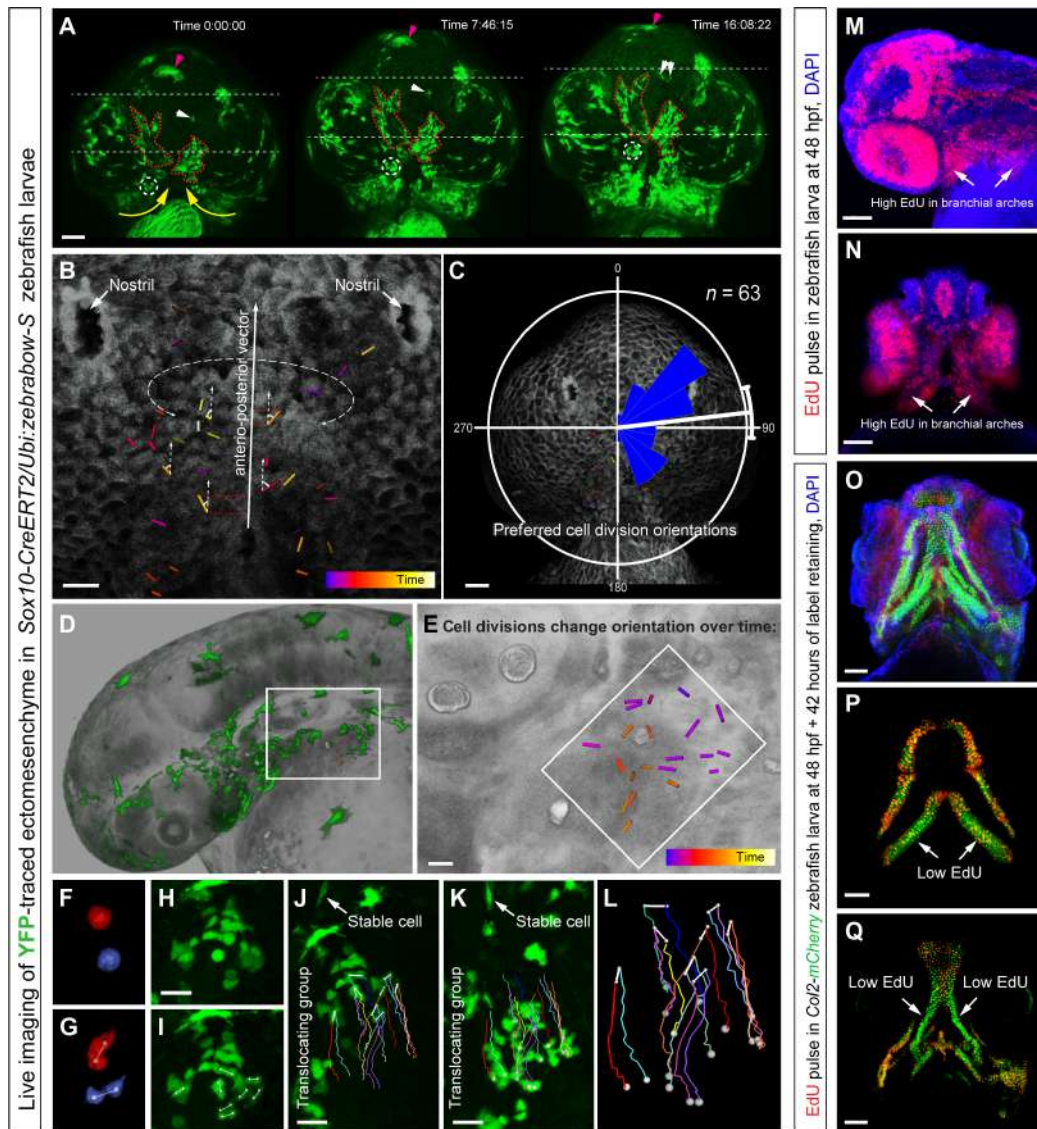


Fig. 6. Live imaging of early zebrafish craniofacial development. (A to L) Live imaging of genetically traced neural crest-derived progenies in *Sox10-CreERT2/Ubi:zebrabow-S* zebrafish larvae between 30 and 56 high-power field (hpf) (A to C) and 30 and 42 hpf (D to L). (A) Ventral view on zebrafish larva head with genetically labeled groups of YFP⁺ cells. Note the spatial stability of translocating labeled groups during organized cell movements in the regions of expanding branchial arches and around the stomodeum. The dotted circle and white arrows show small defined trackable groups of cells. Purple arrows point at the melanocyte. The red dotted line shows how the borders of YFP⁺ groups change over time. Yellow arrows demonstrate the major direction of crowd movement. (B and C) Analysis of oriented cell divisions during live imaging of developing zebrafish head, ventral view. (B) Bars show orientations of individual cell divisions and color code corresponds to the timing of cell division. (C) Rose diagram of orientations of cell divisions. (D to L) Cell divisions in the branchial arch of zebrafish at 30 to 42 hpf, side view. (E) Magnified region from (D). Note that cell divisions change the predominant orientation over time. (F to L) Analysis of the group of cells from the region outlined by the white rectangle in (D). (F and G) Frames from time lapse with two dividing cells from the branchial arch. (H and I) Frame before (H) and immediately after (I) mitosis of several ectomesenchymal cells in the region, side view on the branchial arch. (J to L) Tracking of dividing ectomesenchymal cells and their progeny in the forming branchial arch. (J) First frame of tracking. (K) Final frame of tracking (12 hours). Arrows in (J) and (K) point at the stable YFP⁺ cell that does not change the position in the embryo and serves as a stable orientation anchor for measuring translocation/crowd movement of the labeled group of ectomesenchymal cells. Note that during the displacement of the entire group, most of the cell division products stay proximally close to each other with some rare exceptions [dark brown track in (L)]. Despite this, high intensity of local cellular mixing is achieved owing to proliferation in accordance with modeling results presented in Fig. 2 (A to C). (M and N) EdU incorporation shows proliferation rates in different parts of the developing zebrafish head. Note that a 5-min EdU pulse at 48 hpf immediately followed by the analysis showed high proliferation rates in branchial arches (arrows). (O to Q) Transgenic *Col2a1BAC:mCherry* zebrafish larva's entire head (O) and skeletal elements (P and Q) at 4 days postfertilization (dpf) with incorporated EdU, administered at 48 hpf for 5 min. Note that this EdU label-retaining experiment highlights uneven proliferation in ectomesenchymal chondrogenic progenitors at 48 hpf (5-min pulse). Arrows point at low EdU-retaining regions in the facial cartilages. Scale bars, 50 μ m (A, C, M to O, and Q) and 20 μ m (B, E, and H to K).

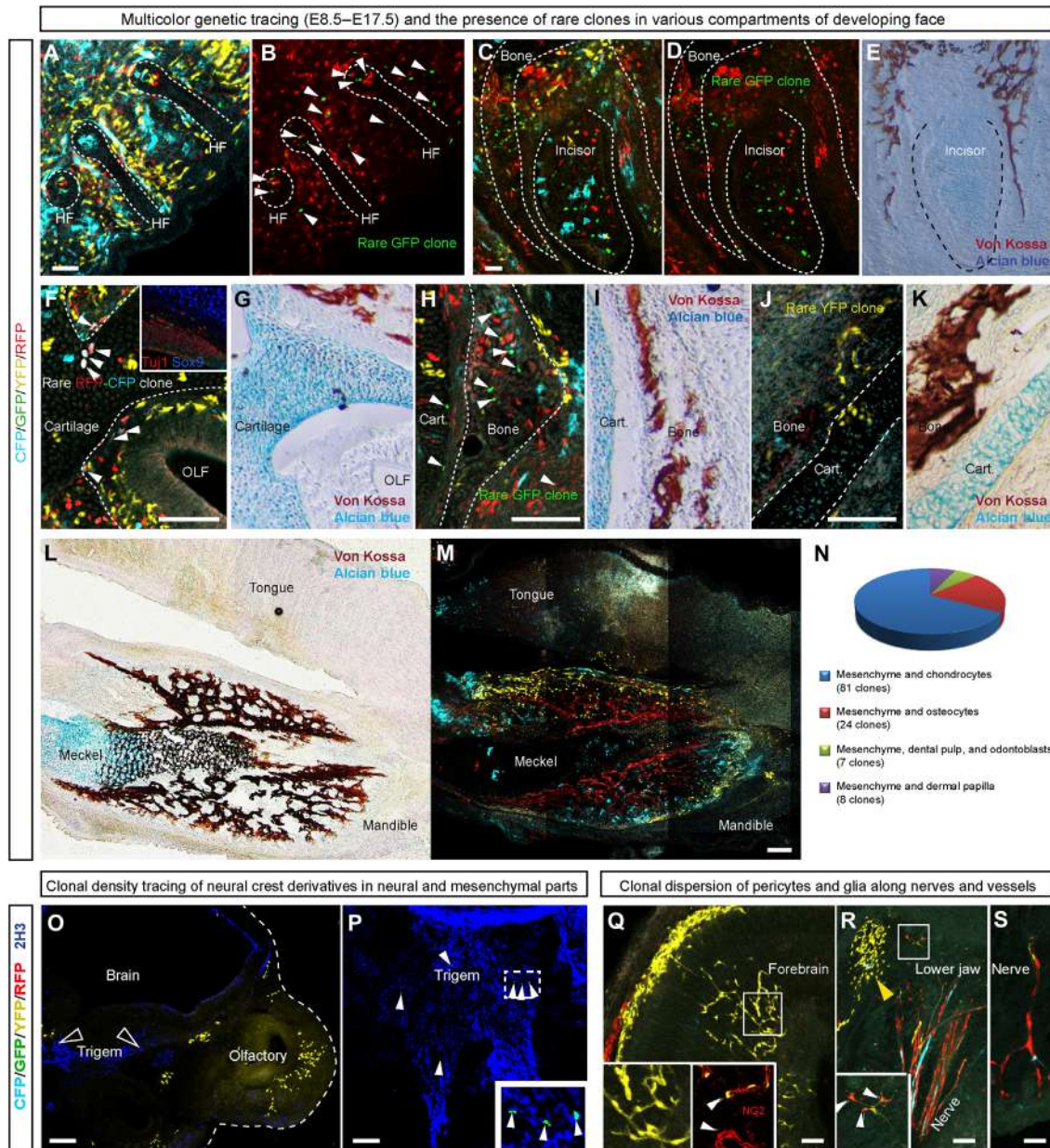


Fig. 7. Cell fate potential of individual neural crest-derived ectomesenchymal clones. (A to I) Genetic tracing of neural crest-derived progeny in *PLP-CreERT2/R26Confetti* embryos. Tamoxifen was injected at E8.5, and the analysis of cell types was performed at E17.5. (A and B) Close-up of the region in the anterior face with outlined whisker follicles. Note that cells of the GFP⁺ rare clone (arrowheads) contribute to both the surrounding mesenchyme and dermal papillae. (C to E) A developing incisor is shown with the dotted line. Note the contribution of the rare GFP⁺ clone to the peridental mesenchyme, osteoblasts, and the dental mesenchymal compartment. (F and G) Cells of the rare CFP⁺/RFP⁺ clone, pointed out by arrowheads, give rise to perichondrial flat cells lining the cartilage, chondrocytes in the olfactory cartilage, and mesenchyme surrounding the olfactory neuroepithelium. (H and I) Arrowheads show cells of the rare GFP⁺ clone that contribute to cartilage (chondrocytes), trabecular bone (osteocytes), and the surrounding mesenchyme. (J and K) Rare YFP⁺ clone contributes to the mesenchyme and chondrocytes of the nasal capsule. (L and M) Localized YFP⁺ and CFP⁺ clones occupy only a part of a lower jaw and contribute to mandibular bone, Meckel's cartilage (in the case of the CFP⁺ clone), and the surrounding loose mesenchyme. (E, G, I, K, and L) Von Kossa staining highlights trabeculae of the facial bones, whereas Alcian blue staining shows cartilage. (N) Diagram representing the occurrence of different cell fate combinations observed within individual clones. (O) Clonal density genetic tracing induced at E8.5 and analyzed at E12.5 in *Sox10-CreERT2/R26Confetti* embryos. Note the absence of genetically traced cells in the neuroglial compartment despite numerous ectomesenchymal clones present in the location. (P) Example of a GFP⁺ rare clone (arrowheads) in the neuroglial compartment that does not include ectomesenchymal derivatives. (Q) Part of the network of pericytes in the forebrain is organized by the single yellow clone. NG2 is a pericyte marker, shown in the inset. (R and S) Several traced neural crest-derived glial clones, including a rare YFP⁺/RFP⁺ double-colored clone (magnified in the inset), follow the nerve fibers in the lower jaw. For comparison, note the compact ectomesenchymal YFP⁺ clone in the upper left corner of the image. Scale bars, 200 μ m. HF, hair follicle.

situations, single clones contributed to the dental mesenchymal compartment and the surrounding osteogenic tissue (Fig. 7, C to E). We often observed that perichondrial cells, chondrocytes, and neighboring mesenchymal patches shared the same clonal origin (Fig. 7, F to K). Osteogenic cells of membranous bones and neighboring mesenchyme also showed clonal relationships (Fig. 7, L and M).

None of the analyzed unique ectomesenchymal clones showed any progeny in the neuroglial compartment (Fig. 7O). Consistently, several rare analyzed clones in the neuroglial compartment did not appear to share the same color code with cells in the ectomesenchymal domain (Fig. 7P).

Embryonic ectomesenchyme-derived pericytes (marked by NG2) were found to spread clonally by dividing along the vessels. This is similar to how glial cells clonally spread along nerve fibers (Fig. 7, Q to S). To conclude, labeled neural crest cells give rise to oligopotent clonal local patches of ectomesenchyme that generate different fates that are necessary in a specific location.

DISCUSSION

The facial region is largely composed of neural crest-derived progenies. The purpose of the present study was to investigate how those progenies dynamically build the face. Previously, an elegant clonal analysis has been performed in the trunk neural crest derivatives that include neurons, glial cells, and melanocytes. Many important questions related to both trunk crest multipotency and techniques concerning Confetti multicolor tracing were resolved in that study (14). However, trunk neural crest and cranial neural crest are different in their ability to give rise to mesenchymal structures. Consequently, knowledge of the clonal structure and cell behavior in relation to early morphogenesis of the face has remained obscure.

We addressed this question with clonal analysis using a multicolor Confetti reporter and found that neural crest cells give rise to well-defined clonal patches (clonal envelopes) of ectomesenchymal tissue in the prospective facial compartment. They demonstrate conspicuous borders and consist of clonal progeny formed from a single labeled neural crest cell. Once formed, these clonal patches persist until at least late embryonic development and most likely postnatally: They occupy certain locations in the face and retain recognizable borders. The patches do not dissolve with developmental time despite some growing heterogeneity inside the clone in terms of intercellular distances. The cells within the clonal envelope are loosely packed and mix locally with the progenies of other neural crest cells. Developmental robustness of the facial compartment might be rooted in a high degree of clonal overlapping in any given locality that is populated by the progenies of at least several individual neural crest cells. Hypothetically, negative somatic mutations occurring in a single migrating neural crest cell or at the level of the neural tube can be compensated by other unaffected neural crest-derived local clonal progenies. Moreover, the intense clonal overlapping among neural crest progenies argues against any somatotopic mapping (37) at the level of the neural tube. The increasing variability in geometrical shape and size of the clones might reflect directional cell behavior unique for a given locality, with different proliferation rates in various compartments of the outgrowing face.

We took advantage of mathematical modeling to sort out these potential mechanisms of clonal behavior. The 3D *in silico* simulations of cell dynamics showed that highly efficient clonal overlapping can be

achieved without migration of individual cells, solely due to the pushing and mingling force of cells as a result of multiple cell divisions in the area. Moreover, the model predicted the existence of a chemical gradient that controls the orientation of cell divisions, to achieve defined clonal envelopes. We set out to test the suggestions from the model regarding both the minor migratory behavior and the directional cell dynamics related to cell divisions with subsequent allocations of daughter cells. Live imaging experiments in zebrafish confirmed our computer model predictions that ectomesenchymal cells do not perform extensive individual migrations and predominantly divide in few orientation planes within a local microdomain. Moreover, similar to the situation in the developing limb (17), we discovered that ectomesenchymal cells execute large-scale, collective, coordinated morphogenetic movements, where the cellular arrangements of microdomains remain well preserved. Such crowd movements, reminiscent of the behavior of viscous fluid, have been previously described (17, 38). The viscous fluid approach was previously used for analyses of biological systems on cellular and organismal levels (39). According to our results, the ectomesenchymal cells in the zebrafish lower jaw translocate or perform crowd movement in relation to the eyes and the brain. This takes place while the stomodeum is displaced anteriorly, presumably as a result of lower jaw mesenchyme outgrowth. The massive relocation of ectomesenchymal cells occurs because of proliferation in the lateral regions of the branchial arches and does not involve independent migration of each cell. This is supported by the fact that differentiating chondrocytes are still moving forward together with the surrounding tissue during lower jaw extension (see movie S3). Thus, it seems that individual ectomesenchymal clones mix and overlap as cells are added because of cell divisions. This causes subsequent mingling with the neighbors without obvious middle- or long-range individual cell migration. However, translocations of large groups of cells (that is, crowd movements) might be responsible for the changes in clonal envelope 3D geometry during critical morphogenetic rearrangements.

The individual shape of clonal envelopes reflects the anisotropic growth of the structure (40, 41) following local orientation cues. Our results show that the cues that orient the plane of cell divisions in the face, at least in part, are represented by the gradient of Wnt5a, which influences the allocation of daughter cells after mitosis and, through this, the general shape. The idea of a Wnt5a gradient is strongly supported by the similarity of the phenotypes resulting from full Wnt5a knockout and overexpression of Wnt5a (21–23). In both cases, the gradient is erased from the tissue, which is phenotypically manifested by the shortening and widening of the face and limbs. Thus, the molecular mechanisms controlling the emission, detection, and interpretation of polarity signals (including noncanonical Wnts) can be partly responsible for the early body plans as well as for the developmental origins of facial diversity (42), especially during early preskeletogenic stages. Despite the strong phenotype in Wnt5a and in other PCP mutants, many parameters related to the shape and placement of different structures are not seriously affected. Therefore, there must be other mechanisms unrelated to directional cell divisions that control the facial shape. Anisotropic proliferation rates in different facial compartments and resulting crowd movements/translocations of cells can provide an alternative way of governing the shape.

Progressively, ectomesenchymal cells that belong to the same clone adopt different fates following odontogenic, chondrogenic, osteogenic, adipogenic, and other directions of differentiation within a spatial

microdomain. Therefore, single neural crest–derived ectomesenchymal early progenitors are oligopotent in the face. Our data do not support the fact that different pools of neural crest cells contribute to prespecified ectomesenchymal populations restricted in their fate potential within the mesenchymal spectrum of fates. However, the results may partly support previously described early fate restrictions in the cranial neural crest and the existence of an early choice between neuroglial and mesenchymal directions of differentiation (15). This renders cranial neural crest cells different in early fate restrictions as compared to cells of the trunk neural crest (14).

Various early embryonic mesenchymal populations, similar to neural crest–derived ectomesenchyme, give rise to multiple differentiated cell types that organize muscle, connective, and skeletal tissues in the head and other compartments, including limbs. Our results show that cellular mechanisms of early facial shaping seem to be very similar to those operating in the limb. Furthermore, recent discoveries of epithelial-to-mesenchymal transition (EMT), a classical property of neural crest (43), in limb bud initiation (16) suggest that similarities between limb and face development are stronger than previously thought. Moreover, a recent study demonstrated that cranial neural crest cells that give rise to mesenchymal derivatives in the head may undergo EMT from a neural fold domain that might not express neural markers (15). If true, it can be defined as a non-neural ectoderm and is possibly similar to analogous sites in regions of future limb buds. For instance, it is widely accepted that facial growth and patterning are regulated by the frontonasal ectodermal zone (FEZ), which includes SHH and FGF8 expression domains (44, 45). The roles of BMPs, endothelins, and other soluble factors in facial development and outgrowth have been thoroughly investigated (44, 46). Variation of signals that affect cartilage and bone development may also influence shaping programs at later stages. This is suggested, for example, by studies on BMP3 mutations associated with the size and varying geometry of the vertebrate skull (47). Apparently, these key signals, including SHH, FGFs, and BMPs, play critical instructive roles in both facial and limb development. It could be speculated that the apical ectodermal ridge secreting FGF8 and the zone of polarizing activity emitting SHH in limb buds might be considered to be deeply homologous to the FEZ in the face. Thus, a blueprint of the cellular and molecular logics that operate in the mesenchyme of the anterior head could become a starting point for the induction of appendages in the more posterior parts of the ancestral body. Some evidence suggest that the origin of paired appendages involved redeployment of genetic programs from the paraxial to the lateral mesoderm (48, 49). Our data highlight a great degree of similarity in clonal dynamics between neural crest– and paraxial mesoderm–derived mesenchyme in the face and branchial arches. Together, our results support a profound similarity between vertebrate face and limb development and, in turn, raise questions concerning a deep homology (50) between these seemingly unrelated structures.

MATERIALS AND METHODS

Experimental design

This study heavily relied on clonal density genetic tracing and on the investigation of clonal envelopes in facial ectomesenchyme both as a series of static pictures and as a dynamic live imaging of mouse and zebrafish embryos, respectively. In silico modeling of clonal envelopes in developing ectomesenchyme helped to visualize and define princi-

ples of clonal overlapping in 3D envelope border formation and other important aspects leading to the prediction of a gradient that orients cell divisions. Investigation of a Wnt5a mouse mutant with deficient polarizing signals confirmed the importance of oriented cell dynamics in facial development.

Mouse strains and animal information

All animal work was approved and permitted by the Ethical Committee on Animal Experiments (Norra Djurförsöksetiska Nämnd; www.djurforsok.info/lagar-regler/) and conducted according to the Swedish Animal Agency's Provisions and Guidelines for Animal Experimentation, and international guidelines and regulations were followed (Institutional Review Board/Institutional Animal Care and Use Committee). Glia-specific genetic tracing mouse strains *PLP-CreERT2* and *Sox10-CreERT2* were previously described (25, 26). Both *PLP-creERT2* and *Sox10-creERT2* strains were coupled to *R26Confetti* mice that were received from the laboratory of H. Clevers (24). To induce genetic recombination of adequate efficiency, pregnant females were injected intraperitoneally with tamoxifen (Sigma, T5648) dissolved in corn oil (Sigma, C8267). Tamoxifen concentration ranged from 1 to 5 mg per animal to obtain a range of recombination efficiency. Wnt5a full knockout embryos were obtained from *Wnt5a^{+/-}* mice (36) at the expected Mendelian proportions. Mesodermal tracing was obtained using *Mesp1-Cre* mouse strain (35) coupled to *R26Confetti* reporter strain. *Sox2^{fl/fl}* mice have been previously described (30) and were coupled to *Wnt1-Cre* (31) that were ordered from the Jackson Laboratory (stock number 003829). For embryo analyses, heterozygous mice of the relevant genotype were mated overnight, and by noon, the plug was considered to be E0.5. Mice were sacrificed by isoflurane (Baxter, KDG9623) overdose, and embryos were dissected and collected into ice-cold phosphate-buffered saline. Subsequently, the samples were placed on freshly prepared 4% paraformaldehyde and, depending on the developmental stage, were fixed for 3 to 6 hours at 4°C on a roller. Afterward, the embryos were cleared in Scale-A2 reagent [4 M urea, 0.1% (w/v) Triton X-100, 10% (w/w) glycerol, distilled water] for 6 hours and imaged in whole-mount mode or, alternatively, the embryos, after fixation, were cryopreserved in 30% sucrose (VWR, C27480) overnight at 4°C, embedded in optimal cutting temperature medium (Histolab, 45830), and cut into 14- to 150- μ m sections on a cryostat (Microm), depending on the subsequent application.

For cyclopamine treatments, three time-mated *PLP-CreERT2/R26Confetti* females were injected with cyclopamine (LC Laboratories) solution that was administered in corn oil via double intraperitoneal injections (30 mg/kg in each injection; days 8 and 9 of gestation). On gestation day 10, we took out and analyzed more than 16 individual embryos.

μ -CT analysis

We used a GE Phoenix v|tome|x L 240 equipped with a 180-kV/15-W maximum-power nanofocus x-ray tube and a high-contrast flat panel detector DXR 250 with 2048 \times 2048 pixels and a 200 \times 200 μ m pixel size. The exposure time was 900 ms for every 2000 positions. The μ -CT scan was carried out at an acceleration voltage of 60 kV and at an x-ray tube current of 200 μ A. The voxel size of the obtained volumes was in the range of 4 to 6 μ m, depending on the size of the embryo head. The tomographic reconstruction was realized using GE Phoenix datos|x 2.0 3D computed tomography software. The 3D and 2D cross section visualizations were performed with VGStudio

MAX 2.2 software. The histogram of the images was adjusted to reach a better contrast of soft tissues.

Fish in vivo experiments

For genetic tracing in the zebrafish model, we used heterozygous hybrids obtained from crossings between *Sox10:ERT²* (51) and *ubi:ZebraBow-S* (52) transgenic fish strains. The recombination was induced by application of 1 μ M 4-hydroxytamoxifen (Sigma-Aldrich) into E3 medium at 16 hpf, and embryos were incubated for 12 hours at 28.5°C. All other manipulations with embryos were performed according to the standard methods described by Westerfield (53). Live imaging was performed using a Zeiss LSM 780 (Carl Zeiss) confocal microscope through existing protocols with minor modifications (54). For further image processing and calculations, we used ZEN 2012 (Carl Zeiss) and Imaris software (Bitplane). For EdU analysis in developing zebrafish, we applied EdU to E3 medium at a concentration of 1.5 mg/ml for 5 min. We used *Col2a1aBAC:mCherry* transgenic fishes to visualize a cartilage in EdU-stained individuals.

Computational model

Individual cells were represented by their location on an underlying unstructured lattice, such as those typically used in finite element computations. The lattice resolution was chosen such that the average cell size is close to the desired biological cell size. Cell division and migration events were executed by inserting a new cell at a lattice site adjacent to the mother cell (division) or by swapping location with an adjacent cell (migration). Unlike many similar implementations of multicellular on-lattice models, we accounted for cell pushing; that is, if a dividing cell attempts to place its progeny at an occupied site, there is a probability that the occupying cell gets pushed to make room for the daughter cell. This means that cells can continue to divide even if all neighboring sites become occupied, rather than becoming quiescent. Because we are interested in capturing naturally occurring variations in the process, our model is stochastic. Stochasticity enters by letting the cell division time and the migration time become normally distributed random variables where the mean and variances are parameters that can be tuned to vary the degree of noise in those processes. The division direction and the migration direction are, in the absence of a polarizing field, uniformly distributed random variables. The degree of randomness in the cell division directions can be modulated by introducing a polarizing field and by tuning via a parameter how strongly the cells respond to this field, allowing us to vary the cell division direction from being completely random to becoming highly directionalized. The model is simulated as an event-driven system by a kinetic Monte Carlo algorithm, where the event with the shortened sampled waiting time is executed in each iteration. Detailed information about the mathematical model is provided in the Supplemental Materials.

Microscopy

Frozen samples were sectioned at 14 to 50 μ m, and the sections were stored at -20°C after drying for 1 hour at room temperature. Confocal microscopy was performed with Zeiss LSM 710 CLSM and Zeiss LSM 780 CLSM instruments. The settings for the imaging of Confetti fluorescent proteins were as previously described (24). The imaging of the confocal stacks was performed using a Zeiss LSM 780 CLSM, Plan-Apochromat 10 \times /0.45 M27 Zeiss air objective, with 23 to 79 optical slices of 12 μ m each with a z-axis shift of 9 μ m for every step. Before whole-mount imaging, the embryos (from E9.5 to E12.5) were cleared

in Scale-A2 reagent for 6 hours. For basic image processing and analysis, we used ZEN 2012 software.

Immunohistochemistry, tissue stains, and EdU analysis

The following primary antibodies were used: goat anti-GFP (fluorescein isothiocyanate) (Abcam; 1:500), goat anti-Sox10 (Santa Cruz Biotechnology; 1:500), anti-neurofilament 2H3 (generated by Developmental Studies Hybridoma Bank; 1:100), Tuj1 (Promega, G712A; 1:1000), NG2 (Millipore, AB5320; 1:200), anti-PH3 (Millipore, clone MC463; 1:1000), 4',6-diamidino-2-phenylindole (DAPI; with Vectashield mounting medium for fluorescence; H-1200, Vector Laboratories Inc.), DCT (gift from V. Hearing; 1:1000), and rabbit anti-Sox2 (Abcam, AB97959; 1:1000). For the detection of the abovementioned primary antibodies, we used secondary antibodies produced in donkey conjugated with Alexa Fluor 405, 488, 555, or 647 (Invitrogen; 1:1000). Slices were mounted with 87% glycerol mounting medium (Merck). EdU (Life Technologies) was injected 2 hours before the embryos were harvested at a concentration of 65 μ g/g. Cells with incorporated EdU were visualized using a Click-iT EdU Alexa Fluor 647 Imaging Kit (Life Technologies). For von Kossa staining of the bone, we submerged the cryosections into silver solution (50 g/liter of silver nitrate in distilled water). Then, we exposed sections to white light from the laboratory lamp for 20 to 50 min. Next, silver nitrate was extensively removed with distilled water during three 7-min washes. After the washes, we placed cryosections into thiosulfate solution (50 g/liter in distilled water) for 5 min. Finally, we performed three sequential 5-min washes in distilled water and mounted microscopic slides with glycerol for imaging. For Alcian blue staining of the cartilage, we used Alcian blue solution (pH 2.5; 1 g of Alcian blue 8GX in 100 ml of 3% glacial acetic acid). Cryoslides were hydrated in distilled water and then kept in 3% acetic acid for 3 min. Then, the slides were transferred to Alcian blue solution and microwaved for 30 s. Afterward, depending on the strength of the signal, the slides were left with Alcian blue solution or were immediately washed in water twice for 5 min and mounted with glycerol.

Image analysis and statistics

All statistical data in the figures are represented as means \pm SEM. Every dot on the graphs in Fig. 1 corresponds to one analyzed clone. The unpaired version of Student's *t* test was used to calculate the statistics (*P* value). All results were replicated in at least three different animals. We used Bitplane Imaris software for volume rendering and digital quantifications of occupied clonal volumes, measuring intercellular distances, automated cell counting, and producing maximum intensity projection images. For example, in Fig. 1 and fig. S1, rare double-colored clones in E9.5 and E10.5 and rare green clones in E17.5 were identified, segmented, and visualized in Imaris. For every clone on the graphs in Fig. 1 (M and N), we calculated 6 to 22 intercellular distances depending on the clonal size in a particular location from several embryos. For analysis of the percentage of occupied clonal volume in Fig. 1L and fig. S4P, we used a 150 \times 150 \times 200 μ m ROI volume (except for the locations where mesenchymal cells represented a narrow layer between the developing brain and the ectoderm; in such cases, one dimension of the ROI volume was reduced accordingly), where we segmented the clonal surfaces using Imaris, calculated total volume encapsulated in cells of the clone, and then subtracted such volume from the total volume of the ROI for every analyzed clone or in different anatomical positions for all color-coded mesodermal derivatives. In Fig. 2, the distances between cells

in single clones were measured using Spots to Spots Closest Distance Xtension in Imaris.

For the analysis of oriented cell divisions in *Wnt5a* mutants with corresponding controls, we performed immunohistochemistry with PH3 antibody on frozen sagittal sections of embryonic heads. Angle of the cell division was calculated as an angle between the cell division axis and the vector drawn through the basisphenoid toward developing nostrils. At least three individual *Wnt5a* mutant embryos were assessed together with higher numbers of littermate wild-type controls. In zebrafish live imaging experiments, dividing cells were tracked manually through the time series. Coordinates of each cell center after cell division were determined. Angle of the cell division in 3D was calculated as an angle between the cell division axis and the vector drawn through the fish body midline from the mouth to the midpoint between nostrils. We performed the actual calculations using vector coordinates derived from 3D space in Imaris. We counted orientations of cell divisions in three fishes between 30 and 52 hpf.

SUPPLEMENTARY MATERIALS

Supplementary material for this article is available at <http://advances.sciencemag.org/cgi/content/full/2/8/e1600060/DC1>

fig. S1. Identification of rare double-color and GFP⁺ clones in neural crest ectomesenchyme in E9.5 to E10.5 embryonic faces.

fig. S2. Clonal mixing and distribution of NCC-derived clones in the embryonic trunk and head through the development.

fig. S3. Defined borders between mesoderm- and neural crest-derived progenies at postnatal and embryonic stages.

fig. S4. Genetic tracing of mesoderm-derived mesenchymal progenies reveals similarities with the neural crest-derived ectomesenchyme.

fig. S5. Live imaging of ectomesenchymal clones and progenitors in the eye shows difference between organized crowd movements and individual migrations.

movie S1. Live imaging of genetically traced neural crest-derived progenies in *Sox10-CreERT2/Ubi:zebraflow-S* zebrafish larvae between 30 and 56 hpf, ventral view.

movie S2. Live imaging of translocating ectomesenchymal clusters in *Sox10-CreERT2/Ubi:zebraflow-S* zebrafish larvae between 39 and 52 hpf, ventral view.

movie S3. Live imaging of genetically traced neural crest-derived progenies in *Sox10-CreERT2/Ubi:zebraflow-S* zebrafish larvae between 30 and 88hpf, ventral view.

movie S4. Live imaging of translocating ectomesenchymal clusters in *Sox10-CreERT2/Ubi:zebraflow-S* zebrafish larvae between 39 and 52 hpf, ventral view.

movie S5. 3D EdU analysis of *Col2a1aBAC:mCherry* zebrafish larva's entire head at 4 dpf corresponding to Fig. 5 (O to Q).

Supplementary Materials and Methods

REFERENCES AND NOTES

1. E. P. Buchanan, A. S. Xue, L. H. Hollier Jr., Craniofacial syndromes. *Plast. Reconstr. Surg.* **134**, 128e–153e (2014).
2. P. A. Trainor, P. P. Tam, Cranial paraxial mesoderm and neural crest cells of the mouse embryo: Co-distribution in the craniofacial mesenchyme but distinct segregation in branchial arches. *Development* **121**, 2569–2582 (1995).
3. V. Franklin, P. L. Khoo, H. Bildsoe, N. Wong, S. Lewis, P. P. L. Tam, Regionalisation of the endoderm progenitors and morphogenesis of the gut portals of the mouse embryo. *Mech. Dev.* **125**, 587–600 (2008).
4. J. Pispal, I. Thesleff, Mechanisms of ectodermal organogenesis. *Dev. Biol.* **262**, 195–205 (2003).
5. R. C. Mootoosamy, S. Dietrich, Distinct regulatory cascades for head and trunk myogenesis. *Development* **129**, 573–583 (2002).
6. G. Couly, P. Coltey, A. Eichmann, N. M. Le Douarin, The angiogenic potentials of the cephalic mesoderm and the origin of brain and head blood vessels. *Mech. Dev.* **53**, 97–112 (1995).
7. A. Achilleos, P. A. Trainor, Neural crest stem cells: Discovery, properties and potential for therapy. *Cell Res.* **22**, 288–304 (2012).
8. M. C. McKinney, K. Fukatsu, J. Morrison, R. McLennan, M. E. Bronner, P. M. Kulesa, Evidence for dynamic rearrangements but lack of fate or position restrictions in premigratory avian trunk neural crest. *Development* **140**, 820–830 (2013).
9. M. Bronner-Fraser, S. E. Fraser, Cell lineage analysis reveals multipotency of some avian neural crest cells. *Nature* **335**, 161–164 (1988).
10. A. Baroffio, E. Dupin, N. M. Le Douarin, Clone-forming ability and differentiation potential of migratory neural crest cells. *Proc. Natl. Acad. Sci. U.S.A.* **85**, 5325–5329 (1988).
11. C. V. Baker, M. Bronner-Fraser, N. M. Le Douarin, M. A. Teillet, Early- and late-migrating cranial neural crest cell populations have equivalent developmental potential in vivo. *Development* **124**, 3077–3087 (1997).
12. E. Nitzan, S. Krispin, E. R. Pfaltzgraff, A. Klar, P. A. Labosky, C. Kalcheim, A dynamic code of dorsal neural tube genes regulates the segregation between neurogenic and melanogenic neural crest cells. *Development* **140**, 2269–2279 (2013).
13. S. Krispin, E. Nitzan, Y. Kassem, C. Kalcheim, Evidence for a dynamic spatiotemporal fate map and early fate restrictions of premigratory avian neural crest. *Development* **137**, 585–595 (2010).
14. A. Baggolini, S. Varum, J. M. Mateos, D. Bettosini, N. John, M. Bonalli, U. Ziegler, L. Dimou, H. Clevers, R. Furrer, L. Sommer, Premigratory and migratory neural crest cells are multipotent in vivo. *Cell Stem Cell* **16**, 314–322 (2015).
15. R. T. H. Lee, H. Nagai, Y. Nakaya, G. Sheng, P. A. Trainor, J. A. Weston, J. P. Thiery, Cell delamination in the mesencephalic neural fold and its implication for the origin of ectomesenchyme. *Development* **140**, 4890–4902 (2013).
16. J. Gros, C. J. Tabin, Vertebrate limb bud formation is initiated by localized epithelial-to-mesenchymal transition. *Science* **343**, 1253–1256 (2014).
17. J. Gros, J. K.-H. Hu, C. Vinegoni, P. F. Feruglio, R. Weissleder, C. J. Tabin, WNT5A/JNK and FGF/MAPK pathways regulate the cellular events shaping the vertebrate limb bud. *Curr. Biol.* **20**, 1993–2002 (2010).
18. B. Boehm, H. Westerberg, G. Lesnicar-Pucko, S. Raja, M. Rautschka, J. Cotterell, J. Swoger, J. Sharpe, The role of spatially controlled cell proliferation in limb bud morphogenesis. *PLoS Biol.* **8**, e1000420 (2010).
19. J. A. Zallen, Planar polarity and tissue morphogenesis. *Cell* **129**, 1051–1063 (2007).
20. R. S. Gray, I. Roszko, L. Solnica-Krezel, Planar cell polarity: Coordinating morphogenetic cell behaviors with embryonic polarity. *Dev. Cell* **21**, 120–133 (2011).
21. R. van Amerongen, C. Fuerer, M. Mizutani, R. Nusse, Wnt5a can both activate and repress Wnt/β-catenin signaling during mouse embryonic development. *Dev. Biol.* **369**, 101–114 (2012).
22. E. R. M. Bakker, L. Raghoebir, P. F. Franken, W. Helvensteijn, L. van Gorp, F. Meijlink, M. A. van der Valk, R. J. Rottier, E. J. Kuipers, W. van Veelen, R. Smits, Induced Wnt5a expression perturbs embryonic outgrowth and intestinal elongation, but is well-tolerated in adult mice. *Dev. Biol.* **369**, 91–100 (2012).
23. H.-Y. H. Ho, M. W. Susman, J. B. Bickoff, Y. K. Ryu, A. M. Jonas, L. Hu, R. Kuruvilla, M. E. Greenberg, Wnt5a-Ror-Dishevelled signaling constitutes a core developmental pathway that controls tissue morphogenesis. *Proc. Natl. Acad. Sci. U.S.A.* **109**, 4044–4051 (2012).
24. H. J. Snippert, L. G. van der Flier, T. Sato, J. H. van Es, M. van den Born, C. Kroon-Veenboer, N. Barker, A. M. Klein, J. van Rheenen, B. D. Simons, H. Clevers, Intestinal crypt homeostasis results from neutral competition between symmetrically dividing Lgr5 stem cells. *Cell* **143**, 134–144 (2010).
25. C. Laranjeira, K. Sandgren, N. Kessar, W. Richardson, A. Potocnik, P. Vanden Berghe, V. Pachnis, Glial cells in the mouse enteric nervous system can undergo neurogenesis in response to injury. *J. Clin. Invest.* **121**, 3412–3424 (2011).
26. D. P. Leone, S. Genoud, S. Atanatoski, R. Grausenburger, P. Berger, D. Metzger, W. B. Macklin, P. Chambon, U. Suter, Tamoxifen-inducible glia-specific Cre mice for somatic mutagenesis in oligodendrocytes and Schwann cells. *Mol. Cell. Neurosci.* **22**, 430–440 (2003).
27. L. Hari, I. Miescher, O. Shakhova, U. Suter, L. Chin, M. Taketo, W. D. Richardson, N. Kessar, L. Sommer, Temporal control of neural crest lineage generation by Wnt/β-catenin signaling. *Development* **139**, 2107–2117 (2012).
28. F. Lescroart, S. Chabab, X. Lin, S. Rulands, C. Paulissen, A. Rodolose, H. Auer, Y. Achouri, C. Dubois, A. Bondué, B. D. Simons, C. Blanpain, Early lineage restriction in temporally distinct populations of *Mesp1* progenitors during mammalian heart development. *Nat. Cell Biol.* **16**, 829–840 (2014).
29. T. Nagase, M. Nagase, N. Osumi, S. Fukuda, S. Nakamura, K. Ohsaki, K. Harii, H. Asato, K. Yoshimura, Craniofacial anomalies of the cultured mouse embryo induced by inhibition of sonic hedgehog signaling: An animal model of holoprosencephaly. *J. Craniofac. Surg.* **16**, 80–88 (2005).
30. R. Favaro, M. Valotta, A. L. M. Ferri, E. Latorre, J. Mariani, C. Giachino, C. Lancini, V. Tosetti, S. Ottolenghi, V. Taylor, S. K. Nocolis, Hippocampal development and neural stem cell maintenance require *Sox2*-dependent regulation of *Shh*. *Nat. Neurosci.* **12**, 1248–1256 (2009).
31. P. S. Danielian, D. Muccino, D. H. Rowitch, S. K. Michael, A. P. McMahon, Modification of gene activity in mouse embryos in utero by a tamoxifen-inducible form of Cre recombinase. *Curr. Biol.* **8**, 1323–1326 (1998).
32. I. Adameyko, F. Lallemand, A. Furlan, N. Zinin, S. Aranda, S. S. Kitambi, A. Blanchart, R. Favaro, S. Nocolis, M. Lübke, T. Müller, C. Birchmeier, U. Suter, I. Zaitoun, Y. Takahashi, P. Ernors, *Sox2* and *Mitf* cross-regulatory interactions consolidate progenitor and melanocyte lineages in the cranial neural crest. *Development* **139**, 397–410 (2012).

33. D. Enshell-Seiffers, C. Lindon, E. Wu, M. M. Taketo, B. A. Morgan, β -Catenin activity in the dermal papilla of the hair follicle regulates pigment-type switching. *Proc. Natl. Acad. Sci. U.S.A.* **107**, 21564–21569 (2010).
34. D. M. Dinulescu, R. D. Cone, Agouti and agouti-related protein: Analogies and contrasts. *J. Biol. Chem.* **275**, 6695–6698 (2000).
35. Y. Saga, S. Miyagawa-Tomita, A. Takagi, S. Kitajima, J. i. Miyazaki, T. Inoue, MesP1 is expressed in the heart precursor cells and required for the formation of a single heart tube. *Development* **126**, 3437–3447 (1999).
36. T. P. Yamaguchi, A. Bradley, A. P. McMahon, S. Jones, A Wnt5a pathway underlies outgrowth of multiple structures in the vertebrate embryo. *Development* **126**, 1211–1223 (1999).
37. M. H. Schieber, Constraints on somatotopic organization in the primary motor cortex. *J. Neurophysiol.* **86**, 2125–2143 (2001).
38. E. Méhes, T. Vicsek, Collective motion of cells: From experiments to models. *Integr. Biol.* **6**, 831–854 (2014).
39. R. David, O. Luu, E. W. Damm, J. W. H. Wen, M. Nagel, R. Winklbauer, Tissue cohesion and the mechanics of cell rearrangement. *Development* **141**, 3672–3682 (2014).
40. O. Kanca, E. Caussinus, A. S. Denes, A. Percival-Smith, M. Affolter, Raeppli: A whole-tissue labeling tool for live imaging of *Drosophila* development. *Development* **141**, 472–480 (2014).
41. M. I. Worley, L. Setiawan, I. K. Hariharan, TIE-DYE: A combinatorial marking system to visualize and genetically manipulate clones during development in *Drosophila melanogaster*. *Development* **140**, 3275–3284 (2013).
42. N. M. Young, D. Hu, A. J. Lainoff, F. J. Smith, R. Diaz, A. S. Tucker, P. A. Trainor, R. A. Schneider, B. Hallgrímsson, R. S. Marcucio, Embryonic bauplans and the developmental origins of facial diversity and constraint. *Development* **141**, 1059–1063 (2014).
43. E. Theveneau, R. Mayor, Neural crest delamination and migration: From epithelium-to-mesenchyme transition to collective cell migration. *Dev. Biol.* **366**, 34–54 (2012).
44. M. Minoux, F. M. Rijli, Molecular mechanisms of cranial neural crest cell migration and patterning in craniofacial development. *Development* **137**, 2605–2621 (2010).
45. D. Hu, N. M. Young, X. Li, Y. Xu, B. Hallgrímsson, R. S. Marcucio, A dynamic *Shh* expression pattern, regulated by SHH and BMP signaling, coordinates fusion of primordia in the amniote face. *Development* **142**, 567–574 (2015).
46. S. Foppiano, D. Hu, R. S. Marcucio, Signaling by bone morphogenetic proteins directs formation of an ectodermal signaling center that regulates craniofacial development. *Dev. Biol.* **312**, 103–114 (2007).
47. J. J. Schoenebeck, S. A. Hutchinson, A. Byers, H. C. Beale, B. Carrington, D. L. Faden, M. Rimbault, B. Decker, J. M. Kidd, R. Sood, A. R. Boyko, J. W. Fondon III, R. K. Wayne, C. D. Bustamante, B. Ciruna, E. A. Ostrander, Variation of *BMP3* contributes to dog breed skull diversity. *PLOS Genet.* **8**, e1002849 (2012).
48. M. Tanaka, Evolution of vertebrate limb development, in *Encyclopedia of Life Sciences (eLS)* (John Wiley & Sons Ltd., Chichester, UK, 2009), p. 1–9.
49. R. Freitas, G. Zhang, M. J. Cohn, Evidence that mechanisms of fin development evolved in the midline of early vertebrates. *Nature* **442**, 1033–1037 (2006).
50. N. Shubin, C. Tabin, S. Carroll, Deep homology and the origins of evolutionary novelty. *Nature* **457**, 818–823 (2009).
51. A. Mongera, A. P. Singh, M. P. Levesque, Y.-Y. Chen, P. Konstantinidis, C. Nüsslein-Volhard, Genetic lineage labeling in zebrafish uncovers novel neural crest contributions to the head, including gill pillar cells. *Development* **140**, 916–925 (2013).
52. Y. A. Pan, T. Freundlich, T. A. Weissman, D. Schoppik, X. C. Wang, S. Zimmerman, B. Ciruna, J. R. Sanes, J. W. Lichtman, A. F. Schier, Zebrafish: Multispectral cell labeling for cell tracing and lineage analysis in zebrafish. *Development* **140**, 2835–2846 (2013).
53. M. Westerfield, *The Zebrafish Book: A Guide for the Laboratory Use of Zebrafish (Danio rerio)* (University of Oregon Press, Eugene, OR, ed. 4, 2000).
54. G. S. O'Brien, S. Rieger, S. M. Martin, A. M. Cavanaugh, C. Portera-Cailliau, A. Sagasti, Two-photon axotomy and time-lapse confocal imaging in live zebrafish embryos. *J. Vis. Exp.* (2009).

Acknowledgments: We thank A. Schier, A. Pan, and C. Nüsslein-Volhard for the fish strains; S. Warner for excellent technical support; M. Karlen and O. Kharchenko for the illustrations; and J. Jaros for technical support with μ -CT. We also thank V. Dyachuk for essential help with mouse experiments. **Funding:** M.K. was supported by the European Molecular Biology Organization Long-Term Fellowship. The work of E.I. was supported by the Russian Fund for Basic Research (grants 14-04-32027, 15-04-07573, and 15-29-02650). K.F., A.S.C., and I.A. were supported by grants from the Swedish Research Council and Karolinska Institutet. I.A. is supported by the Hällsten Research Foundation and the Åke Wiberg Foundation. T.Z. and J.K. were supported by the Ministry of Education, Youth and Sports of the Czech Republic under the project Central European Institute of Technology 2020 (LQ1601). The laboratory of P.S. was supported by grants from the Medical Research Council and the National Institute of Dental and Craniofacial Research. The laboratory of U.S. was supported by the Swiss National Science Foundation. A.H. was supported by the Swedish strategic research program eSENCE, Vetenskapsrådet (VR), and the NIH under award number R01-EB014877-01. This work is solely the responsibility of the authors and does not necessarily reflect the views of the NIH. H. Brismar and H. Blom acknowledge funding support from VR and the Science for Life Laboratory. **Author contributions:** M.K., A.H., and I.A. designed the study and wrote the paper. M.K., D.G., T.Z., M.T., E.I., M.X., A.H., T.Y., J.P., and I.A. performed the experiments and analyzed the data. K.F., J.K., V.P., S.K.N., P.S., E.A., H. Brismar, H. Blom, H.C., U.S., and A.S.C. contributed to the experimental work and study design. All authors read and approved the paper. **Competing interests:** The authors declare that they have no competing interests. **Data and materials availability:** All data needed to evaluate the conclusions in the paper are present in the paper and/or the Supplementary Materials. Additional data related to this paper may be requested from the authors.

Submitted 13 January 2016

Accepted 29 June 2016

Published 3 August 2016

10.1126/sciadv.1600060

Citation: M. Kaucka, E. Ivashkin, D. Gyllborg, T. Zikmund, M. Tesarova, J. Kaiser, M. Xie, J. Petersen, V. Pachnis, S. K. Nicolis, T. Yu, P. Sharpe, E. Arenas, H. Brismar, H. Blom, H. Clevers, U. Suter, A. S. Chagin, K. Fried, A. Hellander, I. Adameyko, Analysis of neural crest-derived clones reveals novel aspects of facial development. *Sci. Adv.* **2**, e1600060 (2016).